MONASH University

The behaviour and performance of geosynthetic reinforced column supported embankments

Daniel John King

Bachelor of Civil Engineering (Hons. 1), Bachelor of Science (Physics)

A thesis submitted for the degree of *Doctor of Philosophy* at

Monash University in 2017

Department of Civil Engineering

Monash University, Melbourne, Australia

April 2017

Abstract

This study investigates the localised and global scale behaviour of geosynthetic reinforced column supported embankments (GRCSEs) by way of a field case study in Melbourne, Australia where a recently constructed GRCSE supported on drilled displacement columns has been extensively instrumented. Post-construction data shows the time-dependent development of arching over the two-year monitoring period and a strong relationship between the development of arching stresses and sub-soil settlement. A ground reaction curve is adopted to describe the development of arching stresses and good agreement is found for the period observed thus far. Four phases of arching stress development (initial, maximum, load recovery and creep strain phase) are shown to describe the time-dependent, and sub-soil dependent, development of arching stresses that can be expected to occur in many field embankments. These findings highlight the need for coupled arching stress-deformation models to describe accurately ultimate limit state conditions, and more importantly serviceability behaviour (i.e., deformation of the embankment) which typically governs the acceptability of a GRCSE design.

This approach contrasts the widely adopted "*two-step"* design approach, which uses limit-equilibrium models that de-couple the arching stress-deformation relationship to describe ultimate limit state behaviour. Of the four phases proposed by the author, the load recovery phase is the most important with respect to load transfer platform design as it predicts the breakdown of arching stresses in the long term due to increasing sub-soil settlement. These concepts are developed further and an approach is presented which provides a means to predict serviceability behaviour, and at the same time, raises questions about the long term performance and the manner in which acceptable performance has been achieved in the short term in several field case studies. In particular, those constructed at, or near, a minimum embankment height.

In addition to the investigation of localised arching stress development in GRCSEs this study also examines the global scale behaviour of embankments. In particular, the geotechnical behaviour associated with lateral sliding and embankment stability, which often governs the acceptability of a given design under global scale serviceability conditions, is studied. Frequently, the complex soil-structure-geosynthetic interaction, the size and the three-dimensional nature of a GRCSE necessitate the use of numerical analysis to assess embankment performance relative to serviceability criteria. However, traditional FEM techniques used in practice to model serviceability behaviour are limited in their ability to model the geotechnical mechanisms associated with column installation, equilibration and group installation effects. The role that column installation effects have on the performance of the GRCSE is highlighted in this study and the behaviour of the columns supporting the embankment is emphasised. It is shown that cracking of the unreinforced columns supporting the embankment is inevitable and that the reduction of lateral resistance provided by the columns should be accounted for in design. The suitability of various numerical approaches currently used in design to model the columns supporting the GRCSE, and the embankment itself, are discussed and recommendations presented.

Declaration

This thesis contains no material which has been accepted for the award of any other degree or diploma at any university or equivalent institution and that, to the best of my knowledge and belief, this thesis contains no material previously published or written by another person, except where due reference is made in the text of the thesis.

Daniel J. King

Department of Civil Engineering

Monash University

Clayton, Australia

April 2017

Publications

The following is a list of journal and conference papers published as part of the research set out in this thesis:

Journal papers

- King, D. J., Bouazza, A., Gniel, J. & Bui, H. H. 2016. The compressibility, permeability and structured nature of the Coode Island Silt. *Australian Geomechanics*, **50**(2), 45 – 62.
- King, D. J., Bouazza, A., Gniel, J., Rowe, R. K. & Bui, H. H. 2017. Load transfer platform behaviour in embankments supported on semi-rigid columns: implications of the ground reaction curve. *Canadian Geotechnical Journal,* **54**(8): 1158-1175. doi: 10.1139/cgj-2016-0406
- King, D. J., Bouazza, A., Gniel, J., Rowe, R. K. & Bui, H. H. 2017. Serviceability design for geosynthetic reinforced column-supported embankments. *Geotextiles and Geomembranes,* **45**(4): 261-279. doi: 10.1016/j.geotexmem.2017.02.006
- King, D. J., Bouazza, A., Gniel, J., Rowe R. K. Bui, H. H. 2018. Geosynthetic reinforced column supported embankment and the role of ground improvement installation effects. *Canadian Geotechnical Journal (accepted)*.
- King, D. J., Bui, H. H., Bouazza, A., Rowe, R. K. & Gniel, J. 2018. Mesh-based and meshfree numerical methods for assessing arching in geosynthetic reinforced column supported embankments. *Geotechnique (in preparation).*
- King, D. J., King, L., Bouazza, A., Gniel, J., Bui, H. H. 2018. The design of geosynthetic reinforced column supported embankments. *Australian Geomechanics (in preparation).*

Conference papers

- King, D. J., Gniel, J., Bouazza, A., Bui, H. H. & Rowe, R. K. 2014. Preliminary observations from a geosynthetic reinforced piled embankment. *Proceedings of the 10th International Conference on Geosynthetics*, Berlin, Germany. 21 – 25 September 2014. German Geotechnical Society.
- King, D. J. & Bouazza, A. 2016. Arching in geosynthetic reinforced column supported embankments - recent findings from a field case study. *Proceedings of the 11th Australian and New Zealand Young Geotechnical Professionals Conference*, Queenstown, New Zealand. 26 – 28 October 2016.
- King, D. J., King, L., Bouazza, A., Gniel, J., Bui, H. H. 2017. The development of arching in geosynthetic reinforced embankments on semi-rigid inclusions. *Proceedings of the 19th International Conference on Soil Mechanics and Geotechnical Engineering*, Seoul, Korea. 17 – 22 September 2017. *(accepted).*
- King, D. J., Haberfield, C. M. H. and Bouazza, A. Global scale numerical modelling of a geosynthetic reinforced column supported embankment. *Proceedings of the 19th International Conference on Soil Mechanics and Geotechnical Engineering, TC 207 – Soil-structure interaction and retaining walls workshop.* Seoul, Korea. 17 – 22 September 2017. *(in preparation).*

Acknowledgements

I would like to thank my supervisor Prof. Malek Bouazza for his mentorship over these past four years. Your support, assistance and our discussions on a range of issues over the past few years has provided much inspiration. In addition, I would like to thank my co-supervisors Dr. Joel Gniel and Dr. Ha Bui for providing valuable input and guidance at various stages of my research. In particular, I would like to thank Joel for encouraging me to pursue my PhD studies and laying the "ground-work" for the field case study as well as Ha for offering valuable insight into the field of computational geomechanics. I am gratefully for the advice and guidance provided by Prof. R. Kerry Rowe on some of the finer points of academic research and writing.

The field case study would not have been possible without the support of Golder Associates and the Regional Rail Link – City to Maribyrnong River (RRLCMR) Alliance. In particular, Anthony Hart and Christian D'Agnolo who provided the design support and co-ordinated the significant approval process required to enable the field case study to proceed. Thanks also to Louie Lu who co-ordinated the construction works and enabled the installation of instrumentation to proceed smoothly. I would also like to thank Dr. Gary Chapman and Dr. Chris Haberfield for their advice during the development of the instrumentation layout and throughout the duration of my candidature. The author gratefully acknowledges the assistance provided by Louis King, Matthew Lumsden, Kevin Nievaart, Mark Taylor and Mike Leach throughout the field work and laboratory testing as well as Simon Bailey and Jared Jordan who assembled, programmed and assisted with the field installation of the data acquisition hardware.

I am also extremely gratefully for having had the opportunity to spend a week at TRI Australasia's lab in Burleigh Heads, QLD with Warren Hornsey who provided access to specialised geosynthetic testing equipment as well as the tour of the GeoFabrics facility on the Gold Coast. In addition to running my first marathon I learnt a lot about geosynthetic that week. This research would not have been possible without the financial support provided by Golder Associates in the form of an "Innovation to Excellence" (i2x) award, Monash University and the in-kind support provided by the RRLCMR Alliance. My doctoral study would not have been possible without the financial support provided by both the Australian Government in the form of an Australian Postgraduate Award and financial support provided by Golder Associates.

I would also like to thank the many friend and colleagues at Monash University who made the past four years that much more enjoyable; Louie King, Daniel Viete, Ben Shannon, Michael Von't Steen, Daniel Borrie, Colin Caprani, Rui (Jerry) Jiang, Lu (Angelina) Zhang, Katrina Pavkova, Gonzalo Guzman, Mayu Heredia, Mohammed Faizel and Ashque Mahbub. Finally, I would like to thank my parents John and Sheryl King for their encouragement and support and my partner Emma for here unconditional support, love and encouragement.

Contents

List of figures

List of tables

Abbreviations and Acronyms

AS	Australian Standard
APGD	Auger pressure grouted displacement
BS	British Standard
CBR	California bearing ratio
CFA	Continuous flight auger
CPT	Cone penetration test
CPTu	Cone penetration test with pore pressure measurement
CT	Computed tomography
DSBR	Differential settlement to base settlement ratio (McGuire, 2011), termed herein differential settlement ratio
EBGEO	Empfehlungen für den Entwurf und die Berechnung von Erdkörpern mit Bewehrungen aus Geokunststoffen (Recommendations for Design and Analysis of Earth Structures using Geosynthetic Reinforcements)
EOD	End of drive
FEM	Finite element method
GRC	Ground reaction curve
GRCSE	Geosynthetic reinforced column supported embankment
LDC	Load displacement compatability
LTP	Load transfer platform
MEMS	Micro Electro-mechanical system
NC	Normally consolidated
OCR	Overconsolidation ratio
PSD	Particle size distribution
RC	Recompression
RL	Reduced level
SPH	Smooth particle hydrodynamics
w/c	Water content in cement slurry

Nomenclature

A_b, A_s	Base area of pile shaft (m^2), area of pile shaft (m^2)
A_c	Projected cone area (m^2)
A_{Lx}, A_{Ly}	Coverage area (m_2) in x-direction, y-direction in EBGEO
A_n	Cone area (A_c) less cone area not affected by pore water pressure (m^2)
A_R	Relative arching ratio (GRC method)
A_{RB}	Relative arching ratio at breakpoint (GRC method)
A_s	Area replacement ratio
a	Column head width (square) (m) *or* CPT cone area ratio = A_n/A_c
a_ϕ	Drucker-Prager constant
B	Width of trapdoor test (m)
B_g	Breakage factor (%)
B_q	Pore pressure ratio = Δu / (q_t - σ_{v0})
b	Equivalent axisymmetric clear spacing (m)
C	Pile setup factor after Ng et al. (2012a,b)
C_a	Empirically derived parameter in Marston-Anderson arching model compression index *or* coefficient of curvature for granular material = $(D_{30})^2/(D_{10} \times D_{60})$ *or* empirical parameter in arching model by Jones (1990)
C_c	Compression index
C'_c	Secant compression index
$C_{c\ max}$	Maximum compression index
$C_{c\ 400-800\ kPa}$	Compression index over stress range 400 kPa to 800 kPa
$C_{c\varepsilon}$	Modified compression index (compression ratio) = $\Delta\varepsilon/\Delta \log \sigma'_v$
$C_{c\varepsilon\ max}$	Maximum modified compression index
C_r	Recompression index
C_u	Coefficient of uniformity = D_{60}/D_{10}
C_α	Secondary compression index
$C_{\alpha\varepsilon}$	Modified secondary compression index = $\Delta\varepsilon/\Delta\log(t)$
c'	Cohesion intercept of Mohr-Coulomb failure envelope in terms of effective stress at failure
c_b, c_s	Cohesion at base of pile, (average) cohesion on shaft of pile (kPa)
c_h	Coefficient of horizontal consolidation (m^2/year)
c_r	Coefficient of radial consolidation (m^2/year)
c_v	Coefficient of vertical consolidation (m^2/year)
$c_{v\ lab/field}$	Coefficient of vertical consolidation assessed in lab/field (m^2/year)
c_v (NC)	Coefficient of vertical consolidation in normally consolidated range (m^2/year)
c_v (RC)	Coefficient of vertical consolidation in recompression range (m^2/year)
D_{max}	Maximum particle size (mm)
D_{10},D_{30},D_{60}	Equivalent particle diameter at 10 %, 30 % and 60 % passing
D_{50}	mean grain size
d	Column head diameter (m) *or* diameter of auger (m)

d_0	Diameter of auger stem (m)
d_{yield}	Yield displacement in bi-linear LDC method
E	Young's modulus (kPa) *or* load efficiency
E_{50}^{ref}	Secant stiffness in standard drained triaxial test (kPa)
E_{oed}^{ref}	Tangent stiffness for primary oedometer loading (kPa)
E_{ur}^{ref}	Unloading/reloading stiffness at small strain (kPa)
e	Void ratio
e_0	Initial void ratio
F_{nf}	Normalised friction ratio
F_r	force acting on pile due to Negative skin friction (kN)
F_1, F_2	Dimensionless parameters in method of Zaeske (2001)
f	Yield function
$f(t)$	Constant of integration (cylindrical cavity expansion theory)
$f(\mathbf{x})$	Field variable (SPH method)
f_s	Sleeve friction (kPa)
f_t	Corrected sleeve friction (kPa)
G	Shear modulus (kPa)
G_s	Specific gravity of solid constituents
g	Plastic potential function
$g(t)$	Constant of integration (cylindrical cavity expansion theory)
H	Maximum drainage distance in one-dimensional consolidation equation (m) *or* Height of soil in trapdoor test (m)
$\overline{H}$	Mean sample height in oedometer test during a load increment (mm)
h_{crit}	Critical height of embankment (m)
h	Embankment height (m) *or* smoothing length (SPH) *or* hardening parameter
h^*	LTP thickness (m)
h^*_{red}	Reduced thickness of LTP (m)
I_1,I_2, I_3	First, second, third stress invariants
I_c	CPTu material index parameter
I_e	Effective moment of inertia
I_p	Plasticity index
I_L	Liquidity index = $(w_0 - w_l)/I_p$
I_R	Rigidity index = G/s_u
J, $J_{2\%}$	Geogrid stiffness, geogrid stiffness of 2 % (kN/m)
J_1, J_2, J_3	First, second, third deviatoric stress invariants
J_i	Bessel function of the first kind and of order i.
$\boldsymbol{j}$	Flux tensor
K	Lateral earth pressure coefficient *or* bulk modulus of soil (kPa) *or* constant in method of Bustmante & Gianselli (1993)
K_{crit}	Critical principal stress ratio
K_E	Krynine (1945) earth pressure coefficient adopted in GRC method
K_s	Modulus of sub-grade reaction (kPa/m)
k	Coefficient of permeability (m/s) *or* parameter in CPT equation by Lunne et al. (1997)
k_c	Drucker-Prager constant
k_v/k_h	Coefficient of permeability in vertical and horizontal directions (m/s)
L	Length of downdrag zone acting on pile
L_t, L_{EOD}	Length of embedded pile at time t, length of embedded pile at end of drive (m)
LS	Linear shrinkage (%)
M	Mass (kg)
m	Slope of critical state line *or* power for stress level stiffness dependency
m_v	Coefficient of volume compressibility
N	Number of blows recorded from standard penetration test
N_c	Bearing capacity factor
N_k	CPT cone factor for calculation of s_u
n	Auger rotation rate *or* empirical constant in hydraulic fracture equation after Soga et al. (2005)
OCR	Overconsolidation ratio
P_A,P_B, P_C	Stress states at points A, B and C on a Mohr's circle
P_f	Fracture (hydraulic) pressure (kPa)
Part A	Load transferred directly to the column (due to arching) (kN/column or kN/unit cell)
Part B	Load part that is carried by the geosynthetic reinforcement and transferred to the columns (kN/column or kN/unit cell)
Part C	Load component carried by the soil between the column heads (referred to as 'subsoil' herein) (kN/column or kN/unit cell)
POP	Pre-overburden stress (kPa)
p	Mean stress
Q_t	Normalised cone resistance = $(q_t - \sigma_{vo})/\sigma'_{vo}$
Q_{ult}, Q_{ub}, Q_{us}	Ultimate pile capacity, ultimate Base, shaft pile capacity
q	Surcharge load on embankment (kPa) *or* normalised distance in SPH method
$q(x)$	Loading on cable in method of Zaeske (2001)
q_c, q_{ce}	Cone tip resistance (kPa), modified cone tip resistance (kPa) in method of Bustamante & Gianselli (1993)
q_t	Corrected cone tip resistance (kPa)
$RF_{installation}$, $RF_{durability}$, RF_{creep},	Geogrid partial factors for installation, durability, creep respectively
R_f	Friction ratio = $100\% \times (f_t/q_t)$

R_t, R_{EOD}	Pile axial capacity- at time (t), at end of drive
$r(x)$	Sub-soil support function in method of Zaeske (2001)
r, r^*	Radius (m), radius where excess pore water pressure is negligible
SRR_{lim}	Limiting stress reduction ratio in Adapted
SRR_{min}	Terzaghi method minimum value of stress reduction
SRR_{term}	Ratio in GRC method stress reduction ratio at terminal condition
S_b	Base settlement of LTP (mm)
$S_{b,d}$	Base settlement beneath diagonal span between columns (mm)
S_c	Surface settlement above column (mm)
S_d	Surface settlement at centre of diagonal span between column (mm)
S_e	Equivalent uniform surface settlement due to base settlement (mm)
S_i	Surface settlement at mid-span between columns (mm)
S_s	Column head settlement due to column shortening (mm)
S_t	Sensitivity parameter for soft soil
S_u	Column head settlement due to compression of founding material (mm)
s, s_x, s_y	Centre-to-centre column spacing (m), centre-to-centre spacing in the x-direction, y-direction (m)
s_u	Undrained shear strength (kPa)
s_u (mob)	s_u mobilised in a full-scale field failure
s_u (DSS)	s_u measured in a direct simple shear test
s_u (FV)	s_u measured by a field vane test
s_u (TC)	s_u measured in a triaxial compression text
s_u (TE)	s_u measured in a triaxial extension test
s_u (UU)	s_u measured in a unconsolidated undrained compression test
T, T_v, T_h	Tensile load in geosynthetic reinforcement, tensile load in vertical direction, horizontal direction (kN)
T_c	Ultimate tensile strength of geogrid (kN/m)
T_d	Design tensile strength of geogrid (kN/m)
T_{ds}	Tensile load due to lateral spreading (kN/m)
T_{rp}	Tensile load due to arching (kN/m)
T_v	Time factor for one-dimensional consolidation in vertical direction
t	Time (years)
t_0, t_f	Initial time, final time (years)
t_{50}, t_{100}	Time to 50 % / 100 % primary consolidation complete (days)
t_p	Time to end of primary consolidation (days)
U%	Average percentage of primary consolidation complete (%)
U	Normalised excess porewater pressure in CPT dissipation test
u	Pore water pressure (kPa)
u_i	Initial porewater pressure in CPT (kPa)
u_0	Hydrostatic porewater pressure (kPa)
u_1	CPT pore pressure measured at sensor location no. 1 (kPa)
u_2	CPT pore pressure measured at sensor location no. 2 (kPa)
u_3	CPT pore pressure measured at sensor location no. 3 (kPa)
v	Velocity (m/s)
v_{cr}	Critical penetration rate (m/s) after Viggiani (1989)
W	Weight function (or kernel)
WPI	Weighted plasticity index = I_p × % passing 0.425 mm sieve
w	Moisture content (%)
w_0	Natural moisture content (%)
w_l	Liquid limit (%)
w_p	Plastic limit (%)
w_s	Shrinkage limit (%)
Y_i	Bessel function of the second kind and i is the order.
z	Distance between top of column and geosynthetic reinforcement layer (m)
z_n	n-number term in cylindrical cavity expansion theory
α	Parameter in the Adapted Terzaghi method *or* separation constant in cylindrical cavity expansion theory *or* inclination of principal stress in PLAXIS
β	Parameter in Svanø et al. (2000) arching model *or* displacement ratio after Carter et al. (1980)
γ	Shear strain
Δf	Maximum sag of geosynthetic reinforcement (mm) in EBGEO
δ	Trapdoor displacement (mm)
δ_A	Trapdoor displacement at point A (mm)
ε	Tensile strain in geosynthetic reinforcement (%)
ε_v	Vertical strain
ε_{v0}	Initial vertical strain
$\dot{\varepsilon}$	Strain rate
θ_A,θ_C,θ_R	Arthur, Mohr-Coulomb and Roscoe shear band inclination angle (°) respectively
κ	Maximum curvature in oedometer e-log(σ'_v) plot *or* constant in the smoothing function in the SPH method
λ	Plastic multiplier *or* Constant in SPH method *or* load recovery index (GRC method)

λ_n	*n*-number term in cylindrical cavity expansion theory
λ_1	Sub-function in Zaeske's arching equation
λ_2	Sub-function in Zaeske's arching equation
μ	Field vane correction factor
μ_n	*n*-number term in cylindrical cavity expansion theory
ν	Poisson's ratio
ξ	Displacement in cylindrical cavity expansion theory (mm)
ρ	Density (kg/m^3)
$\boldsymbol{\sigma}$	Cauchy stress tensor
σ	Total stress
$\dot{\sigma}$	Stress rate
σ'	Effective stress (kPa)
σ'_{p}	Preconsolidation stress (kPa)
σ'_{v}	Effective vertical stress (kPa)
σ'_{vo}	Effective initial vertical stress (kPa)
σ'_{vc}	Applied vertical effective stress in oedometer test
σ_{c}	Stress acting on a column in a GRCSE
σ_{min}	Minimum vertical stress acting on trapdoor (occurs at maximum arching)
σ_{v}	Total vertical stress (kPa)
σ_{v0}	Total initial vertical stress (kPa)
τ	Shear stress (kPa)
ϕ'	Effective friction angle (º)
ϕ'_{cv}	Critical state friction angle (º)
ϕ_{m}	Mobilised friction angle (º)
ϕ_{sec}	Secant friction angle (º)
ϕ_{mob}	Mobilised friction angle (º)
ϕ_{peak}	Peak internal friction angle (º)
ϕ_{μ}	Friction angle due to interparticle sliding(º)
ψ	Dilatancy angle (º) *or* curvature
ψ_{m}	Mobilised dilatancy angle (º)
Ω	Integration domain in SPH method
ω	Dimensionless parameter in tensioned membrane method *or* spin

1 Introduction

In recent decades, increased growth in urban and metropolitan areas and the shortage of available land has led to increased development in areas with poor ground conditions. These sites are often found in coastal areas where much of the world's major cities and global population are found. The low-lying nature of these areas and the presence of geologically recent marine and estuarine deposits are common features and pose a variety of challenges from a geotechnical perspective. Over the past century the number of ground improvement methods available to address these challenges has grown considerable, with continual development, improvement and the introduction of many new techniques. One particular technique that has gained acceptance over the past 30 years is the geosynthetic-reinforced column supported embankment (GRCSE)[1]. This technique was first proposed in Sweden and has been used in Southeast Asia for many years (Magnan 1994). Ooi et al. (1987) describes a site where this technique was used for the Seremban-Air Hitam Toll Expressway in Malaysia in the mid-1980s and Combarieu (1993) describes four sites in France where GRCSEs where constructed in the late 1980s and early 1990s. There are two major factors that have influenced this development; 1) The increased use and acceptance of geosynthetic materials as a construction material and 2) Advances in the capabilities of piling rigs used to install the ground improvement columns.

The ground conditions and long term settlement tolerances are often the major factors governing the choice of ground improvement method. The GRCSE is a semi-rigid ground improvement method and for this reason it is often selected where stringent performance criteria govern the design. In addition, a GRCSE can be constructed relatively quickly compared with other ground improvement types, so is preferable where construction time is limited. As the embankment is supported on semi-rigid inclusions, which carry load through the soft soil to a competent founding material, the overall embankment performs largely independent of the soft soil that may undergo consolidation and long term creep compression. The long term creep settlement of the embankment is therefore, largely eliminated and this is often an important factor in selecting a GRCSE as the ground improvement option.

The key features of a typical geosynthetic reinforced column supported embankment (GRCSE) are shown in Figure 1.1. A GRCSE comprises an embankment, with a load transfer platform (LTP) at its' base, supported on semi-rigid ground improvement that penetrate into a competent founding layer. The LTP is generally a granular material, with one or more layers of geogrid/geotextile at its' base, acting to distribute embankment load to the semi-rigid inclusions. This design approach is also referred to as "basal reinforcement" which may, or may not, include ground improvement. Some examples where GRCSEs are adopted include:

- Transition zones for bridge approach embankments
- Embankment widening

[1] The author recommends, and uses throughout the thesis, the term "column supported embankment" as opposed to "piled embankment". This is discussed further in Section 2.4.

- Embankments requiring vertical retaining walls instead of batter slopes due to site constraints or back-to-back retaining wall embankments
- Warehouses and tank foundations (less common)

Despite the increased use of GRCSEs in practice, there is still considerable debate regarding the suitability of the design methods currently available, particularly in regards to serviceability behaviour which generally governs acceptable performance. The research presented in this thesis is largely an experimental investigation based on a field case study of a recently constructed GRCSE supporting a new rail line in Melbourne, Australia and comprises two major areas of investigation: 1) the localised load transfer platform behaviour and 2) global scale embankment behaviour.

1.1 Geosynthetic materials

In the civil engineering industry, geosynthetic materials have become an accepted construction material over the past few decades alongside steel, concrete and timber. A number of geosynthetic material categories (Table 1.1) exist and a wide variety of geosynthetic products are readily available. Within each category of geosynthetic material, there are geosynthetic products which are able to perform one, or several functions, and can be used for a range of applications. The basic function of a geosynthetic material can include, one or several of the following: reinforcement, separation, (fluid) barrier, filtration, drainage and protection. These basic functions enable the use of geosynthetic materials in applications such as: drainage/erosion control, coastal protection, paved and unpaved roads, railway tracks, containment facilities (tailings ponds, containment of hazardous substances, landfill etc.), subgrade improvement and foundations.

However, it is the use of geosynthetic materials for soil reinforcing applications (slopes, retaining walls and basal reinforcement in embankments) where, arguably, geosynthetics have had their largest impact on geotechnical engineering. In reinforcement applications, a geosynthetic material is incorporated into a soil mass (typically an engineered fill) to create a composite geosynthetic-soil mass. Through frictional interaction and interlocking, the geosynthetic material is able to increase significantly the tensile capacity of the composite soil mass. While many of the geosynthetic materials available are able to perform multiple functions, typically there are geosynthetic products that offers better performance characteristics for an intended application. However, identifying the "preferred" geosynthetic product is often a complex task and requires knowledge of a range of factors, including: short and long term performance, primary and secondary functions, durability, design life, soil pH and aggressiveness, installation damage and finally cost and commercial factors.

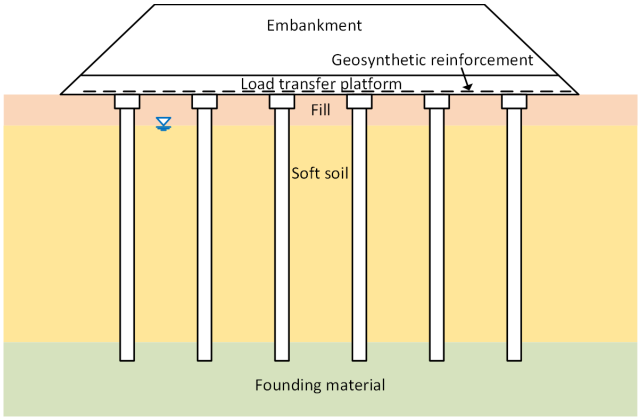

Figure 1.1. Typical Geosynthetic Reinforced Column Support Embankment (GRCSE)

Table 1.1. Categories of geosynthetic products (Shukla et al. 2006) – products relevant to soil reinforcement applications in bold

Geogrid (biaxial, uniaxial) • **Extruded** • **Bonded** • **Woven**	Geomembrane Geonet Geosynthetic clay liner (GCL)
Geotextile • **Woven** • Nonwoven • Knitted • Stitched	Geotextile related products (GTPs) – Geocell, Geofoam, Geomat/Geoblankets, Geomesh, Geopipe, Geospacer, Geostrip

In the context of soil reinforcement, which is primarily reliant on the tensile capacity of the geosynthetic material, it is the category of geogrids and geotextiles with their high tensile capacity, which are most suitable for these applications. Within these categories of geosynthetic materials, further sub-divisions can be made. In Table 1.1, the geogrids and geotextiles are categorised based on manufacturing process. Whilst the manufacturing process alone (generally) does not influence the choice of product, the resulting mechanical properties of the product will affect the choice of product and in this respect, soil reinforcement is generally limited to woven geotextiles and geogrids (Shukla et al. 2006, Lawson 2013). For the case study considered here, the load transfer platform is reinforced with a woven, polyester high tensile strength geogrid.

1.2 Ground improvement

Semi-rigid inclusions (as opposed to piles, which provide rigid ground support) can take the form of concrete columns such as Drilled Displacement Columns (as referred to by their proprietary name Controlled Modulus Columns (CMC) or other cast *in situ* column types, and in most cases, they do not contain steel reinforcement. Although, in some cases driven piles are used. A basal reinforced embankment without ground improvement will generally have an improved FOS against embankment slope failure which enables higher embankment heights and steeper side slopes. However, the overall stress applied to the soft soil is the same and therefore total settlement remains largely unchanged compared with the case of no basal reinforcement. As a result, the choice between the use of basal reinforcement without ground improvement, or with ground improvement (i.e., a GRCSE), is generally governed by allowable total embankment settlement. As mentioned previously, advances in the capabilities of piling rigs over the past few decades have resulted in increased torque capacities, increased productions rates, improved instrumentation monitoring leading to greater quality assurance and control (QA/QC) and overall a significant reduction in the overall cost of installing semi-rigid ground improvement inclusions (Larisch, 2014). The use of semi-rigid ground improvement has become an attractive design option, particularly where this is coupled with an LTP to form a GRCSE.

To understand the benefits offered by a GRCSE, it is necessary to understand the circumstances in which this ground improvement option is adopted. Much like geosynthetics, the choice of a ground improvement method depends on a range of complex factors that includes: geotechnical characteristics of the soil to be treated, short and long term performance, dynamic performance, construction risk and time as well as contractor availability, knowledge and experience. A relatively comprehensive list of ground improvement methods, grouped based on improvement principle is presented in Table 1.2 (modified from Kitazume and Terashi, 2013) .

Table 1.2. Ground improvement methods (modified from Kitazume and Terashi, 2013).

Improvement principle		**Engineering method**	**Ground improvement examples**
Replacement		Excavated replacement	Dredging replacement
		Dynamic replacement	Sand compaction pile
Densification	Dewatering/ compaction	Improvement by displacement and vibration	Sand compaction pile
			Stone column • Dry, wet and bottom feed methods
			Geotextile encased columns (GEC) – displacement method
	Compaction	Vibration compaction	Vibro-flotation/Vibro Compaction
		Impact compaction	Dynamic Compaction
			Rapid impact compaction (RIC)
			Rammed aggregate piers
			High energy impact compaction
Consolidation/ dewatering		Preloading	Preloading
		Preloading with vertical drains	Sand drain
			Prefabricated vertical drains (PVDs)
			Geotextile encased columns (GEC) – replacement method
		Dewatering	Deep well
			Well point
			Vacuum consolidation
		Chemical dewatering	Quick lime pile
Grouting			Cement/Chemical grouting
			High pressure (jet) grouting • Fracture grouting • Jet grouting
Solidification		In-situ mixing	Shallow mixing • Cut-mix injection method • Stabilised bridging layer
			Deep mixing • Dry soil mixing (rotary) • Wet soil mixing (rotary/rotary-jet) • Cutter soil mixing
			Vibro concrete columns
		Plant mixing	Pre-mix mixing
			Light weight soil
		Pipe mixing	Pneumatic flow mixing
Thermal stabilisation		Heating	Thermal PVDs
		Freezing	
Electro-Osmosis			Electro-osmotic consolidation
Blasting		Explosive/blasting	Surface, underwater, hidden explosive methods
Bio-improvement		Microbial	Bioclogging
			Biocementation
Reinforcement		Semi-rigid inclusions	Drilled displacement columns, CMCs etc.
			Geosynthetic reinforced column supported embankment

1.3 Geosynthetic reinforced column supported embankments (GRCSE)

A significant quantity of research has been reported on the topic of GRCSEs over the past two decades as documented in current literature (Han and Gabr 2002, Chen et al. 2008, Briançon and Simon 2011, Filz et al. 2012, van Eekelen et al. 2013, Rowe and Liu 2015). Emphasis of this research work particularly focussed on the description of the complex soil-structure-geosynthetic reinforcement interaction occurring in the load transfer platform (LTP) at the base of an embankment. Owing to the increased use of GRCSEs, national design methods have been developed in several countries such as Germany (EBGEO; German Geotechnical Society, 2010), United Kingdom (BS8006-1; BSI, 2010) and the Netherlands (CUR226; CUR 2010) amongst others. However, the

calculated arching stresses differed considerably in these design methods (Naughton et al. 2005, Lawson 2012) and, in addition, they differed from those measured in the field (Haring et al. 2008, Van Eekelen et al. 2010, Van Eekelen et al. 2012).

A feature common to the design methods used in LTP design, is a general two-step process: Step 1 - assessment of arching and calculation of load on semi-rigid elements (part A load) and load in the un-arched zone (parts B + C load); Step 2 - separation of load in parts B + C, this step calculates the tensile load taken by the geosynthetic reinforcement (part B) as well as the load supported by the subsoil (part C) (Figure 1.2). A significant number of models exist for calculating the arching stresses in Step 1. Van Eekelen et al. (2013) categorised about 20 models as either rigid, limit equilibrium, frictional, mechanical or empirical models while McGuire et al. (2008) presented a parametric analysis of 10 of these models. However, many of these models were shown to provide predictions of arching stresses that differed considerably for various embankment geometries and material properties (Ellis and Aslam 2009b and Lawson 2012) and more importantly, these models have been shown to differ from field behaviour.

As a result, additional models have been developed in recent years such as the concentric arches (CA) model (Van Eekelen et al. 2013) based on extensive laboratory testing (Van Eekelen et al. 2012a, 2012b) and validated against several field case studies (Van Eekelen et al. 2013) as well as a simplified method by Zhuang et al. (2014). Of the large number of models available, the limit-equilibrium models have received the most attention. The model of Hewlett et al. (1988) was adopted in the French ASIRI guideline and suggested as an alternative in BS8006-1 (2010), the model of Zaeske (2001) was incorporated into EBGEO (German Geotechnical Society, 2010) and CUR226 (2010) and more recently the CA model was proposed for the revised Dutch standard CUR226 (2016)

These methods calculate the un-arched stress based on geometric parameters (column spacing s, column head width a, and embankment height h) and LTP material parameters (effective friction angleφ'). The result is a value of un-arched stress acting on the geosynthetic reinforcement layer/sub-soil (Part B +C) which is independent of sub-soil consolidation and time. However, the CA model does describe qualitatively increasing arching stresses due to sub-soil consolidation but the quantitative output of the model is the same as other limit-equilibrium models. This two-step design approach has the effect of de-coupling the arching stress-displacement relationship as the displacement calculated in the second step based on a constant value of arching stress from the first step (independent of displacement).

The relationship between arching stresses and displacement is well documented in trapdoor tests as far back as Terzaghi (1936) and extended further by Iglesia et al. (1999, 2013) who developed the so-called Ground Reaction Curve (GRC) to describe the relationship between arching stresses and displacement. The GRC is calculated based on simple geometric and material properties, similar to limit equilibrium models, and plotted as a function of normalised displacement (displacement/ trapdoor width).

The fundamental mechanisms governing the development of arching as assessed through trapdoor tests and described by the GRC concept has been referred to by only a handful of researchers (Aslam et al. 2008, Ellis et al. 2009a, 2009b, Zhuang et al. 2012, Iglesia et al. 2015) in the context of GRCSE, despite the similarities between the two problems. However, a number of researchers have observed in laboratory and field scale studies variations in arching stresses attributed to sub-soil settlement.

Chen et al. (2008) described a laboratory scale model with two-dimensional bearing elements and sub-soil consolidation controlled by a water bag. Based on stress-displacement plots of measured arching stresses and the

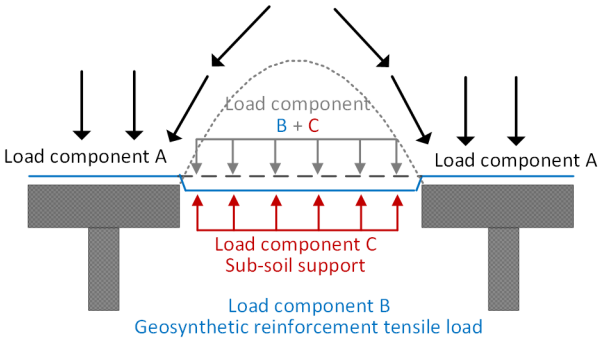

Figure 1.2. Conceptual two-dimensional load distribution in a load transfer platform

stress concentration ratio (SCR), it was noted that "*soil arching is strongly dependent on pile-subsoil relative displacement*" and went further to describe, using terminology similar to that which describes the GRC, a critical relative displacement where arching was most efficient. Similar behaviour was observed by Van Eekelen et al. (2012a) through multiple loading-consolidation steps, with load component A observed to increase during consolidation steps. However, in these laboratory scale models, rather than slow controlled sub-soil consolidation like that which occurs in the field, the subsoil support was removed quickly and the arching stress-displacement relationship was simply described as "increasing" during the consolidation stage. The maximum arching and the break-down of arching at larger displacements as described by Chen et al. (2008) and the GRC was not reported.

Of the limited number of full-scale instrumented embankments described in the literature (Haring et al, 2008, Wachman and Labuz 2008, van Eekelen et al. 2010, van Eekelen et al. 2012), one feature is common throughout; the time-dependent development of arching stresses (measured through earth pressure cell data) which in many cases continued well into the post-construction phase. This time-dependency is a manifestation of the time-dependent consolidation of the soft soil underlying the un-arched zone (i.e., the time dependent loss of sub-soil support). This time-dependent behaviour observed in field studies cannot be described with the existing arching models typically used for GRCSE design. Laboratory testing used to develop the GRC showed that maximum arching occurred at relative small trapdoor displacements. However, at larger displacements, arching began to break down (Iglesia, 1991). In the context of full scale GRCSE, this displacement range for which arching breaks down is expected to occur within the typical displacement range of the geosynthetic reinforcement. The increase of arching stresses acting on the geosynthetic reinforcement at larger sub-soil displacements has important implications for GRCSE design.

1.4 Research hypothesis

The research undertaken herein comprises two major components: 1) localised load transfer platform behaviour and 2) global scale embankment behaviour. It is the author's position that further improvements in the understanding of LTP behaviour, and improvements in the design of GRCSEs, requires the incorporation of sub-soil settlement as a governing parameter in an arching model. In essence, this development reflects a transition from mathematical models predominately describing ultimate state conditions, to models that describe serviceability behaviour through the design life of the LTP. Given the stringent settlement tolerances and performance criteria that typically govern the design of a GRCSE, it is deformation that governs acceptable LTP behaviour, not ultimate state load conditions. The transition to deformation based serviceability design methods is therefore warranted and necessary for advancement of the GRCSE state-of-knowledge.

Chapters 5 to 7 of this thesis are concerned with load transfer platform behaviour and are aimed at validating the author's hypothesis that arching stress development is dependent on the sub-soil settlement/geosynthetic reinforcement deflection in the load transfer platform, and further, validating a relationship that describes this arching stress-deformation behaviour. The implications arising from this hypothesis are then explored in Chapter 7 where the serviceability design of GRCSE is investigated.

Chapters 8 and 9 investigate the role that ground improvement installation effects play in the behaviour of a GRCSE, specifically how they influence global scale behaviour (lateral sliding and overall stability). The installation effects of a single full displacement pile have been investigated by numerous authors (see for example Karlsrud and Haugen, 1986, Coop and Wroth, 1989, Bond and Jardine, 1991, Azzouz and Morrison, 1988, amongst others) and studied analytically using cylindrical cavity expansion theory. These studies having shown that the installation of pile can have a considerable effect on the surrounding ground and the stresses that develops with time around the pile itself. It is hypothesised that the cumulative effects arising due to the installation effects, from the installation of a large number of columns in a dense grid for ground improvement works, have a considerable effect on the global scale embankment behaviour.

1.5 Research aims

The research presented herein is predominately an experimental research study with the main aim of improving the understanding of the mechanisms governing the behaviour of GRCSEs, in order to refine the theoretical models used for GRCSE design. A second research program currently underway at Monash University, aims to further refine these theoretical models for GRCSEs using advanced laboratory testing techniques and will build on the work presented herein.

While many researchers have undertaken parametric studies to assess the variation in arching stresses due to geometric variables such as: column spacing, column head size, embankment height and material properties of the LTP. The intention of this study is to examine the mechanisms governing arching development in GRCSEs and use this knowledge to provide a more rigorous theoretical basis for the design methods employed, and if required, propose a new arching design method. In addition to validating the author's hypothesis, this thesis seeks to address the following aims:

- Highlight the benefits and importance of a LTP design method that incorporates an arching/sub-soil settlement relationship.
- Highlight the need for deformation based serviceability design methods for LTP design in GRCSEs.
- Outline the limitations of current limit equilibrium models under serviceability and ultimate limit state conditions.
- Provide a framework for the development of a LTP design method incorporating the arching/ sub-soil settlement relationship which can be further validated by laboratory scale modelling (by others).

The author has undertaken an extensive review of the historical and current site investigation data along with an extensive program of laboratory testing of the soft soil underlying the site to present a high-quality site characterisation. An extensive amount of field data is presented in this thesis and it is a further aim that this field case study form a benchmark case study on GRCSEs which will be of use for future research into this area.

In addition to investigating the LTP behaviour, this research investigates global scale embankment behaviour and behaviour of the columns supporting the embankment. This includes, column installation effects, the "ground

improvement" effect and the capacity of the semi-rigid inclusions. It is an aim of this study to examine the behaviour of the drilled displacement columns within an effective stress framework in order to understand, if, and how, installation effects affect the global embankment behaviour.

1.6 Methodology

Over the past decade there has been a significant amount of research focused on physical modelling of the LTP behaviour at laboratory scale. By comparison, the number of full-scale embankments with extensive, high quality instrumentation is quite limited. Due to these factors, and partly from opportunity, the instrumentation of a GRCSE recently constructed in Melbourne, Australia has been undertaken and forms the major source of data for this research. The research presented herein is predominately an experimental research study which is supported, where necessary, with analytical and numerical analyses, as well as comparative assessment of data from other laboratory and field studies.

Comparative study of arching methods

Terzaghi (1936) performed one of the earliest systematic studies of soil arching behaviour using the well-known trapdoor test; this led to "Terzaghi's arching theory" (Terzaghi, 1943). In order to assess the merits of this arching theory with others, Terzaghi (1943) suggested that a comparative study is required, along with further experimental study, to compare the results and basic assumptions of the theories. A large number of researchers have studied soil arching through the trapdoor test over the past 70 years since Terzaghi's 1936 study; much of this work is summarised in a comparative study by Tien (1996). However, the study by Tien predates the majority of the arching models developed for GRCSE design, which are currently in use. This research begins with a literature review of the soil arching as observed in trapdoor tests. This provides the theoretical basis for the comparative study undertaken by the author of the arching models currently used for GRCSEs. The emphasis is on assessing the assumptions of these arching models, particularly the limit equilibrium models, within a framework of theoretical soil mechanics and plasticity theory.

Field case study

A recently constructed railway embankment in Melbourne, Australia has been extensively instrumented and monitored by the author since 2013. This forms the main source of data from which the analysis and research presented in this thesis is based. A major advantage of a field case study is that many of the simplifications and assumptions needed for medium/small scale physical models are not required. The real ground conditions, real loads and real stresses are captured directly. In addition, a number of mechanisms in a GRCSE that are difficult to simulate in small scale models, namely column installation effects and overall embankment stability can be observed. However, the inherent variability of sub-surface conditions, variable weather conditions and other factors beyond the direct control of the author mean that the realism of a field case study is also a disadvantage (Wood 2003). The uncertainty introduced into the field data by these factors has been reduced, to the extent that it is practical, through comprehensive documentation of the construction process and detailed site characterisation.

Compared with other case studies, there are several unique features of the present case study. Firstly, the embankment is a widened embankment, as such, there is interaction between the lower and upper level LTPs during and after the various stages of ground improvement works. Secondly, the presence of a fill layer overlying the soft

soil affects the behaviour of the sub-soil beneath the LTP. These features provide unique field data and a basis to understand further the behaviour of GRCSEs.

Laboratory testing and site characterisation

Where laboratory data of the embankment materials was not available as part of the design and construction process, additional laboratory testing has been undertaken to improve the material characterisation. This is particularly important for the numerical analysis undertaken. Calibration of the strain gauges installed as part of the field case study was also required.

In addition, an extensive program of laboratory testing of soft soil samples recovered during the investigation phase and a review of historical and current site investigation data has been undertaken to provide a detailed geotechnical characterisation of the sub-surface conditions.

Analysis of results and analytical techniques

The field case study data is presented and these results are compared with a number of analytical methods used to describe arching behaviour. Similarly, the field data which is used to describe the column installation effects is presented and cylindrical cavity expansion theory is adopted to provide an effective stress framework through which the field data can be interpreted.

Numerical modelling – arching behaviour

Given the considerable amount of time needed to observe the full development of arching stresses, field scale examples are extremely limited. Furthermore, the full development of arching is not expected to be observed by the completion of this present study. Numerical modelling is therefore undertaken as an additional step to further validate the method of arching development adopted by the author. The arching development in a GRCSE and in the analogous trapdoor problem, is a large displacement problem in computational geomechanics, the numerical modelling is therefore undertaken using the mesh based Finite Element Method (FEM) and meshfree Smooth Particle Hydrodynamics (SPH) method. The limitations and advantages of the two computational approaches are discussed.

Comparative study GRCSE field case studies

In addition to the numerical modelling, the GRC arching method is further developed by the author and this understanding of LTP behaviour is used to re-assess previously documented field case studies.

1.7 Layout of thesis

This thesis is separated in two major study areas with the results of the field case study presented in multiple chapters. The LTP behaviour is investigated in Chapter 5 to Chapter 7 and the global scale embankment behaviour and assessment of the ground improvement is presented in Chapters 8 and 9. The thesis comprises the following chapters:

Chapter 1: Introduction

Research background, hypothesis, aims and methodology are outlined.

Chapter 2: Literature review

An overview of soil arching behaviour is presented and a range of arching models currently employed for use in LTP design are described. The key findings from a number of field, laboratory

and numerical studies are discussed and the general design approach is outlined with reference to several design standards. To improve the overall flow of the thesis, aspects of the literature review relating to numerical modelling and global embankment behaviour are presented in Chapter 6 and Chapter 8 respectively.

Chapter 3: Field case study

The field case study and GRCSE embankment design is described along with an overview of the installed instrumentation.

Chapter 4: Laboratory testing and geotechnical site characterisation

The program of laboratory testing on sub-surface materials is described and results presented. This information along with historic and current geotechnical investigation data is used to develop the geotechnical site characterisation.

Chapter 5: Arching and LTP behaviour

Field case study data describing the LTP behaviour is presented. This data is compared with predictions from the ground reaction curve (GRC) method. The relationship between arching development and sub-soil settlement is highlighted and the implications of these findings are discussed.

Chapter 6: Numerical analysis of arching behaviour

Numerical analysis of the arching development using FEM and SPH is presented. The limitations and advantages of the two computational approaches are discussed.

Chapter 7: The GRC design approach and comparative study

The use of the GRC as a design method for GRCSEs is developed further. The author's interpretation of LTP behaviour is compared with a number of other field case studies.

Chapter 8: Column installation effects

Previous laboratory, field and numerical studies of installation effects are described and the field case study data presented. Cylindrical cavity expansion theory is introduced and used as an analytical tool to compare and assess the field data.

Chapter 9: Global scale embankment behaviour

The global scale behaviour is described based on field case study data and the relationship with the ground improvement works outlined in the preceding chapter.

Chapter 10: Conclusions and recommendations for future work

The key research findings as they relate to the research aims are summarised and areas of further research discussed.

2 Literature review

This chapter provides an overview of the behaviour and design of a GRCSE. The two main areas of investigation contained within this study; localised load transfer platform and global scale embankment behaviour, dictates the overall structure of the literature review. To reduce the length of this chapter the background (literature review) to the numerical investigation of localised arching behaviour (Chapter 6) and the global scale behaviour (Chapters 8 and 9) is presented in the respective chapters. Presented in this chapter is a summary of the key points from the literature review in Ch 6, 8 and 9. This chapter begins with a detailed examination of the fundamentals of soil arching behaviour based on studies which have investigated the trapdoor test. The application of arching theory to other geotechnical problems is discussed to provide broader context (Section 2.1.4) and this is contrasted with the various categories of models that have been developed to describe arching in GRCSE design (Section 2.2). A review and discussion on arching behaviour in Section 2.1 and 2.2 concludes with a detailed statement of the research hypothesis previously referred to in Section 1.4.

Methods to assess the second step in LTP design, the membrane action, are described in Section 2.3. This is followed by a discussion on the ground improvement and sub-soil behaviour (Section 2.4). A number of laboratory and field studies along with several failure case studies are described and their key findings, as they relate to the present study, are noted. The design of GRCSEs is a theme throughout this study. To provide the background to these discussions the general GRCSE design principles are outlined in Section 2.6 by way of two contrasting design approaches. In Section 2.7, the various localised and global scale GRCSE limit states are described and the author's position on the global scale behaviour is outlined with reference to Chapters 8 and 9.

In the preceding chapter the components of a GRCSE and the three load components acting on the LTP were described in Figure 1.1 and Figure 1.2 respectively. The main geometric properties of a GRCSE, referred to throughout this thesis, are summarised in cross section and plan view in Figure 2.1*a* and *b*, respectively. These parameters are generally consistent with the notation in EBGEO (German Geotechnical Society, 2010) and McGuire (2011). The latter also presents an extensive list of GRCSE geometric properties and relationships. As the plane of reinforcement is typically very small relative to the height of embankment (*h)*, the assumption is made that the actual height of the embankment is taken as approximately equal to $h + z$, where z is the vertical distance between top of column and geosynthetic reinforcement layer (see Figure 2.1).

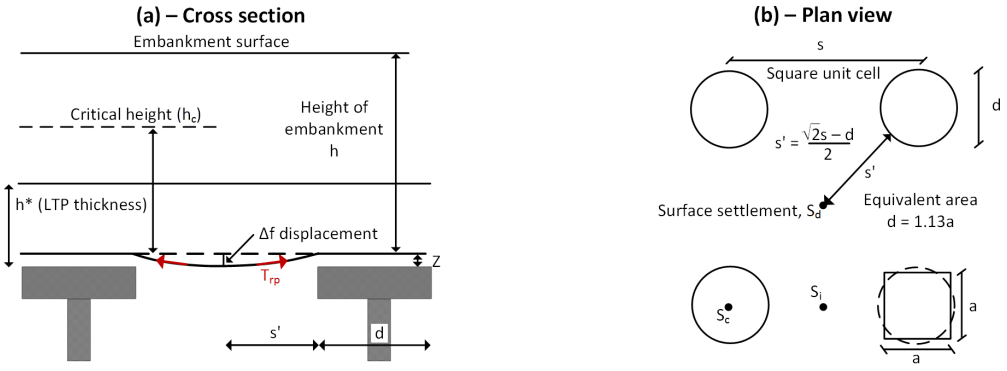

Figure 2.1. Embankment geometry **(a)** cross section and **(b)** plan view

2.1 Soil arching behaviour

As noted by Terzaghi (1943); "*Arching is one of the most universal phenomena encountered in soils in both the field and the laboratory*". This fundamental behaviour occurs when a soil mass moves relative to a stationary soil mass. Shear stresses between the two bodies acts to resist this movement resulting in an increase in stress on the stationary part and decrease in stress on the yielding part. This behaviour is termed "*soil arching*" as it tends to resemble an arch when it forms over a yielding support (Terzaghi 1943). Terzaghi (1943) also noted "*the state of stress that exists due to arching is no less permanent than any other state of stress that relies on shear stress, such as the stress conditions beneath a footing"*, however, it was noted that there are various sources of external disturbance that can have a detrimental influence on the state of stress under static load conditions. The most important of these external disturbances is vibrations (i.e., earthquake loading, vehicular loading etc. in the case of a GRCSE).

The classic trapdoor experiment comprises a mass of dry granular material in a box, which in cross section, has a height of soil H and at its' base a yielding strip of width B with a rigid base on either side (i.e., a two-dimensional plane strain trapdoor test). In a three-dimensional test the yielding strip is either square, or circular, in shape and located in the centre of the box (in plan view). The trapdoor test can be performed with a downward moving (active mode) or an upward moving trapdoor (passive mode). The discussion presented herein is limited to the active mode which is relevant to the GRCSE problem. The trapdoor test is a classic test in soil mechanics that has been studied extensively since the early part of the 20th century and highlights many complex aspects of soil mechanics, these include the development of active and passive zones, radial shear zones and shear banding. Despite the simplicity of the trapdoor test, describing the state of stress (and strain) is exceedingly complex and at this point in time an analytical solution remains elusive (Costa et al. 2009).

In the context of GRCSE, the yielding soil mass is the soft soil (or sub-soil support) between the columns. As this soil beneath the LTP and the LTP itself moves downwards, the state of stress changes as the soil mass located above the columns resists this movement through shear stress. This leads to a redistribution of stress to the columns and an unloading of stress acting on the geosynthetic reinforcement (or sub-soil) between the columns. It is important to note that a trapdoor has a height of granular material equal to *H*, while a GRCSE of height *h* has only the component *h** comprising granular material (Figure 2.1*a*). Typically, the general embankment fill above the LTP is a lower quality engineered fill which may contain an appreciable amount of fines. This can have a significant effect on the arching stress development, particularly where *h** is quite thin relative to the column spacing as soil arching develops through both the LTP and overlying embankment fill. Due to the soil arching behaviour, the geosynthetic reinforcement does not support the overburden stress, but typically, some portion of this stress. The development of arching is a critical component of LTP design; the use of geosynthetic reinforcement in high

embankments would not be feasible otherwise (i.e., if designed to support the overburden stress). In addition, the sub-soil may provide some short term, and in some cases long term support.

Understanding the effectiveness of arching behaviour is fundamental to the GRCSE problem. Much of the understanding of the fundamental mechanisms that govern arching behaviour has come from the study of trapdoor tests. These are described below.

2.1.1 Terzaghi's trapdoor test study

One of the earliest systematic studies of arching behaviour was performed by Terzaghi (1936). Some results from these tests are shown in Figure 2.2 (revised by Evans, 1984) where the load-deformation relationship is shown as a stress reduction ratio (defined as vertical stress acting on trapdoor σ_v divided by the initial overburden stress σ_{v0}) versus the relative displacement (δ/B), where δ, the deflection of the trapdoor, has been normalised with respect to B and is typically expressed as a percentage value. This method of normalising the stress acting on the trapdoor and plotting against relative deformation is used throughout this thesis to quantify arching stress development and enable comparison between tests with differing geometric arrangements. A similar approach is used for arching in GRCSE in later chapters, however, in that case the relative displacement is normalised with respect to the unit cell geometry.

The test data of Terzaghi (1936) shows arching stress development through four distinctive phases; initial arching, maximum arching, load recovery and terminal. The key features of these tests are shown in Figure 2.3 (Terzaghi's studies primarily sought to describe the terminal phase of arching stress). In the context of plasticity theory, the edge of the trapdoor is a singularity point. Terzaghi assessed (correctly) that the region bounded by the zones of high stress (stationary soil mass) and low vertical stress (yielding soil mass) must form a zone of radial shear (Figure 2.3*b*). At a "sufficient" trapdoor deformation, the two failure surfaces propagating from the edge of the trapdoor intersects the surface. This failure surface (at the terminal state) is represented by the lines *ac* and *bd* in Figure 2.3*a*.

The important point is the "*sufficiently large displacement*", referred to by Terzaghi, which is required to mobilise this terminal condition. In the context of GRCSE, the magnitude of displacement would only be achieved if the geosynthetic reinforcement fails and settlement between the columns is both unrestrained and quite large relative to *h*. Terzaghi (1943) also made a number of observations relating to the arching behaviour, and the models used to describe this behaviour, which are relevant to the present study. He noted that the three categories of arching models

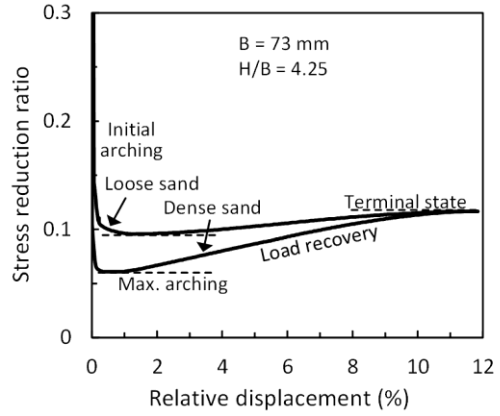

Figure 2.2. Load-deformation results from trapdoor tests (Terzaghi, 1936, revised by Evans, 1984 and modified by the current author)

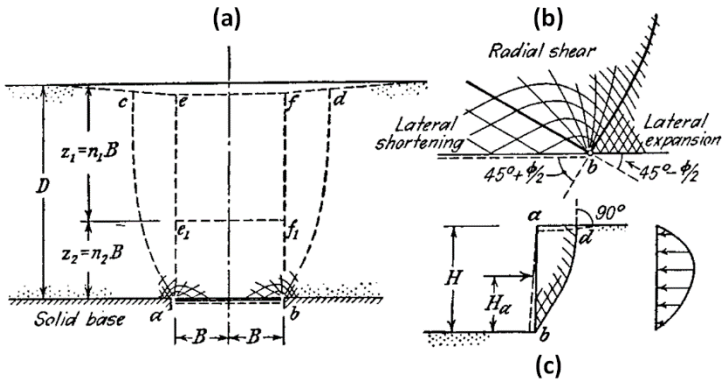

Figure 2.3. Arching as described by Terzaghi (1943) (note Terzaghi defined *B* as been equal to half the trapdoor width)

available at the time gave quite different values for the stress acting on the trapdoor. A similar situation exists at this time for models used to describe arching in GRCSE. To resolve this, it was suggested that a comparative analysis was required along with further experimental studies to compare the results and the basic assumptions of the theories.

A comprehensive comparative analysis of this type has been undertaken by Tien (1996). However, nearly all of the arching models developed for GRCSEs, which are currently in use, have been developed since 1996. The studies which have undertaken a comparative study of arching models used for GRCSE, since the work of Tien (1996), tend to compare the output of the models, rather than the underlying assumptions. These types of studies are numerous; see for example McGuire et al. (2008), Lawson (2012) and Van Eekelen et al. (2011a). There is a need for a comparative study of the type described by Terzaghi and performed by Tien. Fortunately, there is a considerable amount of experimental data available from studies investigating GRCSEs (outlined in Section 2.5) along with information from numerous studies investigating the trapdoor test (Ladanyi et al. 1969, Vardoulakis et al. 1981, Evans 1983, Stone 1988, Iglesia 1991, Ono et al. 1993, Dewoolkar et al. 2007, Costa et al. 2009, Chevalier et al. 2011). This information enables a comparative analysis and assessment of the assumptions underlying the various arching models. This is the aim of Sections 2.1.2 to 2.2.6 which follow.

2.1.2 Other trapdoor test studies

Evans (1983) performed 69 trapdoor experiments using 4 different sand materials and Iglesia (1991) investigated the arching mechanism further with a similar number of centrifuge tests. These studies both focused on describing the soil arching behaviour analytically based on theoretical soil mechanics with the findings supported by physical modelling, and unlike Terzaghi's earlier work they focused on the maximum arching condition as well as the terminal state of arching. These studies contrast greatly with many GRCSE arching models which emphasis the geometric representation of the "soil arch". Similar to the earlier work of Terzaghi, Evans (1983), Ladanyi et al. (1969) and Iglesia et al. (2013) each observed an arching stress-deformation relationship (Figure 2.4) (see also Chevalier and Otani, 2011 amongst others). Iglesia (1991) termed the phases: initial arching, maximum arching, load recovery and terminal.

Terzaghi (1936, 1942), Ladanyi and Hoyaux (1969), Vardoulakis et al. (1981), Evans (1983), Stone (1988), Ono and Yamada (1993), Dewoolkar et al. (2007) and Costa et al. (2009) have developed, in the author's opinion, a relatively consistent interpretation of the arching development which is characterised by the simultaneous development of both internal and external shear bands during an active trapdoor test. The pertinent aspects of arching behaviour are described in the schematic presented in Figure 2.5 (modified from Costa et al. 2009).

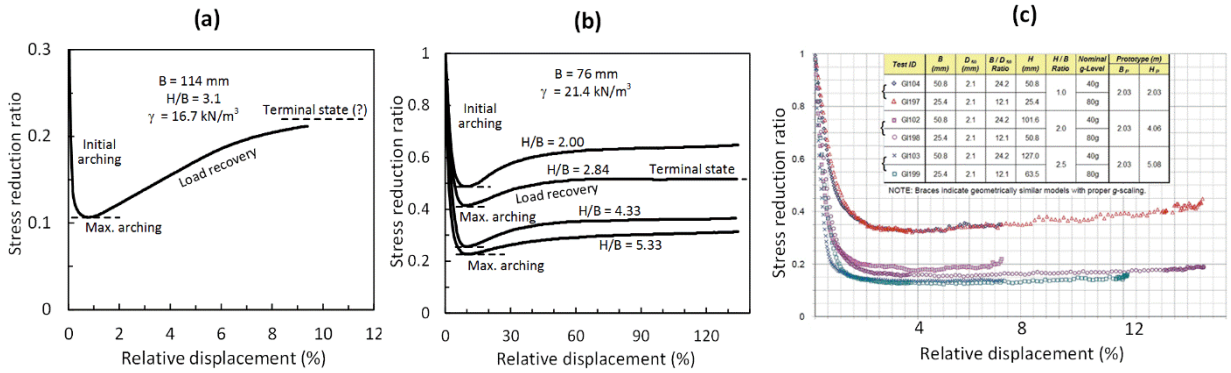

Figure 2.4. Load-deformation arching behaviour observed in trapdoor tests by **(a)** Evans (1983) **(b)** Ladanyi and Hoyaux (1969) and **(c)** from Iglesia (2013).

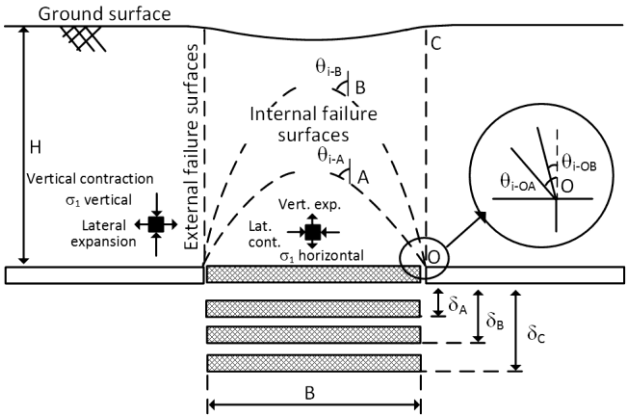

Figure 2.5. Schematic of arching development in shallow active mode trapdoor tests (modified from Costa et al. 2009)

Stone and Wood (1992) and others (Evans, 1983 and Santichaianant, 2002) have shown that internal shear bands propagate from the corner of the trapdoor at an angle, inclined from the vertical, and equal to the dilatancy angle (a variable of relative density and confining stress) at that point in time. The curvature of the shear bands, which approximates the shape of a reuleaux triangle in plane strain, reflects variation in the dilatancy angle as the overburden stress reduces along the length of the shear band.

It is the first internal shear band which broadly characterises the development of maximum arching, and the final external shear band which characterises the terminal phase of arching. Intermittent with these phases are additional internal failure surfaces (shear bands) which develop during the load recovery phase and are associated with the breakdown of the arching mechanism. Given the typical range of sub-soil settlement/geogrid deflection in a GRCSE (i.e., in the order to 100 mm to 150 mm), it is the phases of maximum arching and load recovery (and not the terminal phase) which are of interest to GRCSE. Iglesia et al. (1999, 2013) characterised the load recovery phase of arching as successive triangular failure surfaces (which occur with additional trapdoor displacement), with each failure surfaces forming an apex that is closer to the ground surface (i.e., internal failure surfaces moving upwards) with additional trapdoor displacement.

Evans (1983) used plasticity theory to interpret the arching behaviour and based on the velocity characteristics describing the plastic regions, contended that the internal failure surface must represent a velocity "jump", with plastic flow occurring along this discontinuity as a function of the dilation angle (ψ) (Figure 2.6). The development of the first internal shear band (OA), and the development of the final external shear band (OC), broadly define

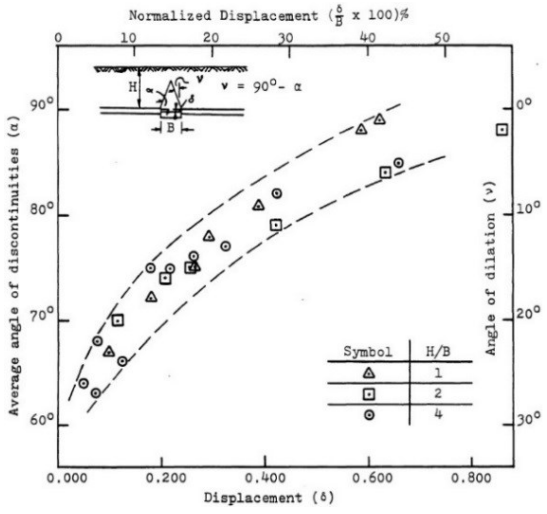

Figure 2.6. Angle of discontinuity in active arching tests (Evans 1983)

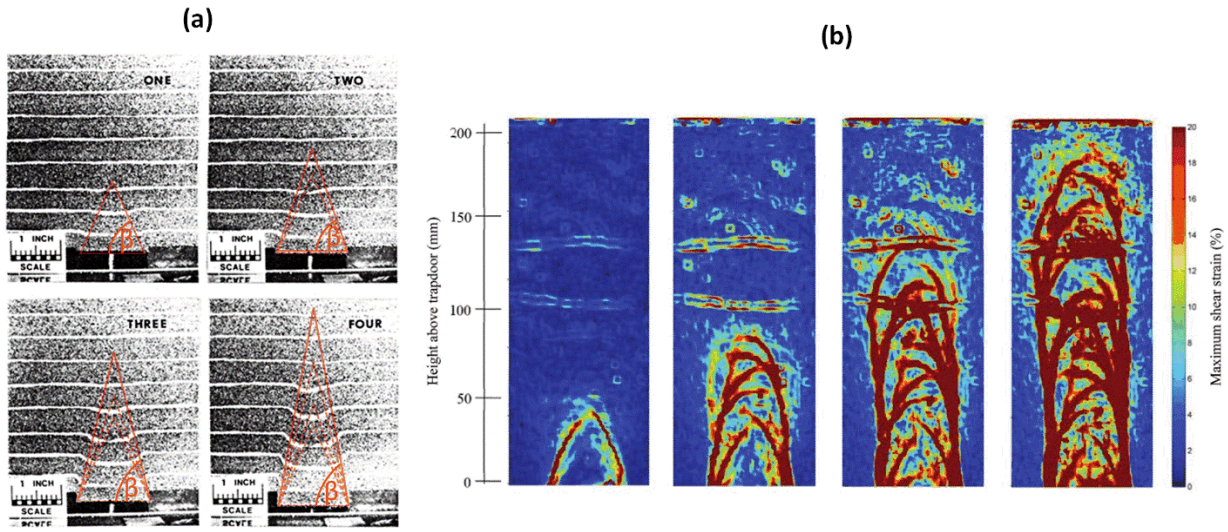

Figure 2.7. Development of failure surface in active mode arching tests **(a)** modified from Evans (1984) and **(b)** Jacobsz (2016)

the failure surfaces which are used to formulate the analytical descriptions of maximum and terminal phases of arching respectively based on limit analysis techniques. These conditions characterise the two extremes of arching deformation; maximum arching at small trapdoor displacement (a failure surface angle of about 60º in Figure 2.6) and a terminal state at very large trapdoor displacement (a sub-vertical failure angle at large displacement in Figure 2.6).

Photographic records (aided by tracer materials in the sand box) of arching development by Evans (1983) are shown Figure 2.7*a*. The progressive development of the internal shear bands is highlighted with red lines. Evans (1983) used this data to develop Figure 2.6. Similar data is presented in Ladanyi et al. (1969). In recent years, advanced imaging techniques have enabled improved visualisation of deformation patterns and localised strain development (shear banding). Stone and Wood (1992) used digitised photographic and radiographic records to relate shear band development to dilatancy angle, and recently, Jacobsz (2016) used Particle Image Velocimetry techniques (Figure 2.7*b*) to provide high resolution imagery of shear band development over a large displacement range.

Iglesia (1991) investigated the arching mechanism using centrifuge testing and developed the Ground Reaction Curve (GRC) (see also Iglesia et al. 1999 and Iglesia et al. 2013). Based on this work it is observed that arching develops rapidly at relatively small displacements; at less than 1 % relative displacement approximately 80% of the maximum arching has developed. Maximum arching generally occurs in the range of 2% to 4% of relative displacement. Three analytical equations (for each stage shown in Figure 2.8) are described below; these are a function of four variables: H, B, ϕ' (effective friction angle) and K (lateral earth pressure co-efficient). The solution to the equations describing the GRC represents three discrete points on the GRC curve. A five-step curve fitting method is described by Iglesia et al. (1999) to plot the GRC (Figure 2.9) and is summarised below:

Initial arching – initial linear portion of the GRC is defined by a linear line originating at stress reduction ratio (SRR) = 1, relative displacement = 0 % and with a gradient of −125 (termed the modulus of arching).

Minimum normalised loading – a flat bottom portion of the GRC curve occurs between the range 2 % < relative displacement < 5 %. The minimum stress reduction ratio value (SRR_{min}) in this range defines the occurrence of maximum arching and is calculated as follows:

$$SRR_{\min} = \frac{\sigma_{\min}}{\sigma_{v0}} = \frac{B}{H}\left(\frac{K_E}{2\cot\phi + \frac{B}{H}K_E} + \frac{\cot\phi}{6}\right) \quad \textbf{(2.1)}$$

Where:

$$K_E = \frac{(\cos\phi)^2}{1-(\sin\phi)^2} \quad \textbf{(2.2)}$$

after Krynine (1945) where $\sigma_{\min}$ is the minimum stress acting on the trapdoor which occurs at maximum arching.

Break point and secant modulus of arching – The break point is the point of maximum curvature located on the curved portion of the GRC between the initial linear portion and the point of minimum normalised loading (maximum arching). This point is located using the secant modulus of arching which, similar to the arching modulus, defines a linear line originating at SRR = 1, relative displacement = 0 and with an approximate gradient of 63. This line intersects the break point at a SRR value defined by a relative arching ratio A_R, the degree of arching relative to maximum arching, and is expressed as follows:

$$A_R = \frac{SRR}{SRR_{min}} = \frac{\sigma_{v0}-\sigma}{\sigma_{v0}-\sigma_{min}} = \frac{1-\left(\frac{\sigma}{\sigma_{v0}}\right)}{1-\left(\frac{\sigma_{min}}{\sigma_{v0}}\right)} \quad \textbf{(2.3)}$$

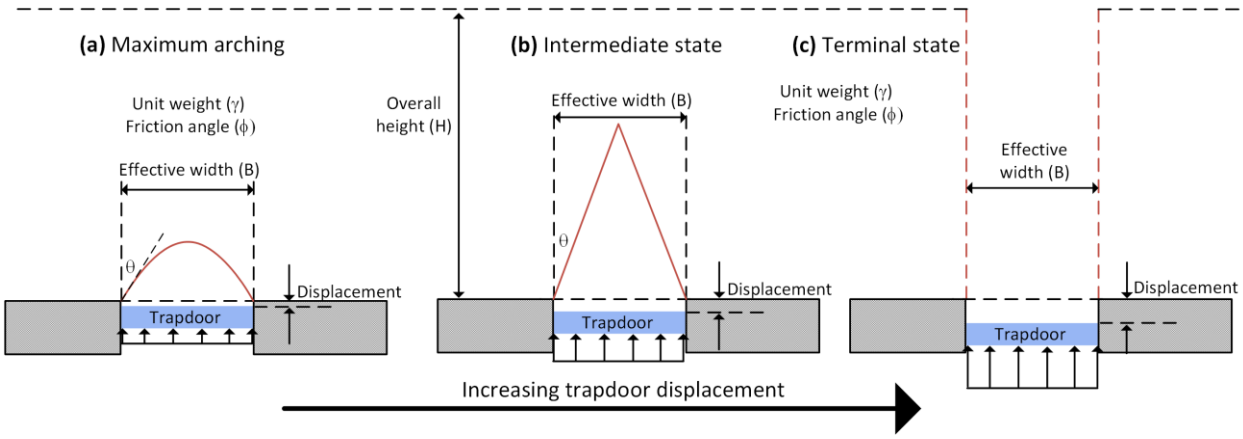

Figure 2.8. Arching geometry as described by the GRC (Iglesia et al. 2013) **(a)** maximum arching, **(b)** intermediate state and **(c)** terminal state

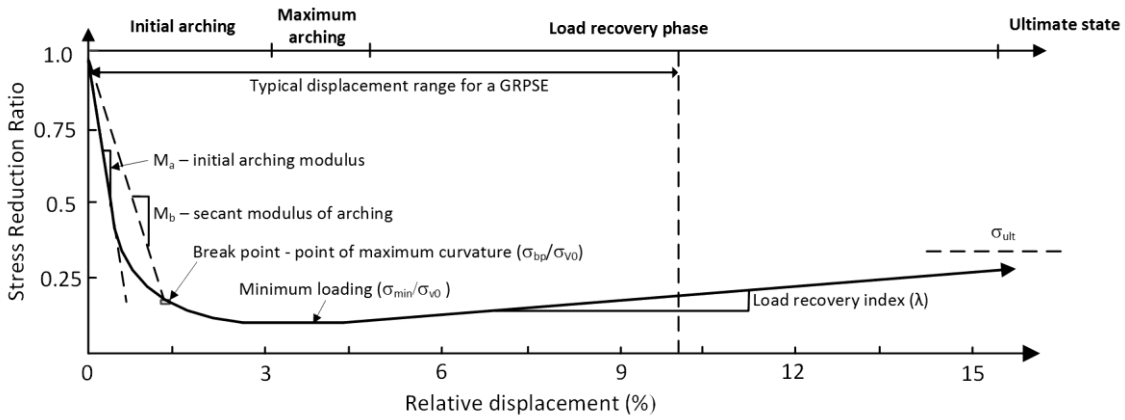

Figure 2.9. Characteristic GRC modified from Iglesia et al. (2011)

The break point occurs at a relative arching ratio A_{RB} defined as:

$$A_{RB} = 1 - 0.41e^{-0.54\left(\frac{H}{B}\right)} \quad \textbf{(2.4)}$$

The secant modulus of arching and break point have been empirically derived from centrifuge experiments by (Iglesia et al. 2013). The GRC is formed by fitting a smooth arc from the initial linear line (Step 1) to the flat portion (Step 2) with the point of maximum arching at the break point.

Terminal normalised loading – the terminal state SRR_{ter} is expressed as follows:

$$SRR_{ter} = \frac{\sigma_v}{\sigma_{v0}} = \frac{B}{2HK\tan\phi}\left[1 - e^{2K\tan\phi\left(\frac{H}{B}\right)}\right] \quad \textbf{(2.5)}$$

Where the earth pressure co-efficient taken as K_E after Krynine (1945)

Load recovery index – the load recovery index is calculated based on the ratios of H/B and B/D_{50} (D_{50} is the mean particle size) and the following empirically derived relationship (Iglesia et al. 1999):

$$\lambda = \left[2.5 + 5.7\log\left(\frac{B}{10D_{50}}\right)\right]e^{-0.65\left(\frac{H}{B}\right)} \quad \textbf{(2.6)}$$

Using these parameters the complete GRC can be developed as shown in Figure 2.9. Iglesia et al. (2013) noted that the intersection of the flat bottom portion of the GRC (zone of minimum loading/maximum arching) and the line describing the load recovery index typically occurs between a relative displacement range of 3 % and 5 %. Herein the author adopts the assumption that this occurs at a relative displacement of 4 %. In addition, it is necessary to curve-fit a smooth arc from the initial arching slope through the breakpoint and to the line defining the maximum arching. This is described in more detail in Section 5.7.3 where the GRC is used to analyse the field data. It is shown that these assumptions have only a minor effect on the derived GRC. While a complete analytical solution of arching stresses development in a trapdoor test does not exist at this point in time, a relatively consistent description of the theoretical aspects has been developed through numerous investigations, spanning many decades. The pertinent aspects of arching behaviour, as they relate to GRCSE, include:

- Deformation dependency
- Initial, maximum, load recovery and terminal phases of arching (see Evans; 1983, Ladanyi and Hoyaux; 1969, and Iglesia; 2013, – summarised in Figure 2.4)
- Progressive shear band development characterising maximum, load recovery and terminal phases of arching (see Figure 2.6, Figure 2.7*a* and Figure 2.7*b*)
- Shear bands developing at an inclined angle equal to the dilatancy angle at that particular point and time in the soil mass (Evans 1983, Stone and Wood 1992, Santichaianant 2002). The inclination of these shear bands, and their height relative to the thickness of the LTP, has important implications for the arching stress development in GRCSE.

2.1.3 Arching behaviour in three-dimensions

When compared with two-dimensional plane strain trapdoor arching, a significant difficulty is encountered when performing laboratory (and field) studies of the three-dimensional arching mechanism; the internal failure surfaces cannot be observed directly through visual observation. As a result, observing the three-dimensional development of

internal shear bands is challenging and only limited studies have successfully visualised this three-dimensional behaviour. This short coming is one of the most difficult to overcome in an experimental study of a GRCSE.

One experimental method which overcomes these difficulties is X-ray computed tomography (CT) scanning techniques which are able to visualise the three-dimensional arching mechanism. Eskişar et al. (2012) used this method in small-scale laboratory tests performed on cylindrical test samples measuring 100 mm in height by 126 mm diameter with four 15 mm diameters columns supporting the soil mass. Three types of sands, two types of geogrid reinforcement and two pile spacings were investigated. Eskişar et al. (2012) note that direct observation of the arching mechanism where geosynthetic reinforced was incorporated was difficult. It is inferred this may have been due to the increased imaging artefacts due to the presence of the geosynthetic layer as well as geosynthetic scaling effects i.e., the geosynthetic was too stiff to permit arching to develop. CT scanning was performed over vertical cross sections and in plan view at various heights about the pile cap. These resulting two-dimensional cross sections were combined to generate three-dimensional images of the small-scale pile arrangement (Figure 2.10).

The X-ray CT scanning technique measures a "CT-value" which can be correlated with density; the method does not directly measure the stress conditions. The following points relate to the laboratory study by Eskişar et al. (2012):

- X-ray CT scanning was performed at 5 mm displacement intervals; the first interval where imaging was performed was at relative displacement of 17%. i.e., in the load recovery phase. If maximum arching did occur, it is unlikely it was measured. The relative displacement of this first interval was well in excess of a typical relative displacement range in GRCSE (i.e., 0% to 10 %).
  The internal failure surface forms an angle with the horizon of 38° for Case 1 (peak internal friction angle ϕ_{peak} = 39.4°), 48° for Case 2 (ϕ_{peak} = 36.0°), 55° for Case 1 (ϕ_{peak} = 33.9°). An increased in friction angle indicates enhanced arching (i.e., shallower arch). See Figure 2.10*a*, *b* and *c* respectively.

Eskişar et al. (2012) summarised the observed internal angle of failure for the four granular material types for the cases with and without geogrid as shown in Figure 2.11. On the basis of these results, Eskişar et al. (2012) concluded that the inclusion of geogrid altered the state of the arching. While this is true, from the discussion outlined in the preceding sections it is evident that it is the difference in base settlement that alters the arching

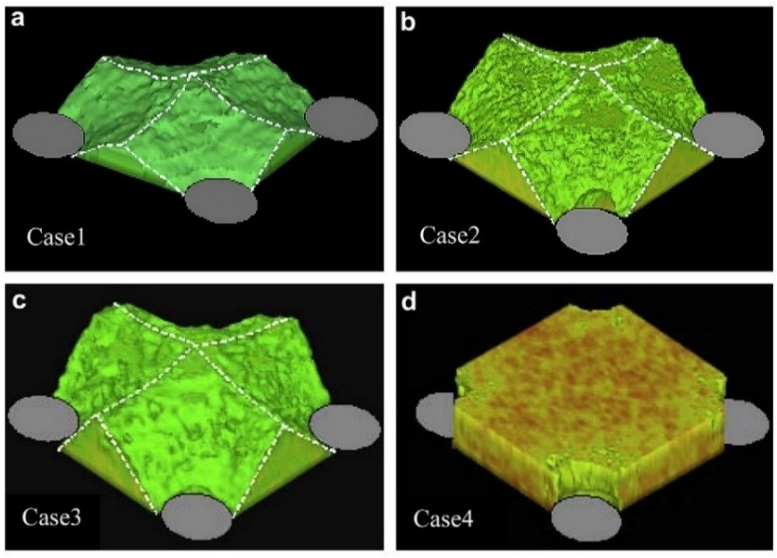

Figure 2.10. X-ray CT scanning - three-dimensional extraction images of arching without reinforcement **(a)** Toyoura sand, **(b)** Silica sand no. 7, **(c)** Silica sand no. 8 and **(d)** dry powder clay, with $s = 3d$ reproduced from Eskişar et al. (2012)

stresses (and not directly due to the inclusion of the geogrid). Without geogrid, the arching conditions transitions to the load recovery phase (at 17 % relative displacement) at the first CT scan. However, with geogrid present, the relative displacement would be much smaller and presumably (the geogrid deflection was not measured) closer to maximum arching at say 5 % relative displacement. i.e., even if the apparatus deflected downward 5 mm (to 17 % relative displacement), the relative displacement of the soil mass is limited by the geogrid deflection. In the author's experience, which is partly borne out from this literature review, the scaling of the geosynthetic for small scale tests is often problematic due to the requirement to scale the geogrid material properties, specifically the stiffness.

2.1.4 Arching observed in other geotechnical applications

The arching effect is also observed in tunnels as the crown of tunnel settles under the overburden stress. Brown et al. (1983) developed the so-called "Ground Response Curves" to assess the optimal time for tunnel support placement (see also Deere et al. 1969) . Arching is also observed in the granular flow of material between vertical wall (i.e., the silo problem), in pile plugging problems and in the formation of caves in karstic terrain (Waltham et al. 2007).

The concept of varying vertical load due to a ground arching effect is observed in underground excavations and it was this application that the GRC method was originally developed to assess. Deere et al. (1969) described the variation in load acting on both the walls and roof of an underground cavern as a function of deformation (Figure 2.12*a*). The ground arch forms between period t_0 and t_f and after time t_f it begins to fail (Blyth et al. 1984); a point of maximum arching is suggested. The deformation occurs as a function of time and Brown et al. (1983) found that this was dependent on rock strength, *in situ* stresses and the shape and size of the excavation. Based on these factors, Brown et al. (1983) developed "Ground Response Curves" which could be used to assess the optimal time for tunnel support placement. Examples of a support placed too early (Case A) and placed at the "optimum" time (Case B) are shown in Figure 2.12*a* after Deere et al. (1969).

Ward (1978) presented data from an experimental tunnel collapse (Figure 2.12*b*). Based on observation and the analysis of five extensometers, the progressive sagging and then collapse of the roof was observed over a period of about 800 days. As noted by Blyth et al. (1984), the behaviour observed by Ward (1978) shows good agreement with the load-deformation curve proposed by Deere et al. (1969). The progressive collapse of tunnel roof is similar (in a conceptual sense) to the progressive arching failure described in trapdoor tests in Sections 2.1.1 and 2.1.2. However, in this case, rock mass characteristics (rock strength, joint set and bedding orientation) play a significant role in the observed failure compared with the soil arching problem.

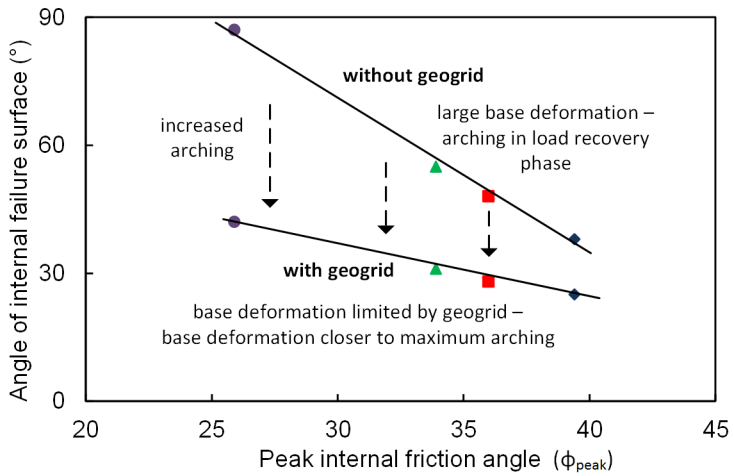

Figure 2.11. Angle of internal failure surface *vs* ϕ_{peak} for cases with and without geogrid (modified from Eskişar et al. 2012)

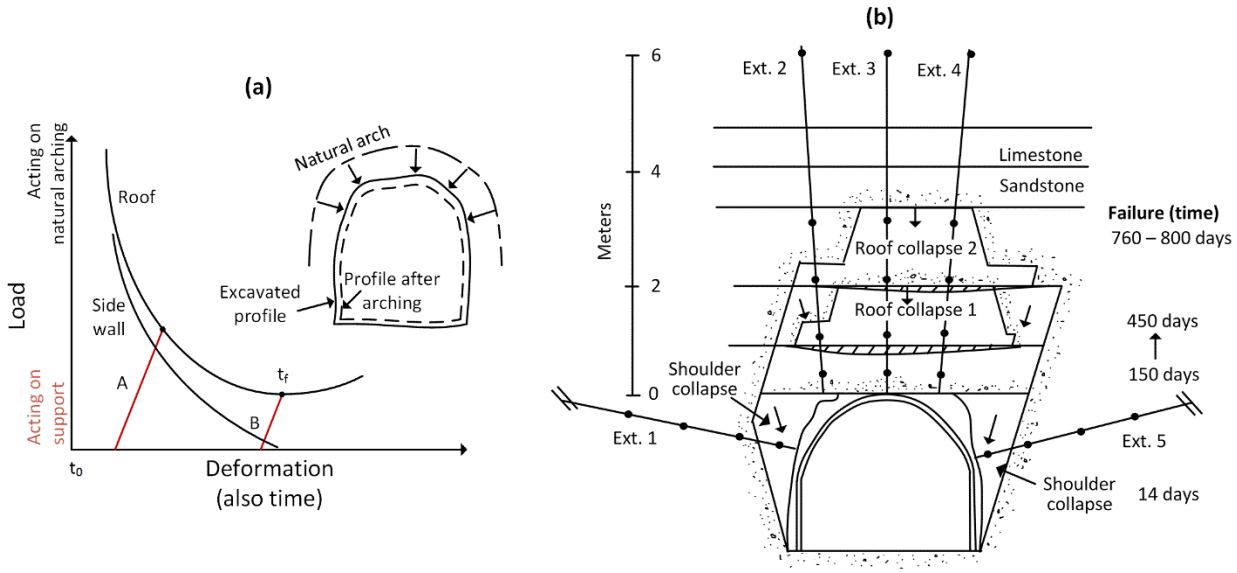

Figure 2.12. (a) Variation in load on roof and side wall due to deformation (and time) in an underground excavation (Deere et al. 1969) and **(b)** the sagging of a tunnel roof and collapse in an experimental tunnel (Ward 1978) from five extensometers (figures modified from Blyth and De Freitas, 1984) .

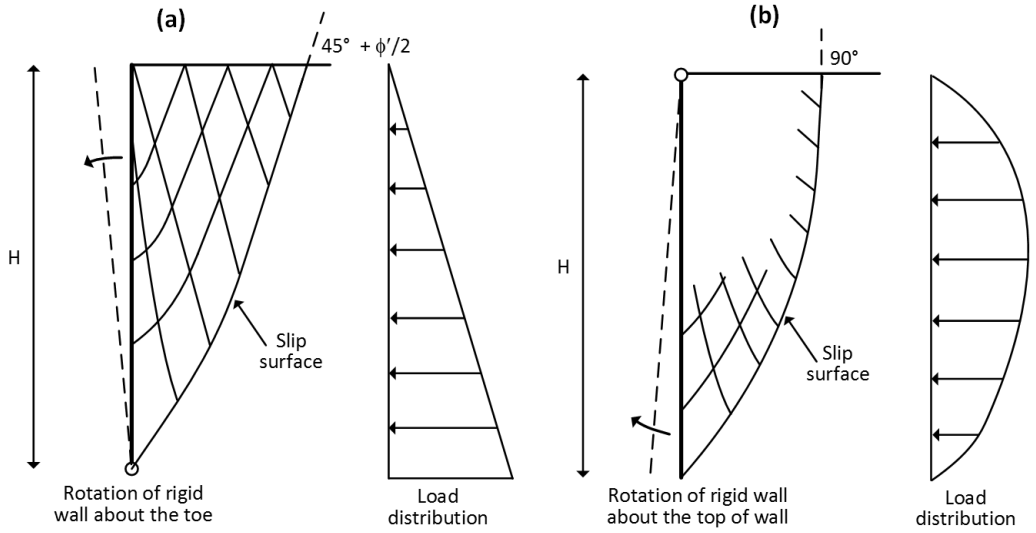

Figure 2.13. Slip surfaces and lateral load distribution acting on rigid rotating wall with a rough interface **(a)** rotation about the base and **(b)** rotation about the top of wall (Terzaghi 1943)

The effects of soil arching are also observed in retaining walls in several forms. A rigid retaining wall is able to yield by either rotation about the toe (Figure 2.13*a*), rotation about the top of wall (Figure 2.13*b*) and lateral translation (not shown). The slip surfaces are shown for two of these cases along with the lateral load distribution acting on the rigid wall for the case of a rough wall (Terzaghi 1943). Paik et al. (2003) adopted the assumption of Coulomb's theory of active earth pressure acting on a retaining wall (Coulomb 1776) and assumed the surface of sliding was planar rather than curved. Based on this assumption, Paik et al. (2003) used concepts presented in earlier work by Handy (1985) to describe the effects of arching behind a rigid retaining wall under active earth pressure.

Handy (1985) developed an arching model based on the arching mechanism which forms in backfilled trenches. In this case, the arching mechanism forms due to shear forces at the vertical interface between the backfill material, which is undergoing settlement, and the more rigid walls of the trench. The model described by Handy (1985) follows from earlier work by Marston and Anderson (1913) which assumed a flat arch with a lateral stress ratio, K, equal to the ratio of principal stress ($K_a = \sigma_1/\sigma_3$). This was shown to be incorrect by Krynine (1945) and was

correctly resolved using a Mohr circle with rotated principle stresses. Krynine's construction (Figure 2.14*a*) of a Mohr circle for arching stresses describes an arching element which is a downwards compressive arch with a surface represented by principal planes of zero shear stress. This is termed, by Handy (1985), as a "Minor principal stress arch".

It can be seen from Figure 2.14 that the principle stresses σ_3 and σ_1, have been rotated with σ_3 representing the plane of the arching element. Stress states A, B and C are represented on the Mohr circle as P_a, P_b and P_c respectively. In order to correctly represent the condition shown in Figure 2.14, Handy (1985) showed that the shape of the plane of minor principal stress must be that of catenary in order to satisfy moment equilibrium (assuming uniform density, thickness and weight throughout). Paik et al. (2003) used this concept to describe the variation in the lateral stress acting on a rigid retaining wall where a soil mass is moving downwards relative to a rigid vertical retaining wall and an assumed rigid planar sliding surface (Figure 2.14*b*). Goel et al. (2008) extended this concept by omitting the assumption of a planar sliding surface and described the stress conditions for a parabolic sliding surface which more closely resembles the sliding surface of a rigid retaining wall that has a rough interface.

Soil arching also occurs in soldier pile walls with timber laggings (King post wall), except in this case, the arching is observed in plan view as the soil mass moves towards the open excavation (Figure 2.15*a*). The more rigid soldier piles take increased lateral load due to soil arching while the load on the horizontal timber laggings is reduced. For this reason, some designers consider the load distribution acting on the timber lagging as an inverse triangular distribution rather than a uniform loading (Figure 2.15*b* and *c*) (as described by Vermeer et al. 2001). Thedeflection of the timber laggings in a soldier pile wall is much smaller than in a GRCSE due to the significantly higher flexural rigidity of the timber laggings compared with geosynthetic reinforcement in a LTP i.e., the arching conditions that develop differ due to difference in the displacement range of the two problems. Van Eekelen et al. (2013) also adopted an inverse triangular stress distribution in the "Concentric Arches" model, which is discussed below.

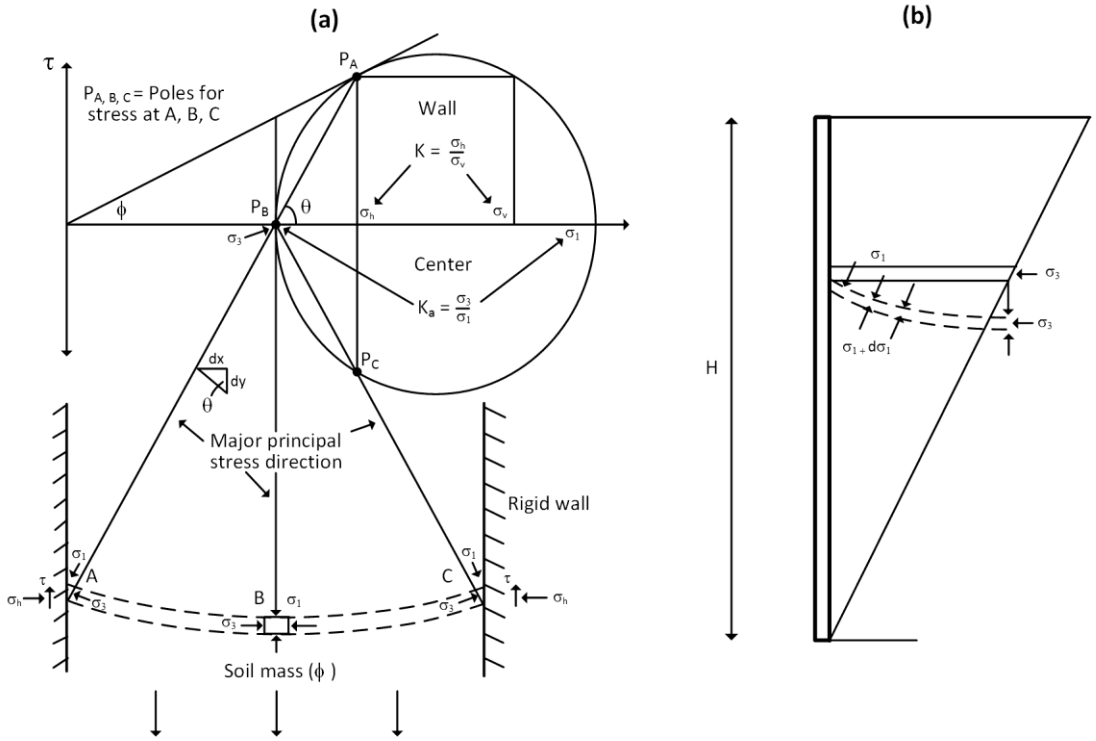

Figure 2.14. (a) Soil arching due to a soil mass settling between two rigid vertical walls (Handy 1985) and **(b)** soil arching concept applied to a retaining wall (after Paik and Salgado, 2003)

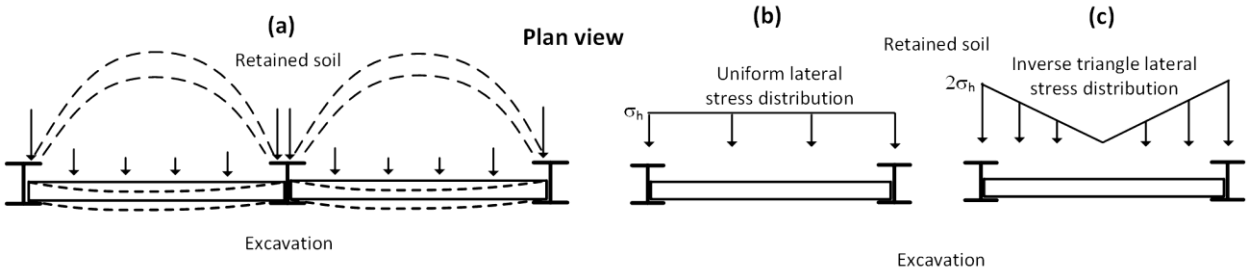

Figure 2.15 (a) Soil arching due to deflection of timber laggings in a soldier pile wall, **(b)** uniform stress distribution acting on timber laggings and **(c)** inverse triangular stress distribution.

Naturally occurring ground arching occurs in natural caves and can lead to a stable arch over a period of time. Typically, the tensile zones in a shallow roof structure will progressively collapse (a process known as stoping), increasing the height of the roof until a stable roof arch is formed. The height of the stable arch relative to the cave width is dependent on rock quality (Waltham et al. 2007). This process was described previously (Figure 2.12*b*) for the man-made experimental tunnel described by Ward (1978), however, in that case, roof stopping continued until a high-strength Sandstone bed was encountered which acted as a beam element and stabilised the tunnel. An arch which forms above a natural cave entirely under compression may be referred to as a "*voussoir arch*" (derived from the French for a stone arch). In many cases, continual roof stoping can continue through to the ground surface leading to the formation of collapse sinkholes, this is particularly common in karstic terrain (Waltham et al. 2007).

This chapter commenced with a quote from Terzaghi; "*Arching is one of the most universal phenomena encountered in soils in both the field and the laboratory*". The preceding examples serve to highlight this point and show that arching manifests itself in numerous natural and man-made geotechnical applications. A feature common to all of these applications is the development of arching over a deformation range. In the soil-structure applications, such as a soil mass sliding behind a rotating retaining wall, or the soil mass movement behind a king post wall, the deformation is often quite small. At the other end of the deformation range, the progressive collapse of roof structure in karstic terrain can lead to the formation of a "voussoir arch" and in some cases continual roof stoping can lead to sinkhole formation. From the work of Ward (1978) and Brown et al. (1983), who developed the so-called "Ground Response Curves", it would seem apparent that in tunnelling applications, the relationship between arching stress development and crown deformation is well understood, at least in a conceptual sense. Arching behaviour and the role of deformation was also highlighted in the small-scale three-dimensional laboratory testing of Eskişar et al. (2012) where the inclusion of geogrid was observed to "alter" the arching stress development due to the change in the deformation. Based on the understanding of arching behaviour outlined in Section 2.1, the arching models for GRCSEs are examined in detail in the following section.

2.2 Models for arching in GRCSEs

A wide range of arching models have been proposed for GRCSEs design. Van Eekelen et al. (2013) categorised the various models under the categories of frictional, mechanical, empirical models, rigid, limit equilibrium and this approach is also adopted here. The aim of this section is to describe the key arching models, how they are formulated and their underlying assumptions. The models I have outlined in greater detail have either been incorporated in design standards or are relevant to the present study. A number of these are summarised graphically at the end of this section in Figure 2.20. This is not intended to be a comprehensive assessment of all available methods as many methods are quite similar and are formulated based on similar assumptions.

The study of Tien (1996) provides, in the author's opinion, the most rigorous assessment of the arching models available at that time. In that study, there was a stronger emphasis on understanding these models within a framework of theoretical soil mechanics with an aim to describe a more generalised model of arching stress development. By contrast, the emphasis of many of the GRCSE arching models would appear to be describing accurately the stress acting on the geosynthetic reinforcement. As with any model which represents an idealisation of the physical behaviour it is necessary to achieve a balance between theoretical robustness and a model that is "fit-for-purpose". Where the purpose here is the engineering design of a GRCSE. A model has only limited use where its' output is restricted to an unrealistically small range of material parameters, geometric conditions or for the present case, a small range of deformation. Such models are particularly problematic where these model limitations are not explicitly stated or those that developed the models have not investigated its' limitations. It is shown in the following section that the divergence between model predications and observed behaviour in GRCSEs is primarily due to differences in the deformation range and that this stems from either a failure by those who develop the models to explicitly state model limitations or because they have not investigated, or understood, the model limitations. The examination of arching in Section 2.1 provides the theoretical background to identify and infer the limitations of the arching models presented in the following sections.

2.2.1 Empirical models

Marston and Anderson (1913) undertook an extensive research program to determine an empirical relationship describing the soil loads on buried pipes (i.e., arching in backfilled trenches). This work was later modified by Jones (1990) and adopted in the first published soil reinforcement design standard, the British standard BS8006-1995 (BSI, 1995) and more recently in BS8006-1 (BSI, 2010) (Corbet et al. 2011, Van Eekelen et al. 2013). Van Eekelen et al. (2011a) suggested further modifications. The modified Marston and Anderson model (Jones et al. 1990) is expressed in the three-dimensional situation for a GRCSE as follows:

$$\frac{\sigma_c}{(\gamma H + q)} = \left(\frac{C_c}{H}\right)^2 \qquad \textbf{(2.7)}$$

Where σ_c is the stress acting on the columns and the material properties are accounted for indirectly by the experimentally derived factor (C_c). The arching stress is calculated independent of the deformation of geosynthetic reinforcement so it is not clear what phase of arching the model describes, further it is not clear if the state of arching stress development in a GRCSE is compatible with the arching stress development in a backfilled trench; the geometric and deformation conditions differ greatly. A model of this type is suitable for a first order calculation of arching stresses. Importantly, it cannot describe the progressive development of arching stresses.

2.2.2 Frictional models

Are number of models are considered in this category. The model of McKelvey III (1994) which extended the frictional model of Terzaghi described in Section 2.1.1 is one such model. Other models include those by McGuire (2011) and Russell et al. (1997). Naughton (2007) proposed a model for preliminary design which calculates the critical height. The model incorrectly predicts an increasing critical height with increasing friction angle (frictional angles 28° and 42°, H_c = 0.92 m and 1.65 m respectively), this contradicts a significant amount of laboratory testing presented previously which shows increased arching with a higher friction angle. Van Eekelen et al. (2013) noted that the frictional models are not typically adopted in European design. It was suggested that this is largely due to the use of a lateral earth pressure coefficient (K) term in these models which is difficult to determine. While these

models are an improvement on the empirical model described in the preceding section as they incorporate material properties directly, they suffer from similar limitations. The deformation of the geosynthetic is not explicitly stated and as a result it is difficult to determine if the state of arching inherently assumed in these models is consistent with the state of arching that develops in a GRCSE.

2.2.3 Models using mechanical elements

These models differ considerably from the preceding models in that they describe the behaviour of the LTP by modelling the components of the LTP (i.e., the columns, fill, sub-soil and geosynthetic reinforcement) as mechanical elements. The Load-Displacement Compatibility (LDC) method is an example of this approach and is based on the work of a number of researchers at Virginia Polytechnic Institute, USA, (see for example Filz and Smith, 2006, Filz and Plaut, 2009, and Filz et al. 2012) . The LDC method expresses the separate elements as a series of differential equations written as a function of base settlement of the LTP (i.e., the boundary conditions for each of the elements are equivalent). The LDC method describes the arching-deformation relationship as bi-linear with the linear portion approximated from the linear-elastic solution for a circular footing on a semi-infinite mass (Poulos et al. 1974) and the limiting stress (SRR_{lim}) established from the Adapted Terzaghi method (Russell et al. 1997), which describes the terminal state of arching. The maximum arching and load recovery phases of soil arching are not described by this bi-linear relationship. This bi-linear arching stress-deformation in incorporated into a method comprising a 10-step procedure and an accompanying Excel spreadsheet titled "GeogridBridge". This is described in further in Section 2.6.2.

Other examples of arching models which incorporate "mechanical elements" include Deb et al. (2007), and Deb et al. (2008) which simulated the soft soil, granular layer, geosynthetic and columns (stone columns) as non-linear spring-dashpots (Kelvin-Voight model), Pasternak shear layer, rough membrane(s) and stiff non-linear Winkler springs, respectively. These models ignored soil arching. A similar publication by Deb (2010) apparently studied the soil arching behaviour by comparing the stress acting on the columns and soft soil. The Pasternak shear layer, which represents the LTP and governs the "arching", describes the transverse shear through the LTP as a linear-elastic, perfectly-plastic shear response. This inherently assumes vertical shear planes through the LTP (i.e., similar to the terminal condition described by Terzaghi); this is gross over simplification of the arching behaviour (see Section 2.1).

Maheshwari et al. (2009) sought to extend the use of mechanical elements further by replacing the Pasternak shear layer (to model the LTP) with a Euler-Bernoulli beam, which accounts for bending deformation, for a basal reinforced embankment. Zhang et al. (2012) adopted the same concept for the case of a GRCSE. The assumptions underlying Euler-Bernoulli beam theory include; 1) small deformation/deflection and 2) cross sections through the beam are perpendicular to the neutral axis (Figure 2.16*a* and *b*) the thickness of the beam is relatively thin compared with its' length. There is a significant body of experimental work investigating GRCSE that shows that these first two conditions are invalidated in most GRCSEs. The output of these mathematical models by Deb (2010) and Zhang et al. (2012) amongst others, do not agree well with laboratory and field data describing LTP behaviour. The approximation of the LTP behaviour using beam theory has a questionable theoretical basis and the studies which have adopted this approach are yet to demonstrate agreement with laboratory of field data.

2.2.4 Rigid arch/fixed models

Rigid arch (or fixed) models are simplistic models that assume a "failure surface" to assess the arching stresses. The force acting on the geosynthetic reinforcement is due to the mass of material beneath this "failure surface"; forces

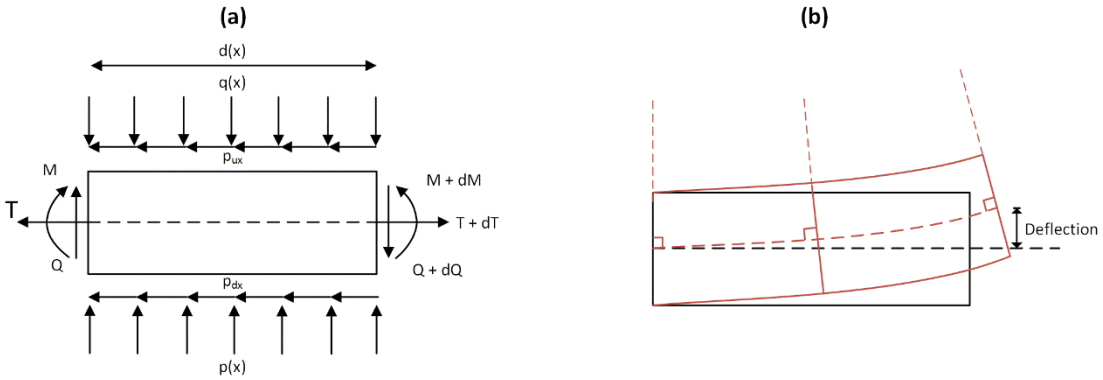

Figure 2.16. Euler-Bernoulli beam segment **(a)** free-body diagram and **(b)** cross sections perpendicular to neutral axis

are not resolved along the failure plane as in limit equilibrium models. Whether this assumed failure surface bears any resemblance to the conditions which develop in reality will largely dictate the success, or otherwise, that these models have in describing the stress conditions acting on the geosynthetic reinforcement.

The "Nordic Guidelines for Reinforced Soil and Fills" (Rogbeck et al. 2004) describes the ultimate limit state condition of arching as a wedge of soil with sides 75° to the horizon (Figure 2.20*a*). This method was extended from the two-dimensional condition described by Carlsson (1987) into three-dimensional by Rogbeck et al. (2004). An initial strain of less than 6 % is recommended and this can be used to assess the mid-span displacement using a simple two-dimensional and three-dimensional force-equilibrium calculation. It is noted that the geosynthetic reinforcement deflection is typically between 100 mm and 200 mm for Swedish cases and that no practical experiences are known where larger displacements have been tolerated. Svanø et al. (2000) adopted a similar approach with a β value defining the angle of the soil wedge (Figure 2.20*b*), where β is measured relative to the horizontal direction. Suggested β values are between 2.5 and 3.5 and the angle of the soil arching to the horizon varies between 68° and 74°.

The Collin method (Collin 2004) considers the LTP to behave as a "beam" element rather than a catenary with four layers of geosynthetic reinforcement at a minimum of 150 mm vertical spacing. The arching behaviour is described by a (rigid) triangular vaulted structure in three-dimensional with 45° slopes (Figure 2.20*c*). Collin et al. (2005) presented a modified beam method which included an additional catenary layer of reinforcement at the base of the LTP. The height of the LTP must be at least equal to half the width of the clear span between columns (s − a). Lawson (2013) showed that the vertical stresses in the area between columns was considerable lower when using the Collin method compared with other limit-state equilibrium models and furthermore, the arching ratio is independent of the s/a ratio which is incorrect.

From the preceding discussion on the relationship between arching stress development and deformation (see Section 2.1) it follows that rigid arch models will provide a "point" on the GRC. This behaviour is highlighted by Evans (1983) in Figure 2.6 where the angle of the discontinuity (failure surface) was found to vary between about 60º and 90º. The questions which follows are; what deformation is required for this "rigid arch" condition to develop? Is this deformation compatible with the geosynthetic reinforcement deflection (i.e., between 100 mm and 200 mm in the ultimate limit state condition)?

The answer is that compatibility is achieved when the geosynthetic reinforced sags and is in (internal) equilibrium with the (external) applied stress acting on it (due to arching). This equilibrium condition will depend on the stiffness of the geosynthetic reinforcement and the dilation angle of the granular material in the LTP (a granular

material with φ >35º is recommended by Rogbeck et al. 2004). For the 70º failure surface to develop the granular material must achieve a dilation angle or at least 20º (see Section 2.1.2). Even if these conditions of dilation angle and geosynthetic stiffness are satisfied, this does not ensure that there is deformation compatibility. In other words, this "rigid arch" condition may develop while the geosynthetic reinforcement is still sagging and not yet in equilibrium.

These methods may in some cases be appropriate for a first-order design check and can be conservative provided the additional requirements in Rogbeck et al. (2004) are followed. However, with improved understanding of GRCSE behaviour the rigid arch models have been (or should be) largely superseded by limit equilibrium models. Rigid arch models rely on assumptions that are (often) not explicitly stated and there is a reasonable likelihood that the state of arching stress that develops in the field, will be inconsistent with the "rigid arch" shape proposed in the model. Furthermore, these models provide no insight into the serviceability behaviour of the LTP, which in many cases will govern whether the LTP design satisfies embankment performance criteria.

2.2.5 Limit state equilibrium models

Limit equilibrium models are the most widely adopted category of arching models and several have been implemented into design standards. The limit equilibrium method is one of three limit analysis techniques, alongside the slip-line method and the well-known limit state analysis theory, which considers lower and upper bounds, and was widely used prior to the introduction of numerical approaches. The limit equilibrium methods in GRCSE design include the Hewlett and Randolph model (1988) which has been adopted in the French ASIRI guideline (2012) and is an alternative arching model in the revised British standard BS8006-1 (2010). Hewlett and Randolph described the soil arch as a series of three-dimensional hemispherical vaults, the two-dimensional representation is shown in Figure 2.20*d*.

Kempfert et al. (1997) followed a similar approach but suggested replacing the three-dimensional hemispherical vaults with a multi-shell arch and incorporating sub-soil support; the latter is a considerable improvement on the method of Hewlett and Randolph. Zaeske (2001) (in German) undertook 1-g laboratory testing of 1:3 scale models and developed this "multi-shell" arching approach using lower bound plastic limit theory (Figure 2.20*e*). The differential equation resulting from the equilibrium of forces acting on a three-dimensional soil element in the radial direction is shown in Figure 2.20*e*. This method is described in English by Kempfert et al. (2004), in the German design method (EBGEO; German Geotechnical Socity, 2010) and Dutch guidelines (CUR226 2010).

The stress distribution due to arching is described by differential equations derived by Zaeske (2001) where the stress acting between the columns (and on the geosynthetic reinforcement) is denoted $\sigma_{zo,k}$. The solution to the differential equations can be obtained either analytically (Equation 2.8) or graphically using the plots in EBGEO.

$$\sigma_{zo,k} = \lambda_1^{\chi}\left(\gamma_k \frac{p_{G+Q,k}}{h}\right) \times \left\{ h\left(\lambda_1 + h_g^2\lambda_2\right) + h_g\left[\left(\lambda_1 + \frac{h_g^2\lambda_2}{4}\right)^{-\chi} - \left(\lambda_1 + h_g^2\lambda_2\right)^{-\chi}\right]\right\} \quad \textbf{(2.8)}$$

$$\chi = \frac{d(K_{crit} - 1)}{\lambda_2 s} \quad \textbf{(2.9)}$$

$$\lambda_1 = \frac{1}{8}(s - d)^2 \quad \textbf{(2.10)}$$

$$\lambda_2 = \frac{s^2 + 2sd - d^2}{2s^2} \quad \textbf{(2.11)}$$

$$K_{\text{crit}} = \tan^2(45^\circ + \frac{\phi'_{\text{k}}}{2}) \quad \textbf{(2.12)}$$

γ_{k}	Characteristic unit weight of soil in the reinforced earth structure (kN/m^3)
ϕ'_{k}	Characteristic value of the friction angle of the reinforced earth structure (°)
$p_{\text{G,+Q,k}}$	Characteristic value of the permanent (G) and variable distributed (Q,k) load on the top of the reinforced earth structure (kN/m^2)
h_{g}	Arch height in m: $h_{\text{g}} = s/2$ for $h \geq s/2$ $h_{\text{g}} = h$ for $h < s/2$
h, s and d	Refer to Figure 2.1

The solution for ϕ'_{k} = 30º is shown in Figure 2.17 for various geometric arrangements. Additional graphical solutions for ϕ'_{k} = 32.5°, 35° and 37.5° are provided in EBGEO (German Geotechnical Society, 2010). Figure 2.17 highlights a number of trends relating to the arching stress condition and embankment geometry:

- For constant d/s ratio, normalised stress decreases (i.e., increased arching development) initially as embankment height increases and then asymptotes. This asymptotic behaviour suggests that a minimum embankment height is needed for arching to develop fully. At h/s = 0.25 for example, the effects of arching are quite small (i.e., $\sigma_{\text{zo,k}}$ is close to the overburden stress).
- The asymptote observed at high h/s values suggests that the magnitude of stress $\sigma_{\text{z0,k}}$ increases for increasing embankment height as might be reasonably anticipated. By comparison, in a rigid arch model, the stress $\sigma_{\text{z0,k}}$ would be constant and independent of h which is incorrect.
- With an increasing d/s ratio (i.e., with a denser layout of rigid elements) a more effective arching mechanism is realised with a lower normalised stress value.

More recently the Concentric Arches model (Van Eekelen et al. 2013), was developed based on extensive laboratory testing (Van Eekelen et al. 2012a, 2012b) and validated against several field case studies (Van Eekelen et al. 2015), was proposed and incorporated into the revised Dutch standard (CUR226 2016). The key difference with this method is the arching development is described as a series of concentric arches which progressively develop

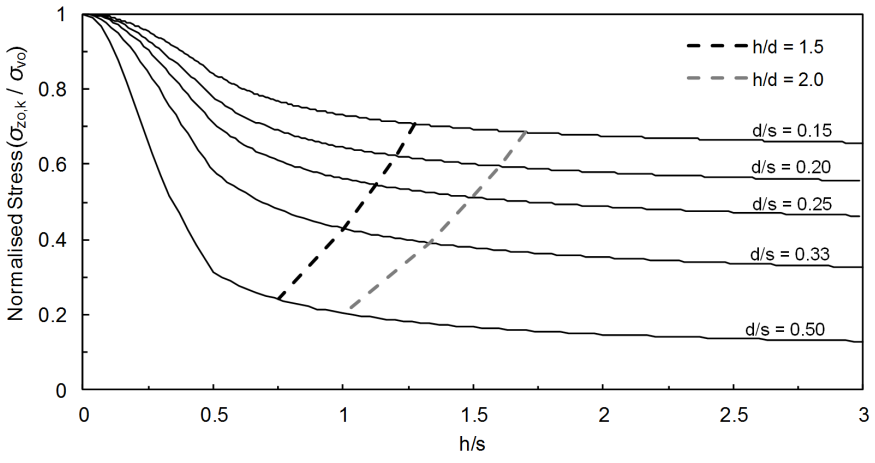

Figure 2.17. Normal stress $\sigma_{\text{z0,k}}$ between rigid point bearing elements for ϕ'_{k} = 30°

(conceptually), however, as noted by van Eekelen et al. (2013) "…*in practical applications, a limit-state version of the model will be applied. In that case, the concentric arches model behaves in a rigid-plastic way and will no longer describe the influence of subsoil consolidation or deformation."* i.e., the progressive arching development, while suggested by Van Eekelen et al. (2015) in the conceptual formulation of their model, is not an output of the model. The other contribution of this Concentric Arches model is that the load distribution acting on the geosynthetic reinforcement which is described as a "inverse triangle" rather than the triangular distribution as assumed in EBGEO (see Section 2.3).

In some respects, limit equilibrium models are not that dissimilar to the "rigid arch" models as they too rely on an assumption regarding the failure surface(s); this is an inherent assumption in any limit equilibrium method. This failure surface can be assumed to form any shape (i.e., a three-dimensional hemispherical vault or multi-shell arches for example) but this may, or may not, bear any resemblance to the true failure surface depending on the dilatancy angle (see Section 2.1). Despite the significant advances that Zaeske's method offers compared with rigid arch models (such as the incorporation of sub-soil support, ensuring force equilibrium along the failure surface) these models also suffer from the same limitations as the rigid arching models; they plot as a "point" on the GRC and may not satisfy deformation compatibility. This is particularly important when considering serviceability behaviour.

2.2.6 Summary – arching behaviour

From the above discussion it is apparent that the categories of rigid, frictional and empirical soil arching models are at this point in time largely superseded by limit equilibrium models which have been specifically developed in recent years for assessing arching stresses in GRCSEs (i.e., Zaeske model and Concentric Arches model). The limit equilibrium models are now widely incorporated in design standards in use throughout Europe. In the author's opinion, the category of mechanical elements, such as the Load-Displacement Compatibility method may offer a viable alternative approach for LTP design. These models have the advantage of being formulated to describe the entire LTP behaviour and not just the arching stress behaviour, however, these model has not found wide spread use beyond North America. Other mechanical elements models, such as those which simulate the LTP behaviour using beam theory, have a questionable theoretical basis and are not considered viable alternatives to established methods in the author's opinion.

The ability of an arching model to describe stress development in an LTP is highlighted in Figure 2.18*a* through the use of an analogy where limit analysis techniques are applied to a material exhibiting pronounced strain softening behaviour. When using limit analysis techniques to assess the collapse load of such a material it is necessary to ignore the strain softening behaviour of the stress-strain curve due to the assumption of perfect plasticity. The validity of an assessed collapsed load, where perfect plasticity is assumed, is dependent on the deformation range, the problem geometry and boundary stress; its' relative position will be somewhere between the bounds of peak and residual shear strength (Chen and Liu 1975). This analogy is equivalent to the behaviour observed during arching stress development where the inverse of the stress reduction ratio is plotted (Figure 2.18*b*).

Typical limit analysis problems are load controlled (i.e., the loading of a footing) and this differs fundamentally with arching stress development in a GRCSE which is displacement controlled (by the geosynthetic reinforcement and sub-soil support). Regardless, while the limiting arching condition is not a collapse load, the model which describes it must still ensure a compatible deformation range if ultimate limit state conditions are to be described successfully using limit analysis techniques. Iglesia (1991) has shown for a trapdoor test that maximum arching occurs within the range of 2 % to 4 % relative displacement. It follows then, that for models which describe

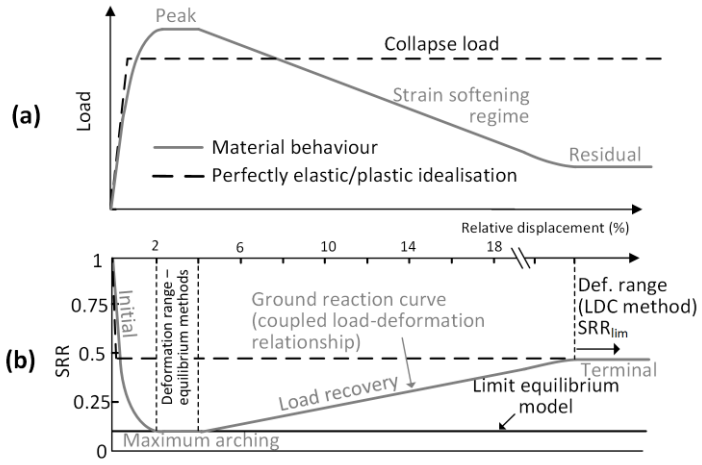

Figure 2.18. (a) Arching analogy with strain softening material and **(b)** arching behaviour

maximum arching, deformation compatibility may only be achieved up to a relative displacement of 4 %. The appropriateness of an ultimate limit state arching model which is formulated to describe maximum arching is questionable on the following basis:

1) This is the least conservative state with respect to the stress acting in the un-arched zone and is analogous to a collapse load formulated to describe peak strength. This is usually avoided for strain softening material as brittle failure will result where peak strength is exceeded.
2) Deformation (base settlement) must be limited to a very small relative displacement range (up to about 4 %). This is difficult to achieve even where very high strength geogrids are adopted. Unless, there is a considerable reliance on sub-soil support, which in itself is questionable at an ultimate limit state condition.

Arching stress development in a GRCSE is therefore a problem of deformation compatibility (Figure 2.19). In Figure 2.19, several arching stress-deformation relationships are shown. These include the bi-linear relationship adopted in the Load-Displacement compatibility (LDC) method (Filz et al. 2012) (described further in Section 2.6.2), the GRC and a constant load-deformation relationship as obtained through a limit equilibrium model (or any of the rigid arch, frictional model, or empirical approaches which decouple the arching stress deformation relationship). The difference in arching stress values depends greatly on the stiffness of the geosynthetic reinforcement (and sub-soil support) which control the base settlement. A model which describes arching in a GRCSE is more complex than the two-dimensional plane strain trapdoor test considered previously due to the three-

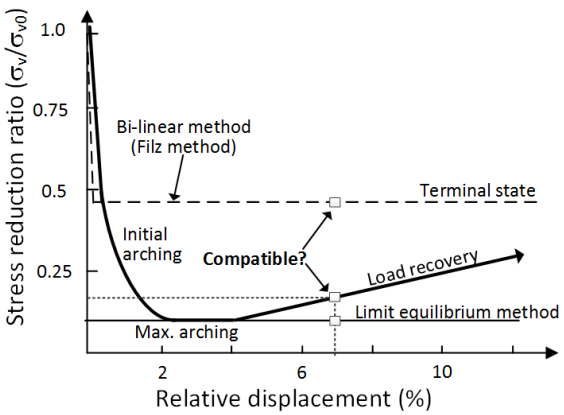

Figure 2.19. Comparison of arching stress-deformation relationships for three models; 1) bi-linear, 2) GRC and 3) limit equilibrium method

dimensional geometric arrangement. However, similar arching behaviour showing initial, maximum, load recovery and terminal phases of arching have been observed for three-dimensional trapdoor tests (see for example Evans, 1983 and Chevalier and Otani, 2011). It is hypothesised that the arching mechanism described in terms of soil material properties and deformation as adopted in GRC method should describe the governing behaviour reasonably well. To account for the differences in geometric conditions; we replace the trapdoor width (B) in the two-dimensional plane strain case with an equivalent axisymmetric condition (i.e., as unit cell representation), defined by column spacing (*s*) and column head diameter (*d*) in the three-dimensional case. When outlining the basis for the Concentric Arches model van Eekelen et al. (2013) noted the following:

> *"Most of the existing arching models assume that a slight deflection of the geotextile is sufficient to create a 'full arch'. However, the measurements showed that A increases with increasing GR deflection (due to subsoil consolidation). The influence of deformation cannot be incorporated in rigid-plastic models such as the equilibrium models [or Concentric Arches model] or frictional models. A new class of models would be needed. This would, however, conflict with the initial principle of keeping as closely as possible to existing design models, and it is beyond the scope of this paper. A 'work-around' is presented in section 4.2: the development of concentric arches."*

It is not clear to the author what the motivating circumstances were which dictated that this new arching model developed and presented in van Eekelen et al. (2013), which was based on an extensive laboratory testing program, should keep "*as closely as possible to existing design models".* The author infers that this suggests developing a limit equilibrium model which follows the underlying "*2-step*" design approach and to that end, the development of the Concentric Arches model was successful. However, given that stringent settlement tolerances and performance criteria typically govern the design of a GRCSE, it is deformation that governs acceptable LTP behaviour, not ultimate state load conditions.

Therefore, it is the author's position that further improvements in the understanding of LTP behaviour, and improvements in the design of GRCSEs, requires the incorporation of sub-soil settlement as a governing parameter in an arching-deformation model. The aim of this thesis is to develop a framework to satisfy these requirements and demonstrate the viability of this approach.

2.2.7 Numerical modelling of arching behaviour

From a computational geomechanics viewpoint, the trapdoor test is a well-known large strain problem and the ability to simulate problems of this type over a large displacement range using current continuum based approach such as the Finite Element Method (FEM) is quite limited (Więckowski 2004). Typically, advanced methods such as Coupled Eulerian-Lagrangian (Qiu et al. 2011, Pucker et al. 2012), point based (meshfree) methods such as smooth particle hydrodynamics (Bui et al. 2008) or the material point method are required. In addition, it was noted in Section 2.1.1 that the corner of the trapdoor is a singularity point; the limitations of modelling such points using FEM are well described by de Borst and Vermeer (1984) and van Langen and Vermeer (1991). It is perhaps then not surprising to find the following note in EBGEO (German Geotechnical Society, 2010):

> "*Comparative investigation of test and analysis results have shown that numerical analysis, e.g. using the finite element method, result in substantially reduced characteristic tensile stresses in the geosynthetic reinforcement…"* and the following recommendation; *"Because cause and effect and their interrelationships are not yet sufficiently clarified, the effect on the geosynthetic reinforcement and the system [LTP] design may not be based on numerical analyses."*

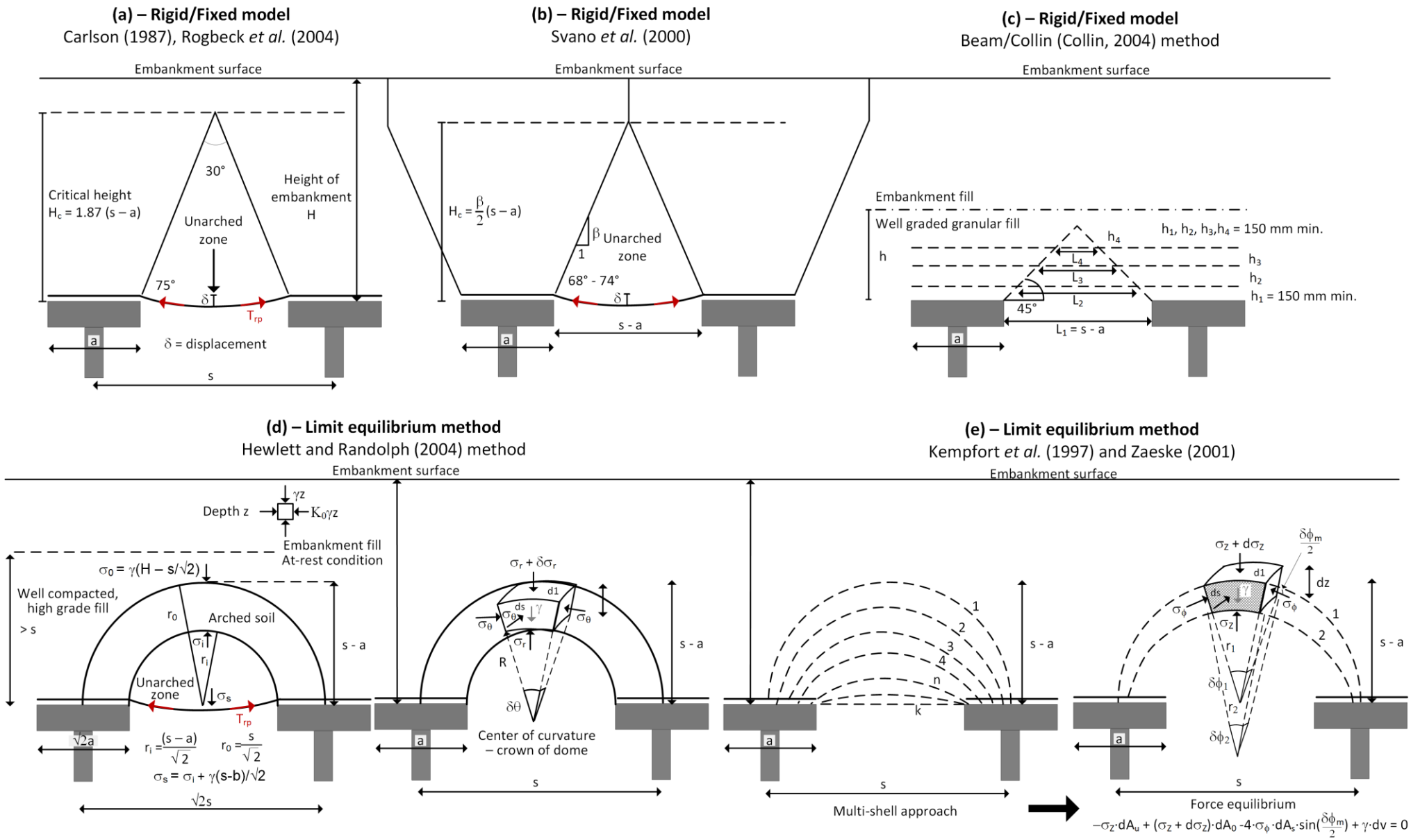

Figure 2.20. (a) Nordic guidelines - Rogbeck et al. (2004), modified from Carlsson (1987) **(b)** Method of Svanø et al. (2000) **(c)** Beam/Collin method (Collin 2004) **(d)** Hewlett and Randolph (2004) method **(e)** Multi-shell arching model Zaeske (2001) (in German) and Kempfert et al. (2004) (in English).

A more detailed literature review of the numerical modelling of soil arching behaviour is presented in Chapter 6 where the objective is to assess the extent to which the GRC can be described by a numerically simulated trapdoor test using the FEM. The two-dimensional finite element modelling software package "PLAXIS" is used here for this purpose. This FEM software package is widely used by practicing geotechnical engineers to perform deformation and stability analysis of various types of geotechnical problems. Based on the numerical analysis of the trapdoor tests, these findings are used to model and explore the development of arching in the field case study. The limitations of this approach are described. To address these limitations, the meshfree method "Smooth Particle Hydrodynamics" (SPH) is introduced in Chapter 6 to model the trapdoor and field arching behaviour. Comparison between the results obtained using these two numerical techniques is presented and the advantages and limitations of each are discussed.

2.3 Membrane behaviour

With knowledge of the stresses acting on the geosynthetic reinforcement, concepts related to membrane theory can be employed to evaluate the force, strain and deflection of the geosynthetic reinforcement. Compared with the large number of arching models available, there are relatively few methods available that describe the geosynthetic reinforcement behaviour in a GRCSE. It is reasonable to note that the difficulties in assessing the behaviour of the geosynthetic reinforcement primarily relate to the uncertainty in the applied stress acting on the reinforcement (i.e., due to arching) rather than difficulties in describing how the membrane will respond to a known applied stress. Geosynthetics do however differ from other civil engineering construction materials (steel, concrete, timber) and soil, in that the polymers which form a geosynthetic undergo significantly greater amounts of creep behaviour (viscoelastic/viscoplastic) under constant load. These characteristics of the geogrid adopted for the case study are described in Section 3.2.1.

In assessing the behaviour of the geosynthetic, it is not just the magnitude of the applied stress but also the distribution of the applied stress (i.e., uniform, triangular or inverted triangular distribution). Van Eekelen et al. (2013) has studied this behaviour extensively and concluded that the applied stress is best approximated as an inverse triangular distribution. The methods available to assess the behaviour of the geosynthetic are well described by Sloan (2011) and are summarised below:

Parabolic method - (Giroud 1995)

This method was one of the earliest developed for GRCSE design and approximates the reinforcement shape as parabolic between two supports. The strain in the geosynthetic reinforcement (ε) is given as a function of clear spacing (s − a) between columns and the maximum deflection at the mid-span (δ) as follows:

$$\varepsilon = \frac{1}{2}\sqrt{1+16(\frac{\delta}{s-a})^2} + \frac{s-a}{8\delta}\ln\left[\frac{4\delta}{s-a} + \sqrt{1+16(\frac{\delta}{s-a})^2}\right] - 1 \qquad \textbf{(2.13)}$$

Giroud (1995) noted that this can be approximated as follows:

$$\varepsilon \approx \frac{8d^2}{3(s-a)^2} \qquad \textbf{(2.14)}$$

Within the strain range of interest for GRCSE the approximate solution is appropriate for most applications (Figure 2.21). This simplistic method highlights an important point; at small values of base settlement (< 50 mm) the strain

mobilised is relatively small (at 50 mm deflection it is less than 1 % strain) due to the planar nature of the reinforcement.

The relationship between ε, tension (T) and a uniform applied stress (σ_v) is used in the Nordic design method and BS8006-1995 (BSI, 1995) amongst others:

$$T = \frac{\sigma_v(s^2 - a^2)}{4a}\sqrt{1 + \frac{1}{6\varepsilon}} \quad \textbf{(2.15)}$$

Tensioned membrane method (Collin 2004)

The tensioned membrane method is described by Collins (2004) as follows:

$$T = \frac{\sigma_v(s - a)\Omega}{\sqrt{2}} \quad \textbf{(2.16)}$$

Where the dimensionless parameters Ω is defined as follows:

$$1 + \epsilon = 2\Omega\sin^{-1}\left(\frac{1}{2\Omega}\right) \quad \textbf{(2.17)}$$

Method of Zaeske (2001)

The method of Zaeske (2001) is used in EBGEO (2010) and enables separation of the Part B and Part C load components acting on the reinforcement. This approach assumes the stress acting over the coverage area (Figure 2.22) can be approximated with an equivalent 2-D line load acting between columns. Load coverage areas A_{Lx} and A_{Ly} are defined for a rectangular column array as follows:

$$A_{Lx} = \frac{1}{2}(s_x s_y) - \frac{d^2}{2}\tan^{-1}\left(\frac{s_y}{s_x}\right)\frac{\pi}{180} \quad \textbf{(2.18)}$$

$$A_{Ly} = \frac{1}{2}(s_x s_y) - \frac{d^2}{2}tan^{-1}\left(\frac{s_x}{s_y}\right)\frac{\pi}{180} \quad \textbf{(2.19)}$$

The method of Zaeske (2001) assesses membrane behaviour by considering the reinforcement as a cable with a line load acting on it. Sub-soil support is also included as a modulus of subgrade reaction (linear elastic spring) which is

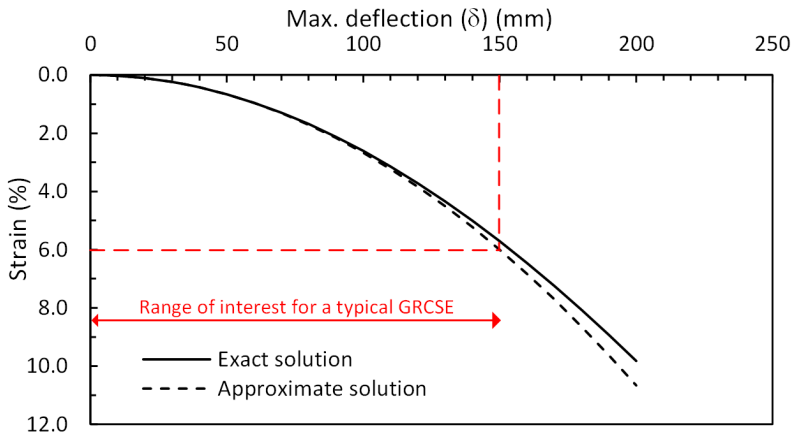

Figure 2.21. Parabolic method (Giroud 1995) – exact and approximate solutions

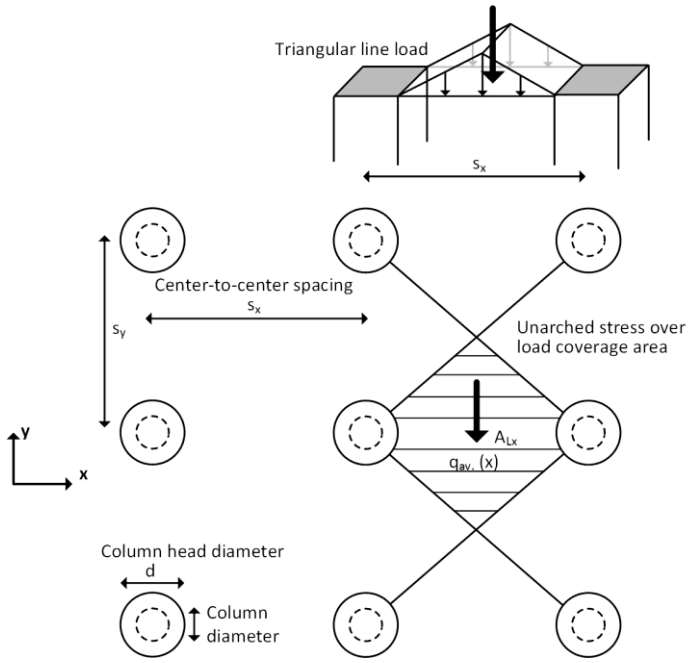

Figure 2.22. Assessment of load acting on reinforcement based on method of Zaeske (2001)

assumed to provide uniform support beneath the cable. This theoretical cable, representing the reinforcement, can be described using the following differential equation:

$$\frac{\mathrm{d}^2 w}{\mathrm{d}x^2} = \frac{q(x) - r(x)}{T} = \frac{q(x)}{T} - \frac{K_s w(x)}{T} \qquad \textbf{(2.20)}$$

w	Vertical deformation of the cable (m)
$r\,(x)$	Sub-soil support (kPa)
x	Horizontal distance (m)
$q\,(x)$	Loading on the cable (kPa)
K_s	Modulus of subgrade reaction (kN/m^3)

The solution (ε_{max} and δ) to Equation 2.20 is based on geogrid stiffness (J) and a triangular load distribution q(x) (Figure 2.23*a*). The factor of 0.5 in Figure 2.23 is included on the net force as this force is proportioned from a unit cell evenly in the x and y direction and q_{av} is the average stress acting in the area between columns was calculated using an arching model. The solution is presented graphically in EBGEO (German Geotechnical Society, 2010) as a function of calculation factors F1, F2 (for square array $s_x = s_y$):

$$F_1 = \frac{0.5(B + C)/a}{J} \qquad F_2 = \frac{K \cdot (s - a)^2_{x,y}}{J} \qquad \textbf{(2.21)}$$

Geosynthetic reinforcement – strain localisation

A common feature of these three methods is that they predict uniform strain (and tension) along the length of the reinforcement which is contrary to experimental data (described below) and numerical analysis (Han et al. 2002, Jones et al. 2010) which observed localisation of strain near the column supports. This behaviour has been

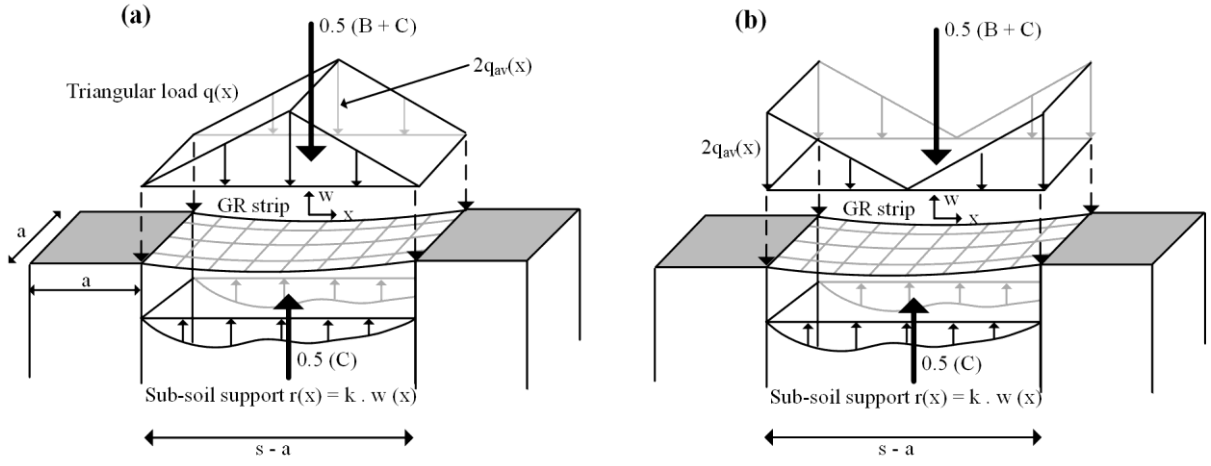

Figure 2.23 (a) Zaeske (2001) triangular load and **(b)** Van Eekelen et al. (2012b) inverted triangular load

investigated extensively by van Eekelen et al. (2012b, 2012c) who proposed using an inverted triangular line load to better represent the load acting on the reinforcement. This is similar to the approach taken to describe the non-uniform load acting on timber laggings in a solder pile wall due to arching as shown in Figure 2.15. If the triangular load is replaced with an inverted triangular load the differential equation is solved (see van Eekelen et al. 2012c) for full derivation) and the following result is obtained:

$$z(x) = -\frac{\mathrm{Q}}{k_{\mathrm{s}} L \alpha}(Me^{\alpha x} + (M-2)e^{-\alpha x} - 2\alpha x) \quad \textbf{(2.22)}$$

$$z'(x) = \frac{T_{\mathrm{v}}}{T_{\mathrm{H}}} = -\frac{Q}{k_{\mathrm{s}} L \alpha}(Me^{\alpha x} - (M-2)\alpha e^{-\alpha x} - 2\alpha) \quad \textbf{(2.23)}$$

$$T(x) = T_{\mathrm{H}}\sqrt{1 + \left(\frac{T_{\mathrm{v}}}{T_{\mathrm{H}}}\right)^2} \quad \textbf{(2.24)}$$

$$\varepsilon(x) = \frac{T(x)}{J} \quad \textbf{(2.25)}$$

Where:

$$\alpha^2 = \frac{k_{\mathrm{s}}}{T_{\mathrm{H}}}$$

To investigate the three-dimensional behaviour of a geosynthetic reinforcement subjected to arching behaviour, Jones et al. (2010) used a mechanical element approach with a uniform stress acting on the soft soil (between the column heads) and a larger uniform stress acting on the column heads with the geosynthetic modelled as a thin, flexible, isotropic, homogeneous plate with a linear stress-strain response. The axial response of the columns and soft soil was approximated with linear springs and the frictional interaction between the geosynthetic and soil is ignored. Various columns head geometries were investigated, including; square, diamond and circular. The resulting tensile strain in the x-direction for a geometry with square column heads is shown in Figure 2.24. The strain concentration near the corner of square column heads is pronounced. By comparison, the circular column heads observed a significantly lower value of peak tensile strain.

2.4 Ground improvement, semi-rigid inclusions and subsoil behaviour

The ground improvement for GRCSEs differs considerable from other forms of ground improvement, such as stone columns and prefabricated vertical drains (PVDs), which typically experience some portion of primary consolidation

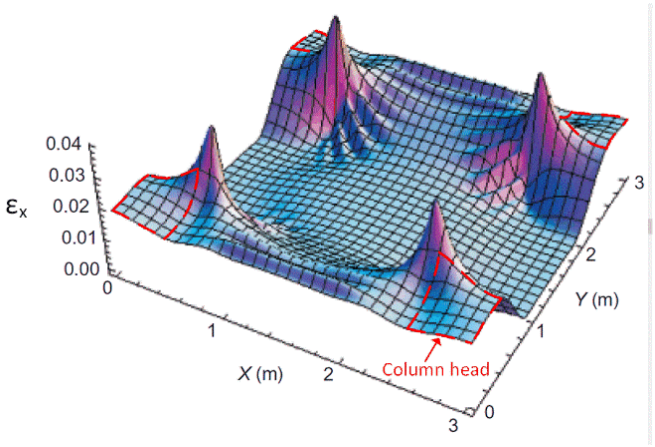

Figure 2.24. Tensile strain in x-direction for geosynthetic membrane overlying square column heads (modified from Jones et al. 2010)

and creep compression in the post-construction phase. By comparison, GRCSEs are supported by semi-rigid columns (and in some cases piles) which generally undergo minimal settlement post-construction (assuming a constant load condition). This is often referred to as semi-rigid ground improvement.

The columns generally comprise either Drilled Displacement Columns which go by a number of names, auger pressure-grouted displacement (APGD) piles is the term frequently used in the North American context, while screw piles or the proprietary named Controlled Modulus Column (CMC) is frequently used in the European context. Prezzi et al. (2005) provide an overview of the European and North-American nomenclature as well as a description of the numerous proprietary drilling tools available to construct displacement piles/columns (e.g. Atlas pile, Fundex pile, De Waal pile etc.).

It is the author's experience, and that of colleagues, that referring to these ground improvement elements as "piles" frequently leads to unnecessary confusion in design scenarios. Namely, whether these "piles" should be designed and tested in accordance with the relevant piling code (i.e., *AS 2159-2009 Piling – Design and Installation* in Australia) where the design and testing criteria are far more onerous than would otherwise be adopted for a ground improvement elements considering their intended use.

The author uses throughout this thesis, and recommends, the term drilled displacement column (or simply column) for ground improvement applications to distinguish from piling applications. It is understood that the term "Controlled Modulus Column" was originally proposed by Menard for similar reasons. Similarly, the term "column supported embankments is recommended in favour of the term "piled embankment" i.e., geosynthetic reinforced column supported embankment (GRCSE). This is consistent with EBGEO (German Geotechnical Society, 2010), which refers to the columns using the generic term "point bearing elements" instead of the term pile. Researchers at Virginia Polytechnic Institute, Virginia, USA (Smith 2005, Jones 2008, McGuire 2011, Sloan 2011, Filz et al. 2012) and other in North America (Collin 2004, Camp III et al. 2006, Wachman et al. 2008, Huang et al. 2009) use the term GRCSE and the distinction between piling and ground improvement applications has been recommended by Gniel et al. (2015) and Larisch (2014) previously.

Other terms used in the literature include "Drilled Displacement Pile" (Brown 2005, Prezzi et al. 2005, Brown et al. 2007, NeSmith et al. 2009, Basu et al. 2010, Park et al. 2012) and "Auger Displacement Pile" (Brown et al. 2000, NeSmith 2002, Hird et al. 2011, Larisch et al. 2012, Larisch et al. 2013) which are used almost interchangeably. Also "Full Displacement Pile" (Pucker et al. 2012) and "Full Displacement Bored Pile" (Busch et al. 2013) are used. The term APGD pile or drilled displacement pile is suitable where these are installed and designed as piles as has

been the trend in recent years in North America (see for example NeSmith and Fox 2009, Brown et al. 2007 and Park et al. 2012). This emerging trend further warrants that a distinction between piling applications and ground improvement applications needs to be made and the author considers that adopting the nomenclature outlined above assists this aim. The installation process, installation effects and installation data from drilled displacement columns are investigated further in Chapter 8.

The columns which support the embankment are designed either as load transfer columns (columns transfer axial load to a more competent unit underlying the soft soil) or settlement reducing columns, the latter is necessary where a competent founding layer is not present within a practical depth. The general design intent of the two column design approaches is much the same. The load-deformation response of the columns under working load will govern the total settlement of the embankment and this generally provides a basis to assess the required socket length into the founding layer or overall shaft length for settlement reducing type columns. In EBGEO (German Geotechnical Society, 2010) it is recommended that the ratio of modulus of subgrade reaction for columns and sub-soil be greater than 75. It is inferred that this criterion is intended to ensure arching development occurs in the intended manner. i.e., that there is relative displacement between the columns and soft soils occurs. As also noted in EBGEO, the inclusion of cement columns will meet, and significantly exceed, this requirement.

The columns supporting a GRCSE can be installed in various geometric arrays. The square column layout (Figure 2.25*a*) is by far the most common. The square arrangement can be rotated 45° to form a triangular arrangement. An equilateral triangular arrangement is also possible (Figure 2.25*b*) as is an isosceles triangular arrangement. Triangular arrangements are generally more difficult from a construability viewpoints and for this reason are less common than a square arrangement. McGuire (2011) provides a detailed overview of various unit cell geometries and the geometric relationships between centre-to-centre spacing (s), clear spacing (s − a), area replacement ratio and spanning ratio. The focus of this study in on the square column layout, these were adopted for the field case study. Most of the findings from this study apply generally to other geometric arrangements. The design actions acting on a column due to global embankment behaviour is discussed further in Section 2.7.

2.4.1 Subsoil behaviour

The sub-soil plays an important role in both the development of arching and the tensile load induced in the geosynthetic reinforcement. In one of the earliest deign methods available for GRCSEs, BS8006-1995 (BSI, 1995),

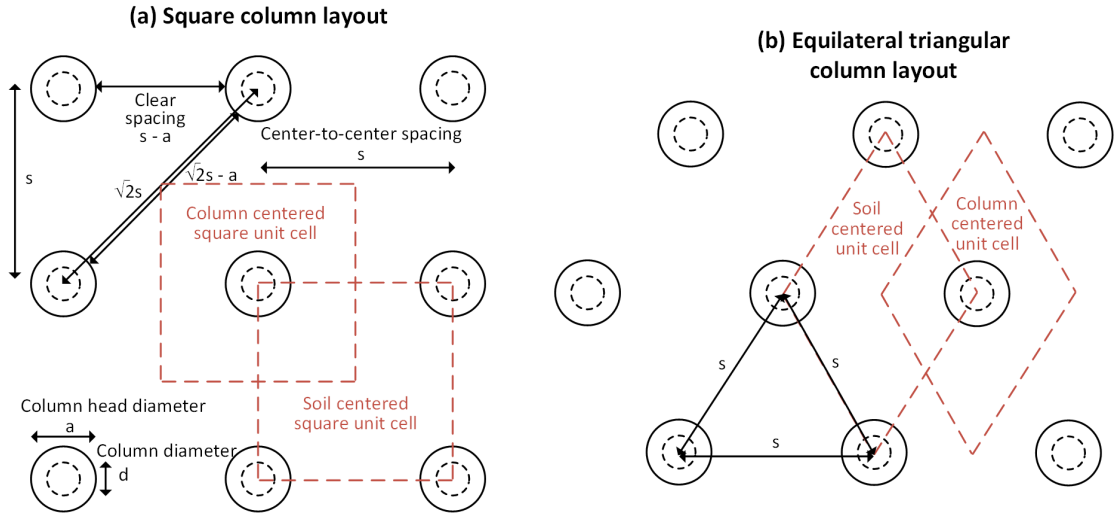

Figure 2.25. (a) Square column layout **(b)** equilateral triangular column layout and unit cells

the sub-soil support was ignored in the LTP design. With the increased use of GRCSE in the late 1990s, there were many who had formed the view that the existing design approaches, such as BS8006-1995 (BSI, 1995) (Hewlett and Randolph method and the method based on Marston and Anderson, 1913), were too conservative for German practice where GRCSEs were becoming more common by the late 1990s (Lawson 2012). The method of Zaeske (2001) developed largely as a result of this perception of conservatism and included sub-soil support in the formulation.

It is the author's view, that the reliance on long term sub-soil support is questionable for ultimate limit state conditions, which the widely-used design methods are formulated to describe, where the design life is typically in the order of 100 years for road and rail infrastructure. For most soft soils, the sub-soil support will gradually diminish through the action of creep compression due to the constant stress (between the columns) acting on the soft soil. The notation that a soft soil can provide constant support, under a constant applied load, over the design life of the structure is highly questionable for ultimate limit state conditions. Almeida et al. (2001), amongst others, expressed a similar opinion based on experiences with soft soil sites in Brazil. To assume otherwise for a soft soil is in most cases likely to be overly optimistic or perhaps suggests that the "soft soil" underlying the site is not so, and that alternative forms of ground improvement may be feasible in the first instance.

The sub-soil support condition is appropriate, and necessary, for serviceability limit state conditions and these are investigated in Chapter 7. Consideration for sub-soil support is also important where the design life is relatively short (i.e., for temporary roadways). For the case study investigated herein, the sub-soil (Coode Island Silt) is expected to undergo significant secondary creep settlement over the design life of the GRCSE and therefore sub-soil support cannot be relied upon in the long term (i.e., the 100-year design life).

The LTP design in EBGEO (German Geotechnical Society, 2010) uses a Winkler spring approach to describe sub-soil support and provides detailed guidance on estimating this modulus of reaction (k_s). Lawson (2012) noted that the representation of a sub-soil support as an elastic spring constant is "*doubtful due to the plastic and time-dependent [sic] nature of soft foundation soils*" and secondly, that this approach was difficult to implement in practice. This is consistent with the author's own experience with GRCSE design. There are several additional factors which may affect the behaviour of the sub-soil and they include: 1) the presence of fill and/or a desiccated layer overlying the soft soil (this may provide increased sub-soil support, at least in the short term) and 2) the requirement to construct a working platform over the soft soil (Figure 2.26). It is uncommon for a LTP to be constructed directly over a soft soil, in most cases, one or more of the above items will be present to ensure constructability. The presence of material overlying the soft soil and underlying the LTP can lead to primary consolidation and/or creep compression of the soft soil. These factors influence the sub-soil support and play an important role in the overall behaviour of the LTP in both serviceability and ultimate conditions. This is investigated further in Chapters 5 to 7.

2.5 Studies into GRCSEs

2.5.1 Laboratory and field studies

A range of laboratory studies have been undertaken to investigate the behaviour of GRCSEs. These studies are typically medium scale laboratory studies and are summarised in Table 2.1. The number of field scale studies (presented in Table 2.2) by comparison is much smaller and these vary greatly in the amount and quality of the

Table 2.1. Laboratory studies into GRCSE

Reference	Model				Measurements	Comments
	Size	Fill material	GR	Sub-soil		
Hewlett and Randolph model (1988)	Not clear	52/100 quartz sand	N/A	Foam rubber chips	Arching stresses	One of the earliest studies into arching development in GRCSE with the Hewlett and Randolph method resulting from this study. This method has been discussed above at Section 2.3.5.
Low et al. (1994)	1.5 m × 0.6 m × 1.0 m high	Sand	With and without geotextile – 200 kN/m tensile strength at 2% axial strain	Rubber foam	Linear bearing elements. Measures column loads.	One of the earliest studies into GRCSEs. Geotextile is not scaled, there is three zones of "sub-soil" across the width of the model. The width of the clear spacing is very small relative to the high strength geotextile used. The sag of the geosynthetic is not consistently scaled to field scale and it is likely that the geotextile will restrict relative displacement to less than 2 %. There is no information on the relative displacement between the geotextile and top of columns. Arching stresses are presented at various geometric arrangements.
Zaeske (2001) and Heitz (2006) (in German)	1.1 m × 1.1 m	Sand	Scaled geogrid	Peat	Deformations, loads, stresses, reinforcement strains	Published in German. The results of this study were used to develop the Zaeske method which was later incorporated into EBGEO. This has been discussed above at Section 2.3.5.
Chew et al. (2006)	3 m × 4.5 m	Sand	Full-scale geotextile	Sub-soil removed	LVDTs[#] to measure geotextile sag, EPCs[*]	Removed subsoil support. Surface settlement observed and contour maps of surface settlement developed. Triangular column arrangement. $h/(s\text{-}a)$ ratio of 0.27 and 0.51 with 0.5 m thick embankment induced 5 cm to 15 cm of surface settlement. $h/(s\text{-}a)$ ratio of 0.53 and 1.0 with 1.0 m thick embankment also induced surface settlement.
Yun-Min et al. (2008)	1.5 m × 1.0 m × 1.3 m high. Planar column elements	Sand	Low-strength, 0.35, 1.4 and 22.5 kN/m at 8% axial strain	Controlled using water bags	Various load pressure cells.	Ground reaction curve behaviour observed. Pressure acting on column heads increases to a peak value then reduces with on-going sub-soil settlement. Notes; "*soil arching is strongly dependent on pile-subsoil relative displacement, and there exists a critical relative displacement.*" While the ground reaction curve behaviour is observed by the authors, this is not explored further. The discussion which follows does not explore the implications of their finding in detail.
Ellis et al. (2009a) and Ellis et al. (2009b)	3×3 and 4×4 column arrangement Centrifuge	Sand	Not used	Polystyrene Styrofoam (EPS)	Vertical stress, three-dimensional surface deformation plots	Introduced the concept of the GRC in GRCSE and demonstrate this behaviour in a three-dimensional prototype GRCSE. Geogrid behaviour was not investigated. A conceptual "Interaction diagram" was proposed to describe the interaction between, geogrid, arching stresses and sub-soil. However, this was not validated or applied to field scale/design, the interaction diagram was used to highlight how these elements interact in a LTP.
Fagundes et al. (2017)	Reduced scale centrifuge models at 20 g-levels, various configurations, h = 1.0, 1.8, 3.2, 5.0 and 7.2 m prototype scale	Hostun sand	$J_{5\%}$ various from 2960 to 16,800 kN/m at prototype scale (very high stiffness)	Mobile tray beneath a layer of sub-soil	Laser displacement under tray and above embankment surface. Instrumented miniature columns	Plot of column efficiency (E) (ratio of load on column divided by total unit cell load) versus normalised mobile tray displacement. Plots of arching stress development with and without geosynthetic are shown. The test without geogrid shows maximum arching and a load recovery phase as expected with maximum arching occurring at 300 mm and only 50 % efficiency. With reinforcement arching achieved an efficiency of close to 100 % (i.e., all load is transferred to columns). The portion transferred to the columns due to arching, and due to geosynthetic reinforcement, cannot be separated due to the limited stress measurements however it can be inferred that the load carried by the geosynthetic must be greater than 50 % (max arching achieved 50 % efficiency). This suggests that the very stiff geosynthetics are carrying a significant portion of the load, and considerable more than in practice.
Girout et al. (2016)			No geosynthetic reinforcement			This laboratory study is similar to Fagundes et al. (2017) and is conducted by largely the same research team. The authors normalise the sub-soil settlement with respect to the thickness of the LTP (rather than the clear spacing as in a trapdoor test), this is unusual. The authors show pronounced arching stress-deformation behaviour with a clear peak and load recovery phase. The authors provide the following comments in relation to this observed behaviour "*[efficiency] reaches a peak, then decreases to a residual value varying with the [LTP] thickness"* and "*In the real case, the settlement of the soft soil would stop while the load transfer towards the pile increases. To analyse the load transfer, the value of the efficiency corresponding to the peak of the load transfer*

						is defined as efficient E_f". The authors do not seem to understand the implications of their finding. The soft soil would not "*stop"* in the field, this depends on its' compressibility and creep compression characteristics. It may however, "*stop"* if a geosynthetic reinforcement is introduced to limit this sub-soil settlement and this would need to occur at a displacement that corresponds to maximum arching if their design analysis is to be based on maximum arching stress conditions.
Chen et al. (2016)	Full-scale 5.5 m by 15 m by 4 m test GRCSE facility	Sand and gravel	130 kN/m UTS geogrid	Water bags	Extensive	This study also observes similar arching stress development and notes that it is similar to that observed by Chen et al. (2008). The measured tensile force is not consistent with the sub-soil settlement. There is over 200 mm of sub-soil settlement before any noticeable increase in tensile strain. The tensile strain rapidly increases after 200 mm "sub-soil settlement" i.e., there "sub-soil" settlement, which appears to be related to the underlying waterbags is not a true representation of the base settlement occurring at the base of the LTP. The development of arching suggests that there is some small amount of base settlement however it would seem that the soil between the water bags and underside of the LTP is not settling as uniformly as the waterbags themselves.

#Linear variable displacement transducers
*Earth pressure cell

Table 2.2. Field scale GRCSE studies

Instrumented GRCSE						
	Author - location	**Type**	**LTP**		**Embankment support**	**Comments**
			Material type, size	**Reinforcement**		
Dutch field case studies	Van Eekelen et al. (2007) – Kyoto Road, Giessenburg.	Shallow height embankment 1.1 m high. In use since November 2005	Hegemann sludge (cement and clay) -	Longitudinal – 350 kN/m UTS Transverse – 400 kN/m UTS	Driven timber piles/columns – 120 mm ∅ (?) with 300 mm ∅ column cap	Long term monitoring over 3.5 year period presented in Van Eekelen et al. (2010) shows load recovery phase of arching. Described in further detail in Chapter 5 and 7.
	Van Duijnen et al. (2010), Van der Stoel et al. (2010) – Houten Railway, Houten.	Embankment, 2.8 m high supporting railway. In use since November 2008	1 m thick granular material (?)	Longitudinal – 450 kN/m UTS Transverse – 600 kN/m UTS	High speed piles (HSP) – 0.22 m ∅ shaft and 0.4 m ∅ cap	First Dutch GRCSE to support a railway. Response of LTP to large (live) rail loads is examined. Sub-soil support is considerable over the 9 months or data presented.
	Van Eekelen et al. (2012) – Woerden highway exit (A12), Woerden	Embankment, 1.53 m to 1.89 m high. In use since June 2009	Crushed, recycled construction material (0 – 40 mm) overlying a sand layer	Longitudinal – 600 kN/m UTS Transverse – 600 kN/m UTS	Driven precast square concrete piles/columns 290 mm. 750 mm square column caps	Long term earth pressure cell data presented. LTP response when subject to passage of heavy truck is assessed.
	Briançon et al. (2008), Briançon et al. (2011) and Briançon et al. (2010) – Test embankment 20 km north-east of Paris, France	5 m high embankment with four design zones	150 mm well-compacted gravel working platform and variable thickness gravel/rockfill (<31 mm)	Varies	380 mm diameter drilled displacement columns	Extensively instrumented test embankment in France comprising four LTP configurations. Described in further detail in Chapter 5 and 7.
	Wachman et al. (2008) and Wachman et al. (2009) – TH241 embankment, St. Michael, Minnesota, USA	3.9 m high embankment	900 mm thick LTP.	Three layers of uniaxial geogrid (Synteen SF 80) – 110 kN/m UTS	300 mm diameter steel tube piles (6.4 mm wall thickness), column cap diameter 0.6 m	Extensively instrumented embankment, earth pressure cells in the sub-soil zone show the complete GRC behaviour including initial, maximum arching and load recovery phase. Described in further detail in Chapter 5 and 7.
	Sloan (2011) and Sloan et al. (2013) – Virginia Tech. CSE test facility			Biaxial geogrid Tensar® BX1500 27/30 kN/m UTS	600 mm diameter concrete columns	Sub-soil modelled with geofoam blocks (expanded polystyrene) which was rapidly dissolved using a natural oil (d-Limonene). Load-deformation arching behaviour was not observed as working condition was rapidly developed (approx. 15mins) and if this behaviour was measured, it has not been presented.

GRCSE case studies – no instrumentation

Author – location	Type	LTP		Embankment support	Comments
		Material type, size	Reinforcement		
Liu et al. (2007)					
Raithel et al. (2008) – railway from Hamburg to Berlin, Germany	1.7 m high GRCSE	Embankment fill comprised cement stabilised fill	400 kN/m UTS uniaxial geogrid in two layers	Mixed-in-Place columns (0.63 m diameter) at 1.5 m square grid	Small post-construction settlement over 6-month period. It is noted in relation to the observed post-construction settlement; "*Also, it has to be considered, that the geogrids, have to deform slightly to become active."*
Livesey et al. (2008) – A614, Goole, East Yorkshire, United Kingdom	Embankment, up to 5 m high at bridge. 9.3 m wide road carriageway, 1:1 embankment batter slopes		Fortrac® R800 in both directions	Driven cast *in situ* (DCIS) piles – 380 mm diameter	Recognised the importance of satisfying serviceability reinforcement strain conditions and noted the limited design advice in design standards. Adopted a number of innovative methods to "pre-tension" the geosynthetic reinforcement to induce the working condition early in the design life of the embankment. This included; 1) placing loose fill between columns, 2) anchoring the transverse reinforcement in a periphery trench and 3) applying heavy compaction on initial fill layers to induce tension in reinforcement The longitudinal reinforcement was also extended 30 m beyond the last row of piles in the transition zone.
Gwede and Horgan (2008) – A650, Bingley Relief Road, West Yorkshire, United Kingdom	2 m high GRCSEs over a length of 440 m. Peat deposits 2 m to 11 m thick underlie the embankment.		600 kN/m UTS biaxial woven geotextile (longitudinal /transverse)	350 mm square precast concrete piles – 2.5 m square grid	Design issues relating to serviceability reinforcement strain are also raised, similar discussion to Livesey et al. (2004). Reinforcement strain was further limited to 3- 4 % with an estimated mid-span deflection of 170 – 200 mm. Additional construction measures to induce the "working condition" included: 1) placement of loose compressible soil between column caps, 2) thin initial layers of LTP fill with heavy compaction and 3) 2 m high rolling fill surcharge to induce final settlement prior to road surfacing. The working platform was removed after construction such that the LTP directly overlies the soft soil (peat) in the as-built condition.
Fok et al. (2012) – Breakwater bridge realignment project, Geelong, Victoria, Australia.	Shallow height embankment, 1.5 m high	600 mm thick layer of crushed rock	Three layers of biaxial geogrid (strength ?)	450 mm diameter CMCs	First use of a GRCSE to support a roadway in Victoria, Australia. Static load testing of CMCs to demonstrate ultimate capacity.

Other field case studies

Author - location	Type	LTP		Embankment support	Comments
		Material type, size	Reinforcement		
Lawson (2013) - M74 Completion project in Glasgow, UK	Four major intersections with 13 approach embankments/GRCSEs. Embankment height ranged from 4 m to 12 m.	50 mm – 150 mm of sand between column heads. High frictional fill layer between geotextile layers.	Woven polyester geotextile – Longitudinal – 100 to 200 kN/m UTS Transverse – 400 to 1,600 kN/m UTS	275 mm precast concrete piles	Very high strength geotextile adopted.
Lawson (2013) - A1/N1 project in Ireland	Dual carriageway, 3 m high embankment.	Granular embankment fill (?)	Woven polyester geotextile – Longitudinal – 600 kN/m UTS Transverse – 800 kN/m UTS	Precast concrete piles with precast 0.5 m square column heads	800 mm thick working platform overlying soft soil.

instrumentation installed; interpretation of the field data from these studies is challenging. A number of these field case studied are examined further in Chapter 7 where the serviceability behaviour is investigated.

2.5.2 Failure case studies

A limited number of failure case studies are documented in the literature, two of which are described below.

Rossorry Quay development

A housing development was planned at a site bordering the River Erne in Enniskillen, Northern Ireland and is described in High Court proceedings (Coghlin 2005) and is also reported by Zhuang et al. (2012). The site is low lying, subject to flooding and is underlain by highly compressible alluvial clay and peat. Due to the low-lying nature of the site and the underlying soft soil it was necessary to raise the site level by about 3 m and support the proposed development, which included roadways, two- and three-storey townhouses and four-storey apartments, on columns with a geosynthetic reinforced load transfer platform. The ratio of embankment height to clear span ratio ($h/(s\text{-}a)$) was 1.5 in this case.

The poor ground conditions necessitated the need for a working platform comprising a considerable thickness of crushed rock (generally about 500 mm) to support the piling rig(s). This working platform was however up to 1.5 m thick in parts and was situated below the LTP. As a result, the working platform was unsupported and its' applied stress caused considerable primary consolidation of the underlying soft soil and peat. It is inferred that this induced a loss of sub-soil support condition at some time after the completion of construction and that the loss of sub-soil support condition induced (or allowed) considerable sagging of the geogrid. The loss of sub-soil support is accounted for in ultimate limit state design, however, the geogrid layers installed were of a low stiffness and geogrid sag was excessive, this was estimated by Zhuang et al. (2012) to be about 400 mm at the mid-span between columns. Despite the height of the embankment (h = 3 m) the base settlement was large enough that this led to surface settlement; embankment failure was therefore due to the serviceability reinforcement strain condition.

While the geogrid underwent significant deformation, it is not clear if the geogrid ultimately ruptured and subsequently failed under an ultimate limit state condition. Regardless, the LTP and embankment failed first under a serviceability condition and this occurred progressively and led to worsening cracking of the buildings supported on the GRCSE. Whether the LTP satisfied ultimate limit state conditions at some later time is only of importance if this

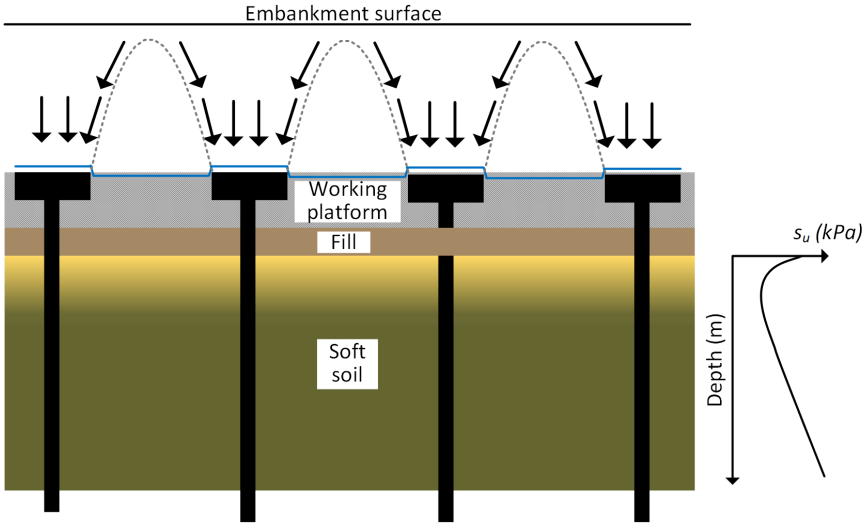

Figure 2.26. Example of sub-soil conditions beneath LTP

induces a brittle failure mechanism. However, this was not the case. If the ultimate limit state condition occurred, the buildings were already condemned by that time as is of little importance. Whether the LTP satisfied, or otherwise, ultimate limit state conditions at some time after the failure is a trivial consideration in this case. This failure mechanism highlights the need to consider and design for serviceability limit state conditions even where the embankment height may be considerable greater than minimum height requirements. This case study is examined further in Chapter 7 where the serviceability design of GRCSE is investigated further.

Road embankment in South Carolina

The construction of a roadway in South Carolina also experienced a serviceability reinforcement strain failure similar to the preceding case study and is described by Camp III et al. (2006). The roadway was constructed over a length of about 310 m using vibro-concrete columns (0.6 m diameter) at 2.5 m centre-to-centre spacings and enlarged heads of 0.9 m diameter to support the embankment. The maximum embankment height was 1.1 m and this gives a ratio of embankment height to clear span ratio of just 0.4. The LTP was 600 mm thick and comprised three layers of Tensar BX 1200 geogrid. As noted by Camp III et al. (2006) this was too thin to permit arching to fully develop through the embankment LTP and embankment fill.

Shortly after completion differential settlement of about 50 mm was encountered at the road surface and the owner of the asset (presumably the road authority) was forced to close the roadway (Camp III et al. 2006). The failure was summarised by Camp III et al. (2006) as follows; "*Within the original design calculations, the relationship between the strain within the tensioned membrane and the vertical displacement (i.e., embankment settlement between columns) was not recognised. The computations of the geosynthetic strains, vertical displacements, and geosynthetic tension force were uncoupled from one another."* This is consistent with the discussion outlined in Section 2.2.5 where the short-comings of de-coupling the arching stress-deformation in the design of a GRCSE have been discussed.

2.6 Design methods for GRCSEs

A number of national design standards have been developed over the past two decades for GRCSE design. A common feature of recent design revisions is the use of limit equilibrium models to describe arching behaviour and incorporation of sub-soil support. The model of Hewlett et al. (1988) was adopted in the French ASIRI guideline and suggested as an alternative in BS8006-1 (2010), the model of Zaeske (2001) was incorporated into EBGEO (German Geotechnical Society, 2010) and CUR226 (2010) and more recently the CA model was proposed for the revised Dutch standard (CUR226 2016).

These standards adopt the "two-step" design approach outlined earlier. The German standard, EBGEO (German Geotechnical Society, 2010) is presented in detail below to highlight this approach. The author is familiar with several projects in Australia where this method has been used (see also Hamidi et al. 2009 who describes other Australian GRCSEs). This is compared with the Load-Displacement Compatibility method (Filz et al. 2012) in Section 2.6.2 which employ a coupled arching stress-deformation relationship with base settlement as a governing parameter. A common feature of the various LTP design methods is the consideration of vertical stress only. Additional lateral stresses acting on the geosynthetic reinforcement due to embankment spreading, lateral sliding etc., is considered through separate analytical calculations. Typically, numerical analysis is required to assess global embankment behaviour under serviceability conditions, this is discussed further in Section 2.7. The discussion presented below is limited to point bearing semi-rigid elements (or point bearing rigid piles). The design of linear bearing elements follows a similar course; however, these are rarely used.

Other design methods included the Nordic design guidelines (Rogbeck et al. 2004), the Collin method (Collin et al. 2005), used in the U.S.A. and the design method of the Public Work Research Center in Japan (described by Eskişar et al. 2012) amongst others.

2.6.1 German Standard – EBGEO

The design of GRCSEs is covered in Chapter 9 of the German design standard EBGEO (German Geotechnical Society, 2010). An English version was published in 2011. Much of the analysis is based on the limited equilibrium model, and theory of elastically embedded membranes, described by Zaeske (2001) (in German) and summarised by Kempfert et al. (2004) in English. A basic outline of the design process for ultimate limit state conditions in the LTP is summarised as follows:

1. Specification of embankment geometry (see Figure 2.1) as well as minimum and maximum geometry ratios
2. Assessment of arching behaviour in accordance with the method of Zaeske (2001) (Section 2.2.5); the stress acting on the sub-soil/geosynthetic reinforcement ($\sigma_{zo,k}$) is calculated
3. The stress $\sigma_{zo,k}$ is used to calculate the effect on the geosynthetic reinforcement using the method outlined in Section 2.2.5. This includes a procedure for assessing a weighted estimate of modulus of subgrade reaction (k_s) i.e., a linear elastic spring constant to simulate sub-soil support.
4. Two procedures are outlined for assessing the additional load acting on the reinforcement layers due to lateral sliding/spreading.

EBGEO (German Geotechnical Society, 2010) provides a number of notes and recommendations relating to minimum embankment height, numerical modelling of LTP behaviour, dynamic loads and serviceability behaviour which are relevant to the present study. The minimum ratio of $d/s \geq 0.15$ and maximum ratio of $(s - d) \leq 3.0$ m for static loads and $(s - d) \leq 2.5$ m provide practical upper bounds on column spacing and column head size. It is however, the ratio of embankment height to clear spacing which often governs the geometric arrangement for shallow height embankments.

For "*predominately static loads*" this is $h/(s - d) \geq 0.8$ and "*a higher ratio is recommended for high variable loads [dynamic loads]*". It is noted that the negative impact of the variable loads for $h/(s - d) \geq 2.0$ is negligible. i.e., $h_{crit} = 2.0\ (s - d)$. In the draft version of the EBGEO (German Geotechnical Society, 2010), Raithel et al. (2009) notes that the minimum embankment height is specified as $(s - d) \leq 1.4\ (h - z)$ which is considerably higher than the value adopted in the final version of EBGEO (German Geotechnical Society, 2010). This trend towards shallower embankments is consistent with other design standards, presumably due to an improved understanding of the LTP behaviour, arising from the large number of research studies investigating GRCSEs as outlined in Section 2.5.1 (Table 2.1 and Table 2.2). The importance of the minimum embankment height requirement is assessed in detail in Chapter 7.

In EBGEO (German Geotechnical Society, 2010) the procedure to estimate the modulus of subgrade reaction includes two cautionary notes. One states that the use of this procedure; "*may lead to considerable over- or under-estimation of the subgrade reaction"* and *"... [the] design method is highly sensitive in terms of the subgrade approach used*." The difficulties in describing the subgrade support using a linear elastic spring (Winkler spring approach) has been highlighted by Lawson (2012). EBGEO also notes that numerical analysis may not be used to assess LTP *"Because cause and effect and their interrelationship are not yet sufficiently clarified."* as noted in Section 2.2.7. In regards to the effects of dynamic loading on the embankment, EBGEO notes that "*arch*

deterioration" may occur if the limiting embankment heights specified are not adhered to and it notes that this may lead to increased strain in the geosynthetic reinforcement.

EBGEO (German Geotechnical Society, 2010) provides the following advice in relation to the amount of base settlement required to achieve the design reinforcement strain (ultimate) condition:

"*The reinforcement is strained during [construction] of the [GRCSE] in layers and in particular during installation and compaction of the initial soil layers."* and

"*Generally, the serviceability analysis is governed only by the additional deformations in the [GRCSE] occurring after its [construction], due to the actions described in Section 9.4 [of EBGEO]."*

It is also noted in EBGEO (German Geotechnical Society, 2010) that creep strain should be limited to ≤ 2 % and "[for] *certain applications (e.g. transport structures sensitive to deformation or [other example]) it may be necessary to further limit additional strains [creep strains] in terms of the [geosynthetic reinforcement] sag Δf.*" However, no further advice is given as to how to achieve this.

EBGEO (German Geotechnical Society, 2010) assumes that the "ultimate" condition described by the "two-step" design process develops during construction, it follows then, that the only additional strain that develops in the reinforcement layers is due to creep strain under constant load. As part of this present study it is shown that this assumption is not valid for the majority of field embankments, and it follows then, that the development of this "ultimate condition" will occur post-construction. Understanding serviceability behaviour therefore requires an understanding of the coupled arching stress-deformation behaviour which forms part of the arching hypothesis stated in Section 2.2.6 and is the focus of Chapters 5 to 7.

2.6.2 Load-Displacement Compatibility Method

The Load-Displacement Compatibility (LDC) method was originally described by Smith (2005) and has since been reinfed (see Filz and Smith; 2006, Jones; 2008, Sloan; 2008, McGuire; 2011, and Filz et al. 2012). The design of the GRCSE is a 10-step design procedure with an associated spreadsheet application titled "GeogridBridge" used to solve the differential equations describing base settlement. The 10-step design procedure is outlined below:

1. **Design parameters –** design parameters are specified.
2. **Geotechnical site investigation information –** Subsurface information, stratigraphy, field and laboratory data and groundwater information are collected. Subsurface profile developed.
3. **Initial design values** – s and a (or d) must meet the following 3 criteria:
   a. $h / (s - a) \geq 1.0$
   b. $s - a \leq 2.4$ m
   c. $A_s \geq 0.10$

   Where A_s is the (surface) area replacement ratio.
4. **Bridging (LTP) layer –** a bridging layer comprising sand or gravel (SP, SW, GW or GW material, in accordance with USC system for soil classification) is recommend for the bridging layer. The following properties are required: γ, ϕ', E and v. The thickness of the bridging layer h^* should meet the following criteria:
   a. $h^* \geq 0.9$ m
   b. $h^* \geq s - a - h^*_{red}$

      h^*_{red} is an amount the bridging layer can be reduced if an upper layer of strong soil exists at the site.

5. **Embankment fill material** - Material properties for embankment fill are the same as the bridging layer.
6. **Load requirements for semi-rigid elements** – The LDC method recommends that columns be designed to carry the entire unit cell embankment load plus surcharge load (i.e., $s^2(\gamma h+q)$).
7. **Geosynthetic reinforcement** – the layers of reinforcement are selected and stiffness specified
8. **Calculate base settlement** – the embankment settlement (S_{total}) which is a function of maximum base settlement ($S_{b,max}$), embankment compliance settlement (S_E), column compression (S_c) and compression of founding material (S_U). This is shown in Figure 2.27.
9. **Iterations** – if the settlement tolerance exceeds design requirements then the above process is repeated by either reducing s, increasing A_s, using a stiffer geosynthetic reinforcement (higher J) and/or stiffer columns.
10. **Geosynthetic details** – separation between layers of geosynthetic and overlap distances are specified.

The stress distribution acting on the unit cell and the relationship between the "mechanical elements" is shown in Figure 2.28. The LDC method quantifies arching behaviour with parameters $\sigma_{col,geotop}$, $\sigma_{col,geobot}$, $\sigma_{soil,geotop}$ and $\sigma_{soil,geobot}$ which are described in Figure 2.28. Equilibrium is achieved as a function of the dependent variable d. Where d is the relative differential settlement between the column head and the subgrade soil. To assess the arching component ($\sigma_{col,geotop}$ and $\sigma_{soil,geotop}$) the arching stress deformation relationship is defined by a bi-linear relationship as noted previously and shown in Figure 2.18*b* and Figure 2.19. The initial component of the bi-linear relationship is

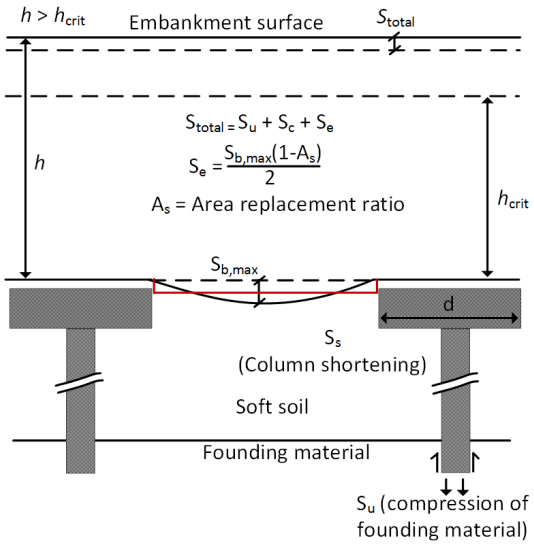

Figure 2.27. Calculation of total surface settlement where $h > h_{crit}$ (LDC method)

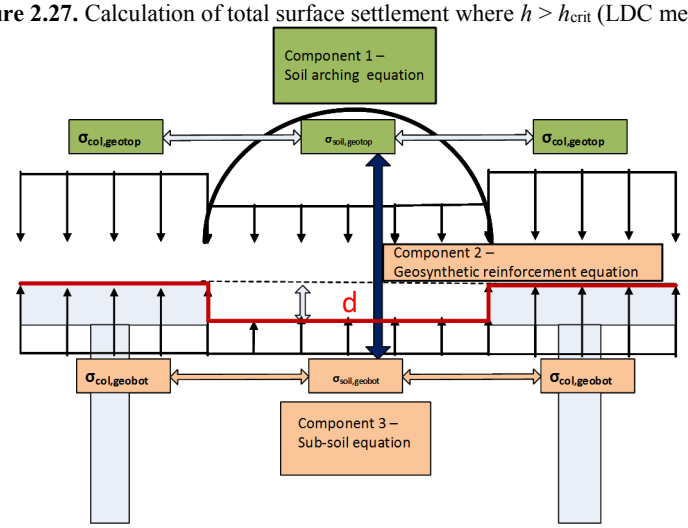

Figure 2.28. LDC method

based on the assumption that the column head "pushing up" into the soil mass above can be approximated by the linear-elastic solution for the displacement of a circular loaded area on a semi-infinite mass described by Poulos and Davis (1974).

$$\rho_z = \frac{\pi}{2}(1-\nu^2)\frac{p_{\text{av}}^2}{E} \tag{2.26}$$

Re-arranged for the GRCSE situation to obtain:

$$d = \frac{\sqrt{\pi A_c}(1-\nu_f)(\sigma_{\text{col,geotop}} - \sigma_{\text{soil,geotop}})}{2E_{\text{f}}} \tag{2.27}$$

When $d = 0$ there is no arching and therefore the stress reduction ratio is equal to unity. It is necessary to impose a limiting stress condition, this is achieved by describing the lower limit value of stress reduction ratio using the Adapted Terzaghi method, a frictional method as described in Section 2.2.2. This stress is termed SRR_{lim} and described as follows:

$$SRR_{emb} \geq SRR_{\text{lim}} = \frac{\gamma}{\alpha(\gamma H + q)}(1 - e^{-\alpha H}) \tag{2.28}$$

The differential settlement at which yielding occurs is as follows:

$$d_{\text{yield}} = \frac{\sqrt{\pi A_c}(1-\nu_f)(1-SRR_{\text{lim}})(\gamma H + q)}{2a_{\text{s}}E_{\text{f}}} \tag{2.29}$$

Based on this formulation, the value of SRR_{emb} decreases linearly from 1 to SRR_{lim} as d increases from 0 to d_{yield}. For values of $d > d_{\text{yield}}$ the value of stress reduction ratio is equal to SRR_{lim}. This is the so-called bi-linear expression described in Figure 2.18*b* and Figure 2.19. This stress is used to assess the behaviour of the geosynthetic reinforcement ($\sigma_{\text{soil,geotop}}$ and $\sigma_{\text{soil,geobot}}$). To calculate the subsoil stress ($\sigma_{\text{col,geobot}}$ and $\sigma_{\text{soil,geobot}}$) the calculation procedure considers a sub-soil that is granular or fine-grained in nature. For the fine grain case the calculation procedure considers recompression and primary consolidation. This is a considerable improvement over the method of Zaeske which describes the sub-soil as a linear-elastic spring by comparison.

2.7 Global embankment design

The design of a GRCSE requires consideration of a number of limit state conditions. These are shown in Figure 2.29 and include; overall stability, lateral sliding, column group extent, vertical load shedding, column group capacity and surface deformations (Lawson, 2012). The limit states relating to LTP behaviour include; vertical load shedding (arching stress development) and surface deformation. These have been discussed in preceding sections and are the subject of Chapters 5 through to 7. Throughout this thesis these limit states are referred to as localised GRCSE behaviour. The remaining four limit states relate to global embankment behaviour and include the behaviour of the embankment, the columns and the interaction with the LTP. These four limit states can be sub-divided based on the load conditions acting on the columns; axial (column group capacity) and lateral (overall stability, lateral sliding and column group extent).

To assess the column group capacity limit state (i.e., axial capacity) the applied load can be assumed to result from the full weight of the unit cell plus design surcharge load (dead load or live load) (i.e., assume no sub-soil support). The axial capacity of an isolated column can be assessed by various design methods. These approaches relate unit base and shaft resistance to CPT tip resistance q_{c} or SPT blow count N (Bustamante; 1993, 1998;

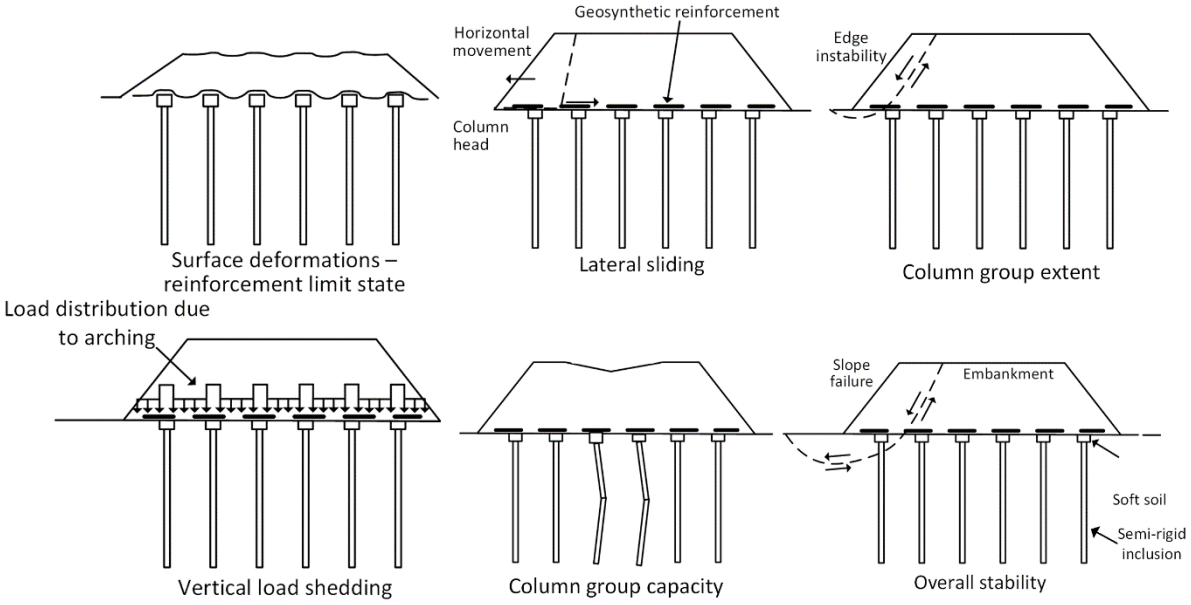

Figure 2.29. Various limit states for design of GRCSEs (after Lawson, 2012)

NeSmith; 2002 and Brettman and NeSmith; 2005, for example). While these methods may provide a means to calculate bearing capacity, they provide limited insight into installation effects which is discussed further below.

Where the columns act as load transfer columns the typical axial load is quite small relative to the ultimate capacity of say a 450 mm diameter constant modulus column. For example, a shallow height embankment of say a 2 m height may have working column loads of less than 100 kN. For columns acting as load transfer columns (which is typically the case), the axial capacity and axial group capacity is rarely a critical design limit state (there are however a number of constructability issues that require consideration, these are described further in Chapter 8). For columns designed to act as settlement reducing columns, the axial capacity or axial load-deformation behaviour of the columns will control total settlement and is therefore an important consideration.

Assessment of lateral behaviour of the columns typically represents the governing design action for unreinforced concrete columns due to their limited lateral and shear capacity. EBGEO (German Geotechnical Society, 2010) provides several ultimate limit state design calculations that must be satisfied. Some general design concepts relating to lateral loading of the columns are outlined below. The assumption is made that the transverse geosynthetic reinforcement layer must carry the embankment lateral thrust (i.e., due to an active earth pressure). It follows then, that the longitudinal and transverse layers of geosynthetic reinforcement will carry differing lateral loads. To enable the geosynthetic reinforcement to carry lateral load an adequate bond length is required. This is achieved either through the use of thrust block or alternatively with a "wrap around length". This load is denoted T_{ds} and is illustrated in Figure 2.30. The longitudinal layer will carry a tensile load due to arching (T_{rp}) only while the transverse layer will carry the load $T_{rp} + T_{ds}$. For this reason, it often uneconomical to use bi-axial geosynthetic reinforcement due to the different ultimate tensile strength requirements of the longitudinal and transverse layers of geosynthetic reinforcement. As a result, the transverse layer is often designed to have a higher ultimate tensile capacity than the longitudinal layer.

Assessment of global scale embankment behaviour is quite challenging at laboratory scale with most studies primarily focused on assessing the load transfer platform behaviour and arching rather than global stability and lateral sliding mechanics. A large number of these studies were described in Section 2.5.1 (Table 2.1 and Table 2.2). A review of numerous studies that have investigated the global scale behaviour of GRCSEs (Masse et al. 2004, Liu

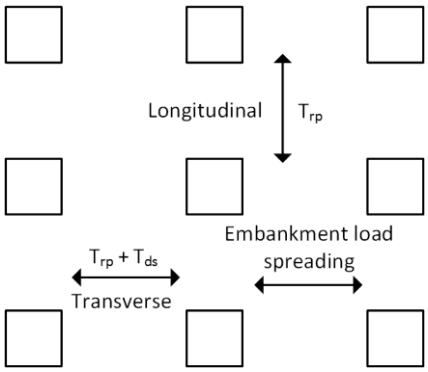

Figure 2.30. Longitudinal and transverse ultimate limit state load conditions for GRCSE based on EBGEO (Germany Geotechnical Society, 2010)

et al. 2007, Jenck et al. 2009, Chatte and Lauzon 2011, Ariyarathne et al. 2012, Zhang et al. 2013, Nunez et al. 2013 and Bhasi and Rajagopal 2013, 2015) indicates that numerical analysis techniques are by far the preferred method of analysis for assessing global scale GRCSE behaviour, particularly serviceability behaviour. The study of global scale GRCSE mechanisms through full-scale case studies, laboratory scale physical modelling and centrifuge modelling is far less common.

However, current FEM numerical techniques are limited in their ability to model large strain problems such as pile installation (Więckowski 2004) and generally advanced methods such as Coupled Eulerian-Lagrangian (CEL) (Qiu et al. 2011, Pucker et al. 2012) or point based (meshfree) methods such as smooth particle hydrodynamics (SPH) (Bui et al. 2008) or the material point method (MPM) are required. In some cases, "work-around" methods are adopted within a FEM analysis to account for installation effects. Wong et al. (2012) and Gniel et al. (2015) consider the columns supporting a GRCSE as "geotechnical" elements, which are assumed to be cracked and are modelled as plate elements with little to no bending stiffness. However, in many cases, installation effects are ignored entirely (i.e., columns are "wished into place" in a numerical simulation), or not acknowledged, and no position is taken as to the effect that this assumption has on the numerical output.

Whilst this short-coming may sound like a trivial matter, it is well known from field scale observations of pile installation effects, particular for driven piles (Randolph et al. 1979, Coop et al. 1989, Lehane et al. 1994, Eigenbrod et al. 1996), and through the use of analytical methods such as cylindrical cavity expansion techniques (Carter et al. 1979, Randolph et al. 1979, Randolph 2003) and the strain path method (Baligh 1985, Sagaseta et al. 2001) that the installation of full displacement piles can induce lateral displacement and excess pore water pressure in the vicinity of the pile shaft. This has also been shown recently for an isolated full-scale controlled modulus column (Suleiman et al. 2015) and for a large diameter cast *in situ* concrete pipe pile (Liu et al. 2009) that were both extensively instrumented. A limited number of studies have described group installation effects; Poulos (1994) investigated the effects of driving a pile adjacent to a pile in clay, O'Neill et al. (1982) investigated installation effects for a group of steel tube piles and Kitazume et al. (2007) assessed the stability of a group of deep soil mixed columns.

Part of this field scale study of a GRCSE is aimed at investigating these installation effects and their effect, or otherwise, on the global scale behaviour of the GRCSE. The cumulative column installation effects, which are relevant for GRCSEs due to the large number of columns/piles installed in a dense array, are considerable more difficult to assess. However, it is thought that a reasonable approximation and insight into group installation effects can be gained by considering the installation of multiple columns within the framework of cavity expansion theory; this is done to assist with and aid the interpretation of the field data.

One of the benefits frequently cited to justify the construction of a GRCSE is the rapid speed of construction permitted compared with unsupported geosynthetic reinforcement embankments, where it is often necessary to monitor the excess pore water pressure responses as the embankment is raised, to ensure that an adequate factor of safety for embankment stability is maintained. As embankment load in a GRCSE is (predominately) transferred directly to the founding unit through load distribution in the load transfer platform, the behaviour of the soft soil is generally considered to be of little importance when considering embankment behaviour. However, the author considers that the rapid speed of construction can be expected to be detrimental to embankment performance due to the lack of time available to allow dissipation of excess pore water pressure (due to installation effects) arising due to ground improvement works. It follows then that if the rapid speed of construction of a GRCSE is to be promoted as a benefit then the interaction between installation effects and embankment behaviour should be considered. The aim of Chapters 8 and 9 is to investigated these concepts further using cylindrical cavity expansion theory as a framework to aid the interpretation of the field data.

2.8 Summary

A considerable amount of research has been undertaken over the past two decades on the topic of GRCSE (see Table 2.1 and Table 2.2). Over this period of time a number of limit equilibrium models have emerged and these are now widely used for the design of GRCSEs. Examples include the Hewlett and Randolph, Zaeske and Concentric Arches models. At this time these models have largely surpassed a variety of other arching models such as empirical, frictional and rigid arching models due to the advantages that limit equilibrium models are perceived offer over other categories of arching models.

All the available GRCSE arching models have to this time been developed to describe ultimate limit state conditions. However, it has been shown by numerous practioners and researchers that serviceability criteria typically govern the suitability and acceptance of a given GRCSE design. This has also been highlighted in Section 2.5.2 by way of two failure case studies. Limit equilibrium models are also formulated within a general "*two-step*" design approached whereby the steps to assess arching and membrane behaviour are separated. This approach precludes the use of an arching models that describes arching as a deformation dependent process. Arching as a deformation dependent process has also been highlighted in Section 2.1 and in a range of geotechnical problems in Section 2.1.4, some examples include; pile plugging, tunnel supports, backfilled trenches and in granular flow between vertical walls (i.e., the silo problem), retaining walls, King post walls and in the formation of sinkholes in karstic terrain. Many other examples exist. The current approaches available for assessing arching development in GRCSEs assume that a state of arching will develop post-construction under a small amount of geosynthetic reinforcement sag and/or sub-soil settlement. It is assumed that the deformation conditions implicitly in these limit equilibrium models are consistent with the deformation that occurs when a GRCSE is in service.

This assumption is incorrect in nearly all cases due to; 1) deformation compatibility is not explicitly stated as a requirement when using the current limit equilibrium models and 2) the stiffness of the geosynthetic reinforcement or the role of the sub-soil support may not enable deformation compatibility to be achieved post construction. Understanding arching stress development is an important step in understanding serviceability behaviour. This investigation aims to highlight the benefits of utilising an arching stress-deformation relationship to understand serviceability behaviour by way of a full scale experimental investigation coupled with numerical and analytical investigation.

The limitations in assessing arching stress behaviour using conventional continuum based numerical techniques such as the Finite Element Method has also been described (Section 2.2.7). These limitations are well described by de Borst and Vermeer (1984) and van Langen and Vermeer (1991) and are described further in Chapter 6. To address these limitations, it is proposed to use the meshfree method, Smooth Particle Hydrodynamic to examine arching stress behaviour further. In addition, another large displacement problem that is difficult to simulate using conventional continuum based numerical methods is installation effects that arise during pile or column installation. While these effects have been studied extensively the emphasis is generally on understanding how the installation influences the pile behaviour itself rather than the surrounding ground. A more expansive literature review on this behaviour is presented in Chapter 8. These effects become significant when installing a large number of full displacement columns in a dense grid for the purposes of ground improvement for a GRCSE. It is proposed to utilise cylindrical cavity expansion theory to investigate further these effects and as a means to interpret and understand the field case study data.

3 Field case study

As part of this research project, a field case study has been undertaken to assess the behaviour of a GRCSE. This chapter presents information relating to the field case study and includes embankment design and construction information as well as a description of the installed instrumentation. A detailed geotechnical site characterisation and description of sub-surface conditions, based on geological and geotechnical information and additional material testing, is presented in Chapter 4. The results from the field case study are presented in Chapter 5 onwards.

3.1 Introduction

The Regional Rail Link project was a $5.3 billion project comprising 47.5 km of new rail, and significant rail upgrades in the west of Melbourne, linking the regional rail lines of Geelong, Ballarat and Bendigo with Melbourne (DOT 2014). At the time, the project was the largest public transport infrastructure project in Australia (DOT 2014). Works for the project begun in 2009 and were completed in June 2015 with much of the major construction work completed during the period between 2011 and 2013. The project was delivered through 7 separate (design and construct) work packages with Work Package B delivered by the Regional Rail Link – City to Maribyrnong River (RRLCMR) Alliance which comprised a number of engineering design firms, construction contractors and other stakeholders. An overview of the Regional Rail Link project and the location of Work Package B is indicated in Figure 3.1.

The portion of the Regional Rail Link alignment which Work Package B covered differed from other sections of the alignment due to its' geological setting. Approximately 80 % of the 4.5 km (Work Package B) alignment is located within the Yarra Delta (Figure 3.2) and is underlain by soft soils. The flat and extensive Quaternary aged

Figure 3.1. Regional Rail Link project overview (from DOT, 2014)

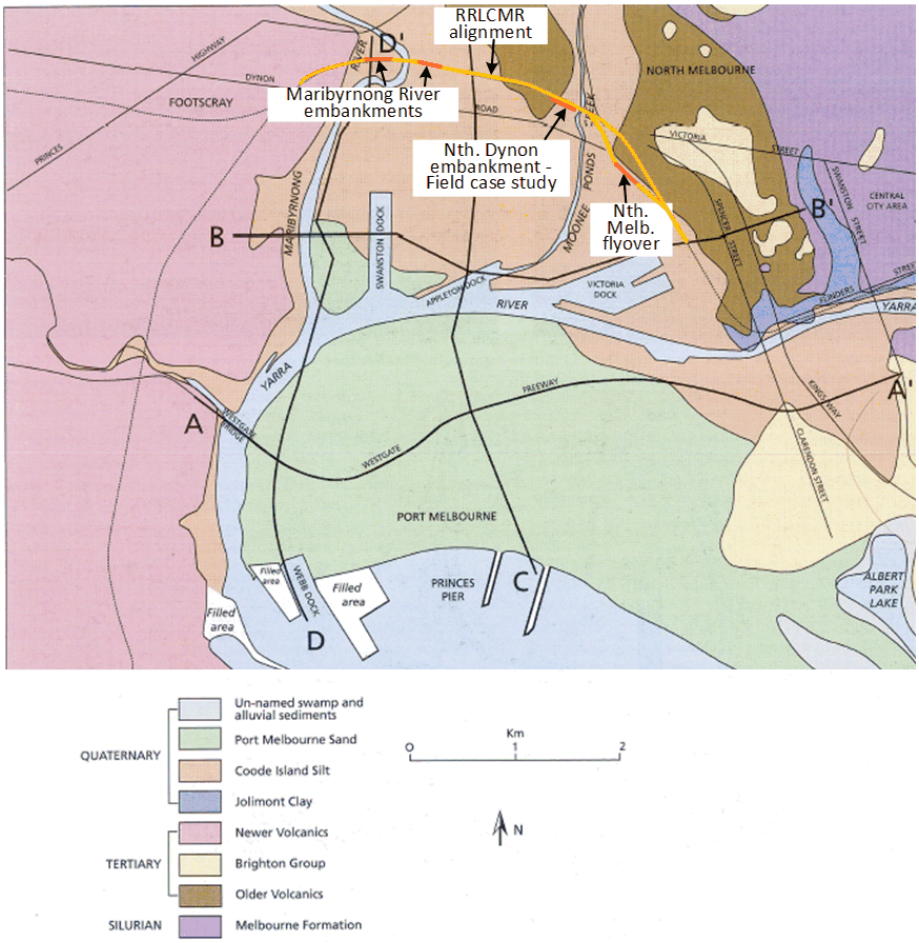

Figure 3.2. Surface geology of the Yarra Delta (modified from Cupper et al. 2003) with GRCSEs and approximate extent of RRLCMR alignment shown.

Basaltic "Werribee Plains" generally define the western limit of these works. The Yarra Delta comprises a complex sequence of Quaternary aged sediments (Yarra Delta Group) and Tertiary aged units overlying bedrock (VandenBerg 1973, Neilson 1992). The surficial geological unit present in the Yarra Delta Group is the Coode Island Silt, a soft soil present over large portions of inner Melbourne and well documented in the local geotechnical literature (Hughes et al. 1980, Ervin 1992, Ervin et al. 2001, Ervin et al. 2004, Day et al. 2007, Srithar 2010). The presence of Coode Island Silt beneath much of the rail alignment posed considerable design challenges from a geotechnical perspective for the Alliance. Underlying this Coode Island Silt is the Fishermens Bend Silt which forms the founding unit for the semi-rigid inclusions installed as part of the ground improvement works. As part of Work Package B four GRCSE (shown in Figure 3.2) were constructed over a combined length of about 760 m. Of these embankments, the North Dynon embankment was adopted as the field case study for this research project, due largely to its location away from more sensitive rail infrastructure and ease of site access. One of the Maribyrnong River GRCSEs is described separately by Gniel et al. (2015).

3.2 North Dynon ground improvement and embankment design

The design of the North Dynon embankment was completed between May 2012 and April 2013. The final embankment design comprised 4 design areas which differed largely as a result of the varying sub-surface conditions, specifically the thickness of the underlying Coode Island Silt. The ground improvement and geosynthetic reinforced embankment was constructed as part of the design zone *1a* at the eastern end of the embankment,

adjacent to the Moonee Ponds creek where the Coode Island Silt is thickest. The field case study focuses on this 60 m long ground improvement zone. The other 3 areas of embankment design had more favourable ground conditions which did not require ground improvement and they are not investigated as part of this study. At the eastern end of the embankment adjacent to the Moonee Ponds creek it was a requirement to minimise the embankment footprint within the flood plain of the creek and as a result a near vertical gabion wall was designed and constructed in favour of embankment batter slopes. In order to construct the widened embankment without adversely affecting the existing operational rail line, it was necessary to construct the LTP as a split-level design comprising a lower and upper platform. Other aspects of the design are summarised below with further details provided in the following sections:

- Drilled displacement columns are 450 mm diameter, installed with a minimum 2 m socket into the underlying stiff to very stiff clay Fishermens Bend Silt (or underlying Moray Street Gravels) and were designed for a working load of 700 kN. Each column had an enlarged 1 m square head constructed at the ground surface by excavating 1 m square by approximately 600 mm deep and backfilling with concrete, typically, while the column shaft was still wet.
- Columns were typically spaced on a square 2.5 m by 2.5 m grid, or 2.0 m by 2.0 m near the eastern end of the embankment. However, these spacing vary considerably due to geometric constraints.
- The LTP comprised a 650 mm thick layer of 75 mm minus rockfill with not more than 5% fines.
- Two layers (longitudinal and transverse) of 200 kN/m ultimate tensile strength uniaxial geogrid (ACEGrid® GG200-I) were used for the reinforcement of the LTP. The transverse geogrid was placed 100 mm above the base of the LTP and a 100 mm separation layer separates the overlying longitudinal geogrid layer.
- The height of gabion baskets varied along the length of the wall, at the location of instrumentation Area #2 the wall is 3 m in height (i.e. three gabion baskets high). At the far eastern end of the embankment, the gabion wall is 6.5 m high.

Plan views showing the layout of the columns for the North Dynon embankment ground improvement works are shown in Figure 3.3 and Figure 3.4. Note that the orientation of the two drawings is different. Cross sections of the embankment at the two instrumented areas, Area #1 and Area #2, are presented in Figure 3.5 and Figure 3.6, respectively. The construction of the embankment commenced in early March 2013 and was largely completed by mid-November 2013. A timeline of construction activities is presented in Table 3.1 and the embankment height during construction for Area #1 and Area #2 is shown in Figure 3.7*a* and *b* respectively. Note that time zero corresponds to 3 May 2013 at 8:00 am when the first instrumentation reading was taken. The embankment height is measured relative to the top of the column heads (RL + 2.0 m) in Figure 3.7*a* and *b*. The instrumentation was mostly installed at the base of the LTP; the overburden pressure acting on the instrumentation can be (approximately) inferred from the height of embankment shown in Figure 3.7.

A number of events had a considerable impact on the construction sequencing, these are described below:

1. The split-level LTP design meant that ground improvement works were undertaken in stages. The lower ground improvement area was completed as part of Stage 1 and 2 while ground improvement works for the upper area was completed as part of Stage 3a and 3b works.
2. The construction schedule was delayed for approximately 3 months due to the need to relocate a number of underground assets near the eastern end of the embankment. There was a 3 month period between Stage 1 and 2 works.

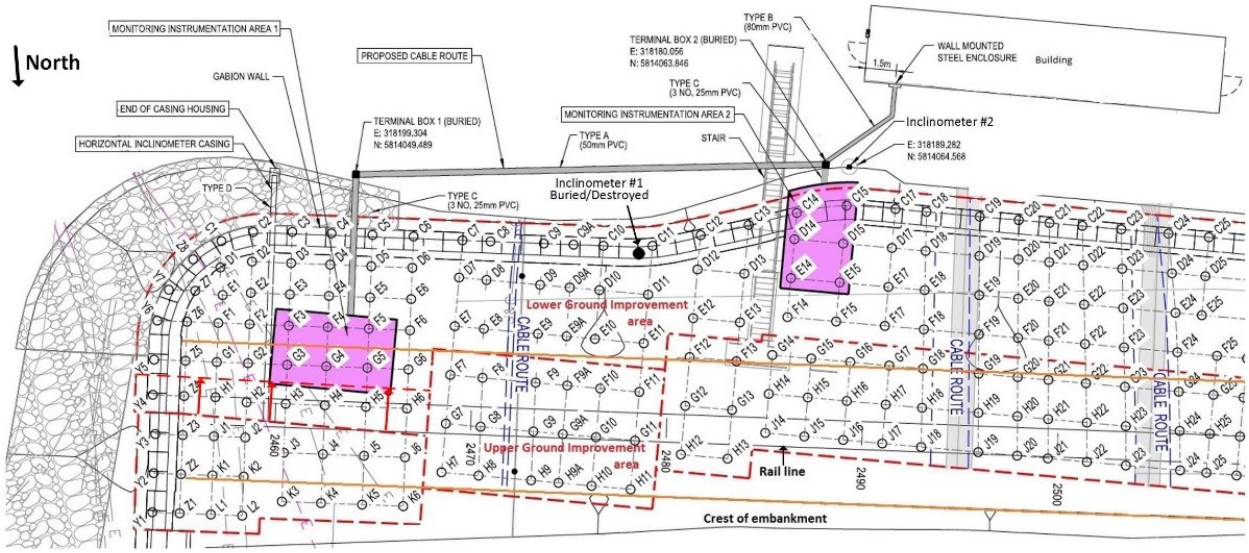

Figure 3.3. North Dynon ground improvement area (exert from design drawings[2]) showing instrumented areas

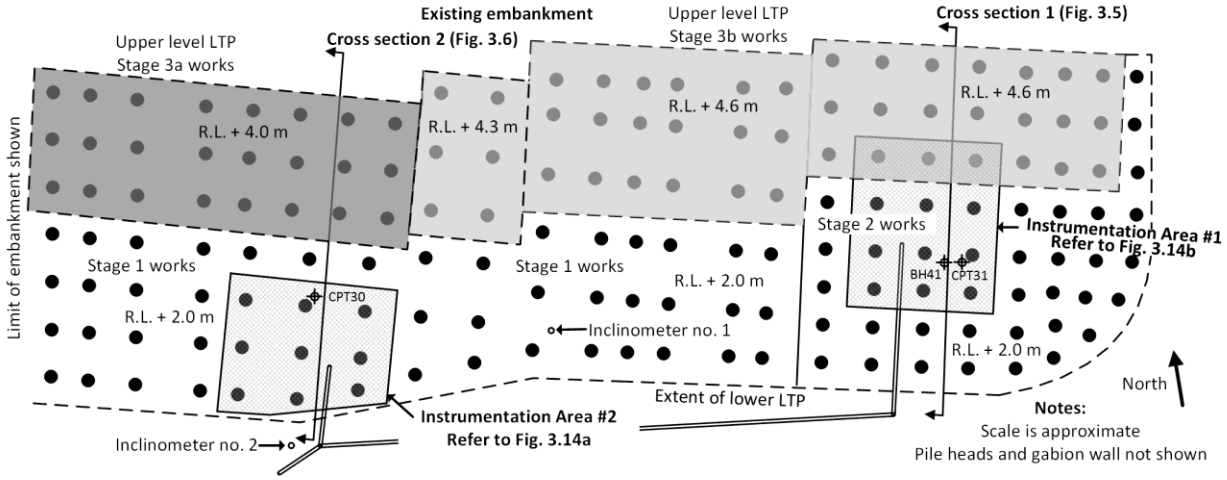

Figure 3.4. Instrumentation areas and North Dynon ground improvement area

[2] Drawing provided for information purposes only and should not be used in place of the original design drawings. Drawing is modified from the original. Underground services have been removed from the drawing for clarity. Note that the design drawings are oriented (approximately) south upwards which is standard convention for rail design drawings in Melbourne. All drawings and figures developed by the author and presented herein are oriented north upwards as shown in Figure 3.4.

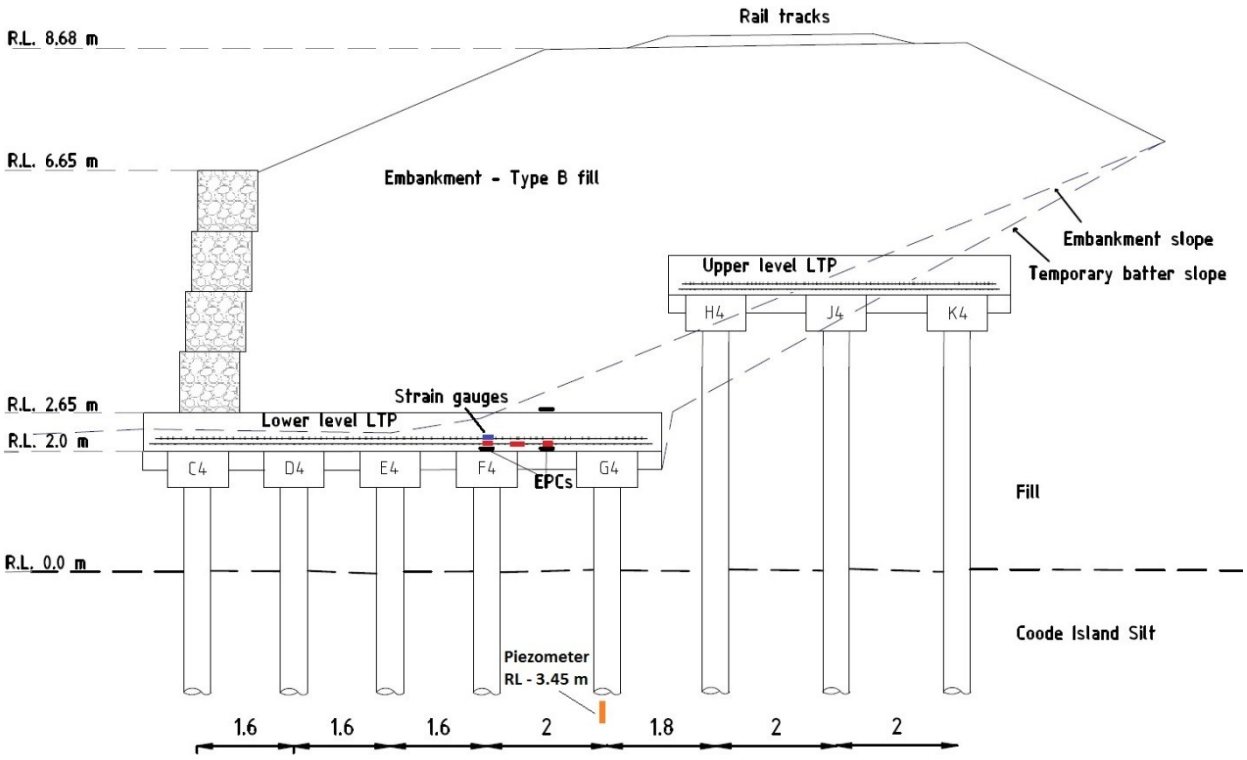

Figure 3.5. Area #1 - Cross Section

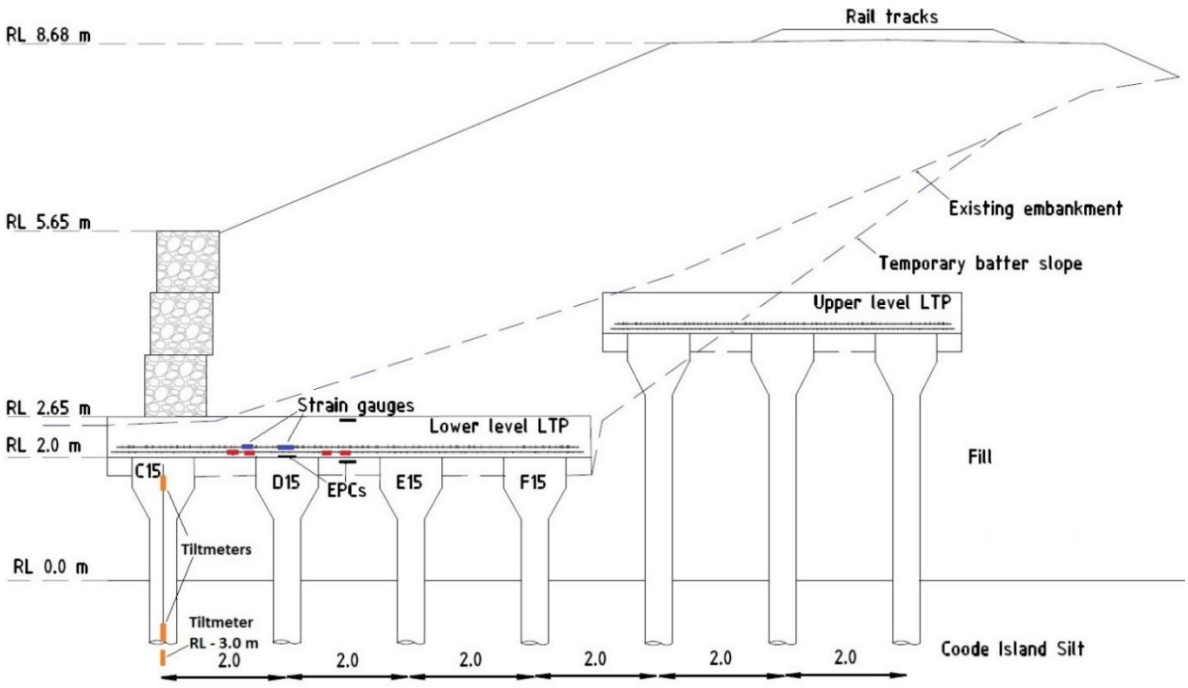

Figure 3.6. Area #2 - Cross Section

Table 3.1. Timeline of embankment construction

Date	Days Elapsed	Activity	Comment
1920s		Construction of historic rail (approach) embankment and bridge	
1968 to 1971		Replacement of historic rail bridge and extension of historic rail (approach) embankments towards creek	
1984		Golder Associates geotechnical investigation	Investigations into settlement issues associated with 1971 extended embankment
1991		Additional consultant geotechnical investigation	
1984 to mid-1990s		On-going settlement monitoring	
2009 to 2011		Various Geotechnical investigations completed for Regional Rail Link	
Mid 2012		Design of Nth Dynon embankment commences	
August 2012		Research case study proposed	
		2013	
14 to 17 Jan.		Geotechnical investigation – detailed design	CPT26 to CPT31. Borehole BH41
8 to 12 March		Inclinometer 1 and 2 installed.	
14 to 27 March		Stage 1 Ground Improvement works	
8 to 10 April		Stage 1 Additional Ground Improvement works	
17 to 23 April		Breaking back column heads	
28 April to 7 May		Instrumentation installation - Area #2	
6 May		LTP construction	
3 May 8:00am	0	First instrumentation reading	
4 May to 20 June	48	Lower portion of embankment constructed (lifts 1 and 2)	
24 to 29 June	57	Stage 2 Ground Improvement works	
5 to 13 July	71	Stage 3a Ground Improvement works	
9 to 16 July	74	Instrumentation installation - Area #1	
7 August	96	Automated data logger installed	Instrumentation measured on a 4 hour time cycle
17 July to 8 Sept.	128	Remaining lower portion of embankment constructed (lifts 1 and 2)	
11 to 17 Sept.	137	Stage 3b Ground Improvement works	
1 Sept. to 24 Oct.	174	Embankment lifts 3 to 7	
24. Oct.	174	Post-construction period commences	

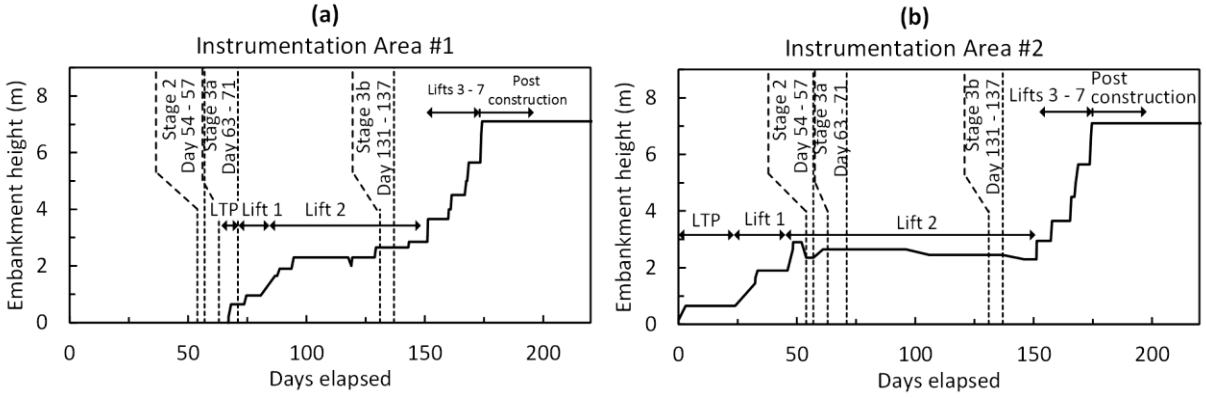

Figure 3.7. Embankment construction timeline **(a)** Area #1 and **(b)** Area #2

3. For these reasons, instrumentation in Area #2 was installed first. This occurred during April 2013 after Stage 1 works. The instrumentation in Area #1, located at the far eastern end of the embankment, was installed several months later after Stage 2 works were completed.
4. Due to the scheduling of the ground improvement works, the embankment lifts were not simultaneous along the length of the embankment. Hence, for most of the construction period the embankment height varied between the two instrumented areas.
5. Embankment construction required a total of seven (7) embankment lifts plus track formation. The lower portion of the embankment construction involved ground improvement works (Stage 1 and 2) as well as construction of the LTP, two levels of gabion baskets and embankment lift no. 1 and 2. Following this, upper level ground improvement works (Stage 3a and 3b) took place between about days 50 and 150.
6. Embankment lifts 3 to 7 involved considerably smaller quantities of earthworks and a shorter length of gabion wall construction; embankment progressed rapidly during these phases to final track level.

3.2.1 Construction material verification

Information relating to the materials used for the embankment construction are summarised in the following section. Much of this information was provided to the design team during the construction phase[3]. This information, along with the laboratory data in Chapter 4, forms the basis for the material parameters adopted in the analyses presented in Chapter 5 onwards.

Embankment fill (RFI0582 and RFI0672) - the engineering fill used for bulk (embankment) earthworks was specified as Type B (or better) compacted in accordance with VicRoads Section 204 – Earthworks specifications. The Type B fill material was required to meet the following requirements (Golder 2013):

- *Free of organic content, topsoil and deleterious or perishable matter such as timber and plastic.*
- *Maximum size of the materials shall not be greater than 100mm.*
- *Target range of % fines passing 0.075 mm sieve is between 15 and 50.*
- *Plasticity Index (I_p) is no greater than 30 or Weighted Plasticity Index (WPI) of the materials is no greater than 1500. WPI is defined as I_p x % passing 0.425 mm sieve.*

The embankment fill material was predominately sourced from an excavation elsewhere within the rail corridor and re-used for the construction of the North Dynon embankment. Given the materials' location and quality it is likely that this historic fill was previously placed under some engineering controls although no records are available to confirm this. The embankment fill is predominately silty sandy gravel (GM) (AS 1726), comprising 40 % - 55 % gravel, approximately 30 % sand, and the remaining portion comprising low-plasticity inorganic fines. Laboratory testing including Particle Size Distribution (PSD) and California Bearing Ratio (CBR) tests were performed on four no. bulk soil samples of this material, results are summarised in Table 3.2.

Embankment fill – compaction records (RFI1464) – design specifications required the embankment fill material to be placed in loose layers not exceeding 300 mm and compacted to 95 % standard compaction; the upper 1 m of the embankment was compacted to 98 % standard compaction. The results of 12 compaction assessments using the nuclear gauge method (AS1289 2007) indicated an average field dry and wet unit weight (average *w* of 13.3 %) of 19.2 kN/m^3 and 21.7 kN/m^3 respectively.

[3] The request for information (RFI) numbers shown in parenthesis refer to the document naming protocol used on the project and have been included for the authors reference

LTP rockfill material (RFI0724) – The LTP comprised a 650 mm thick layer of well graded, 75 minus granodiorite rockfill that was locally supplied, and is known as Oaklands Junction Granodiorite. The PSD curves showing lower/upper limits and a typical profile, along with values of coefficient of curvature (C_c), uniformity coefficient (C_u) and equivalent particle diameters at 10%, 30 % and 60% passing (D_{10}, D_{30} and D_{60}) are presented in Figure 3.8. Additional rockfill material properties provided by the supplier are presented in Table 3.3. The rockfill is of considerable importance for this research as the arching primarily occurs in this unit and this material was specifically chosen by the designers to enhance arching. A review of the material behaviour of rockfill and additional laboratory testing is presented in Chapter 8 where the load transfer platform is modelled using numerical techniques.

Table 3.2. Laboratory test results - embankment fill (prior to embankment construction)

Test	Sample no. 1	Sample no. 2	Sample no. 3	Sample no. 4
% gravel	42	42	56	47
% sand	3	32	30	32
% fines	55	26	14	25
Plastic limit w_p (%) / Liquid limit w_l (%)	23/35	23/34	24/34	23/34
USCS soil description	Gravelly CLAY (CL – CI)	Clayey sandy GRAVEL (GC)	Clayey sandy GRAVEL (GC)	Clayey sandy GRAVEL (GC)
CBR	13.0	20.7	16.4	23.0
Max. dry unit weight (kN/m^3)	17.9	18.1	18.0	18.1
Optimum moisture content (%)	15.2	14.5	14.7	14.4
Field moisture content (%)	13.6	13.5	13.3	13.5

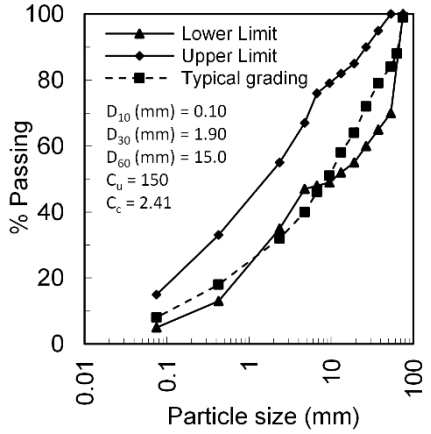

Figure 3.8. Particle-size distribution for LTP 75 mm minus rockfill

Table 3.3. LTP rockfill material properties

Test	Value
w_p (%)	19
w_l (%)	23
Plasticity Index (%)	4
I_p x % passing 0.425 mm	72
CBR at 98% standard compaction	45
Coefficient of permeability at 98% standard compaction (m/sec.)	2 x 10^{-8}
Swell (%) at standard compaction	0.0
Modified maximum dry density (kN/m^3) and optimum moisture content (%)	2.14 at 8.2

LTP geogrid (RFI0967) – the geosynthetic reinforcement for the LTP was specified as a uniaxial geogrid with not less than 200 kN/m ultimate tensile strength at 10 % strain (Golder 2013). The geogrid adopted, ACEGRID® - GG200, is manufactured by Ace Geosynthetics and distributed by a local supplier, Global Geosynthetics. Some of the key product specifications from the manufactures datasheet are summarised in Table 3.4. The relationship between the characteristic tensile strength and the working tensile strength of the geogrid is shown in Figure 3.9 and is calculated based on Equation 3.1. The isochronous curves for the geogrid are shown in Figure 3.10. The value of tensile strength and stiffness adopted in the various analyses undertaken in this research varies depending on the stress/strain range and the time frame considered. This is described separately for each analysis presented. Additional tensile testing was undertaken as part of the strain gauge calibration process and is described in Chapter 4.

$$T_{\mathrm{d}} = \frac{T_{\mathrm{c}}}{f_{\mathrm{c}} \cdot f_{\mathrm{d}} \cdot f_{\mathrm{e}} \cdot f_{\mathrm{m11}} \cdot f_{\mathrm{m12}}} \qquad \textbf{(3.1)}$$

where T_{d} is the long term design tensile strength of the geogrid, T_{c} characteristic tensile strength, f_{c} partial factor for creep effects of embankment design life, f_{d} partial factor for installation damage, f_{e} partial factor for environmental effects, f_{m11} partial factor relating to consistency of manufactures reinforcement and f_{m12} partial factor relating extrapolation of long term creep data. These factors for ACEGRID® 200 are shown in Table 3.5.

Table 3.4. ACEGrid® GG200 uniaxial polyester geogrid – manufacturer material properties

Mean ultimate tensile strength (kN/m)*	Characteristic ultimate tensile strength (kN/m)*†	Geogrid characteristic strength at 5 % strain (kN/m) †
219	206	132

*Cross direction strength is 30 kN/m. Strain at short term ultimate strength is 10 %. From results of wide-width tensile tests (ISO 10319), tested in machine direction and reported in manufacturers literature

†Characteristic strength is the statistical 95 % (2 standard deviations) confidence limit

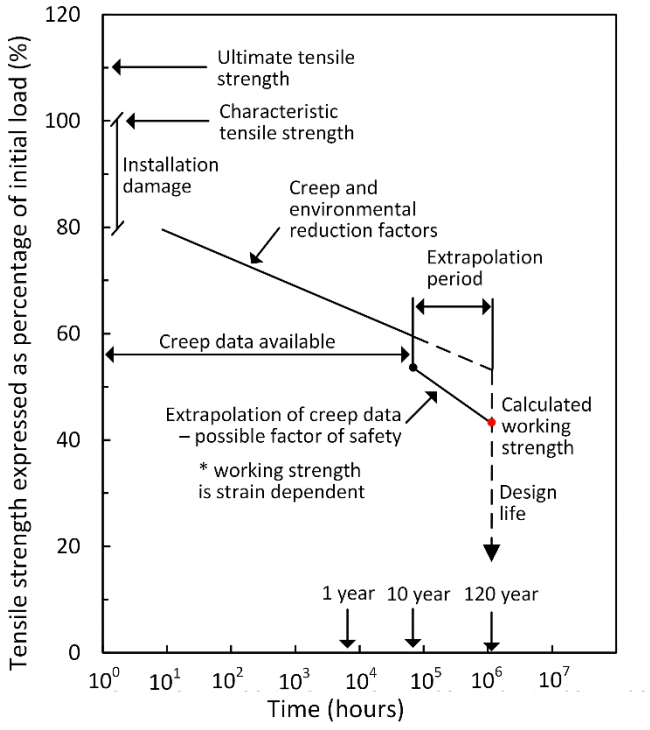

Figure 3.9. Partial factor reductions for calculations of long term working strength (modified from AceGrid® datasheet)

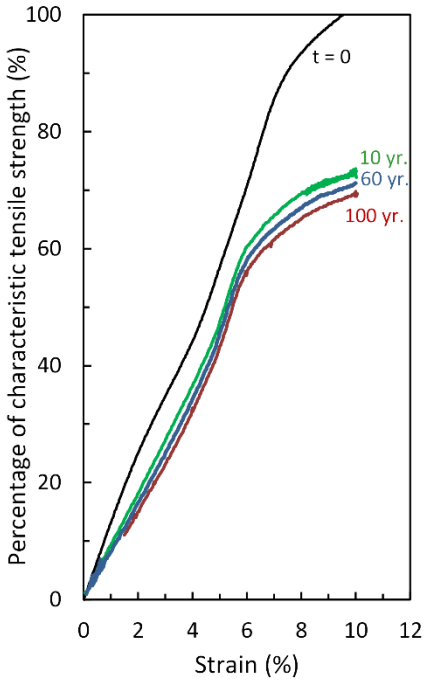

Figure 3.10. Characteristic long term tensile strength-strain-time isochronous curves for AceGrid®

Table 3.5. AceGrid® GG200 partial factors (from AceGrid® datasheet)

	f_d*	f_c	f_e	f_{m11}	f_{m12}
10 year design life	1.05	1.37	1	1.0	1.0
60 year design life		1.41	1.05		
120 year design life		1.45	1.1		

*f_d is based on gravel less than 50 mm. In lieu of an alternative value for the 75 mm minus rockfill used in this case study this value is adopted here. The partial factor is close to 1 and this assumption is not expected to significantly affect the strength and stiffness values adopted in the analysis presented in the following chapters.

Gabion basket and Terramesh panels (RFI1022) – the gabion wall is comprised of Galmac® coated Gabion baskets and 2 m integral Terramesh panels (tails) manufactured by Maccaferri Pty. Ltd. Installation was in accordance with the product guidelines Maccaferri (2003). Maccaferri Gabion basket and Terramesh panel datasheets are available through the supplier website (Geofabrics 2015).

Gabion wall - geosynthetic reinforcement – Maccaferri Paralink 100 and Paralink 200 geogrids where used as the geosynthetic reinforcement for the gabion walls. The Paralink 100 reinforcement was typically used and extended back 6 m into the embankment for each gabion level. At the eastern end of the gabion wall, where the wall is at its highest, Paralink 200 was adopted, extending back between 10 m and 12 m into the embankment. Datasheets are available on the Maccaferri (2015) website.

Gabion basket rockfill (RFI1365) – the rockfill material used in the gabion basket was to be dense, durable, free of soil and vegetable matter, non-acid forming and meeting the criteria (Golder 2013) below (relevant Australian Standards (AS) are indicated in parenthesis):

- *Los Angeles value B grading (AS 1141.23) ≤ 20%*
- *Aggregate dry strength (AS 1141.21) ≥ 200 kN*
- *Aggregate wet strength (AS 1141.21) ≥ 100 kN*
- *Aggregate wet/dry strength variation (AS 1141.21) ≤ 50%*
- *The aggregate size should be 100 – 200 mm with not more than 5 % passing 75 mm. If there is a shortage of suitably sized material then rock of less than 100 mm diameter (e.g. railway ballast of suitable quality) can be used to fill the centres of the baskets.*

The rockfill used for the gabion baskets is a Newer Volcanics Basalt. Initially laboratory test results indicated a Los Angeles value of 23 % (exceeding design criteria) and an aggregate dry and wet strength of 192 kN and 110 kN respectively. Wet/dry strength variation was 43 %. Additional laboratory test data was supplied to verify the Los Angeles value, the data indicated a Los Angeles value of 19 %.

North Dynon embankment post-construction survey monitoring (RFI2750) – survey monitoring of the gabion wall and embankment commenced at the completion of construction and was on-going at the time of publication (late 2016). This data is presented in Chapter 9 where the full-scale embankment mechanisms are examined.

3.2.2 Ground improvement works

The ground improvement works for the North Dynon embankment comprised the installation of 297 drilled displacement columns to depths ranging from 12 m to 23 m (depth from lower ground improvement area). The installation of the columns was completed using a MAIT HR 360-800 – piling rig (Figure 3.11). The rig has a mast height of just over 33 m, operational weight of 138 tonne and a maximum stroke of 27.0 m. The generic piling rig

Figure 3.11. Mait HR 360-800 piling rig

specifications for the Mait HR800 are available online. The piling rig is typically used by the contractor for installation of continuous flight auger (CFA) piles. However, for this project the CFA flights were replaced with a conventional Kelly bar drilling system and a specialised drilling tool. The construction of a drilled displacement column is similar in many respects to the non-displacement CFA pile, the main difference been the drilling tool used. The construction methodology for a drilled displacement column is outlined in detail in Chapter 8 where the installation effects are examined.

3.2.3 Survey of ground improvement works

As the column heads were cast *in situ* they were, in some cases, cast greater than the design 1 m by 1 m size specified. From a design viewpoint, this was not considered overly problematic as this reduced the clear spacing between column head locations. However, for the post-construction analysis undertaken as part of this research, the variable clear spacing makes the analysis of instrumentation results more difficult. For this reason, the column heads in Area #2 were "broken back" by the author using a combination of concrete cutting and jack hammering. Over the course of 3 days (17 to 19 April 2013) the column heads were cut (approximately) square to the original 1 m by 1m dimensions. Before and after photos of Area #2 with the array of column heads visible is shown in Figure 3.12 and Figure 3.13. Site survey of the column heads was undertaken and these "as-built" survey dimensions were used to locate the column heads during the instrumentation installation. This was necessary to ensure that the instrumentation could be placed in the correct location relative to the column heads once these were covered (and obscured) by the LTP rockfill. At the location of Area #1 forma-tube was used to construct circular 1.0 m diameter column heads.

3.3 Instrumentation

As the field case study involved the instrumentation of a functioning rail line a significant amount of planning, investigation and approvals were required before instrumentation could be installed. A detailed instrumentation plan was developed in 2013 by the author along with the specification, procurement and installation of instrumentation. The following instrumentation was installed:

- Earth pressure cells
- Strain gauges (including dummy gauges)
- Vertical and horizontal inclinometer casing

Figure 3.12. Column heads following removal of the hardstand (17 April 2013)

Figure 3.13. Area #2 column heads after "breaking-back" (19 April 2013)

- Tiltmeters
- Piezometer
- Data acquisition hardware

The instrumentation was installed in two general areas; Area #1 and #2, both are located in the lower ground improvement area (Figure 3.3 and Figure 3.4). The instrumentation layout plan is shown in Figure 3.14. A photograph of Area #1 at the completion of Stage 2 works is presented in Figure 3.15. Similar photographs of Area #2 are presented in Figure 3.12 and Figure 3.13.

Area #1 is located near the centre of the lower ground improvement area and was intended to assess the general LTP behaviour. However, due to subsequent design changes, the "step" between the lower and upper ground improvement areas was shifted from between column row J-H to row H-G. As a result, the upper level LTP is

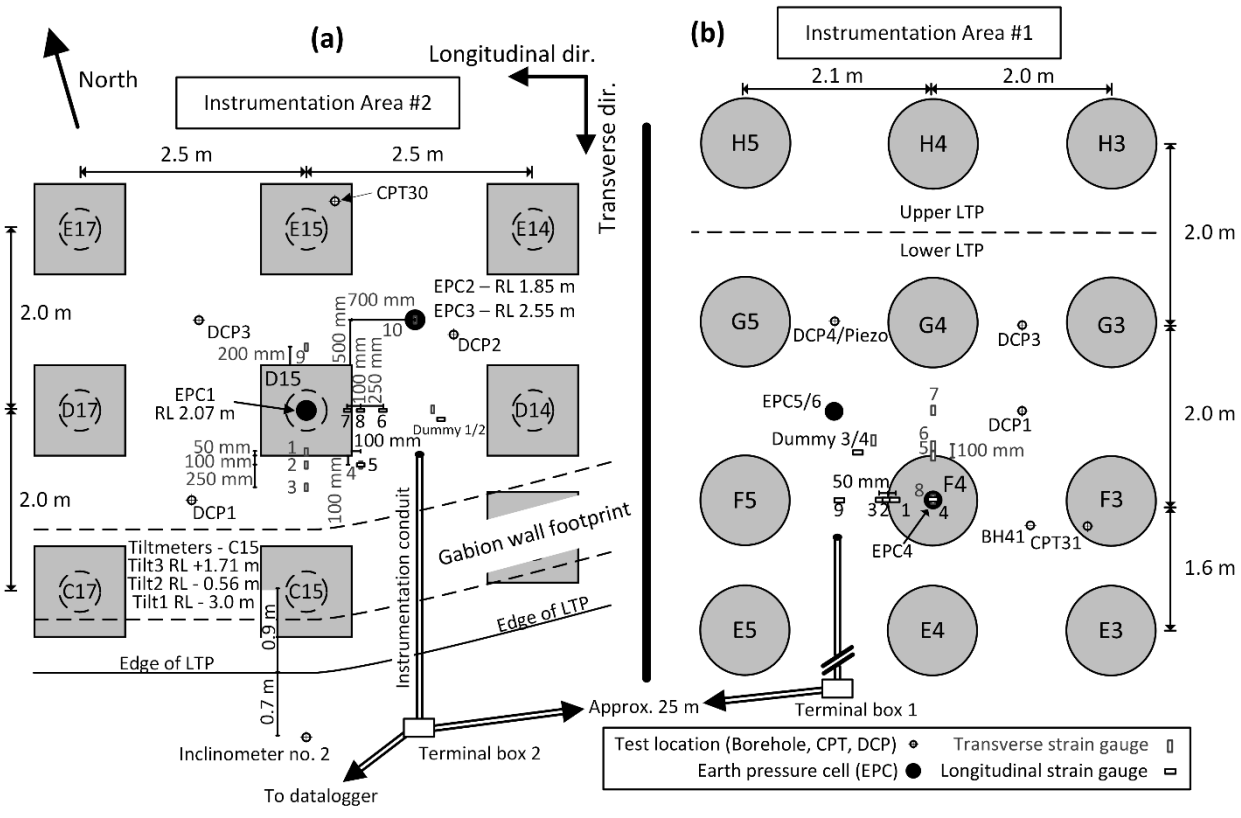

Figure 3.14. (a) Area #2 plan view and **(b)** Area #1

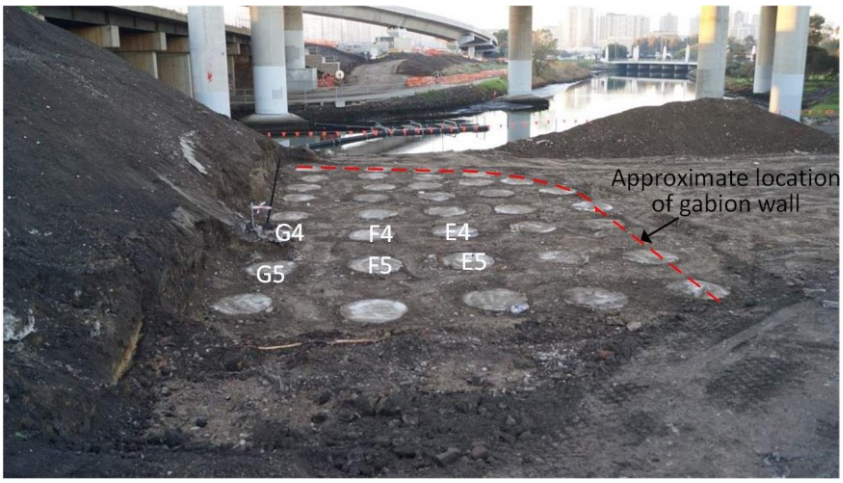

Figure 3.15. Photograph of Area #1 and lower ground improvement area

located immediately adjacent to the Area #1; this was not the intention of the original instrumentation design and has had a considerable effect on the LTP behaviour which is described later. Area #2 is near the edge of the embankment, beneath the gabion wall. The intention was to assess the difference between the longitudinal and transverse forces in the LTP, due to the lateral load from the overlying gabion wall and embankment.

In addition to the instrumented areas, two vertical inclinometer casings were installed. Inclinometer no. 1 was installed near column C11 to assess the lateral soil displacement associated with the installation of the adjacent columns. This casing was temporary and was not accessible following the completion of ground improvement works. Inclinometer casing no. 2 was permanent and was installed beyond the footprint of the LTP to assess both the lateral soil displacement associated with column installation as well as global embankment behaviour (i.e., lateral spreading of the embankment). Two horizontal inclinometers were also installed adjacent to Area #1. One casing was situated below the LTP and the other near the surface of the LTP; these were installed to assess the vertical deflection of the LTP.

3.3.1 Earth pressure cells

Earth pressure cells were installed within the LTP material to measure the vertical stresses associated with the arching mechanism. Within each instrumented area three earth pressure cells were installed (six total). The earth pressure cells installed were supplied by HMA – Geotechnical Systems Australia Pty. Ltd. and are Geokon Model 4800 circular earth pressure cells. The cells installed are 230 mm in diameter and 6 mm thick (aspect ratio of approximately 38). They comprise a flexible upper and lower circular plate welded around the periphery and are intended for stress measurements within soil masses (as opposed to earth pressure cells with a rigid back face which are intended for stress measurements at the soil-structure interface).

A thin cavity between the plates is filled with de-aired hydraulic oil and connected to an external diaphragm via a thin tube. The sensors used to measure diaphragm movement are typically available in two general forms: strain gauge and vibrating wire type, the installed cells are of the latter type. The earth pressure cells produce a vibrating wire frequency as its output, this is calibrated against a known applied external pressure as part of the factory calibration. The earth pressure cells also have a built-in temperature sensors to account for temperature induced expansion and contraction of the hydraulic oil. Two of the installed earth pressure cells are shown in Figure 3.16. The arrangement of earth pressure cells installed in Area #2 is described below (earth pressure cells are named EPC1 to EPC6 and are numbered based on the order of installation):

- EPC1 – Centre of column D15. 100 mm above column head.
- EPC2 – Centre of grid D15-D14-E15-E14. 150 mm below the base of the LTP
- EPC3 – Centre of grid D15-D14-E15-E14. 100 mm below the top of the LTP

The earth pressure cells installed in Area #1 where installed in a similar manner to Area #2, i.e., EPC1 is similar to EPC4, EPC2 to EPC5 etc.

- EPC4 – Centre of column D15. 100 mm above column head.
- EPC5 – Centre of grid D15-D14-E15-E14. 150 mm below the base of the LTP
- EPC6 - Centre of grid D15-D14-E15-E14. 100 mm above the top of the LTP

The arching mechanism is shown conceptually along with earth pressure cells installed in Area #2 in Figure 3.17. EPC1 is installed beneath the 2 layers of geosynthetic reinforcement and measures the sum of component A (arching stress) and component B (tensile load); the applied load acting on the head of the column. EPC2 is beneath both layers of geogrid, near the centre of a column grid, and measures load component C (sub-soil support). EPC3 is 100 mm above the LTP and measures stresses near the so-called "crown of the soil arching". This will depend on the arching stress development and the height which the crown of the soil arch forms. Based on this understanding of

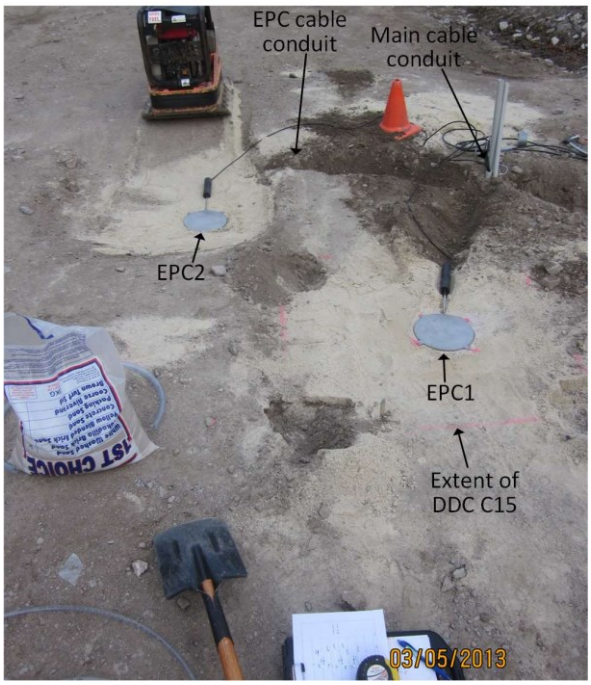

Figure 3.16. Installation of earth pressure cell

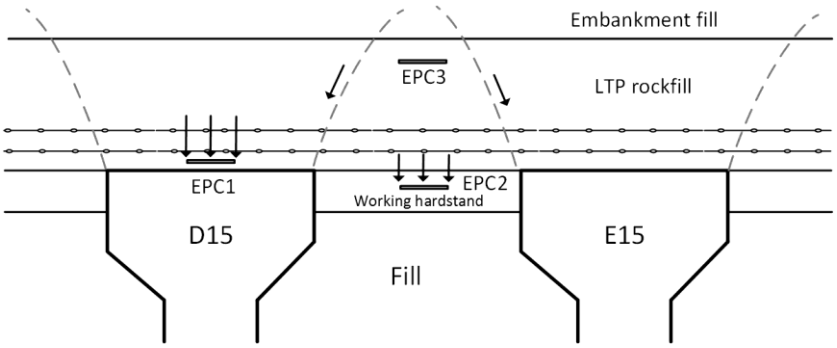

Figure 3.17. Area #2 – theoretical load distribution

Table 3.6. Factors affecting earth pressure cell performance – after Dunnicliff (1988)

Factor	Description of Error	Correction method	Geokon Model 4800
Aspect ratio (cell thickness / diameter)	Cell thickness alters stress fields around cell	Use relatively thin cells ($T/D < 1/10$)	$T/D = 1/38$ Satisfied
Soil/cell stiffness ratio	May cause cell to under- or over register. Error will change if soil stiffness changes	Design cell for high stiffness and use correction factor	
Size of cell	Small cells subject to scale effects and placement errors Large cells difficult to install and subject to non-uniform bending	Use intermediate size of cell; typically, 230 – 300 mm diameter	230 mm diameter cell Satisfied
Stress-strain behaviour of soil	Measurements influenced by confining conditions	Calibrate cell under near-usage conditions	
Placement effects	Physical placement and backfilling causes alteration of material properties and stress field around cell	Use placement technique that causes minimum alteration of material properties and stress field	Bedding material compacted with Bedding sand necessary to protect cells from rockfill.
Eccentric, non-uniform and point loads	Soil grain size too large for cell size used Non-uniform beddings cause non-uniform loading	Increase active diameter of cell Take care to maximise uniformity of bedding Particle diameter to cell diameter < 1:10 Weiler et al. (1982)	Rockfill does not meet this requirement. A bedding material is required.
Proximity of structures and other embedded instruments	Interaction of stress fields near instruments and structures	Use adequate spacing	
Orientation of cell	Changing orientation of cell while placing fill	Use appropriate placement methods	
Concentration of normal stresses at cell edge	Causes cell to under – or-register, depending on soil/cell stiffness ratio	For hydraulic cell, use grooved thick active face and thin layer of liquid	Satisfied (Geokon 2011)
Deflection of active face	Excessive deflection of active face changes stress distribution by arching	Design cell for low deflection Use thin layer of liquid in hydraulic cell	Satisfied (Geokon 2011)
Corrosion and moisture	May cause failure of cell	Use appropriate material and high quality waterproofing.	Manufacturers design addresses these issues. Cell placement is above the water table. Main concern is wiring connections between cell and instrumentation enclosure.
Temperature	Temperature changes cause change of cell reading	Design cell for minimum sensitivity to temperature, if significant temperature is likely, measure temperature and apply correction factor calculated during calibration	Cells have incorporated temperature sensor and correction factor available in manufacturer calibration sheets. Temperature range in embankment relatively stable.
Dynamic stress measurement	Response time, natural frequency, and inertia of cell cause errors	Use appropriate type of cell and instrumentation	Dynamic measurements are not proposed as part of this research.

the load distribution, the stress range of the installed earth pressure cells was specified. This is necessary to ensure that applied stresses (including construction phase stresses) do not exceed the cells limits and that the cells have sufficient sensitivity in the stress range which they experience. EPC1 and EPC4 were specified as 1 MPa cells while the remaining 4 cells are 350 kPa cells. The relationship between the earth pressure cells and arching stress distribution is similar for Area #1.

Earth Pressure Cell Installation

A number of earth pressure cell installation techniques were considered. In general, the literature describing the measurement of *in situ* stresses (Peattie et al. 1954, Thomas et al. 1969, Dunnicliff 1988, Theroux 2000, Theroux et al. 2001, Dave et al. 2011, Talesnick 2013) focuses on two aspects of measurement:

1) earth pressure cell specifications (cell diameter, thickness, aspect ratio and other cell characteristics) and
2) Properties of the soil in which the earth pressure cell is located.

The factors affecting the measurement of *in situ* soil stress, after Weiler et al. (1982) and modified by Dunnicliff (1988), are presented in Table 3.6. Regarding the earth pressure cell specifications (aspect ratio, size of cell, concentration of normal stresses at cell edge, corrosion, moisture and temperature), these are controlled by the cell manufacturer and it is shown in Table 3.6 that these meet the requirements suggested by Dunnicliff (1988). The other factors affecting earth pressure cell performance (placement effects, non-uniform point loads, proximity of other structures and orientation of cell) were addressed, as far as practical, based on extensive review of the literature by adopting the installation technique described. The earth pressure cells were installed in a thin layer (100 mm thick above and below) of bedding sand in order to 1) minimise the potential for localised "point loads" occurring due to larger rockfill particles acting directly on the cell face (and affecting the cell pressure) and 2) protect the cells from the rockfill and compaction stresses imparted during the earthworks compaction. The bedding layer was prepared by excavating into the compacted zone a 1 m by 1m area with an excavator and blade bucket. The bottom layer of moist bedding sand (below the cell) was compacted using a vibratory plate (Wacker Neuson – DPU 4045Ye); this provided marginal improvement in the compaction of the loosely placed sand. The cells were placed and an upper layer of bedding sand was placed and lightly compacted with the same vibratory plate.

Fill material was then placed over the earth pressure cells (rockfill over earth pressure cells 1,2 and 4,5 and embankment fill over earth pressure cells 3,6) with the first lift of 300 mm loose thickness compacted with earthworks equipment to 95% standard compaction in accordance with design specification. Area #2 was compacted with a 15-tonne vibratory smooth drum roller (DynaPac CA51) and Area #1 with a 10-tonne vibratory smooth drum roller (Caterpillar CS533E). Given the granular nature of the bedding sand and rockfill, along with the relatively thin loose layer thickness compacted it is inferred that a relatively uniform compactive effort is close to the one used for the overlying material (i.e., 95 % standard compaction).

3.3.2 Strain gauges

Strain gauges were installed to measure the strain of the longitudinal and transverse geogrid layers installed within the LTP. The gauges installed are Vishay Micro-Measurements® type CEA-06-250UN-350 and measure 10 mm × 3 mm, gauge factor of 2.12 (varies) and have a relative resistance of 350 Ohm. The Vishay Micro-Measurements® EP type gauges for large strain applications (VMM 2010a) were not considered necessary for this application as design geogrid strains were not expected to exceed about 4 % over the project life; general purpose CEA type gauges were therefore adopted. The strain gauges were installed in pairs on the machine direction geogrid ribs with one rib

separating the pair. For Area #2, four pairs of gauges were installed on the longitudinal geogrid, six pairs on the transverse geogrid and two dummy gauges (22 gauges total) were installed (Figure 3.14*a*). For Area #1, five pairs of gauges were installed on the longitudinal geogrid layer, four pairs on the transverse layer and two dummy gauges (20 gauges total) were installed (Figure 3.14*b*). To calibrate against thermally induced strain, dummy gauges on 5 cm pieces of geogrid separate from the reinforcement layers were installed in the rockfill in both instrumentation areas. The gauges were installed in accordance with the detailed procedure described by Oglesby et al. (1992) for bonding strain gauges to woven polyester (PET) geogrids and follows many of the general recommendations in the VMM literature (VMM 2010b, 2010c, 2010d, 2011).

The strain gauge application procedure is a six-step procedure and is as follows:

1) **Design drawings**, survey co-ordinates and markers were used to peg out the location of the longitudinal and transverse geogrid layers on-site. Lengths of geogrid (typically 20 m by 5 m) were taken to a warehouse were the gauges were installed indoors under controlled conditions. In the warehouse the location of the various column heads was marked out on the geogrid with spray-paint and the strain gauge locations identified relative to the columns.

2) **Surface preparation** was in general accordance with Vishay Micro-Measurements® literature (VMM 2011) and involved physically removing the polymer coating using a scalpel over an area 25 mm by 9 mm (rib width) to expose the polyester fibres at the midpoint of a machine direction rib. Isopropyl alcohol and M-Prep neutraliser was applied separately to clean the bonding surface and then allowed to air dry.

3) The **Bonding surface** was prepared over the 25 mm by 9 mm by applying Vishay Micro-Measurements® M-Bond AE-10 two-part epoxy resin. Installation tape, rubber pads and clamps were used to ensure an even epoxy surface. As the work was performed in the winter months, heaters were required to ensure the temperature dependent curing times were met (VMM 2010b); 2 hours greater at a temperature > 20° degrees.

4) **Gauge application** required lightly sanding the epoxy bonding surface with 200 grit sandpaper and then 400 grit sandpaper. The surface preparation technique described in step 2 was then repeated and strain gauges applied using epoxy resin, installation tape, rubber pads and clamps similar to step 3.

5) **Soldering** of strain gauges was done with a three lead wire attachment in accordance with literature (VMM 2010c, 2010d). M-Line rosin solvent was applied post-soldering to remove any residual solder flux.

6) Two **protective coatings** were applied, the first was a thin application of a general purpose base coating, M-Coat A, which was applied to provide general waterproofing. This was followed by a thick coating of a general purpose gap filler to provide mechanical protection to the gauge. The gauge wires were then feed through protective rubber tubing. In order to protect the gauges during transportation the tubing was attached to the geogrid with duct tape and wooden splits were placed beneath gauges, this also helped to prevent any load been applied to the gauge wiring and the solder joint which is particularly prone to breakage/debonding.

Similar strain gauge application procedures for high-density polyethylene (HDPE) and polypropylene (PP) geogrids are described by McGown et al. (1995), Gnanendran et al. (2001), Bathurst et al. (2003), Zarnani et al. (2004), amongst others. Hsu (2008) also reports laboratory strain gauge tensile tests on PET woven geogrid samples. The key differences with the application method above, compared with HDPE/PP geogrids applications, is the two-step epoxy resin application and the requirement to remove the outer polymer coating from the geogrid. The surface preparation, soldering and steps taken to protect the gauges during transportation are similar.

The initial strain gauge calibration was undertaken as Monash University in mid-2013 using an Instron (model 5982) 100 kN loading apparatus. Metal clamps were used to clamp the geogrid (Figure 3.18*a*) with varying clamping pressures (by varying the applied torque to mounting bolts), and clamping methods adopted in an attempt to reduce clamping pressure (to avoid geogrid damage at the clamp location) whilst also minimising clamp slippage. An example of typical strain applied to the PET woven geogrid (AceGrid® GG200) is shown in (Figure 3.18*b*). Four no. tensile tests without strain gauges were recorded and a number of additional geogrid samples were tested to failure to assess clamping effects. Two no. tensile tests were performed with strain gauges attached with localised strain gauge readings measured using a Tokyo Sokki Kenkyujo - TC-32K Handheld data logger/strain gauge readout unit (see Section 3.3.7).

Global geogrid strain was measured based on the crosshead displacement of the load cell. However, the results indicated that some clamp slippage occurred, as evidenced by comparing the geogrid load-strain test results with the manufacturer's characteristic curve, indicating the true global strain in the geogrid was less than that measured based the crosshead displacement of the load cell machine. In addition, the majority of geogrid samples experienced premature rupture at, or near, the clamps at about 6 % (geogrid failure is expected at 10 % in accordance with the manufactures datasheet, see Figure 3.10). The difficulties encountered relating to clamping of the high strength geogrid are consistent with the discussion and results of Müller-Rochholz et al. (2000) who provides a comprehensive overview of different clamping systems for high strength geosynthetic testing. The limited number of strain gauge tests did however provide an initial, approximate calibration factor up to about 6 % global strain.

Further strain gauge calibration testing was completed in July 2014 at TRI Australasia's specialist geosynthetic testing facility in Burleigh Heads, Queensland. These tests were performed in accordance with ASTM D6637 – 11 and were also tested using an Instron (model 5982) 100 kN loading apparatus. A key difference with this geogrid tensile testing was the use of purpose built high strength hydraulic roller clamps (manufactured by Humphrey Products in Michigan, USA) that have been designed for the purposes of testing high tensile strength geogrids. Due to the nature of the clamping mechanism, crosshead displacement measured by the loading cell cannot be used to accurately measure global geogrid strain for these clamps. Global geogrid strain was therefore measured using the Instron – Non-contacting Standard Axial Video Extensometer 2 (SVE2). This approach provides a direct, high resolution, non-contact measure of global geogrid strain and removes errors associated with clamp slippage typically encountered with the testing of high tensile strength geosynthetic materials (Shinoda et al. 2004). Some samples were not of a sufficient length to mount in the roller clamps, in this case they were tested using high capacity Curtis Industries "Geo-grips", which have an applied grip/load capacity equivalent to 4536 kg (10,000 lb).

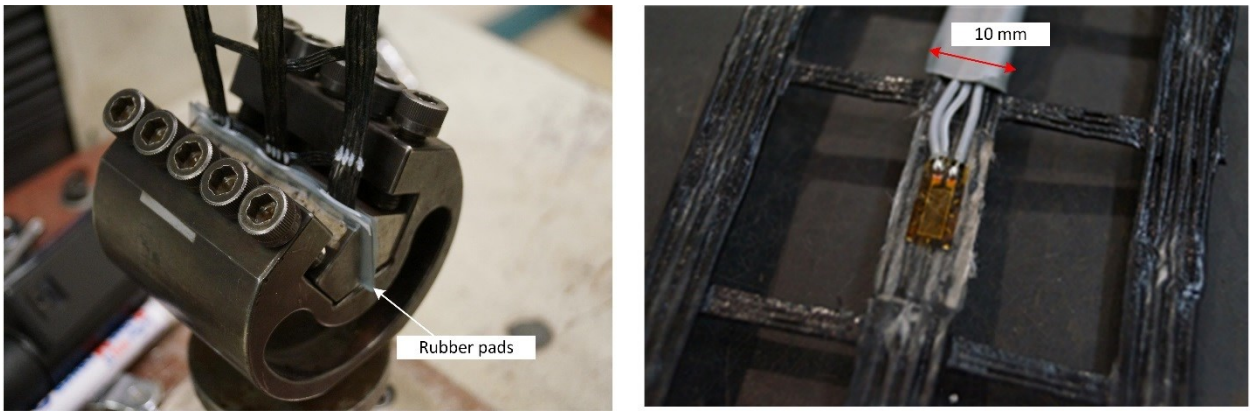

Figure 3.18. (a) Strain gauge clamps used for 2013 tensile tests at Monash University and **(b)** typical strain gauge on PET woven geogrid

The results of the tensile load testing are presented in Figure 3.19 together with the manufacturer's geogrid characteristic curve. Tensile tests and strain gauge calibration tests (denoted with SG in Figure 3.19 and Figure 3.20) were performed and typically terminated in the range of 4 % to 6 % global strain where strain gauges failed. Within the expected working strain range of the geogrid (0 % to 6 %), the characteristic curve plots as a lower bound of the laboratory test results as expected. By comparison, the earlier tests performed with metal clamps

The results of the strain gauge laboratory calibration are presented in Figure 3.20. Test no. 1 was damaged during soldering and not tested, test no. 3 showed an erratic gauge response. The reason for this is not clear based on a visual inspection of the strain gauge application and comparison with the other samples. Of the six gauges tested, four showed a reasonably linear response up to a global strain of 3.0 %, sample no. 6 deviated somewhat from the other four samples. Based on these results, global strain is calculated with a calibration factor 0.82. The calibration factor obtained is dependent on a range of factors; the predominant factors include: geosynthetic material type, ultimate tensile strength, and strain gauge application procedure. This has been shown by Bathurst et al. (2002), who summarized the calibration factors obtained from 12 studies; a range of 1.0 to 2.0 for mostly low strength geogrids was shown. These calibration factors indicate that the application of glue–epoxy creates a localized stiff spot (i.e., strain gauge reading is less than global strain). By contrast, the application of the strain gauge to the high strength (200 kN/m) PET geogrid used in the present study creates a localized "soft" spot; in the present study, a calibration factor of 0.82 was obtained. The localized gauge reading is therefore greater than the registered global strain.

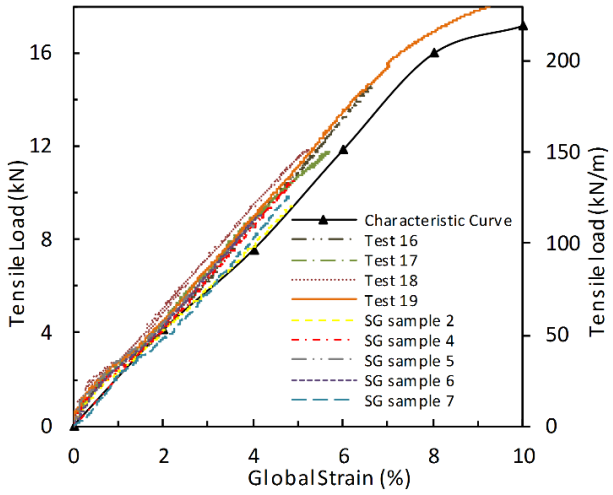

Figure 3.19. Tensile load testing of ACE Geogrid

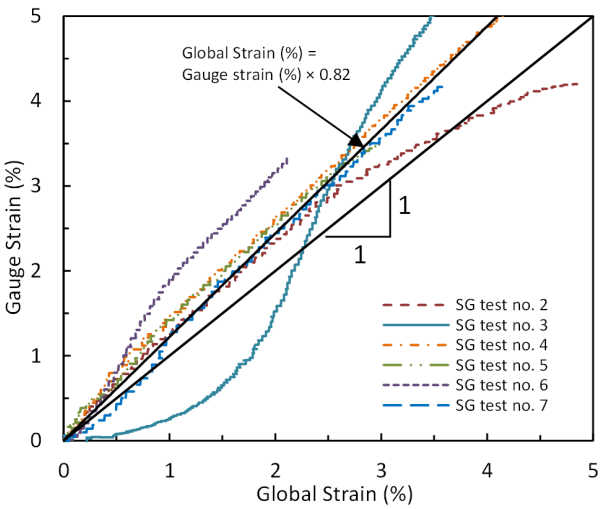

Figure 3.20. Strain calibration testing – Gauge strain *vs* global geogrid strain

Laboratory testing by Oglesby et al. (1992) using this gauge application technique on similar high-strength (T_{ult} = 133 kN/m) woven PET geogrid observed similarly consistent behaviour although with a slightly lower calibration factor.

3.3.3 Vertical inclinometer

Vertical inclinometers no. 1 and 2 were installed on 8 and 12 March 2013 respectively using a specialist drilling contractor. The boreholes were advanced using a combination of solid auger and then washbore drilling techniques. These drilling works were performed under the supervision of the author. It was necessary to advance the boreholes sufficiently below the expected column installation depth to ensure that the base of the inclinometer casing remained fixed during ground improvement works. The installation depth for Inclinometer no. 1 was expected to be considerable deeper than inclinometer no. 2 based on the site investigation information available at the time. The inclinometer casing has an outer diameter of 70 mm and an inner diameter of 58.50 mm that has four equally spaced machined grooves that guide the inclinometer probe along the length of the borehole; these grooves define the A+/A- and B+/B- axes. The inclinometer casing used has a coupling system with a watertight O-ring seal (see Figure 3.21); the use of solvent cements was not required.

The total length of inclinometer 1 casing installed was 22.14 m (8 no. 3 m lengths). A 25 mm diameter polytube/grout tube was progressively fixed to the outside of the casing as each length was installed into the borehole. The casing was also progressively filled with water as each length was installed to counter the casing buoyancy in the drilling fluid. The installation method was in accordance with the installation manual provided by the manufacturer (GSA 2005). The grout comprised 1 part cement, 0.3 parts bentonite and 4.5 parts water and was batched in a 44-(imperial)-gallon drum (200 litres) using the drilling rig pump with a suction hose and jet grout to ensure a consistent mix. The grout was then pumped into the tremie grout tube, displacing the drilling fluid to the surface. This grout mixing configuration and procedure is in accordance with Mikkelsen (2002). The grout ratio adopted is in between ratios described by Mikkelsen (2002) for instrumentation grouted into soft and hard clays. Inclinometer no. 1 was installed to about 250 mm below the surface of the piling hardstand. A 150 mm protective casing was placed over the casing to protect the inclinometer casing during ground improvement works (Figure 3.22).

The method of installation for inclinometer 2 was the same as inclinometer 1. Inclinometer 2 is offset 1.6 m from the centre of column C15 and 700 mm from the edge of the LTP (Figure 3.3 and Figure 3.4). The borehole for inclinometer 2 was advanced to a depth of 18.2 m; a total of 18 m of casing was installed. Both inclinometer casings were surveyed (top of casing) following installation to determine the elevation and orientation of the top of inclinometer casing. The top of inclinometer 1 casing was surveyed at RL + 1.95 m, 50 mm below the top of the column heads. The toe of the inclinometer casing is at RL − 20.19 m. The four adjacent columns adjacent to inclinometer no. 1 were installed to RLs of between − 14.0 and − 15.7 m; the base of the inclinometer casing is over 4 m below the deepest installed column and is therefore considered fixed and stable as intended.

Inclinometer 2 has a top of casing RL of + 2.10 m and toe of casing at RL - 15.9 m. Adjacent columns were installed to depth of between RL − 12.41 m and − 14.13 m. One column, D17, was installed at a radial distance of 4.4 m to RL − 15.50 m. The bottom tip of this column head is 0.4 m above the toe of the inclinometer. However, the geometry of the drilling tool (see Chapter 8, Figure 8.2) suggests that minimal lateral movement would be expected at, or below, the toe level. This is confirmed by the results of inclinometer 1 (Section 8.4.2) where a lateral movement of 0.5 mm at the bottom tip of drilling tool was recorded at a radial distance of 1.96 m. With

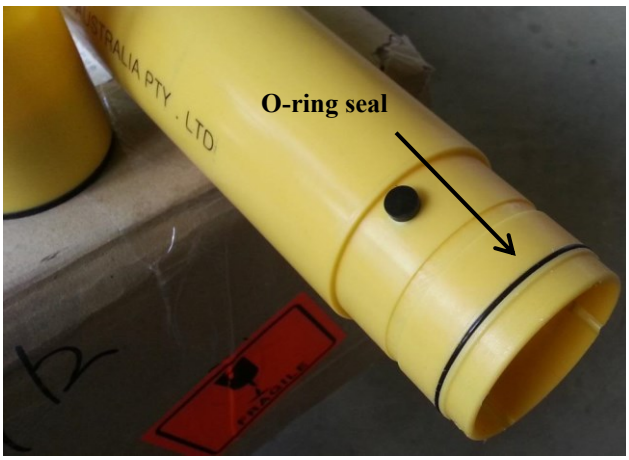

Figure 3.21. Vertical inclinometer casing

Figure 3.22. Inclinometer no. 1

consideration for the radial distance of column D17, the effect this column installation had on the toe of the inclinometer casing is at most 0.5 mm and likely less. This casing is also considered fixed and stable. Measurements from the inclinometer casing are taken using an inclinometer probe that is first lowered to the base of the casing and then progressively raised with measurements taken at 0.5 m intervals. The standard industry sign convention for the inclinometer probe and output data is shown in Figure 3.23 and Figure 3.24. Note the probe A/B axes refer to the orientation of the two accelerometers housed in the probe and differ from the axes in the inclinometer casing. The probe has a check sum standard deviation of 8 (0.08 mm) and 16 (0.16 mm) in the A-axis and B-axis respectively. The standard deviation provides a measure of the random placement error (Mikkelsen 2003).

The difference is due to the positioning of the probe wheels in the grooves which are required to have a wheel clearance tolerance. For this reason, all inclinometer surveys were performed by surveying the inclinometer with the probe A axis. This requires four passes for a single inclinometer reading. The B+/B− inclinometer probe data is therefore not used and the more reliable primary A+/A− probe data is used to measure inclination in both casing directions.

Two initial baseline readings from inclinometer 1 were taken on 12 and 13 March prior to the commencement of ground improvement works, these readings showed good agreement. The top of casing survey data and baseline readings were used to determine the co-ordinates of the fixed inclinometer casing toe. The baseline reading for inclinometer 2 was taken on 13 March. Note that the data for both inclinometer 1 and 2 has been converted to local X-Y co-ordinate systems where the Y-Axis corresponds to the direction transverse to the rail embankment and the X-Axis the longitudinal direction.

3.3.4 Tiltmeters

It was proposed to instrument an outer row of columns in order to assess the long term behaviour lateral deflection of the outer row of columns supporting the gabion wall. A range of options were considered, strain gauges and rebar strainmeters “sister bars” were considered, however, it was considered that determining the deflected shape and structural behaviour of the columns based on isolated strain readings would be difficult. A vertical inclinometer provides a more direct measure, however, the location the column below the gabion wall meant that readings would not be possible. Cast *in situ* tiltmeters providing a measure of inclination at various depths in the column were considered a reasonable compromise. Three no. Slope Indicator – MEMS (Micro Electro-mechanical systems) bi-axial tiltmeters were installed in column C15. This column is immediately adjacent to Area #2 (see Figure 3.6 and

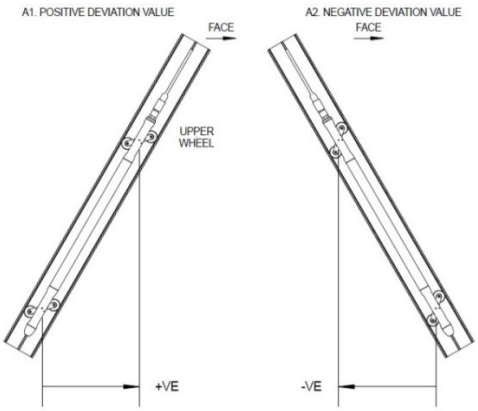

Figure 3.23. Sign convention for inclinometer probe A-axis (reproduced from RST Instruments, 2010)

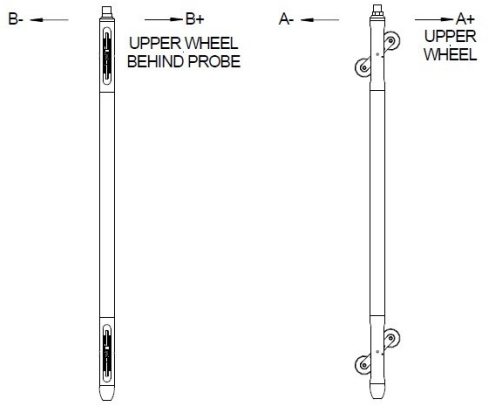

Figure 3.24. Inclinometer probe axes (reproduced from RST Instruments, 2010)

Figure 3.14*a*); inclinometer 2 is 1.6 m from the centreline of column C15 in the direction transverse to the embankment.

The MEMS tiltmeters have an inclination range of ±10°, resolution of 9 arc seconds, repeatability of ±22 arc seconds and measures 32mm in diameter and 190 mm in length. The tiltmeters also have a temperature sensor for temperature corrections. The tiltmeters were mounted (bolted) inside a 400 mm length of 50 mm diameter PVC pipe (Figure 3.25) with washers used on the mounting thread to act as spacers at the top of the tiltmeter (Figure 3.26) and

Figure 3.25. Inclinometer mounted in 50 mm diameter PVC

Figure 3.26. Top of mounted inclinometer

Figure 3.27. Base of mounted inclinometer

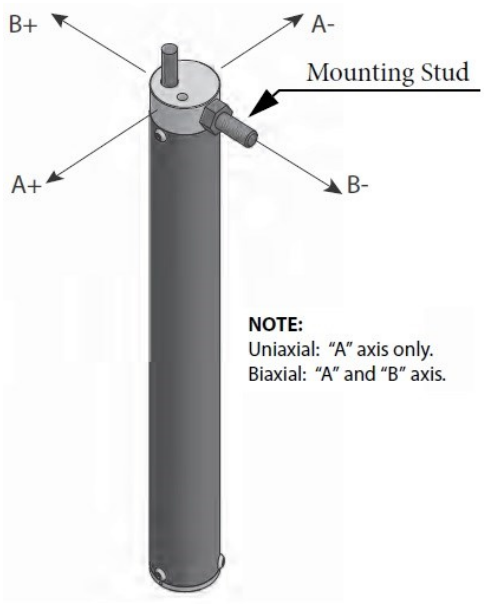

Figure 3.28. Slope indicator MEMS bi-axial tiltmeter from (reproduced from DGSI, 2009)

Figure 3.29. Author installing tiltmeters into column

Table 3.7. Tiltmeter installation details

PVC Pipe configuration	Depth (m)	RL (m)
Top of PVC pipe/Top of LTP	0	+2.65
Top of column head	0.65	+2.00
Tiltmeter no. 3	0.94	+1.71
Tiltmeter no. 2	3.21	−0.57
Tiltmeter no. 1	5.00	−3.00
Bottom of PVC pipe	5.95	−3.25

at the base (Figure 3.27). This ensured the tiltmeters were mounted securely and initially as close to vertical as possible. The short sections of PVC were joined with couplers to form a continuous length of PVC pipe 5.905 m in length (Figure 3.29). The installed length of instrumented PVC had a 655 mm stick up (above the column head at RL + 2.0 m), the tiltmeter instrumentation was installed immediately after the column shaft and column head was excavated. The tiltmeter details are presented in Table 3.7. It was necessary to leave the base of the PVC pipe open to avoid the instrumentation becoming buoyant, this meant advancing the tiltmeter casing slowly to allow the grout to flow up the annulus of the PVC pipe. The verticality of the PVC pipe was checked at surface with a spirit level and the tiltmeter sensors were checked for any significant deviation periodically during the installation to maintain verticality.

3.3.5 Horizontal inclinometer

Two (2) horizontal inclinometer casings were installed between column rows 2 and 3 in Area #1, see Figure 3.3. The horizontal inclinometer casing is 85 mm OD and was installed to provide a continuous profile of the LTP settlement. One casing was placed at the base of the LTP, the second directly at the top of the LTP. Both horizontal inclinometer casings installed are configured in a "one-way" arrangement. A separate 30 mm conduit was placed adjacent to the inclinometer casings and a pulley cable feed through the casing and return conduit. This pulley allowed the inclinometer probe to be pulled from the toe of the embankment to the end of the horizontal casing near the centre of the embankment. The probe was then pulled back towards the toe of the embankment with readings taken at 0.5 m intervals. The bottom and top horizontal inclinometer casing was installed on 9 and 10 July 2013

(Day 67/68) respectively. A baseline reading of the horizontal inclinometer casing was taken on 17 July 2013 (Day 75). Unfortunately, due to a number of design changes, the casing housing (access point) is no longer accessible and post-construction readings could not be taken.

3.3.6 Piezometers

The piezometers were proposed so that the pore pressure behaviour associated with the consolidation of the Coode Island Silt could be assessed. In addition, the piezometers were to be used to assess pore water changes associated with the installation of the columns. The piezometers are manufactured by Geotechnical Systems Australia (GSA) Pty. Ltd. and are GSA – Model 1200 vibrating wire piezometers with a pressure range of 350 kPa. The piezometers are 22 mm in diameter, 136 mm in length (Figure 3.30). It was proposed to install four no. piezometers in the general vicinity of Area #1. Piezometers were installed using a "push-in" place method immediately prior to the commencement of the Stage 2 ground improvement works. The piezometer was housed in a GSA push-in cone (Figure 3.30 and Figure 3.31). The housing and piezometer were advanced using a 1-inch steel tube casing which slides over the push-in housing and rests on the cone tip.

Lengths of steel tube casing were progressively joined as the piezometer was advanced. The bucket of an excavator was used to provide the "push" for the piezometer installation. The push-in piezometer was installed on 24 and 27 June 2013 (Day 52 and 55); a total of 5.55 m of casing was installed from RL + 2.1 m. The piezometer is at RL −3.45 m. The casing was extracted upwards a sufficient height to expose the ports near the base of the push-in cone. Due to time constraints only one piezometer was installed.

3.3.7 Data acquisition hardware

Data from the instrumentation has been measured and recorded using both manual readings and later automated data acquisition hardware that was installed between 5 and 7 August 2013 (Day 94 to 96). The first automated reading was taken on 7 August 2013 at 12:50pm. Prior to this, readings were taken manually from the terminal boxes located near the two instrumented areas (Figure 3.3). The vibrating wire sensors (earth pressure cells and piezometer) were taken using the GSA – Model 9120 vibrating wire readout unit (Figure 3.32). Strain gauge readings were taken using a Tokyo Sokki Kenkyujo TC-32K handheld data logger/strain gauge readout unit (Figure 3.33). Manual tiltmeter readings were taken using a 12-volt car battery and a Protek 608 Digital Multimeter.

Figure 3.30. Vibrating wire piezometer and push-in cone

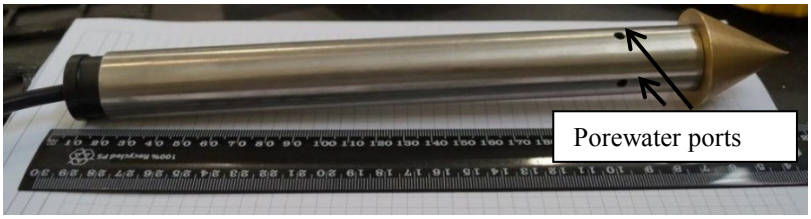

Figure 3.31. Assembled piezometer and push-in cone

Figure 3.32. GSA - Model 9120 vibrating wire readout unit

Figure 3.33. Tokyo Sokki Kenkyujo - TC-32K Handheld data logger

Assembling of the enclosure, data acquisition hardware and programming was done at the Golder Associates' warehouse. The enclosure was securely mounted to the outer wall of a building adjacent to the embankment (Figure 3.35). The author installed all instrumentation cabling on-site and wired the instrumentation sensors into the instrumentation enclosure once it was mounted (Figure 3.34 and Figure 3.35). The installed hardware was supplied by Campbell Scientific Australia and comprised a CR1000 data logger connected to 3 no. AM16/32B multiplexers. One multiplexer, with an AVW200 interface, receives the earth pressure cells and piezometer vibrating wire instrumentation. The second multiplexer, receives the three tiltmeter sensors. The third multiplexer, with a 4-wire 350 Ω wheatstone bridge completion circuit (4WFBS350), receives the strain gauges sensors. A NextG modem was also installed for wireless transmission of the site data to the Golder network. The instrumentation enclosure initially ran on a 12 V 40AH battery, a permanent power source (solar panel) was installed at a later date.

3.3.8 Ongoing instrumentation monitoring

The majority of the data was collected remotely via the data acquisition hardware. On-going periodic site visits, at 6-monthly intervals, were arranged to take readings from inclinometer 2 and undertake inspection of site and embankment. Considerable delays were encountered with site access and the installation of the permanent power source; this has caused intermittent power loss where the battery power supply has run too low. This predominately occurred about 18 months after embankment completion, much of the embankment behaviour was largely static at this time. Interpretation between period of data loss is possible without introducing any significant source of uncertainty.

Figure 3.34. Instrumentation enclosure and wiring

Figure 3.35. Instrumentation enclosure location

4 Geotechnical site characterisation and laboratory testing

This chapter outlines the geotechnical characterisation of the sub-surface conditions at the North Dynon case study site. An overview of relevant historic information, geological information, geotechnical site investigation data and the geotechnical properties of the main sub-surface materials; the existing and historic embankment fill, Coode Island Silt and Fishermens Bend Silt is outlined. A summary of geotechnical properties is provided at the end of the chapter along with a geotechnical long section.

The Coode Island Silt is the dominant sub-surface material within the stratigraphy owing to its highly compressible nature and low undrained shear strength. As noted in the previous chapter, the Coode Island Silt is present throughout the inner parts of Melbourne and is of interest to the local geotechnical profession. The geotechnical characterisation undertaken as part of this case study produced a significant amount of high quality laboratory data from testing of the Coode Island Silt and this presented an opportunity to provide an update on the previous publications by Ervin (1992) and Srithar (2010). King et al. (2016a) provides new insight into the compressibility and structured nature of the Coode Island Silt. Due to the length of the paper it is presented in Appendix B. A summary is presented within this chapter.

4.1 Historic information

The existing embankment, which was widened as part of the Regional Rail Link project, was constructed as part of the Essendon rail line in the early 20th century and is close to 100 years old. The historic information relating to the existing embankment, described below, provides a useful long term case study of an embankment founded on Coode Island Silt. It provides a baseline for embankment performance, with which to compare and assess, the performance of the current widened embankment.

The rail lines crossing the Moonee Ponds creek immediately to the north of the site forms the alignment of one the earliest rail lines in Victoria – the Williamstown rail line, between Spencer Street station and Newport Station (Waugh 2000, ARHS 2014). The rail line generally follows the northern extent of the Yarra Delta, with major crossings at the Moonee Ponds creek and the Maribyrnong River, and was officially opened on 13 January 1859. A second rail crossing of the Moonee Ponds creek, at the location of the North Dynon embankment, appears on the Victorian rail maps in 1890. It is understood that the existing 8 m high historic embankment was constructed along with the historic high level Moonee Ponds creek timber rail bridge as part of construction of the Essendon Flyover in 1922 (Wong 2015).

Between the period of 1968-1971 the existing timber rail bridge crossing Moonee Ponds Creek, comprising 35 spans, each spanning 3.05 m was demolished and replaced with the current reinforced concrete bridge which comprises seven 9.15 m spans. By shortening the overall length of the bridge it was necessary to extend the approach embankments by 15 m on the western side and 28 m on the eastern side (Golder 1984b). This was done without ground improvement with the existing timber bridge piles were cut at ground surface and left in place. This likely provided some form of embankment support. In the mid-1980s, structural distress was noted in the end spans

of the bridge on both the eastern and western sides of the bridge, although this was observed to be more severe on the eastern side. This is described in a number of reports by Golder Associates in the 1980s and by a second consultant in the 1990.

As part of these investigations it was observed that the structural distress was consistent with, and due to, significant post-construction settlement of the extended sections of the approach embankments. Which had been constructed without ground improvement. It was suggested that this post-construction settlement, accompanied with associated horizontal movement, was imparting excessive lateral load on both bridge abutments and first bridge spans, consequently leading to the structural distress observed (Golder 1984b). In suggesting this mechanism for the observed structural distress, it was noted that 13 years had passed since the construction of these extended embankments and that initial (elastic) and primary consolidation was complete at the time of assessment (mid-1980s); the continuing settlement which had been observed was due to on-going creep settlement. It was noted as part of the 1980s investigations that the creep rate of settlement for Coode Island Silt observed at numerous locations throughout Melbourne was generally about 1.5%/log cycle. Long term settlement monitoring was recommended; the results from May 1984 to June 1990 are generally consistent with the predicted rate of creep settlement (VicRoads 1990). It is this existing embankment, founded on the Coode Island Silt without ground improvement and continuing to undergo long term settlement, which has been widened as part of this present case study.

4.2 Site geology

The geology of the Yarra Delta is well described by Neilson (1992) based an extensive geological information (Pritchard 1910, Bell et al. 1967, Neilson 1988) as well as a large number of public and private geotechnical borehole records. The paper by Neilson (1992) is part of the "Engineering Geology of Melbourne" book which is well known in the local profession and comprises chapters describing the geological units in the Melbourne region in terms of their geological and engineering properties. The complimentary chapter by Ervin (1992) provides a comprehensive overview of the geotechnical properties of the soils comprising the Yarra Delta Group. The site geology encountered at the North Dynon embankment is typical of the Yarra Delta region, with the geological units encountered generally consistent with those described by Neilson (1992) and Ervin (1992).

The extent of the Yarra Delta and its relationship to the North Dynon embankment was shown in Fig 3.2 (from Cupper et al. 2003) . The bedrock in the Yarra Delta region is the Silurian aged Melbourne Formation and is found below about RL – 23 m in the small number of boreholes which extended to this depth. Bedrock is between 5 m and 15 m below the toe of the columns which were installed. Overlying the Melbourne Formation are the Tertiary aged units which included the Werribee formation (a soil unit) and the Older Volcanics Basalt (Neilson, 1992) amongst others. The pre-Quaternary geology of the Yarra Delta is shown in Figure 4.1. This figure indicates the presence of the Older Volcanics immediately to the north and underlying the western portion of the embankment and is generally consistent with site investigation data. The presence of the Older Volcanics generally defines the more favourable conditions at the western end of the North Dynon embankment were ground improvement was not required. The Quaternary aged Yarra Delta Group sediments have been deposited over this pre-Quaternary surface.

Addition geological maps from the construction of the Citylink – Western Bypass viaduct structure, aligned in an approximately north-south and 10 m to the east of the embankment, showing the spatial distribution of the Werribee Formation and Older Volcanics are presented in Appendix A1. These maps are generally consistent with Figure 4.1. The field case study, however, is focused on the design zone where ground improvement was

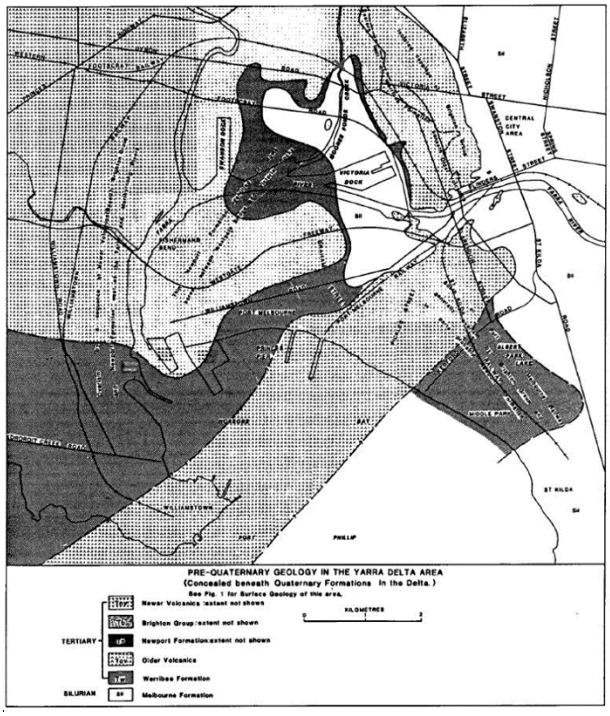

Figure 4.1. Pre-Quaternary geology in the Yarra Delta region from Neilson (1992)

undertaken, and at this location, the Quaternary aged Yarra Delta sediments directly overlie the Silurian aged bedrock. For this reason, the Tertiary aged units underlying the western portion of the embankment have not been investigated further.

Complex sub-surface conditions in the Yarra Delta region is generally the norm rather than the exception. As with many urbanised areas there has been a significant number of geotechnical investigations which have assessed the material behaviour and presence of the various geological units. In particular, there has been a significant amount of literature published on the Coode Island Silt; the settlement characteristics have been described by Donald et al. (1962), Jackson (1969), Walker et al. (1977), Anantasech (1984), McDonald (1988), Ervin (1992, 1996), Day et al. (2007) and Srithar (2010). In addition, information from large basement excavations in Coode Island Silt (Ervin et al. 2001, Ervin et al. 2004), assessments of strength characteristics (Hughes et al. 1980, Nagalingam 1986, Paul et al. 2014) and treated Coode Island Silt for soil mixing applications (Bouazza et al. 2006, Rex et al. 2008, Stanley et al. 2010, Islam et al. 2013) provide additional information on the behaviour of Coode Island Silt in various geotechnical applications.

This information provides a significant volume of background information for the laboratory testing of the Coode Island Silt which has been undertaken and is presented in this chapter and Appendix B (see King et al. 2016a). A summary of site stratigraphy at the location of the North Dynon ground improvement works is presented in Table 4.1. The presence and depth of the Moray St. gravels underlying the Fishermens Bend Silt is difficult to confirm based on the available geotechnical information. However, this is of minor importance for the present study as the embankment behaviour is governed by the behaviour of the Fill units, Coode Island Silt and Fishermens Bend Silt.

4.3 Geotechnical site investigation data

An extensive amount of geotechnical site data comprising boreholes, cone penetration tests (CPTs), test pits and laboratory data from site investigations, both historic and as part of the Regional Rail Link project, has been

gathered and analysed. The data is summarised below in chronological order with the site investigation plan in Figure 4.2 showing the test locations; data directly relevant to the field case study is highlighted in red. Figure 4.2 shows the location of the Moonee Ponds creek bridge, which was the subject of an earlier geotechnical investigations; a large number of boreholes and CPTs are located near the bridge abutments. The elevated Citylink viaduct (Western Bypass) can be seen, along with Moonee Ponds creek beneath. The alignment of the North Dynon embankment closely follows the alignment of the CPTs (CPT26, CPT28, CPT29, CPT30 and CPT31) that were performed as part of the detailed site investigation for RRLCMR. The embankment supports the Standard Gauge Headshunt rail line; a shunting line that joins the North Dynon lead track near the Radcliffe Street bridge at the western end of the embankment. The as-built rail alignment is slightly longer than that indicated in Figure 4.2 and terminates adjacent to the Moonee Ponds Creek bridge abutment.

Table 4.1. Stratigraphy of the North Dynon site, descriptions from Neilson (1992)

Age	Name	Description
Recent	Fill	Variable. Comprises general (uncontrolled) filling of the site area as well as controlled engineered fill placed to form the rail embankments
Quaternary aged Yarra Delta Group	Coode Island Silt	Soft dark grey-brown silty clay with shells
	Fishermens Bend Silt	Stiff yellow-grey silty clay; in parts sandy clay
	Moray Street Gravels	Dense sands, gravels and irregular clay beds
Silurian	Melbourne Formation	Mudstone with lesser interbedded fine sandstone

1984 Investigation (Golder 1984b) - four no. boreholes

Test no.

- GA1984_001*
- GA1984_002*
- GA1984_003*
- GA1984_004*

* (incorrectly labelled as GA19754_xxx in Figure 4.2)

Comments

Borehole GA1984_001 was excavated to 26.7 m depth (approx. R.L. – 25.7 m) for characterisation of Yarra Delta sediments. Borehole terminated in Melbourne Formation. The remaining boreholes were shallow boreholes for the purpose of slope stability analysis and terminated in Coode Island Silt. Closely spaced field vane tests were performed in the Coode Island Silt in the shallow boreholes. These were performed in accordance with the method given in AS 1289.F2.1 – 1977 "Determination of the Shear Strength of a Soil - Field Test using a Vane", 31 tests were performed. The vane shear apparatus used had a diameter of 74 mm and length of 140 mm. To conduct tests, the borehole was advanced to a depth 0.4 m above the test depth, the vane shear was then pushed to the test depth interval by hand or by using the drill rig hydraulics (Golder 1984b). Shear vane data is presented in later in this chapter with the Coode Island Silt characterisation.

1990 Investigation – five boreholes and eight CPTs

Test no.

- B90-1033P
- B90-1534P
- B90-1535P

(P) - Piezometer installed in boreholes

- B90-1536I
- B90-1537I

(I) - Boreholes drilled to bedrock

- C90-008
- C90-030
- C90-031
- C90-035

- C90-036
- C90-038
- C90-039
- C90-040

Cone penetration tests

RRL project - eight boreholes and two CPTs

Test no.

BH1225
Hydrometer analysis (7.0-7.45 m, 13.0-13.45 m)
PSD (16.0-16.27 m, 19.0-19.29 m, 22.0-22.24 m, 28.0-28.30 m)
BH1226
BH1267

BH1251
Hydrometer analysis (2.5 – 2.95 m, 5.0 – 5.45 m, 8.0 – 8.45 m)
PSD (2.5 – 2.95 m, 8.0 – 8.45 m)
BH1252
Hydrometer analysis (3.0 - 3.45 m, 5.0 – 5.45 m)

CPT1201

CPT1224
In-situ pore pressure dissipation test at depths of 17.01 m and 22.94 m.

BH1290^
BH1291^
BH1292^
BH1293^
^Boreholes BH1290-BH1293 completed as part of supplementary investigation by others.

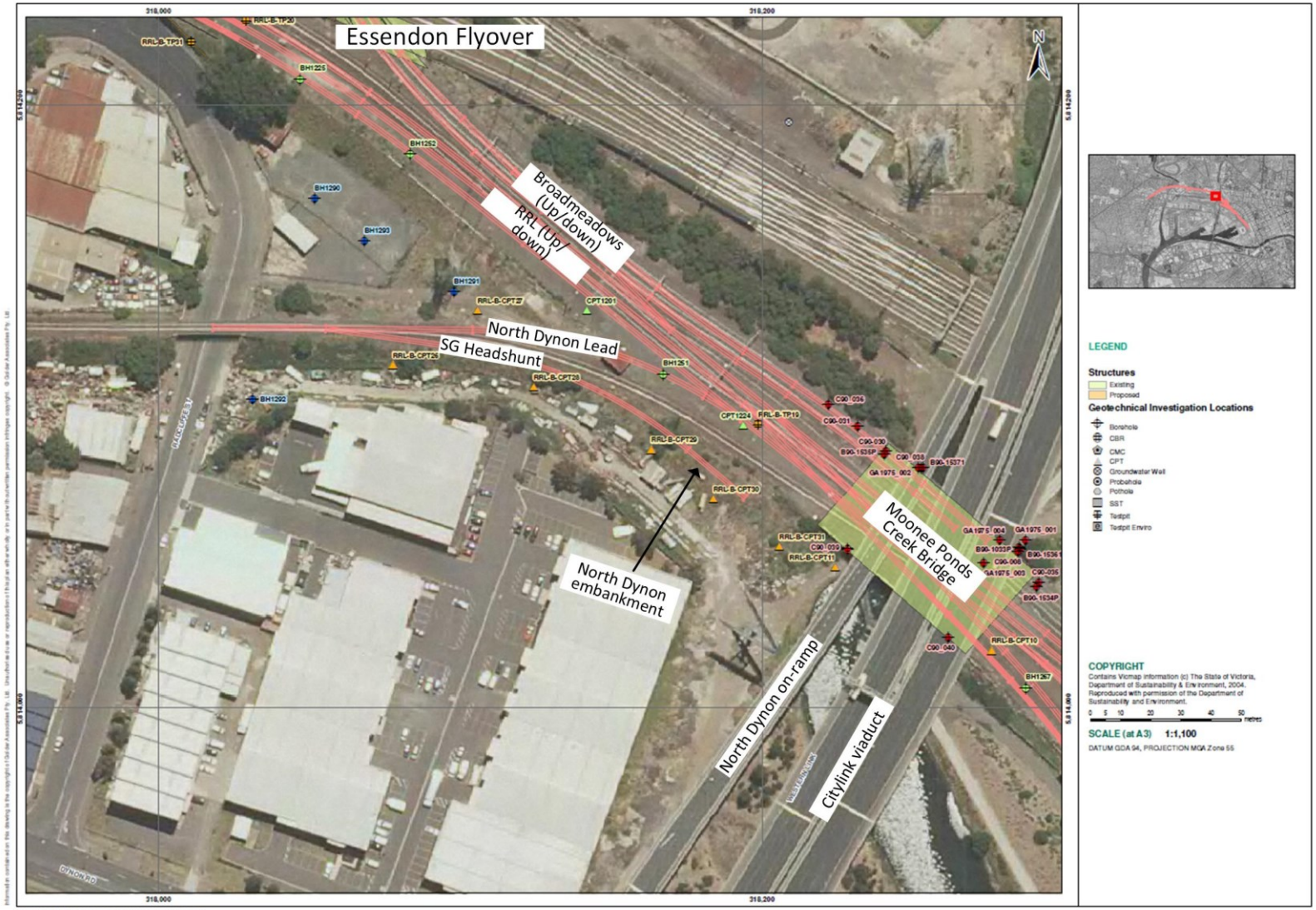

Figure 4.2. Geotechnical site Investigation Plan (modified from Golder, 2013)

RRLCMR project - one test pit, one borehole and eight CPTs

Test no.

RRL-B-TP19	RRL-B-CPT26	RRL-B-CPT29	RRL-B-BH41
Shallow test pit for rail subgrade design	RRL-B-CPT27	RRL-B-CPT30	Inclinometer no. 1
	RRL-B-CPT28	RRL-B-CPT31	Inclinometer no. 2
RRL-B-CPT10	CPTs performed as part of detailed design.		Borehole and two no. inclinometers for research project.
RRL-B-CPT11	All CPTs predrilled through the Fill units.		

4.4 Geotechnical site characterisation

4.4.1 Sub-surface conditions

The subsurface materials encountered during the various phases of geotechnical investigation include; Historic Embankment Fill, General Fill, Coode Island Silt and Fishermens Bend Silt. These units are described below based on laboratory and field testing. The fill material which forms the Historic Embankment was generally of a better quality than the General Fill which overlies the Coode Island Silt beyond the embankment footprint. For this reason, these units are described separately.

4.4.2 General Fill

Additional field testing was undertaken by the author both during and following the completion of the ground improvement works. During the site investigation works the CPTs were generally pre-drilled to avoid potential obstructions in the Fill units. As a result, there was limited data on the strength characteristics of the General Fill unit that forms the sub-soil beneath the LTP. Several Dynamic Cone Penetrometer (DCP) tests were performed in Areas #1 and #2 to assess the strength of the General Fill unit, the results are shown in Figure 4.3 and Figure 4.4. The location of the various DCP tests were shown in the instrumentation drawings presented in Chapter 3 (Figure 3.14*a* and *b*). These tests were typically performed to depths of about 2 m (Fill/Coode Island Silt interface) and indicate that the majority of the Fill is of a firm (s_u = 25 to 50 kPa) to stiff (s_u = 50 to 100 kPa) consistency.

4.4.3 Historic Embankment Fill

The fill material which comprises the Historic Embankment is inferred to have been sourced and placed under some form of engineering control, although no records to confirm this exist (the Historic Embankment dates back to the early 1920s). The embankment batter slopes are generally at angles of about 3H:1V where the embankment overlies the Coode Island Silt, further to the west where sub-surface conditions improve these batter slopes steepen to greater than 2H:1V. These factors, and the long term stability of the embankment, attest to a fill material of "reasonable" quality (the settlement issues at the bridge abutment related to the overstressing of the underlying Coode Island Silt and do not suggest poor quality Embankment Fill).

Standard penetration tests (SPT) performed in Historic Embankment in boreholes BH1225, BH1226, BH1227, BH1251, BH1252 and CPT1201 (pre-drilled borehole), are presented in Figure 4.5. These *N* values have been corrected with the SPT overburden pressure correction factor of Gibbs et al. (1957) and have an average value of 19 with some scatter. The corrected SPT *N*-values suggest a very stiff (s_u = 100 to 200 kPa) consistency or a density index of medium dense. Photographs of sections of exposed cuts in the batter slopes of the existing Historic Embankment are shown below in Figure 4.6. The exposed soil is predominately Gravelly CLAY. The clay is high plasticity, yellow brown in colour, has sub-angular gravel fragments of basalt. It is inferred that the origin of this material is weathered Tertiary Aged Older Volcanics Basalt which has been excavated and re-compacted. It is

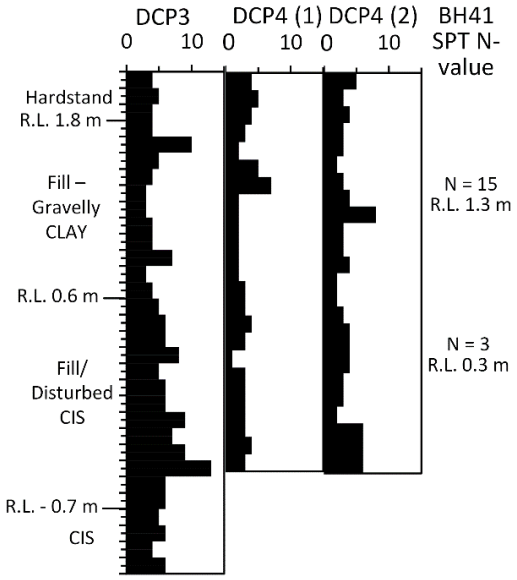

Figure 4.3. Area #1 - DCP testing and SPT results for General Fill unit

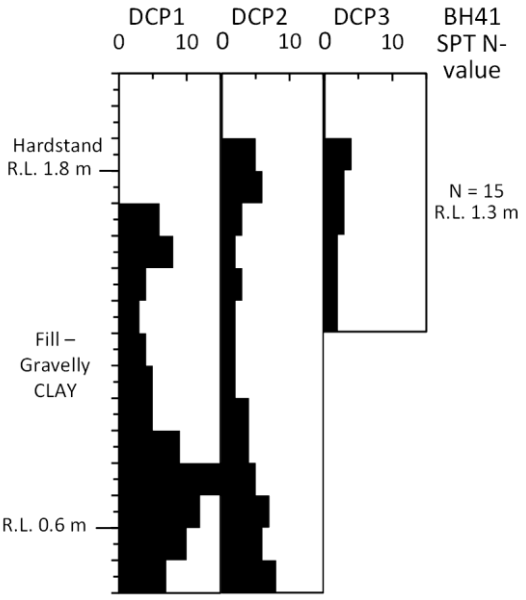

Figure 4.4. Area #2 - DCP testing and SPT results for General Fill unit

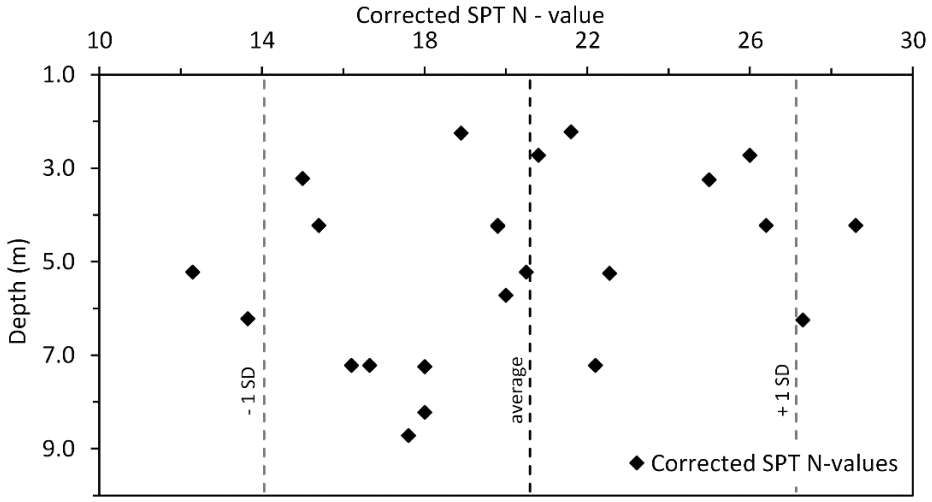

Figure 4.5. Historic Embankment Fill material – corrected SPT *N*-values

probable that the Embankment Fill material was sourced from excavations into the Older Volcanics several hundred meters to the west were this unit outcrops, and was used as borrowed material to construct the Historic Embankment across the low-lying ground (underlain by Coode Island Silt) adjacent to Moonee Ponds Creek.

4.4.4 Coode Island Silt

Within the Yarra Delta group of sediments, the near-surface Coode Island Silt, is of particular importance owing to its wide spatial distribution, low undrained shear strength (s_u typically increases from about 15 kPa to 40 kPa at depth) and its considerable thickness of up to 25 m in parts. Despite their geological names, the Coode Island Silt encountered is almost exclusively a silty clay while the Fishermens Bend Silt is an over-consolidated clay to sandy clay. A detailed description of the sub-surface conditions, laboratory testing and assessment of *in situ* testing of the Coode Island Silt data was presented in King et al. (2016a). A modified version is presented in Appendix B. Laboratory testing performed included: Atterberg limits, particle size distribution (PSD), 15 automated oedometer tests and 8 manual oedometer tests with an extended (one-week) creep incremental load stage. Selected results from

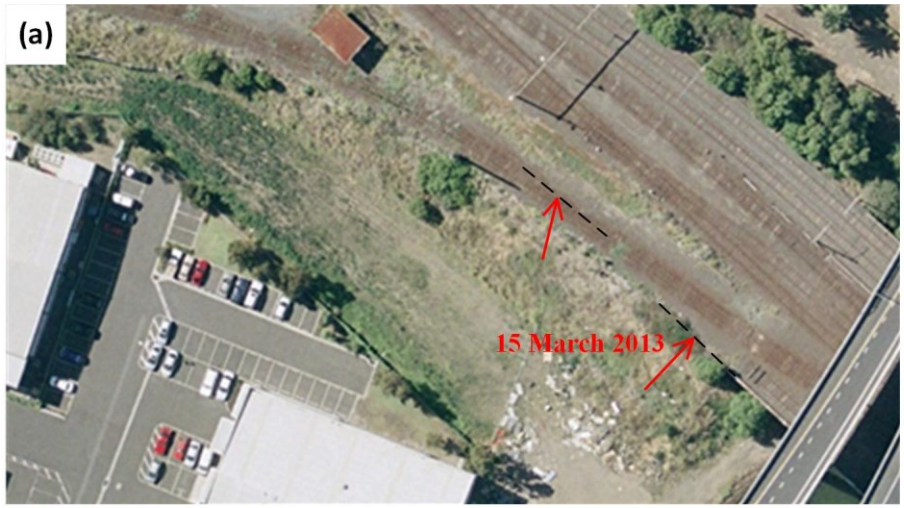

Aerial Image (3 March 2006) – Historic Rail Embankment showing the location of various exposures of Historic Embankment Fill material during construction of the North Dynon embankment

15 March 2013 – Stage 1 ground improvement works, temporary batter slope and exposed Historic Embankment Fill in vertical cuts (approximate R.L. 2.0 to 2.7 m)

29 June 2013 – embankment construction, exposure of existing rail embankment (R.L. 4.3 m), Fill material is inferred to be derived from weathered Tertiary aged Older Volcanics Basalt.

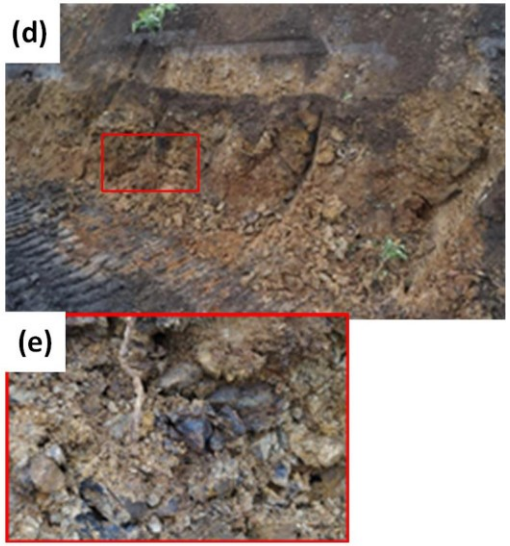

Figure 4.6. (a) Aerial image dated 3 March 2006, **(b)**, **(c)** field observations of Historic Embankment Fill, **(d)** and **(e)** close up of fill material from Figure 4.6*c*.

Appendix B are presented below, with a particular emphasis on the settlement characteristics of the Coode Island Silt, which are relevant for the settlement analysis in Chapter 5.

A geological long section of the ground improvement zone (chainage 2450 m to 2515 m) where the instrumented sections of the embankment are located is presented in Figure 4.7*a*. The Moonee Ponds creek is at approximately chainage 2420 m to 2440 m and CPT11 is at chainage 2445 m. The thickness of the Coode Island Silt can be seen to increase considerably towards the eastern end of the embankment adjacent to the creek. As-built records of the installed columns have been used here to refine the geological long section. The corrected cone tip resistance (q_t) profiles of CPT29, CPT30 and CPT11 are presented in Figure 4.7*a*, *b*, *c* and *d*, respectively. In addition, the soil behaviour type zone is shown, this is calculated based on the CPTu material index (I_c) (Equation 4.1 after Jefferies and Been 2006) and the values presented in Figure 4.7.

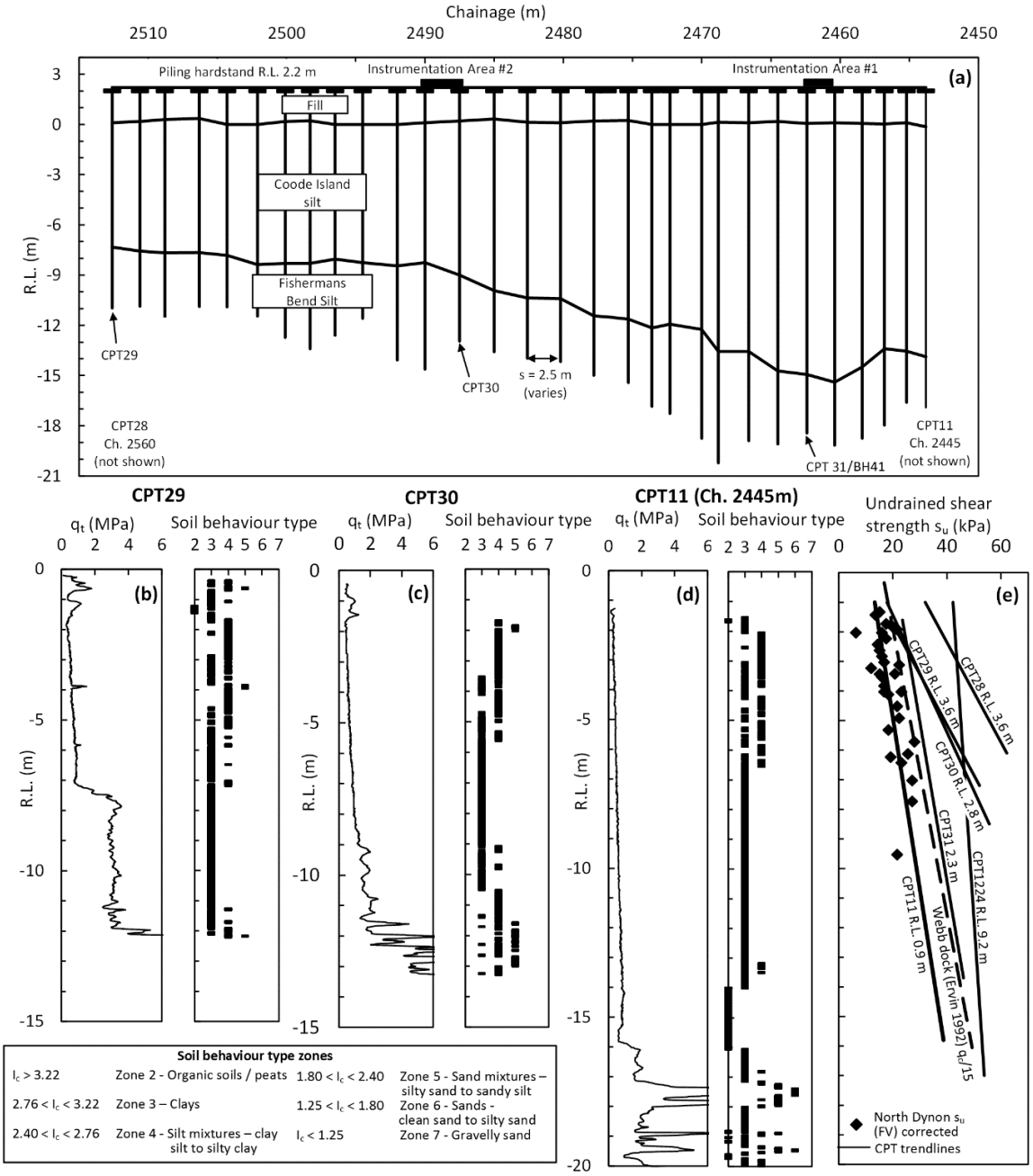

Figure 4.7. (a) Embankment long section. Corrected cone tip resistance profiles and soil behaviour type **(b)** CPT29, **(c)** CPT30, **(d)** CPT11 and **(e)** Undrained shear strength s_u profile – various CPTs, vane shear data adjacent to CPT11 from King et al. (2016a)

$$I_c = \sqrt{\{3 - \log(Q_t[1 - B_q] + 1\}^2 + \{1.5 + 1.3\log(F_r)\}^2} \quad \textbf{(4.1)}$$

The three normalised CPTu parameters are calculated as follows: normalised cone tip resistance $Q_t = (q_t - \sigma_{v0})/\sigma'_{v0}$, normalised friction ratio $F_r = 100\ \% \times f_s/(q_t - \sigma_{v0})$ and normalised porewater pressure $B_q = (u_2 - u_0)/(q_t - \sigma_{v0})$. Where f_s is sleeve friction, u_2 pore water pressure, σ_{v0} total vertical stress, σ'_{v0} effective vertical stress and u_0 is the hydrostatic porewater pressure. The undrained shear strength profile (s_u) for various CPTs has been calculated as $s_u = (q_c - \sigma_{v0})/N_k$ (Figure 4.7*e*). CPT11 has been calibrated against (corrected) *in situ* shear vane tests performed in the immediate vicinity of this test location. A cone factor (N_k) of 15 was found to provide an excellent fit with a linear trendline through the shear vane data (Figure 4.7*e*); this compares well with similar locally calibrated CPT profiles reported by Ervin (1992) and Srithar (2010).

The borehole stratigraphy, Atterberg limits and SBT zones from BH41 as well as the q_c profile from CPT31 are shown in Figure 4.8*a*, *b*, *c* and *d*, respectively. Ladd et al. (2003) suggest using the vertical strain ε_{v0} of the oedometer samples measured at overburden stress (σ'_{v0}) to provide an indication of relative disturbance between samples at equivalent depths, this is shown in Figure 4.8*e* along with the specimen quality designation (SQD). In addition to assessing relative sample disturbance, ε_{v0} for the manual tests (LIR = 1.0) and automated tests (LIR= 0.3) are compared in Figure 4.8*e*. This comparison provides an indication of the relative quality of the resulting S-shaped oedometer curve in *e*-log(*p*) space for the two test methods. This is discussed further in Appendix B. Based on the pre-consolidation stress (σ'_p) profile obtained from the laboratory investigation it was found that the expression $\sigma'_p = k(q_t - \sigma_{v0})$, with a value of $k = 0.3$ by Lunne et al. (1997), provided an excellent correlation between the cone resistance (CPT31 adjacent to BH41) and the pre-consolidation stress (King et al. 2016). Values of secant compression index (C'_c) calculated from the automated oedometer test data are also reported by in Appendix B.

4.4.5 Fishermens Bend Silt

Ervin (1992) described the Fishermens Bend Silt as predominately a silty clay, mottled grey to yellow brown in colour and varying from low to high plasticity with fissuring of the clay often observed. The Fishermens Bend Silt has a marine origin and the mottled colour and fissuring has been suggested as indicative of sub-aerial weathering of the Fishermens Bend Silt prior to the deposition of the Coode Island Silt (Neilson 1992). It was also noted by Ervin (1992) that plasticity generally increased towards the mouth of the Yarra River. The split spoon sample of Fishermens Bend Silt recovered from BH41 between R.L. – 16.52 and – 16.92 m is shown below in Figure 4.9.

The geotechnical properties of the Fishermens Bend Silt unit assessed here are based on CPT tests and only a limited number of laboratory results as the BH41 terminated at R.L. – 17.02m, about 4 m into the Fishermens Bend Silt unit. There is however a significant amount of data published by Ervin (1992) and Donald et al. (1962) which provides a reasonable basis for comparison and assessment of material parameters which have not been directly measured. The Atterberg limit test results from the North Dynon site are shown in Table 4.2 along with the Lower Yarra River crossing data described by Donald et al. (1962) and data from a range of sites described by Ervin (1992). The North Dynon site and Arts Centre site are both located in the upper parts of the delta and despite being located in different tributaries of the delta show similar characteristics.

One of better available sources of information on the s_u of the Fishermens Bend Silt is from Donald et al. (1962) (Figure 4.10) and describes the variation of s_u (FV) and s_u(TC) against moisture content. Ervin (1992) previously noted that the Fishermens Bend Silt was typically very stiff and at only a few sites was it encountered to be of a stiff

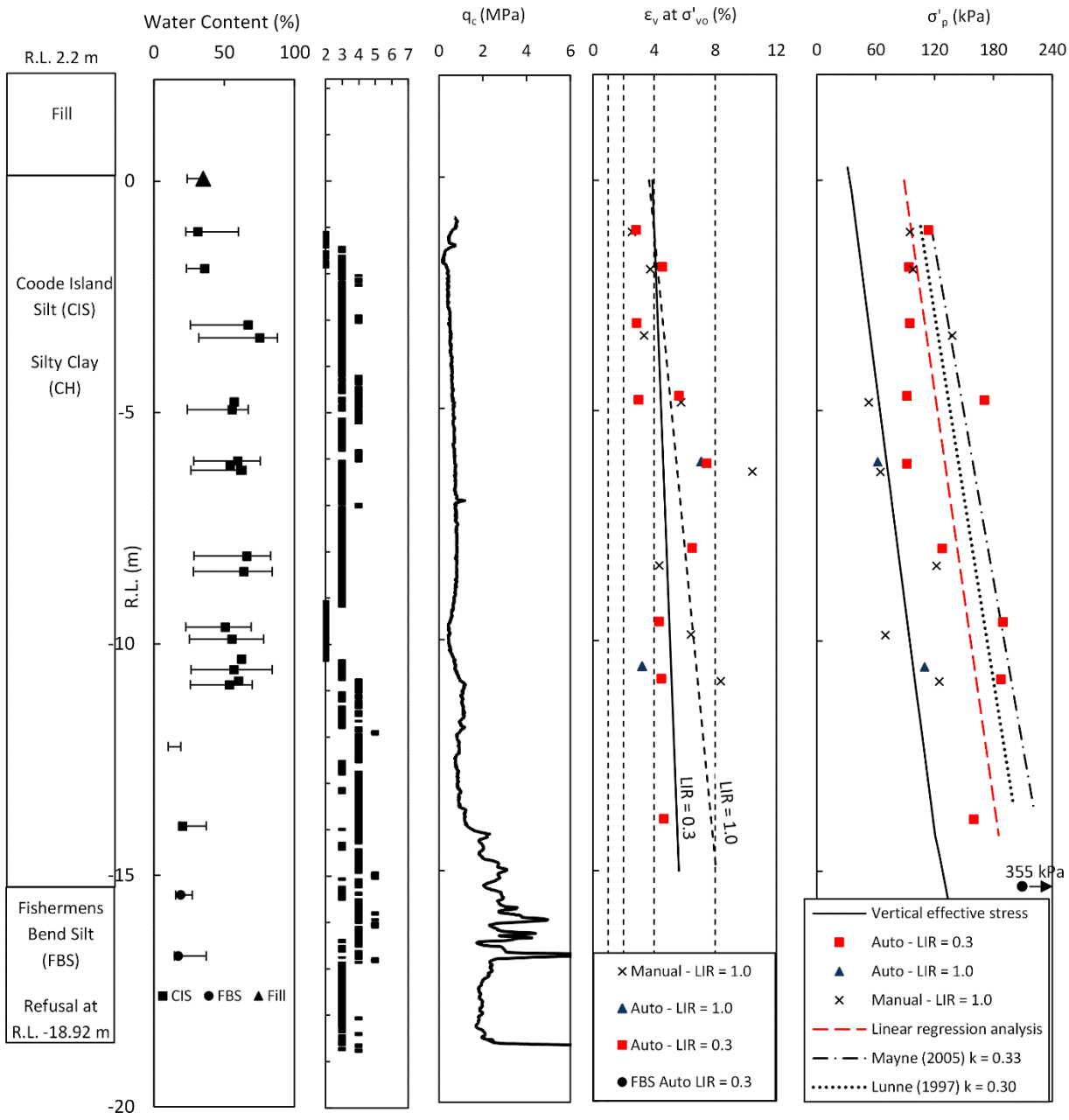

Figure 4.8. CPT31; **(a)** Soil profile, **(b)** Atterberg limits, **(c)** SBT zones and **(d)** q_c profile. (e) BH41 vertical strain at *in situ* overburden pressure from oedometer tests and **(f)** pre-consolidation stress profiles from laboratory tests and CPT correlations

Figure 4.9. Split spoon sample taken of Fishermens Bend Silt taken at R.L. – 16.52 m to – 16.97m

consistency, this interpretation likely reflects the spatial distribution of sites described by Ervin (1992), many of which were located in the upstream areas of the delta. At the mouth of the Yarra river, where Donald et al. (1962) obtained their data, approximately half of the samples are of stiff consistency. This is generally consistent with the increased plasticity towards the mouth of the Yarra river and by inference the higher moisture content. The two no. samples from North Dynon had moisture contents of about 20 % which, based on Figure 4.10, indicates the consistency of at least very stiff. This is consistent with the CPT q_c profiles presented in Appendix A2 and the undrained shear strength describe below.

Ervin (1992) calculated the q_c/s_u ratio by comparing CPT profiles with laboratory test results (CU and UU triaxial tests). Assessment of the q_c/s_u ratio at Appleton and Webb dock from 11 no. tests results indicated an average value of 18 with a range of 7.4 to 26. By comparison, 10 no. test results at Ingles street indicated an average q_c/s_u ratio of 21 with a range of 14 to 36. It was noted by Ervin (1992) that this range is likely due to significant variation in the undrained shear strength of the Fishermens Bend Silt and is not due solely to test procedures.

Analogous to a CPT cone penetrating clay at depth is a deep pile of circular cross section penetrating a clay at depth, in this case the bearing capacity has a factor $N_c = 9$, this provides the lower bound for the cone factor. However, the cone factor typically varies from 11 to 30. The reason for this difference in stiff clays is due largely to two factors; strain rate effects and the role of fissures. This is discussed at length by Terzaghi et al. (1996) based on 100 mm diameter UU triaxial tests which were noted to provide the most useful source of data for comparison. The time to failure for a typical UU tests is about 1200 seconds compared with about 2 seconds for a CPT test, this

Table 4.2. Atterberg limit test results and data reproduced from Ervin (1992) and Donald et al. (1962)

Location	**No. of results**	**w_l (%)**		**I_p (%)**		**LS (%)**		**w (%)**	
		Range	Ave	Range	Ave	Range	Ave	Range	Ave
North Dynon	2	27-37	32	12-22	17	-	-	17-19	18
Arts Centre	2	33-57	36	20-28	24	-	-	-	-
South Melbourne	56	23-80	40	4-53	22	2-17	10	17-46	28
Appleton Dock	3	77-92	85	42-69	58	8-19	12.5	40-55	45
Port Melbourne	2	53-59	56	36-38	37	12	12	-	-
Webb dock	5	40-102	68	21-79	49	9-26	17	29-35	31
Lower Yarra crossing	50?	60-100	85	50-70	63	-	-	-	-

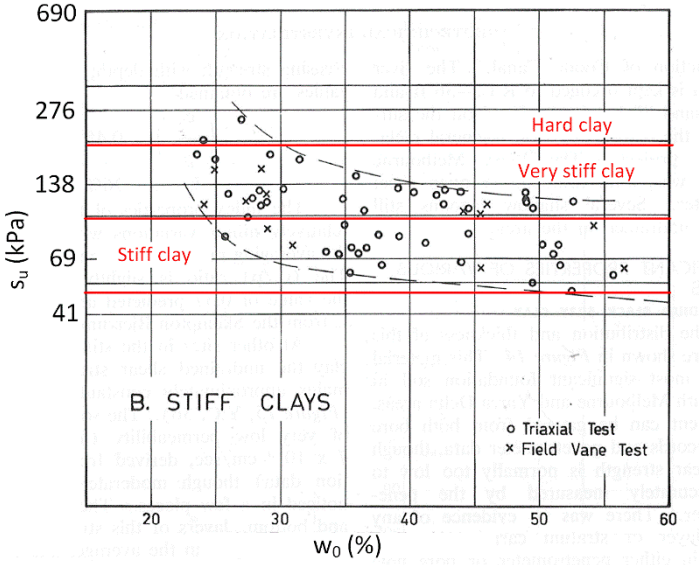

Figure 4.10. Undrained shear strength of the Fishermens Bend Silt vs w_0 (%) (modified from Donald and Ellwood 1962)

difference in strain rate introduces a factor of about 1.2 (Terzaghi et al. 1996) and increase the N_k from 9 to 11. The further increases in N_k relate to the role and fissure spacing and plasticity as shown in Figure 4.11.

For the Appleton and Webb Dock sites described by Ervin (1992) the average plasticity index was 58 and 49 respectively. The average value of N_k assessed for these sites (assessed as q_c/N_K not q_{net}/N_k) was 18 which, based on Figure 4.11, indicates closely spaced fissures in the range of 1/8 to 1/4 times the cone diameter (i.e., 4 mm to 9 mm). It is likely that the significant variability in N_k noted by Ervin (1992) is related to the variability in the plasticity index of the Fishermens Bend Silt, which was also noted, and perhaps to a larger extent, variability in the spacing of fissures.

Based on the average N_k factor obtained by Ervin (1992), the variation of N_k as a function of plasticity index, a reduced plasticity index at the North Dynon site (I_p = 20 %) and assuming the extent of fissuring is approximately similar between sites, a value of N_k = 15 is adopted for the North Dynon site. The CPT q_t profiles for CPT29, CPT 30, CPT31 and CPT11 are shown in Figure 4.12*a* to *d* along and the interpreted s_u profiles in Figure 4.12*e*. From this interpretation, it can be seen that s_u varies from 75 kPa to 122 kPa beneath the majority of the ground improvement area. Effective strength parameters assessed by Ervin (1992) are presented in Table 4.3.

The compression ratio assessed from an automated oedometer test performed on the Fishermens Bend Silt sample at R.L. – 15.41 is shown in Table 4.4 along with data from Ervin (1992). Ervin (1992) also noted the average recompression ratio was 9 % of the average compression ratio. The σ'_p was assessed to be 355 kPa and the OCR calculated to be 2.7. The data in Table 4.4 had OCR values ranging from 1.4 to 6.9 with no apparent trend evident (Ervin 1992), the average of the data was 3.5.

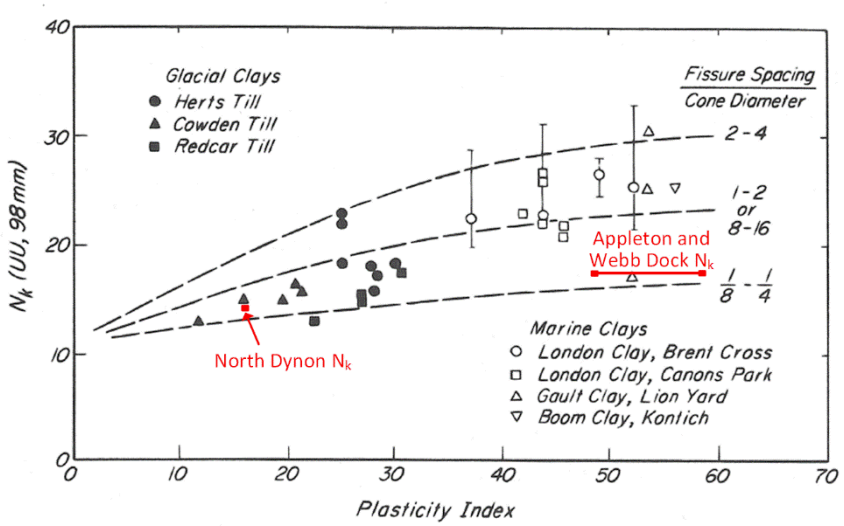

Figure 4.11. Cone factor N_k (UU) for stiff fissured clays (reproduced from Terzaghi et al. 1996)

Table 4.3. Fishermens Bend Silt – laboratory data from Erin (1992)

Location	Test Method	No. of results	Effective cohesion c' (kPa)		Friction angle ϕ' (degrees)	
			Range	Average	Range	Average
Webb Dock	CUPP*	2	15, 40	-	33, 22.5	-
Webb Dock	DSX#	6	25 to 75	42	19 to 25	22
Appleton Dock	DSX#	10	10 to 60	34	11 to 25	20

* CUPP – Consolidated undrained triaxial tests with pore pressure measurements
# DSX – Direct shear test

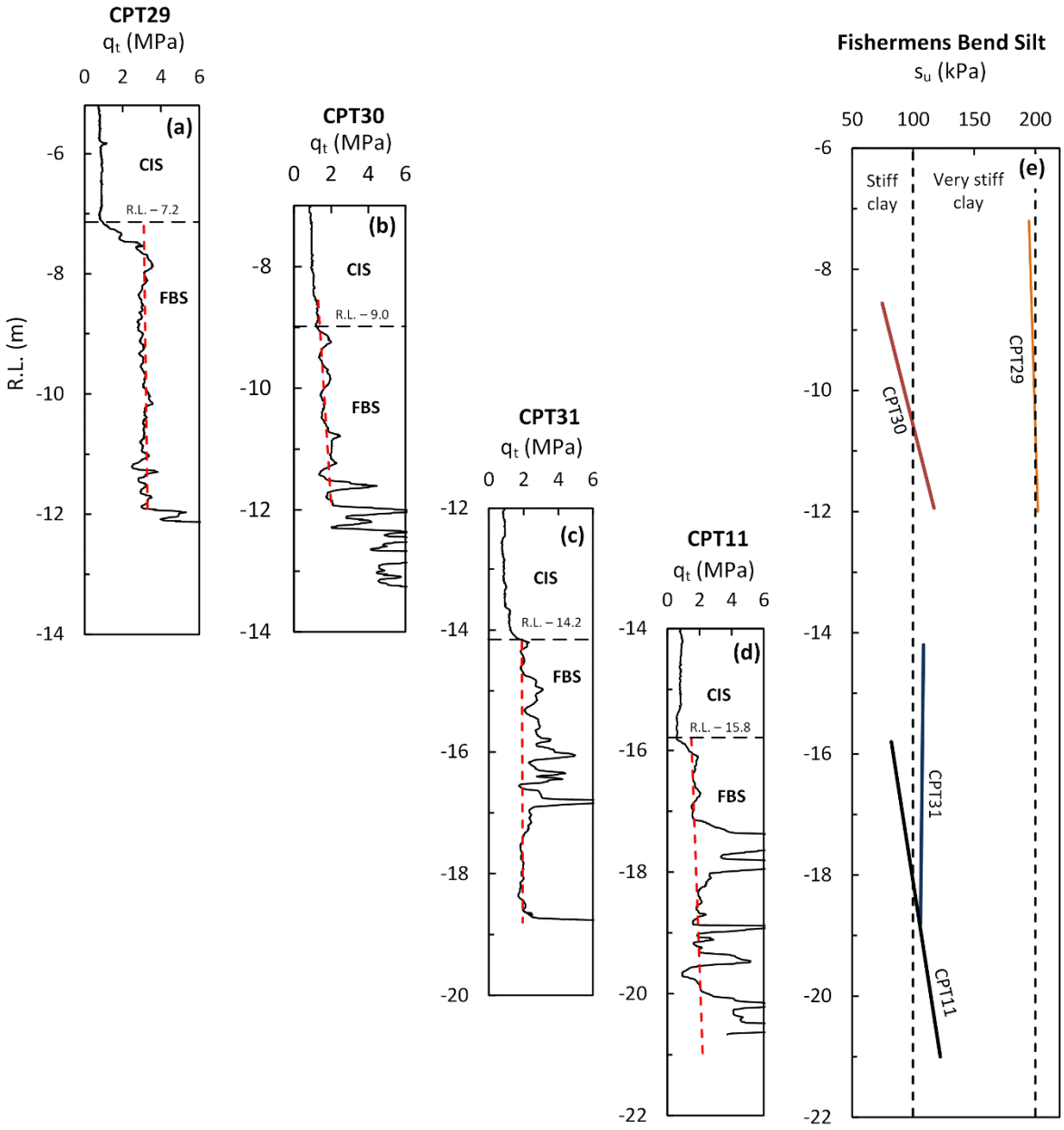

Figure 4.12. Fishermens Bend Silt q_t profiles for **(a)** CPT29 **(b)** CPT30 **(c)** CPT31 **(d)** CPT11 and **(e)** s_u profiles based on CPT interpretation

Table 4.4. Fishermens Bend Silt compression ratio data from Ervin (1992) together with data from current study

Location	No. of results	Compression ratio $C_c/(1+e_0)$	
		Range	Average
North Dynon*	1	-	0.11
South Melbourne	13	0.063 to 0.197	0.140
Ingles Street	7	0.177 to 0.300	0.227
Appleton Dock	2	0.270 to 0.319	0.295
Port Melbourne	2	0.145 to 0.188	0.167
Webb Dock	5	0.075 to 0.0164	0.127

*current study

4.5 Groundwater

Groundwater was recorded at a depth of 0.8 m (R.L. 0.17 m), 0.8 m (R.L. 0.18 m) and 0.6 m (0.37 m) in Golder boreholes GA1984_001, GA1984_002, GA1984_001 respectively. These boreholes were located immediately

adjacent to the Moonee Ponds Ck. and it is noted in a number of historic design reports that this GW level would have been expected to vary to some extent with the tidal influenced creek level, although it is not clear the extent of this influence. The two instrumented areas are located at a distance of 30 m and 50 m from the creek where the influence of tidal variation is likely minimal; this is confirmed by the consistent readings in the installed piezometer. Based on the available measurements and the piezometer data presented in Chapter 8 the groundwater level is measured at 0.6 m R.L.

4.6 Geological long section

The design geological long section (Appendix A1, Figure A12) has been updated based on the design and construction phase information described in Chapters 3 and 4. Importantly this long section is based on the interpretation of installation data from the columns, which were typically installed at a 2 m centre to centre spacing. The interpretation of the Drilled Displacement Column installation records is described in Chapter 8 were the pile installation effects are examined. Using the column installation records reduces the need to interpret between CPT test locations (typically 20 m apart), and as a result, the uncertainty in the sub-surface conditions is significant reduced over the study area.

4.7 Summary of findings

An extensive schedule of laboratory testing, assessment of field data and review of existing published literature has been undertaken for the Coode Island Silt and Fishermens Bend Silt to characterise, as accurately as possible, the geotechnical material properties. This has resulted in the summary of the geotechnical properties outlined in Table 4.5 and Table 4.6. The parameters presented are used in the analytical and numerical analyses presented in Chapters 5 to 9.

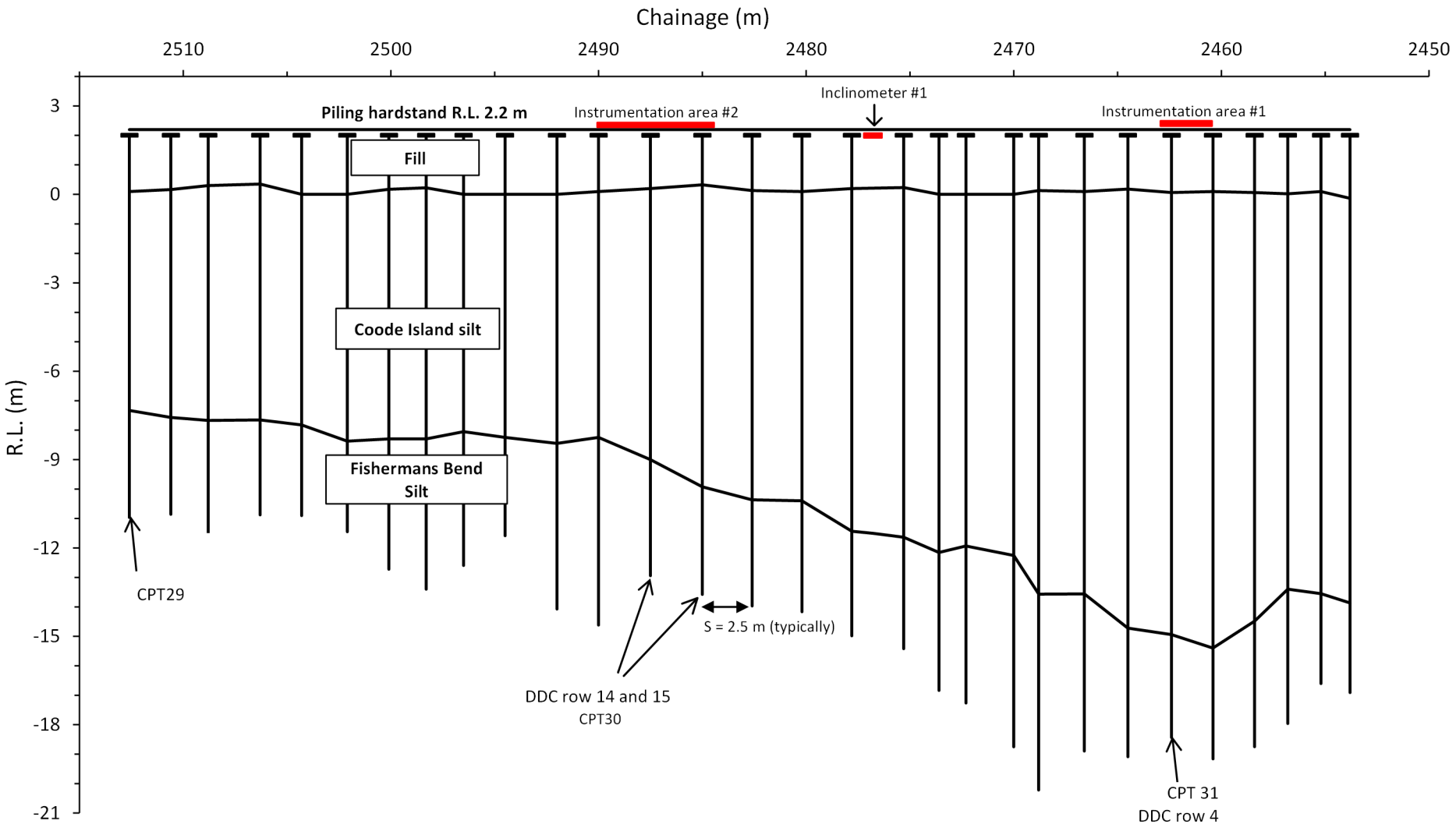

Figure 4.13. Geological long section of North Dynon embankment ground improvement area

Table 4.5. Summary of Coode Island Silt geotechnical properties

Index properties												
Unit name	**Soil type**	w_L **(%)**		w_p **(%)**		I_p **(%)**		**LS (%)**	w **(%)**		γ_d **(kN/m^3)**	γ_b **(kN/m^3)**
		Range	Ave.	Range	Ave.	Range	Ave.		Range	Ave.	Ave.	Ave.
Coode Island Silt	Predominately Silty CLAY (with sand lenses)	34 - 88	64	23 - 32	24	14 - 56	45	-	20 – 75	52	0.91	15.9
		Figure B1*a* (Appendix B)							Figure B2*a*, B6*b*		Figure B2*b*	

Compressibility							
Void ratio (*e*)	$C_{c\ max}$	$C_{c\ 400-800\ kPa}$	C_r	$C_{\alpha\varepsilon}$	$C_{\alpha\varepsilon\ max}$	C_α/C_c	σ'_p **(kPa)**
$e =$ 0.028 w	$C_{c\ max} =$ $(1+ e_0)\times5.07\times10^{-4}\ w^{1.66}$	$C_c =$ $0.0031w^{1.25}$	$C_r = 0.07C_c$	Varies due to σ'_{vc}/σ'_p	$1.3 < \sigma'_{vc}/\sigma'_p < 1.7$	0.039	$\sigma'_p =$ $0.30(q_t - \sigma'_{v0})$
Figure B2*a*	Figure B9*b*		Oed. data and Ervin (1992)		Figure B14	Figure B16	Figure B6*h*

Time rate of consolidation				**Strength**				
c_v **(RC) (m^2/year)**	c_v **(NC) (m^2/year)**	$c_{h\ field}$ **(m^2/year)**	k_v **(m/s)**	s_u **(kPa)**		S_t	c' **(kPa)**	ϕ' **(°)**
				Instrumentation Area #1	Instrumentation Area #2			
1.3 to 3.4	0.1 to 0.4	2.1 to 10.5	10^{-11} to 10^{-9}	26 kPa + 1.75 kPa/m depth	18 kPa + 5.1 kPa/m depth	4 – 8	7	30
see Figure B12		Figure B12*c* and Figure B13		Figure B19*d*		Figure B11	Ervin (1992) (average)	

Table 4.6. Summary of Fishermens Bend Silt geotechnical properties

Unit name	**Soil type**	w_L **(%)**		w_p **(%)**		I_p **(%)**		**LS (%)**	w **(%)**		γ_d **(kN/m^3)**	γ_b **(kN/m^3)**
		Range	Ave.	Range	Ave.	Range	Ave.		Range	Ave.	Ave.	Ave.
Fishermens Bend Silt	Sandy CLAY/Clayey SAND	27 and 37	32	15 and 25	24	12 and 22	17	-	17 and 19	18	1.42	1.89
		Table 4.2							Table 4.2		Ervin (1992) & Oed. test result	

Compressibility				**Strength**			
Void ratio (e)	$C_c/(1+e_0)$	C_α	C_r	s_u **(kPa)**		c' **(kPa)**	ϕ' **(°)**
0.91 (Ave.)	0.11	-	$C_r = 0.09C_c$	Instrumentation Area # 1	Instrumentation Area # 2	34 - 42	20 -22
Ervin (1992)	Table 4.4	-	Oed. data and Ervin (1992)	75 – 117 kPa	≈110 kPa		

5 Field case study – localised behaviour

This chapter comprises the material presented in King et al. (2017a) merged with the associated supplementary material. The focus of the chapter is on the behaviour of the LTP (i.e., localised GRCSE behaviour) based on the analysis of the earth pressure cell and strain gauge data from the field case study. The second publication based on the field case study (King et al. 2017e) is presented in Chapters 8 and 9 and focuses on global scale embankment mechanisms and pile installation effects, as assessed through the vertical inclinometer, tiltmeter, piezometer and post-construction survey data. Some preliminary field observations based on field data have also been presented King et al. (2014). Reference is made throughout this chapter to the embankment plan view and cross sectional drawings presented in Chapter 3 (Figures 3.3 to 3.6), construction timeline in Table 3.1 and Figure 3.7, instrumentation layout plans (Figure 3.14*a* and *b*) and the geotechnical site characterisation in the preceding chapter.

5.1 Temperature behaviour

In order to interpret accurately the earth pressure cell and strain data it is necessary to account for temperature effects. The variation in ground temperature in the instrumented areas is summarised here and used to correct the earth pressure cell and strain gauge data presented below. The temperature variation in instrumentation Area #2 as measured by the earth pressure cells is shown in Figure 5.1. Instrumentation was installed in the winter months of 2013, an increase of about 6°C was measured from the period of installation to the following summer, after this period seasonal variation is evident. The mean monthly temperature data from a nearby weather station (BOM 2015) is also plotted, the instrumented zone shows a peak temperature approximately 3 months after the peak atmospheric temperature in summer and vice versa for winter.

The long term seasonal ground temperature variation for Area #2 can be approximated by a sinusoidal function with a mean temperature of 16.9 °C and a seasonal fluctuation of ±2.0 °C. Similarly, for Area #1 a mean

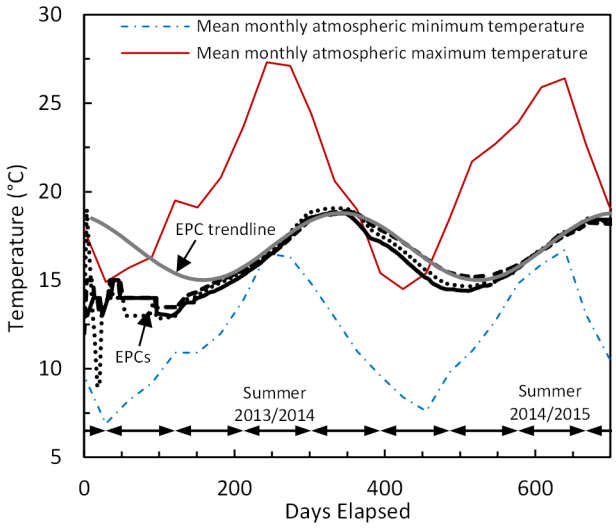

Figure 5.1. Instrumentation Area #2 - earth pressure cell temperature data.

temperature of 19.0 °C and a seasonal fluctuation of ±1.0 °C provides a good fit. The difference in ground temperature behaviour is due to the depth of soil cover (3.5 m in Area #2 compared with 7 m in Area #1) and proximity to the gabion wall (3 m in Area #2 compared with 8 m in Area #1), see Figures 3.3 to 3.6. The temperature profile and seasonal fluctuations are generally consistent with the ground temperature depth-profile described by Bouazza et al. (2011), Wang et al. (2014) and Singh et al. (2015) for a geothermal pile site in the Melbourne region where ground temperatures have been extensively monitored.

5.2 Instrumentation Area #1 – earth pressure cell data

The earth pressure cell data for Area #1 is shown in Figure 5.2 along with embankment height. Between days 65 to 80 the measured stresses match closely with the overburden stress. Partial arching is observed to develop between days 81 and 87 as the embankment height increased from 1.0 m to 1.9 m. This was observed as an increase in stress of 25 kPa for EPC4 and an increase of only 12 kPa for EPC5. A significant increase in the measured stress is observed between days 131 and 135 during the Stage 3b works (Figure 5.2). This increase in stress correlates well with the installation of drilled displacement column associated with the Stage 3a works, similar behaviour is observed in Area #2. However, the columns are installed at much closer radial distances in Area #1 and as a result the variation in earth pressure cell stress is considerably larger. It is shown in Chapter 7 that this increase in stress correlates well with the installation of columns associated with the Stage 3a works, similar behaviour is observed in Area #2. However, compared with Area #2, the columns are installed at a much closer radial distance; the response measured by the earth pressure cells is considerably larger.

The stress measured by EPC4 is shown to reduce considerably after each of the embankment lifts 3 to 7 and is decreasing during the post construction period. This observed behaviour is not consistent with a typical development of the arching mechanism in a GRCSE. There a number of mechanisms that may cause this behaviour. Firstly, the possibility that EPC4 is not functioning correctly is considered. However, given the response of EPC4 during the embankment lifts and Stage 3a works it appears that the earth pressure cell is functioning correctly. This behaviour is due to a "shadow" effect caused by the upper LTP, which is situated immediately adjacent to and above Area #1 (Figure 3.5). As embankment lifts are constructed it is inferred that load within the embankment soil mass is distributed to the more rigid upper LTP. In effect, this causes a "virtual" reduction in the height of overburden material acting in Area #1. As partial arching is inferred to have developed above Area #1 prior to embankment lifts

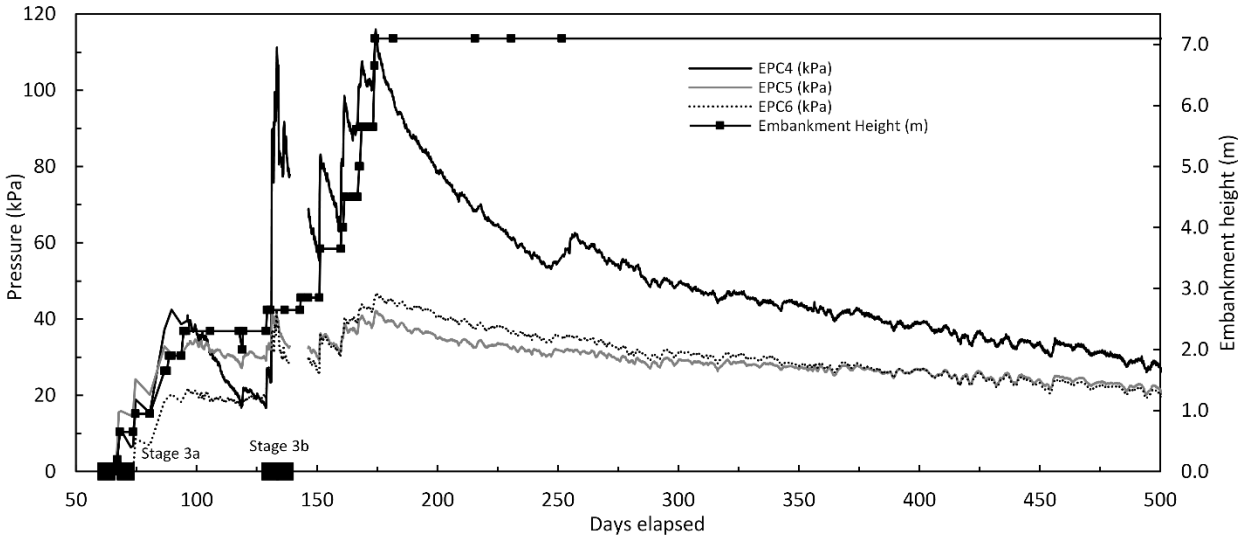

Figure 5.2. Earth pressure cell data – Area #1

3 to 7, this unloading of the overburden stress occurs primarily along the existing arching stress paths i.e., load component A (measured by EPC4 and to a lesser extent EPC6). The stress in the un-arched zone (measured by EPC5) shows only a minor reduction by comparison.

5.3 Instrumentation Area #1 – strain gauge data

For the field based strain gauges the dominant factors influencing the strain readings are temperature, lead-wire resistance, transverse sensitivity and moisture. The effects of temperature on the strain readings can be seen on both a daily and seasonal scale however it is the seasonal variation which has a more significant effect on strain readings, particularly given the small strains observed to date. The daily variation is due to temperature differences between the 4 arms of the wheatstone bridge (strain gauge and the 3 arms of the wheatstone bridge located in the instrumentation enclosure) which are assumed to be at the same temperature when calculating strain. The measured daily strain is plotted along with datalogger temperature and the (constant) soil mass temperature in Figure 5.4. This temperature data shows daily strain and temperature variation during a 10-day period in the summer months. Significant daily heating/cooling (approximately 20°C/day) of the northerly facing instrument enclosure (in the southern hemisphere the northern facing aspects are the "sunny" side) can be seen. The instrumented LTP remains at a constant temperature over this time. On a number of occasions in the early morning hours it can be seen that the enclosure and strain gauge are at approximately the same temperature (about 18°C). This represents a "true" strain reading unaffected by temperature. The variation in strain due to the heating of the enclosure on day 277 causes a strain fluctuation of about -10 με (-0.001 % strain) from this "true" strain reading as the enclosure is heated from 18°C to about 30°C. This daily temperature fluctuation is negligible relative to the strain gauge resolution required (i.e., about ±0.1%) and relative to other sources of potential gauge error. For this reason, a daily temperature correction has not been applied nor is it required to be applied.

Seasonal temperature induced strain can be assessed based on the temperature variation of the soil mass presented in Figure 5.1. Note that seasonal variation is very small at ±2°C for Area #2 and ±1°C for Area #1. However, greater seasonal temperature variation is seen during the period of installation where the instrumented zone equilibrates (by about 5°C) between the winter of 2013 when it was installed and the following summer. Seasonal temperature variation occurs within the instrumented areas after the summer of 2013/2014. The apparent strain caused by the initial equilibration period is shown for dummy gauge 1 and 2 in Figure 5.5 along with the seasonal temperature variation for Area #2. Based on this data, a strain temperature correction factor of about 35 με/°C is calculated. This is considerably lower than the value of 170 με/°C calculated by Zarnani et al. (2004) for

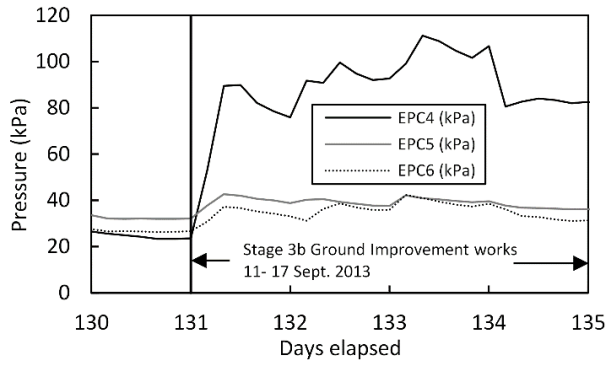

Figure 5.3. Earth pressure cell data during Stage 3b works – Area #1

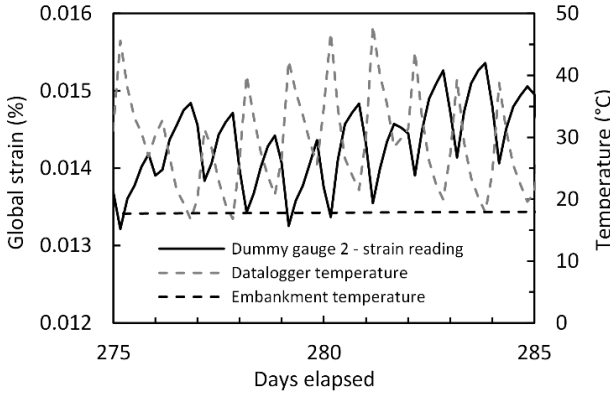

Figure 5.4. Temperature (daily) induced strain

strain gauges installed on HDPE and the thermal expansion coefficients for HDPE and polyester of 120 με/°C and 123 με/°C respectively. There a several factors which explain this behaviour. Strain gauges on geogrid do not measure "true" geogrid strain due to thermal expansion/contraction as these uniaxial gauges are designed to be relatively insensitive to transverse strain. i.e., across a geogrid ribs (refer to Figure 3.18*b*). In addition, the strain gauges do not measure strain induced by thermal expansion/contraction occurring in the direction normal to the plain of the strain gauge (or are highly insensitive to strain in this direction). That is to say, the strain gauges measure strain, including thermally induced strain, primarily in axial direction of the geogrid ribs, strain in the non-axial direction is not fully registered.

This is not a shortcoming, it is the uniaxial strain in the geogrid that is of interest. Further, the dummy gauges are free to expand/contract in this axial direction, the reinforcement layers are not. In particular, the reinforcement layers are not free to contract, as they are resisted by the vertical stress (due to soil arching) acting on these reinforcement layers. This is evident when the temperature correction factor is applied to the strain gauges. Rather than eliminating seasonal temperature variation, a sinusoidal pattern is introduced and it is apparent that thermally induced strain in the unconstrained dummy gauges is greater than in the constrained geogrid layers. For this reason, and due to the extremely small magnitude of seasonal variation (±0.02 %) a seasonal temperature correction is not applied to strain readings nor is it necessary to apply such a correction.

The strain gauge data for transverse and longitudinal layers of geogrid in Area #1 is presented in Figure 5.6*a* and *b*, respectively. In addition, the response of the strain gauges during the Stage 3b works (Days 131 to 137) is shown in Figure 5.6*c* and *d* for the transverse and longitudinal geogrid layers, respectively. Note that columns were installed on day 131 and 132. It is inferred that the tensile strains induced in the geogrid layers during the Stage 3b works is due to a heave mechanism resulting from the large and temporary porewater pressure increases in the Coode Island Silt during the installation of the columns i.e., upward deflection of the geogrid layer. The temporary increases in the strain gauges cannot be explained by a downward sagging geogrid layer and is consistent with the increasing stress observed by EPC5/6 (Figure 5.6).

Due to the influence of the upper level ground improvement works and the upward deflection of the geogrid layer, it is somewhat more difficult to assess the long term behaviour of the geogrid. In addition, it is shown later in this chapter that the subsoil settlement (to date) is quite small, resulting in only a small amount of geogrid strain. Of the transverse strain gauges, only gauges 5E and 5W develop realistic tensile strains, while gauges 6W and 7E measure either constant and/or compressive strains over the long term. Gauges 5E/5W indicate an average increase in tensile strain of about 0.04 % from day 150 to day 300. Beyond this period the gauges are relatively stable. Of the longitudinal gauges, gauges 4S and 1N indicate increasing tensile strain of about 0.05 % between days 150 to 300. The remaining gauges are either constant and/or decreasing in strain over the long term; this may be due to the

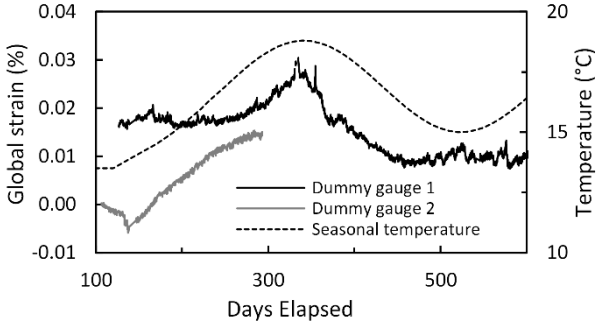

Figure 5.5. Temperature (seasonal) induced strain

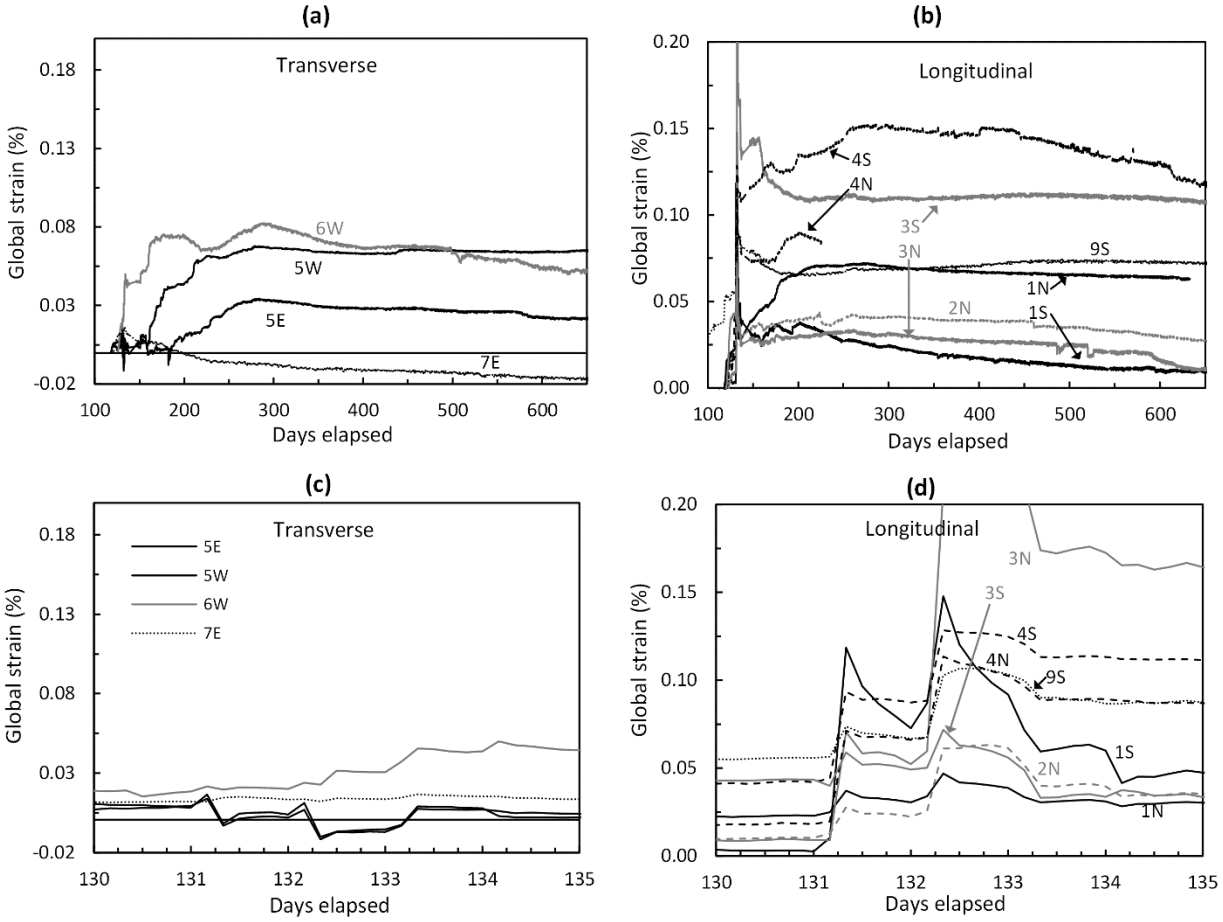

Figure 5.6. Strain gauge data: **(a)** longitudinal geogrid **(b)** transverse geogrid **(c)** longitudinal geogrid - Stage 3b works **(d)** transverse geogrid - Stage 3b works

reduction in the tensile strains induced during the Stage 3b works.

On the basis of the results presented it is difficult to comment on the strain concentration described by Han et al. (2002), Jones et al. (2010) and Zhuang et al. (2015) other than to note that minimal strain was observed at the mid-span between drilled displacement column heads (gauges 7E and 9S) and higher strain was observed to develop in the gauges located near the edge of the circular pile heads (gauges 1N, 5E and 5W) and centre of pile head centre (4S). Whilst these strain readings do not confirm the expected concentrated strains near the edge of the pile head, the results do not contradict this behaviour either. Given the small amount of sub-soil settlement which is inferred to have occurred to date, more time is required for sub-soil settlement to occur and the geogrid behaviour (increased tensile load) to fully develop.

5.4 Instrumentation Area #2 – earth pressure cell data

The EPC data for Area #2 is shown in Figure 5.7 along with the embankment height. Only the first 400 days are plotted to show the development of the arching stresses more clearly. The measured stresses match closely with the overburden stress during the first 20 days (LTP placement; Figure 5.7). Partial arching is observed as an increase in EPC1 and a reduction in EPC2 after embankment lift #1 (days 34 to 46) where the embankment height increased from 0.65 m to 1.90 m. By day 80 the arching behaviour is well established. However, there are two events which had a considerable effect on the measured stresses and were related to where columns were installed as part of the Stage 3a and 3b works. The measured data shows that the arching collapses on day 136 and again on day 137 as a result of the installation of several columns near the already constructed lower LTP. On days 136, 137 and 138 the

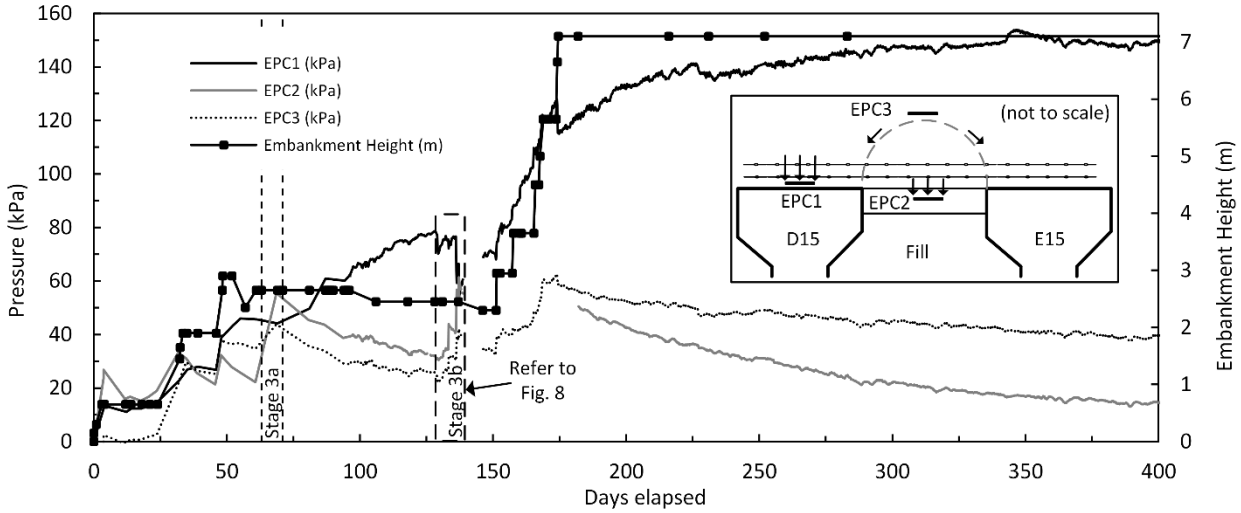

Figure 5.7. Earth pressure cell data for Area # 2

arching stresses are observed to collapse and both EPC1 and EPC2 return to an overburden stress condition (57 kPa).

The location of the upper level columns relative to the lower level LTP and instrumentation area was shown in Figure 3.6. Figure 5.8 shows that the variation in arching stresses between days 130 and 139 matches with the installation of the nearby columns. Note that the arching lost due to drilled displacement column installation was re-established shortly after drilled displacement column installation, as is evident after working days 133, 136 and 137 and after the Stage 3a works. A power outage caused loss of data between days 139 and 146. The ground improvement installation effects are examined further in Chapters 8 and 9.

5.5 Instrumentation Area #2 – strain gauge data

At this point in time it is difficult to undertake detailed analysis of the strain gauge data as the sub-soil settlement is estimated to be quite small (discussed later in this chapter), i.e., the geogrid has only been partially mobilised at this time. The transverse strain gauges (Figure 5.9*a*) show a variable response over the small strain range presented; this is primarily due to the small subsoil settlement over the period being examined. The initial strain in the geogrid layers at placement (in some areas the geogrid was tauter than in others areas) is also likely a contributory factor. This was the first of four layers of geogrid installed and some difficulties were encountered with transportation and installation that were rectified with the installation of the next three layers of geogrid. A number of these gauges failed, others showed quite an erratic response, only a small number of gauges indicated long term strains that are

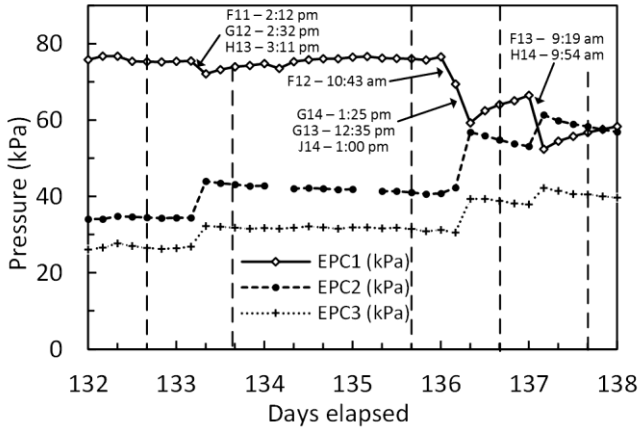

Figure 5.8. Earth pressure cell data for Area #2 - Stage 3b works

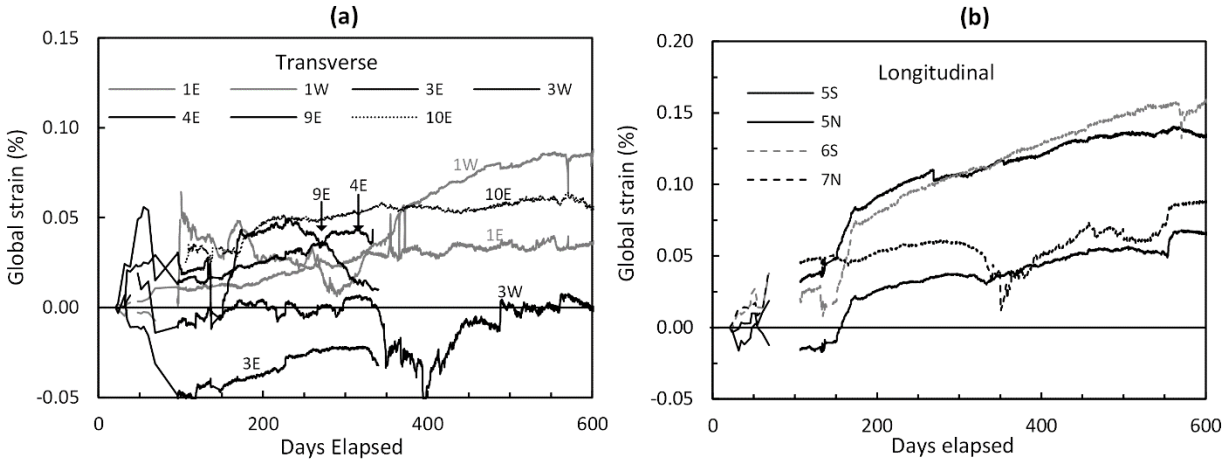

Figure 5.9. Strain gauge data - Area #2: **(a)** transverse and **(b)** longitudinal

consistent with the expected membrane action. A number of longitudinal strain gauges showed erratic results, however, four of these gauges indicated increasing strain between days 150 to 180 (embankment lifts 3 to 7) and gradual increase post-construction. Tensile strain of about 0.10 % to 0.15 % was observed to have developed in the geogrid layer. These small values of tensile strain observed are consistent with the geogrid having only a minor role at that point in time. As the geogrid is fully mobilised in the future, further analysis of the strain gauge data will be possible. These values of strain data observed to date are compared with predictions of the sub-soil settlement in later sections of this chapter and good agreement is found. The strain gauge results do not appear to indicate increased strain in the transverse layer compared with the longitudinal layer due to lateral spreading of the embankment. This is assessed further in Chapters 8 and 9.

5.6 Analysis of results

The following sections examine the development of the arching stresses with emphasis on the relationship between the sub-soil settlement and the arching stresses. The development of arching stresses in Area #1 shows similar behaviour with a reduction in vertical stress in the area between columns. However, it is difficult to assess the arching stress development further due to the influence of the upper level LTP that is located immediately adjacent to the Area #1 and the inferred reduction in the overburden stress. The analysis is therefore concerned with Area #2. This analysis involves four steps and provides the basis by which a designer can evaluate the development of arching stresses. The output of this analysis is compared with the data observed to date and predicted arching stresses for the remaining design life of the embankment are presented.

1. **Overburden stress** – knowledge of the overburden stress is required, this is assessed using a two-dimensional plane strain finite element model.
2. **Ground Reaction Curve** – a predicted GRC curve describing the relationship between arching stresses and sub-soil settlement is developed based on the procedure described by Iglesia et al. (1999). This is compared with the measured arching stresses.
3. **Settlement analysis** - as no direct measurement of the sub-soil settlement is available the sub-soil settlement is assessed through a detailed settlement analysis and compared with the GRC.
4. **Strain gauge results** – the development of tensile strain in the geogrid layers due to the downward sagging of the geogrid is used to back-calculate geogrid deflection and also compared with the GRC.

5.6.1 Overburden stress

The stress reduction ratio is a parameter typically used to quantify the degree of arching. It is defined as σ_v'/σ_{v0}' where σ_v' is the stress acting in the area between columns and σ_{v0}' the initial effective overburden stress. The overburden stress can be assessed by a simple one-dimensional calculation at the location of EPC2; a value of 70.4kPa is obtained. To account for geometry of the embankment and the presence of the gabion wall (Figure 3.6), a two-dimensional plane strain finite element analysis was performed to more accurately assess σ_{v0}'. At the location of Area #2 (3.6 m of overburden material), σ_{v0}' was assessed to be 74 kPa. Details of the numerical analysis are presented in Appendix C1.

The stress in the un-arched zone measured by EPC2 is used to assess the stress reduction ratio. The assumption is made that the load taken by the geogrid layer is negligible, this is a valid assumption for the initial period of arching assessed and it will be shown that the strain gauge readings validate this assumption. The EPC data presented previously is re-produced in Figure 5.10 with the stress reduction ratio values shown for two periods where arching stresses develop; between Stages 3a and 3b works and post Stage 3b works. After Stage 3a works, the stress reduction ratio curve reduces from an initial value of 1.0 to 0.58 before the arching collapses due to the Stage 3b works. The arching develops again over a period of nearly 1.5 years as the stress reduction ratio reduces to 0.08. In the following section, it is shown that these measured arching stresses can be calculated using the GRC (Iglesia et al. 1999, 2013).

5.6.2 Ground Reaction Curve

The GRC describes the relationship between the stress reduction ratio and relative displacement (defined as trapdoor displacement / trapdoor width × 100%), or in the context of a GRCSE, a relationship between the development of arching stresses and sub-soil settlement. This was first described by Iglesia et al. (1999) primarily for tunnelling applications based on centrifuge modelling and was presented in further detail to describe more generally the development of arching in a soil mass (Iglesia et al. 2011, 2013). The GRC is calculated based on two geometric parameters (height of soil mass above trapdoor H and trapdoor width B), material parameters of the granular material above the trapdoor (friction angle ϕ and mean particle size D_{50}) and the equations presented in Section 2.1.2 after Iglesia et al. (1999, 2013). An example of a GRC is shown in Figure 5.11.

5.6.3 Load transfer platform behaviour

To apply the GRC concept to the field case study it is necessary to convert the three-dimensional embankment

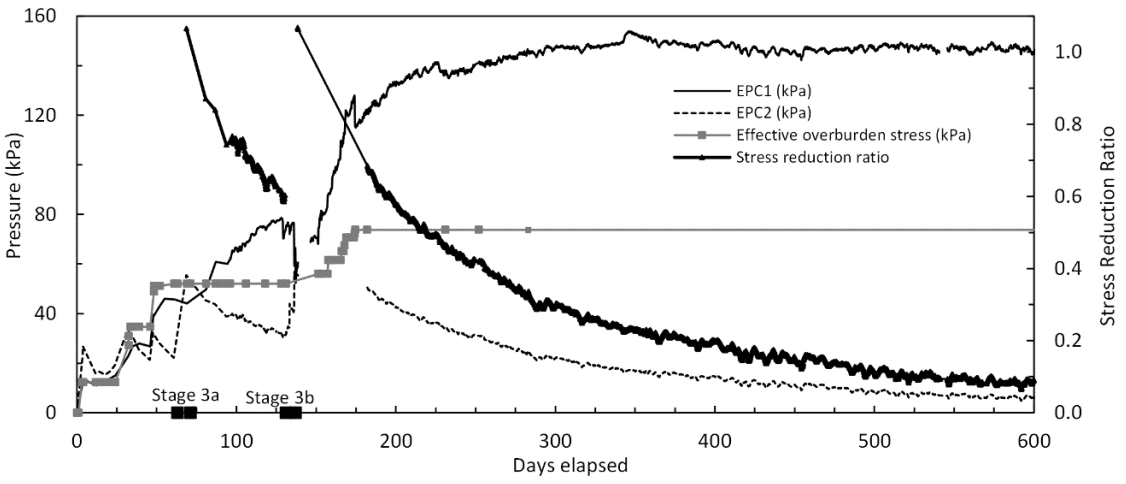

Figure 5.10. Stress reduction ratio for Area #2

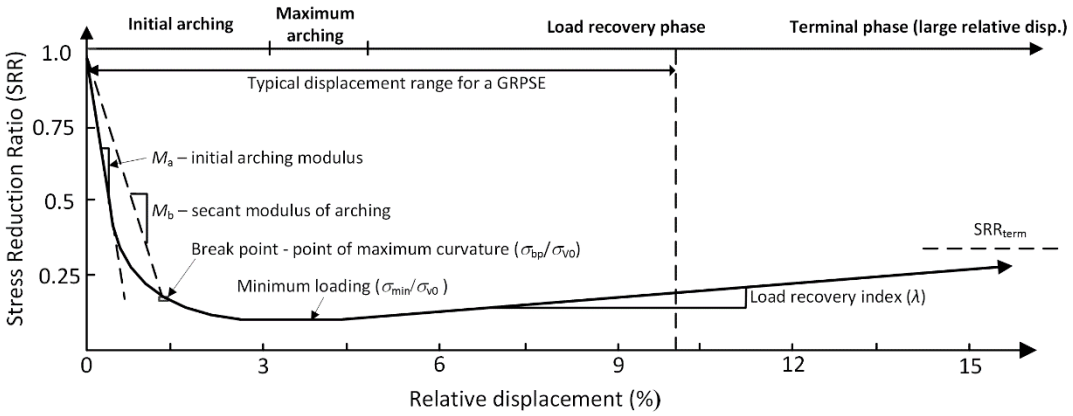

Figure 5.11. Characteristic Ground Reaction Curve (GRC) (modified from Iglesia et al. 2011)

geometry to an equivalent two-dimensional axisymmetric unit cell with parameters h (height of overburden material) and an equivalent axisymmetric clear spacing (b). The embankment geometry at Area #2 is shown in Figure 5.12 and has been converted to an equivalent axisymmetric unit cell based on an equal area concept. A value of b = 1.42 m is calculated and a value of h = 3.9 m is adopted as this gives a value of overburden stress $\boldsymbol{\sigma'_{v0}}$ equal to 74 kPa (assessed in the preceding section). A ϕ of 50° and a mean grain size (D_{50}) of 9.7 mm are selected for the rockfill material based on the laboratory data presented in Section 3.2.1 (Appendix D). The predicted GRC, based on Figure 5.11 and Figure 5.12 has been calculated based on the equations presented Iglesia et al. (1999, 2013) and is shown in Figure 5.13.

The stress reduction ratio values can be converted to a stress value by multiplying by the overburden pressure (σ'_{v0} = 74 kPa). Iglesia et al. (2013) noted that the intersection of the flat bottom portion of the GRC (zone of minimum loading) and the load recovery index line typically occurred between a relative displacement range of 3 % and 5 %. Thus, it is assumed herein to occur at a relative displacement of 4 %. To describe the portion of the GRC between the straight line initial arching and maximum arching, Iglesia (1991) noted that a smooth arc with a point of maximum curvature at the breakpoint, should be fitted. The author has investigated various curve fitted functions (polynomial functions of various order, log, exponential and power function) applied to a varying number of data points. The best fit was found using a linear regression analysis with a third order polynomial fitted between the following six data points:

- Three data points are evenly spaced along the linear line of initial arching between stress reduction ratio values of 0.6 and 0.8
- A data point at the breakpoint
- Data points at maximum arching at relative displacement values of 2 % and 3 %.

The author has not explored the mathematical uniqueness of this curve fitted function, however, the analysis undertaken suggests that the variance between the smooth arcs that can be fitted through these data points, to satisfy the above criteria is minor. The resulting variability in the GRC due to the curve fitting requirement is minimal (i.e., in the order of about SRR ± 0.03).

Based on the observed ground pressure at EPC2 (Figure 5.10), the stress reduction ratio reduced from 1.0 to about 0.6 between Stage 3a and 3b works (day 68 to 131). Using the GRC, which establishes a relationship between arching stress development and sub-soil settlement, the phase of arching development and an estimate of sub-soil settlement can be assessed based on the observed EPC data. The variation in stress reduction ratio between Stage 3a

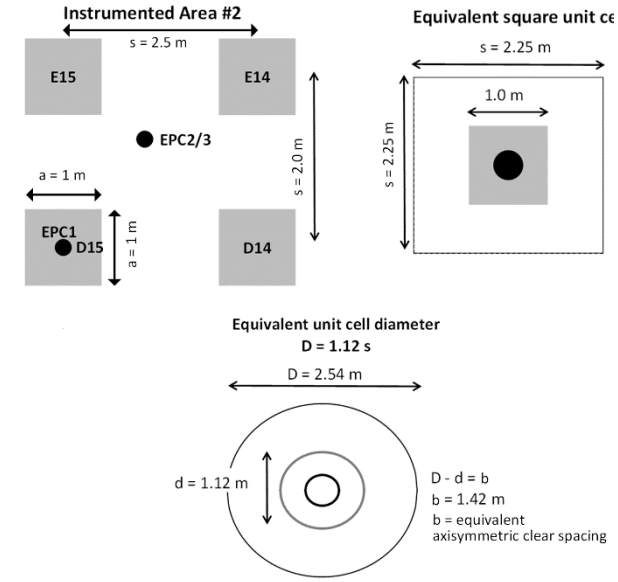

Figure 5.12. Equivalent unit cell – Area #2

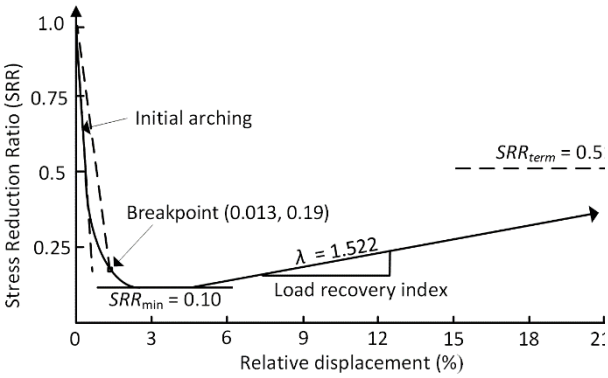

Figure 5.13. Predicted GRC – Area #2

and 3b, and the predicted GRC (Figure 5.13), suggests that this arching stress development is consistent with an initial arching phase. In the 500 day period after Stage 3b works (Figure 5.14), however, the development of maximum arching is evident and during this period the characteristics of the GRC match very well with the measured data. The measured data exhibits a flat bottom portion which matches well with the predicted minimum value of stress reduction ratio of 0.11. In addition, a localised point of maximum curvature, a characteristic of the GRC (breakpoint), is observed in the measured data at day 397, stress reduction ratio = 0.19. The linear line extending from the origin to the break point is termed the secant modulus and has a gradient of 63 in Figure 5.11.

The gradient of initial arching is 125 in Figure 5.11 and is calculated in Figure 5.14 based on the location of the observed breakpoint. This (theoretical) initial modulus of arching shown in Figure 5.14 matches well with the inferred data (extrapolated 5th order polynomial) through the period of data loss. To assess the development of the arching stresses in further detail using the GRC, it is necessary to convert the arching stress *versus* time data (Figure 5.10) to an arching stress *versus* sub-soil settlement plot by establishing a relationship between time and sub-soil settlement. This is done by fitting the measured stress reduction ratio curve in Figure 5.14 to the predicted GRC in Figure 5.13 by matching the characteristic features; breakpoint, flat bottom portion and initial straight line arching phase. The result is the relative displacement axis shown in Figure 5.14 (upper horizontal axis) which establishes a

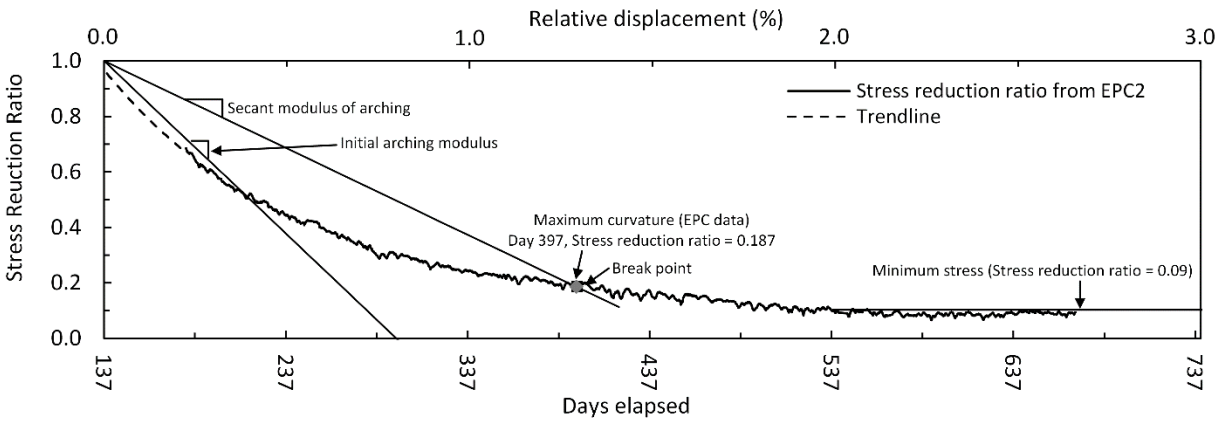

Figure 5.14. Instrumentation Area #2 – SRR based on EPC2 with GRC features

relationship between days elapsed and sub-soil settlement. From these relative displacement values, the magnitude of sub-soil settlement can be calculated by multiplying by *b* (1.42m). The back-calculated sub-soil settlement where maximum arching (relative displacement = 2 %) is inferred to commence is calculated to be about 28 mm at day 537 (Figure 5.14).

5.6.4 Comparison with settlement analysis

For the settlement analysis of sub-soil in Area #2 the compressibility of the 2 m thick stiff to very-stiff fill layer, overlying the Coode Island Silt, is ignored under the low applied stresses acting in the un-arched zone; the settlement analysis focuses on assessing the time-dependent primary consolidation of the underlying Coode Island Silt. The applied stress acting on the upper surface of the Coode Island Silt is calculated from sub-soil stress (EPC2) (Figure 5.15). The stress is applied incrementally and the settlement calculated incrementally using a macro enabled spreadsheet. The proportioned stress acting on the upper surface of the Coode Island Silt is also shown in Figure 5.16. The total applied stress acting on the Coode Island Silt has been calculated by assuming load spreading through the fill unit based on the ratio of the surface area between pile heads, and the surface area at the upper surface of the Coode Island Silt (less the area of the drilled displacement column shafts) a ratio of 4.0/4.9 is calculated from the Area #2 geometry (Figure 5.16). The stress distribution with depth in the Coode Island Silt is calculated based on the embankment width (12 m) and a 2:1 method stress distribution. The Coode Island Silt is sub-divided into 3 sub-layers with the parameters adopted for the settlement analysis (Table 5.1) based on the laboratory testing described in Chapter 4 and King et al. (2016a). The settlement analysis shown does not include secondary compression. The results of the settlement analysis are presented in Figure 5.18.

The time-rate of settlement was assessed using the time-U (%) relationship described by Srithar (2010) which was back-calculated from field scale settlement data from Coode Island Silt sites (c_v = 2 m^2/year and H = 2.3 m). It is noted that this settlement analysis is highly sensitive to the time rate of settlement parameters c_v (coefficient of consolidation) and H (maximum drainage length). The results of a second analysis with H = 4 m is shown in Figure 5.18 to highlight this point. The difficulties in assessing accurately the presence of minor sand lenses (i.e., representative values of c_v and H) in the Coode Island Silt is discussed in Chapter 4 and Appendix B (see Srithar, 2010 and King et al. 2016a).

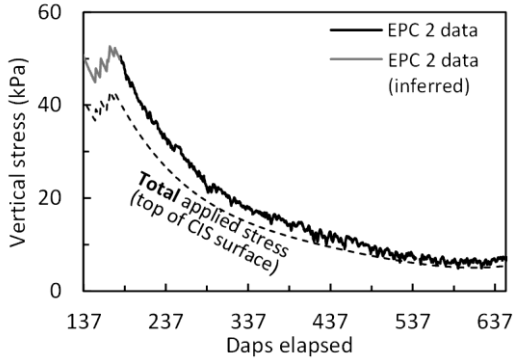

Figure 5.15. Applied load for Area #2 settlement analysis

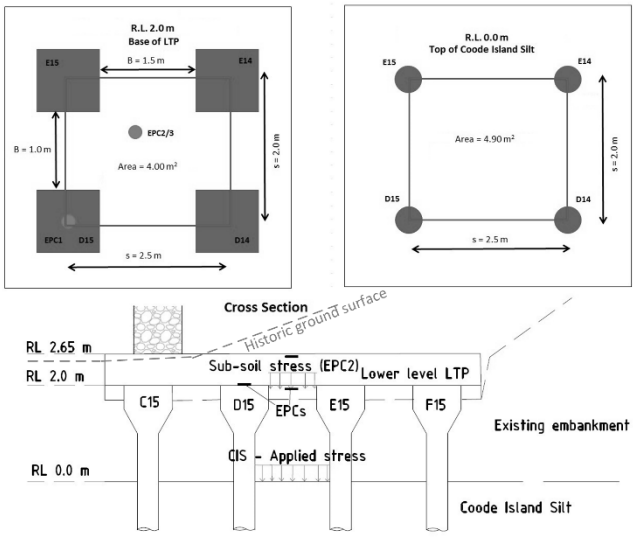

Figure 5.16. Calculation of applied stress on upper surface of the Coode Island Silt based on embankment geometry

Table 5.1. Coode Island Silt consolidation parameters adopted for settlement analysis

Thickness of Coode Island Silt (m)	σ'_p (kPa)*	e_0	$C_{c\ max}$	C_r	C_α	c_v (m^2/year)	H (m)
1.7 (upper)	64 kPa (RL 0 m) + 20 kPa/m depth	1.0	0.4	0.03	0.002	2.0†	2.3‡
7.3 (mid)		1.5	1.5	0.11	0.006		
2.6 (lower)		1.0	0.4	0.03	0.002		

*Correlated from CPT30 q_c using expression by Lunne et al. (1997) and k = 0.3
†Based on laboratory and field testing of Coode Island Silt samples – refer to Appendix B, Section B.1.4 and B.2.3.
‡H value adopted satisfies Time - U(%) relationship reported by Srithar (2010), refer to Appendix B, Section B.1.4 and B.2.3.

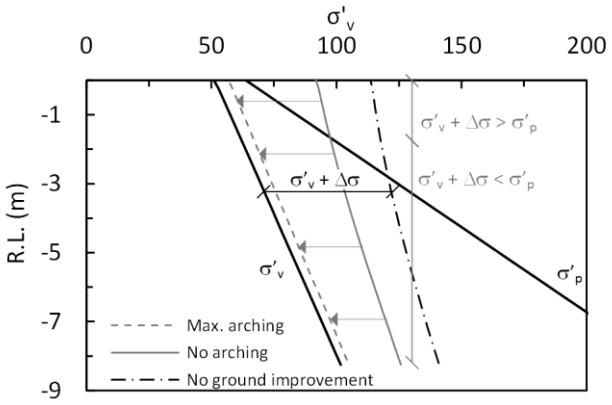

Figure 5.17. Profile of applied stress with depth

The variation in applied stress acting on the Coode Island Silt with depth is shown in Figure 5.17. The initial applied load at stress reduction ratio = 1.0 through to maximum arching (stress reduction ratio = 0.09) is shown along with the case of no ground improvement. Based on this assessment, only the upper few meters of Coode Island Silt is in the normally consolidated range, and this occurs only for a short period of time. Most the primary consolidation behaviour with depth occurs in the re- compression range. In Figure 5.18 the consolidation is about 80 % complete and the remaining consolidation under the applied stress of 8 kPa is negligible. As result, the long term behaviour at maximum arching (applied stresses of about 8 kPa) will be dominated by creep compression which is not described in the results in Figure 5.18. The settlement analysis presented ignores the load transfer to the drilled displacement column and the "*ground improvement effect*" in the Coode Island Silt due to the ground improvement works, thus, the plotted settlement represents the upper bound of settlement with time.

5.6.5 Comparison with strain gauge results

Based on the strain gauge results presented in Figure 5.18 the deflection of the geogrid layer can be estimated using the simplified expression of Giroud (1995) for an assumed parabolic sagging geogrid spanning a clear span ($s - a$) and strain (ε) of membrane (or geogrid):

$$\text{Maximum deflection} = (s - a)\sqrt{\frac{3\varepsilon}{8}} \qquad \textbf{(5.1)}$$

For this case, the geogrid strip between columns D15 and D14 (Figure 3.14) in Area #2 is considered, $s - a$ = 1.5 m. Based on the average strain (ε) of gauges 5N, 5S and 6N, the deflection is calculated using Equation 5.1 and presented in Figure 5.18. Maximum geosynthetic sag can also be assessed using the design charts by Zaeske (2001) and presented in EBGEO (German Geotechnical Society, 2010). Based on a maximum strain ε_{max} of 0.1 %, the $\Delta f/L_W$ value is 0.21 where Δf is the deflection of the geogrid layer and L_W the clear spacing (1.5 m). A maximum

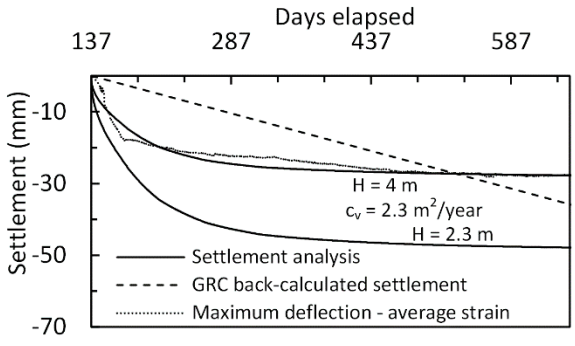

Figure 5.18. Maximum deflection of geogrid and sub-soil settlement

deflection of 32 mm is obtained from this method. Although both of these calculations ignore the localisation of strain in the geogrid layer as well as the three-dimensional nature of the membrane deflection, the estimated deflection is generally consistent with the settlement analysis and the back-calculated settlement from the GRC.

5.6.6 Long term behaviour

From the settlement data presented in Figure 5.15 there is reasonable agreement between the three predictions of sub-soil settlement (strain gauge, settlement analysis and back-calculated from arching stress development using the GRC) over the 500 day post-construction period shown. However, it is clear that the assumed linear relationship between back-calculated settlement (from the GRC) and time is incorrect (bottom and top horizontal axes in Figure 5.14) As the applied stress acting on the Coode Island Silt reduces, and settlement transitions from settlement predominately due to normal consolidation, then consolidation in the re-compression range and finally creep compression. Thus, the relationship between sub-soil settlement and time is non-linear. At this time, the measured EPC data has shown arching stress development up to maximum arching; it is difficult to assess the non-linear relationship between sub-soil settlement and time without further EPC data to define fully the GRC. For this reason, a linear relationship is assumed which despite the limitations of this assumption, shows reasonable agreement with the settlement analysis and strain gauge assessment of sub-soil settlement (Figure 5.18).

The most important feature of the GRC with respect to the LTP behaviour is the transition from maximum arching to a load recovery phase associated with the breakdown of the arching mechanism. This has important implication for the design of the geogrid layer as this suggests the stress acting on the geogrid layer will begin to increase at some time in the future, and will continue to increase to the ultimate value of stress reduction ratio, unless displacement in the un-arched zone is arrested by the geogrid layer. The development of arching described by the GRC invokes the following question: At what relative displacement will loss of subsoil support occur? Without a direct measurement of the sub-soil settlement, accurately assessing when the loss of subsoil support will occur is difficult in this particular case due to variability of the sub-surface conditions caused by the presence of the 2 m thick fill unit and the interaction between the fill and column head and shaft.

In addition, the ground improvement effect on the Coode Island Silt due to the installation of an array of full-displacement columns has likely improved the strength characteristics and reduced the compressibility of this unit (while acknowledging that it is extremely difficult to quantify this "*ground improvement effect*" based on the currently available knowledge of pile/column installation effects). While these various factors introduce uncertainty into the assessment of the rate of sub-soil settlement, there is sufficient data available (Ervin 1992, Srithar 2010) over much of the Yarra Delta to suggest that in the long term, sub-soil support provided by the Coode Island Silt

cannot be relied upon. This is due to its long term measured rate of creep settlement which occurs under little or no applied stress. Loss of subsoil support is, therefore, expected to occur for this embankment.

On this basis, the maximum sag of the geogrid can be calculated by ensuring load compatibility between the un-arched stresses (a variable which is a function of geogrid deflection) and geogrid tensile load. This is calculated based on the square unit cell shown in Figure 5.16 with the tensile load and stiffness in the geogrid calculated as follows:

$$\text{Tensile load T (kN)} = \frac{\sigma_v(s^2 - a^2)}{4a}\sqrt{1 + \frac{1}{6\varepsilon}} \quad \textbf{(5.2)}$$

$$\text{Stiffness J (kN/m)} = \frac{T}{\varepsilon} \quad \textbf{(5.3)}$$

where s and a are geometric variables, centre-to-centre spacing and width of square column cap respectively, ε is geosynthetic strain and σ_v is the stress acting in the area between columns calculated from the predicted GRC in Figure 5.13 and the maximum deflection calculated from Equation 5.1. The stiffness of the geogrid layer installed is 2600 kN/m ($J_{2\%}$, from Fig 3.18) and in this analysis, it is assumed that the sub-soil settlement is equal to the maximum sag. The results of this analysis are presented in Figure 5.19*a* and *b* in terms of settlement required and stiffness required for equilibrium respectively. This analysis shows for example that when σ_v = 8 kPa (i.e., at maximum arching), the installed geogrid layer would need to settle 87 mm to achieve equilibrium. At present the geogrid settlement is estimated to be about 30 mm.

Alternatively, the analysis can be considered in terms of a required stiffness, at relative displacement = 4 %, σ_v = 8 kPa and the geogrid deflection of 57 mm, the geogrid layer would need a stiffness in excess of 10,000 kN/m. From Figure 5.19, it can be seen that equilibrium is achieved in the load recovery phase at relative displacement = 7 %, stress reduction ratio = 0.14 (10.1 kPa) and with the maximum geogrid sag of 100 mm, ε = 1.31 % and T = 34.5 kN/m. Whilst designing the geogrid layer to limit the deflection to within the range of maximum arching (2 % < relative displacement < 4 %) may seem like an efficient approach; Figure 5.19*b* indicates that the geogrid layer required would need to be of an extremely high stiffness to limit deflection to within this 30 mm to 60 mm range.

Based on the development of arching stresses predicted by the GRC for Area #2 and the analysis presented, four phases of LTP behaviour occurring over the design life of the embankment are proposed (Figure 5.20). To date only Phase 1 has been fully observed, the embankment is currently in Phase 2 with the Phase 3 and 4 predicted to occur

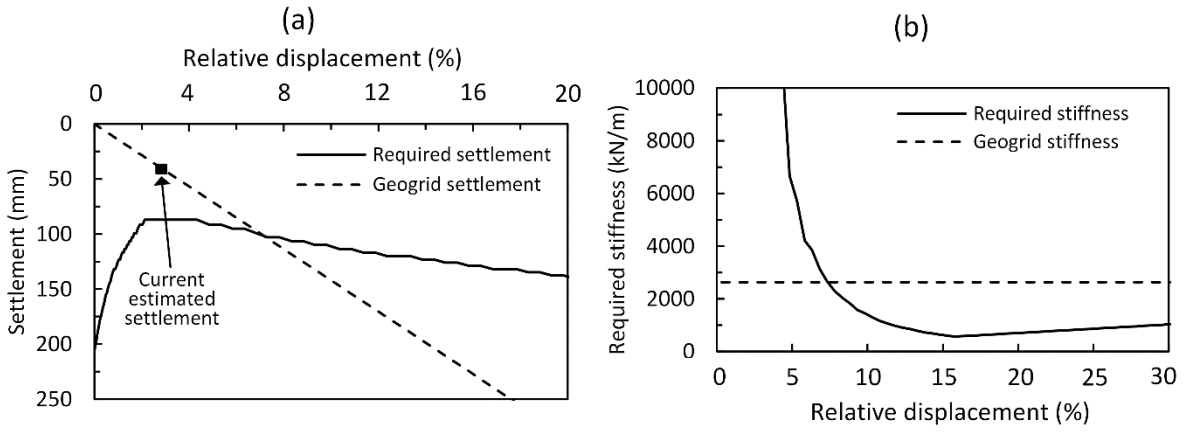

Figure 5.19. Calculated geogrid equilibrium at loss of sub-soil support (a) required settlement (b) required stiffness

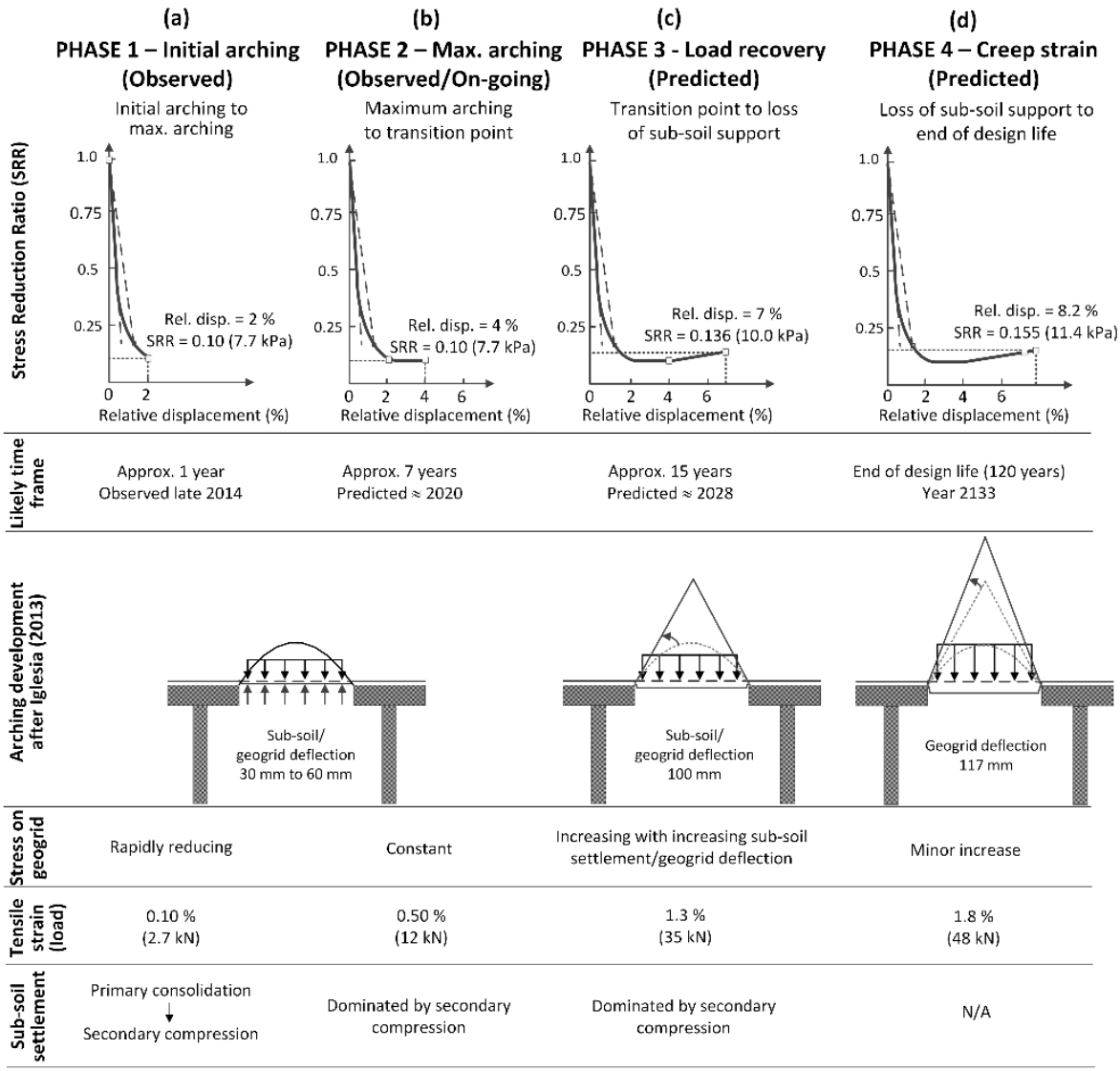

Figure 5.20. Four phases of arching development based on application of GRC method to Area #2 – **(a)** Initial arching **(b)** Maximum arching **(c)** Load recovery **(d)** Creep strain

over the design life of the embankment. The transition from Phase 2 to Phase 3 is predicted to occur in about year 2020 and a working tensile strain of 1.3 % is predicted to develop in about year 2028 at the end of Phase 3 (sub-soil settlement of 100 mm). The rate of sub-soil settlement under the current applied stress is due to creep settlement which has been estimated based on a lower bound rate of creep settlement of 5 mm/year based on data presented by Ervin (1992).

The creep strain occurring in the geogrid layers during Phase 4 can be calculated from the manufacturer's isochronous curves describing the long term tensile strength-strain-time relationship. The tensile load at the end of Phase 3, is calculated to be 15 % of the mean ultimate tensile strength. The creep induced tensile strain which is predicted during Phase 4 (85 years) is calculated to be approximately 0.5 % and the end of design life strain is predicted to be approximately 1.8 % with a maximum geogrid deflection of 117 mm. No attempt has been made here to assess the concentration of tensile strain in the geogrid near the edge of the column head, the values of tensile strain are presented using a simplified analysis to highlight how the development of arching stress affects the geogrid layers, the predicted values of tensile strain are approximate only. It is the intention of this research project

to continue with long term monitoring of the LTP behaviour to observe the predicted phases of arching development.

5.6.7 Discussion and comparison with design methods

This section compares the observed results and predicted arching stress based on the GRC method with the methods of Zaeske (2001) and van Eekelen et al. (2013). These three methods use the same material parameter inputs (γ_{bulk} and ϕ') and similar geometric inputs (s, a and h). The stresses acting in the area between the columns have been converted to a stress reduction ratio value (stress divided by overburden pressure of 74 kPa) and shown in Figure 5.21. The three methods predict a value of stress reduction ratio within a reasonably small range of between 0.06 and 0.10, with the GRC and the method of Van Eekelen showing good agreement with the measured data at maximum arching. As both the method of Zaeske and Van Eekelen are derived independent of sub-soil settlement, the calculated values of stress reduction ratio are constant with respect to time and sub-soil settlement. For the purpose of design, a constant "design" value of stress acting on the geogrid in the un-arched zone may be appropriate, provided of course that this value is representative, and on the safe side, of the ultimate stress acting on the geogrid layer through its' design life.

However, unlike other common methods, the GRC method has the ability to describe the development of arching stresses through the design life of the embankment. Most importantly, the development of arching stresses described by the GRC (Figure 5.20) implies that adopting a design stress for the geogrid based on maximum arching is not conservative unless:

1) the geogrid is designed to limit deflection to a value of relative displacement less than 4 %, this requires a geogrid layer of very high stiffness and in most cases will not be feasible, or
2) design assumes long term sub-soil support which limits sub-soil settlement to less than 4 % relative displacement (which requires knowledge of the long term sub-soil performance and more importantly an understanding of how arching stresses develop).

The analysis presented suggests that the stress acting on the geogrid layer in Phase 3 is approximately 50 % larger than that acting during maximum arching (Phase 2). As a result, designing the geogrid layer based on an arching model that predicts stresses at maximum arching and/or on the basis of stresses observed shortly after the completion of embankment construction, where maximum arching is likely to be occurring, may result in geogrid that is under-designed in the long term.

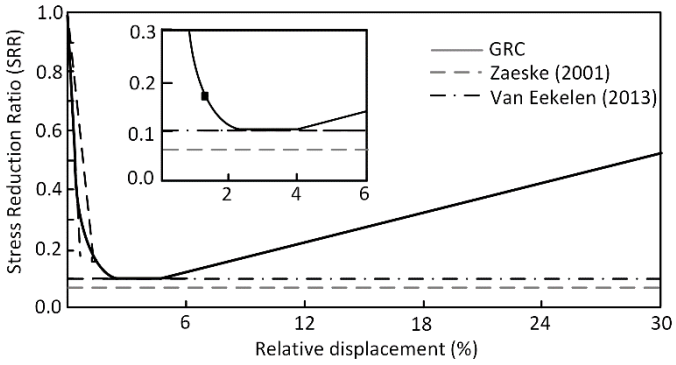

Figure 5.21. Comparison of arching stresses – various methods

5.6.8 Further evidence of ground reaction curve behaviour in field studies

Field scale studies that have observed sub-soil settlement and arching stresses simultaneously are quite limited. The most conclusive data showing the arching stress development as a function of sub-soil settlement at field scale comes from the TH 241 embankment near St. Michael, Minnesota, USA (Wachman and Labuz 2008). The vertical stress measured at the base of the LTP over a 250 day period show the characteristic features of the GRC; initial, maximum and load recovery phases of arching as proposed herein. The authors have indicated the phases of arching development on the original data[4] reported by Wachman and Labuz (2008) (Figure 5.22*a*).

The arrangement of the EPCs and triangular grid layout of columns is shown in Figure 5.22*b*. In a separate field case study, van Eekelen et al. (2010) presented instrumentation data recorded over a 3.5 year period for the Kyoto Road embankment project in Holland. The authors, similar to the above case, have indicated the inferred periods of arching development (initial, maximum arching and load recovery phase) on the original data which describes the vertical stress acting on the sub-soil (load component C) (Figure 5.23*a*). This data highlights that over the long term the stresses at acting maximum arching do not represent the long term arching stresses that will prevail over the remaining design life of this embankment. The layout of the columns, arrangement of the EPCs, a method used to assess sub-soil stress by van Eekelen et al. (2010) is shown in Figure 5.23*b*.

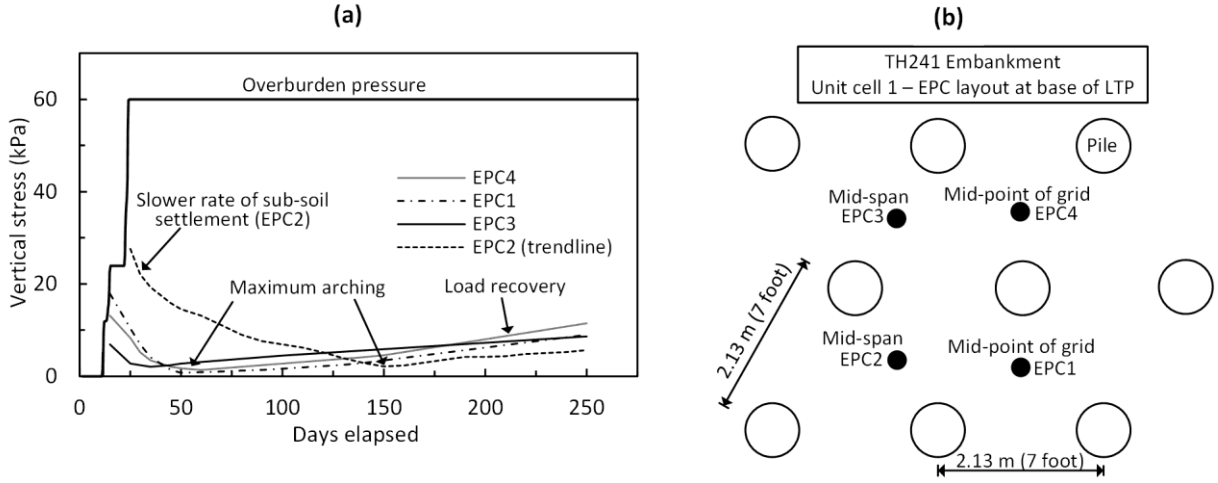

Figure 5.22. (a) EPC data for TH 241 embankment and **(b)** instrumentation layout plan (modified from Wachman and Labuz 2008)

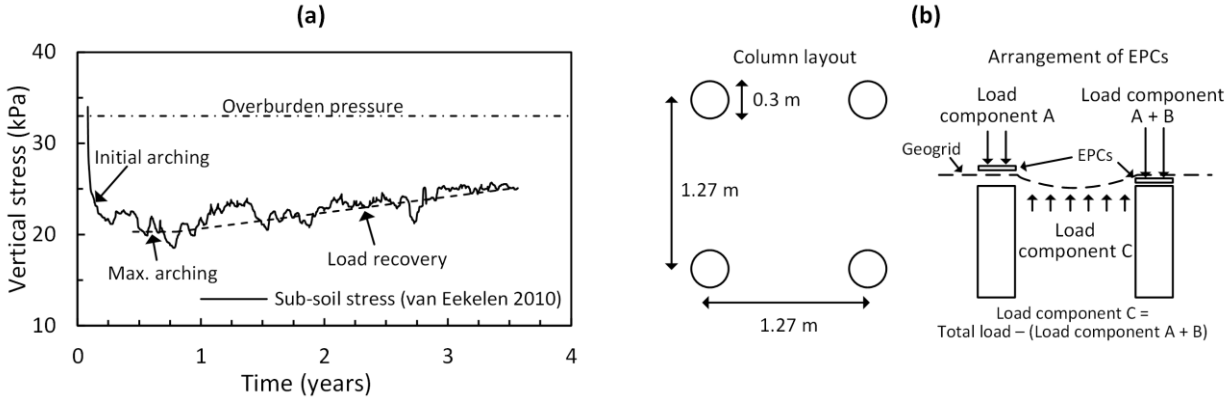

Figure 5.23. Kyoto road data **(a)** Sub-soil stress (modified from van Eekelen et al. 2010) and **(b)** EPC and column layout

[4] The original data has been digitised in Figure 5.22 as a trendline through the original data points

5.7 Discussion

The field data and analysis presented above is not without limitations inherent to most field scale studies. In this case they include: (a) variability of the sub-surface conditions, particularly the fill unit and settlement characteristics of the Coode Island Silt, and (b) the effects of the upper level ground improvement works on a partially constructed embankment introduces uncertainty and limits the extent to which the LTP behaviour can be accurately analysed. However, this uncertainty primarily relates to the assessment of the sub-soil settlement and assessing when the various phases of arching will occur. Based on the field data of Wachman and Labuz (2008) and van Eekelen et al. (2010) described above as well as extensive laboratory testing which have observed maximum arching (Terzaghi 1936; Ladanyi and Hoyaux 1969; Evans 1983; Iglesia et al. 1999, 2013, Chen et al. 2008; Ellis and Aslam 2009a, 2009b), the authors consider that there is sufficient evidence to suggest that the load recovery phase will occur.

However, it is difficult to assess precisely when this will occur. The prediction that stress acting on the geosynthetic reinforcement will begin to increase over the long term has considerable importance in LTP design. It has been shown that the geosynthetic layer must have an unrealistically high stiffness in order to achieve equilibrium at maximum arching stresses and as a result, in most cases, equilibrium between stress acting between the columns and the geosynthetic layer will occur in the load recovery phase unless the sub-soil support is provided. For this particular case study, extensive data is available (see Ervin 1992) which indicates that significant long term settlement of the Coode Island Silt can be expected under small or zero applied stress. As a result, sub-soil support is unlikely to be permanent over the design life of the embankment. The authors consider that the reliance on sub-soil support in (ultimate limit state) design is problematic given that the arching stress development in the load recovery phase occurs under a positive feedback loop (i.e., increasing settlement will lead to increasing stress leading to further settlement, etc.). In addition, creep induced settlement is often significant for road and rail embankments which typically have a design life in the order of 100 years. The “equilibrium” conditions which establish shortly after embankment completion, at maximum arching and with sub-soil support, are not likely to prevail over the design life of the embankment in many cases and may not be representative of the ultimate limit state.

A design of the geosynthetic layer based on the value of stress in the area between columns achieved under equilibrium conditions with no sub-soil support in the load recovery phase (see Figure 5.20*c*), is in the authors opinion, a prudent ultimate limit state design value which the geosynthetic layer can be designed to resist. The design approach outlined in this chapter and summarised in Figure 5.20 differs from the widely adopted “2-step” design approach found in various design standards (EBGEO 2010; German Geotechnical Society, 2010, BS8006-1; BSI, 2010, and CUR; CUR 2016) where an arching model is used to calculate the stress acting in the area between columns in Step 1 independent of sub-soil settlement, and in Step 2, the stress in the area between columns from Step 1 is used to assess geosynthetic behaviour. This “2-step” approach is at odds with the coupled relationship between arching stresses and sub-soil settlement highlighted in this chapter.

Furthermore, the constant values of arching stresses predicted by the limit equilibrium models provide little insight into the phases of arching development described by the GRC (initial, maximum and load recovery phase) that have been outlined in this chapter. The authors consider that the concept of arching development in phases (Figure 5.20), provides knowledge that would be highly beneficial to designers and is important for understanding the development of arching stresses, the interaction with the geosynthetic reinforcement and the overall behaviour of a load transfer platforms.

Much of the analysis presented above focuses on assessing the stresses acting in the area between columns for ultimate limit state design of the geogrid. Another equally important consideration is the impact on embankment deformations as these phases of arching development occur. A common feature observed in many field case studies, and shown here also, is sub-soil settlement occurring for a considerable period post-construction. For the case study presented here, the sub-soil settlement is predicted to increase from the present value of about 50 mm to about 100 mm as phase 2 and 3 occur over the next 12 years (Figure 5.20). For the case study considered here this is not expected to adversely affect rail performance due to the height of the embankment (see Chapter 7). However, the authors consider that this behaviour has considerable implications for shallow height embankments where this continuing sub-soil settlement may lead to surface deformation.

The authors recommend that further development of arching models for the purpose of load transfer platform design should incorporate sub-soil settlement as a governing parameter. While the GRC method describes these phases, further validation of the GRC method with various geometric and material properties is required. In particular, the properties characterising the GRC and developed based on the two-dimensional trapdoor tests, require validation (or otherwise) based on three-dimensional column-supported embankment tests. In the opinion of the author, the GRC parameters (Figure 5.11) of interest include: the empirically derived initial and secant arching modulus values of 63 and 125 respectively, the relative displacement range of maximum arching (2 % < relative displacement < 4 %), the relative displacement range at which maximum arching transitions to the load recovery phase (3 % < relative displacement < 5 %), and finally, how the equivalent relative displacement is assessed (i.e., is it assessed based on the settlement at the edge of the column head, or the displacement where maximum sag occurs (as assumed here), or is there some other value representative of the sub-soil settlement that should be used?) The results of the analysis presented in this chapter suggest that the characteristic parameters of the GRC are, at the least, reasonable for describing the three-dimensional arching associated with column-supported embankments, however further validation is required.

5.8 Findings

The instrumentation of a GRCSE in Melbourne, Australia has been undertaken with over 2 years of post-construction data presented. The measured data has shown the time-dependent development of arching stresses during the post-construction period and it has been further demonstrated, through analysis of the data, that this behaviour is due to the sub-soil settlement in the area between columns. The relationship between arching stresses and sub-soil settlement has been observed previously in laboratory trapdoor tests (Terzaghi 1936; Ladanyi and Hoyaux 1969; and Evans 1983 amongst others), small-scale centrifuge trapdoor models (Iglesia et al. 2011, 2013), column-supported embankment centrifuge models (Ellis and Aslam 2009a, 2009b) and small scale column-supported embankments (Chen et al. 2008) and is shown here at field scale. Reasonably good predictions of the stress reduction ratio at maximum arching have been made based on the method of Zaeske (2001), van Eekelen et al. (2013) and with the GRC method.

However, it has been shown that the GRC method can describe the development of arching stresses from initial arching to maximum arching, and in addition, has been used to predict the development of arching stresses in the future. The concept of the arching development described by an initial, maximum and load recovery phase is a concept that the authors consider to be particularly useful in understanding LTP behaviour and one which would greatly benefit designers. The load recovery phase is the phase of most importance for LTP design. The concept that the arching stresses begin to break-down in the long term with increasing sub-soil settlement has been shown to

occur in embankment field case studies (Wachman and Labuz 2008; van Eekelen et al. 2010), in extensive laboratory testing used to develop the GRC method (see Iglesia 1991) and by a limited number of researchers investigating column-supported embankments (Chen et al. 2008; Ellis and Aslam 2009a, 2009b). This has important implication for the design of the geogrid layer, and perhaps more importantly, has considerable implication concerning long term embankment performance, particularly concerning surface settlement of shallow height embankments. While the GRC and the concept of arching development in phases have been discussed previously by others, given the implications highlighted in here, the authors consider that further research into the role of sub-soil settlement in the development of arching stresses, and particularly the load recovery phase, is warranted.

6 Numerical modelling of arching behaviour

In this research, numerical modelling is used to further investigate the arching behaviour observed in the field case study and described in the preceding chapter using the concept of the GRC (Iglesia et al. 2013). The corner of the trapdoor is described as a singularity point in plasticity theory; the limitations of modelling such points using FEM are well described by de Borst and Vermeer (1984) and van Langen and Vermeer (1991). In addition, the trapdoor test is a well-known large strain problem and the ability to simulate problems of this type over a large displacement range using current Finite Element Method (FEM) numerical techniques is quite limited (Więckowski 2004). Typically, advanced methods such as Coupled Eulerian-Lagrangian (Qiu et al. 2011, Pucker et al. 2012), point based (meshfree) methods such as smooth particle hydrodynamics (Bui et al. 2008) or the material point method (MPM) are required.

The objective of this chapter is to assess the extent to which the GRC can be accurately simulated in a numerically simulated trapdoor test using FEM. A two-dimensional finite element modelling software package "PLAXIS" is used herein for this purpose. This FEM software package is widely used by practicing geotechnical engineers to perform deformation and stability analysis of various types of geotechnical problems. Based on the numerical analysis of the trapdoor tests, these findings are used to model and explore the development of arching in the field case study. To address the limitations associated with the FEM approach, the meshfree method "Smooth Particle Hydrodynamics" (SPH) is introduced later in the chapter and used to model the trapdoor and field arching behaviour. Comparison between the results obtained using these two numerical techniques are discussed.

As the arching in the field case study occurs primarily through the LTP rockfill material, a literature review into the material behaviour of rockfill along with laboratory test results are presented in Appendix D with a summary of this work presented in this Chapter.

6.1 Finite Element Method (FEM)

The two-dimensional FEM numerical analysis presented in the following sections has been carried out using the PLAXIS Anniversary Edition (AE.02) version (2014 version). The software package is a user-friendly Windows based software, with a graphical user interface with allows the input of geometry, soil/rock layers, structures and loading sequences. The software is capable of simulating non-linear and time-dependent soil/rock behaviour in plane strain or axisymmetric conditions.

Some features of the software, that are relevant to the numerical analyses presented in the following sections, include:

- Advanced constitutive soil models such as the Hardening Soil Model (outlined later in this chapter).
- One dimensional elements used to simulate geogrid layers. These are slender elements with normal stiffness and no bending stiffness. These elements can sustain only tensile force and cannot sustain compressive force.

- Interface elements used to simulate the behaviour at the soil-structure interface. These are particularly important when modelling soil-structure interaction problems such as the trapdoor problem and for modelling soil-geogrid interaction.
- Consolidation analysis based on Biot's theory of consolidation enabling the simultaneous calculation of both deformation and groundwater flow with time-dependent boundary conditions in saturated (and partially saturated) soils (Galavi 2010).
- An embedded pile row feature which describes a row of piles installed in the out-of-plane direction (Sluis 2012) and is intended to simulate the three-dimensional pile-soil interaction behaviour in a two-dimensional plane strain model.

6.1.1 Linear elastic perfectly plastic model (Mohr-Coulomb model)

The Mohr-Coulomb model is one of the simplest constitutive model available in PLAXIS and is often used in geotechnical practice in lieu of more complex constitutive models. It describes soil behaviour as isotropic linear elastic with a perfectly plastic yield surface that is fixed by model parameters. In other words, a yield surface that is not affected by plastic straining. Modelling of soil problems using an isotropic linear elastic formulation can be useful to obtain a first order estimate of deformation under working conditions where the soil is not expected to reach a failure condition. However, even under these pre-failure conditions, soil will typically show a non-linear stress-strain response that in most cases is not isotropic. The inability of the Mohr-Coulomb model to simulate the stress-dependency, stress-path dependency and anisotropic stiffness are some of the limitations of the model. In addition, if the soil is unloaded under modest strain conditions, rather than returning to its original condition, in most cases it will develop irrecoverable deformation i.e., plastic deformation (Wood 2003). Some aspects of the stress-strain-stiffness response of a Mohr-Coulomb material are shown in Figure 6.1 where typical soil behaviour is shown in Figure 6.1*c*, *d* and this is compared with Mohr-Coulomb approximated behaviour in Figure 6.1*a*, *b*.

To describe the mechanisms of plastic deformation a yield surface function f is needed. Early works into soil plasticity (1950 – 1965) were influenced by the developments of metal plasticity theory; under moderate strain

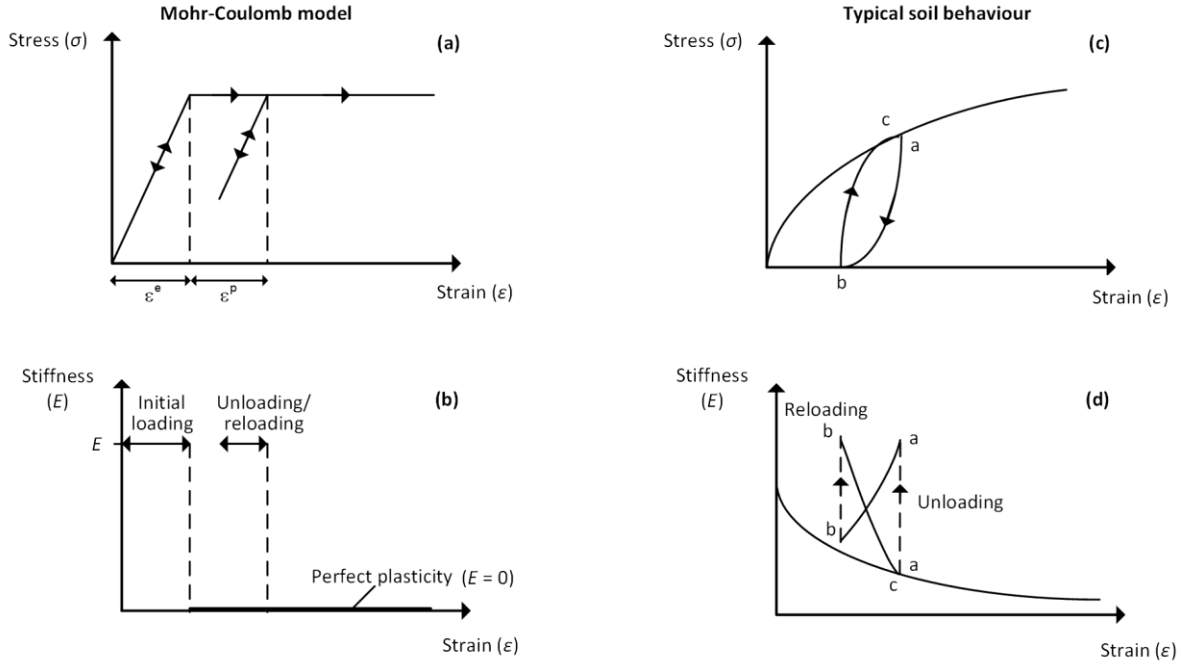

Figure 6.1. Mohr-Coulomb model; **(a)** stress-strain response and **(b)** stiffness response. Typical soil behaviour; **(c)** stress-strain response and **(d)** stiffness response (after Wood, 2003)

mild steel is well described by a perfectly plastic material. Metal plasticity theory typically employed the associated flow (flow is associated to the yield function). This is also referred to as the normality (plastic potential function forms a vector perpendicular to the yield surface) hypothesis (Chen et al. 1985). Using an associated flow rule, the yield surface function and plastic strain rates ($\underline{\dot{\varepsilon}}^p$) are described as follows:

$$\underline{\dot{\varepsilon}}^{\mathrm{p}} \approx \frac{\partial f}{\partial \underline{\sigma}} \tag{6.1}$$

Note: rates are denoted with an overdot as shown in Equation 6.1. However, it has been shown that this hypothesis does not hold well for soil. For this reason, on-going research into soil plasticity incorporated a plastic potential function $\boldsymbol{g}$ and a non-associated flow hypothesis ($\boldsymbol{g} \neq \boldsymbol{f}$) to better describe soil plasticity behaviour (Vermeer et al. 1984). This largely arose due to the need to better describe soil dilatancy behaviour. The material parameter that characterises shear dilatancy is the dilatancy angle (ψ) and this is incorporated into the plastic potential function $\boldsymbol{g}$ (i.e., $\boldsymbol{g}$ is function of $\underline{\sigma}$ and ψ):

$$\underline{\dot{\varepsilon}}^{\mathrm{p}} = \lambda \frac{\partial g}{\partial \underline{\sigma}} \tag{6.2}$$

Where λ is the plastic multiplier. For purely elastic behaviour λ is zero, in the case of plastic behaviour λ is positive. In PLAXIS the model requires five basic parameters: 1) Young's modulus E; 2) Poisson's ratio ν to describe isotropic linear elastic behaviour, 3) Cohesion c, 4) Friction angle ϕ to describe the perfectly plastic yield surface and 5) Dilation angle (ψ) to describe the volume change accompanying failure (plastic potential function) on the yield surface.

6.1.2 Elastic-plastic with isotropic cap hardening (Hardening Soil model)

Compared with the Mohr-Coulomb model which has a perfectly plastic yield surface fixed in principal stress space, the yield surface of the Hardening Soil model has an isotropic (work) hardening yield surface that can expand due to plastic shearing. The model is also capable of distinguishing between shear hardening and compression hardening and is well described by Schanz et al. (1999). The Hardening Soil model also features a deviatoric stress – axial strain relationship which shares similarities with the well-known hyperbolic model (Duncan et al. 1970). However, the Hardening Soil model offers a number of advantages over the hyperbolic model, namely, that it is based on plasticity theory rather than elasticity theory, it includes soil dilatancy and a yield cap (Brinkgreve et al. 2011). As is common with many advanced constitutive models, the improved ability to describe material behaviour requires additional material parameters. The Hardening Soil model requires seven parameters:

- Power for stress level dependency of stiffness (m)
- Secant stiffness in standard drained triaxial test (E_{50}^{ref}) (kPa)
- Tangent stiffness for primary oedometer loading ($E_{\mathrm{oed}}^{\mathrm{ref}}$) (kPa)
- Unloading/reloading stiffness ($E_{\mathrm{ur}}^{\mathrm{ref}}$) (kPa)
- A failure surface defined by the Mohr-Coulomb failure criterion (c, ϕ, ψ)

A relationship between a number of these parameters under loading for a standard drained triaxial test is illustrated in Figure 6.2. A significant portion of the numerical analysis presented in the following sections is concerned with the behaviour of granular materials with high friction angle and under relatively low confining stresses. These conditions are conducive for optimising dilatant behaviour. Accurately describing this behaviour is therefore an

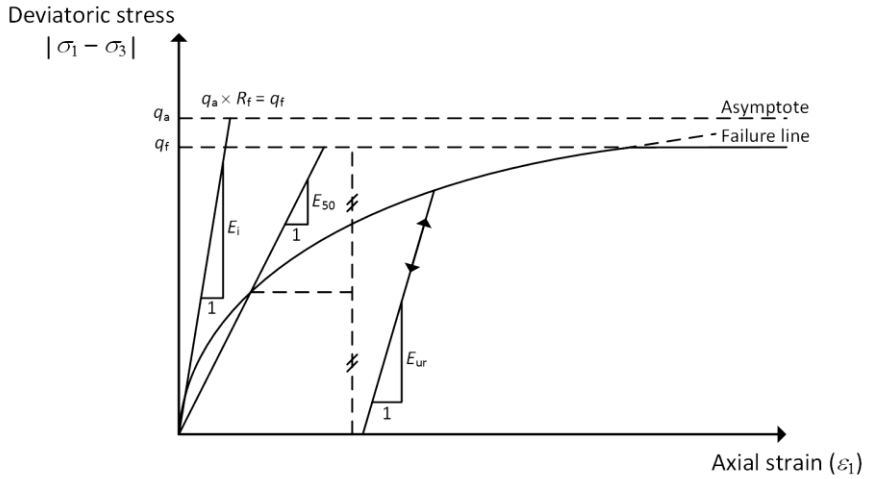

Figure 6.2. Hyperbolic deviatoric stress-strain relationship under drained triaxial conditions (modified from Brinkgreve et al. 2011)

important step in the numerical analyses presented in this chapter. The Hardening Soil model describes the shear hardening flow using the following linear form:

$$\dot{\varepsilon}_v^p = \sin\psi_m \, \dot{\gamma}^p \qquad \textbf{(6.3)}$$

Where ε_v^p is the plastic volumetric strain rate and γ^p is the plastic shear strain rate. The shear hardening flow rule describes the relationship between the rates of plastic shear strain and volumetric plastic strain. In order to incorporate Equation 6.1 into the formulation of the Hardening Soil model the following conditions are imposed on the mobilised dilatancy angle ψ_m:

For $\sin\phi_m < 3/4 \sin\phi$ $\quad \psi_m = 0$

For $\sin\phi_m \leq 3/4 \sin\phi$ and $\psi > 0$ $\quad \sin\psi_m = \max\left(\dfrac{\sin\phi_m - \sin\phi_{cv}}{1 - \sin\phi_m \sin\phi_{cv}}\right)$ **(6.4)**

For $\sin\phi_m \geq 3/4 \sin\phi$ and $\psi < 0$ $\quad \psi_m = \psi$

If $\phi = 0$ $\quad \psi_m = 0$

Where the mobilised friction angle $\sin\phi_m = \dfrac{\sigma_1' - \sigma_3'}{\sigma_1' + \sigma_3' - 2c\cot\varphi}$ **(6.5)**

And the critical state friction angle (ϕ_{cv}) is defined as $\sin\phi_{cv} = \dfrac{\sin\phi - \sin\psi}{1 - \sin\phi \sin\psi}$ **(6.6)**

Figure 6.3 illustrates the relationship between the mobilised dilation angle and mobilised friction angle for a material with Hardening soil properties; $\phi = 40°$ and $\psi = 0°$. These conditions imposed on the mobilised dilation angle, are explained further by Schanz et al. (1996) and correspond to the stress-dilatancy theory by Rowe (1962). In short, Rowe's theory describes a material that contracts at small stress ratios ($\phi_m < \phi_{cv}$) and dilates at higher stress ratios ($\phi_m > \phi_{cv}$).

While the Hardening Soil model is an advanced constitutive model it is not without short comings. As the name perhaps suggests, the hardening isotropic cap is not able to describe softening behaviour and de-bonding effects associated with soil dilatancy. This particularly short-coming is shown to be important in the analyses presented in the following sections.

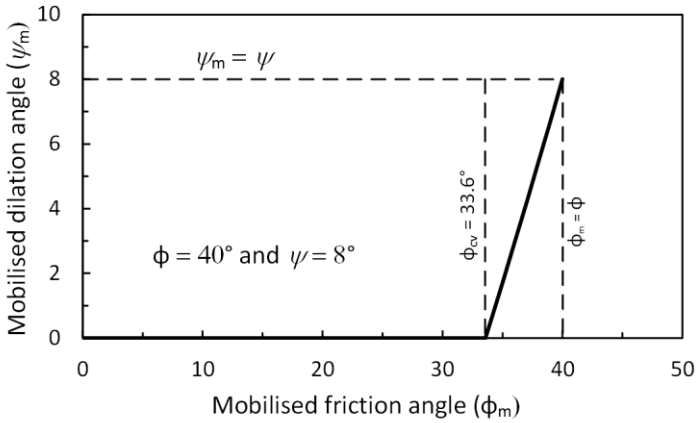

Figure 6.3. Mobilised dilation angle *vs* mobilised friction angle in Hardening Soil model

6.2 FEM trapdoor model

Preliminary two-dimensional plane strain modelling of an active trapdoor based on the physical modelling of Iglesia et al. (1999, 2011, 2013) has been undertaken to attempt to describe the relationship between the arching mechanism and displacement using numerical analysis. The results of 27 trapdoor tests are presented by Iglesia et al. (2011) for various geometric conditions (trapdoor spacing B and height of soil mass H) using coarse sand and various sized glass beads. The coarse sand is known as "*New Jersey 4/14 sand*" where 4 and 14 refer to U.S. standard sieve sizes through which sand particles pass and are retained respectively. New Jersey 4/14 sand is between 1.41 mm (Size #14 sieve) and 4.76 mm (Size #4 sieve) with D_{50} equal to 2.1 mm. The "sand" contains approximately equal portions of coarse grain sand (600μm to 2 mm) and fine grain gravel (2 mm to 6 mm), and in accordance with AS 1726 (1993) is described as a Sandy GRAVEL or Gravelly SAND; for simplicity, the term sand is used below. Additional material properties are described in Table 6.1.

Direct shear tests at a normal stress of 49 kPa and 98 kPa on New Jersey 4/14 sand indicated a friction angle ϕ of 39°. The void ratio was approx. 0.70 for these tests. The sand was "poured" into the trapdoor box and tamped regularly, this process achieved bulk densities typically around 1600 kg/m^3 (Iglesia et al. 2011). The preliminary modelling described below is based on the prototype model geometry from test No. GI103. This test was selected based on the H/B ratio which satisfies the minimum critical height condition ($H > 1.5B$), although other tests could equally have been adopted.

The physical modelling by Iglesia et al. (2011) used centrifuge modelling. To demonstrate similitude between scaled models and prototype models it is typical for centrifuge modelling to undertake a modelling-of-models exercise. The validity of this exercise, and hence the centrifuge modelling, is demonstrated by testing scaled models of the same prototype under various g-levels and plotting the results in dimensionless/normalised space. In this case, the results of the centrifuge modelling are presented as normalised trapdoor load against normalised displacement. Test results GI104 (40 g level) and GI197 (80 g level), GI102 (40 g level) and GI198 (80 g level), GI103(40 g level) and GI199 (80 g level) for New Jersey 4/14 sand are presented in Figure 6.4. Similar behaviour between the 40 g and 80 g models is evident and thus validating the centrifuge modelling approach adopted. The geometric conditions of the centrifuge model and equivalent prototype parameters adopted for the numerical analysis based on Test GI103 are described in Table 6.2. The PLAXIS model geometry for the two-dimensional plane strain analysis is presented below in Figure 6.5. The model geometry is relatively simple and consists of two areas; a soil mass and the trapdoor zone. The trapdoor zone is modelled as a linear elastic non-porous zone with full fixities. To control fully the development of arching in the soil mass, the trapdoor is simulated with a uniform applied displacement across the

Table 6.1. New Jersey Sand 4/14 geotechnical properties after Iglesia et al. (2011)

Material Properties			
Specific gravity G_s	2.66	Max./min. void ratio e_{max}/e_{min}	1.0/0.43
Average particle size D_{50}	2.1 mm	Max./min. dry density $\gamma_{dry\ max}/\gamma_{dry\ min}$	1860/1330 kg/m^3
Uniformity co-efficient $C_u = D_{60}/D_{10}$	1.7	Sample dry density γ_{dry}	1660 kg/m^3
		Relative density D_r	70 % (medium dense-dense)

Table 6.2. Small scale test no. GI103 geometry and prototype model (Iglesia et al. 2011, 2013)

Small scale centrifuge test[1]						Prototype[2]		
B (mm)	H (mm)	B/D_{50} Ratio	Model width (mm)	H/B	g-level	[3]Width (m)	B_p (m)	H_p (m)
50.8	127.0	24.2	330	2.5	40g	13.2	2.03	5.08

[1] Iglesia et al. (2011) [2] Iglesia et al. (2013) - scaled from parameters B_p and H_p

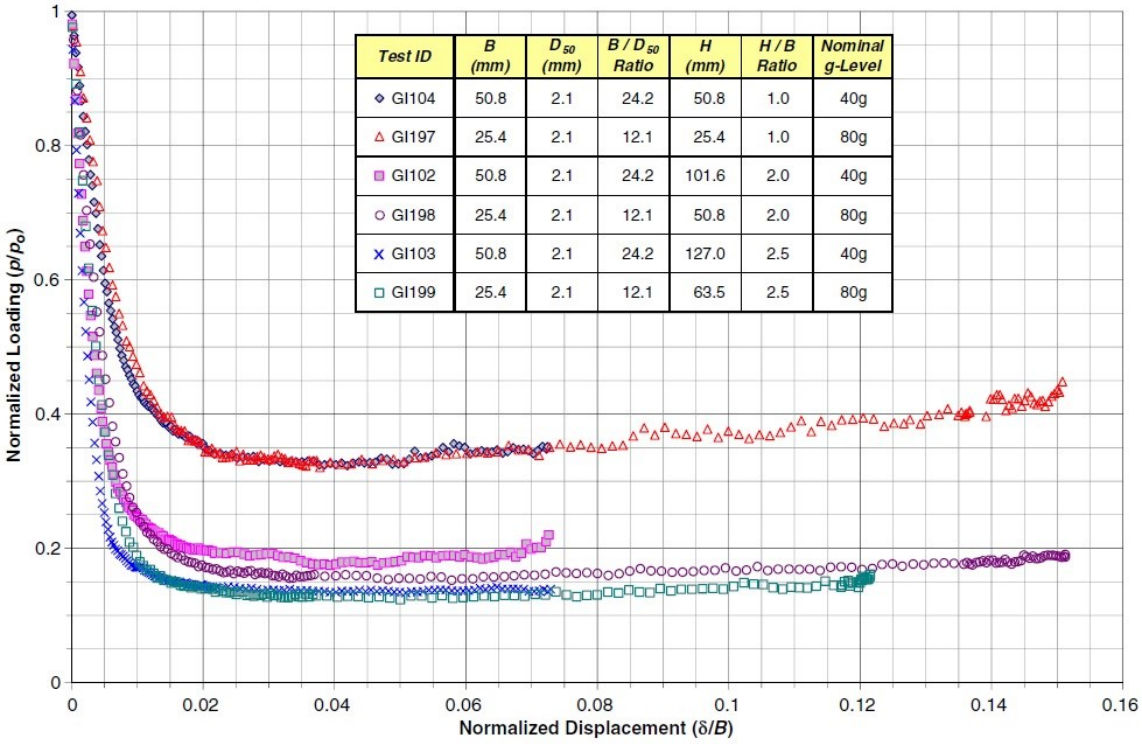

Figure 6.4. From Iglesia et al. (2013) – modelling of coarse sand at 40g and 80 g

width of the trapdoor. This displacement is progressively increased through each phase. Relative displacement (δ/B) values of 0.1 %, 0.25 %, 0.5 %, 0.75 %, 1.0 %, 2.0 %, 4.0 %, 8.0 % and 15 % are modelled, however, convergence issues are typically encountered prior to the final phases been reached. The horizontal model boundary at the base of the soil mass has full fixities and horizontal fixities on the sides of the model. Additional geometry lines are included within the soil mass to assist with mesh refinement.

The PLAXIS user manual (Brinkgreve et al. 2011) provides practical advice on the use of interface elements for soil-structure interaction problems. Van Langen et al. (1991) present a detailed treatment of displacement singularity points in plasticity problems using FEM techniques with solutions to a trapdoor and pile penetration problem presented. An example of a singularity point occurring where a rigid object with rough sides punches into a cohesive material is shown in Figure 6.6 (after Van Langen and Vermeer, 1991) and based on the analytical solution of Hill (1950).

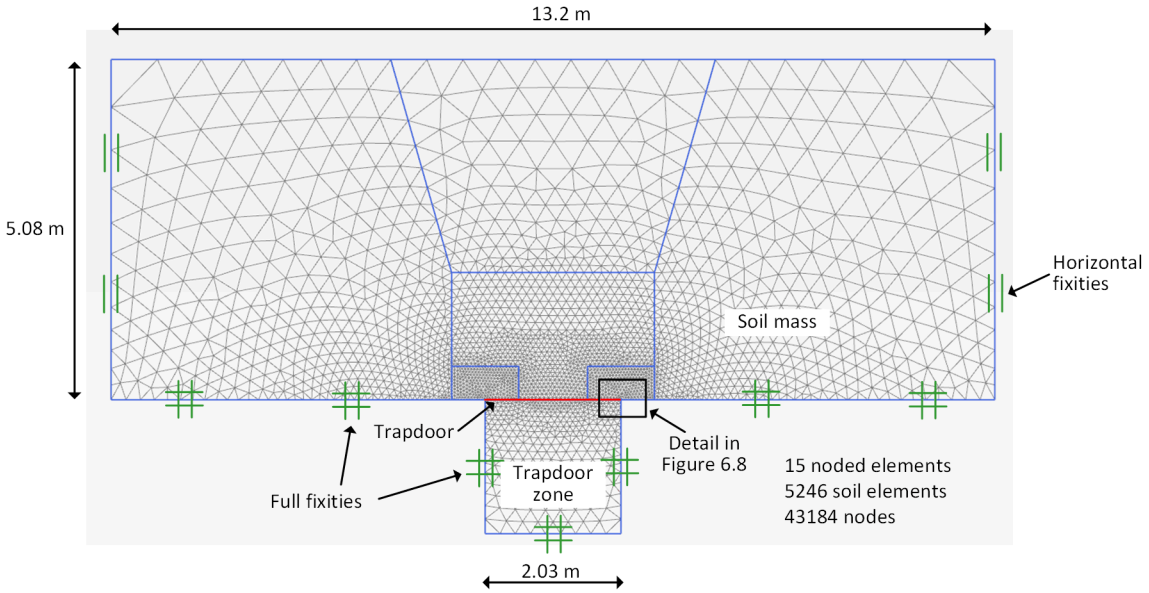

Figure 6.5. Two-dimensional plane-strain model geometry for preliminary trapdoor analysis

Van Langen et al. (1991) describe two techniques that can be implemented to deal with these singularity points in plasticity problems. The first approach is to "smooth out" the displacement continuity by prescribing a displacement over a small transition zone (Figure 6.7*a*). This approach was used by De Borst et al. (1984) to assess the trapdoor problem, the results of this investigation are discussed later. The second approach is to use an interface element at the location of the singularity point (Figure 6.7*b*).

The interfaces at the singularity point and soil-structure model boundaries are described below, five interfaces have been included in the FEM trapdoor models (four are shown in Figure 6.8):

- *Horizontal trapdoor interface* – this interface acts at the trapdoor-soil interface.
- *Soil slip interface* – this interface extends vertically from the edge of the trapdoor into the soil mass. This is discussed in further detail below. *Vertical trapdoor interface* - this interface describes the interaction between the trapdoor zone and vertical wall. For the trapdoor model this is not of interest. However, when considering the interaction between sub-soil and columns in later models this interface is very important.
- *Horizontal model interface* – this interface acts between the soil mass and the base of the model
- *Vertical model interface* – this interface acts at the vertical walls of the soil mass (see Figure 6.5).

There are two methods available in PLAXIS to generate the material properties at the interface; 1) a material set is

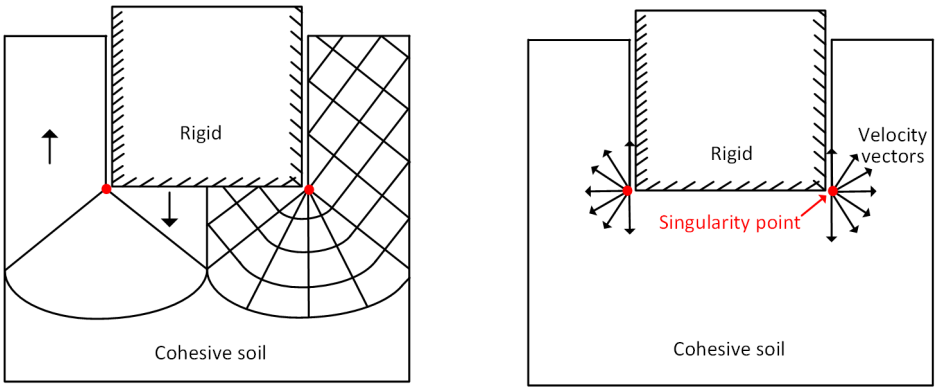

Figure 6.6. Rigid material with rough sides punching into a cohesive material **(a)** slip line field after solution of Hill (1950) and **(b)** singular velocity corner points (after Van Langen and Vermeer, 1991).

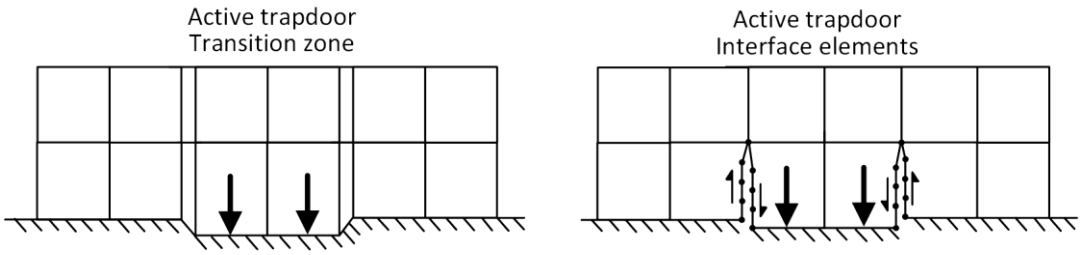

Figure 6.7. Techniques to address singularity point; **(a)** transition zone and **(b)** interface elements

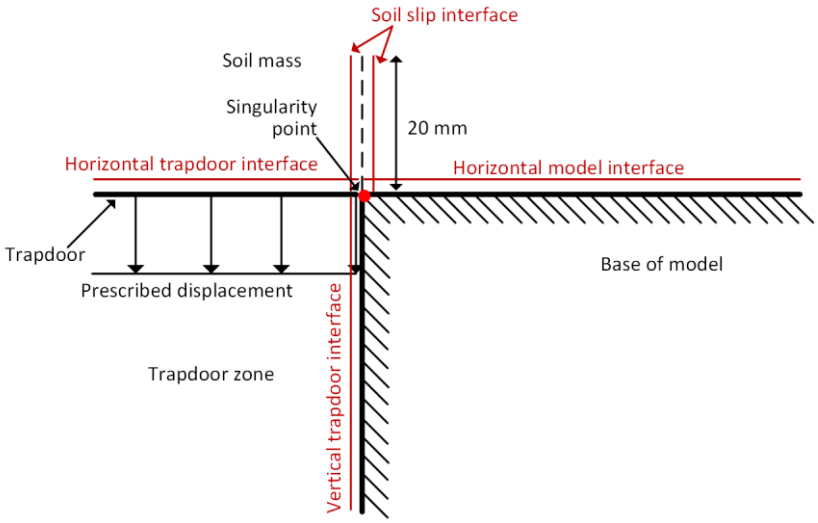

Figure 6.8. Interface elements (in red) at singularity point (corner of trapdoor) as modelled in PLAXIS models presented herein.

assigned directly to the interface, or 2) material properties are generated based on the adjacent soil with a strength reduction factor (R_{inter}) applied. For the models presented here the soil-structure interfaces are modelled with R_{inter} = 0.9. This reduction factor applies to both strength and stiffness parameters. For the soil slip interface, no strength reduction applies and R_{inter} = 1.0; slip is still possible due to the inclusion of the interface elements.

It will be shown in subsequent sections that the soil behaviour and arching mechanism is particularly sensitive to the use of interfaces and the interface parameters. Five models have been developed initially to investigate the effects of the dilation angle and the constitutive model (Table 6.3). For these models describing granular material behaviour, drained behaviour is considered and cohesion is equal to zero in all cases.

6.2.1 General observations

The displacement fields ($|u|$) at various values of relative displacement are shown in Figure 6.9 for Model 4. The discussion below outlines the general behaviour based on the results of Model 4. Comparison between models 1 to 6 and a discussion on the effect of varying dilatancy angle is presented later. With only minimal trapdoor

Table 6.3. Description of FEM trapdoor models 1 to 5

Material Type	Model type	E (MPa)	E_{50}^{ref} (MPa)	E_{oed}^{ref} (MPa)	(E_{ur}^{ref}) (MPa)	m	ν	ϕ' (°)	ψ (°)
1	M-C*	35	-	-	-	-	0.33	39	0
2									6
3	H-S#	-	35	35	105	0.6			0
4									6
5									12

* Mohr-Coulomb model, # Hardening soil model

displacement, a "soil arch" is evident as a wedge forming immediately above the trapdoor. This wedge has the form of a Reuleaux triangle on two sides, with a flat base on the bottom. This wedge is symmetric about the model centreline. This shape is approximated reasonably well by an isosceles triangle, and this is the approach taken by Iglesia (1991) and Iglesia et al. (2013) to describe maximum arching in the GRC method. In addition to the wedge that is evident by about 1 % relative displacement, an approximate log spiral shear plane propagates from the singularity point; these failure planes are identical to those described by Ono et al. (1993) and are illustrated in Figure 6.9*c*. Vardoulakis et al. (1981), Evans (1983), Iglesia (1991) and Iglesia et al. (2013) also observed these failure planes experimentally. From Figure 6.10, where shear strain (γ) is plotted, the development of shear bands present as localised bands of higher shear strain is evident. The most prominent shear bands are the log spiral failure plane and the interior shear band defining the "arch" which define the extent of the radial shear zone. Intermediate shear bands are also evident between these two.

De Borst et al. (1984) presented FEM results of a passive (upward moving) trapdoor test using a thin transition zone to model the singularity point (Figure 6.11). The corresponding relative velocity contours at arching phases termed "Pre-peak", "At-peak" and "Post-peak" are indicated Figure 6.11. The normalised relative displacement

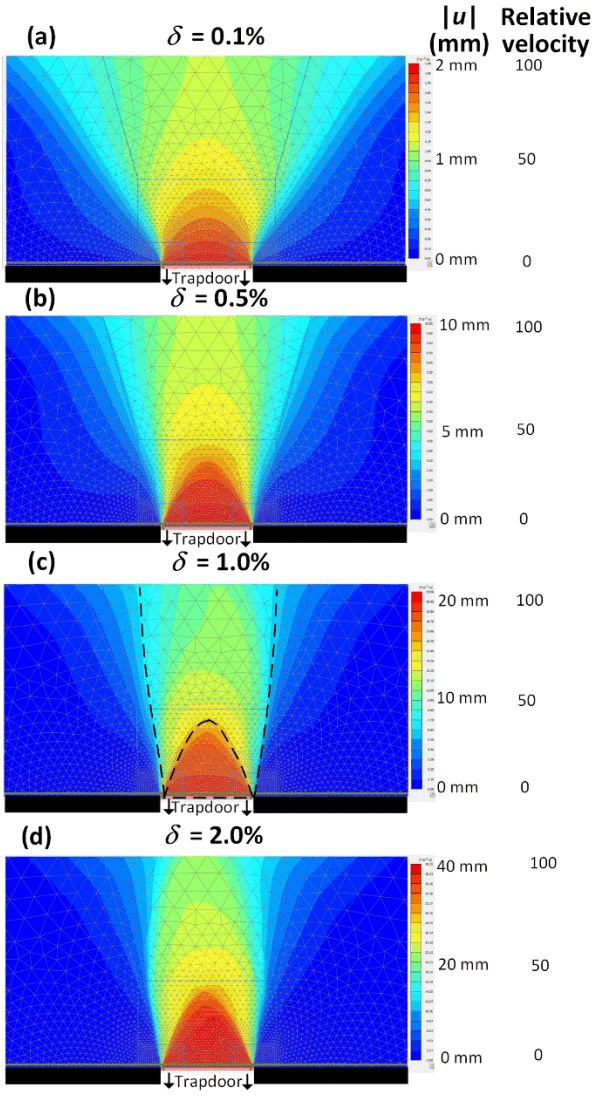

Figure 6.9. Displacement fields **(a)** 0.1 % **(b)** 0.5 % **(c)** 1 % and **(d)** 2 %

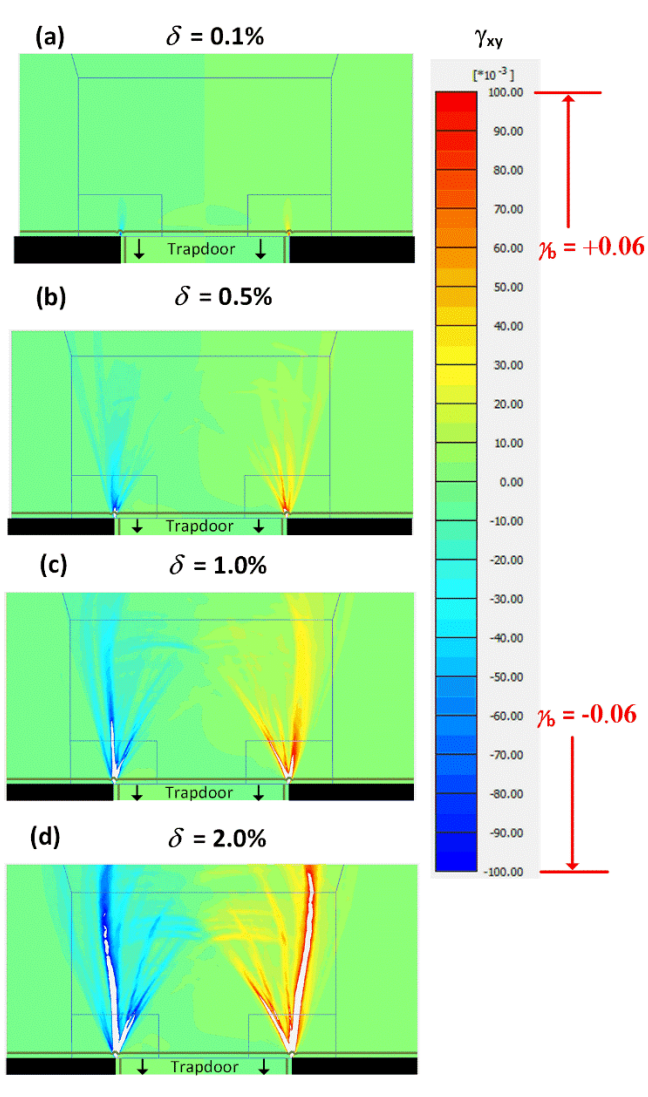

Figure 6.10. Development of shear banding **(a)** 0.1 % **(b)** 0.5 % **(c)** 1 % and **(d)** 2 %

includes an unknown shear modulus (G) term and for this reason, the data cannot be converted to an equivalent relative displacement. Regardless, from the material behaviour, the author has interpreted the observed behaviour as Initial arching, Maximum arching and Load recovery and this is evident in the normalised load-displacement graph. In describing this result, De Borst et al. (1984) noted:

> *"The most surprising observation of this curve is probably the strong macro softening behaviour which occurred although the material model assumed was elastic-ideally plastic, or in other words, no softening of the material itself was assumed"*

And went further to highlight the physical grounds of their finding:

> *"...., the softening behaviour may be attributed to the numerical procedure for a minor part, but the strong softening behaviour which is displayed by the curve of [Figure 6.11b], has physical grounds. This also emanates when we look at the relative velocity contours as depicted in [Figure 6.11c, d, e]."*

The velocity contours produced by De Borst et al. (1984) describing "Pre-Peak" and "At-Peak" are similar to those presented in Figure 6.9. The "Post-peak" behaviour, however, cannot be modelled here using FEM due to convergence issues. The similarities between the two solutions is promising.

6.2.2 Shear band development

At this point, it is important to distinguish between the various phase of arching behaviour and their relevance to the

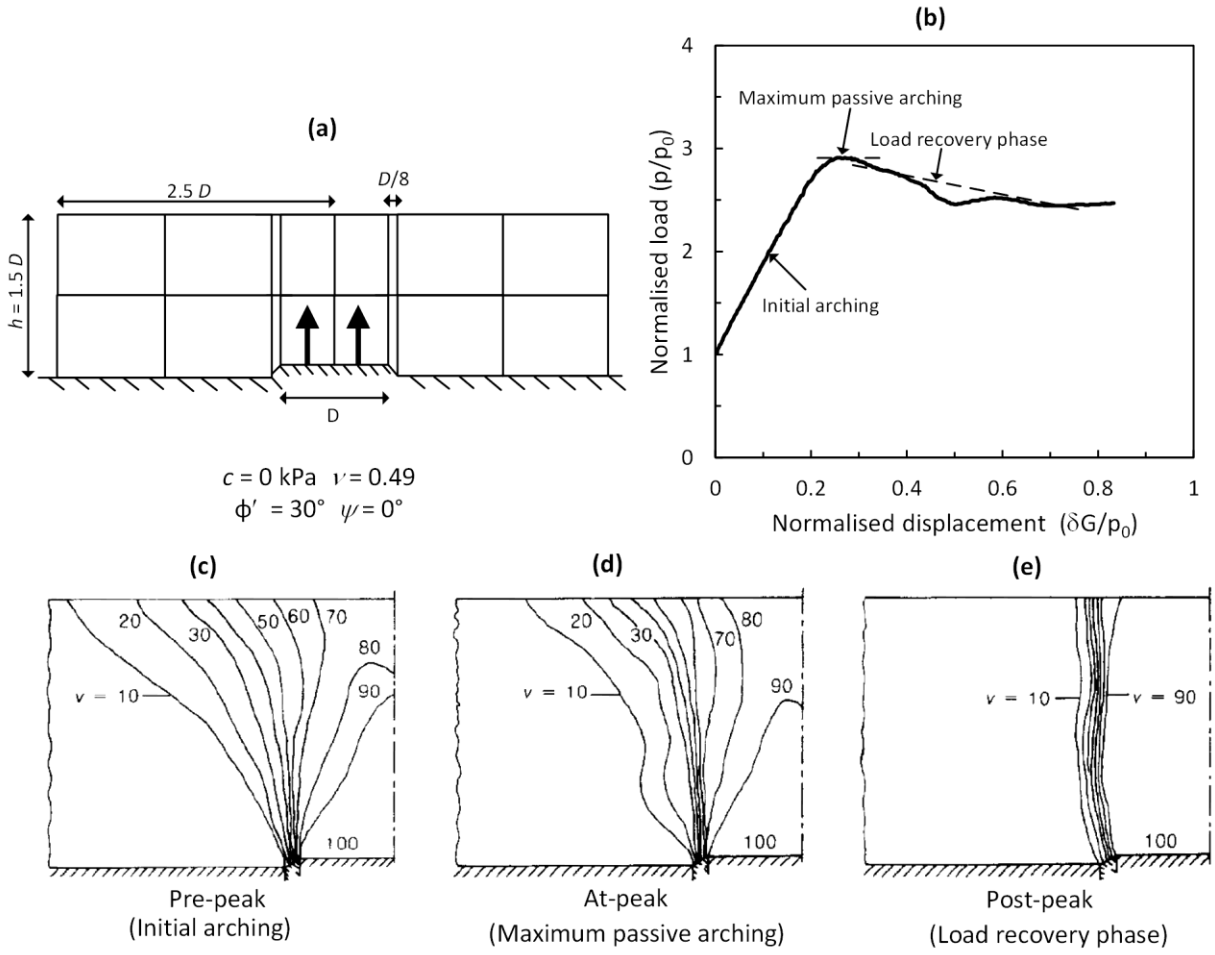

Figure 6.11. (a) FEM model geometry, **(b)** normalised load-displacement curve and relative velocity contours at **(c)** pre-peak, **(d)** at-peak and **(e)** post-peak from De Borst et al. (1984).

problem at hand. The log spiral failure plane is typically used to describe the failure condition at the terminal state using limit analysis techniques. This has been described by Terzaghi (1943), experimentally by Vardoulakis et al. (1981) and numerically by De Borst et al. (1984) amongst others. Although Vardoulakis analysed this failure plane as a vertical plane. This terminal condition occurs at very large relative displacements (greater than about 30 %) and is rarely of interest in assessing LTP behaviour as the geosynthetic reinforcement is included to prohibit these very large displacements from occurring. It was shown in the literature review that relative displacements up to about 10 % are generally of interest for GRCSE. At a displacement range less than about 10 % the failure plane(s) defining the "soil arch" are the main focus as these dictate the maximum arching condition and the load recovery phase of arching. These can be seen as progressively developing shear bands in Figure 6.10. However, it is noted that the log spiral shear band develops simultaneously with the internal shear bands.

Shear bands are defined as localised bands of intense shearing and are observed regularly in granular materials, rocks and metals (Vermeer et al. (1984). Experimentally, shear band development is observed in granular material as a relatively smooth deformation pattern initially and then a quite sudden change to a deformation pattern where deformation is confined to narrow bands. These shear bands are generally bounded by material discontinuities of the velocity gradient, the stresses and its rates (Vardoulakis et al. 1981). The shear band will often propagate from the boundary of the soil body and can pass through the entire soil body or terminate within the soil body. The inclination of shear bands has been studied extensively (see for example Roscoe 1970, Arthur et al. 1977, Vardoulakis 1980, Vardoulakis et al. 1981, Vermeer 1982, Bolton 1986, Chu et al. 1996, Saada et al. 1999, Alshibli et al. 2000, Gajo et al. 2007 among others). One of the earliest solutions describing shear band development for a frictional material is the Mohr-Coulomb criterion:

$$\theta_c = \left(45^\circ + \frac{\phi_m}{2}\right) \qquad \textbf{(6.7)}$$

Where ϕ_m is the mobilised friction angle and θ_c is the angle of the shear band relative to the minor principal stress axis. Roscoe (1970) theory described the angle of inclination as follows:

$$\theta_R = \left(45^\circ + \frac{\psi_f}{2}\right) \qquad \textbf{(6.8)}$$

Where ψ_f is the dilation angle at failure. Vermeer (1982), however, showed that the solutions of Coulomb and Roscoe are limits on the angle of inclination and that the initiation of a shear band in a granular material is dependent on a hardening parameter (h) (Figure 6.12). When loading first commences, h takes on a very large value, this progressively reduces with further loading. Shear band formation is first possible when the hardening parameter reduces to a critical hardening value (h_c), at this time the inclination angle can be approximated as follows (where $h = h_c$):

$$\theta_A = 45^\circ + \frac{1}{4}(\phi_m + \psi_f) \qquad \textbf{(6.9)}$$

Which is equivalent to the experimentally derived value given by Arthur et al. (1977) (θ_A). Vermeer (1982) noted that in many cases, secondary and boundary effects often prohibit the onset of shear banding at inclination θ_A. The frictional effects on the end platens of a triaxial cell are one example. Where this occurs, non-unique solutions at an inclination other than θ_A occurs. This process is known as bifurcation and is well described by Vardoulakis et al. (2004).

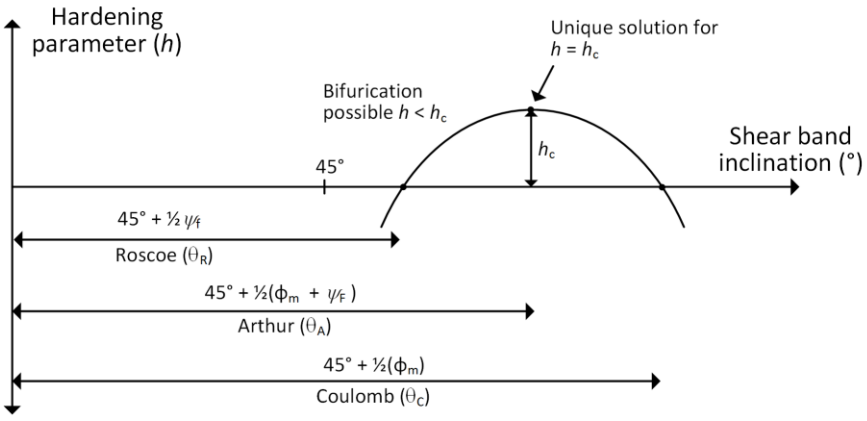

Figure 6.12. Shear band inclination modified from Vermeer et al. (1984)

The shear bands observed in the radial shear zone in Model 4 at 2 % relative displacement are examined in Figure 6.13 where the α angle is plotted. The sign convention adopted in PLAXIS to define the orientation of the major principal stress axis (α angle) is shown in Figure 6.13. This vector field is compared with the analytical solution described by Evans (1983) (Figure 6.13*b*), excellent agreement is found when comparing the average orientation. However, note that when comparing the α vectors from the PLAXIS model with those of Evans (1983) (Figure 6.13*b*), the α vectors are rotated 180° due to the PLAXIS sign convention. In the wedge above the trapdoor the major principal stress axis is horizontal, this is shown as a broad red area with α = - 90°. A second triangular wedge at the edge of the trapdoor is also evident with major principal stresses oriented near-vertical (~5°). Between these two zones is a radial shear zone. The progressive development of shear bands in the radial shear zone was evident in Figure 6.10 as concentrated zones of shear strain. At the location of these shear bands, the α angle can be seen to change suddenly when compared with the smooth pattern shown by Evans (1983) in the radial shear zone. This is consistent with the description presented above and is shown in the graph beneath the PLAXIS plot of shear strain in Figure 6.13.

A cross section through the radial shear zone (A – A′) in Figure 6.13 has been plotted and three shear bands (orientation −21°, −13° and +2°) have been are analysed in detail. A unit element of soil is shown at the bottom of Figure 6.13 with major principal stresses applied and the shear band orientation is shown at the bottom of the figure. The α angle and the orientation of the shear bands are plotted along the cross section and these are aligned with the shear bands analysed in the PLAXIS output. The discontinuous nature of the shear bands is evident as sudden changes in the orientation of the major principal stress direction at the boundaries either side of the shear band. Numerical instability also accounts for some portion of the irregular variation in the major principal stress direction along the cross section.

The principal stress at the shear band locations has been assessed along the length of the shear band and shows only minor variation. This average α orientation along shear band 1 is – 63°, for shear band 2 – 55° and for shear band 3 – 40° has been calculated. The difference between the major principal stress orientation and shear band orientation was found to be 42° ± 1°. The equations defining the orientation of the shear bands θ_A, θ_C and θ_R are each defined as measured relative to the minor principal stress axis. The shear band orientation relative to the minor principal stress axis is therefore 48° ± 1°. This shows excellent agreement with Roscoe's criteria (Equation 6.7), where ψ is 6° for model 4 described in Figure 6.13.

However, it is not clear if the numerically simulated localisation of the deformation observed in Figure 6.13, i.e.,

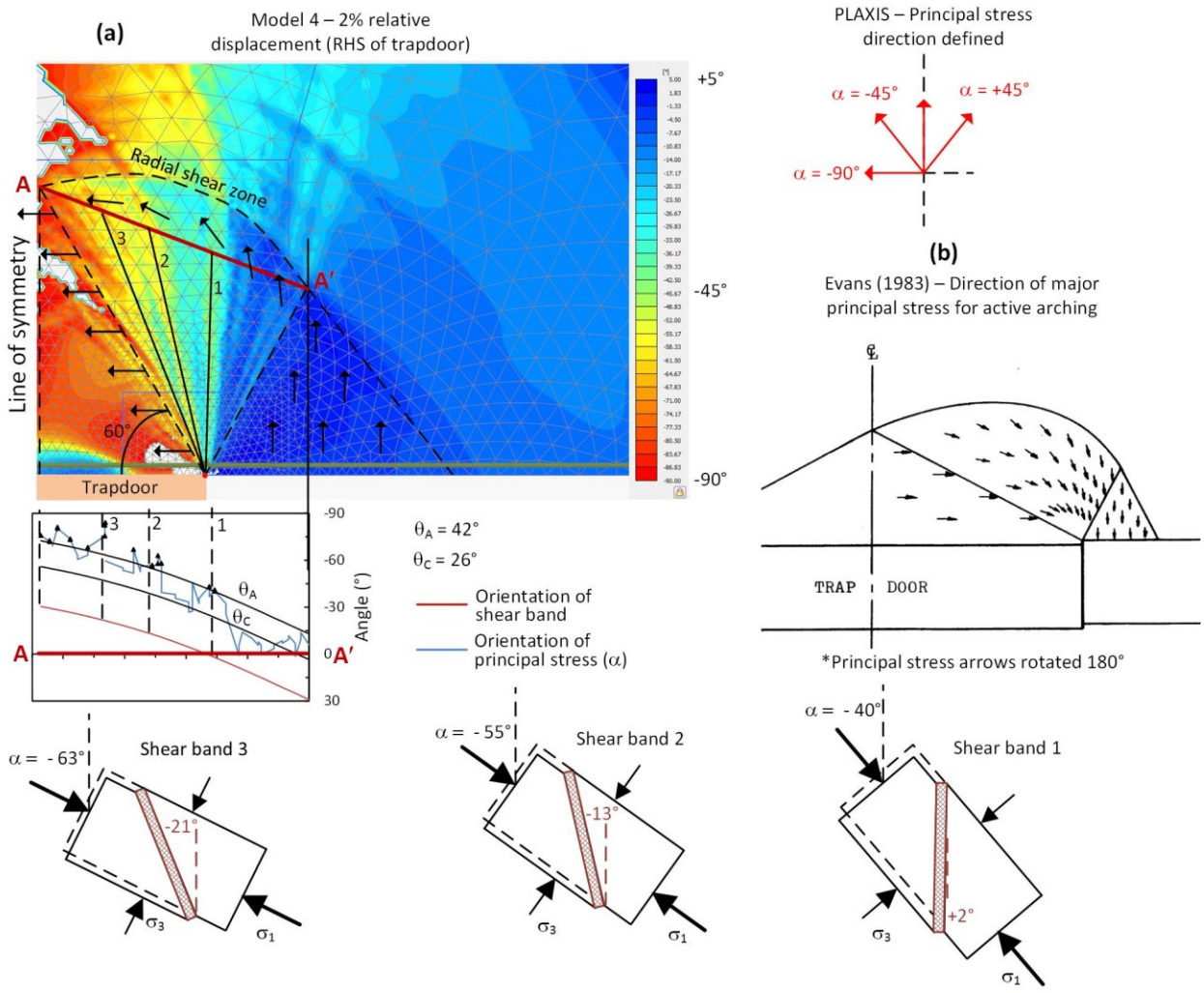

Figure 6.13. Model 4 at 2 % relative displacement; **(a)** direction of major principal stress and shear band orientations and **(b)** direction of major principal stress after Evans (1983).

the development of shear banding, is due to formulation of the hardening soil model. Brinkgreve et al. (2013) describes in the PLAXIS Scientific Manual under the heading "*Implicit integration of differential plasticity models*" that the incremental plastic multiplier ($\Delta\lambda$), calculated when determining Equation 6.2 through an iterative procedure, is written as:

$$\Delta\lambda = \frac{f(\underline{\sigma}^{\mathrm{tr}})}{d+h} \qquad \textbf{(6.10)}$$

$$\text{where} \quad \mathrm{d} = \left(\frac{\partial f}{\partial \underline{\sigma}}\right)^{\underline{\sigma}^{\mathrm{tr}}} \underline{\underline{D}}^{e} \left(\frac{\partial g}{\partial \underline{\sigma}}\right)^{\mathrm{i}} \qquad \textbf{(6.11)}$$

Where $\underline{\underline{D}}^{e}$ is the elastic material matrix for the current stress increment, $\underline{\sigma}^{\mathrm{tr}}$ is the auxiliary stress vector, referred to as the elastic stresses or trial stresses and h is the hardening parameter defined previously. Brinkgreve et al. (2013) note that for perfectly plastic models (i.e., Mohr-Coulomb models) $h = 0$, for linear hardening models h is constant and for non-linear hardening models, h the increment of the plastic multiplier is obtained using a "*Newton-type iterative procedure with convergence control*". The details of the numerical implementation are not clear. However, the orientation of the shear bands (being defined by θ_R) suggests that h is zero.

6.2.3 Vertical stress on trapdoor

The overburden pressure for this model is 77.6 kPa and in Figure 6.14 the reduction in vertical effective stress acting on the trapdoor is shown. The vertical effective stress reduces to about 40 kPa at a relative displacement of just 0.1% highlighting how arching stresses developing at very small trapdoor displacement. To assess how this vertical stress varies with increasing trapdoor displacement a cross section is taken across the width of the model at a level 10 mm above the trapdoor (on the trapdoor side of the interface element, see Figure 6.8). The variation in vertical stress across the width of the model is shown in Figure 6.15. There is a local maximum vertical stress at the mid-point of the trapdoor and a significant increase in vertical stress just outside the edge of the trapdoor. The average trapdoor stress has been assessed and is used to calculate the stress reduction ratio at various values of relative displacement for each model (Figure 6.16).

The numerically derived GRCs for each of the five models fall within a relatively small envelope with the models with a higher dilation angle showing a lower value of stress reduction ratio. The Mohr-Coulomb model (Model 1 and 2) tends to show strong bi-linear response (i.e., initial and maximum arching) with the value of maximum arching reached at just 0.5 % relative displacement. This is not consistent with experimental data described by Iglesia et al. (2011) for test GI103 (Figure 6.4). The Hardening-Soil model tends to approach maximum arching more gradually and reach minimum value of stress reduction ratio (SRR_{min}) at about 1.0 % relative displacement. However, this too does not agree well with the experimental data. The values of SRR_{min} for the five models vary between 0.16 and 0.19 and does not show a load recovery phase prior to numerical convergence issues. The experimentally derived SRR_{min} is 0.12 between about 2% and 4 % relative displacement. The gradient of the load recovery portion of the GRC is relatively shallow for the sand modelled in test no. GI103.

The numerically derived GRCs in Models 1 to 5 show some of the features of the experimentally derived GRC. An initial arching phase that is approximately linear and the progressive development of maximum arching. However, despite the two soil constitutive models adopted and the range of dilation values adopted, the envelope of numerically derived GRCs from Models 1 to 5 does not agree well with the experimental data. Maximum arching is

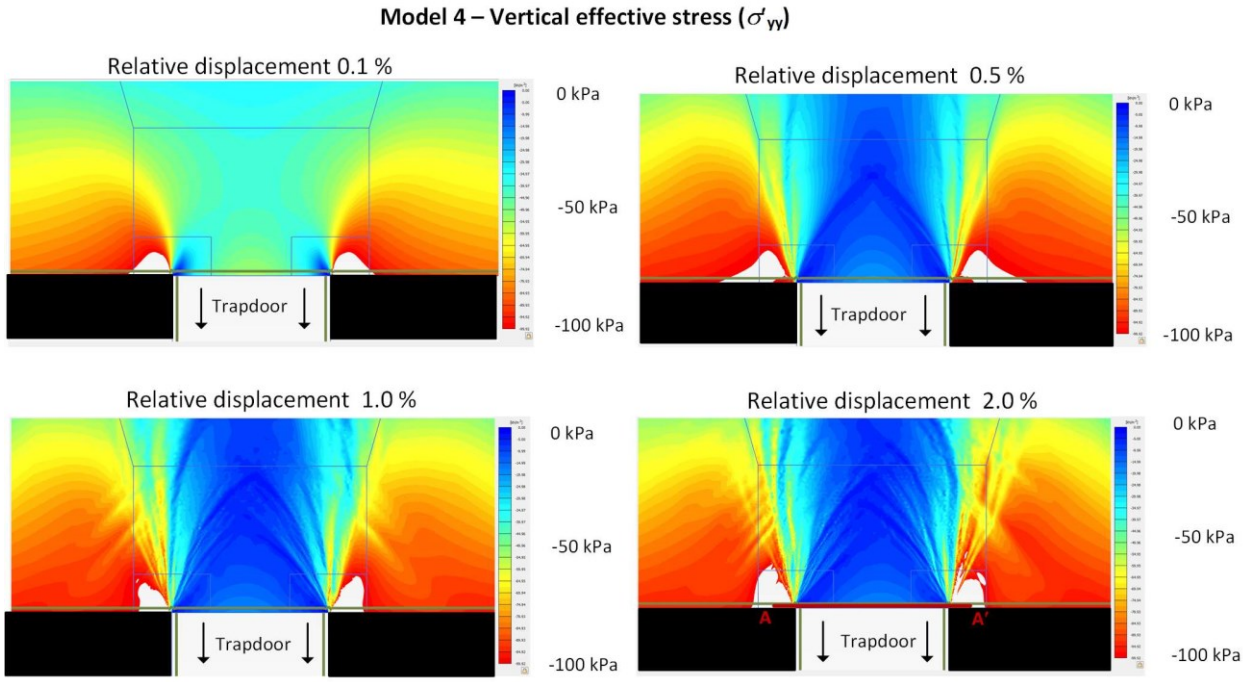

Figure 6.14. Development of vertical stress (σ'_{yy}) acting on trapdoor

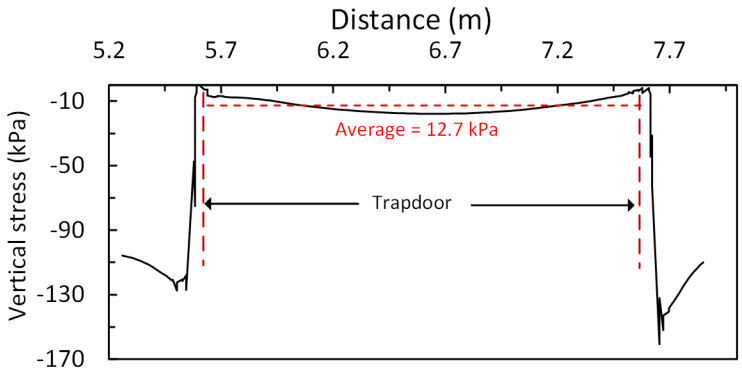

Figure 6.15. Vertical stress distribution – cross section A – A′ at 2 % relative displacement.

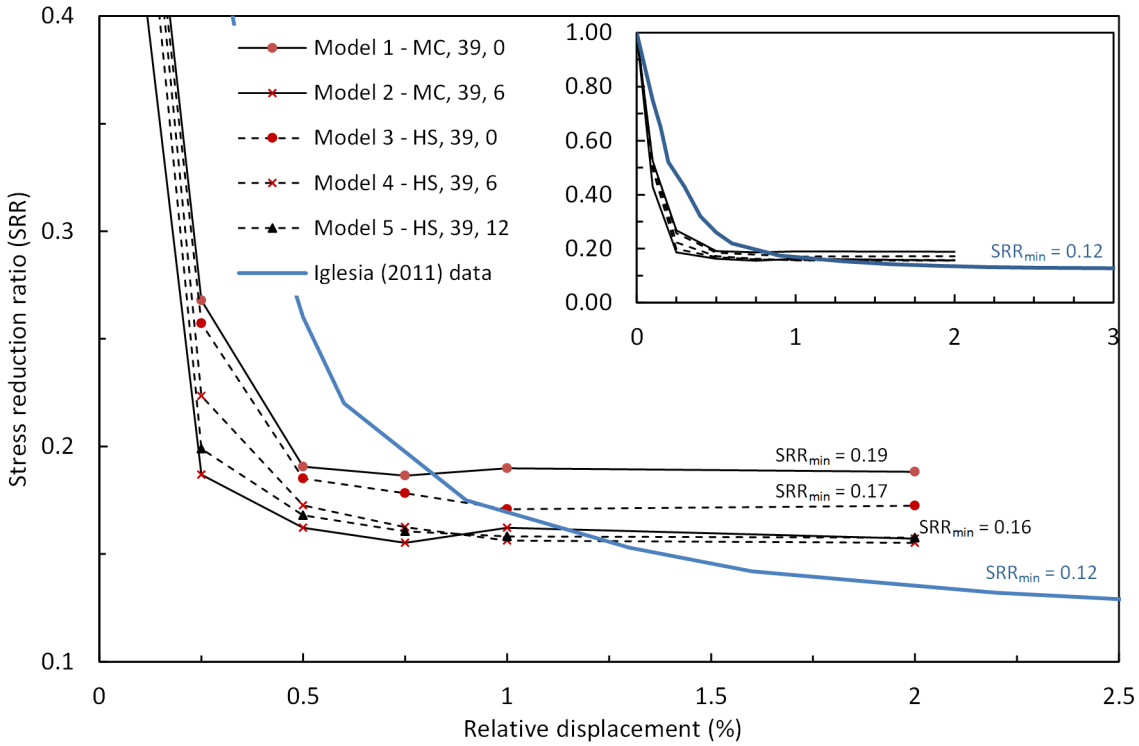

Figure 6.16. Stress reduction ratio for Model 1 to 5 and data from 4.

under estimated and the model appears to be more "sensitive" to trapdoor displacement than the experimentally derived data. Furthermore, shear banding in the numerical models develops at about 1.0 %, preceding maximum arching, and casting doubt on the accuracy of the numerically derived values of maximum arching as the shear banding continues to develop at is well formed at 2 % relative displacement where maximum arching has been observed to occur in physical modelling.

More importantly, the range of relative displacement modelled is limited to just 2 %. In the preceding chapter, it was noted that the range of interest for typical GRCSEs is up to 10 % relative displacement. Re-meshing techniques have been used by the author to extend the relative displacement range through to 5 % in Model 4, however, the SRR_{min} value remains constant from 1 % to 5 %. Based on the development of shear banding in Figure 6.10 it is expected that sliding along shear band discontinues and localised strain softening behaviour leads to the breakdown of arching and the load recovery phase observed in physical modelling.

Based on the shear band development described above, there is uncertainty in the numerically derived results up to and beyond maximum arching. There is little basis to support a level of confidence in the numerical FEM results

beyond maximum arching and into the load recovery phase as there is no indication of destablisation (load recovery phase) or that the model will trend towards a Terzaghi type failure mechanism. The model tends to indicate a constant collapse load or a constant state of stress defined at maximum arching. Where these results are relied upon at large relative displacements, erroneous conclusions are likely and these conclusions are generally on the unsafe side from a design perspective. That is to say, they under predict the ultimate stress acting on the geosynthetic reinforcement.

6.3 North Dynon case study

Data from the North Dynon embankment, described in Chapter 5, calculated sub-soil settlement to be about 2% relative displacement. In this section the arching observed in the North Dynon embankment at Area #2 is modelled using a two-dimensional axisymmetric model to simulate the unit cell described in the preceding chapter. The axisymmetric FEM model is compared with the field data and with the predicted GRC which was shown to give good agreement in the preceding chapter. The limitations of the plane strain analysis have been outlined in the preceding sections and as such, the aim of this section is to investigate how these limitations affect the interpretation of field behaviour when traditional FEM numerical techniques are used to assess the development of arching. The meshfree method – Smooth Particle Hydrodynamics (SPH) is introduced in the next section and compared with the FEM numerical results. In the North Dynon embankment the soil arching develops predominately through the Rockfill unit; accurate modelling of this unit is therefore particularly important to assess the arching behaviour. An overview of rockfill material behaviour is presented and the difficulties in assessing accurately rockfill material properties using conventional laboratory equipment are discussed.

6.3.1 Rockfill

The Rockfill unit adopted for the case study is a 75 mm granodiorite rockfill known as Oaklands Junction Granodiorite. The general characteristics of the Rockfill (C_u, C_c, D_{10}, D_{30}, D_{50}) were summarised in Chapter 3 in Table 3.3. In Figure 3.8 a Particle-size distribution curve was presented. Given the important role the Rockfill plays in development of arching in the North Dynon case study, a literature review of rockfill material behaviour has been undertaken (Appendix D). The key findings of this literature review are summarised below along with an overview of the Rockfill material properties derived from large-scale direct shear box testing on scaled rockfill material.

- The breakage factor of the rockfill used in LTP design will generally be negligible under the low confining pressures found in most GRCSEs. To satisfy this condition the rockfill must be comprised of good quality rockfill material (rockfill grade C or better, UCS > 125 MPa, is suggested).
- The dilative component is likely to form a significant component of the rockfill shear strength at peak shear strength. For the rockfill used in the LTP this effect is considerable under even modest compactive effort and increases with increasing compaction. Heavy compaction of the LTP is not recommended due to the potential for increased installation damage to the geosynthetic reinforcement layers. A well-graded rockfill assists with the reducing the required compactive effort.
- The increase in peak shear strength due to dilation will lead to a significant strain softening of rockfill material (see data from Charles and Watts, 1980 in Figure D7).
- Increased rockfill angularity will increase the friction angle at low confining pressures however this may also increase the potential for installation damage to the geosynthetic reinforcement layers.

6.3.2 Rockfill laboratory testing

Due to difficulties finding a suitable sized direct shear box test apparatus owing to the large particle size of the rockfill, the parallel gradation technique originally developed by Lowe (1964) has been used to assess the shear strength properties of the Rockfill unit. Based on the principles of similitude Lowe (1964) is postulated that realistic shear strength properties can be obtained from a scaled laboratory rockfill that are representative of the field rockfill when using the parallel gradation technique. This technique is frequently used to assess the shear strength properties of large-scale rockfill (i.e., D_{max} greater than 500 mm) for rockfill dams (see Indraratna et al. 1993 and Varadarajan et al. 2003). For the scaling of 75 mm minus rockfill to the laboratory 26 mm minus rockfill the parallel gradation technique was used and is expected to provide a reasonable representation of the full scale rockfill shear strength. To further validate the measured material properties of the laboratory scale rockfill, these properties were compared with those predicted using the equations described by Douglas (2003) (see below and Appendix D) which are based on the data presented in Figure 6.17.

Testing was performed using the Monash University's Constant Normal Stiffness direct shear apparatus (Haberfield et al. 2003) (Figure D9). Samples were tested at confining pressures of 50 kPa, 100 kPa and 200 kPa, results are shown in Figure D10*a*, *b* and *c* respectively. Values of ϕ'_{sec} of 51°, 49° and 44°, and dilation angles 14°, 14° and 11° were measured at confining pressures of 50 kPa, 100 kPa and 200 kPa respectively. The range of confining stress (σ_n) of interest is in the order of 50 kPa to 100 kPa for GRCSEs and over this stress range the relationship suggested by Douglas (2003) to relate ϕ'_{sec} with σ_n (Equation 6.12) shows good agreement with the laboratory data.

$$\phi'_{sec} = 35.95 + \frac{77.73}{\sigma'^{.3974}_n} \quad \textbf{(6.12)}$$

Similarly, the power expression suggested by Charles et al. (1980) to describe the curved Mohr-Coulomb failure envelope (Equation 6.13) was found to provide a reasonable fit of the laboratory data over the stress range of interest with parameters A = 3.1 and b = 0.78.

$$\tau = A(\sigma')^b \quad \textbf{(6.13)}$$

6.3.3 Rockfill deformation parameters

Fell et al. (2005) provides guidance on the assessment of Young's modulus (E) for rockfill used in concrete faced

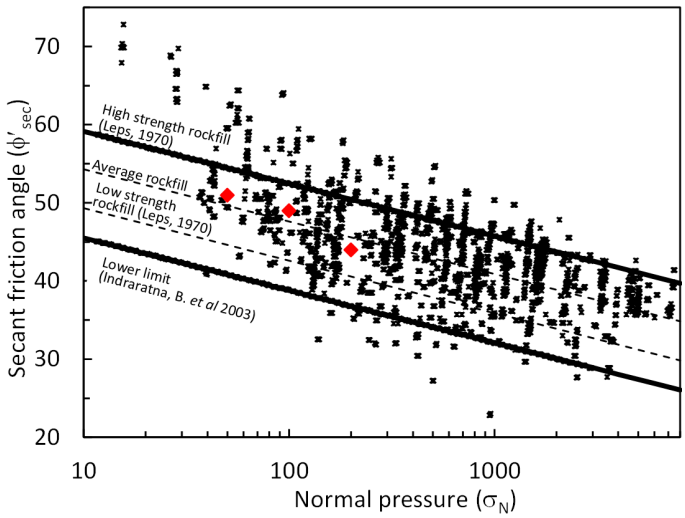

Figure 6.17. Secant friction angle (ϕ'_{sec}) with normal stress (σ_n) – modified from Douglas (2003) with North Dynon Rockfill data shown (red diamond)

ranging from 39° to 56°. Soroush et al. (2006) adopted a value of 0.8 for the failure ratio (R_f) and a power factor (m) ranging from 0.35 to 0.5. Without additional laboratory data the reference Young's modulus at 50 % peak strength (E_{50}^{ref}) is taken as 60 MPa for a dense granular material.

6.3.4 FEM – two-dimensional axisymmetric without geogrid

In Chapter 5 a unit cell was used to describe the development of arching in instrumentation Area #2. (Figure 5.12). The axisymmetric model (Figure 6.18) has a radius of 1.26 m and the column head a radius of 0.56 m. With the exception of the column head, the vertical boundaries are modelled with horizontal fixities, the column head is modelled as fully rigid. The sub-soil (General Fill unit) is not modelled explicitly, instead a prescribed displacement is used at the Rockfill-subsoil interface initially, similar to the previous trapdoor models. As outlined in Chapter 5, the overburden pressure was calculated to be 74 kPa (refer to Section C1 in Appendix C). An equivalent height of soil equal to 3.93 m is adopted in the axisymmetric model to generate an initial overburden pressure of 74 kPa. This comprises a 0.65 m thick Rockfill layer (the LTP) overlain by a 3.28 m thick Embankment Fill layer. The geogrid is omitted to allow arching stresses to develop unimpeded. Material properties are summarised in Table 6.4. Rockfill parameters were outlined in the preceding sections. The Embankment Fill material properties were described in Chapter 3.

Interface elements are again used to model the singularity point at the corner of the column head as previously outlined for the trapdoor test (Figure 6.8). However, the trapdoor soil-structure interface, termed the "*horizontal trapdoor interface*" is replaced with a "*soil slip interface*" that extends 20 mm horizontally from the corner point. Relative displacement (δ/B) values of 0.1 %, 0.25 %, 0.5 %, 0.75 %, 1.0 %, 2.0 %, 4.0 %, 6.0 %, 8.0 % and 10 % are applied as prescribed displacements at the Rockfill – Sub-soil interface. The global mesh factor is 0.02 with mesh refinement applied near the corner point, the Rockfill layer and in the bottom portion of the Embankment fill layer.

6.3.5 FEM - two-dimensional plane strain without geogrid

Three plane strain models have been developed to allow direct comparison with the results of the axisymmetric model and the SPH model presented later in the chapter (at this time, the SPH code has not been developed to model axisymmetric conditions). The three plane strain cases are as follows:

1. Plane strain model with clear spacing equal to 1.42 m
2. Plane strain model with clear spacing equal to 1.50 m
3. Plane strain model with clear spacing equal to 1.50 m and far field vertical boundaries (model width 8 m).

The plane strain models have a global mesh factor of 0.02. Case 1 is shown in Figure 6.19. The clear spacing of 1.5 m is equal to the spacing between columns D15 and D14 in Area #2 (Figure 5.12). All other aspects of the model are the same as the axisymmetric model described previously. The GRC from the axisymmetric model and the three plane strain cases are shown in Figure 6.20. The predicted GRC developed in Chapter 5 for the Rockfill material is also shown. The results are generally consistent with those shown previously for the trapdoor model. The maximum arching develops between about 1% and 2 % relative displacement and then remains relatively consistent, in this case through to 10 % relative displacement. condition (Figure 6.22*a*), transitions to a passive stress state as the wedge of soil contracts laterally and expands in a vertical direction due to the unloading of the initial overburden stress (Figure 6.22*b* and *c*). It is not clear if the behaviour observed beyond about 2 % relative displacement is a function of the inability of the constitutive model (i.e., the hardening soil model) to describe the strain softening

behaviour along the initial shear bands (that define maximum arching and the triangular wedge). As result, this may be forcing additional shear bands through the passive wedge. The behaviour simulated in Figure 6.22*c* is not consistent with physical modelling by (Jacobsz 2016) shown in Figure 2.7*b*.

Table 6.4. Axisymmetric FEM model based on North Dynon embankment material properties

Material Type	Model type	γ_{dry} (kN/m^3)	E (MPa)	E_{50}^{ref} (MPa)	E_{oed}^{ref} (MPa)	(E_{ur}^{ref}) (MPa)	ν	c′ (kPa)	ϕ′ (°)	Ψ (°)
Embankment fill	M-C* (Drained)	19	30	-	-	-	0.30	5	30	0
Rockfill (LTP)	H-S* (Drained)	20	-	60	$0.8\times E_{50}^{ref}$	$3\times E_{50}^{ref}$	0.35	0	50	14

* Mohr-Coulomb model, # Hardening soil model

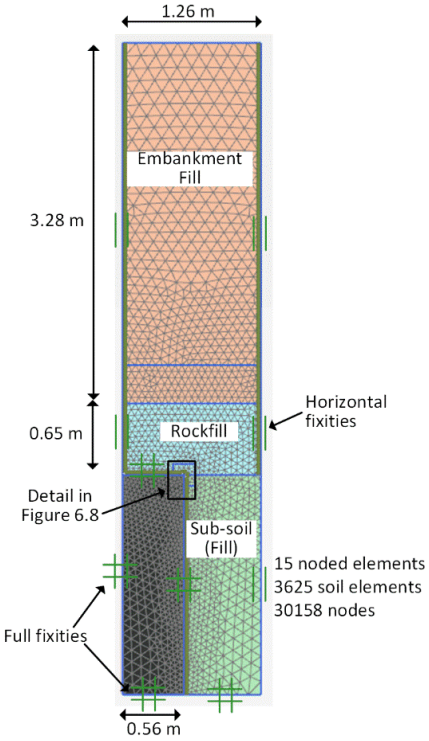

Figure 6.18. Two-dimensional plane strain model geometry

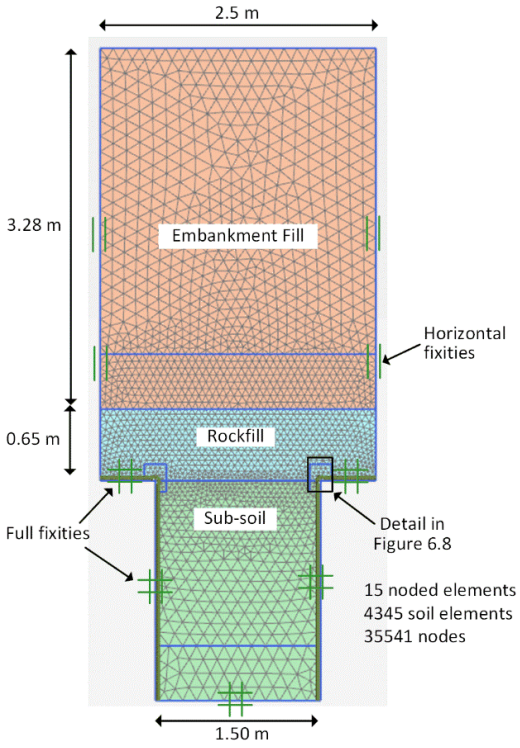

Figure 6.19. Two-dimensional plane strain model geometry

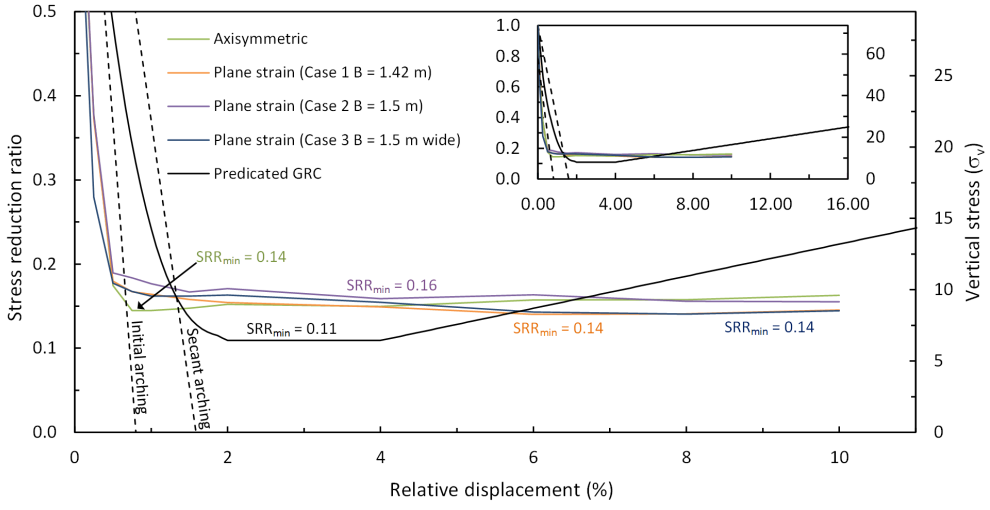

Figure 6.20. Theoretical GRC and curves from FEM analysis

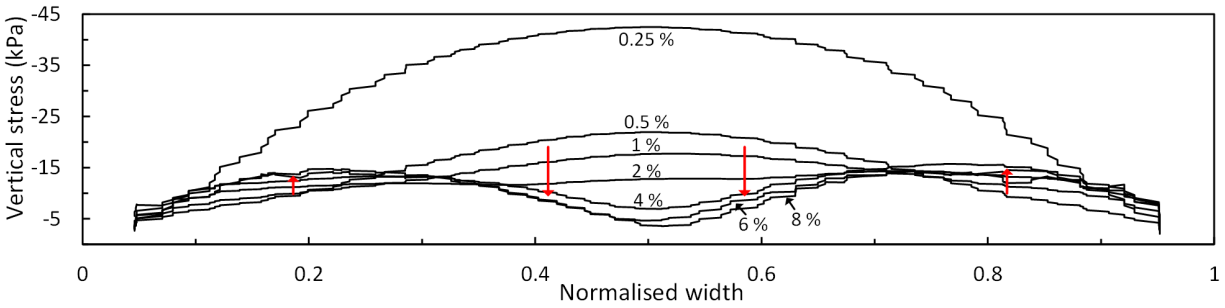

Figure 6.21. Vertical stress acting on subsoil zone as a function of relative sub-soil displacement

This condition at maximum arching is consistent with the description suggested by Evans (1983) and shares similarities with the development of arching stresses described by Van Eekelen et al. (2013). This development of arching, described by Van Eekelen et al. (2013) was used as the conceptual basis for the so-called "Concentric Arches" model. Similar numerical modelling by Van der Peet (2014) describe the development of principal stress axes as shown in Figure 6.22 , however this model does not describes the phases of arching outlined in the literature review (i.e., initial, maximum, load recovery and terminal).

Prescribed displacement

The benefit of using a prescribed displacement at the Rockfill/Fill interface is that the relationship between arching stresses and displacement can be easily established and a GRC developed. However, a shortcoming of this approach is that soil-structure interaction, which is occurring along the vertical sides of the column head, is ignored. By prescribing the displacement at this location, the soil mass is forced to shear at the corner of the column head. However, in a GRCSE, frictional interaction between the sub-soil and the vertical face of the column heads will reduce settlement. This raises an important distinction between arching stress development observed in a trapdoor experiment and arching stress development observed in a GRCSE. In the trapdoor model the relative displacement occurs at the edge of the column head and this locally behaviour rapidly initiates shearing of the soil mass. In the GRCSE, soil-structure interaction on the vertical sides of the column heads will limit the localisation of relative displacement.

To investigate how the prescribed displacement affects the arching stress development, the plane strain Case 2 (*B*

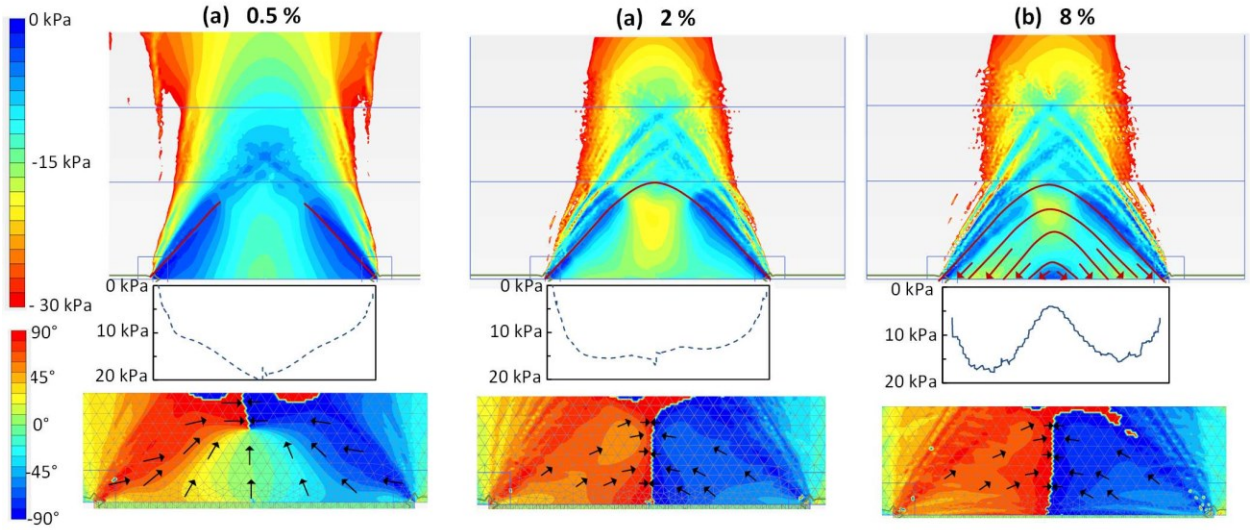

Figure 6.22. Development of stress conditions in the triangular wedge of soil undergoing settlement **(a)** initial arching **(b)** transition to maximum arching and **(c)** load recovery phase

= 1.5 m) is modelled by applying a prescribed displacement at the Fill-Coode Island Silt interface, 2 m below the LTP. Numerical difficulties are encountered where the GRCSE geometry is modelled directly as the fill attempts to separate from the underside of the column head at the location(s) indicated in Figure 6.23*a*. For this reasons, the GRCSE geometry shown in Figure 6.23*a* is approximated by the model geometry shown in Figure 6.23*b*.

The frictional interaction on the vertical sides of the column heads is expected to affect the nature of the sub-soil settlement at the base of the LTP. To investigate these effects the strength reduction factor (R_{inter}) acting on the interface termed "Vertical trapdoor interface" (Figure 6.8) is modelled with values of 0.5, 0.75 and 1.0. A value of 1.0 indicates a "rigid" interface and therefore no strength reduction, a value of zero indicates a frictionless surface. The resulting settlement profiles at Rockfill/Sub-soil interface is shown in Figure 6.24*a* where a 150 mm prescribed displacement is applied at the Fill/Coode Island silt interface. The effects of increased frictional interaction on the vertical face of the column head can be seen as a vertical transitional shear zone which increases in width with increasing R_{inter} value. These results indicate that a prescribed displacement applied at the Rockfill/Sub-soil interface approximates the settlement profiles in Figure 6.24*a* quite well. More importantly, when comparing the resulting GRCs for the models with R_{inter} values, there is negligible difference in the results. Given the approach adopted to

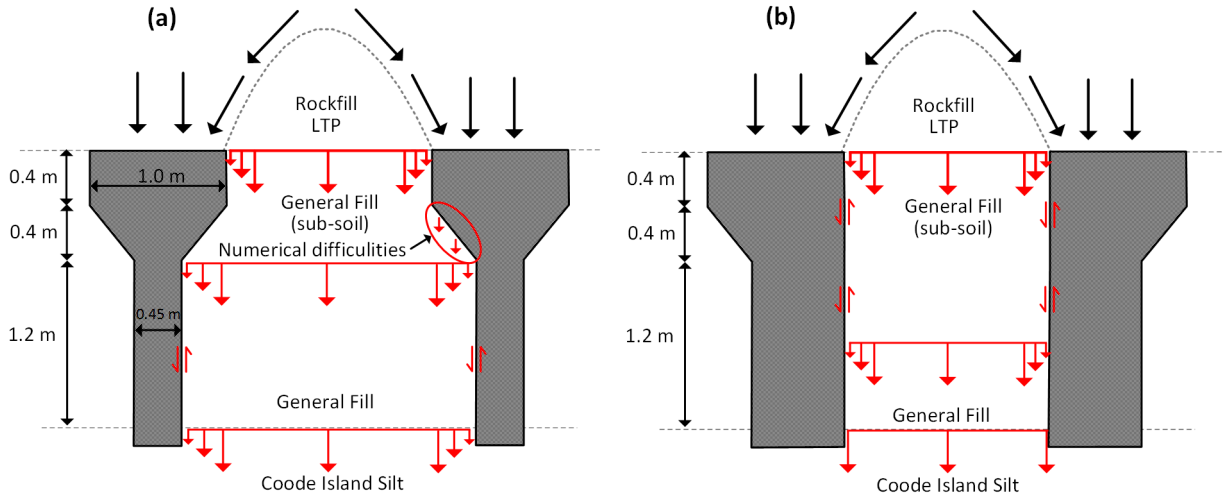

Figure 6.23. Settlement of sub-soil (General Fill) - **(a)** GRCSE and **(b)** approximated condition in FEM analysis

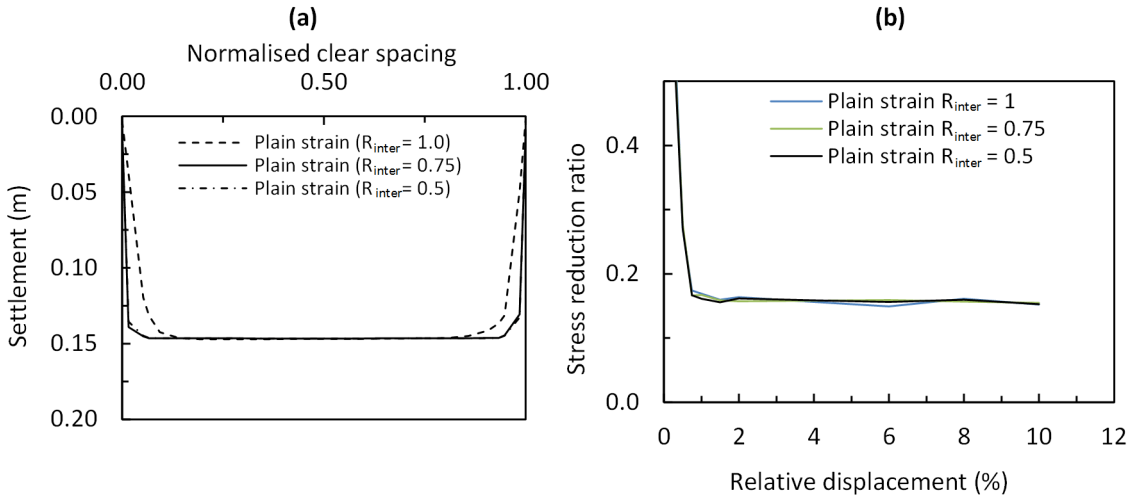

Figure 6.24. Profile at Rockfill/Sub-soil interface with varying R_{inter} values **(a)** settlement and **(b)** GRCs

assess the arching stress development, this result is significant. These results support the approach of modelling the small-scale behaviour adopted throughout this chapter and indicates that a prescribed displacement applied at the base of the LTP can be used to model localised LTP behaviour (as done in this Chapter) as an alternative to explicitly modelling the sub-soil and column head and reasonable results obtained. That is to say it is not necessary to model the entire GRCSE to achieve accurate simulation of the localised LPT behaviour and arching stress development. Ideally, the entire GRCSE would be modelled, however, this comes at the expense of mesh refinement in the LTP area, and as a result, detailed assessment of the localised LTP behaviour (i.e., the shear band development described at Section 6.2.2 above) is difficult.

6.4 Other FEM numerical investigations into arching in GRCSEs

Numerous authors have undertaken FEM studies of full scale GRCEs and drawn a variety of conclusions based on the arching stresses calculated in the numerical simulations. In many cases, the output of the numerical simulation is compared with the analytical methods found in various design standards which describe ultimate limit state conditions. These are often presented without reference to the limitations outlined in the preceding chapter which include:

- shear bands development (Roscoe 1970, Arthur et al. 1977, Vardoulakis 1980, Vardoulakis et al. 1981, Vermeer 1982, Bolton 1986, De Borst et al. 1993, Chu et al. 1996, Saada et al. 1999, Alshibli et al. 2000, Gajo et al. 2007)
- large relative displacement of the soft soil relative to the rigid pile heads (De Borst et al. 1984, Vermeer et al. 1984, Van Langen et al. 1991)
- the singularity point at the corner of the pile heads (De Borst et al. 1984, Vermeer et al. 1984, Van Langen et al. 1991)

For example, Bhasi et al. (2015) and Bhasi et al. (2015a) presents full-scale three-dimensional numerical simulations of GRCSEs and compares the numerical output with analytical methods such as the method of Zaeske, BS8006-2010 and Hewlett and Randolph method. In Bhasi et al. (2015a) where floating columns are simulated the relative displacement between the sub-soil and column is in the order of only 40 mm to 50 mm; the reinforced LTP is not in equilibrium and the arching stresses which develop are those occurring during initial arching and maximum arching. In Bhasi et al. (2015) settlement is in the order of 70 mm. In both studies, the effects of soft soil creep are not considered (the soft soil is modelled as a modified Cam Clay model) and there is no discussion as to whether or not the ultimate condition is achieved in the LTP. It would appear, that the authors have assumed that the conditions that develop in the model are commensurate with the ultimate condition. As outlined in the preceding chapter, the conditions that develop shortly after end-of-construction (or alternatively the conditions that develop where primary consolidation is complete in the Modified Cam Clay model) are generally not consistent with the ultimate state condition as the LTP is not in equilibrium.

The comparison between the numerical output presented within these studies, which describes initial arching and maximum arching in the short term, with the various design standards which describe ultimate limit state conditions (when a LTP is assumed to be in equilibrium) in the long term, is therefore meaningless and incorrect. Furthermore, the issues outlined above are not discussed and it is not clear if the authors have considered how these effects will influence the results of their numerical output. There is no information presented in Bhasi et al. (2015) and Bhasi et al. (2015a) that suggests that the limitations outlined in this chapter are not equally encountered in their studies.

A number of other studies have adopted a similar approach. Jenck et al. (2009) simulated the entire GRCSE as a unit cell using a Modified Cam Clay to model soft soil beneath the LTP. While the obvious benefits of including (reinforced) columns to support the embankment compared with the case of no piles are shown, the efficacy of the LTP in the unit cell is described and it is clear that a maximum arching condition is obtained similar to the field case study in the preceding chapter. Again, the LTP is not in equilibrium. The plots of surface settlement are therefore not indicative of the long term condition which may see surface settlement as the base of the LTP (due to creep), and as a result, potentially greater surface settlement. The creep behaviour of the soft soil which affects the LTP behaviour in the long term cannot be assessed with the Modified Cam Clay adopted in the study of Jenck et al. (2009). The second portion of the study considers global embankment behaviour with columns "wished into place" and using gross cross sectional member properties. Installation effects are not discussed and it is not clear if they have been considered. The limitations of this approach are investigated in Chapters 8 and 9.

Ariyarathne et al. (2012) investigates and compares various two-dimensional representations of the GRCSE unit cell as well as a three-dimensional global scale GRCSE using Mohr-Coulomb and Modified Cam Clay models within ABAQUS standard FE software. A detailed parameters study of the "load transfer" (i.e., arching development), pore water pressure development and settlement of columns and soft soil is presented. This study suffers from the same limitations as those described previously for Bhasi et al. (2015) and Bhasi et al. (2015a). The arching condition described is one of maximum arching with a LTP that is not in equilibrium. Whilst their numerical simulation may "calibrate" with the short term field case study data (in the same way the Chapter 5 field case data over a 2 year period could erroneously be said to "validate" the PLAXIS simulations in the preceding Section 6.3) this does not, and cannot simulate long term ultimate limit state behaviour due to the numerical limitations (outlined in this chapter) encountered when simulating the geotechnical mechanics outlined in the Chapter 5 based on analysis of the 2 year post-construction field data.

Nunez et al. (2013) models the test GRCSE constructed at the Chelles test site (Briançon et al. 2011) including all 96 columns across four test zones. The output is compared with the predictions of various analytical models. The limitations are the same as those outlined in the preceding paragraphs in that only a maximum arching condition is achieved and the LTP is not in equilibrium. Nunez et al. (2013) does refer to some of the observed differences in their numerical and experimental simulation; "*The differences in the stress efficacies between the experimental and numerical results in zone 2R might be caused by the assumptions of a continuum model… Some authors, including Chavalier (2008) and Jenck et al. (2009b), have studied load transfer on pile-reinforced soils using discrete [element] modelling. The latter authors highlighted the differences between the response of discrete and continuum models, particular near the pile head."* The finding of Nunez et al. (2013) is not new, as outlined at the beginning of the chapter the limitations in simulating the arching stress development in trapdoor test using continuum based numerical simulation, which apply equally to the numerically simulated arching stress development in a GRCSE, are well documented.

Similarly Zhuang et al. (2012) presented a three-dimensional numerical simulation of a GRCSE using the FE package ABAQUS (version 6.6). In that study, the development of arching stresses is plotted as a function of relative displacement and are limited to between 2% and 4%. Points of "*maximum arching"* are described. However, the reasons for limiting the arching stress development to these low relative displacement values is not explained; presumably this was because of mesh distortion and numerical convergence issues similar to those described above. These numerical results are at best useful in describing the initial and maximum arching development but do not describe a LTP in equilibrium. These findings are surprising, as Zhuang (2009) previously

studied arching stress development in GRCSEs extensively and refers to the concept of the GRC. Yet in Zhuang et al. (2012), the load recovery phase is not described, nor is there any discussion as to why the numerical simulation could not simulate the arching stress development described in the author's previous studies (such as Zhuang et al. 2012a). To address the limitations outlined above using a continuum based FEM approach, meshfree numerical methods are investigated in the following sections.

6.5 Alternative numerical techniques

The problems encountered highlight some of the limitations in FEM when applied to large deformation problems. Similar issues are encountered where pile penetration and post-failure analysis problems such as; slope instability, debris flows, soil behaviour due to liquefaction etc. are considered. Many of these problems stem from the main disadvantage of FEM – mesh distortion (Więckowski 2004). Remeshing can help to solve problems associated with severe mesh distortion however this procedure is complicated, time consuming and has limitations in three-dimensional modelling (Bui et al. 2011). Alternative approaches with the finite element method framework include the Coupled Eulerian-Lagrangian method which can be used in conjunction with adaptive mesh techniques to avoid mesh distortion issues (Henke 2010, Qiu et al. 2011). The Coupled Eulerian-Lagrangian method is used by Pucker et al. (2012) and Larisch et al. (2014) to simulate the installation of drilled displacement columns. Some findings from those studies are discussed in Chapter 8.

The Discrete Element Method (DEM) offers an alternative method to numerical methods formulated in the finite element framework, however, the modelling of individual particles is limited to several hundred thousand and therefore small-scale simulations (Bui et al. 2008, Liu et al. 2010). Chevalier et al. (2011) used DEM to simulate three-dimensional trapdoor results using 6 mm (±0.2 mm) glass beads, the results of both the experimental and numerical work are shown in Figure 6.25. The numerical results show the progressive arching stress development including; initial, maximum and load recovery phase of arching with only minor divergence occurring at a relative displacement > 10 %. Another approach to large strain problems is the large group of computational approaches knows as "group of particle" or "point-based" methods. These are commonly referred to as meshfree methods. A common feature of these methods is the mapping of the state variables to points (or numerical "particles") that are not connected to a mesh (Więckowski 2004). Więckowski (2004) categorises these methods into four groups based on the approximation technique used: 1) moving weighted least square approximation, 2) Kernel methods, 3) partition of unity methods and 4) the material point method. A comprehensive overview of meshfree methods is

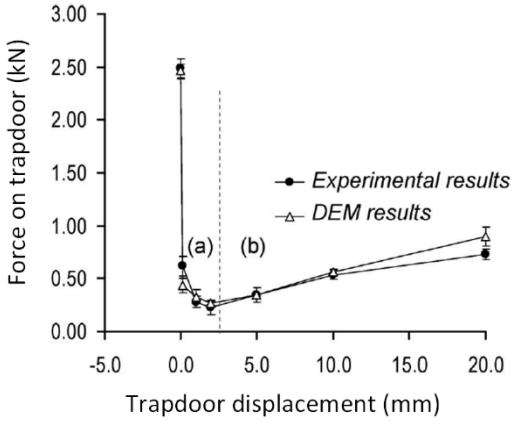

Figure 6.25. Experimental and DEM results reproduced from Chevalier et al. (2011)

given in the book by Liu (2009) as well as Belytschko et al. (1996), Więckowski (2004), Idelsohn et al. (2006) and Nguyen et al. (2008).

Smooth Particle Hydrodynamics (SPH) belongs to the group of meshfree methods known as Kernel methods and was one of the earliest meshfree methods developed (Liu et al. 2010). The method was originally developed to solve problems in astrophysics (Gingold et al. 1977, Lucy 1977) and later in fluid dynamics and then in solid mechanics (Libersky et al. 1991). Bui et al. (2008) was the first to implement SPH for describing the behaviour of geomaterials and has since refined the method considerably (Bui et al. 2011, Bui et al. 2013). Although other meshfree methods could have been implemented, the SPH method was the most readily available meshfree method available to the author. In the following section SPH is used to assess the development of arching based on the trapdoor test modelled using FEM in the preceding section.

6.6 Smooth Particle Hydrodynamics (SPH)

The SPH code employed herein was primarily developed by Dr. Ha Bui (co-supervisor) as part of his PhD research and has been further refined over the past decade. The SPH code has been employed primarily because it is expected to resolve the major difficulties associate with modelling the trapdoor problem; mesh distortion. Modelling of the large displacement trapdoor problem over the required relative displacement range (0 to 10 %) requires the issues associated with mesh distortion and shear band formation to be addressed. The SPH framework does not suffer from convergence issues due to mesh distortion and/or the formation of discontinuities, such as shear bands, within the problem geometry. The SPH code has been applied to a wide range of geotechnical problems including;

- Desiccation induced cracking in soils (Bui et al. 2015) where the thermo-hydro-mechanical processes associated with clay soil crack initiation and propagation induced by moisture and heat transfer have been simulated.
- Slope stability analysis and slope failure simulation (Bui et al. 2009, Bui et al. 2011) – studies have implemented SPH to study the failure surface in embankments and model post-failure debris flow. The ability to simulate these flows in one of many geotechnical problems where meshfree methods offer significant advantages over mesh-based methods such as the FEM.
- Retaining walls (Bui et al. 2014) – simulation of model scale two-dimensional segmental retaining wall collapse mechanisms.
- Soil-structure interaction modelling (Bui et al. 2008) – soil-structure interaction at very large deformation has been investigated.
- Coupled soil-water modelling (Bui et al. 2009) – SPH framework has been applied to saturated soil problems. The work in this area is ongoing.
- Granular flow modelling (Bui et al. 2008, Bui et al. 2009) – this has been a major area of investigation.
- Seepage failure and erosion modelling

Examples of these applications are presented at; https://sites.google.com/site/hhbuiinfo/sph-applications

While the SPH method outlined below has many advantages as a meshfree methods compared with FEM there are also many limitations. Unlike the PLAXIS software the SPH code employed herein is not a commercial software and does not have a graphic user interface, nor does it have the range of constitutive models available within the PLAXIS framework. This approach incurs a considerable time penalty compared with the graphical user interface found in the PLAXIS software where problems geometries can be quickly generated and assigned material

parameters. The advantages of the SPH method comes at the expense of useability and ease of implementation, which is common where a more advanced numerical framework is implemented. The two models which are presented in the following sections have been implemented and executed by Dr Bui based on input parameters from the author. The interpretation of the output files has then been completed by the author.

6.6.1 SPH method for soil mechanics

An overview of the theoretical aspects of the SPH method as it is employed herein is presented below. A more detailed derivation of the SPH method is presented in Appendix C, Section C2 and is based on the work of Bui et al. (2008). The derivation describes the basic SPH framework and includes the governing SPH and soil constitutive equations.

SPH Framework

In the SPH method the motion of a continuum is modelled as discrete numerical "particles". These "particles" are distinct from the particles which make up a soil mass. The "particles" in a SPH computation are assigned a mass and carry field variables such as; density, velocity, energy, temperature etc. The field variables form a continuous field taken by interpolation of the surrounding particles using a weighted summation (or kernel function) that is inversely proportional to the radius. There are two main steps within the SPH method which form the basis for the SPH framework; **(1) Kernel approximation** – the first step is to represent the field functions, and its derivatives, in continuous form as approximate integral representations using a smoothing function (or kernel function) and **(2) Particle approximation** – the problem domain (Ω) is represented as a set of discrete numerical particles which are used to approximate the field variables on the location of these particles i.e., discretisation. The particles represent the material properties and can also be used for integration, interpolation and differencing. In a SPH formulation, particles can be fixed within a Eulerian framework or move in a Lagrangian framework (Liu et al. 2010), the former is adopted in the present study.

Kernel approximation

This interpolation process is based on an integral representation of a field function f (**x**) as:

$$\langle f\ (\mathbf{x})\rangle = \int_{\Omega} f(\mathbf{x}')W(\mathbf{x} - \mathbf{x}', h)\, d\mathbf{x}' \qquad \textbf{(6.15)}$$

Where W is the smoothing function or kernel, Ω is the integration (problem) domain that contains $\boldsymbol{x}$, and h is the smoothing length which defines the influence domain of W. The adopted smoothing function must satisfy three conditions; unity condition, delta function property and compact support condition. The choice of kernel or smoothing function is very important in an SPH formulation as it directly affects the accuracy, efficiency and stability of the numerical approach (Bui et al. 2008, Liu et al. 2010). For the SPH adopted herein, the cubic B-spline function, proposed by Monaghan et al. (1985), is adopted (see Bui et al. 2008). This is formulated as follows:

$$W_{ij} = \alpha_d \begin{cases} \frac{2}{3} - q^2 + \frac{1}{2}q^3, & 0 \le q < 1 \\ \frac{1}{6}(2-q)^3, & 1 \le q < 2 \\ 0 & q \ge 2 \end{cases} \qquad \textbf{(6.16)}$$

Where α_d is the normalisation parameter, which is $15/(7\pi h^2)$ for two-dimensional space and q is the normalised distance between particles i and j which is defined as $q = r/h$. The parameter k (refer to Appendix C for details) is equal to 2 for the numerical analyses presented herein and defines the support domain as shown in Figure 6.26.

Particle approximation

The integral representation of a field function f (**x**) (Equation 6.13) is discretised for *N* number of particles as follows:

$$\langle f\ (\mathbf{x})\rangle \approx \sum_{j=1}^{N} \frac{m_j}{\rho_j} f(\mathbf{x}_j) W(\mathbf{x} - \mathbf{x_j}, h) \qquad \textbf{(6.17)}$$

Where j = 1, 2, …, N are particles within the support domain, as shown in Figure 6.26, m_j and ρ_j are mass and density respectively. The particle approximation of the field function f (**x**) and the partial derivative of the field function $\partial f(\mathbf{x})/\partial \mathbf{x}$ can be expressed in condensed form for a particle i, as follows:

$$f(\mathbf{x}_i) \approx \sum_{j=1}^{N} \frac{m_j}{\rho_j} f(\mathbf{x}_j)\, W_{ij} \qquad \textbf{(6.18)}$$

$$\langle \frac{\partial f(\mathbf{x})}{\partial \mathbf{x}} \rangle \approx -\sum_{j=1}^{N} \frac{m_j}{\rho_j} f(\mathbf{x}_j) \cdot \frac{W_{ij}}{\partial \mathbf{x_j}} \qquad \textbf{(6.19)}$$

$$W_{ij} = W(\mathbf{x_i} - \mathbf{x_j}, h) \quad \text{and} \qquad \textbf{(6.20)}$$

$$\frac{\partial W_{ij}}{\partial \mathbf{x_j}} = \left(\frac{\mathbf{x}_i - \mathbf{x}_j}{r}\right) \frac{\partial W_{ij}}{\partial r} \qquad \textbf{(6.21)}$$

Where r is the relative distance between particles i and j and is defined as $r = |x_i - x_j|$. The discretised versions of field function f (x) (Equation 6.18) and the partial derivative of the field function $\partial f(x)/\partial x$ (Equation 6.19) are used to discretised the soil constitutive equations as well as the equations of mass and momentum conservation.

SPH Governing Equations

The governing equations are the mass conservation equation:

$$\frac{\partial \rho}{\partial t} = -\rho \frac{\partial v^{\alpha}}{\partial x^{\alpha}} \qquad \textbf{(6.22)}$$

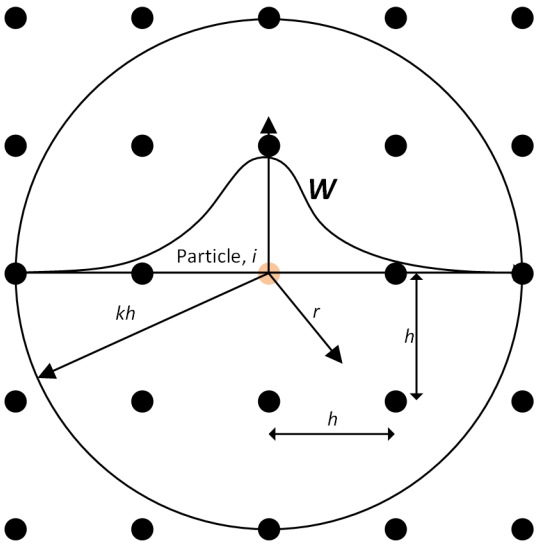

Figure 6.26. Example showing numerical "particles" in SPH simulation with smoothing function and support domain

where t is time, ρ is density and v is velocity. The equation is presented using Einstein summation convention (where α denotes Cartesian components x, y and z). The momentum conservation equation is as follows:

$$\frac{Dv^{\alpha}}{Dt} = \frac{1}{\rho}\frac{\partial \sigma^{\alpha\beta}}{\partial x^{\alpha}} + g^{\alpha} \tag{6.23}$$

where β denotes Cartesian components x, y and z and g is gravity. The governing equations are then discretised using Equations 6.18 and 6.19 and the following discretised form of the mass and momentum governing equations is obtained:

$$\frac{\mathrm{D}\rho_i}{\mathrm{D}t} = -\sum_{j=1}^{N} m_j \left(v_i^{\alpha} - v_j^{\alpha}\right) \cdot \frac{W_{ij}}{\partial x_i^{\alpha}} \tag{6.24}$$

$$\frac{\mathrm{D}v_i^{\alpha}}{\mathrm{D}t} = -\sum_{j=1}^{N} m_j \left(\frac{\sigma_i^{\alpha\beta}}{\rho_i^2} + \frac{\sigma_j^{\alpha\beta}}{\rho_j^2}\right)\frac{W_{ij}}{\partial x^{\beta}} + g^{\alpha} \tag{6.25}$$

SPH soil constitutive model

The SPH method developed herein adopts an elastic-perfectly plastic model with a Drucker-Prager yield criterion to describe the yield surface. The derivation follows a similar course for other elastic-perfectly plastic models such as the Mohr-Coulomb model described in detail in Brinkgreve et al. (2011), Wood (2003) and summarised at Section 6.1.1 above. The expression for the stress-strain relationship for an elastic-perfectly plastic material is as follows:

$$\dot{\sigma}^{\alpha\beta} = 2G\dot{e}^{\alpha\beta} + K\dot{\varepsilon}^{\gamma\gamma}\delta^{\alpha\beta} - \dot{\lambda}\left[\left(K - \frac{2G}{3}\right)\frac{\partial g}{\partial \sigma^{mn}}\delta^{mn}\delta^{\alpha\beta} + 2G\frac{\partial g}{\partial \sigma^{\alpha\beta}}\right] \tag{6.26}$$

Where α and β are free indices and m and n are dummy indices, $\dot{\lambda}$ is the rate of change of the plastic multiplier (λ), g is the plastic potential function, $\dot{\sigma}^{\gamma\gamma}$ is the sum of the three normal stress components (i.e., $\dot{\sigma}^{\gamma\gamma} = \dot{\sigma}^{xx} + \dot{\sigma}^{yy} + \dot{\sigma}^{zz}$), v is poisson's ratio and K is the bulk modulus which is related to the shear modulus (G) as follows:

$$K = \frac{E}{3(1-2v)} \quad \text{and} \quad G = \frac{E}{2(1+v)} \tag{6.27}$$

The deviatoric shear strain rate tensor ($\dot{e}^{\alpha\beta}$) is defined as follows:

$$\dot{e}^{\alpha\beta} = \dot{\varepsilon}^{\alpha\beta} - \frac{1}{3}\dot{e}^{\gamma\gamma}\delta^{\alpha\beta} \tag{6.28}$$

With regards to the plastic potential function (g), both an associated and non-associated flow rule can be incorporated into the SPH code with the later used in the models presented herein. This has the form:

$$g = \sqrt{\mathrm{J}_2} + 3I_1 \sin\psi \tag{6.29}$$

Where ψ is the dilatancy angle. The yield function f adopted is the Drucker-Prager yield criterion (Drucker et al. 1952) which is written as follows:

$$f(I_1, J_2) = 0 = \sqrt{\mathrm{J}_2} + \alpha_{\phi} I_1 - k_c \tag{6.30}$$

Where k_c and α_ϕ are the Drucker-Prager constants (Figure 6.27*a*), I_1 is the first stress invariant of the Cauchy stress tensor and J_2 is the second deviatoric stress invariant. These are defined as follows (Yu 2007):

$$I_1 = \sigma_{xx} + \sigma_{yy} + \sigma_{zz} \quad \text{and} \qquad J_2 = \frac{1}{2} s^{\alpha\beta} s^{\alpha\beta} \tag{6.31}$$

The constants k_c and α_ϕ can be related to the Mohr-Coulomb material constants c and ϕ in various ways. Two examples are shown in Figure 6.27*b*, in one example the Drucker-Prager yield criterion circumscribes the Mohr-Coulomb yield surface in the second it middle circumscribes the Mohr-Coulomb yield surface. An alternative approach is to match the yield surface so that they give identical collapse loads in plane-strain conditions (Drucker et al. 1952), as is adopted herein:

$$\alpha_\phi = \frac{\tan\phi}{\sqrt{9 + 12\tan^2\phi}} \quad \text{and} \qquad k_c = \frac{3c}{\sqrt{9 + 12\tan^2\phi}} \tag{6.32}$$

The final discretised form of the stress-strain relationship with a non-associated plastic flow rule is as follows (details are presented in Appendix C, Section C2):

$$\frac{\mathrm{D}\sigma_i^{\alpha\beta}}{\mathrm{D}t} = \sigma_i^{\alpha\gamma}\dot{\omega}_i^{\beta\gamma} - \sigma_i^{\gamma\beta}\dot{\omega}_i^{\alpha\gamma} + 2G\dot{e}_i^{\alpha\beta} + K\dot{\varepsilon}_i^{\gamma\gamma}\delta_i^{\alpha\beta} - \dot{\lambda}_\iota\left[9K\sin\psi\,\delta^{\alpha\beta} + \frac{G}{\sqrt{J_2}}s_i^{\alpha\beta}\right] \tag{6.33}$$

With the rate of change of the plastic multiplier ($\dot{\lambda}$) for a non-associated plastic flow rule is expressed as follows:

$$\dot{\lambda} = \frac{3\alpha_\phi K\dot{\varepsilon}^{\gamma\gamma} + \left(\frac{G}{\sqrt{J_2}}\right)s_i^{\alpha\beta}\dot{\varepsilon}_i^{\alpha\beta}}{27\alpha_\phi K\sin\psi + G} \tag{6.34}$$

For large displacement problems it is necessary to employ a stress rate that is invariant with respect to rigid body motion for the constitutive equations. Bui et al. (2008) adopts the Jaumann stress rate ($\dot{\hat{\sigma}}^{\alpha\beta}$):

$$\dot{\hat{\sigma}}^{\alpha\beta} = \dot{\sigma}^{\alpha\beta} - \sigma^{\alpha\gamma}\dot{\omega}^{\beta\gamma} - \sigma^{\gamma\beta}\dot{\omega}^{\alpha\gamma} \tag{6.35}$$

Where $\dot{\omega}$ is the spin rate tensor defined as:

$$\dot{\omega}^{\alpha\beta} = \frac{1}{2}\left(\frac{\partial v^\alpha}{\partial x^\beta} - \frac{\partial v^\beta}{\partial x^\alpha}\right) \tag{6.36}$$

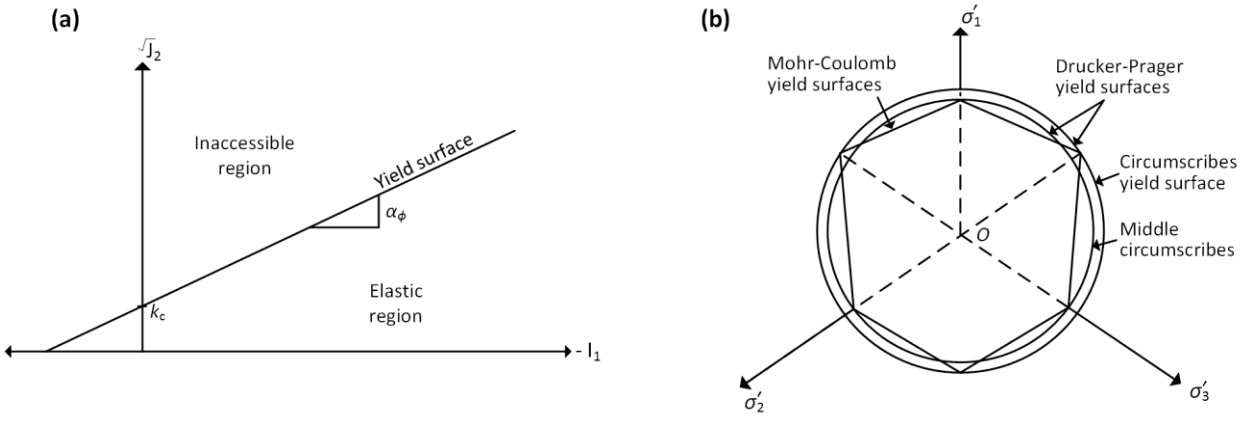

Figure 6.27. Drucker-Prager yield criterion; **(a)** – I_1, $\sqrt{J_2}$ space and **(b)** π-plane ($\sigma_1 + \sigma_2 + \sigma_3 = 0$) (after Bui, et al 2008)

It is also necessary to discretise the strain rate tensor ($\dot{\epsilon}^{\alpha\beta}$) and the spin rate tensor, these are written as follows:

$$\dot{\epsilon}^{\alpha\beta} = \frac{1}{2}\left(\frac{\partial v^{\alpha}}{\partial x^{\beta}} + \frac{\partial v^{\beta}}{\partial x^{\alpha}}\right) = \frac{1}{2}\left[\sum_{j=1}^{N} \frac{m_j}{\rho_j}\left(v_j^{\alpha} - v_i^{\alpha}\right) \cdot \frac{\partial W_{ij}}{\partial x_i^{\beta}} + \sum_{j=1}^{N} \frac{m_j}{\rho_j}\left(v_j^{\beta} - v_i^{\beta}\right) \cdot \frac{\partial W_{ij}}{\partial x_i^{\alpha}}\right] \quad \textbf{(6.37)}$$

$$\dot{\omega}^{\alpha\beta} = \frac{1}{2}\left(\frac{\partial v^{\alpha}}{\partial x^{\beta}} - \frac{\partial v^{\beta}}{\partial x^{\alpha}}\right) = \frac{1}{2}\left[\sum_{j=1}^{N} \frac{m_j}{\rho_j}\left(v_j^{\alpha} - v_i^{\alpha}\right) \cdot \frac{\partial W_{ij}}{\partial x_i^{\beta}} + \sum_{j=1}^{N} \frac{m_j}{\rho_j}\left(v_j^{\beta} - v_i^{\beta}\right) \cdot \frac{\partial W_{ij}}{\partial x_i^{\alpha}}\right] \quad \textbf{(6.38)}$$

Other aspects of SPH numerical implementation

In Appendix C, Section C2, provides a brief overview of several aspects of the numerical implementation that are specific to the SPH method, these include; artificial viscosity, tensile instability and time integration. These are described in detail in Bui et al. (2008). The SPH model described herein is written in Fortran 90 and is implemented through a command line prompt and run through a Fortran compiler.

6.7 SPH trapdoor model

The SPH model is implemented by generating an array of numerical "particles" uniformly placed on a square lattice with particles at the vertices. Unlike the FEM simulation where the mesh can be refined, no refinement of initial particle placement is performed for SPH. In the simulations presented below dx = 50 mm (h = 1.2dx; therefore, the initial smoothing length h is equal to 60 mm) and a value Δt is equal to 1.073 × 10^{-4} seconds. There are 13,200 numerical particles modelled with 1819 boundary particles (representing solid boundaries). Value of friction angles of 39° and 42° are modelled and various values of Young's modulus are modelled. The results of Tests 1 to 4 are shown in Figure 6.28. These tests each show similar behaviour at maximum arching with a value of stress reduction ratio equal to, or slightly greater than, 0.2. The simulations show similarities with the results of the FEM analysis presented in Figure 6.16. The effects of a varying the dilation angle are shown in Figure 6.29 where the increasing dilation angle can be seen to influence the maximum arching by slightly reducing SRR_{min}. The results of these three simulations are similar to those obtained for other two tests shown in Figure 6.28. i.e., the load recovery behaviour is not observed and the model shows a bi-linear response which is similar to the output obtained from the FEM simulations presented in Section 6.3.

In addition to the stress reduction ratio plots versus relative displacement in Figure 6.28, the deviatoric plastic strain and total strain is shown in Figure 6.30*a* and *b* respectively. These two figures show the strain fields at a relative displacement of approximately 20 % where surface deformation can be seen.

6.8 Comparison with FEM approach

The SPH method overcomes a number of issues encountered in the FEM simulation, these include; shear bands development, severe mesh distortion at the corner point of the trapdoor (i.e., the singularity points) and associated with the large displacement of the trapdoor relative to stationary soil mass. A number of simulations have been run and a parametric study of the material parameters has been undertaken, several of these results are presented in Figure 6.28 and Figure 6.29. However, it is apparent that like the FEM simulations, the maximum arching behaviour is not accurately simulated, and more importantly, the load recovery phase is not simulated. Simulating the load recovery phase was the primary reason for investigating the SPH method for the trapdoor test and GRCSE in the first instance. The differences in the physical modelling of Iglesia et al. (2013) and the SPH simulations can be

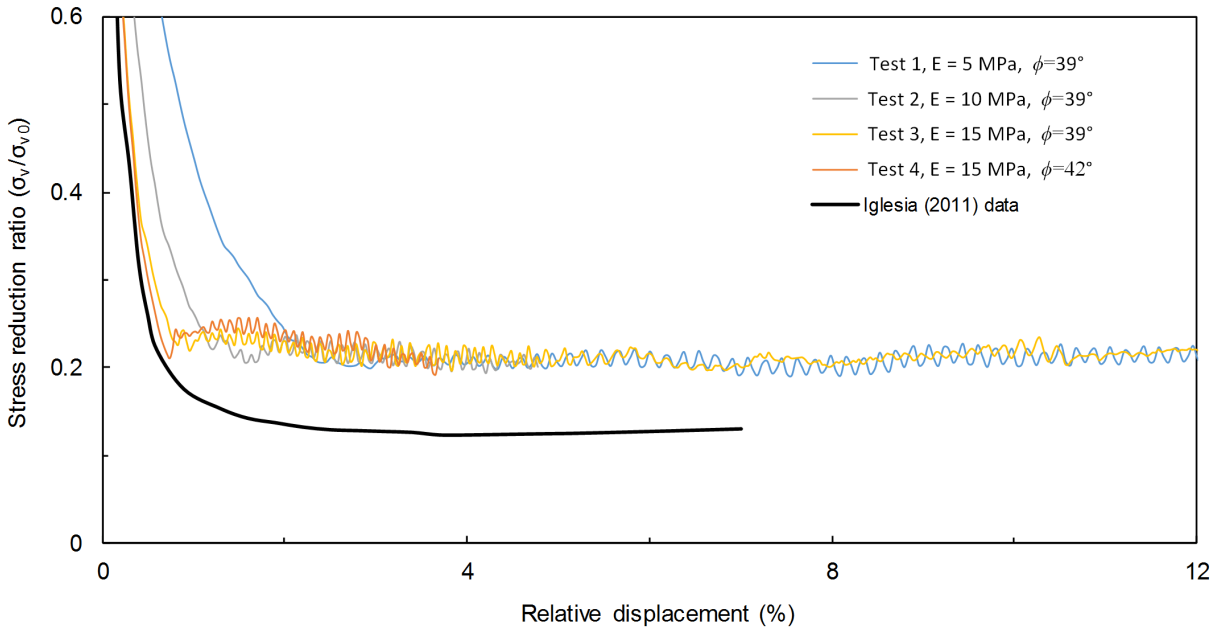

Figure 6.28. SPH model results - normalised trapdoor loading versus relative displacement

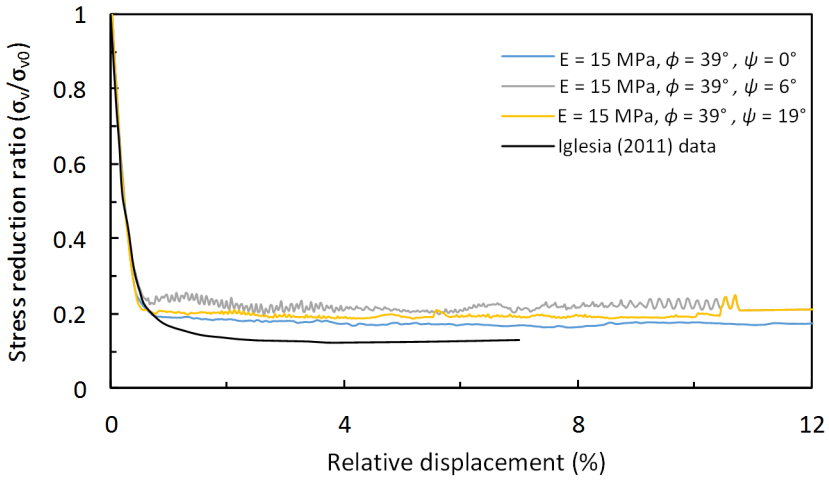

Figure 6.29. SPH model results (dilation angle) – normalised trapdoor loading versus relative displacement

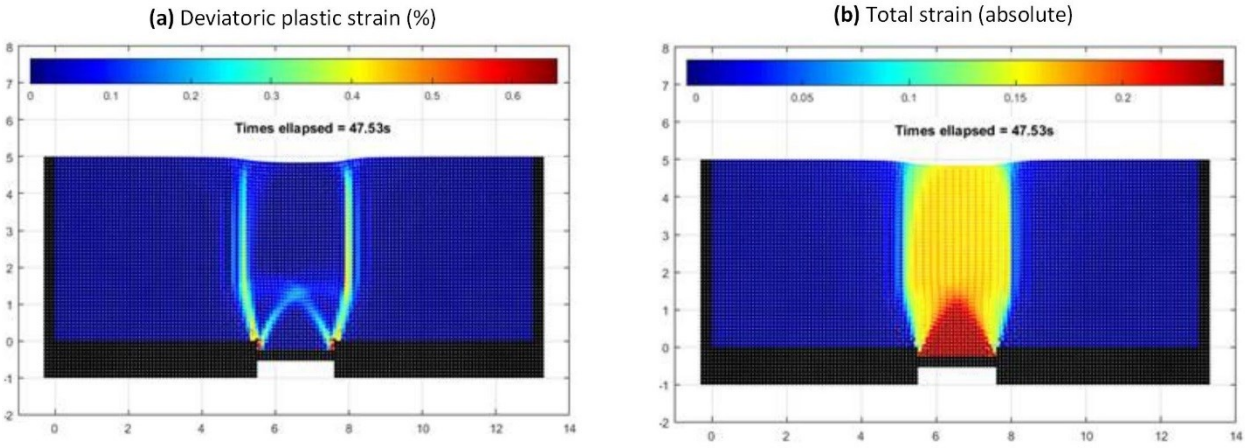

Figure 6.30. SPH model results **(a)** deviatoric plastic strain and **(b)** total strain

attributed broadly to two factors:

1) Limitations (errors) within the SPH numerical framework. These may be related to, for example; tensile instability, the use of the artificial viscosity or other factors associated with the numerical implementation of the SPH method (see Appendix C, Section C2), or;
2) Limitations in the constitutive model adopted within the SPH framework.

Based on the significant number of applications (described at the start of Section 6.6) where the SPH has been shown to provide good agreement with physical modelling, it is the author's opinion that the limitations associated with the constitutive model are the primary reason for the inability to simulate the ground reaction curve. However, a significant amount of further work is required to demonstrate this conclusively and it is beyond the scope of the author's study to undertake such work. At the time of writing, work is on-going to address the limitations associated with the constitutive model and it is proposed to present this work in King et al. (2018). Some of limitations which will be addressed as part of this on-going work are described below.

The elastic perfectly plastic constitutive model with a Drucker Prager yield criterion does not simulate the response of the granular material at large strain. Some fundamental aspects of granular material behaviour are described in Appendix D as part of the literature review of the rockfill behaviour. These aspects of granular material behaviour are also applicable to the sand used in the centrifuge trapdoor tests described by Iglesia et al. (2013) and simulated in this chapter. As noted by Lee et al. (1967) the measured shear strength of a granular material comprises four components: sliding friction (ϕ_μ) ± dilation (ψ) + particle rearranging + particle crushing. The angle of interparticle sliding friction (ϕ_μ) is a function of the roughness, texture and hardness and ranges from 20° to 40°, more commonly it is between 25° to 35° (Terzaghi et al. 1996). The measured friction angle of the New Jersey 4/14 sand used in the study by Iglesia et al. (2013) has a friction angle ϕ of 39° at a normal stress of 49 kPa and 98 kPa. The critical friction angle (ϕ'_{crit})is the sum of the purely frictional sliding friction component, ϕ_μ and the frictional component due to particle rearranging and particle crushing which is typically in the range of 5° to 6° (Terzaghi et al. 1996). The mobilised friction angle (ϕ'_m) can therefore be described as follows:

$$\phi'_m = \phi'_{\text{crit}} + \psi \qquad \textbf{(6.39)}$$

For the New Jersey 4/14 sand the dilatancy angle is estimated to be in the range of 4° to 8°. The shear and volumetric response of a sand of this type while exhibiting the shear and volumetric characteristics shown in Figure 6.31 (after Rowe, 1962). In Figure 6.31 the peak shear strength, which occurs simultaneously with the peak mobilised dilatancy angle, is shown as is the strain softening behaviour and at large strain a critical state where $\Delta V = 0$. An elastic-perfectly plastic idealisation is shown in orange. Unlike the elastic-perfectly plastic model with a Drucker-Prager yield criterion, the Hardening Soil model in PLAXIS incorporates a shear hardening rule, i.e., a relationship between the rate of plastic volumetric strain and the rate of plastic shear strain. This is a function of dilatancy angle in the Hardening soil within the PLAXIS and has been outlined in Section 6.1.2 and based on the stress-dilatancy theory by Rowe (1962). There is no such equivalent formulation within the constitutive model employed here within the SPH framework. However, more importantly, the strain softening behaviour is not described in the SPH constitutive model.

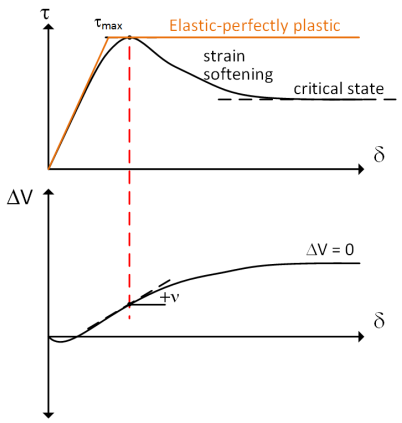

Figure 6.31. Shear and volume change in direct shear test of dense granular material (after Rowe, 1962)

6.9 Summary of findings

The deformation range of interest for GRCSE is up to 10 % relative displacement. This was described in the literature review and has been discussed based on the data from the field case study in Chapter 5. In this chapter, FEM was used to model the GRC over this displacement range and number of computational difficulties were encountered. It was shown that it is difficult to achieve reliable results beyond the development of maximum arching due to the effects described below (these have been investigated numerically and through physical modelling in numerous studies):

- shear bands development (Roscoe 1970, Arthur et al. 1977, Vardoulakis 1980, Vardoulakis et al. 1981, Vermeer 1982, Bolton 1986, De Borst et al. 1993, Chu et al. 1996, Saada et al. 1999, Alshibli et al. 2000, Gajo et al. 2007)
- large relative displacement of the soft soil relative to the rigid pile heads (De Borst et al. 1984, Vermeer et al. 1984, Van Langen et al. 1991)
- severe mesh distortion at the corner of the pile heads, i.e., at the singularity point (De Borst et al. 1984, Vermeer et al. 1984, Van Langen et al. 1991)

Despite varying the material parameters (within reasonable limits) the maximum arching observed in the tests performed by Iglesia et al. (2013) was not accurately simulated. The development of shear banding, which is highlighted in Figure 6.10 shows quite clearly that the formulation of discontinuities within the soil mass is likely the primary reason for the difficulties in simulating maximum arching stress conditions as the shear band formation precedes the maximum arching stress development. The presence of these shear bands then poses significant on-going convergence issues where the tests is continued to greater values of relative displacement. Whilst this may seem like an obvious finding, it is evident from numerous publications that the limitations of FEM applied to arching stress development in a trapdoor tests, or a GRCSE which suffers from the same limitations, are not fully appreciated, and if these limitations are understood, there is no discussion as to the effects this introduces into the numerical analysis.

Numerous authors have undertaken FEM studies of full scale GRCSEs and drawn a variety of conclusions based on the arching stresses calculated in the numerical simulations. In many cases, the load transfer mechanisms assessed in the numerical simulation are compared with the analytical methods describing ultimate limit state conditions despite the clear limitations in simulating ultimate behaviour using the FEM. These are often presented without reference to the limitations outlined above. Some examples of this have been discussed at Section 6.4 and

include the studies of Bhasi et al. (2015), Bhasi et al. (2015), Jenck et al. (2009), Ariyarathne et al. (2012), Nunez et al. (2013), (Briançon et al. 2011) and Zhuang et al. (2012) amongst others.

To address these difficulties, meshfree methods are required. In the present study the SPH method has been introduced, although there are a number of other meshfree methods which could equally be used. The SPH method has been employed primarily to resolve the major difficulties associate with modelling the trapdoor problem; mesh distortion. Modelling of the large displacement trapdoor problem over the required relative displacement range (0 to 10 %) requires the issues associated with mesh distortion and shear band formation to be addressed. The SPH framework does not suffer from convergence issues due to mesh distortion and/or the formation of discontinuities, such as shear bands, within the problem geometry. However, while the issues associated with mesh distortion and shear band development were overcome a number of significant limitations were found with the constitutive model adopted within the SPH framework; the elastic-perfectly plastic model with a Drucker-Prager yield criterion. While this constitutive model may provide reasonable results for small strain problems, for large displacement problems, such as the trapdoor problem and the LTP behaviour in a GRCSE, where the failure mechanisms are strongly influenced by localised dilative behaviour. As a result, this constitutive model is inadequate as it cannot describe the strain softening behaviour or the stress-dilatancy behaviour of the type described by Rowe (1962). The limitations of the constitutive model are not insurmountable and can be addressed, however, it is beyond the scope of the author's study to undertake such work. At the time of writing, work is on-going to address the limitations of the constitutive model

Rockfill

The author is of the opinion that the use of rockfill is an economical approach to optimising the arching development in a LTP (this was the basis for its use in the field case study). The author advocates the use of rockfill in the LTP construction. A discussion on rockfill behaviour has been included at Section 6.3.1 to 6.3.4 and in Appendix D. The main benefit being that the soil arching is increased, however, this must be considered relative to the detrimental effects, such as increased installation damage to the geosynthetic layer. Further, a more pronounced maximum arching will also typical lead to a more pronounced load recovery phase (this is dependent on D_{50}, see Equation 2.6).

7 Serviceability behaviour in GRCSEs

This chapter comprises the material presented in King et al. (2017b) and further investigates localised LTP behaviour. In the preceding chapters the relationship between sub-soil settlement and the development of arching stresses was shown based on the field case study data and investigated further through numerical analysis. In this chapter, the arching stress-deformation relationship is extended to investigate serviceability behaviour and it is shown that a coupled arching stress-deformation relationship, which has been well described in trapdoors tests (Terzaghi 1943, Ladanyi et al. 1969, Vardoulakis et al. 1981, Evans 1983, Stone 1988, Iglesia 1991, Ono et al. 1993, Dewoolkar et al. 2007) and the present field case study, is necessary to describe accurately the serviceability behaviour of GRCSEs. This is at odds with limit equilibrium models which calculate arching stress as a constant with respect to deformation and time. It is shown that the arching stress-deformation relationship is particularly important for GRCSE geometries whose embankment height is below the critical height described by McGuire (2011). The serviceability behaviour is investigated by way of an analytical example and the findings are used to examine a number of previously published field case studies.

7.1 Background

Despite the acceptance of limit-equilibrium models for LTP design in GRCSEs, there is a significant quantity of experimental data describing the development of arching as a deformation dependent process. The pertinent aspects of arching behaviour have been discussed in the Chapter 2. While the deformation dependent development of arching stresses is at odds with these limit equilibrium models, the limit equilibrium models may be suitable for LTP design, provided that the value of arching stress is representative, and on the safe side, of the ultimate stress acting on the geogrid layers through its design life. This arching stress-deformation compatibility issue is highlighted in Figure 7.1 where the transition from initial conditions, to the so-called “ultimate” long term condition in an LTP is shown. A bi-linear arching stress – deformation relationship (as used in the load-displacement compatibility (LDC) method, see Section 2.2.3 and 2.6.2) , is also shown for comparison.

Herein, the author uses the term “serviceability condition” to describe the LTP behaviour between the initial and “working condition”. The long term working condition describes the equilibrium condition where the base settlement of the LTP is no longer influenced by the consolidation and/or creep settlement of the sub-soil (i.e., negligible creep settlement/permanent sub-soil support) or the loss of sub-soil support. The ultimate condition, as defined here, is the end of design life condition, which includes consideration of the creep strain in the reinforcement. The constant value of arching stress predicted by limit equilibrium models is only achieved when the required deformation is reached and this may or may not coincide with the long term working condition.

For road and rail applications, often, it is stringent surface settlement tolerances that necessitate the use of a GRCSE design approach in the first instance. To describe the deformation of a GRCSE, and confirm the suitability of an adopted design, knowledge of the time-dependent development of arching stress development is required. The limit equilibrium models in EBGEO (German Geotechnical Society, 2010), BS8006-1 (BSI, 2010) or (CUR226

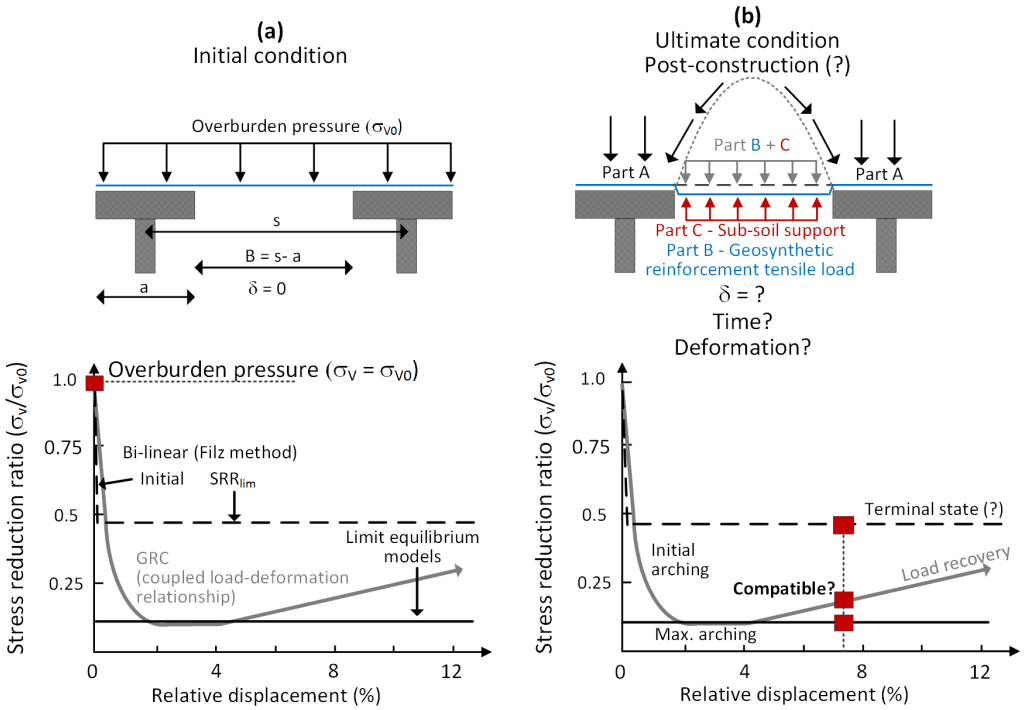

Figure 7.1. (a) Initial condition with no sub-soil settlement and **(b)** long term ultimate limit state design condition in GRCSE

2016) do not explicitly state, or provide a means to assess, how much deformation is required to achieve this state of "arching" which they simulate? Or what period of time is required? Or what happens to arching stresses if the base settlement differs from the amount of settlement inherently assumed in these models. While post-construction base settlement of the LTP, and/or geogrid deflection, in the LTP is not in itself a serviceability concern, this post-construction behaviour can translate to surface settlements and failure under serviceability tolerances; particularly in shallow embankments.

EBGEO (German Geotechnical Society, 2010) provides the following advice in relation to the amount of base settlement required to achieve the design reinforcement strain ("ultimate") condition: "*The reinforcement is strained during [construction] of the [GRCSE] in layers and in particular during installation and compaction of the initial soil layers."* and "*Generally, the serviceability analysis is governed only by the additional deformations in the [GRCSE] occurring after its [construction], due to the actions described in Section 9.4 [of EBGEO (2010)]".* EBGEO (2010) goes further to also note "… [for] *certain applications (e.g. transport structures sensitive to deformation or [other example]) it may be necessary to further limit additional strains [creep strains] in terms of the [geosynthetic reinforcement] sag Δf.*" However, no further advice is given as to how to achieve this.

There is a considerable amount of instrumentation data from field case studies showing reinforcement strain developing post-construction. Analysis of field case studies (Haring et al. 2008, Wachman et al. 2009, Van Duijnen et al. 2010, Van Eekelen et al. 2010, Briançon et al. 2011, Van Eekelen et al. 2012, King et al. 2017a) indicates that this is the norm rather than the exception. This is observed in instrumented GRCSEs as a time-dependent increase in geogrid strains, sub-soil settlement and the development of arching stresses; which is coupled to the on-going deformation of either the sub-soil, geosynthetic reinforcement, or both. Furthermore, creep strain in the geosynthetic reinforcement layers is not the cause of additional base settlement, in most cases the additional (post-construction) deformation is due to the time-dependent sub-soil consolidation. The difficulties in assessing serviceability limit state behaviour in GRCSEs using limit equilibrium models has been noted by a number of authors (Gwede et al. 2008, Haring et al. 2008, Livesey et al. 2008, Wong et al. 2012, Gniel et al. 2015).

In contrast to the aforementioned design standards, a number of researchers have developed design methods that placed a greater emphasis on directly quantifying the embankment surface settlement. The LDC method (Filz et al. 2012) is a good example of this approach. This method is formulated to ensure compatibility between the sub-soil settlement, geosynthetic deformation and arching (Filz et al. 2006). The total surface settlement is the sum of column shortening (S_s), compression of the founding material (S_u) and the settlement due to base settlement (S_e). The component S_e is approximated as equal to half the maximum sag of the reinforcement ($S_{b,max}$) while accounting for the area replacement ratio (A_s) (as suggested by Russell et al. 2003) . To avoid differential settlement, Filz et al. (2012) recommend a minimum embankment height greater than the critical height (H_{crit}) as defined by McGuire (2011)(see Figure 2.27). The critical heights define the height about the reinforcement plane where differential settlement is zero and is discussed further later in this Chapter. Despite the merits of this design method, which is formulated with base settlement as a governing parameter, this approach to GRCSE design has not found widespread use beyond North America; the two-step design approach is still favoured in the majority of design methods. The intention of this Chapter is to highlight the limitations of the "2-step" design approach when applied to serviceability behaviour, and in addition, outline and highlight the benefits of a serviceability design approach that adopts a coupled arching stress-deformation relationship.

7.2 Arching

The arching stress-deformation relationship was described in Chapter 2 and the pertinent aspects of arching behaviour summarised in Section 2.1.2. Based on the arching stress-deformation relationship, it follows then that limit equilibrium arching models, which assume a fixed geometric shape to simulate "soil arching", describe what is a "snapshot" of some point on the arching stress-deformation curve. In many cases, this "snapshot" describes the maximum arching condition. These models simulate the observed arching stress behaviour only when the observed base settlement (either sub-soil settlement and/or deflection of the reinforcement) is compatible with the base settlement inherently assumed in the model. However, the soft soil that provides sub-soil support will typically undergo time-dependent consolidation and long term viscoplastic (creep) behaviour and the polymers used in geogrids are themselves viscoplastic materials, which show strain, stress and temperature dependent creep behaviour. The incompatibility between observed, and inherently assumed, base settlement makes the use of limit-equilibrium models to describe arching stress development challenging.

Another important aspect of the arching behaviour that relates to GRCSE is the height of the initial internal shear bands (OA). For a trapdoor test comprising good quality granular material that mobilises a very high dilatancy angle ($\psi = 30°$), the initial shear band (OA) will have a height of $0.87(s - a)$. This is akin to the crown of a "soil arch" at maximum arching. Where $\psi = 15°$, the height increases to $1.86(s - a)$. This interpretation applies for a trapdoor test comprising a single granular material. By contrast, a GRCSE will typically have an LTP of compacted granular material of about 600 mm thick underlying embankment fill. If the clear spacing ($B = s - a$) exceeds 0.7 m (for the case $\psi = 30°$), the initial shear banding will extend through the upper surface of a 600 mm thick LTP and into the fill material. However, in many GRCSEs, a dilation angle is considerably less than 30° and the clear spacing is greater than 0.7 m; in these cases, the initial failure surface will extend into the embankment fill material, which often comprises poorer quality material. This has implications for many arching models used for GRCSE design that assume an arching shape that simulates this initial failure surface with a fixed geometric shape.

Only a small number of researchers have recognised the arching stress-deformation behaviour in the context of GRCSE. Ellis et al. (2009b) observed the phases of arching described by the GRC in centrifuge models of GRCSEs

and suggested that an "interaction diagram" incorporating the GRC could be used in LTP design. Zhuang (2009) investigated the use of the GRC method for GRCSEs using FEM analysis and applied this approach to the analysis of several case studies (Zhuang et al. 2012). Chen et al. (2008), Chen et al. (2016), Girout et al. (2016) and Fagundes et al. (2017) observed and described various phases of an arching stress-deformation relationship in laboratory scale models but did not report the GRC.

In contrast to the limit equilibrium models, which describe the arching stress-deformation relationship as a constant, the LDC method describes this relationship as bi-linear. The maximum and load recovery phases of the arching stress-deformation relationship are, however, not described by the bi-linear relationship (Figure 7.1). Compared with the constant and bi-linear relationships, the GRC method describes the four phases of soil arching and was shown in Chapter 5 to provide a reasonable predication of arching stress development in the field case study. The concept of an arching stress-deformation relationship is further developed here, and used along with the differential settlement ratio and plane of equal settlement concepts (McGuire 2011), to investigate the serviceability behaviour of GRCSEs.

7.3 The plane of equal settlement

The progressive breakdown of the arching mechanism in the load recovery phase was illustrated by Jacobsz (2016) who used Particle Image Velocity techniques to better capture shear bands progressively propagating through the granular materials. This was observed visually as a triangular like volume of material propagating towards the surface with increasing trapdoor deformation. Others have investigated this behaviour analytically (Costa et al. 2009) and it is this behaviour which leads to the progressive development of surface deformation in a GRCSE. McGuire (2011) investigated the development of surface deformation in GRCSEs due to settlement at the base of the LTP based on laboratory and numerical analysis. The surface settlement at the mid-span between columns (S_i), the diagonal span between columns (S_d), above column (S_c) and $S_{b,max}$ was assessed and used to calculate a differential settlement ratio (termed Differential Surface to Base Settlement Ratio, DSBR by McGuire, 2011) (Figure 7.2).

McGuire (2011) proposed the relationship in Equation 7.1 to describe H_{crit} (termed herein the McGuire line), plotted as normalised embankment height (H/d) versus normalised clear spacing (s'/d). The clear spacing term (s') is the maximum distance from the edge of column to the boundary of a unit cell (Figure 7.2*b*) and d is the diameter of a column head. For square column heads of width a these are converted to an equivalent (equal area) diameter (i.e., $d = 1.13a$).

The expression for H_{crit} is based on the experimental observations of McGuire (2011) and seven other studies that observed H_{crit}, including: Demerdash (1996) (data point 31), (Ellis et al. 2009a, 2009b) (data point 32) and Sloan (2011) (data point 41) amongst others. Data points describing the reported (and not reported) differential settlement from 25 case studies (Numbers 1 to 25) and 16 experimental students (Numbers 26 to 44) were compiled by McGuire (2011) and are reproduced in Figure 7.3. This data compiled by McGuire (2011) provides a means to quantitatively identify GRCSE geometries which may be subjected to differential surface settlement from those which are unlikely to be subjected to differential settlement. While McGuire (2011) proposed a static line to represent this boundary, experimental observations of arching development (see Jacobsz, 2016 and Evans, 1983 amongst others) show that shear banding will progressively propagate towards the surface if sub-soil is not restrained; i.e., this plane is a function of sub-soil settlement. The line of critical height described by Equation 7.1 is

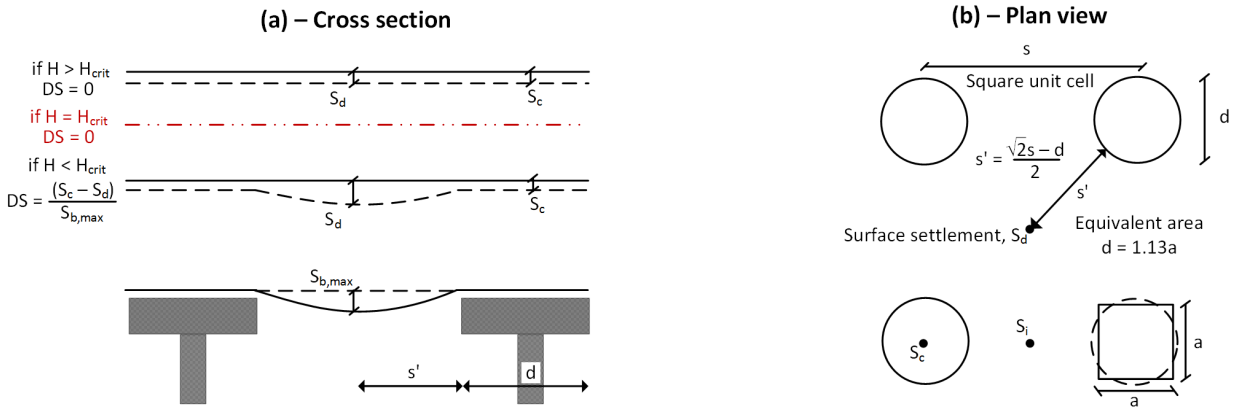

Figure 7.2. (a) Cross section of GRCSE geometric properties and **(b)** Plan view (after McGuire 2011)

interpreted by the author as an upper limit for GRCSEs that undergo "typical" deformation beneath the LTP (in the order of 150 mm of base settlement).

$$\frac{H_{crit}}{d} = 1.15\left(\frac{s'}{d}\right) + 1.44 \qquad \textbf{(7.1)}$$

The considerable number of case studies and experimental data that show agreement lends merit to Equation 7.1. On this basis, the GRCSE geometries that may be subjected to surface differential settlement and require further examination of serviceability deformation can be identified; the majority of these are shallow height embankments. The field case study described in Chapter 5, the TH241 embankment (Wachman et al. 2009) and a French test embankment (Briançon et al. 2011) all plot above the critical height line i.e., the surface deformation serviceability limit state condition is not likely to be critical for these embankments.

It is evident that a number of case studies plot beneath the McGuire line. In addition, three failure case studies

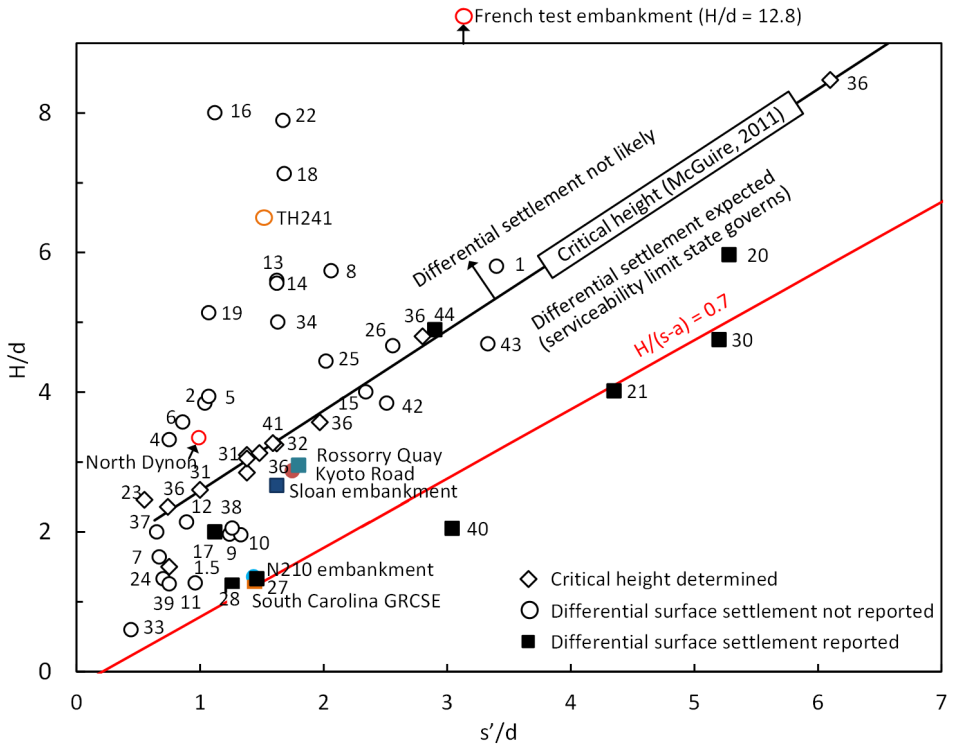

Figure 7.3. GRCSE geometry and field case studies (data modified from McGuire (2011)

are shown: 1) Rossorry Quay development, Enniskillen, Northern Ireland (Coghlin 2005), 2) Large-scale experiments by Sloan et al. (2013), 3) South Carolina roadway embankment (Camp III et al. 2006). Furthermore, two case studies plot below this critical height line and to date have not reported differential settlement: 1) N210 embankment (Haring et al. 2008) and 2) Kyoto Road (Van Eekelen et al. 2007).

McGuire (2011) proposed Equation 7.2 to describe the differential settlement ratio and a number of these contours are plotted in Figure 7.4. The minimum embankment height of $0.7(s - a)$ for the partial arching condition (BS8006-1; BSI, 2010), minimum H for static load conditions $0.8(s - a)$ (EBGEO; Germany Geotechnical Society, 2010), and minimum H in CUR226 (CUR, 2015) of $0.66(\sqrt{2}s - a)$ all plot below the McGuire line (the a term is converted to an equivalent d value in Figure 7.4). The differential settlement ratio is the ratio between surface settlement and base settlement (see Figure 7.2*a*). If the base settlement beneath the LTP is known, then these contours can be utilised to assess the surface settlement and the serviceability behaviour of a GRCSE. It is important to recognise that while differential settlement approaches zero at the McGuire line in a typical GRCSE, uniform total settlement will occur above this line. This can be assessed as the sum of components S_s, S_u and S_e (see Figure 2.27).

$$\text{Diff. sett.} = \min\left\{\left(0.115\frac{s'}{d} - \frac{H}{10d} + 0.144\right)\tan\left(\min\left\{\begin{matrix}1 - SBR_c \\ 83^\circ \\ 135\left(\frac{s'}{d}\right)^{-0.7}\end{matrix}\right\} \times \frac{\pi}{180}\right)\right\} \qquad \textbf{(7.2)}$$

Where SBR_c is the ratio of surface settlement above a column to base settlement ($S_c/S_{b,max}$) calculated as follows:

$$SBR_c = \left(1 - \frac{1}{16}\left(5 - \frac{H}{d}\right)^2\right)\left(1 - 4\left(1 + \frac{H}{d}\right)^{-2}\right) \qquad \textbf{(7.3)}$$

7.4 GRCSE behaviour below the McGuire line

There are a number of GRCSEs situated below the McGuire line that have reported differential settlement, a number that have failed and numerous case studies that have not reported differential settlement. A number of the case

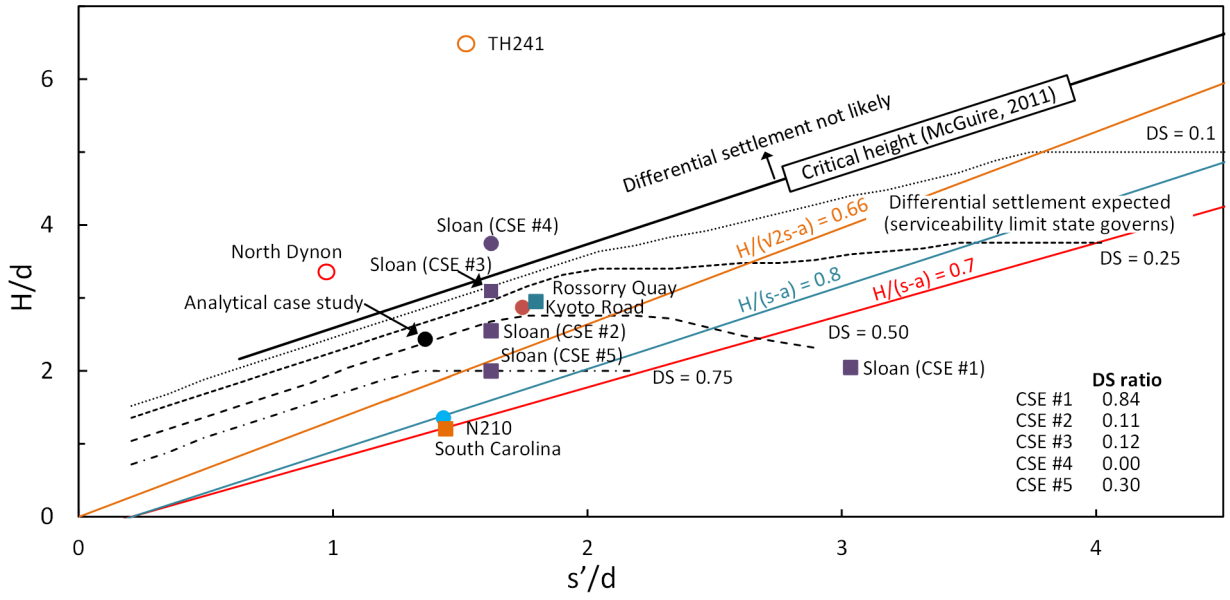

Figure 7.4. Differential settlement ratios for serviceability assessment in GRCSEs

studies which have not reported differential settlements share geometric similitude with failure case studies, the reasons for differences in post-construction differential surface settlement can be attributed to 1) minimal base settlement or 2) base settlement occurring entirely during the construction phase. It is also possible that some of these case studies have experienced long term differential settlement but have not reported it.

Assessing the base settlement requires an understanding of the magnitude, and more importantly, the time rate of settlement in order to assess the magnitude of construction phase, and post-construction phase settlement. In the short term, immediately after a GRCSE comes into service, it is the sub-soil settlement that controls the base settlement, and with increasing base settlement, the geosynthetic reinforcement (geogrid) layers are mobilised. The development of tensile load in geogrid layers can be reasonably well predicted as a function of base settlement, however, the sub-soil is more difficult to predict and is the subject of the analysis in the following section.

7.5 Sub-soil behaviour

To explore the complex time-dependent interaction between arching stresses and base of LTP settlement, the coupled load-deformation response of the sub-soil is investigated using an analytical example. The GRC method (Iglesia et al. 1999, 2013) is used to describe the deformation dependent arching stress and this is applied to an idealised GRCSE and stratigraphy (Figure 7.5). The time-dependent sub-soil settlement response is investigated for a range of soil parameters, including: over consolidation ratio (OCR), compression index (C_c) and the coefficient of vertical consolidation (c_v). The fill can be thought to represent either a working platform constructed over a soft soil, a fill layer or a stiff desiccated crust layer typically encountered near surface at soft soil sites. The compressibility of this layer relative to the underlying soft soil is assumed to be negligible and settlement induced by this layer is not considered. The embankment comprises a 0.6 m thick LTP and 1.6 m of embankment fill. Columns are 450 mm diameter at 2.5 m centre-to-centre spacing with 0.8 m square column heads. From Figure 7.4 the differential settlement ratio is assessed to be 0.5. Soil parameters relevant to the analysis are presented in Figure 7.5. The response of the sub-soil is described by the GRC and is solved using Terzaghi's one-dimensional consolidation (Equation 7.4), where u is porewater pressure, z is the vertical distance, t is time and c_v the vertical coefficient

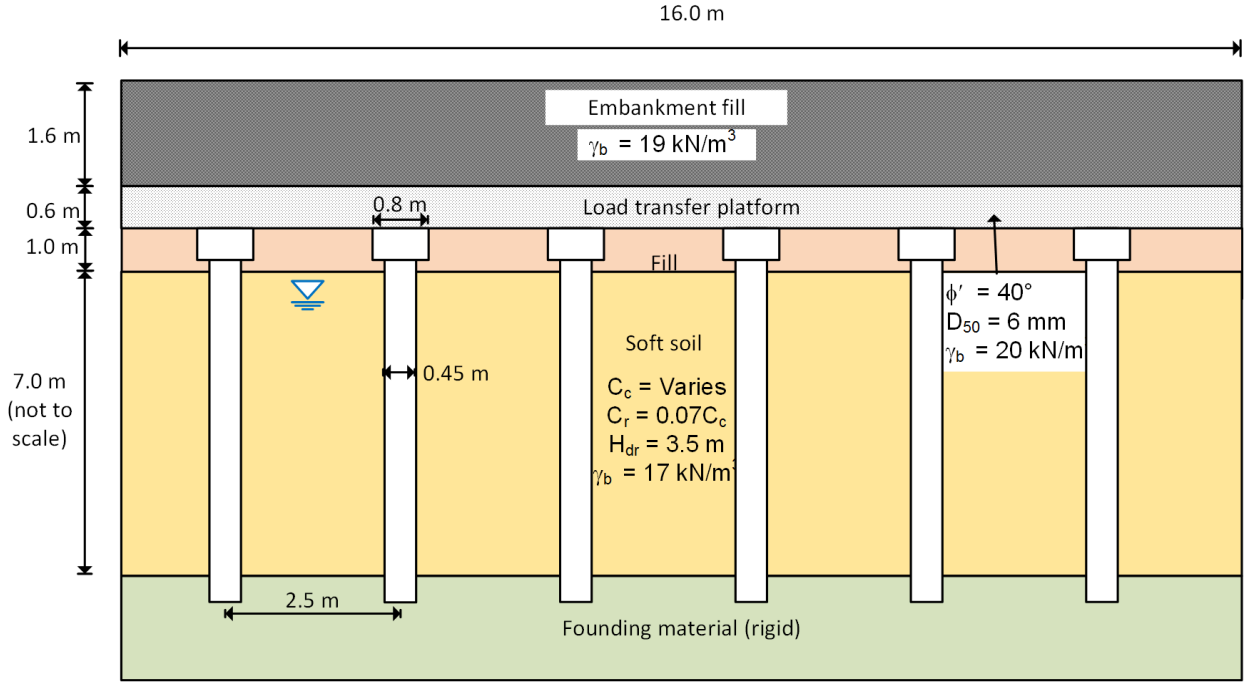

Figure 7.5. Idealised stratigraphy and GRCSE for analytical study

of consolidation. The interaction with the columns is not considered in this analysis and as a result the magnitude of primary consolidation settlement predicted is an upper-bound (secondary compression is not considered).

$$\frac{\partial u}{\partial t} = c_{\mathrm{v}} \frac{\partial^2 u}{\partial z^2} \tag{7.4}$$

The primary consolidation (S_{c}) is calculated in the usual manner as a function of the C_{c}, C_{r}, σ_{p}, e_0 and effective stresses. Elastic settlement varies under the applied stress and is negligible under maximum arching; for this reason it is not included. The distribution of the stress in the area between columns and acting at the base of the LTP is assumed to be a 1:1 load spread through the fill unit (the area ratio is 0.89). The percentage of surface settlement due to primary consolidation (U%) is calculated using a time-dependent series function (Equation 7.5)(Terzaghi et al. 1996). The solution is a function of the one-dimensional time factor for vertical consolidation T_{v} (Equation 7.6), where H_{dr} is the maximum vertical drainage distance.

$$U\% = 100\ (\%) \times \left\{1 - \sum_{n=0}^{\infty} \frac{8}{(2n+1)^2 \pi^2} \mathrm{e}^{-\left[\frac{(2n+1)^2 \pi^2}{4} T_{\mathrm{v}}\right]}\right\} \tag{7.5}$$

$$T_{\mathrm{v}} = c_{\mathrm{v}} \frac{t}{H_{\mathrm{dr}}^2} \tag{7.6}$$

7.5.1 The ground reaction curve

The theoretical GRC for the GRCSE shown in Figure 7.6 is developed using the procedure described by Iglesia et al. (1999, 2013). To apply the GRC concept to the field case study the embankment geometry is converted to an equivalent two-dimensional axisymmetric unit cell with parameters H = 2.2 m and b = 1.92 m. The initial vertical stress (σ'_{v0}) is 42 kPa. Iglesia et al. (2013) noted that the intersection of the flat bottom portion of the GRC (zone of minimum loading) and the line describing the load recovery index typically occurs between a relative displacement range of 3 % and 5 %. Thus in this analysis, it is assumed to occur at a relative displacement of 4 %.

The solution to Equation 7.5 due to a deformation dependent applied stress, calculated from the theoretical GRC, is solved iteratively using a macro enabled spreadsheet application. After each time-step the settlement is calculated and the stress acting is updated based on the GRC. The time-step is variable, with a small time-step used during the initial arching phase as the change in arching stresses with respect to time is greatest during this period. The output of the analysis is settlement versus time and sub-soil stress versus time graphs over a 10-year period considered.

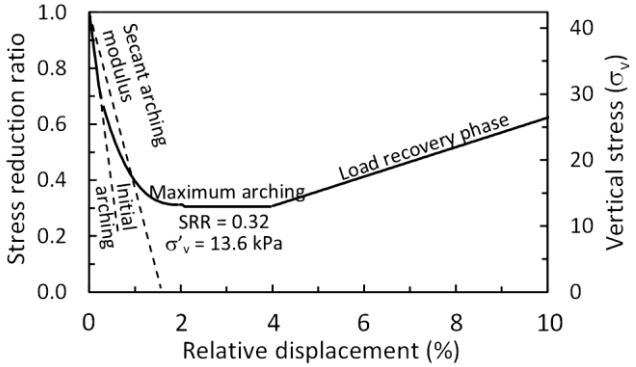

Figure 7.6. Theoretical Ground Reaction Curve (GRC)

7.5.2 Soil parameters

Settlement vs time plots for 48 combinations of soft soil parameters are presented in Figure 7.7. The OCR values increases from left to right with values of 1.0, 1.3, 1.6 and 1.9 assessed. Values of vertical coefficient of consolidation equal to 0.5 m^2/year, 1.0 m^2/year, 1.5 m^2/year and 2.0 m^2/year are described in Figure 7.7*a*, *b*, *c* and *d* respectively. With the exception of Figure 7.7*a*, where primary consolidation is 70 % complete, primary consolidation is largely complete in the remaining cases at the end of the 10 year period considered. Various values of C_c are plotted with the applied stress conditions indicated by line type. The loss of sub-soil support condition is assumed to occur at 100 mm settlement for comparative purposes. For the three soil parameters assessed (c_v, C_c and OCR), c_v has the least impact on the settlement response (compare vertical plots).

The influence of soil compressibility (i.e., C_c) is as expected, with more compressible sub-soil achieving the loss of sub-soil condition much quicker. However, the most pronounced effect is observed with variation in OCR. At values of OCR > 1.6 the primary consolidation is complete in the recompression range, settlement is significantly reduced, and there is insufficient settlement for the load recovery phase of arching to develop. For these scenarios, the long term sub-soil support will depend on the amount of creep compression over the remaining design life.

7.5.3 Pre-consolidation stress

The effect of varying OCR is assessed further in Figure 7.8*a* and *b* where values of C_c equal to 0.75 and 1.0 respectively and c_v equal to 1.5 m^2/year are modelled. In Figure 7.8*c*, the settlement response due to the arching stresses predicted using the Concentric Arches method (σ_v = 13.6 kPa, SRR = 0.32; calculated in accordance with procedure outlined in (Van Eekelen et al. 2013)) and a bi-linear stress (σ_v = 30.4 kPa, SRR_{lim} = 0.72 calculated in accordance with procedure outlined in Filz et al. 2012) are shown. The plots show the time-dependent stress acting in the area between columns and the resulting settlement. The differences in settlement (and stress) response between the three values of OCR is pronounced.

This settlement response is due to the applied stress with depth, and its relationship with the pre-consolidation stress with depth, as shown in Figure 7.9*a*. The applied stress with depth profile (red line) is the effective stress profile at maximum arching. The thickness of soil in the normally consolidated range at maximum arching reduces considerably as the OCR ratio increases. At OCR = 1.5, the thickness of soil in the normally consolidated range is confined to the upper 0.5 m. A similar response (not shown) is also observed when values of pre-overburden stress (POP), defined as $\sigma'_p = \sigma'_v$ + POP value, between 10 kPa and 15 kPa are used (Figure 7.9*b*). The analysis presented highlights that the sub-soil response is dominated by the applied stress conditions in the upper portion of the soft soil. It was for this reason that the 1 m thick fill layer was included in the analysis. It follows then, that the overall thickness of the soft soil has only minimal effect on the sub-soil response. While that has not been shown here, it can be demonstrated using the analysis outlined above.

7.5.4 Differential settlement

If it is assumed that the embankment comes into service at t = 3 months, for the soft soil properties OCR=1.3, C_c = 0.75 and c_v = 1.0 m^2/year, the base settlement at end-of-construction would be 37 mm (Figure 7.7*b*). The loss of sub-soil support is specified here as 100 mm (i.e., the geogrid is designed with sufficient stiffness to fully support the stress acting between columns at 100 mm deflection), this leads to 32 mm of differential settlement post-construction based on the differential settlement ratio of 0.5 (Figure 7.4). The question of how long this will take is difficult to answer, the analysis indicates 3.82 years when the mobilisation of the geogrid tensile load is ignored.

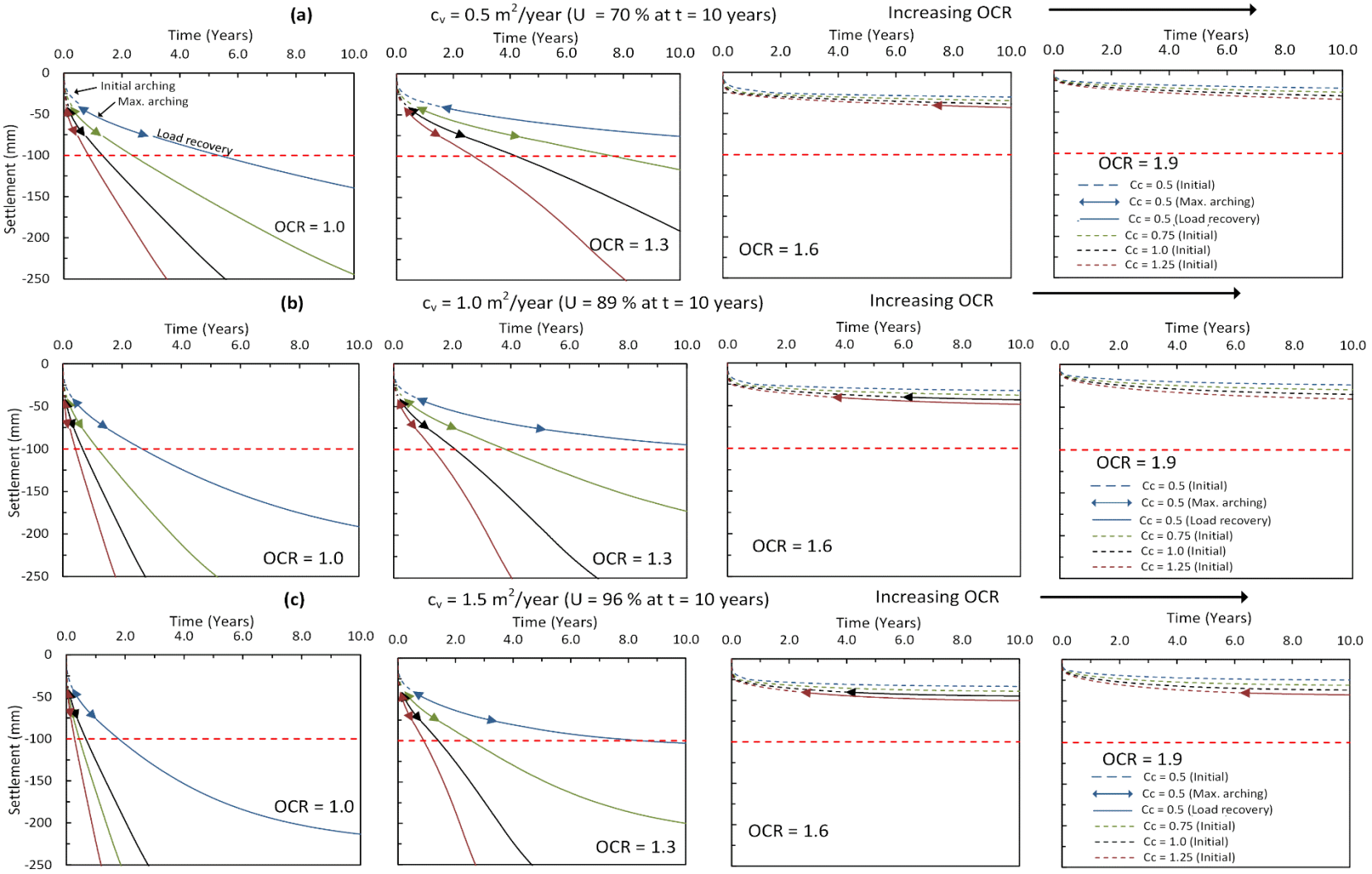
(a)
c_v = 0.5 m²/year (U = 70 % at t = 10 years)
Increasing OCR
Time (Years)
Settlement (mm)
Initial arching
Max. arching
Load recovery
OCR = 1.0
OCR = 1.3
OCR = 1.6
OCR = 1.9
Cc = 0.5 (Initial)
Cc = 0.5 (Max. arching)
Cc = 0.5 (Load recovery)
Cc = 0.75 (Initial)
Cc = 1.0 (Initial)
Cc = 1.25 (Initial)
(b)
c_v = 1.0 m²/year (U = 89 % at t = 10 years)
(c)
c_v = 1.5 m²/year (U = 96 % at t = 10 years)

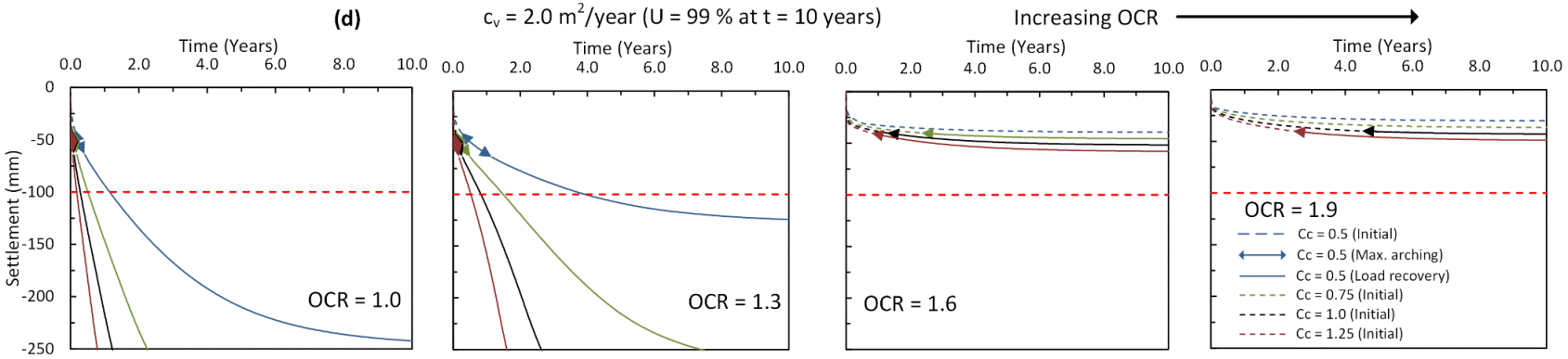

Figure 7.7. OCR Settlement *vs* time plots – using GRC and soil parameters; **(a)** c_v = 0.5 m²/year **(b)** c_v = 1.0 m²/year **(c)** c_v = 1.5 m²/year (d) c_v = 1.5 m²/year

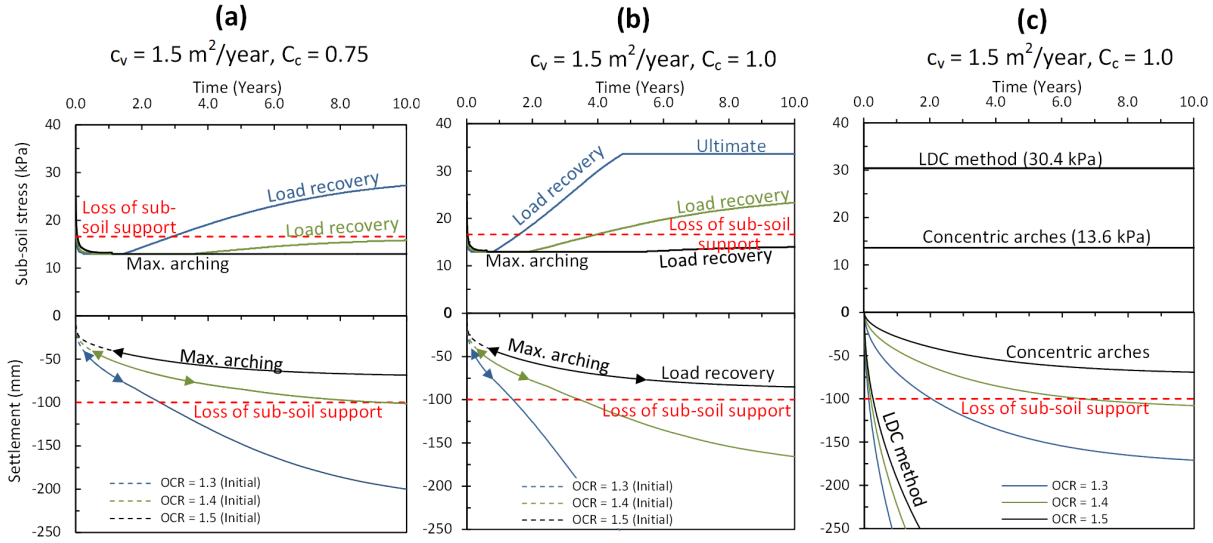

Figure 7.8. Settlement/stress *vs* time **(a)** using GRC and soil parameters; c_v = 1.5 m²/year, C_c = 0.75, **(b)** using GRC and soil parameters c_v = 1.5 m²/year, C_c = 1.0 and **(c)** using Load-Displacement compatibility method (bi-linear) method and Concentric Arches model and soil parameters c_v = 1.5 m²/year, C_c = 1.0

The mobilisation of tensile load will progressively reduce the applied load on the sub-soil thereby slowing the rate of sub-soil settlement; the analysis presented in Figure 7.7 and Figure 7.8 is therefore a lower-bound of the time required to achieve the loss of sub-soil support.

Furthermore, the assumption of a one-dimensional consolidation ignores the interaction between the installed columns, ground improvement effects and the three-dimensional consolidation effects. It is likely that the 100 mm sub-soil settlement would still be achieved but would occur as result of creep compression; this may take in the order of 5 to 10 years for this example. If for example, a serviceability tolerance of 20 mm was specified, then stiffer reinforcement could be adopted to limit maximum deflection to 77 mm.

This time-dependent interaction between the stresses acting between columns, sub-soil and geosynthetic reinforcement highlights an important aspect of LTP behaviour when considering the response of the LTP due to arching stresses alone. Even for the near normally-consolidated soils (left side in Figure 7.7), it is difficult to fully mobilise the long term working condition in the construction phase as the vertical stress, which induces sub-soil settlement, is progressively transferred to the reinforcement, thereby slowing the mobilisation of the working condition. The condition is worse for embankments with a "stiffer" sub-soil (right side of Figure 7.7). Where the working condition is not mobilised under primary consolidation, the working condition can, and in most cases is, developed due to long term creep compression.

7.5.5 Others factors affecting the sub-soil settlement

The difficulties in achieving the working condition under the action of arching stresses alone have been highlighted in the preceding section. Another factor which can induce the working condition it the additional load acting on the soft soil due to an unsupported working platform; as has been highlighted in field case studies in Brazil (Almeida et al. 2008). In these cases, the additional unsupported stress, caused by the 0.6 m to 1.0 m thick working platform was sufficient to induce about 400 mm of sub-soil settlement and enabled the working condition to be mobilised during the construction phase. The effect of this unsupported fill can be used to the advantage of the designer and enable

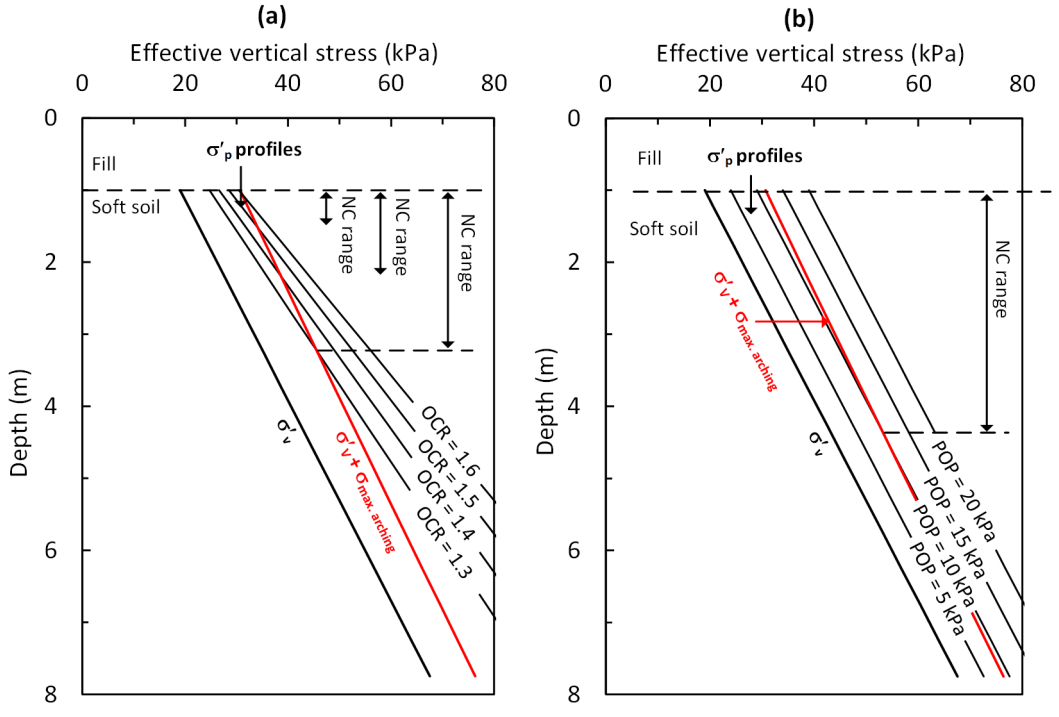

Figure 7.9. Applied stress at maximum arching with depth **(a)** various OCR profile and **(b)** various POP profiles

the working condition to be quickly mobilised; the settlement analysis presented can be modified to account for this behaviour. Alternatively, this can also be a disadvantage depending on designers understanding of the complex soil-structure-geosynthetic interaction occurring in the LTP.

7.5.6 Progressive collapse in GRCSEs

When the base settlement of a GRCSE is unrestrained the stress acting in the area between columns progressively increases in the load recovery phase. This has been measured in numerous experimental studies (see Chapter 2), was observed visually by the progressive development of shear banding/failure surfaces (Ladanyi et al. 1969, Evans 1983, Jacobsz 2016) and can be predicted using the GRC method. Long term deformation can occur due to consolidation and creep settlement of the sub-soil. The response of the arching mechanism to earthquake loading, cyclic dynamic loading (vehicular traffic) and other sources of dynamic loading (i.e., nearby construction works) is, however, not well understood. The response of earthquake loading may cause the partial, or complete, collapse of the arching mechanism and re-establishment of overburden stress conditions. The partial collapse of soil arching was shown in model scale tests under cyclic dynamic load by Heitz et al. (2008) and was observed in the field case study when columns were installed (at > 8 m) adjacent to the partially constructed GRCSE (see Chapter 5). Both studies highlight the sensitivity of the arching mechanism to external disturbance.

The re-establishment of overburden conditions will lead to further deformation and the re-establishment of some arching condition. However, the shear banding/failure surface, previously developed in the LTP, means that maximum arching will not re-establish, rather a weaker state of arching will develop (load recovery phase). This behaviour generates a positive feedback loop (i.e., increasing base settlement will lead to increasing stress leading to further base settlement, etc.) and will lead to progressive failure if enough sources of external disturbance are provided over the design life of a GRCSE. For the typical 100 year design life, at least one or more sources of external disturbance can, or should, be expected and engineering mechanisms employed to mitigate this risk. Some authors have suggested the removal of geosynthetic reinforcement under certain circumstances (i.e., for a thick fill layer beneath the LTP as suggested by Wong and Muttuvel, 2012), the reinforcement provides an engineering mechanism to guard against unrestrained base settlement under the progressive collapse mechanism outlined. Given the limited understanding at this time of the response of soil arching in GRCSE to dynamic loading, the removal of geosynthetic reinforcement is not recommended by the author.

The progressive collapse mechanism described above arises when the phases of arching stress development are considered, by contrast, the constant arching stress condition predicted by limit equilibrium models (and the bi-linear model), trend towards, a long term state of “equilibrium” under arching stresses; regardless of sub-soil deformation (Figure 7.8*c*) or soft-soil parameters (compare Figure 7.7 and Figure 7.8*c*). This is a short-coming of these arching models and can lead to erroneous conclusions regarding the long term performance of LTP (and GRCSE) behaviour.

7.6 Field case studies

The geometry, reinforcement details, sub-soil support conditions and other details of the field case studies considered are summarised in Table 7.1. Further details can be found in the references listed in Table 7.1. The emphasis is on describing the arching stress development and the relationship with the sub-soil settlement and/or geosynthetic reinforcement deflection. The first case studies described are failure case studies, where the relationship between base settlement and differential surface settlement is clearer. For the case studies that have not

Table 7.1. Geometric and material properties from field case studies

Fully instrumented field embankments						
Author – location (end of construction	**Embankment height (m)**	**LTP**			**Embankment support**	**Comments**
		Material type, size	**Reinforcement**	**Sub-soil support**		
Sloan et al. (2013) – Virginia Tech. test facility (CSE #2) and Sloan (2011)	1.25 m	40 mm minus gravel (ϕ_{peak} = 48 - 56°) for LTP and embankment	Biaxial geogrid (27/30 kN/m UTS*)	Geofoam for sub-soil. Injected a chemical compound to dissolve/ remove the sub-soil support (Part C = 0); this was noted to have occurred over a period of several hours.	600 mm diameter concrete columns (no heads) at 1.8 m square spacing	Load-deformation arching behaviour was not observed as working condition was rapidly developed (approx. 15mins).
Rossorry Quay(Coghlin 2005, Zhuang et al. 2012), Enniskillen, Northern Ireland	2.5 to 3.0 m	1.5 m thick granular LTP. From bottom - 200 mm, geogrid, 300 mm, geogrid, 300 mm, geogrid, 700 mm	Uniaxial geogrid (280 kN/m UTS) and (×2) (420 kN/m UTS)	Unsupported piling hardstand 0.5 m (up to 1.5 m) overlying very soft (lacustrine) clay and peat up to 10 m thick	Precast driven piles with 0.75 m heads at 2.75 m square spacing	Very large sub-soil settlement, loss of sub-soil support (Part C = 0)
South Carolina roadway	1.1 m	600 mm thick gravel (ϕ>32°)	Biaxial geogrid (3/6.7 kN/m UTS)	Sandy fill (2 m) overlying very soft clay (~6.5 m), loose clayey sand (~2 m), firm calcareous clay	600 mm diameter vibro-concrete columns with 910 mm enlarged head at 2.5 m triangular spacing	Very large sub-soil settlement, loss of sub-soil support (Part C = 0)
Van Eekelen et al. (2007) – Kyoto Road, Giessenburg. (November 2005)	1.1 m	Hegemann sludge (cement and clay) -	Longitudinal – 350 kN/m UTS Transverse – 400 kN/m UTS		Driven timber piles/columns – 120 mm diameter (?) with 300 mm diameter column cap at 1.27 m square spacing	Long term monitoring over 3.5 year period presented in Van Eekelen et al. (2010) shows load recovery phase of arching.
N210 GRCSE (Haring et al. 2008)	1.15 m	32 mm minus gravel (ϕ = 33°) for LTP and embankment	Longitudinal – 600 kN/m UTS Transverse – 350 kN/m UTS	Peat (1.5 m) overlying, soft clay (6.5 m), sand (13.5m)	Precast driven piles (290 mm) on rectangular array – 2.35 m (longitudinal) by 2.28 m (transverse).	Peat/very soft material was placed between the column heads to induce the working condition.
French test embankment (Briançon et al. 2011) – four design zones (2R and 4R described here)	5 m	0.65 m thick LTP. From bottom – 150 mm trafficking layer, 200 gravel, geogrid, 200 mm, geogrid, 100 mm	Biaxial geogrid (55/55 kN/m) – two layers	Clayey fill (1.5 m) overlying soft clay (1 m thick), firm to stiff sandy clay (6 to 8 m). See Rowe et al. (2015).	Controlled Modulus Columns (CMCs), 390 mm diameter, square array, 2 m spacing.	The measured settlement of the 5 m high embankment in zone 1R (no piles) of 230 – 260 mm suggests that the sub-soil response cannot be considered "typical" of a GRCSE.
		150 mm trafficking layer	None			

*Ultimate tensile strength

reported differential settlement, the aim is to understand the nature of the base settlement that has occurred to date, i.e., was base settlement limited by the reinforcement stiffness? Did base settlement occur during construction? Or is base settlement on-going due to either primary consolidation of the sub-soil and/or creep compression?

7.7 Failure case studies

7.7.1 Large-scale experiments – Sloan (2013)

The large-scale test CSE #2 (Sloan et al. 2013) is examined here; a further four large-scale tests are described in Sloan (2011). In this test the working condition was achieved within several hours by rapidly dissolving the geofoam sub-soil support. The measured sub-soil deflection was between 150 to 175 mm. The earth pressure cells were arranged within the column to measure the total column load (Part A + B) and additional earth pressure cells were placed immediately above the geogrid layers (6 cm, 9 cm and 43 cm above) to measure the stress in the area between columns (Figure 7.10). These earth pressure cells measuring stresses in the area between columns did not appear to function correctly after the sub-soil support was dissolved. Measured values varied from 0 kPa and 4 kPa.

A large amount of experimental work demonstrates that these near zero vertical stresses values are not possible under the action of arching alone (see Section 2.1). In addition, the measured vertical stress in the area between columns is not compatible with the stress required to induce the measured tensile strain (in excess of 4 %) and deflection of the geogrid. For these reasons, it is difficult to examine the aching stress development in more detail other than to note that 96 % of the calculated vertical load in the tributary unit cell area of the column was transferred to the column through a combination of arching and load transfer through the geogrid layers. The measured differential settlement ratios from the five large-scale tests described by Sloan (2011) were presented in Figure 7.4 and reasonable (conservative) agreement with the contours of differential settlement ratio calculated from McGuire (2011) is indicated.

7.7.2 Rossorry Quay development and South Carolina roadway

The failure of a GRCSE in South Carolina, U.S.A. supporting a roadway (Camp III et al. 2006) and of a LTP supporting a proposed housing development (Rossorry Quay development) in Enniskillen, Northern Ireland (Coghlin 2005) were both designed with multiple layers of low strength geogrid in accordance with the so-called Guido method (Guido et al. 1987). Both sites were underlain by very soft soil leading to a loss of sub-soil support

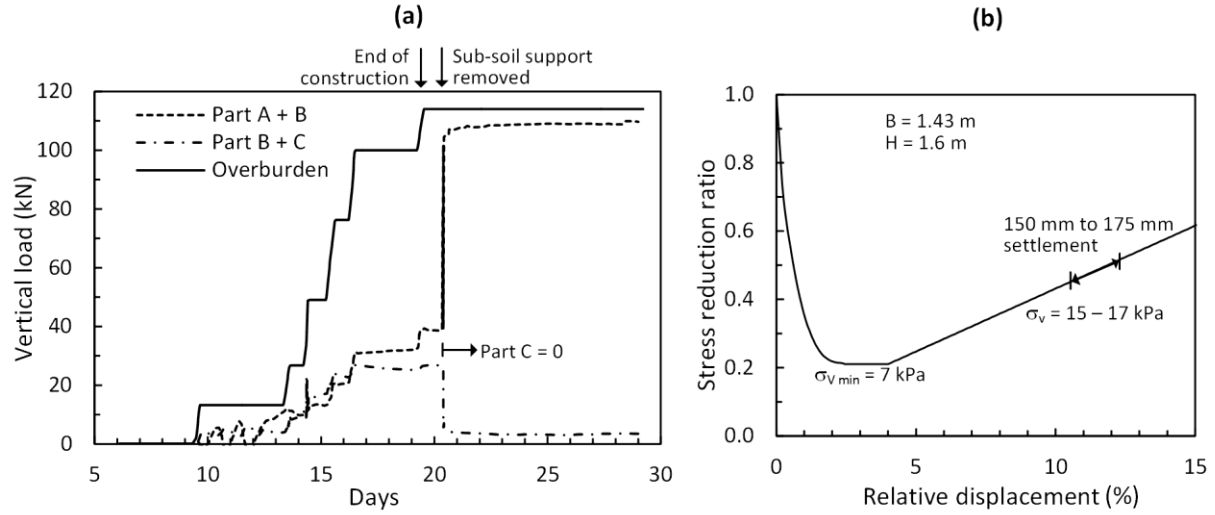

Figure 7.10. Large-scale experiments by Sloan et al. (2013); **(a)** load measured by earth pressure cells and **(b)** theoretical GRC with predicted arching stresses

condition and failed under a reinforcement strain condition which led to surface deformation (serviceability failure). In the South Carolina case, the differential settlement was reported to be approximately 50 mm shortly after the road opening; the tolerance was 20 mm.

In the Rossorry Quay case study, the full extent of the serviceability issues took about 2 years to develop (after the construction of numerous residential houses and roadways). The base settlement was significantly aided by the unsupported working platform, which varied from 0.5 m up to 1.5 m. While it is perhaps easy to dismiss these case studies due to the design method adopted, the current specified minimum embankment heights permits these geometric designs despite the high risk of surface differential settlement. For the South Carolina case, the differential settlement ratio is close to 1.0 and approximately 0.3 for the Rossorry Quay case. While EBGEO (German Geotechnical Society, 2010) notes that reinforcement sag may need to be limited to control differential settlement, it is questionable, if a designer could limit maximum sag and long term reinforcement creep strain to less than 20 mm in order to meet surface differential settlement tolerances, given the differential settlement ratio is estimated to be close to unity. Even where high stiffness geogrid polymer types are adopted (i.e., using polyamide fibre geogrid reinforcement).

7.8 Case studies which have not reported differential settlement

7.8.1 N210 National Road

The development of arching stresses in the N210 National Road between Krimpen aan den Ijssel and Bergambacht, the Netherlands is described by Haring et al. (2008) for a 50 m test section. Haring et al. (2008) notes that the analytical methods available at the time were not able to calculate surface deformation, which are the main interest for the designer. However, the importance of developing the working condition was understood and to achieve this; "*very loose and soft peaty material*" was placed between the column heads. The instrumentation was placed in two test areas; MV1, which was subjected to extensive traffic loading (discussed here) and 2) MV2 which was preloaded with 1.6 m of fill.

Instrumentation data from earth pressure cells and strain gauges is presented in Figure 7.11 as a component of unit cell force along with the total unit cell load. Construction was complete at day 30 and the arching stresses can

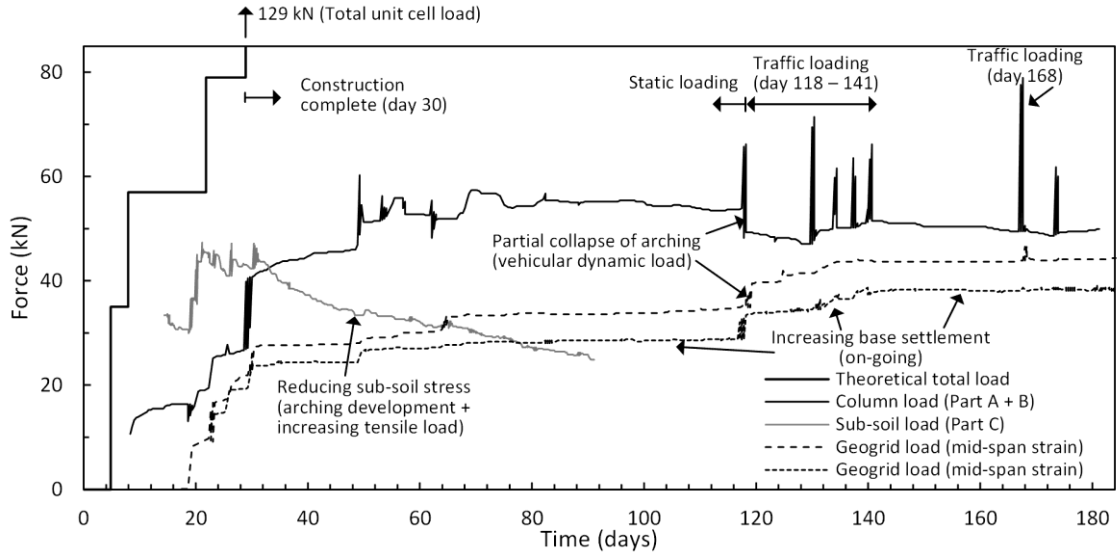

Figure 7.11. N210 GRCSE instrumentation monitoring – construction and post-construction phase (modified from Haring et al. 2008)

be seen to develop as increasing load on the column and a reduction in the sub-soil support. The placement of soft material between column heads has enabled a rapid increase in the geogrid load during construction. The geogrid load (deflection) can be seen to increase continually over the 5 month period post-construction while at the same time arching stresses can be seen to gradually develop (increasing column load) i.e., equilibrium in the LTP was not achieved. In addition, two periods of dynamic (vehicular) loading on the embankment between day 118 and 141, and again on day 168, can be seen to partially collapse the arching. The response of the arching mechanism to dynamic loading in this thin embankment is consistent with the embankment height to clear span ratio being too shallow. As a result, full arching cannot develop and surficial loading is acting directly on the geogrid layers. A number of hydrostatic settlement gauges and pipes as well as settlement plates were installed in the embankment. However, this data was not presented in the original publication.

The instrumentation indicates that base settlement (likely primary consolidation) was on-going 5 months after the embankment was completed. The embankment geometry suggests a differential settlement ratio at, or close to, unity (Figure 7.4). It is difficult to conceive how the base settlement which has progressively developed in this embankment over the 5-month period shown has not manifested into a measurable amount of surface settlement or that the dynamic action of vehicular loading, which caused a direct increase in base settlement (geogrid strain), has not induced measurable surface rutting. In Van Eekelen et al. (2015) it is noted that the new N210 road went into operation in 2010 and that "*problems with the GR installation in the test field may have resulted in unexplainable measurements. The road surface, however, has remained settlement-free during the first four years of using the road.*" Unfortunately, no deformation data is presented to validate what is a surprising statement given the experimental observations at a number of other case studies (Camp III et al. 2006, Britton et al. 2010, McGuire 2011, Sloan 2011) and, in particular, the South Carolina roadway failure case which had geometric similitude and experienced significant differential surface settlement. Dynamic loading due to vehicular traffic can be expected to incrementally increase the base settlement over the design life of the GRCSE, as a result, it is conceivable that surface differential settlement may develop in the long term.

7.8.2 Kyoto Road project

In the Kyoto Road project (Van Eekelen et al. 2010), long term instrumentation data is presented in Figure 7.12. It can be observed that maximum arching occurred at about August 2006 (20 kN in van Eekelen et al. 2010 Fig 8 – Load component C), about 10 months' post-construction, and over the 3 year period to 2009 the component of force acting on the sub-soil gradually increased to about 25 kN. It is suggested that the arching development is in the load recovery phase as arching is becoming less efficient with increased sub-soil settlement. This is, in-part, supported by the findings of Van Eekelen et al. (2010) who notes:

> "*A heavy dynamic load, however, can cause a sudden short term decrease of arching (A decreases and B increases suddenly). The Kyoto Road experiences both sudden reductions in arching and an on-going development of the arching during several months (increasing A) or years (decreasing B).*"

The researchers have described, in this case, the progressive collapse mechanism outlined above. The sudden reductions in arching and subsequent re-development of arching must be accompanied by deformation (i.e., base settlement). The continual collapse of the arching due to these effects and the incremental increase in base settlement with time raises questions about the long term potential for surface differential settlement. These effects are similar to those observed in the N210 embankment during the periods of dynamic (traffic) loading (Figure 7.12).

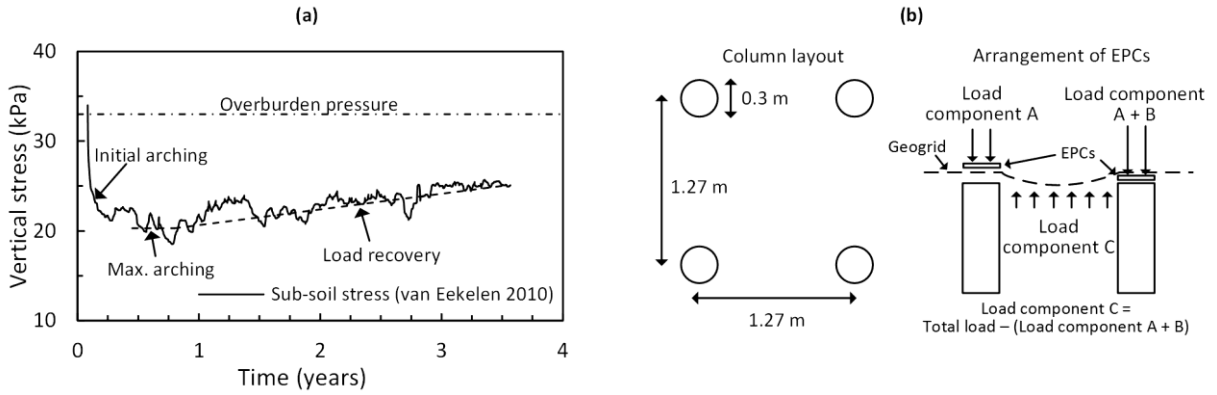

Figure 7.12. Kyoto Road GRCSE **(a)** sub-soil stress inferred from EPC data **(b)** Column layout plan and instrumentation

7.9 Full height embankments

7.9.1 French test embankment

A full-scale experimental GRCSE was constructed 20 km northeast of Paris, France (Briançon et al. 2011). Additional information on the material properties of the GRCSE is presented in Rowe et al. (2015) who undertook a three-dimensional numerical simulation of the GRCSE. The embankment is 5 m high and comprises four zones, however, only zones 1R (no ground improvement), 2R (no LTP) and 4R (a LTP reinforced with two geogrid layers) are assessed here (Figure 7.13).

In Case 2R, where embankment fill directly overlies the installed columns, the overburden pressure is 92.5 kPa and σ_v in the sub-soil zone at the completion of construction is 83 kPa (SRR = 0.90) and trends towards 88 kPa (SRR = 0.95). The reciprocal stress increase on the column due to an SRR of 0.90 is 570 kPa and is consistent with the measured value on the column. The measured data suggests negligible "soil arching" occurs in the embankment fill and that the columns act in isolation with load transfer in the embankment fill occurring along near-vertical failure planes (external failure surfaces in Figure 2.5) extending upwards from the columns; i.e., as described by the three-dimensional Adapted Terzaghi Method (Russell et al. 1997). The description of the embankment fill by Briançon et al. (2011) "marly and chalky natural soil", the high optimum moisture content (w_{opt} = 29 %) and low bulk density (18.5 kN/m^3) suggest a poor quality fill which is consistent with the lack of arching observed.

In zone 4R the arching condition is indicated as a failure plane extending through LTP granular material (650 mm thick) and through 4.35 m of cohesive material. The GRC assumes that the ultimate conditions occur through a

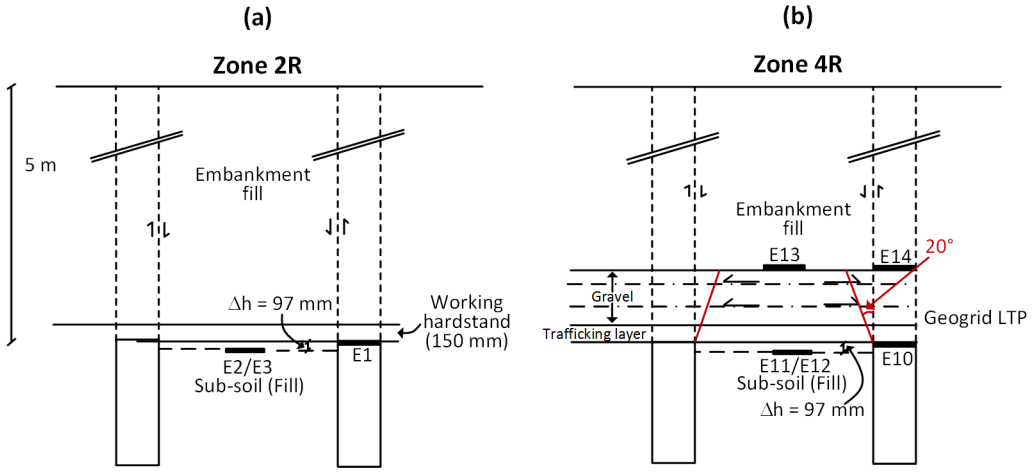

Figure 7.13. Inferred load distribution for French test embankment; **(a)** zone 2R and **(b)** zone 4R

single granular material, which is not the case here; the failure surface propagates through the embankment fill. The SRR ratio was measured to be 0.45 and is consistent with the SRR at the terminal state of arching calculated with the GRC method.

The soil arching/vertical load transfer that develops in zone 2R through the embankment fill is minimal and this influences the arching development in the LTP which is not confined to the LTP which is too thin relative to the adopted geometric spacing of the columns (without column heads) to enable maximum arching to develop entirely in the LTP. The significant difference in the shear strength properties of the LTP material and embankment fill material make interpretation of the arching development (internal shear band development), and comparison with arching models difficult. Furthermore, this test embankment shows a very stiff sub-soil response beneath the LTP at this site compared to the response that would typically be expected for a soft soil site. The 5 m high embankment in zone 1R (without ground improvement) completed (~90%) primary consolidation in just 40 days with only 230 mm of settlement measured.

7.9.2 TH-241 column supported embankment

The vertical stress measured at the base of the LTP in the TH241embankment (Wachman and Labuz, 2008) shows the characteristic features of the GRC with the initial, maximum and load recovery phases of arching apparent over the 250 day period shown (Figure 7.14*a*). The arrangement of the earth pressure cells and triangular grid layout of piles is shown in Figure 7.14*b*. Interestingly, where this data is presented in Wachman et al. (2009), only the first 90 days of data was presented as the authors stated that they wanted to eliminate the effects of frozen soil.

A review of the original data in Wachman and Labuz (2008) by the present author suggests that much of the measured settlement (about 170 mm) is real and consistent with the underlying sub-soil which comprises about 9.1 m of highly organic silty loams and peat underlain by 6.1 m of silty organic soils (there is limited sub-surface information provided). The temperature inversion as the ground begun to heat in spring (April) 2007 suggests some temperature dependence in the settlement system. However, the progressive development of arching stresses (Figure 7.14*a*) is consistent with on-going sub-soil settlement, furthermore, there does not appear to be any evidence of temperature induced effects coinciding with the winter of 2006/2007 (day 66 to 155), nor with the heating of the ground in spring 2007 (day 210 onwards) in the earth pressure cell data (Figure 7.14*a*).

7.10 Discussion

The bi-linear arching stress-deformation relationship used in the LDC method uses the Adapted Terzaghi Method (Russell et al. 1997) to describe the limit stress (SRR_{term} in Section 2.6.2) that achieved at the yield displacement (d_{yield}):

$$SRR_{\text{term}} = \frac{\gamma}{\alpha(\gamma H + q)}(1 - e^{-\alpha H}) \qquad \textbf{(7.7)}$$

Where

$$\alpha = \frac{4aKtan(\phi)}{A_s} \qquad \textbf{(7.8)}$$

Russell et al. (1997) used a lateral earth pressure coefficient (K) of 1.0, while Russell et al. (2003) used a value of 0.5, in the modified version (Equation 7.7) adopts K = 0.75. The Terzaghi (1943) method was converted from two-dimensional to three-dimensional for GRCSE analysis by Russell et al. (1997), however, it is important to

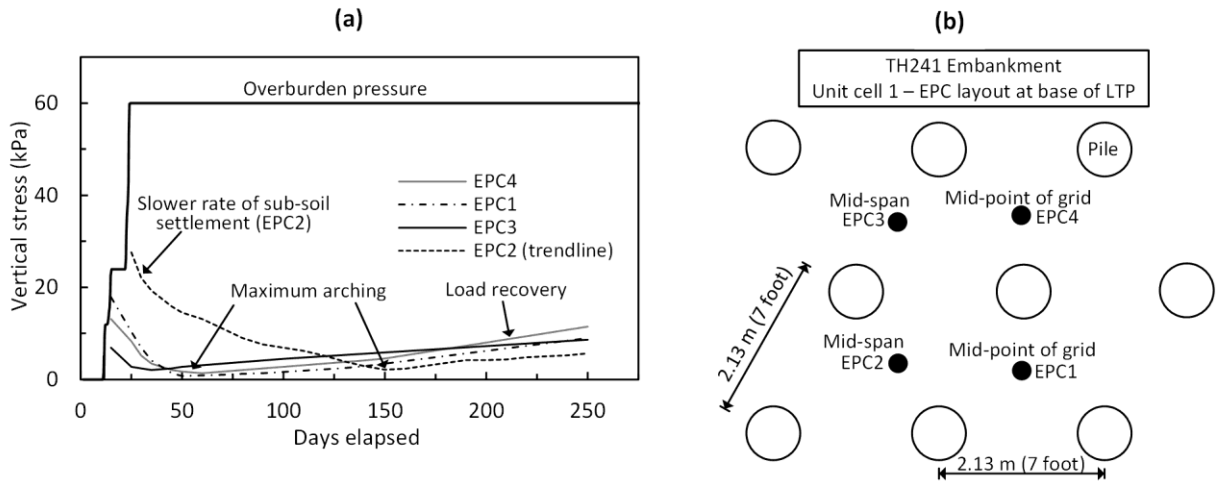

Figure 7.14. (a) EPC data for TH241 embankment and **(b)** instrumentation layout plan (modified from Wachman and Labuz, 2008)

understand the assumptions of the original method which are described by Terzaghi (1943) "*The simplest theories are those in the third category [i.e., Terzaghi method] which are based on the assumption that the surfaces of sliding are vertical. Fortunately, the sources of error associated with this assumption are clearly visible. In spite of the error the final results are fairly compatible with the existing experimental data.*" The failure surface described in this method is a terminal state of "arching" (OC in Figure 2.5) and requires large settlement to develop, typically more than about 30 % relative displacement in well-compacted granular material. The GRC method uses this approach to describe the terminal condition; these methods are identical at large displacement. However, it is the deformation range at less than about 10 % relative displacement that is of interest for GRCSE, and over this range, the GRC describes better the key features of arching stress development (i.e., initial, maximum and load recovery phases).

There is however, a case to be made for the use of the Adapted Terzaghi Method for shallow embankments where it is likely that the arching will breakdown due to dynamic loading effects, acting on, or near, the apex of the shear bands characterising maximum arching (point A in Figure 2.5). In this case, the terminal state is not reached through excess deformation (i.e., by following the GRC to the terminal phase) but is induced by external disturbance. This is consistent with the observations of Haring et al. (2008) who described the break-down of arching, coinciding with the commencement of dynamic loading on day 188 onwards after the "static" period prior to day 118, and the regular break-down of arching measured, and described by Van Eekelen et al. (2010), in the Kyoto Rd embankment. Filz et al. (2012) also noted that the Adapted Terzaghi Method can be modified to account for vertical shearing through more than one layer of embankment fill (i.e., LTP and embankment fill material), such as in the French test embankment and these shallow embankments. The downside of using the Adapted Terzaghi Method is that the rate of sub-soil settlement will be over-estimated initially (Figure 7.8*c*) when assessing serviceability behaviour.

It is suggested that the LDC method could be further refined by incorporating the GRC for high embankments (above the McGuire line). The framework used to develop the LDC makes this modification possible. The use of the GRC method enables the breakdown of the arching mechanism (load recovery phase) and associated increase in stress in the area between columns to be described and the progressive failure mechanism to be described. This is particular important in high embankments where this mechanism is more likely to occur. The use of a constant or a bi-linear arching stress-deformation relationship does not enable this mechanism to be described.

The differential surface settlement in GRCSE geometries below the McGuire line is controlled by the differential settlement ratio and the base settlement of the LTP which is controlled by, and limited by, the sub-soil settlement and geosynthetic reinforcement layers. The method outlined by McGuire (2011) and presented graphically in Figure 7.4 enables this ratio to be estimated. The accuracy of any assessment of base settlement is highly dependent on the level of the geotechnical site investigation conducted and this should be proportionate to the risk of differential settlement induced serviceability issues. While the magnitude of base settlement can be controlled by the specification of the reinforcement and the magnitude predicted using concepts related to membrane theory (Parabolic method by (Giroud 1995), Kempfert et al. (2004) method, etc.). It is considerably more difficult to predict the time-rate of sub-soil settlement.

Furthermore, detailed site investigation is not normally undertaken; this is often justified on the basis that the underlying soft soil does not greatly influence the GRCSE behaviour as the embankment load is transferred via the LTP to the columns that then by-passes the soft soil. However, it has been shown here, that soft soil behaviour, largely controls the serviceability behaviour of shallow GRCSE through the time-dependent relationship between the applied load at maximum arching and the pre-consolidation stress profile and creep settlement. In general, accurately assessing σ'_{p} and the secondary compression index (C_{α}) is both difficult and expensive. A design based on serviceability limit state conditions should reflect the uncertainty in these material parameters and the inherent difficulties in assessing accurately the time rate of sub-soil settlement.

In addition, the soft soil thickness, compressibility and time rate of consolidation varies considerable along the length of a GRCSE; the rate of base settlement will vary between unit cells leading to further differential settlement. The use of the GRC method to describe the development of arching and its relationship with the serviceability, working and ultimate conditions in a GRCSE (as they have been termed here) is shown in Figure 7.15. The critical period with respect to differential and total settlement coincides with the period where the LTP is in the serviceability condition in the years after embankment construction, this may be in excess of a decade if sub-soil settlement is controlled by creep settlement.

In the author's opinion, the LDC method (Filz et al. 2012), which is formulated to ensure compatibility between vertical stress and deformation, provides a more robust analytical framework to describe the complex soil-structure-geosynthetic interaction in a GRCSE compared with the current two-step design approaches which utilise limit equilibrium models (Concentric arches, (Van Eekelen et al. 2013) Hewlett et al. (1988), Zaeske (2001). The elastic spring constant used to model sub-soil support in both the Concentric arches and Zaeske model is replaced by soft soil parameters, C_{c}, C_{r} and σ'_{p} in the LDC method. This is a considerable improvement and enables the time-dependent sub-soil consolidation process to be modelled and pre- and post-construction base settlement of the LTP to be calculated. The issues with the arching stress-deformation relationship in the LDC method has, however, been outlined.

7.11 Conclusion

While a complete analytical solution of arching stresses development in a trapdoor test does not exist at this point in time, a relatively consistent description of the theoretical aspects has been developed through numerous investigations, spanning many decades. The pertinent aspects of arching behaviour, as they relate to GRCSE, include:

- Deformation dependency

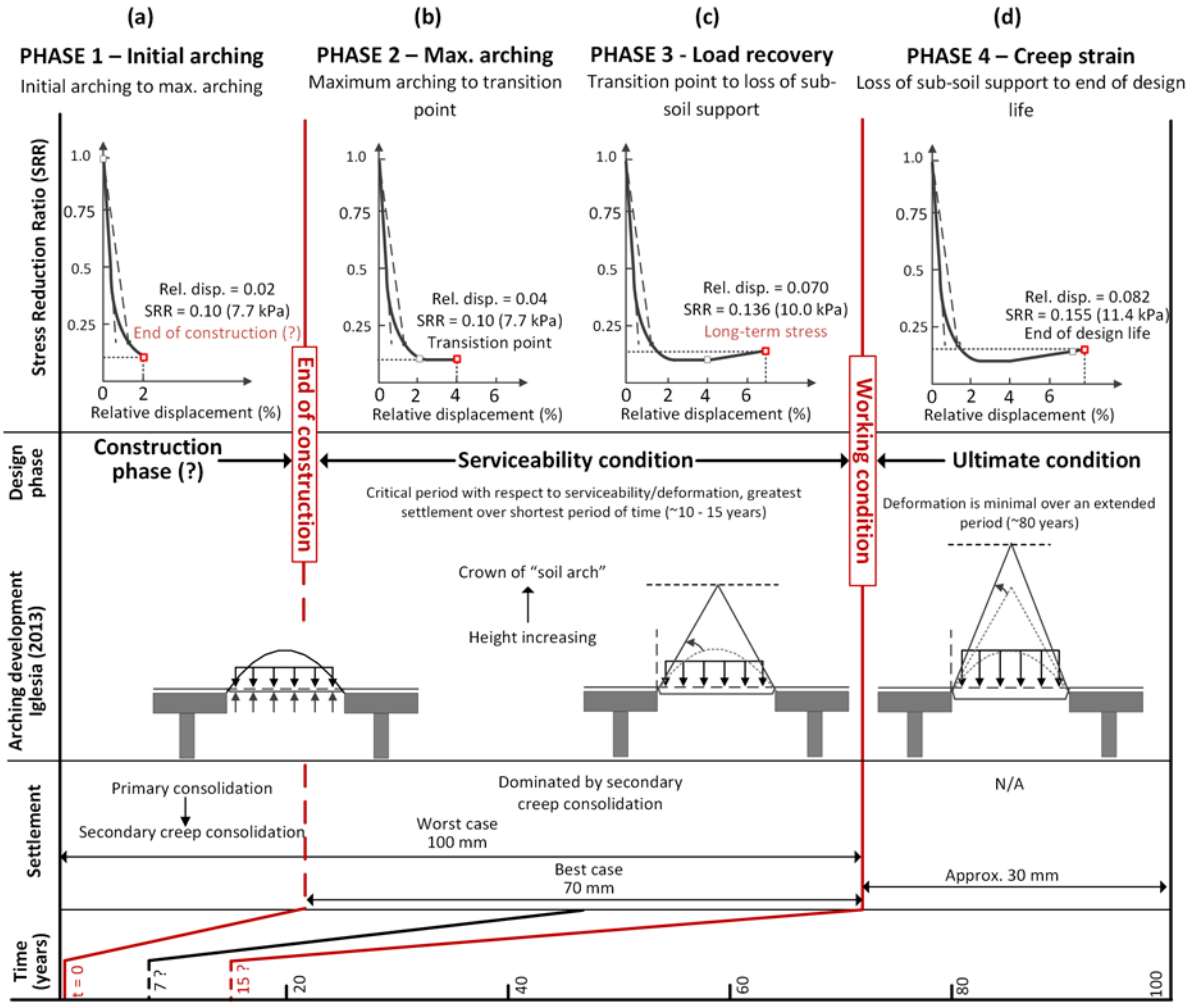

Figure 7.15. Ground reaction curve design method **(a)** Initial arching **(b)** Maximum arching **(c)** Load recovery and **(d)** Creep strain

- Initial, maximum, load recovery and terminal phases of arching
- Progressive shear band development characterising maximum, load recovery and terminal phases of arching
- Shear bands developing at an inclined angle equal to the dilatancy angle at that particular point and time in the soil mass (Evans 1983, Stone and Wood 1992, Santichaianant 2002). The inclination of these shear bands, and their height relative to the thickness of the LTP, has important implications for the arching stress development in GRCSE.

In recent times, a large number of arching models have been developed in association with GRCSE research. Many of these models are at odds with, and in some cases directly contradict, a large amount of well-established research into the theoretical aspects of the arching phenomena. The author considers that further improvements in the understanding of LTP behaviour, particularly the reinforcement strain serviceability limit state, requires the incorporation of base settlement as a governing parameter in a coupled arching stress-deformation model. It has been shown here, that this is necessary to describe accurately serviceability behaviour; models which assume a constant value of arching stress cannot describe serviceability behaviour. Given the stringent settlement tolerances and performance criteria that govern the design of most GRCSEs, deformation typically governs acceptable GRCSE design and this transition is therefore warranted and necessary for the advancement of the GRCSE state-of-knowledge in design.

It has been shown here, that where a coupled arching stress-deformation relationship is adopted, that the development of the working condition under the action of arching stresses alone is difficult, for most soft soil sites. The development of the working condition often occurs post-construction, and in many cases, long term creep compression controls the development of the working condition. In contrast to the traditional view of GRCSE behaviour, the compressibility and time-rate of settlement of the sub-soil plays an important role in the serviceability behaviour of GRCSE. In particular, the parameters σ_p and C_α. Often, these are not assessed accurately as part of site investigation works for GRCSEs.

The LDC method is formulated with base settlement as a governing parameter and ensures compatibility between arching stress development, sub-soil settlement and geosynthetic reinforcement deflection. In the author's opinion, this offers a more robust analytical framework compared with the widely adopted two-step design approach which utilises limit equilibrium models and de-couples the arching stress-deformation relationship. However, the validity of the bi-linear arching stress-deformation relationship adopted in the LDC method is questionable for high embankments. The work of McGuire (2011) and Sloan (2011) provides a method to estimate the relationship between surface deformation and base settlement (see Figure 7.4) and at the same time, raises questions about the long term performance, and the manner in which acceptable performance has been achieved in the short term in several field case studies. Furthermore, the validity of arching models for these shallow embankments, which are shown to be susceptible to traffic loading, has been highlighted. The Adapted Terzaghi Method is likely the most suitable for these shallow embankments subjected to dynamic (traffic) loading, however, this method will over-estimate the rate of sub-soil settlement when assessing serviceability behaviour.

In the author's experience, there has been a trend in recent year to design at, or near, the limits of the recommended minimum embankment height specified in (BSI, 2010) of $0.7(s - a)$. Generally without detailed consideration for the differential settlement or deformation tolerances. In a number of failure case studies (Coghlin 2005, Camp III et al. 2006) it was excessive deformation of the LTP that translated to surface deformation and rendered the asset (roadway, foundation platform for housing) unserviceable. It is often stringent differential settlement tolerances that necessitate the design and construction of GRCSEs in the first instance, and the author considers that the risks associated with differential settlement induced serviceability concerns are not fully conveyed in the widely used design standards (BS 8006-1; BSI 2010, EBGEO; German Geotechnical Society 2010, CUR 226; CUR 2015) which enable the design and construction of GRCSEs below the McGuire line, and in particular those designed near the minimum embankment height of $0.7(s - a)$.

8 Ground improvement installation effects

8.1 Background

Chapters 8 and 9 examine installation effects associated with the ground improvement works and global embankment behaviour based on data from the field case study. Whilst the analysis of the global embankment behaviour and installation effects are closely related, and draws on similar data, the amount of material and topics covered necessitated the separation of these chapters.

In this chapter, an overview of the drilled displacement column construction methodology and installation data is described. A number of field, laboratory and numerical studies that have investigated pile installation effects are reviewed to highlight the typical behaviour that can be expected where full displacement piles are installed into a soft soil. Cylindrical cavity expansion theory is introduced to provide a framework with which the observed field behaviour can be interpreted. The field behaviour is assessed based on the piezometer, tiltmeter, inclinometer and survey data, which is presented in term of pore water pressure fields, displacement fields and cumulative displacement fields. The axial capacity of the two test columns installed within the North Dynon embankment are also assessed and compared with the dynamic load test results.

The importance of sub-soil settlement in understanding the localised embankment behaviour has been highlighted in the preceding three chapters and it was noted in Chapter 5 and 7 that accurate assessment of the sub-soil settlement presented a considerable source of uncertainty due to difficulties in assessing the "ground improvement" effect in the Coode Island Silt. Investigating the installation effects is expected to offer insight into the soft soil ground improvement and the affect this has on the sub-soil settlement. However, installation effects (Chapter 8) are investigated with the primary aim to understand how ground improvement with semi-rigid inclusions affects global embankment behaviour (Chapter 9).

The findings relating to installation effects are presented at the end of this chapter. The main findings are however left for the conclusion of Chapter 9. The field data presented in this Chapter and the bulk of Chapter 9 is from King et al. (2017e). The data and analysis presented here is applicable to other GRCSEs where the ground improvement comprises the installation of full-displacement type columns which is the case for the majority of GRCSEs.

8.2 Overview of installation

The construction of a drilled displacement column is similar in many respects to the non-displacement continuous flight auger (CFA) pile and has largely evolved from this piling technique. The main difference is the drilling tool used for drilled displacement columns which fully displaces the soil during the installation phase. NeSmith (2002) and Basu et al. (2009) provide a detailed description of the construction process. A summary is presented below and illustrated in Figure 8.1 (after Bottiau, 1998):

- The drilling rig is positioned over the target location; the drilling tool penetrates the ground with a combination of clockwise rotation and downward force (crowd pressure).
- As the drilling tool advances, soil is transported up the lower auger section, progressively compressed, and displaced laterally.
- The drilling tool is advanced to termination depth. For the case study considered here, termination depth occurred when a minimum 2 m penetration into the Fishermens Bend Silt was achieved. In this case the operator was required to monitor the rig instrumentation to confirm minimum penetration had been achieved. Alternatively, in many cases, the columns are installed to a target depth or drilled to practical refusal.
- Concrete is then pumped through the hollow auger stem as the drilling tool is extracted and simultaneously rotated clockwise. The displacement body of the drilling tool assists in maintaining a positive concrete pressure in the grouted portion of the pile during extraction. Rotation of the drilling tool and the reverse flight augers above the displacement body ensures that any collapsed material is displaced laterally as the drilling tool is extracted.
- If required, reinforcement can be installed into the fresh concrete for piling applications.

Similar to a CFA pile, installation data is recorded during installation, this generally comprises time, depth, mast inclination, torque, drilling stem rotation rate and penetration rate. During the concreting phase, additional data is recorded and includes; concrete slurry pressure and lifting speed, which is often used to infer an "as-built" profile. The use of data acquisition hardware for the monitoring and verification of the drilled displacement column installation (i.e., quality assurance requirements) is an integral part of the ground improvement works that enables the delineation of the sub-surface materials and increased confidence that founding conditions and column integrity are achieved. The rig instrumentation forms an important part of the drilled displacement column construction and is described in detail by NeSmith et al. (2006a) and Piscsalko et al. (2004). The drilling tool used for the case study (shown in Figure 8.2) is a progressive displacement type, based on the classification described by Larisch et al. (2013). The drilling tool dimensions are listed in Table 8.1.

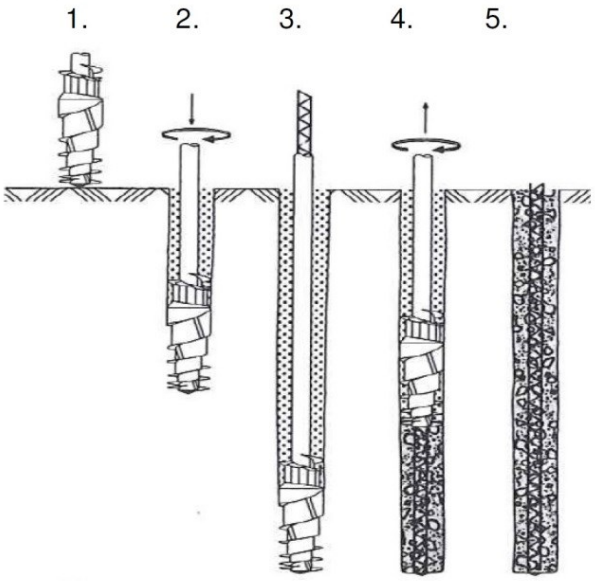

Figure 8.1. Installation process for a drilled displacement pile/column (from Bottiau 1998)

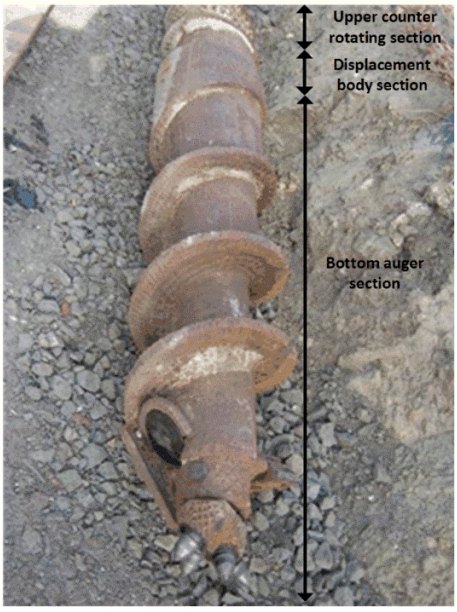

Figure 8.2. Drilling tool used installation of columns at North Dynon embankment case study

8.2.1 Installation data

The data produced during the installation of a drilled displacement column comprises separate drilling and concreting phase data. An example of the rig output is presented in Figure 8.3 and includes penetration (speed) rate, torque, rotation rate, lifting speed, concrete pressure and column profile. The Coode Island Silt/Fishermens Bend Silt interface (top of socket) has been interpreted by the author and is also shown at a depth of 10.4 m. The columns installed as part of the case study typically progressed at a penetration rate of approximately 2 m/minute with the concreting phase typically taking a similar amount of time (typically, drilling and concreting took between 15 to 30 minutes per column depending on depth). As the drilling tool penetrates the founding unit the most noticeable increase is observed in the drilling torque (Figure 8.3). The speed rate and pitch are largely consistent, with a minor drop observed over the final 2 m.

The response of the rig is related to auger mechanics and the drilling process of the Continuous Flight Auger (CFA) piles, from which the drilled displacement column technology originates. To avoid excessive flighting during the drilling of a CFA pile, the ratio between the rate of cutting (at the base of the auger) and rate of soil transportation up the auger flights must be correctly maintained. If for example, the rotational rate is too high compared with the downward penetration rate, this may lead to an insufficient volume of soil being transported up the auger flights. As a result, lateral earth pressures acting along the shaft of the partially filled auger shaft causes soil to feed from the sides rather than the base of the auger (i.e., side loading). This can result in a reduction in lateral earth pressure, increased disturbance along the pile shaft and can lead to potential instability (Fleming 1995).

Table 8.1. Dimensions of drilling tool

Auger detail	Dimension (mm)
Outer auger diameter	450
Inner auger diameter	250
Upper counter-rotating auger section height	500
Displacement body height	1000
Bottom auger section height	1000
Total length	2500

This is particularly problematic in loose granular soils. Viggiani (1989) proposed a critical penetration rate (v_{cr}) to minimise the potential for excessive flighting:

$$v_{cr} = nl\left(1 - \frac{d_0^2}{d^2}\right) \quad \textbf{(8.1)}$$

Where n is auger rotation rate, l pitch of the auger flights, d auger diameter and d_0 diameter of auger stem. For this reason, the rotational rate is generally coupled with the penetration rate during installation either automatically by the on-board computer or manually by the rig operator. Therefore, to maintain the required rotation rate relative the penetration rate the piling rig must vary the torque applied. Aspects of auger mechanics related to displacement piling techniques are discussed further by Fleming (1995), Slatter (2000), and Larisch (2014). Regardless, the drilling mechanics relating to torque, penetration and rotation are essentially the same for a drilled displacement columns as they are for a CFA pile and control the installation process. However, for the drilled displacement columns considered here the role of auger mechanics are less important than for a CFA pile as the auger section is limited to the bottom 1 m of the drilling tool. This response is observed in the installation data in Figure 8.3. It is the author's understanding that the automation of this installation process varies between rigs and is dependent on manufacture, the type of on-board software and degree of operator input. Bauer (2013) provides an overview of their technologies currently available including a description of their automated drilling software.

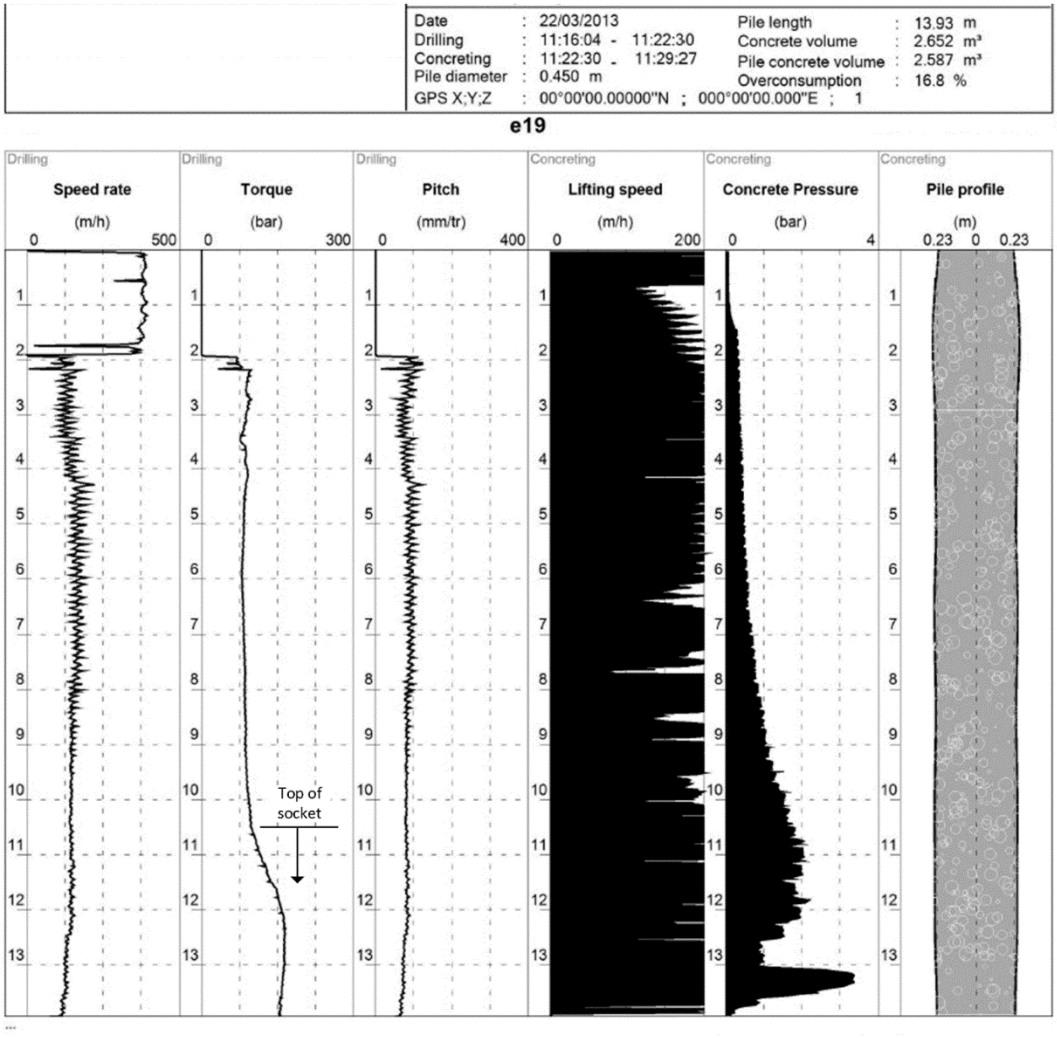

Figure 8.3. Typical drilled displacement column installation data

To the author's knowledge the method developed by NeSmith (2003) termed the "installation effect" is the only method, currently available and specifically developed for full displacement auger piles/columns that can assess axial capacity real time during installation. NeSmith (2003) found that the combination of torque and penetration rate "*provided a relatively simple, reliable indicator of subsurface conditions and relative capacity over a fairly wide range of conditions.*" NeSmith's assessment is generally consistent with the author's interpretation of the installation data described above.

8.2.2 Crowd pressure

Another parameter affecting the installation process that has not been mentioned is the vertical load applied to the drill tool. This is referred to as a "crowd pressure". The typical installation of a column is shown in Figure 8.4. For most soft soils, the main line winch is required to provide a pull-back force to counter the combined weight of the drilling head, Kelly bar and drilling bit, this reduces the net vertical force on the drill bit (Figure 8.4 – Step 1) and allows the penetration rate to be achieved. As the overburden pressure increases and/or a stiffer stratum is encountered, the pull-back force is reduced (Figure 8.4 – Step 2) and in some cases a pull-down force is applied to aid penetration into the founding material (Figure 8.4 – Step 3).

The author's experience is that the ability to apply, measure and record this pull-down/back force varies greatly between piling rigs. For the field case study, only one of the rigs used for ground improvement works had

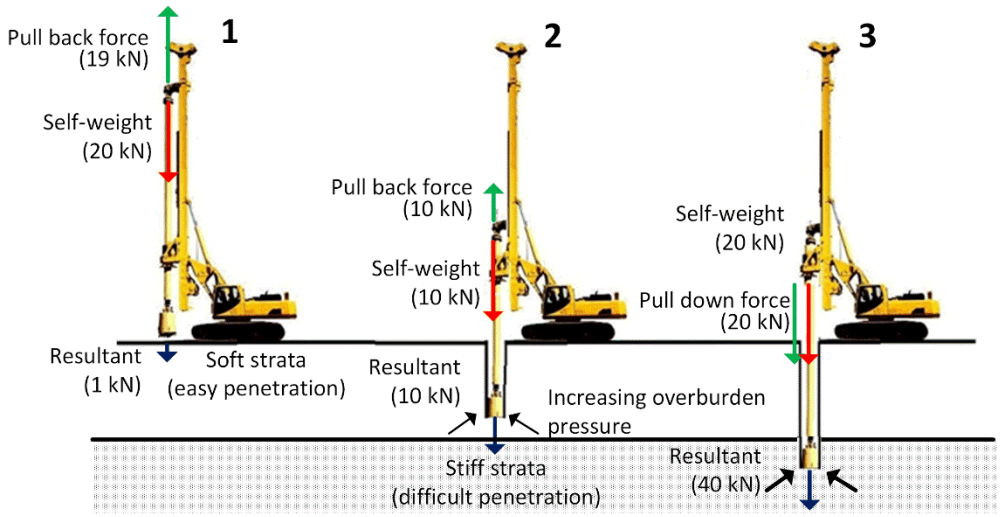

Figure 8.4. Drilled displacement column installation – example of applied loads (Surenee Piling, 2015)

instrumentation that measured pull-down/force, however, it did not permanently record the data. The effects of penetration rate, rotation rate, torque and crowd pressure are considered based on cylindrical cavity expansion theory introduced in the next section and laboratory and numerical studies investigating drilled displacement columns.

8.3 Installation effects

8.3.1 Stress and deformation

The current understanding of installation effects has mostly been developed from studies investigating driven piles. Knowledge from these studies forms the basis with which installation effects associated with drilled displacement columns are interpreted for the present case study. Some notable studies investigating the behaviour of driven piles include:

- Research at Cambridge University to develop the cylindrical cavity expansion theory (Carter et al. 1979, Randolph et al. 1979). Described in further detail below.
- Instrumented closed-ended steel tube piles installed into the heavily over-consolidated London clay (Bond et al. 1991) and the soft clay deposit at the Bothkennar test site, Scotland (Lehane et al. 1994)
- Instrumented closed-ended steel tube piles in heavily over-consolidated clay and normally consolidated estuarine clay (Coop et al. 1989).
- The installation of displacement piles was also studies extensively at the Norwegian Geotechnical Institute (e.g. Karlsrud and Haugen 1986)
- At Massachusetts Institute of Technology, Azzouz et al. (1988) for example, described an instrumented model pile with a piezo-lateral stress cell tested at numerous sites. A number of tests were performed at sites underlain by Boston Blue Clay, a sensitive marine clay. The strain path method (Baligh 1985) also resulted as part of this extended research program in the 1980s.

The installation effects associated with a driven pile are well described by Randolph (2003) and summarised briefly here. The three fundamental mechanisms described below, in a generalised form, are applicable to full displacement columnar elements used to support a GRCSE. The **installation** of a full displacement pile results in severe distortion

of the soil in the immediate vicinity of the pile. In the case of a drilled displacement column, this distortion includes the effects of auger mechanics as soil is rotated and transported up the auger flights, densified and displaced laterally. In the vicinity of the pile tip the strain fields resembles spherical cavity expansion while further up the pile shaft the strain field merges to resemble cylindrical cavity expansion where the soil outside the immediate distorted zone is displaced radially outwards.

At the completion of pile installation, an excess pore water pressure field exists around the installed shaft due to: 1) an increase in total stresses as the soil is displaced outwards to accommodate the pile volume and, to a lesser extent, 2) a change in the mean effective stress due to shearing of the soil. After the installation of a driven pile, the **equilibration** phase commences immediately as excess pore water pressure dissipates radially. The soil in the vicinity of the pile undergoes (inward) radial consolidation, and as a result, increases in strength. In the third phase, pile **loading** is resisted by shaft friction and base pressure.

8.3.2 Cylindrical cavity expansion theory

Given the difficulties in modelling the drilled displacement column installation effects numerically, cylindrical cavity expansion theory is adopted here to provide a framework to quantitatively compare the cumulative installation effects with the measured field behaviour. Cylindrical cavity expansion theory broadly falls within the "effective stress concepts" for pile design and is a method used to assess pile bearing capacity (Randolph 2003, Yu 2013). The application of cylindrical cavity expansion theory to piling problems is complex and is not routinely employed in practice. It is adopted here because it enables as assessment of the inadvertent effects that column installation has on the surrounding ground, adjacent columns and the embankment itself.

Whilst not all the installation effects are detrimental to embankment performance, the excess pore water pressure and displacement field, which develop due to installation effects often are; particularly where a large number of columns are installed, in a dense array, as is typical for ground improvement works associated with a GRCSE. The zones along a pile shaft where cylindrical cavity expansion theory is broadly applicable (Yu 2013) where described above and are indicated in Figure 8.5. These zones broadly resemble the sub-surface conditions encountered in the field case study; Zone A – Fill, Zone B - Coode Island Silt and Zone C – Fishermens Bend Silt.

The cylindrical cavity expansion solutions developed by Randolph et al. (1979) describe the excess pore water pressure and displacement field for the soil mass surrounding a driven pile and is summarised below. The cavity expansion solution relies on the assumption that the axisymmetric deformation occurs in an elastic-perfectly plastic

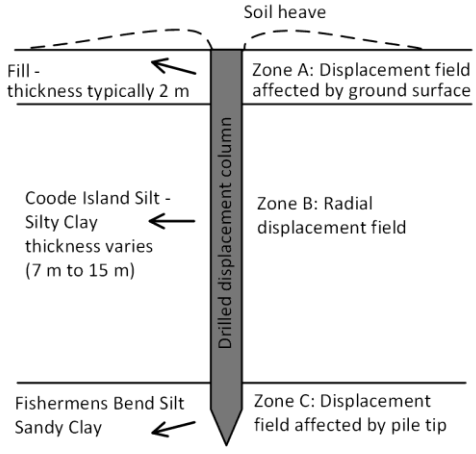

Figure 8.5. Soil displacement after pile installation (after Yu, H-S. 1995)

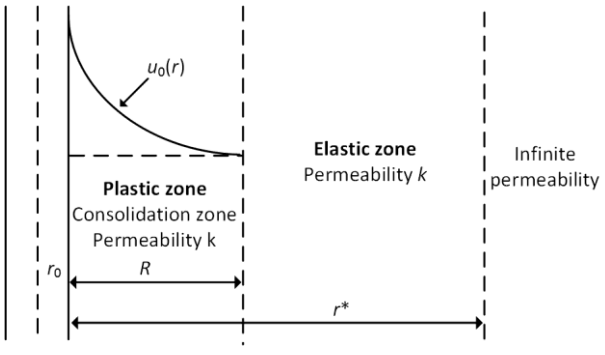

Figure 8.6. Cylindrical cavity expansion parameters

material, therefore the only degree of freedom permitted is in the radial direction. The limitations of an elastic-perfectly plastic constitutive model applied to the present problem are described later. The geometric parameters and initial excess pore water pressure distribution are defined in Figure 8.6 and described below.

Based on the axisymmetric conditions the governing equations are developed in cylindrical co-ordinates in terms of the radial, circumferential and vertical stresses (σ_r, σ_θ and σ_z respectively) and strains (ε_r, ε_θ and ε_z respectively) using Hooke's law, radial equilibrium and continuity of the volumetric strain rate along with Darcy's law to describe the flow of excess pore water pressure due to a pore water pressure gradient. The first governing equation describing the variation of excess pore water pressure (u) with time (t) is as follows:

$$\frac{\partial u}{\partial t} = c\left[\frac{1}{r}\frac{\partial}{\partial r}\left(r\frac{\partial u}{\partial r}\right)\right] + g(t) = c_r \nabla^2 u + g(t) \qquad \textbf{(8.2)}$$

$$c = \frac{k}{\gamma_w} G^* = \frac{k}{\gamma_w}\frac{2G(1-\nu)}{(1-2\nu)} \qquad \textbf{(8.3)}$$

Where r is the radius, $g(t)$ constant of integration and the coefficient of radial consolidation (c_r) is defined by Equation 8.6 where k is the (radial) permeability of the soil, γ_w unit weight of water, G the shear modulus and ν is poisson's ratio. With the exception of the constant of integration the governing equation for pore water pressure is identical to Terzaghi's one dimensional consolidation equation. The second governing equation describing the variation of radial displacement ξ due to consolidation at radius r is:

$$\frac{\partial \xi}{\partial t} = \frac{k}{\gamma_w}\frac{du_0}{dr} + c\left\{\frac{\partial}{\partial r}\left[\frac{1}{r}\frac{\partial}{\partial r}(r\xi)\right]\right\} - \frac{f(t)}{r} \qquad \textbf{(8.4)}$$

Where $f(t)$ is a constant of integration. The general solution to the governing equations (Equation 8.2 and Equation 8.4) is found by applying r and ξ boundary conditions (7 in total) and through the use of Bessel functions. Boundary conditions for radial displacement (Equation 8.5i to iii) and pore water pressure (Equation 8.5iv to vii) are as follows:

$\xi = 0$ at $t = 0$ for $r \geq r_0$ **(8.5) (i)**

$\xi = 0$ at $r = r_0$ for $t \geq t_0$ **(ii)**

$\xi \rightarrow 0$ as $r \rightarrow 0$ for $t \geq 0$ **(iii)**

$u = u_0$ at $t = 0$ for $r \geq r_0$ **(iv)**

$u \rightarrow 0$ at $r \rightarrow \infty$ for $t \geq 0$ **(v)**

$u \rightarrow 0$ at $t \rightarrow \infty$ for $r \geq$ r0 **(vi)**

$\frac{\partial u}{\partial r} = 0$ at $r = r_0$ for $t > 0$ **(vii)**

However, to avoid difficulties with the Bessel functions at large radi ($r \rightarrow \infty$) it is necessary to modify the boundary conditions and introduce the term r^* which is the radius at which the increases in excess pore water pressure during radial consolidation (i.e., outward radial flow of porewater) is negligible. This value of r^* is usually between 5R and 10R (Randolph et al. 1979), where R is the radius of the plastic zone. The eighth boundary condition is therefore $u = 0$ at $r > r^*$, in addition the permeability is defined as infinite at $r > r^*$. Using the separation

of variables technique, with a separation constant – α^2, the general solution to the governing equations is written in the following form:

$$u = Be^{-\alpha^2 t}[J_0(\lambda r) + \mu Y_0(\lambda r)] \quad \textbf{(8.6)}$$

$$\xi = \frac{B}{G^*\lambda} e^{-\alpha^2 t}[J_1(\lambda r) + \mu Y_1(\lambda r)] + h(r) \quad \textbf{(8.7)}$$

Where J_i is a Bessel function of the first kind and Y_i is a Bessel function of the second kind. Subscript i indicates the order of the Bessel functions. i.e., Y_1 is a 1st order Bessel function of the second kind. The linear combination of $J_i(\lambda r) + \mu Y_i(\lambda r)$ is known as a cylinder function of ith order. By applying boundary conditions to the zero and first order cylinder functions these equations can be expressed as follows:

$$C_1(\lambda r_0) = J_1(\lambda r_0) + \mu Y_1(\lambda r_0) = 0 \quad \textbf{(8.8)}$$

$$C_0(\lambda r^*) = J_0(\lambda r^*) + \mu Y_0(\lambda r^*) = 0 \quad \textbf{(8.9)}$$

The generation of excess pore water pressure during full displacement pile installation is due to two factors: (1) changes in effective stresses caused by the shearing and remoulding of the soil mass and (2) changes in the total stresses due to the outward expansion of the soil as the pile (or drilling tool) is installed. Randolph et al. (1979) used the expression for excess pore water pressure proposed by Hill (1950) and Gibson et al. (1961) for an elastic-perfectly plastic soil as follows:

$$u_0 = 2s_u \ln\left(\frac{R}{r_0}\right) \qquad r_0 \le r \le R \quad \textbf{(8.10)}$$

$$u_0 = 0 \qquad R < r < r^* \quad \textbf{(8.11)}$$

Where $R = r_0(G/s_u)^{1/2}$. By substituting the initial excess pore water pressure into the general solution, the final solution for u and ξ over the radial domain is written as follows:

$$u = \sum_{n=1}^{\infty} B_n e^{-\alpha^2 t} C_0(\lambda_n r) \quad r_0 \le r \le r^* \quad \textbf{(8.12)}$$

$$u = 0 \qquad r > r^* \quad \textbf{(8.13)}$$

$$\xi = \frac{1}{G^*}\sum_{n=1}^{\infty} \frac{B_n}{\lambda_n} e^{-\alpha^2 t} C_1(\lambda_n r) + \frac{C_u}{G^*}\left[r \ln\left(\frac{r}{R^*}\right) - \frac{r_0^2}{r}\ln\left(\frac{r_0}{R^*}\right)\right] \qquad r_0 \le r \le R \quad \textbf{(8.14)}$$

$$\xi = \frac{1}{G^*}\sum_{n=1}^{\infty} \frac{B_n}{\lambda_n} e^{-\alpha^2 t} C_1(\lambda_n r) + \frac{C_u}{G^* r}\left[R^2 \ln\left(\frac{R}{R^*}\right) - r_0^2 \ln\left(\frac{r_0}{R^*}\right)\right] \quad R \le r \le r^* \quad \textbf{(8.15)}$$

$$\xi = \frac{F(t)}{r} \qquad r > r^* \quad \textbf{(8.16)}$$

$$B_n = \frac{4c_u}{\lambda_n^2} \frac{[C_0(\lambda_n r_0) - C_0(\lambda_n R)]}{\left[r^{*2} C_1^2(\lambda_n r^*) - r_0^2 C_0^2(\lambda_n r_0)\right]} \quad \textbf{(8.17)}$$

Where ½ + ln(R) = ln(R^*). As the Bessel functions are periodic there are an infinite number of μ and λ values which satisfy Equation 8.8 and 8.9. The solutions are found by non-dimensionalising the time axis as $\tau = ct/r_0^2$ and by

replacing the λ_n term with z_n/r_0. This cancels the $-\alpha^2$ constant introduced in the general solution; the $e^{-\alpha^2 t}$ term in Equations 8.12, 8.14 and 8.15 becomes $e^{-\frac{\tau r_0^2}{c_h} z^2}$. The author has found these solutions by rearranging Equation 8.8 and 8.9 in terms of μ and combining to form the following expression:

$$0 = \frac{J_0\left(\frac{z_n r^*}{r^0}\right)}{Y_0\left(\frac{z_n r^*}{r^0}\right)} - \frac{J_1(z_n)}{Y_1(z_n)} \qquad \textbf{(8.18)}$$

The roots of Equation 8.18 are approximately periodic and to find terms z_n the modified secant method (Chapra and Canale 2010) root finding algorithm, with an initial guess based on the (approximate) periodic spacing, was used. This enables the equations for u and ξ to be solved using a macro enabled spreadsheet applications to find a finite number of z_n terms, 2500 z_n terms have been used in the solutions presented here. The accuracy of the solution obtained at $t = 0$ can be compared with the exact solution (Equation 8.10); the agreement is excellent. Randolph et al. (1979) have previously noted that reasonable accuracy can be obtained with around 50 terms. Examples of various excess pore water pressure solutions (Equation 8.12) at various times are shown in Figure 8.7, these solutions are used to assess the piezometer data presented later in this chapter. These solutions indicate a plastic zone of radius $R = 2.54$ m, excess pore water pressure of 121 kPa at the column/soil interface which reduces to 0 kPa at radius R. As excess pore water pressure dissipates radially outward with time, excess pore water pressure is reduced at the pile/soil interface and increases at values of $r > R$, although this increase is minor. The assumption of negligible increase in pore water pressure at r^* (taken as $10R \approx 25$ m) is reasonable based on the solutions presented.

In order to describe the displacement field the following expression for radial soil displacement (Δr) was proposed by Carter et al. (1980):

$$\Delta r = \sqrt{r^2 + \beta r_0^2} - r \qquad \textbf{(8.19)}$$

Where β is the displacement ratio, which is the ratio of net to gross cross sectional area of a pile being driven. For a solid (driven) pile $\beta = 1$, however, for open ended steel tube piles the value of β is significantly less than 1 and depends on the extent to which a soil plug develops in the base of the pile during installation. Given that a drilled displacement column is a full displacement pile the value of β should be 1, similar to a driven pile. However, it will be shown that the displacement fields which develop due to drilled displacement column installation are significantly over-predicted when $\beta = 1$ is used. The radial displacement field from Equation 8.19 is shown in Figure 8.8 along with the long term radial consolidation ($t \rightarrow \infty$) solution which represents the equilibration phase (Equation 8.14 and 8.15). The long term radial displacement is the sum of the initial radial displacement and long term radial consolidation. The closed form analytical solution for cylindrical cavity expansion in a (drained) cohesive-frictional material by Yu et al. (2002) is also shown for comparison, this solution is approximately equivalent to the long term case.

The work presented above was developed to simulate the driven pile installation effects by considering an expanding cylinder in an elastic perfectly plastic material and was based on earlier studies which were aimed at interpreting the pressuremeter test (e.g. Gibson et al. (1961); Palmer (1971) and Hughes et al. (1977)). This research was further extended by Randolph et al. (1979) to describe an expanding cylinder in a work-hardening soil (i.e., modified Cam-Clay). Since this time, a number of other researchers have extended this concept by considering

idealised soil models of increasing complexity. Carter et al. (1986) presented an analytical solution for cavity expansion in a non-associated Mohr-Coulomb material and Yu et al. (1991) developed a solution for a dilatant elastic-plastic material. A relatively comprehensive overview of these methods is provided by Yu (2013). Detailed analysis of the stress conditions arising due to column installation is beyond the scope of this research. However, some results arising from research into this topic are briefly discussed here to provide a basis to interpret the field data presented later in this chapter.

In Figure 8.9*a* the initial effective stress conditions in cylindrical co-ordinates (σ'_r, σ'_θ and σ'_z) are shown along with pore water pressure (similar to Figure 8.6) immediately after installation. Near the pile, the radial stress increases while the circumferential and vertical stresses both reduced. Randolph et al. (1979) showed that the same analysis performed with OCR = 8 lead to tensile circumferential stress (σ'_θ) in the range of $6 < r/r_0 < 10$ and noted:

"it has been assumed in the Cam-clay model that the soil will sustain these tensile strains. In reality, however, cracks radiating from the pile axis may occur. These cracks will be self-healing close to the pile where the soil is severely remoulded under positive effective stress. The main effect of the presence of cracks further from the pile will be to hasten the dissipation of the excess pore pressures due to the resulting increase in radial permeability"

At larger radi, the initial stress distribution approaches the *in situ* condition with the radial and circumferential stresses equal to σ'_h and the vertical stress (σ'_z) equal to σ'_v. The at-rest earth pressure coefficient is 0.55 i.e., at large radi $\sigma'_h = 0.55\sigma'_v$. As the excess pore water pressure dissipates radially in a manner similar to that described in Figure 8.7, the stress distribution transitions from the post installation condition (Figure 8.9*a*) to the long term condition (Figure 8.9*b*).

As radial consolidation occurs during the equilibration phase, the value of post-installation σ'_r stress (~$2.5s_{u0}$) doubles to value of ~$5s_{u0}$. This time-dependent increase in radial stress acting at the pile-interface is responsible for producing higher shaft capacities for driven piles compared with non-displacement pile types (e.g. bored pile). This is often referred to as "set-up" and is the reason why higher pile sets are observed during pile "restrike" tests performed a period of time after installation (see for example restrike test data by Samson et al. 1986, Preim et al. 1989 and Hussein et al. 1993). Randolph et al. (1979) describe two important findings from their research: (1) a method to assess pile shaft capacity based on effective stresses and (2) a measure of increased undrained shear strength which is an indirect result of the effective stress approach to pile analysis. The long term undrained shear strength $s_{u(\infty)}$ is presented as a function of initial undrained shear strength s_u in Figure 8.10. At the pile interface the

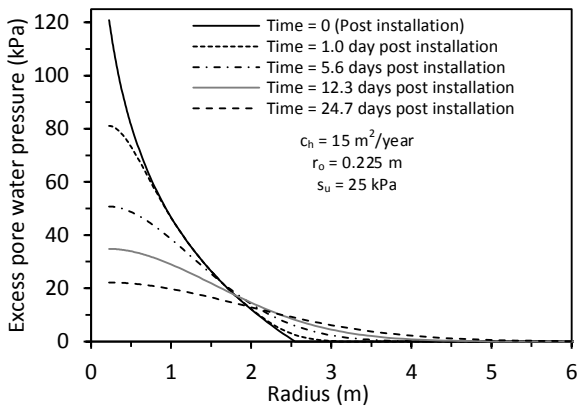

Figure 8.7. Axisymmetric time-dependent cylindrical cavity expansion solutions

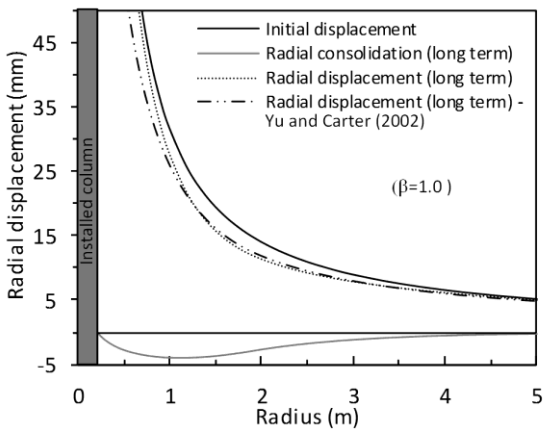

Figure 8.8. Radial displacement field – installation and equilibration

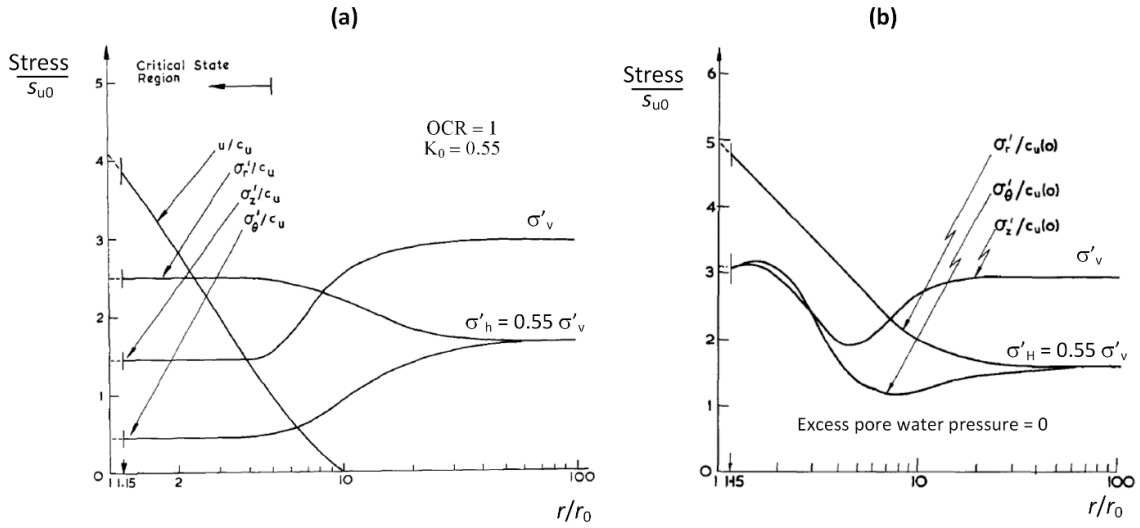

Figure 8.9. Effective stress distribution in the soil (OCR = 1) surrounding a driven pile (a) immediately after installation and (b) after consolidation (reproduced from Randolph et al. (1979)

increase in s_u is as much 60 % and reduces approximately linearly on a semi-log scale as a function of normalised radial distance. The radial distance over which undrained shear strength increases is important when considering group effects for columns installed in a closely spaced array as will be shown later in the chapter.

8.3.3 Previous field and laboratory studies

In recent years a small number of studies have investigated drilled displacement piles/columns with effects such as penetration rate, rotation rate, torque and crowd pressure described. A full-scale study by Suleiman et al. (2015) assessed the installation of an isolated 315 mm diameter Controlled Modulus Column. The variation in pore water pressure and displacement as the drilling tool was installed, and then extracted, is shown in Figure 8.11*a* and *b* respectively. The instrumentation was installed into a very soft sandy silt with a c_v of 149 m^2/year; dissipation of excess pore water pressure is expected to be very rapid. The significant reduction in horizontal stress after the drilling tool passes is particularly interesting. This reduction in stress must be accompanied with a corresponding change in radial strain in the soil mass at the pile shaft interface. i.e., inward "squeeze" around the perimeter of the column. This is examined in Section 8.5.

Larisch et al. (2014) installed four full-scale piles at a site in Lawnton, Queensland, Australia as part of a study investigating drilled displacement piles. Lateral displacement due to pile installation is shown in Figure 8.12*a* where Pile B is the CFA pile, Pile C is the progressive displacement pile and Pile D the rapid displacement pile. The

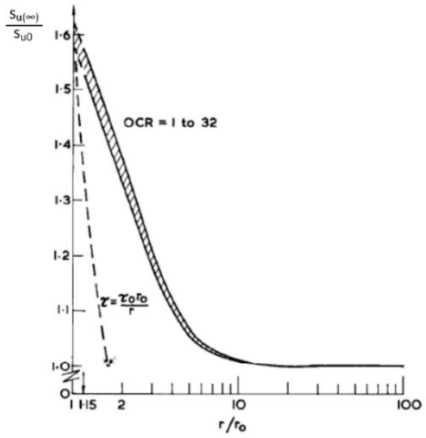

Figure 8.10. Long term undrained shear strength gain due to pile installation (from Randolph et al. (1979)

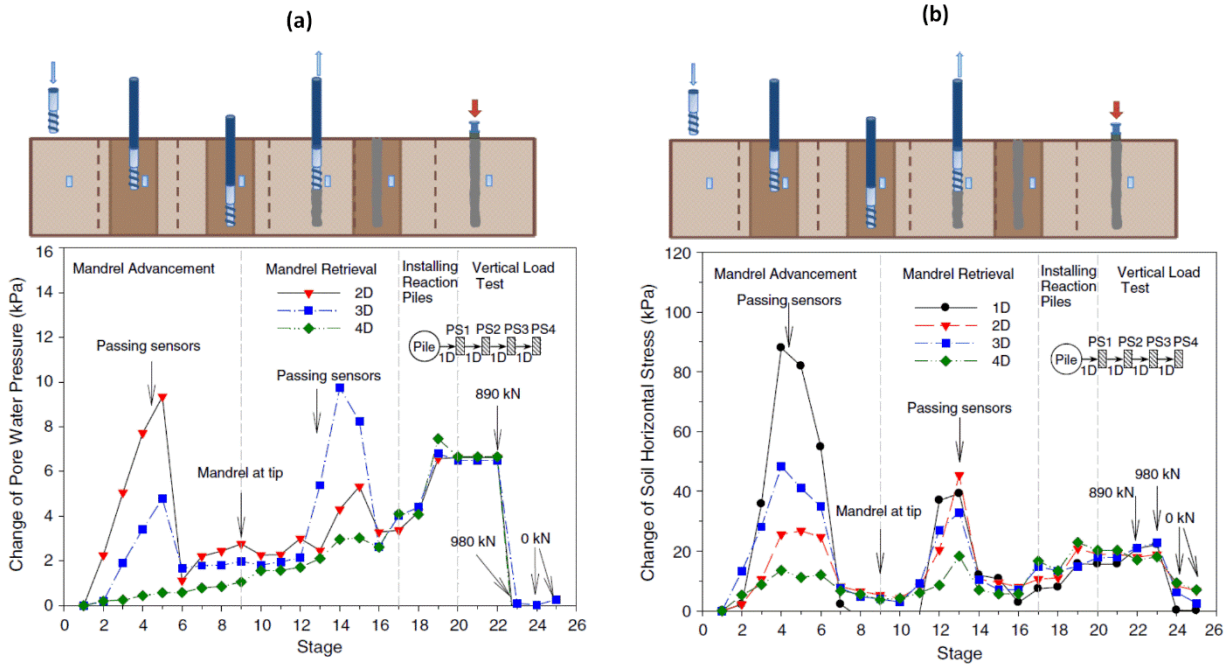

Figure 8.11. Variation in **(a)** pore water pressure and **(b)** horizontal stress during installation and extraction of a Controlled Modulus Column drilling tool (reproduced from Suleiman et al. (2015)

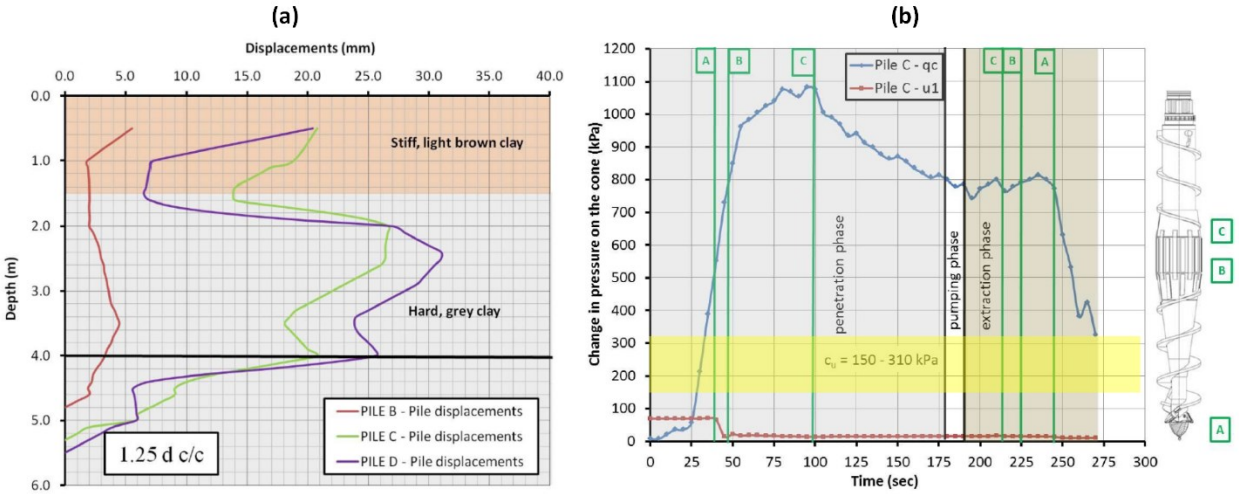

Figure 8.12. (a) Lateral displacements due to the installation and **(b)** variation in CPT q_c and pore water pressure due to pile installation (reproduced from Larisch et al. (2014)

variation in q_c and porewater pressure was measured by a raked CPT positioned at an offset of 225 mm from the pile face (1 diameter from centreline) and at 1.5 m depth. The measured response during the installation and extraction of Pile C is shown in Figure 8.12*b* along with a cross section of the drilling tool. A similar progressive displacement drilling tool was used for the North Dynon case study. The variation in stress during installation peaks as the displacement body (point B to C) passes the CPT sensors, the pore water pressure shows a rapid and significant 400 kPa reduction. The negative pore water pressures are likely due to dilation of the hard clay. The rapid reduction in pore water pressure and constant pore water pressure observed prior to, and immediately after point B of the drilling tool passes the sensor, is unusual and may be due to cavitation in the CPT pore water pressure sensor due to the high negative pore water pressures induced (this typically occurs when these pressures exceeds 100 kPa, see Lunne et al. 1997) . Similar to variation in horizontal stress described above by Suleiman et al. (2015), horizontal pressures reduced significantly once the displacement body passed the sensors.

Hird et al. (2011) developed a small-scale model to describe the installation of a drilled displacement pile using a mixture of transparent amorphous silica particles, a blend of mineral oils and reflective seeding particles. Particle image velocimetry (PIV) techniques (White et al. 2003) were used to develop displacement fields. The author noted that due to the limited transparency of the soil the plan dimensions of the model are smaller than intended leading to boundary effects. Figure 8.13 presents the displacement fields for three tests performed with variable rotational rates, v_{cr} (neutral), $2v_{cr}$ (fast), $0.5v_{cr}$ (slow) and a constant penetration rate. The effect on the auger cutting and transportation mechanisms can be seen by comparing the different cases. In Case (b) drilling is the dominant mechanism compared with Case (c) where the rotational rate is low and penetration is achieved through a pushing action; the difference in the displacement field at the base of the auger is evident.

These results suggest that the relationship between penetration and rotational rate may have some influence on the confinement at the pile base. However, it is noted that the rotational rates differ significantly from v_{cr} and likely representative of extreme cases of over- and under-drilling. The automation available in most modern piling rigs (and mechanical limitations of the rig itself) is likely to limit the potential for over- and under-drilling such that the behaviour shown at laboratory scale by Hird et al. (2011) is unlikely to occur in practice expect in extreme or unusual circumstances. As a result, if these results are extrapolated to full scale it is likely that the influence that these variables have in practice (i.e., at full scale), under typical installation conditions, will be overstated. This is not to suggest that studying the influence of these variables at laboratory scale is not without merit. The author is suggesting that care is however required to translate these results to field behaviour. In addition, the displacement fields are predominately vertical near the displacement body of the auger suggesting that boundary effects are indeed quite significant for these laboratory models.

Ng et al. (2012a, 2012b) investigated the pile "setup" behaviour for steel H-piles driven into cohesive soils and proposed the following expression to describe the time-dependent increase in normalised pile capacity:

$$\frac{R_t}{R_{\mathrm{EOD}}} = \left[C \log_{10}\left(\frac{t}{t_{\mathrm{OED}}}\right) + 1\right]\left(\frac{L_t}{L_{\mathrm{EOD}}}\right) \qquad \textbf{(8.20)}$$

Where (L_t/L_{EOD}) is the normalised embedded pile length factor, t is time and EOD is end-of-drive. The relationship describes a normalised pile capacity that increases linearly with respect to log time, the gradient of this increase is the pile setup factor (C). This expression is based on the earlier method of Skov et al. (1988). The University of Florida side shear setup (SSS) program (Bullock et al. 2005a, 2005b) investigated "setup" in driven piles and similarly proposed a linear log time expression of the general form shown in Equation 8.20 to describe the time-dependent increase in pile capacity. Bullock et al. (2005a) also showed that the percentage gain in capacity increased considerably as the undrained shear strength of a soil reduced; "setup" is more pronounced in softer cohesive soils. The linear pile setup behaviour with respect to log time was also reported by Svinkin et al. (1994) and numerous studies have shown an increase in pile capacity after driven pile installation. Chow et al. (1998) noted that three types of stratigraphic profiles can lead to a reduction in pile capacity after installation: (1) strong soils that dilate during pile driving, (2) weak and metamorphic rocks and (3) sands confined by a cofferdam or closely spaced piles. The primary cause in these cases was the dissipation of negative pore water pressures that built up during pile driving.

The studies outlined in the preceding sections indicate that upon installation of a full displacement column, an increase in effective radial stress and a reduction in both circumferential and vertical stresses in the vicinity of the column is expected. These effects will be noticeable to a radial distance of approximately 20 column radi. It is

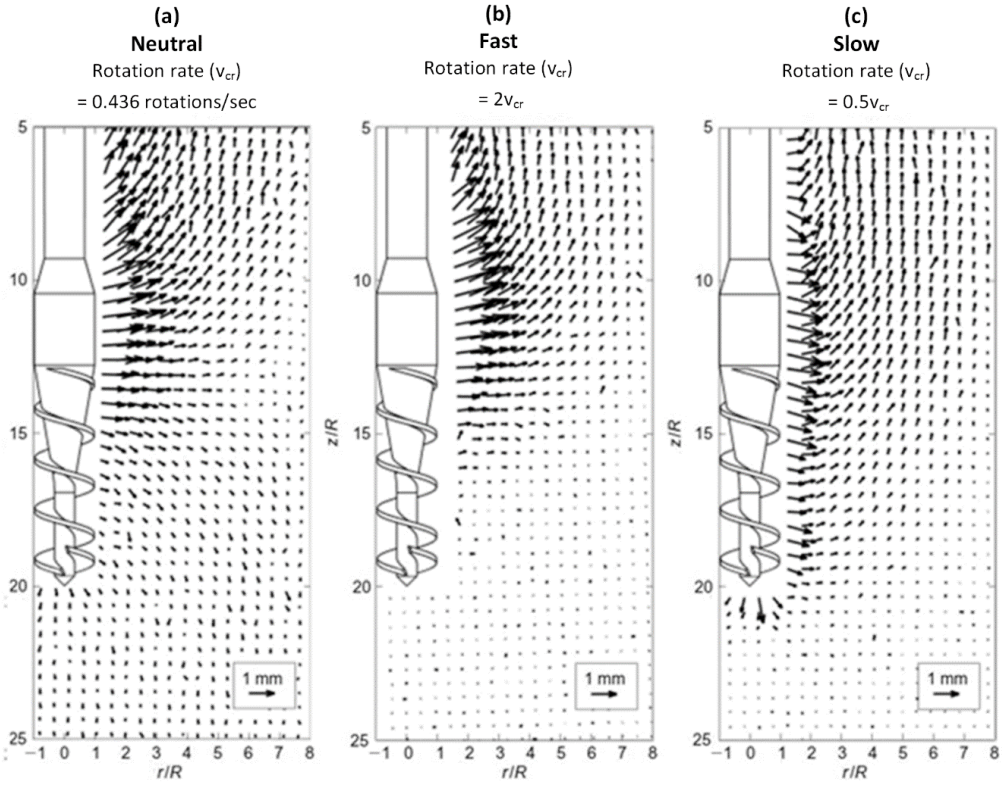

Figure 8.13. Drilled displacement column installation for three rotational speeds; **(a)** neutral **(b)** fast **(c)** slow (after Hird et al. 2011)

conceivable that the reduction in circumferential stresses can induce tensile stresses and potentially (vertical) cracking of the Coode Island Silt. In the long term, radial, vertical and circumferential stresses will increase in the vicinity of the column with these increases being greatest in the radial and circumferential stress directions. The undrained shear strength may increase by a factor of 1.6 at the soil/column interface and be negligible at a radius of about 10 column radi. The stresses predicted by cylindrical cavity expansion theory may approximate the conditions during the installation of the auger head but will change where the drilling tool is removed and the *in situ* stress conditions are defined by the head of concrete slurry (see data from Suleiman et al. 2015). The variability in the installation parameters (rotation rate, penetration rate and pull-down force) will influence the *in situ* stress conditions however these effects are likely to be minor, relative to magnitude of change in *in situ* stresses described by a generalised cylindrical cavity expansion solution (i.e., Figure 8.9) as these variables are reasonably uniform between installed columns (all installed with same piling rig). The conditions leading to a reduction in column/pile capacity described by Chow et al. (1998) above are not applicable to the present study; for the Coode Island Silt "setup" is expected to be significant.

8.3.4 Previous numerical studies

Current FEM numerical techniques are quite limited in their ability to model large strain problems such as pile installation (Więckowski 2004) and generally advanced methods such as Coupled Eulerian-Lagrangian (Qiu et al. 2011, Pucker et al. 2012), point based (meshfree) methods such as smooth particle hydrodynamics (Bui et al. 2008) or the material point method (MPM) are required. The use of techniques such as the Coupled Eulerian-Lagrangian method to investigate geomechanics problems is a relatively recent development and has been implemented in several studies recently. Some findings of these numerical studies are briefly discussed below.

Pucker et al. (2012) simulated the installation of the drilled displacement column using a Coupled Eulerian-Lagrangian Method (CEL) within the Abaqus software. The simulation describes the time-dependent rotation and penetration of a three-dimensional Bauer drilling tool (Figure 8.14*b*). The cylindrical soil mass modelled is a Mai Liao Sand (Figure 8.14). Three different relative densities (D_r = 80%, 50% and 20%) and two penetration/rotation relationships ($v_r = 5v_z$ and $v_r = 10v_z$) were modelled. Using Equation 8.1 the author has evaluated the critical penetration ratio to be $v_{cr} = 7.82v_z$ based on the drilling tool dimensions (d_0 = 0.32m, d = 0.51 m and l = 0.21m).

Results from Pucker et al. (2012) showing the variation in reaction force and rotational moment (torque) against depth are presented in Figure 8.15. The difference in torque between the two velocity ratio cases is small for the models described (Figure 8.15*c* and *d*). The difference in reaction force is however significant, with the lower

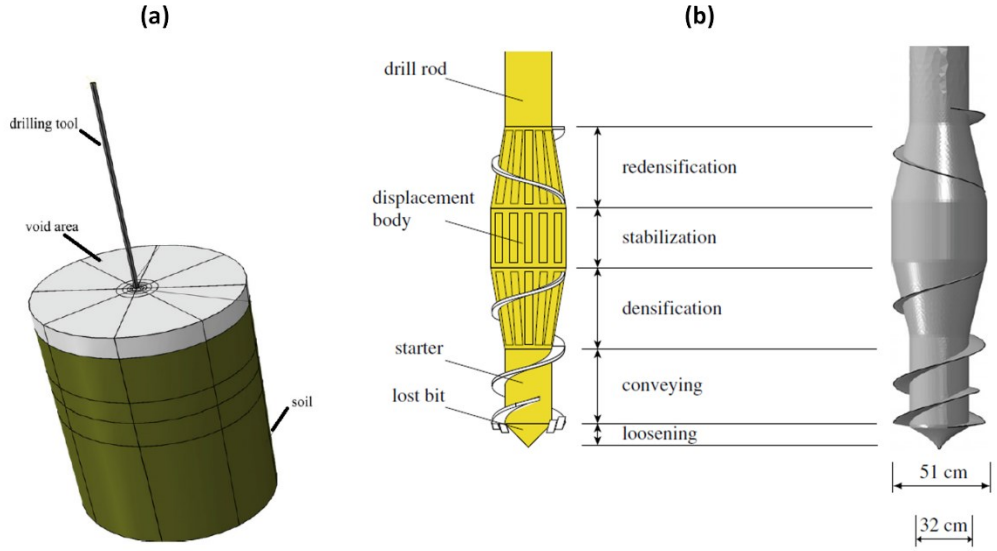

Figure 8.14. (a) Numerical model and **(b)** Bauer drilling tool reproduced from Pucker et al. (2012)

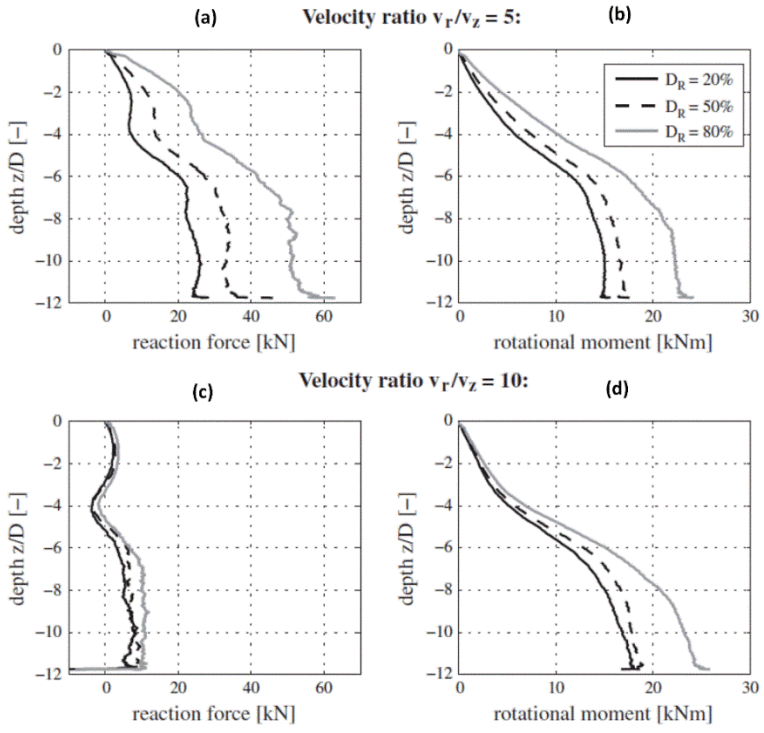

Figure 8.15. Reaction force and rotational moments from column installation (reproduced from Pucker et al. 2012).

velocity ratio case (Figure 8.15*a*) indicating a considerably higher reaction force; the difference in torque is a factor of 6 for the dense sand and suggests that the installation mechanism is predominantly a pushing action.

In addition to full scale field tests of drilled displacement piles, Larisch et al. (2014) also undertook numerical modelling of the field tests. A two-dimensional axisymmetric FE model in Abaqus was developed with the 450 mm diameter drilling tool modelled as a 1.5 m high rigid cone with a 60° cone angle. A numerical technique termed the "zipper technique" Henke (2010) was used to separate the soil mass along the vertical axis of symmetry. This technique does not model the auger rotation or auger mechanics and more closely resembles the penetration of a CPT cone. The soil modelled is a hypo-plastic constitutive model for clay developed by Mašín (2005). The deviatoric effective stress, displacement and pore water pressure fields are shown in Figure 8.16*a*, *b* and *c*, respectively. The displacement field is relatively uniform along the length of the shaft and suggests a cylindrical cavity expansion approximation in this area may be reasonable. At the base of the pile there is an effective stress bulb of about 400 kPa and a 750 kPa pore water pressure bulb is indicated. Negative pore water pressure equal to about 250 kPa along the pile shaft are suggested.

In addition to the method described above there are other "work-around" methods that have been implemented in standard FE analysis software to simulate pile installation effects. Satibi (2009) investigated floating GRCSEs and assessed three methods to simulate the stress fields at the pile interface after installation (Figure 8.17). In these models the earth pressure co-efficient (K) at the pile interface is back-calculated from field tests and is then simulated in the numerical model. In the K_0 approach the K value is applied directly to the soil, the other two methods are either displacement or stress controlled cavity expansion approaches. These methods are primarily concerned with simulating the axial- deformation response of the pile rather than simulating the effects of installation on the surround soil mass and are therefore not suitable for the present study.

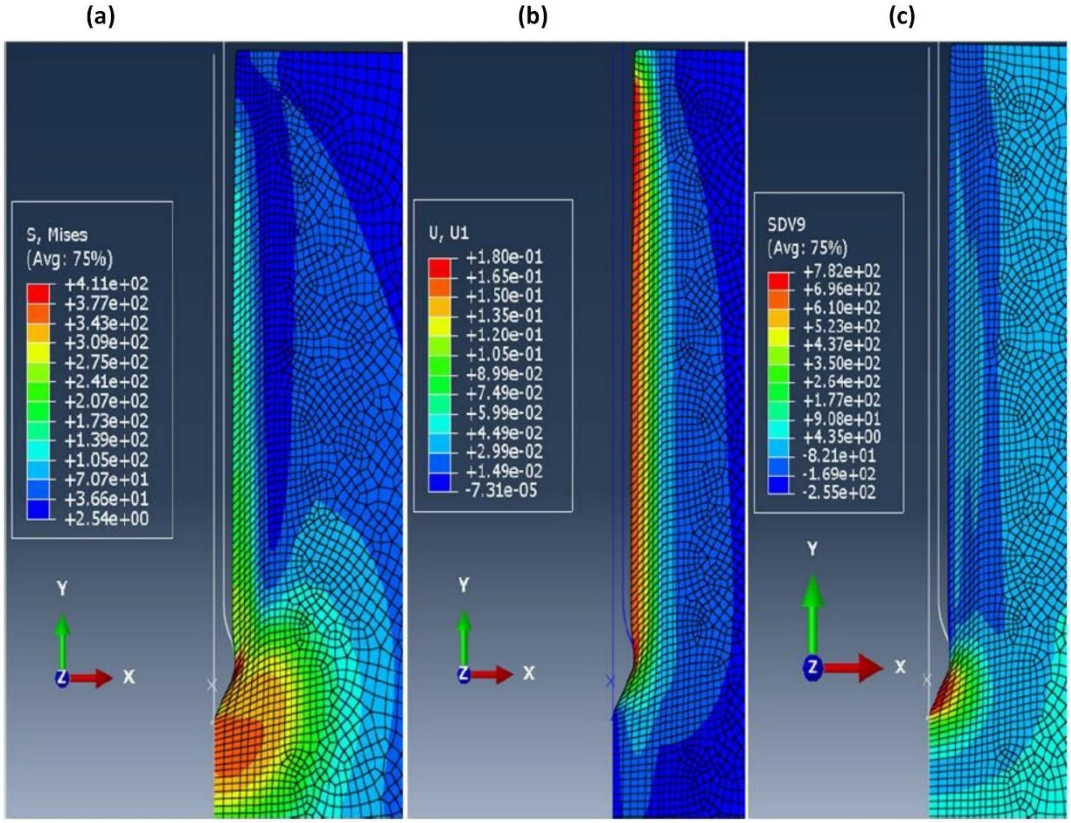

Figure 8.16. Drilled displacement pile installation modelled by Larisch et al. (2014) **(a)** Deviatoric effective stress (von Mises stress in kPa) **(b)** Soil displacement (mm) and **(c)** pore water pressure (kPa)

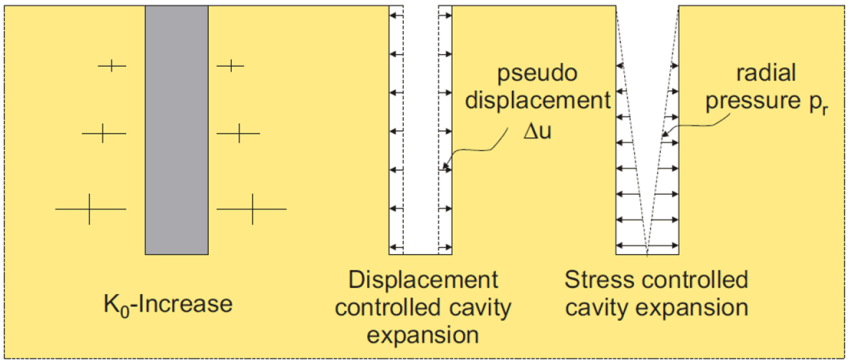

Figure 8.17. Alternative methods for simulating radial stress field due to pile installation (after Satibi, 2009)

The installation effects associated pile installation are a challenging problem in geotechnical engineering, and for the case of drilled displacement columns, are particularly challenging due to the influence of additional variables which include: crowd pressure, rotation rate, penetration rate and torque. At this time, explicitly modelling the installation of a drilled displacement column into soft soil (i.e., hydro-mechanical response) is largely beyond the means of even the most advanced numerical techniques currently available in computational geomechanics. The CEL method used by Pucker et al. (2012) describes the drilled displacement pile installation into dry granular material while the hydro-mechanical response described by Henke (2010) and Larisch et al. (2014) required simplifications to the model geometry to achieve their results. Extending these numerical studies of isolated columns to explore group effects using computational methods is not feasible at this time, and in any instance, is beyond the scope of this study. These physical and numerical modelling studies do however, provide an indication of the likely behaviour that can be expected due to the installation of a column as described at the conclusion of Section 8.3.3. This understanding of installation effects is used as a basis to understand the installation effects arising in the field case study which are assessed throughout the remainder of this Chapter and Chapter 9.

8.4 Field case study – installation effects

Field case study data from the piezometer, inclinometer, tiltmeters and survey data is presented below to assess the installation effects. Details of the method of installation and location of the instrumentation was presented in Chapter 3. A plan view of the North Dynon embankment is presented in Figure 8.18 with the various areas of the GRCSE assessed in this chapter indicated.

8.4.1 Installation effects – pore water pressure

Data from the piezometer in Area #1 (Figure 8.19) shows the long term pore water pressure dissipated to a hydrostatic condition over a period of approximately one year. Two major increases in pore water pressure were observed during construction, the first occurred the day after the installation of the columns (day 57) and coincided with the commencement of Stage 2 works and the second coincided with the Stage 3b works. During Stage 2 the pore water pressure increased by approximately 70 kPa and a maximum pore water pressure of 127 kPa was measured. An approximately exponential decay of pore water pressure was observed after installation. The piezometer readings were taken manually during this time making detailed assessment of installation effects difficult. The data recorded during Stage 3b works was recorded on 4-hour intervals allowing analysis that is more detailed.

The measured increases in pore water pressure are due to: (1) increase in the sub-soil stress due to the embankment

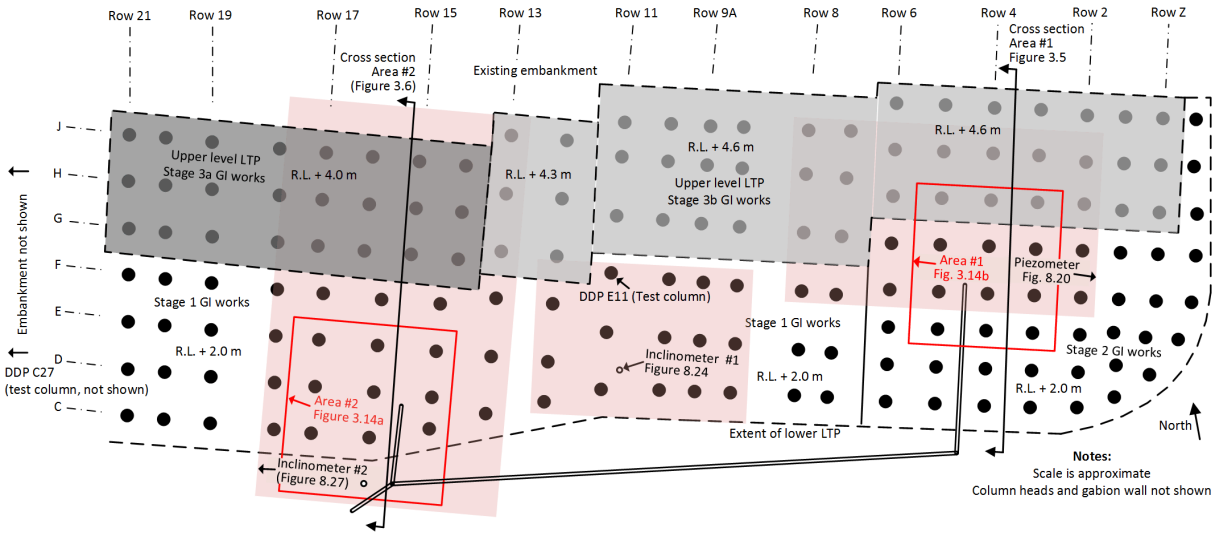

Figure 8.18. North Dynon embankment plan view

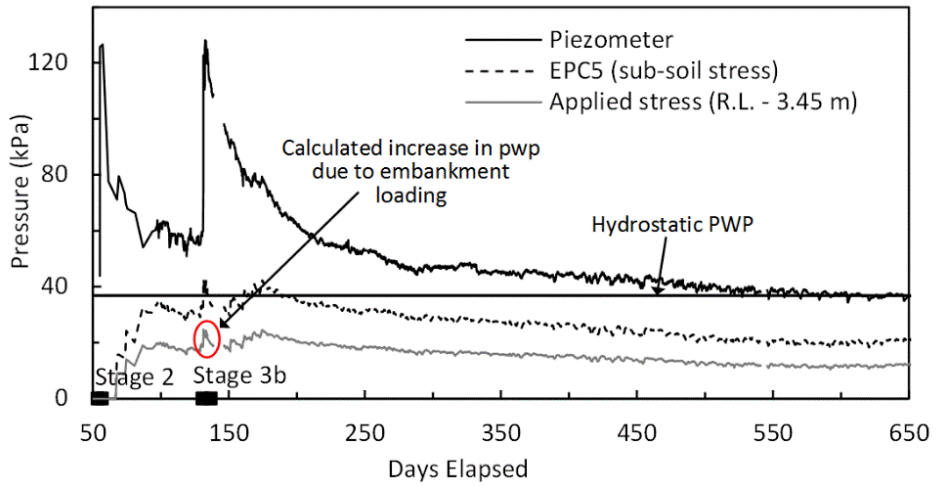

Figure 8.19. Long term piezometer data

load, and (2) increase due to column installation. Regarding point 1, the stress acting in the area between the columns was measured by EPC5 (see Section 5.3). By assuming a 1.5V:1H stress distribution with depth through the fill and Coode Island Silt units the applied vertical stress acting at the level of the piezometer can be estimated. This applied stress shown in Figure 8.19 indicates that most of the pore water increase was due to embankment loading between Stage 2 and Stage 3b works and during Stage 3b where the increase in pore water pressure was 70 kPa, the calculated increase in applied stress due to embankment loading is just 6 kPa. The majority of the measured pore water pressure increase can be attributed to column installation effects and shows a response similar to that observed by O'Neill et al. (1982) for a driven pile group installed into an over-consolidated clay.

A detailed plan view in Figure 8.20 indicates the location of the columns installed near Area #1 during the Stage 3b works between days 130 to 134. The response of the piezometer, EPCs and strain gauges during Stage 3b works is presented in Figure 8.21*a*, *b* and *c* respectively. The instrumentation layout in Area #1 was shown Figure 3.14*b*. A daily increase in pore water pressure can be observed during the working hours (7 am to 5 pm), at the completion of the day's work, partial dissipation of excess pore water pressure occurs overnight. The daily data indicates upper maxima of measured pore water pressure in the range of 125 to 130 kPa and is consistent with the maximum pore water pressure observed on day 57 during Stage 2 works.

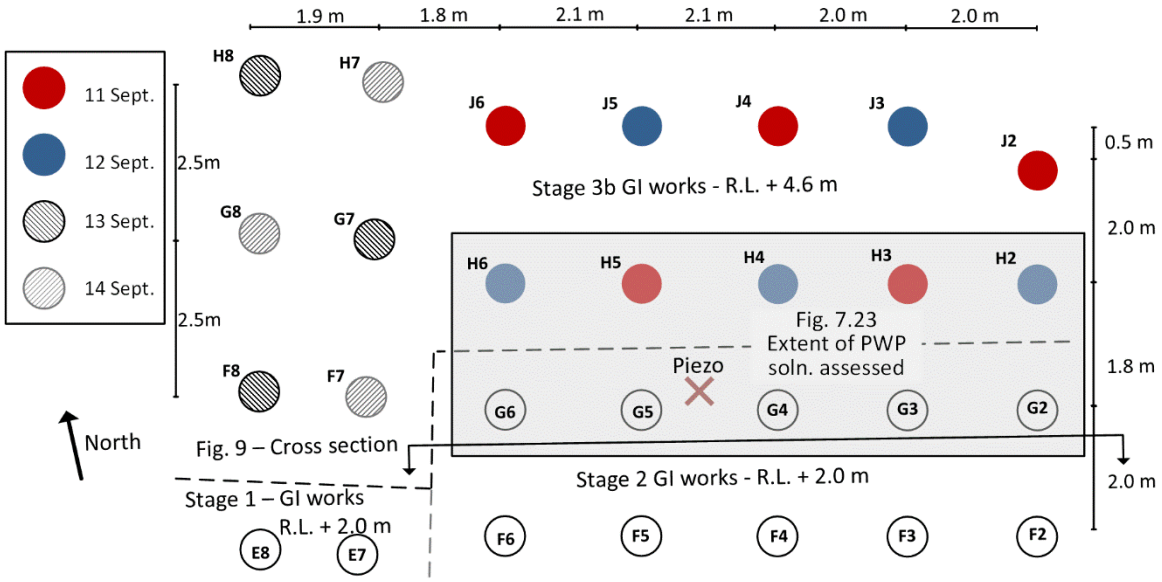

Figure 8.20. Layout of drilled displacement columns near Area #1

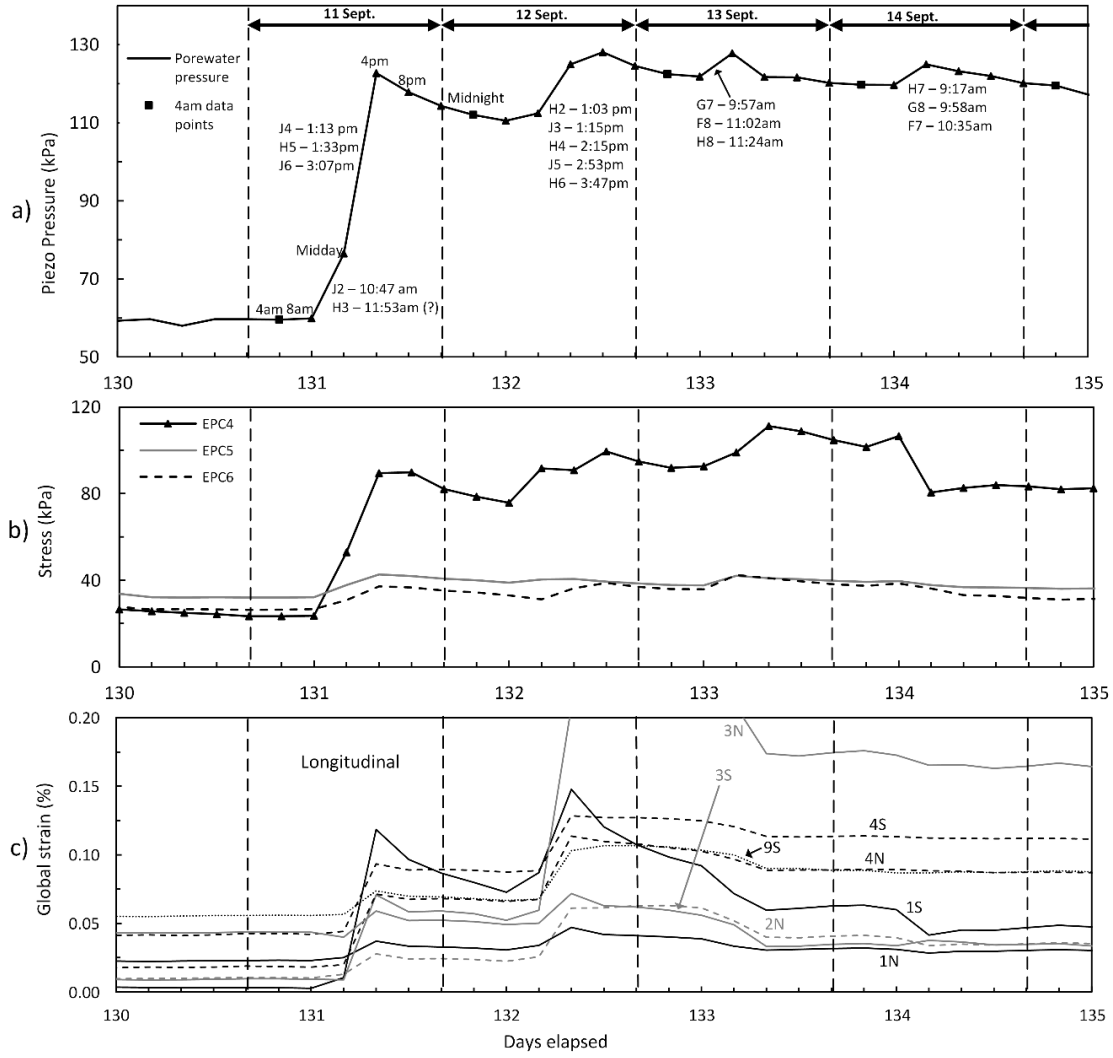

Figure 8.21. Response of **(a)** piezometer, **(b)** earth pressure cells and **(c)** longitudinal strain gauges to column installation

The EPCs show a similar response during this period despite the overburden pressure (2.7m height of embankment) being constant. It is inferred that the significant increase in vertical stress acting on the EPCs is due to uplift pressures generated in the Coode Island Silt. This effect is most pronounced on the column (EPC4) where it is inferred that the uplifted column is resisted by a passive arching mechanism (where the column is now the yielding support in a trapdoor analogy) which develops in the overlying soil mass as indicated in the Area #1 cross section (Figure 3.5). Similarly, uplift pressure acting in the area between the columns is inferred to cause the geogrid to deflect upward, resulting in tensile strain development (Figure 8.22). By comparison the transverse geogrid layer showed no significant strain development over the same period (see Figure 5.6 in Chapter 5). The difference in the response of the transverse layer compared with the longitudinal layer is due to the location of the anchorage zones. The anchorage zone of the transverse layer is located near the boundary of the lower and upper load transfer platform. The entire anchorage zone is uplifted as a result and minimal strain develops in the transverse layer. By comparison, the longitudinal layer is anchored at a distance sufficiently away from the installed columns, allowing the geogrid layer to resist uplift pressures. The result is the increased strain measured shown in Figure 8.21*c*.

As this uplift pressure in the Coode Island Silt dissipates following column installation (Figure 8.19), these tensile strains are also observed to reduce as the uplift pressure reduces (see long term strain readings in see Figure 5.6*a*, *b* in Chapter 5). The relatively uniform and temporary response of all longitudinal strain gauges during both of these periods (Figure 8.21*c*) is consistent with the uplift/heave mechanism described; the observed behaviour cannot be explained by tensile strain induced by downward sagging of the geogrid (i.e., membrane action due to arching stresses).

To provide a quantitative interpretation of the pore water pressure data, the pore water pressure response due to the installation of ten columns between 11 and 12 September was modelled based on the cylindrical cavity expansion theory outlined above. Over an area of 9 m by 7 m, and based on the Coode Island Silt properties at R.L. – 3.45 m (depth of piezometer), s_u = 25 kPa and G = 3200 kPa (see Chapter 4), the time-dependent axisymmetric equations for each column installation were solved. Based on these parameters, axisymmetric solutions plotted at various times after installation are presented in Figure 8.23, these solutions provide an indication of the magnitude

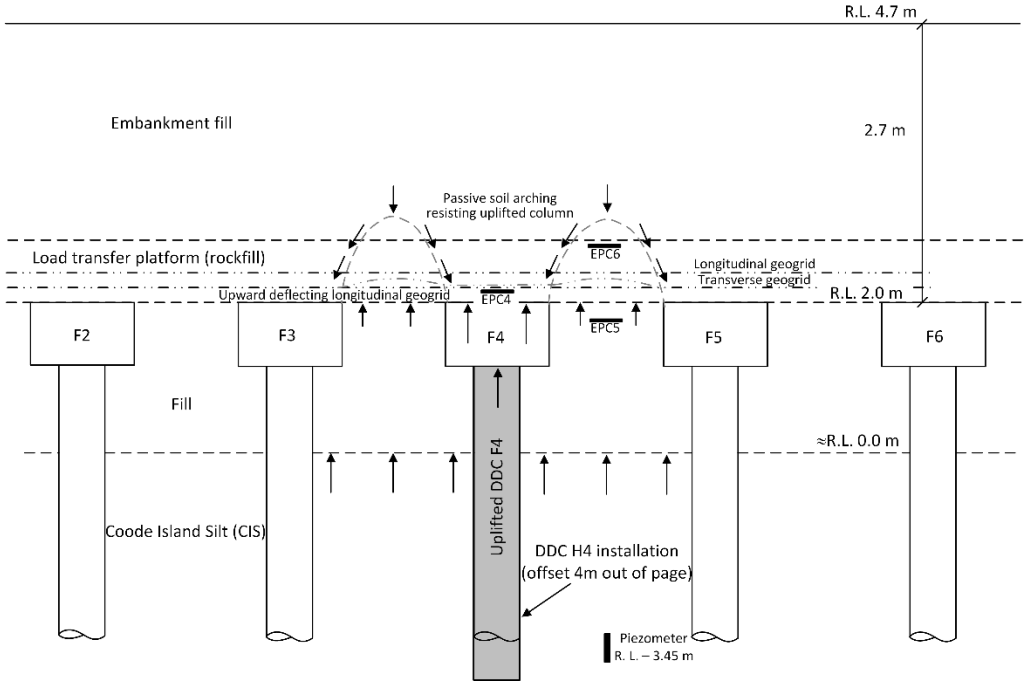

Figure 8.22. Inferred applied loadings acting on Area #1 during Stage 3b works

of pore water pressure increase in the vicinity of an isolated column as well as the rates of pore water pressure dissipation. The calculated excess pore water pressure surfaces were super-imposed in a spreadsheet application to assess the cumulative installation effect. Solutions at day 131 midday and 4 pm, day 132 at 8 am and 4 pm and day 133 at 8 am are presented (Figure 8.23*a*, *b*, *c*, *d* and *e*, respectively) representing the major periods of pore water pressure installation and equilibration. Figure 8.23*f* compares measured and calculated excess pore water pressure. The excess pore water pressure was calculated as absolute pore water pressure reading less the initial pore water pressure of 59.9 kPa (see Figure 8.19). The magnitude of discrepancy in pore water pressure between the calculated solutions and measured pore water pressure is considerable and the zone of influence predicted by cylindrical cavity expansion theory is not consistent with the observed data.

The initial pore water pressure distribution (Figure 8.7) reduced to 0 kPa at a radius of 2.54 m. This is not consistent with the increase in pore water pressure observed following the installation of columns J2 and H3 located

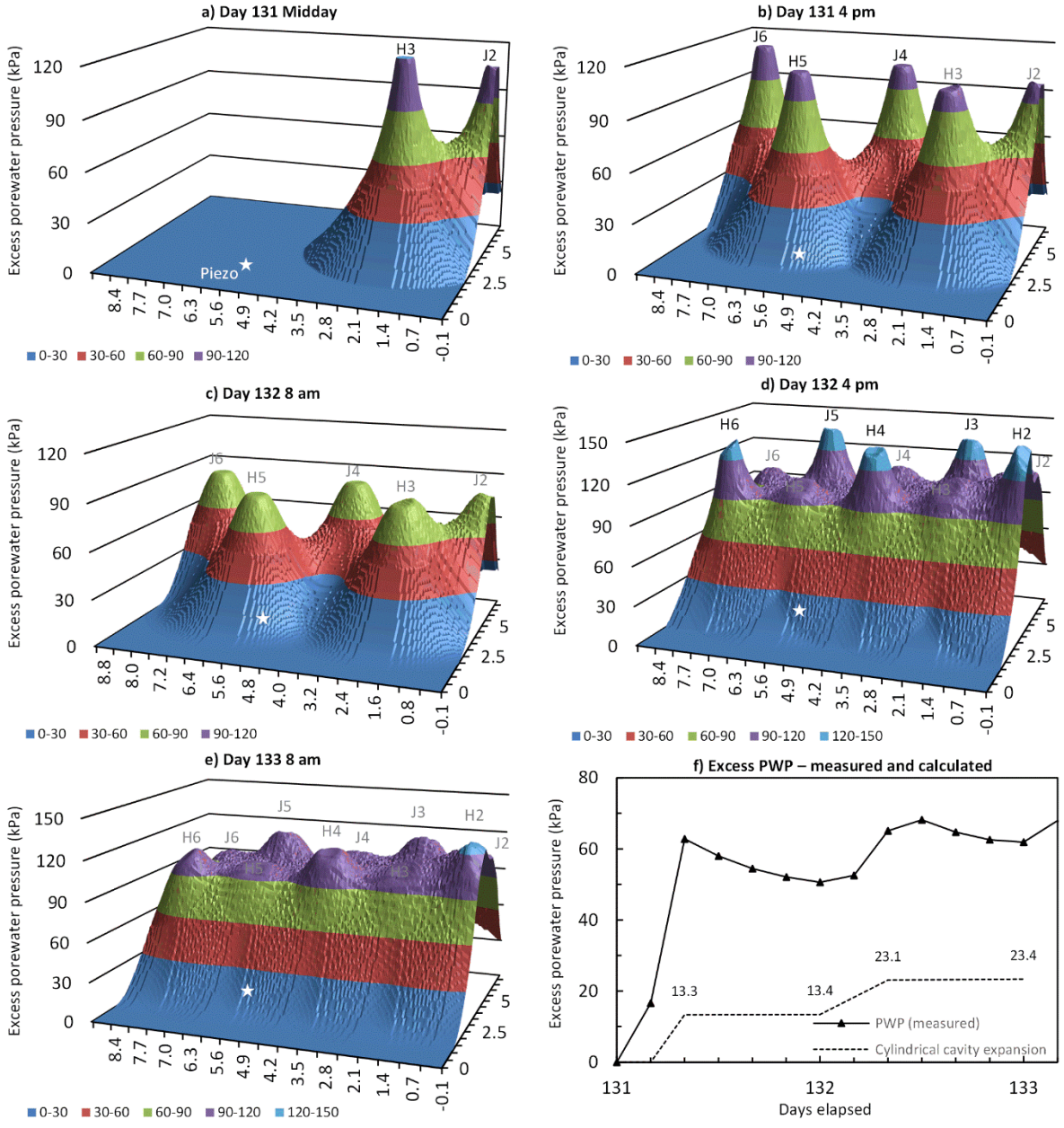

Figure 8.23. Porewater pressure development based on cylindrical cavity expansion theory; **(a)** day 131, midday, **(b)** day 131 at 4 pm, **(c)** day 132 at 8 am **(d)** data 132 at 4 pm **(e)** day 133 at 8 am and **(f)** plot of measured and calculated excess pore water pressure

at a radial distance of 13.9 m and 8.1 m respectively. Similarly, increases in pore water pressure were observed on days 133 and 134 due to columns installed at radial distances greater than 12.4 m and 11.4 m respectively. Increases in pore water pressure at a radial distance > 2.54 m were predicted to occur as part of the equilibration phase (Figure 8.7), however these increases were minor and did not increase until a number of day after installation. The cylindrical cavity expansion theory described above was developed for an elastic perfectly-plastic soil model to predict excess pore water pressure; shear induced pore water pressure is not described by this approach. Some portion of the difference in calculated and observed pore water pressure can be attributed to this effect, however, for slightly over- consolidated soil such as the Coode Island Silt this contribution is expected to be relatively small (Randolph 2003). It follows then that the difference arises due to the initial pore water pressure distribution adopted at the time of installation.

Hydraulic fracturing of clays due to column installation

It is inferred that the differences in the initial pore water pressure distribution is due to fracturing of the Coode Island Silt in the vicinity of the column shaft due to cumulative columns installations. This is suggested by an apparent upper bound of pore water pressure in the range of 125 kPa to 130 kPa observed on days 55, 57, 131, 132, 133 and 134, and in particular, the pore water pressure response on days 131 and 132 where five columns were installed on both days approximately symmetrical to the piezometer location. A similar pore water pressure response of about 60 kPa (day 131) would reasonably be expected on day 132 however the increase is just 17 kPa. This suggests an upper bound of excess pore water pressure of between 65 kPa and 70 kPa (125 kPa and 130 kPa absolute pore water pressure) in Figure 8.23. This result is consistent with the cylindrical cavity expansion results described in Section 8.3.2 which predict tensile stresses for certain soil conditions and a significant reduction in circumferential stresses for the soft soil encountered here. The superimposition of stress fields due to multiple column installations is hypothesised to lead to the development of tensile stresses (in the horizontal direction due to multiple circumferential stress reductions) and localised fracturing of the soil mass. It is inferred that through fracturing a significant portion of the excess pore water pressures in the immediate vicinity of the columns rapidly dissipate outward through vertical fractures orthogonal to the minor (circumferential/horizontal) principal stress axis. This forms a broad area of excess pore water pressure in the order of 70 kPa (130 kPa absolute pore water pressure) and results in higher pore water pressures generated at larger radi than was predicted in Figure 8.7. This behaviour has been previously shown for displacement piles by Massarsch et al. (1977), Randolph et al. (1979) and Asaoka et al. (1994). The hydraulic fracturing of soils due to deep mixed columns by Shen et al. (2003) and Shen et al. (2004) and in grouting applications by Gottardi et al. (2008) and Marchi et al. (2013) is also well documented.

Marachi et al. (2013) provides an overview of various theoretical and empirical equations used to calculate the fracturing (hydraulic) pressure, P_f, in clays. These theoretical approaches are generally based on cylindrical cavity expansion theory applied to soil models with either a tensile or shear failure criteria. Based on a considerable amount of experimental data, Marchi et al. (2013) showed that while conditions such as initial stress, strength, stiffness, OCR and moisture content influence P_f, the key factor is the confining pressure σ_0 (initial minor principal stress). The equation proposed by Soga et al. (2005) (Equation 8.21) describes a shear failure criteria where n is an empirical factor and s_u the undrained shear strength. Based on experimental data plotting P_f vs σ_0 it was shown that the linear gradient (n value) of data for soils with a liquidity index (I_L) = 0.5 was typically 1.0.

$$P_f = \sigma_0 + n s_u \quad \textbf{(8.21)}$$

$$P_f = \sigma'_0 + u + ns_u \quad \textbf{(8.22)}$$

Equation 8.21 can be reinterpreted in terms of effective stress and porewater pressure (Equation 8.22). As the hydraulic fracture pressure and the porewater pressure are the same in this case, this expression simply states that a shear failure criteria will occur when the negative (tensile) minor effective stress (circumferential) is less than, or equal to, the undrained shear strength. The effective stress conditions immediately after installation were shown in Figure 8.9*a* where it was shown that σ'_θ was reduced significantly from the initial *in situ* σ'_{h0} value. In addition, it can be seen that the zone of influence is in the order of 50 r/r_0, or about 11.25 m. It is hypothesised that the cumulative reduction in σ'_θ due to multiple column installation will eventually induce tensile stress conditions leading to fracturing of the soil mass. This then allows excess pore water to radiate further than would otherwise be expected. Shen et al. (1999) have previously shown this to occur for deep soil mixed applications, with vertical fractures first occurring then horizontal fractures developing due to cumulative installation.

8.4.2 Installation effects – lateral deformation

Inclinometer #1

The location of Inclinometer #1 and its axes along with date, time and location of adjacent columns is presented in Figure 8.24. The column installations and inclinometer readings took place between 12 March to 3 April 2013 and are listed in Table 3.1. Also, shown in Table 3.1 is the radial distance (r) from inclinometer to columns, r/D ratio and time between installation and the subsequent inclinometer reading. Due to site constraints, the inclinometer readings were generally taken at either the start or end of the work day. The data is described by five phases, where a phase is one or more column installations followed by a reading. The inclinometer was decommissioned after the last reading taken on 3 April 2013.

The incremental lateral displacement for the five phases and sub-surface conditions are shown in Figure 8.25 along with the predicted lateral displacement based on Equation 8.19. The general shape of the lateral displacement profile observed is relatively consistent between the various phases. Large lateral movement in the Coode Island Silt, particularly near the upper surface is observed and the magnitude of lateral movement correlates with the radial distance. A maximum of lateral displacement of up to 60 mm is consistently observed at about 2 m below the fill-Coode Island Silt interface (R.L. −2 m) and it appears that the overlying stiff fill unit acts as a lateral restraint.

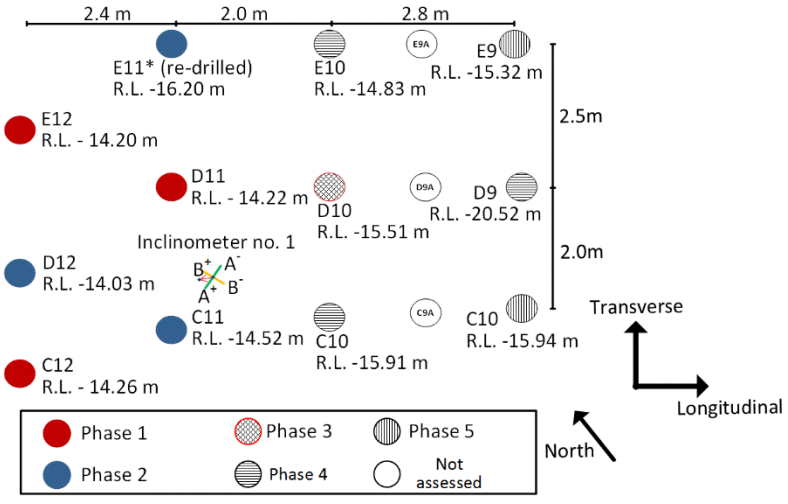

Figure 8.24. Inclinometer #1 and column locations

Table 8.2. Inclinometer #1 timeline

Activity	Date & Time	Time from column install to reading (hours:minutes)	Phase	Radial distance (m)	*r*/*D*
C12	15 March 2:17 pm	3:39	**Phase 1**	3.47	7.7
E12	15 March 2:45 pm	3:11		3.99	8.9
D11	15 March 3:22 pm	2:34		1.71	3.8
Inclinometer reading	15 March 5:22 pm				
E11	16 March 3:22 pm	2 days, 4:00	**Phase 2**	4.15	9.2
D12	18 March 1:49 pm	3:41		3.06	6.8
C11	18 March 2:41 pm	2:49		1.12	2.5
Inclinometer reading	18 March 5:30 pm				
Inclinometer reading	20 March 3:47 pm		**Phase 2b**		
D10	25 March 2:26 pm	17:47	**Phase 3**	2.41	5.4
Inclinometer reading	26 March 8:13 am				
E10	26 March 10:43 am	21:32	**Phase 4**	4.48	10.0
C10	26 March 11:21 am	20:54		1.96	4.4
D9	26 March 12:03 pm	20:12		5.13	11.4
Inclinometer reading	27 March 8:15 am				
C9	27 March 10:49 am	4 days 2:11	**Phase 5**	4.92	10.9
E9	27 March 10:21 am	4 days 2:39		6.28	14.0
Inclinometer reading	3 April 1:00 pm				

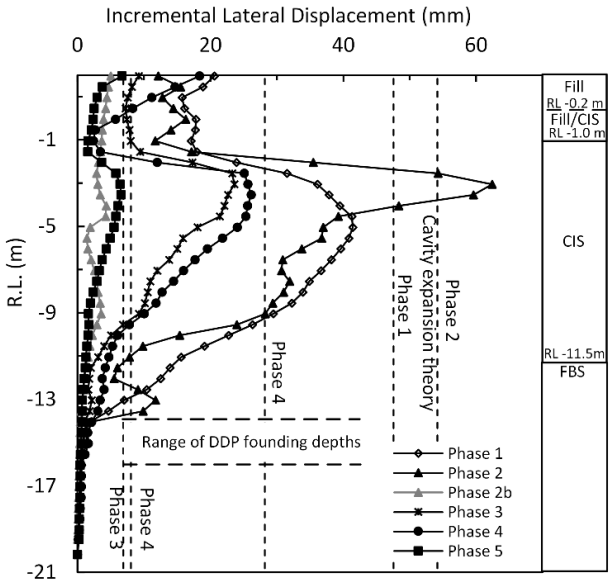

Figure 8.25. Incremental lateral displacement for Phases 1 to 5 – Inclinometer #1

However, Larisch et al. (2014) also observed similar behaviour in a soil profile comprising stiff clay overlying hard clay. It is inferred that this displacement response is dominated by soil heave during the first few meters of penetration (i.e., resembles spherical cavity expansion). The volumetric soil heave due to installation is well described by Larisch et al. (2014). The displacement response transitions to a primarily lateral response at about 2 m (4.4D) for Larisch et al. (2014) and at about 4 m (8.8*D*) in this case. The consistent response observed from multiple columns installations at the two sites, with identical drilling tools and installation methods, suggests that ground conditions influence the heave response and that heave failure mechanism extends to a deeper depth where weaker ground conditions exist at the ground surface (i.e., the North Dynon site).

This lateral displacement profile observed results in three points of inflexion in the profile; this has important implications when back calculating the internal bending moments of the column in Section 9.2. The lateral displacement profiles at the toe of the columns shows negligible movement (< 2mm) and matches closely with the shape of the auger head. It is likely that the stress condition at the shaft interface, near the base, is more closely

resembling that of a non-displacement piles i.e., a K_o stress condition. The majority of the increase in shaft capacity is therefore likely to occur further up the shaft (at least 1.5 m above the toe) where the displacement body has fully displaced soil laterally. See Table 8.1 for drilling tool dimensions.

However, assessment of lateral displacement provides only limited insight into the three-dimensional nature of the problem. A vector diagram showing the directional and magnitude of lateral movement at R.L. −3.55 m is presented in Figure 8.26. Displacement vectors are inversely scaled based on the radial distance (i.e., vector length ≈ 1/r) and a resultant vector for each phase is shown. The resultant phase vectors do notalign precisely with the measured soil movement, although the general agreement is good (Figure 8.26). This is due to time-dependent effects, with different columns in different phases of equilibration, which are not described by the linear superimposition of vectors. However, the general agreement is reasonable as the magnitude of soil displacement is dominated by the installation phase. The effect of the additional columns installed beyond the extent shown in Figure 8.24 is also a contributory factor in the difference between resultant phase vectors and measured direction of soil movement.

Inclinometer #2

Inclinometer #2 was installed to assess column installation effects and long term embankment behaviour. The information is presented below in a similar manner to Inclinometer #1 above. The installed columns adjacent to Inclinometer #2 are shown in Figure 8.27. Additional information relating to the installed columns and inclinometer readings is presented in Table 8.3. The lateral movement associated with the various phases (Figure 8.28) is similar to the response measured by inclinometer #1, although the general magnitude of movement is less. This is consistent with the increased radial distance of inclinometer #2 relative to the installed columns. Figure 8.29 presents a vector diagram of soil movement at R.L. −2.9 m assessed by Inclinometer #2. The directional component of soil movement is predominately in the transverse direction away from the embankment (−ve Y-axis) with a minor component of movement in the longitudinal direction (+ve X-axis). This is consistent with the spatial distribution of the Stage 1 columns (Figure 3.4).

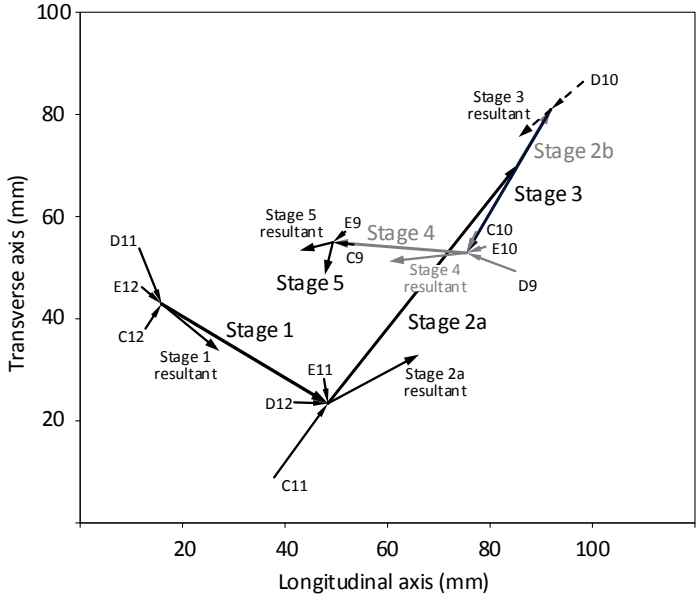

Figure 8.26. Vector diagram (R.L. -3.5m) – Inclinometer #1

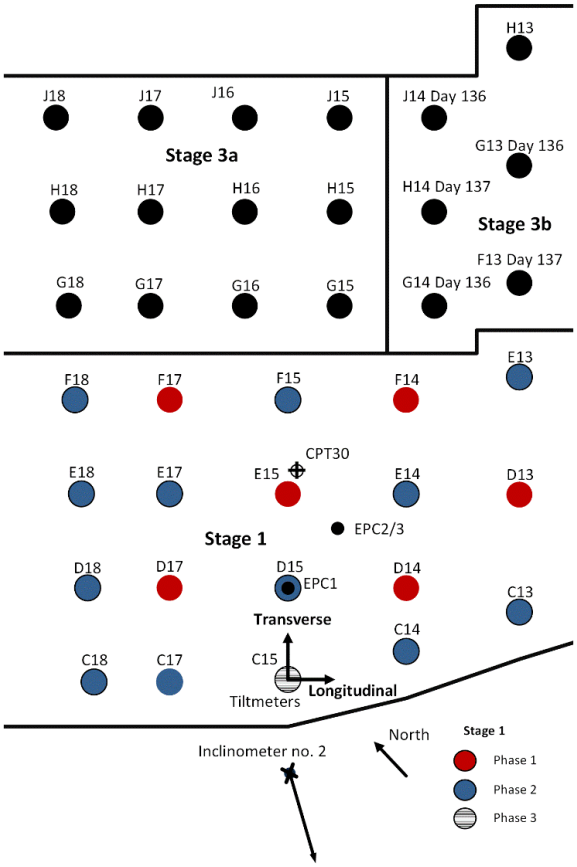

Figure 8.27. Inclinometer #2 – Layout of columns

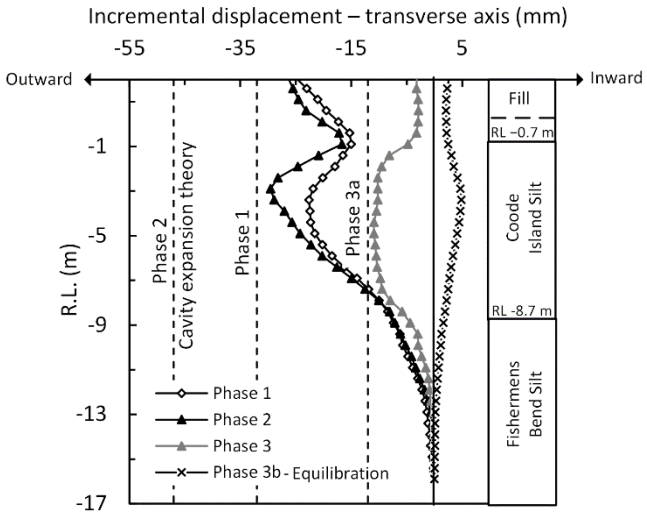

Figure 8.28. Inclinometer #2 Y−axis displacement Stage 1 works

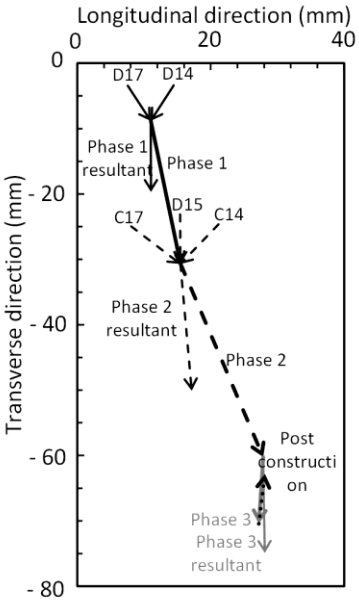

Figure 8.29. Lateral movement at R.L. −2.9 m (Plan View) - Inclinometer #2

Table 8.3. Inclinometer #2 readings – Stage 1 timeline

Activity	Time - install to next reading (hours:minutes)	Phase no.	Angle (°)	Radius (m)	r/D	Cavity exp. soln (mm)	Resultant radius (m)	Cavity exp. soln Vector resultant (mm)
D17 - 15 March 11:13 am	3:27	Phase 1	11	4.68	10	5.4	3.58	4.1
F17 - 15 March 11:34 am	3:06		26	8.34	19	3.0	7.55	2.7
E15 - 15 March 11:58 am	2:42		43	5.96	13	4.2	5.90	4.2
D14 - 15 March 12:38 pm	2:02		75	4.68	10	5.4	4.26	4.9
F14 - 15 March 12:56 pm	1:44		60	8.34	19	3.0	8.22	3.0
D13 - 15 March 2:01 pm	0:39		82	7.69	17	3.3	6.55	2.8
Resultant - Inclio reading 15 March 2:40 pm			231			24.0		21.8
F15 - 16 March 10:58 am	9 days 22:40	Phase 2	43	7.96	18	3.2	7.86	3.1
E17 - 16 March 11:34 am	9 days 23:16		7	7.39	16	3.4	6.56	3.0
D15 - 18 March 11:16 am	7 days 23:32		43	3.96	9	6.4	3.91	6.3
C17 - 18 March 11:56 am	7 days 22:52		-9	3.18	7	7.9	2.32	5.8
E14 - 18 March 12:06 pm	7 days 22:42		66	6.46	14	3.9	5.50	3.3
C14 - 18 March 12:25pm	7 days 22:23		87	3.61	8	7.0	2.20	4.3
E13 - 18 March 1:09 pm	7 days 21:39		73	9.75	22	2.6	7.59	2.0
C13 - 18 March 1:33 pm	7 days 21:15		98	5.98	13	4.2	2.65	1.9
D18 - 22 March 11:33 am	3 day 23:15		-4	5.80	13	4.4	4.56	3.4
F18 - 22 March 11:50 am	3 day 22:58		14	9.14	20	2.8	8.56	2.6
C18 - 25 March 12:51 pm	1 day 21:57		-21	4.54	10	5.6	2.56	3.1
E18 - 25 March 1:14 pm	1 day 21:34		7	7.39	16	3.4	6.56	3.0
Resultant - Inclio reading 26 March 10:48 am			214			55		42.0
C15 - 27 March 9:23 am	3:37	Phase 3a	48	2.04	5	12.3	2.04	12.3
Resultant - Inclio reading 27 March 1:00 pm						12.3		12.3
Inclio reading - 5 July	100 days	Phase 3b						

8.4.3 Installation effects – cumulative

Multiple columns were installed for Stage 3a and 3b works; these installation effects are assessed through the data from Inclinometer #2. The dates of the inclinometer readings and their relationship with the various stages of ground improvement works are shown in Table 8.4. Various cumulative and incremental inclinometer profiles are plotted in the transverse (Y-axis) direction (Figure 8.30). The longitudinal movement (X-dir.) during this period was minimal. The first three cumulative profiles show the lateral displacement due to Stage 1, Stage 3a and Stage 3b works. The fourth profile shows the long term behaviour over a period of 660 days (day 160 to 741). The lateral displacement measured during this period corresponds to the period where the Coode Island Silt has undergone long term equilibration and is observed as 10 mm of movement towards the embankment. A further five incremental profiles are shown which describe the installation and/or equilibration phases associated with Stage 3a, Stage 3b works and the long term condition. For these phases, installation causes movement away from the embankment and equilibration cause movement towards the embankment. The response due to the Stage 1 works (Figure 8.28) was the same.

The equilibration causes inward movement of the columns that is in a direction opposite to the outward movement of the embankment caused by lateral spreading and/or embankment instability. The equilibration imposes lateral movement and loadings on the columns that are not typically considered, or recognised, when describing GRCSE behaviour based on numerical analysis that ignored installation effects.

8.4.4 Effects on arching

The collapse of the arching due to the Stage 3b works was observed by the EPCs and tiltmeters (Figure 8.31) and was discussed briefly in Section 5.5 and 5.6 where the Area #2 instrumentation was presented. Based on the inclinometer data (Figure 8.30), the tiltmeter data (Figure 8.31) and the strong correlation with the installation times, it is likely that the primary cause of the arching collapse is lateral movement of the soil mass where arching is occurring (i.e., in the rockfill material). Vibrations caused by the piling works (rig tracking, drilling etc.) may be

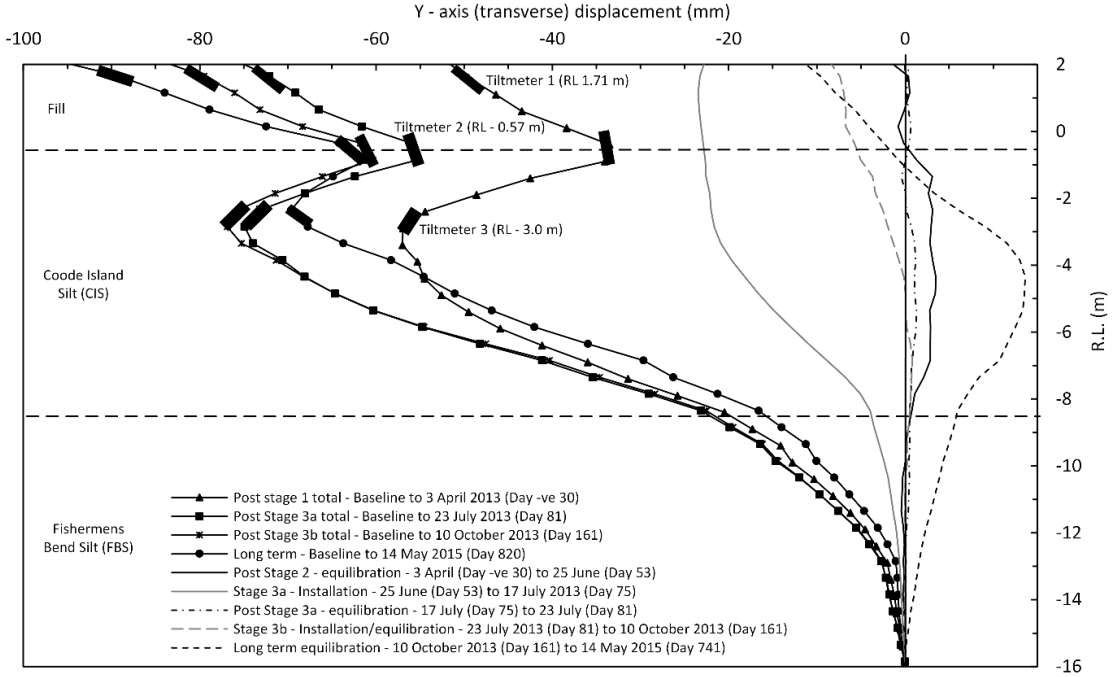

Figure 8.30. Inclinometer #2 long term data

Table 8.4. Long term readings – Inclinometer #2 readings

Date & Time	Days elapsed	Phase
13 March	-51	Baseline
14 – 27 March (4 readings)	-50 to -37	Stage 1 GI works - Installation
3 April	-30	Stage 1 GI works - equilibration
17 May	14	
21 May	18	
28 May	25	
4 June	32	
20 June	48	
25 June	53	
5 July	63	
5 to 13 July (no readings)	63 to 71	Stage 3a GI work - Installation
23 July	81	Equilibration
11 to 17 Sept. (no readings)	131 to 137	Stage 3b GI work - Installation
10 October	160	Equilibration
14 May 2015	741	

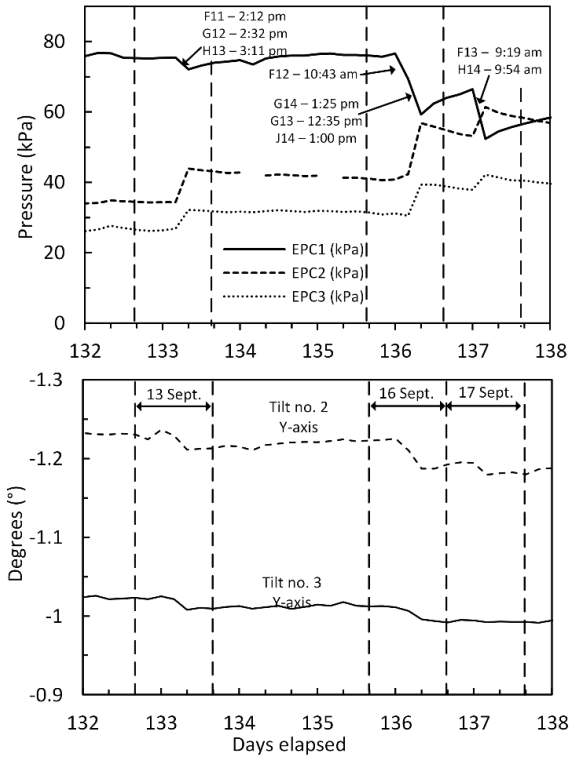

Figure 8.31. EPC and tiltmeter response during Stage 3b works

expected to contribute, however one would expect to observe this throughout the Stage 3b works, which it is not the case. The nearest column installed as part of Stage 3b was G12 at a distance of 8.2 m (12.4 D). Columns installation on day 133 were at > 10.2 m (20D). From Equation 8.19 the lateral displacement is predicted to be 5.0 mm at 5 m and 2.5 mm at 10 m offset. These predictions, and the observed behaviour, highlight the susceptibility of the arching stresses are to external disturbance. The behaviour observed here suggests that just several millimetres of lateral movement is sufficient to cause the arching to collapse. However, as described in Chapter 5, the arching stress quickly redevelop as the sub-soil settlement occurs under stresses close to the overburden pressure (i.e., 55 kPa in Figure 8.31).

This behaviour highlights an important aspect of the arching stress-deformation relationship that is seldom recognised in GRCSEs. If arching collapses, in order for the arching stresses to reform this must be accompanied with sub-soil settlement and/or deflection of the geogrid layer for arching stresses to re-develop. Theoretically, this could lead to the geogrid layer being overstressed if repeatedly subjected to stresses close to the overburden pressure (assuming it was designed for much lower stresses such as those encountered near maximum arching). Earthquake loading, traffic loading and other forms of dynamic loading may provide the necessary repetitive conditions for this failure mechanism to develop over the long term. This was discussed previously in Section 7.5.6.

8.5 Interpretation of installation effects

By normalising the lateral displacement profiles from inclinometer #2 (Figure 8.32*d*), a reasonably consistent profile of lateral deformation with depth is evident. Similar profiles were observed by Skinner et al. (2003), Larisch (2014) (Figure 8.12) and Suleiman et al. (2015). These differ considerably from the uniform lateral deformation predicted by cavity expansion theory and it is of interest to explore the reasons for this. A β value equal to 1 in Equation 8.19 is used to describe the installation of a rigid body such as a driven pile. By using a β value of less than 1 in the radial displacement equation (Equation 8.19) previous researchers (Pestana et al. 2002) have been able to make reasonable prediction of lateral displacement for steel tube piles. Using linear optimisation it was found that $\beta = 0.55$ provides a good estimate of the maximum lateral displacement in the Coode Island Silt. There are several factors which may explain a $\beta < 1$: (1) the column immediately after installation is not rigid and is therefore not consistent with an expanding rigid cavity, (2) the displacement fields do not achieve a true cylindrical cavity expansion, where displacement is radial only due to the first item as well as the auger mechanics and crowd pressure creating a significant component of vertical displacement. However, a value of $\beta < 1$ does not explain the non-uniform deformation with depth. It is postulated that the observed behaviour can be explained by the effective stress and pore water pressure conditions at the column/soil shaft interface as outlined below:

Maximum lateral displacement

The initial axisymmetric displacement field due to the drilling and extraction of the auger head can be approximated by a modified cylindrical cavity expansion displacement field using a reduced value of β and Equation 8.19. A value of $\beta = 0.55$ was found to reasonably predict the maximum lateral displacement in this case.

Effective stress condition at column interface

After the drilling tool has been extracted, a state of equilibrium must exist between internal and external fluid pressures at the column/soil interface as well as effectives stresses at the column/soil interface. The radial effective stress (σ_r') acts inwards and can be predicted using cylindrical cavity expansion theory (e.g. Figure 8.9). For a driven pile, σ_r' acts on the (rigid) pile shaft, however, for a column comprising a liquid slurry this stress is out-of-balance at

the end of the concreting phase. The out-of-balance effective radial stress must lead to "relaxation" of radial stresses at the pile shaft immediately after construction and inward radial strains.

An advancing and retracting drilling tool does not fully satisfy the assumptions of cylindrical cavity expansion, however, as an approximation the assumption of cylindrical expansion would appear to be reasonable. The end of installation stress predicted by cylindrical cavity expansion likely provides a reasonable prediction of the stress conditions at a depth within the soil mass at the moment the drilling tool passes (see Figure 8.11). However, as the drilling tool is advanced, or extracted further, stresses relaxation ($\sigma'_r \rightarrow 0$) at the interface will alter the stress conditions established. Based on cylindrical cavity expansion theory outlined earlier, and assuming a modified Cam-Clay material, the value of σ'_r can be predicted from Equation 8.23. Immediately after installation, the soil adjacent to the column fails and the effective stress is given by the condition at the critical state line for the modified Cam-Clay material (Randolph et al. 1979) as follows:

$$\sigma_r' = s_u \left[\left(\frac{\sqrt{3}}{M} \right) + 1 \right] \qquad \textbf{(8.23)}$$

$$\text{where } M = \frac{6\sin(\emptyset')}{3 - \sin(\emptyset')}$$

For the Coode Island Silt considered in Figure 8.23 at R.L. -3.55 m (s_u = 25 kPa and ϕ = 30°), the value of σ'_r is equal to 68 kPa or 2.7s_u. The variation in effective radial stress with depth is shown in Figure 8.32*c*. These results indicate that stress "relaxation" will vary considerably with depth and primarily as a function of undrained shear strength. The rebound of the soil mass at the interface will be most pronounced at the base of the pile. The most compelling data supporting this hypothesis is from Suleiman et al. (2015). The variation in horizontal stress during drilling was shown to cause a significant increase in horizontal stress followed by a significant decrease as the displacement body passed the push-in place sensor. This was shown during both drilling and extraction. It is inferred from the instrumentation description in Suleiman et al. (2015) that the push-in place total pressure cells (with pore water pressure sensors) are oriented with the plane of measurement in the circumferential direction and the normal to this plane is in the radial direction. i.e., the "horizontal" stress described by Suleiman et al. (2015) is a radial stress, circumferential and vertical stresses act perpendicular to the instrument. This was shown as a function of installation stages in Figure 8.11*b*. This time-dependent behaviour is shown in Figure 8.33.

Lateral movement of the soil mass was also directly measured by Suleiman et al. (2015) both during, and after the installation of the Controlled Modulus Column using a shape acceleration array. While the inward lateral movement may be explained by radial consolidation it was also shown that excess pore water pressure dissipated (see Suleiman et al. 2015) in about 3 minutes at radi of 2D, 3D and 4D when the drilling tool was at bottom depth and stationary. Radial consolidation of the soil mass does not explain the inward lateral displacement measured as there was no excess porewater pressure present. This behaviour is due to the unloading of radial stresses at the column interface.

It is postulated that the radial stresses at the column/soil interface will be approximately zero immediately after installation. However, as the column is in a liquid state it is not possible to demonstrate the resulting reduced shaft capacity. The analysis presented has postulated that the effective radial stresses that are predicted to occur from cylindrical cavity expansion theory for driven piles at the time of installation will not eventuate for drilled displacement piles.

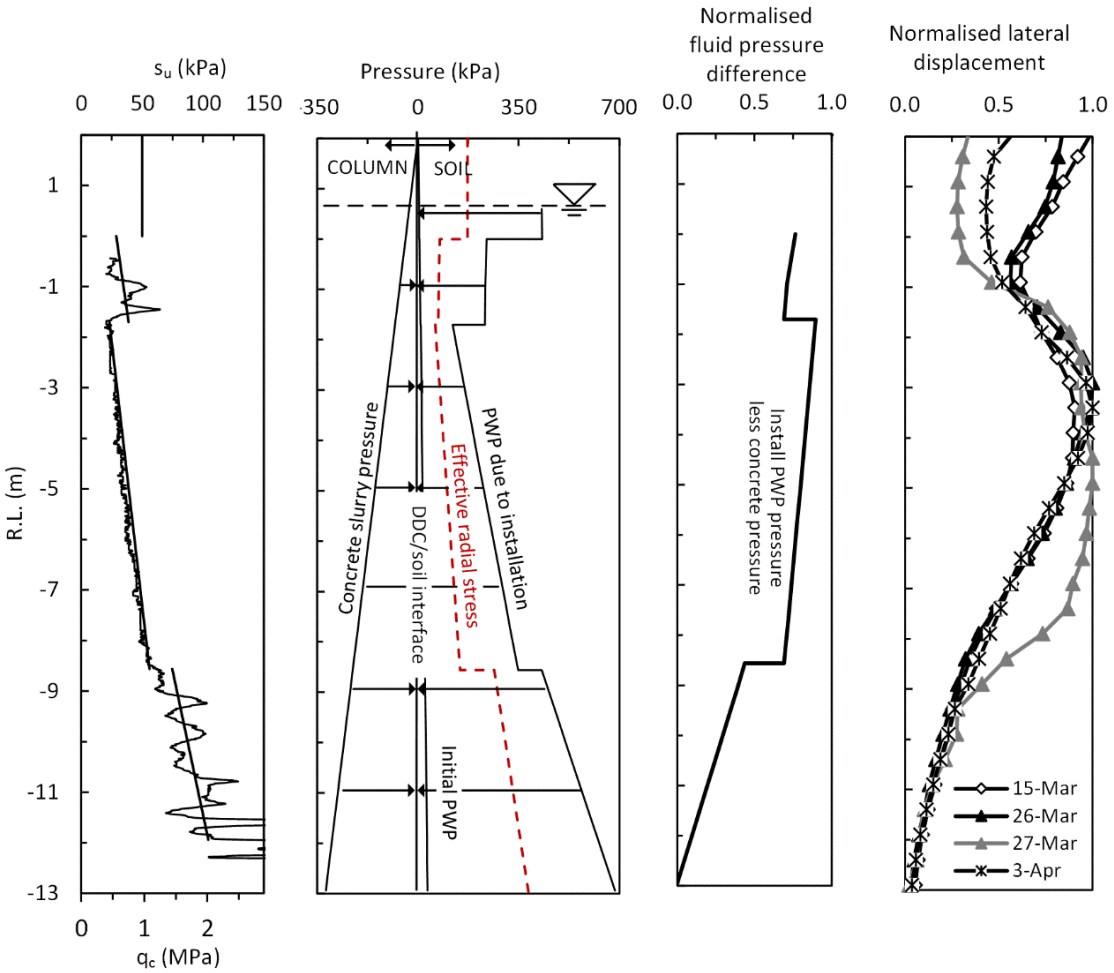

Figure 8.32. (a) Undrained shear strength profile CPT30, **(b)** pressure acting at column/Soil interface immediately after pile installation, **(c)** normalised pressure difference and **(d)** normalised lateral displacement

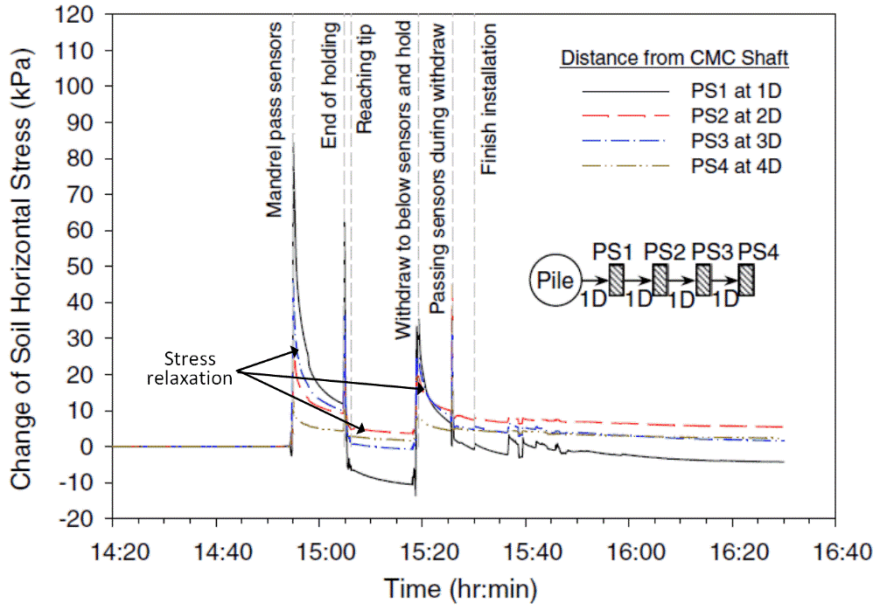

Figure 8.33. Time-dependent variation in horizontal (radial) stress during column installation (after Suleiman et al. (2015)

However, while installation stresses are not expected to develop, the time-dependent increase in effective radial stresses due to radial consolidation is expected to play a considerable part in the development of the stress conditions surrounding the column. In Figure 8.9*a* and *b* the installation stresses and long term stresses due to driven

pile installation into a normally consolidated clay were compared and it was shown that effective radial stress increased by about 100 % over this period. It follows then that the shaft capacity mobilised will be strongly time-dependent as the stress conditions at the shaft interface (σ'_r) increase from a near zero value as radial consolidation occurs.

Out-of-balance fluid pressure at column interface

During the concreting phase the withdrawal rate is varied in order to maintain a target grout pressure, this is described in detail by NeSmith (2002). The concept of constructing the column based on grout pressure reflects the varying external pressure acting at the pile interface (Figure 8.32*b*) and is further supported by observations described by NeSmith (2002), that under a constant withdrawal rate, grout pressures were higher in dense sands and reduced as the auger head based through loose sand and soft fine grained material. Whilst the slurry pressures during the concreting phase may match the pore water pressure at the interface, and in many cases exceed this pressure, this condition is temporary and cannot be controlled once the auger head is removed. Once this occurs the grout pressure reverts to a hydrostatic condition.

The drilled displacement columns are unique in that the curing of the concrete slurry occurs in a soil mass with lateral stresses and pore water pressure that have increased significantly due to the installation process. The fluid pressure at the column/soil interface immediately after extraction of the drilling tool comprises an internal fluid pressure; the concrete slurry in a hydrostatic condition (assumed density $\gamma = 2180$ kg/m^3) and an external fluid pressure; the pore water pressure acting at the interface. This is shown in Figure 8.34 where the internal and external fluid pressure is shown as a function of radius. The pore water pressure acting can be predicted from Equation 8.10 and is also shown in Figure 8.32*c* where the inverse normalised pressure difference at the interface is calculated as $1 - (\sigma_{pd}/\sigma_{pd.max})$ where σ_{pd} is defined as pore water pressure minus slurry pressure. The positive normalised pressure difference indicates that over the entire depth the net fluid pressure acting at the interface is inward. This pressure difference will result in an inward flow of pore water into the concrete slurry. At RL −3.45 m, shown in Figure 8.34, this net inward flow will approximately occur to a radius of about 0.4 m from the centre of the column (approximately 150 mm radial distance from the interface). After approximately one day the external pore water pressure is calculated to dissipate (assuming outward radial drainage only) to less than the concrete slurry pressure. The flow of groundwater will then revert to outward radial flow only (i.e., as typically encountered for displacement piles. Note that the out-of-balance fluid pressure is greater in the near surface fill and in the Fishermens Bend Silt.

This inward flow and interaction with the concrete has the potential to be problematic for three reasons; 1) the concrete slurry is initially curing in a liquid state when excess pore water pressures are greatest, 2) Coode Island Silt is a well-known acid sulphate soil and its porewater is highly aggressive towards concrete and 3) the interaction with the ground water occurs around the periphery of the columns where concrete cover may be required. Therefore, it is of interest to assess the potential for any detrimental effects on the concrete curing around the periphery of the column. The rate of flow at the interface is a complex transient groundwater flow problem governed by a time-dependent (increasing) permeability of the concrete slurry and an external (decreasing) pore water pressure dissipating with time. A first order approximation can however be obtained by applying Darcy's law. The variation in permeability of typical concrete is shown in Figure 8.35 as a function of water content (w/c) and time. The initial permeability of the concrete slurry will be in the order of 10^{-5} to 10^{-6} m/s (Hilsdorf et al. 2004). Based on the construction records which indicated a slurry w/c of 0.7, aggregate size of 7 mm and Figure 8.35*a*, the permeability of the hardened concrete will be in the order of 10^{-12} m/s. It follows then that the initial inward flow of porewater

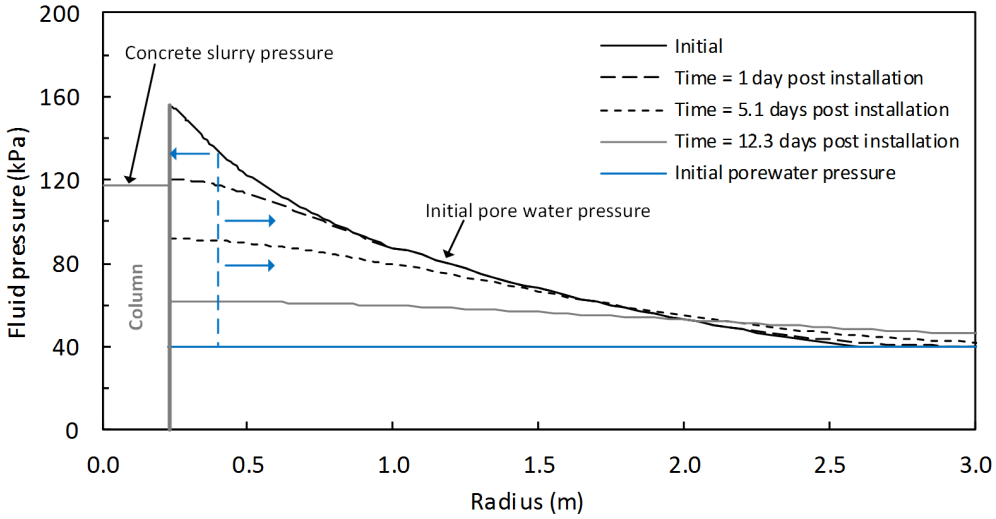

Figure 8.34. Fluid pressure at a function of radius at RL – 3.45 m

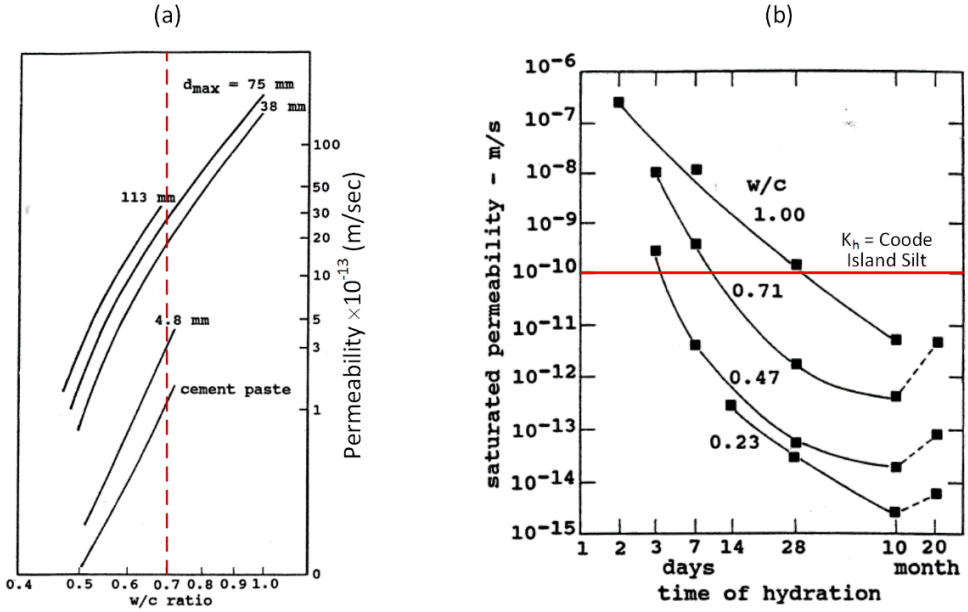

Figure 8.35. Permeability of typical concrete **(a)** *vs* w/c ratio (USBR 1975) and **(b)** *vs* time (Nyame et al. 1981)

will be controlled by the lower permeability of the remoulded Coode Island Silt.at the interface. This is estimated to be in the order of 10^{-10} m/s (see *e*-log (k_v) plot in Figure B12*c* in Appendix B).

If the inward flow is approximated by describing the flow between 0.225 m < *r* < 0.4 m under a 20 kPa pressure difference and permeability of 10^{-10} m/s the calculated flow rate through the column interface per meter depth of column is approximately 0.1 litres/day. The outer 50 mm of the column has a volume of 33 litres and so by comparison this calculated inflow is negligible. This is due largely to the very low permeability of the remoulded soil at the interface that is likely to significantly restrict inward flow more than the concrete slurry permeability and the rapidly dissipating excess pore water pressure in the soil mass. In addition, analysis presented earlier in this chapter indicates the hydraulic fracturing of the soil mass is likely to limit these large excess pore water pressures from developing in the first instance.

Concreting phase

Based on the analysis presented here, a number of questions are raised regarding the validity of the plots of drilled displacement column cross sectional area produced based on instantaneous grout pressure and withdrawal rate (see

Figure 8.3 for the profile for column E19). These construction records are frequently used to "validate" the construction methodology and confirm that the design cross sectional area of the column has been achieved; this approach is questionable as it bears no relationship with the pressure-deformation behaviour at the shaft/soil interface. The pressure-deformation relationship at the interface governs the final cross sectional area of the column. This current approach, in the author's opinion, provides a misleading interpretation (on the unsafe side) of the column cross sectional area.

While some may refer to the extensive number of dynamic and static load tests as proof of the suitability of the construction method it is highly likely that any reduction in the cross sectional area of the column is offset considerably by the increase in radial stresses at the shaft interface. Perhaps the most important factor favouring the construction approach of a column, is that the constructed column (or pile) must be allowed to cure before been tested; this ensures that a considerable period of "set-up" time occurs, typically 28 days, during which time radial stresses at the shaft interface increase as excess pore water pressure and radial consolidation occurs.

These issues raised suggest that further research is required to understand the pressure-deformation behaviour at the column interface, without a more comprehensive understanding of this behaviour it is difficult to: (1) confidently confirm the conditions at the column/soil interface, and perhaps more importantly (2) assess the radial stresses acting on the column shaft.

8.5.1 Installation records and founding conditions

The column installation records for the field case study were reviewed by the design engineers in order to confirm (or otherwise) the integrity of the installed columns and that the minimum 2 m socket into Fishermens Bend Silt unit had been achieved. A more detailed assessment of the installation records is presented below.

The torque profiles for columns installed adjacent to CPT31, CPT30 and CPT29 are shown in Figure 8.36*a*, *b* and *c* respectively along with CPT q_t profiles and soil behaviour type data. Calculation of these parameters was described in Appendix B. The design minimum 2 m socket was evaluated on-site by the rig operator and some of the difficulties in achieving this are highlighted below. The inferred top of socket assessed from both the CPT and installation records is shown in Figure 8.36. In general, the torque response matches quite well with the CPT q_t profile. However, the depth to the top of the pile socket interpreted from the installation record is typically deeper than the CPT q_t assessed depth.

This is attributed to two factors: (1) the difference in strength at the interface and (2) the response of the auger as it penetrates the founding unit. The difference in strength at the interface was most pronounced at the western end of the embankment (CPT29). However, at the eastern end (CPT31) where the Coode Island Silt is thickest, the undrained shear strength at the base approaches that of the underlying Fishermens Bend Silt and an increase in torque at the interface was not obvious. In these cases, generally the approach was to consider the interface to occur where the torque exceeded 100 bar which was known to be conservative based on calibration of the ground improvement rigs at the start of the project.

Concerning the second factor, generally the increase in torque at the interface correlated with the penetration of the enlarged body of the drilling tool rather than the penetration of the toe of the drilling tool (depth is defined as the distance from ground surface to the toe of the drilling tool). The increase in torque due to penetration of the interface was generally found to trail the auger toe penetration by 0.4 m to 1.0 m. This response is analogous to the CPT probe penetrating a stiffer stratum (see for example Robertson, 2010; Ahmadi et al. 2005), however, with the added

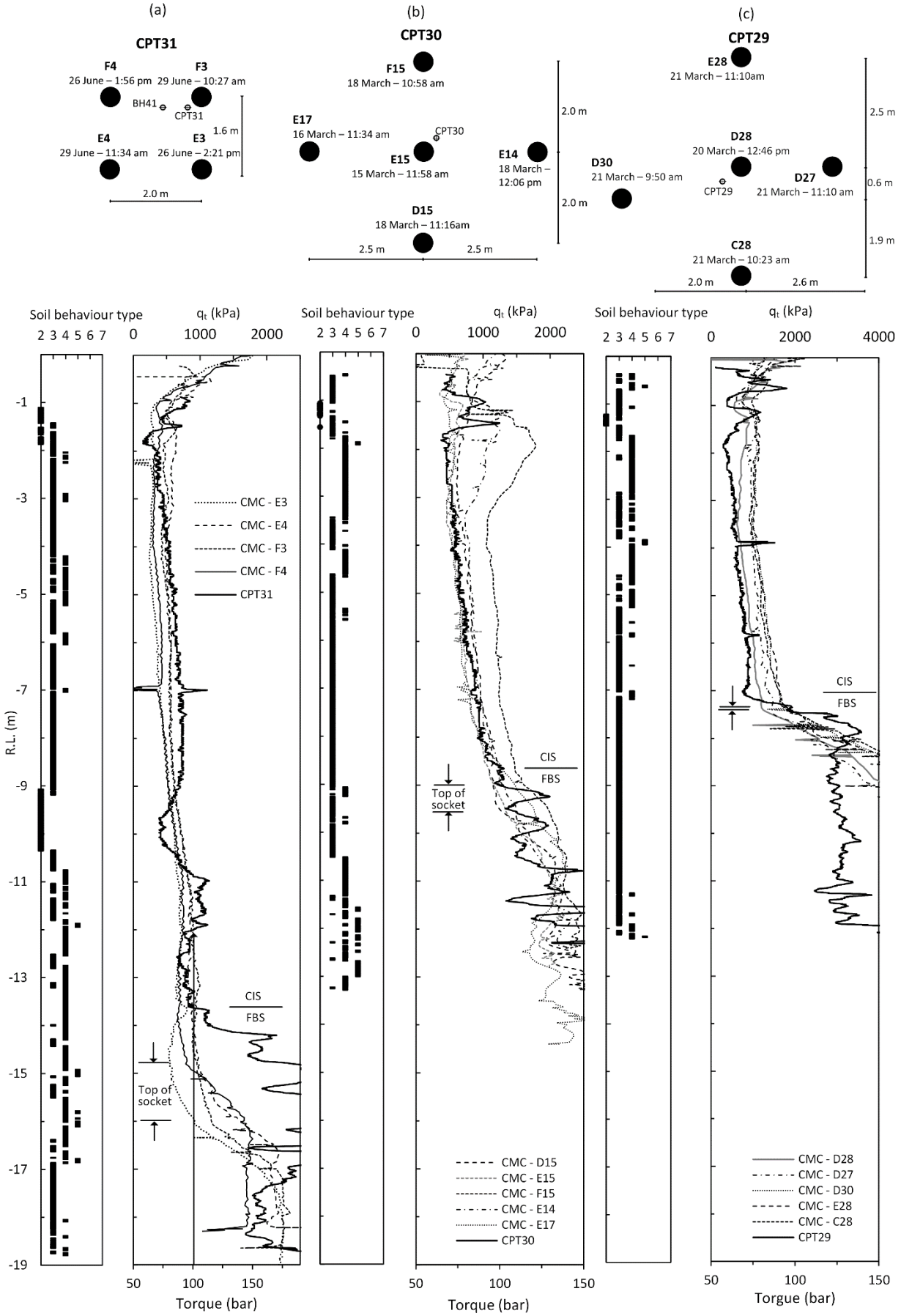

Figure 8.36. CPT and adjacent columns – plan view, soil behaviour type, q_c and torque reading **(a)** CPT31, **(b)** CPT30 and **(c)** CPT29

complication of variable auger mechanisms (crowd pressure and rotational rate in particular). As outlined earlier in this chapter, the relationship between auger mechanics, pore water pressure and stress fields is not well understood at present and therefore, interpreting this behaviour in practice is difficult and requires a degree of engineering judgement.

These factors highlight some of the difficulties encountered in achieving an efficient ground improvement works when subjected to variable ground conditions. However, even closely spaced columns surrounding the CPTs shows variation in torque profiles of between 10% to 20%. This variation is attributed to two factors: (1) Time of installation – F4, E15 and D28 were the first columns installed adjacent to CPT31, CPT30 and CPT29 respectively and showed the lowest torque profile with depth. As more columns were installed, the *in situ* stresses and pore water pressure increased making further penetrations more difficult. The second factor is the location of the columns relative to the historic embankment. Columns on north side showed greater penetration resistance (the northern side is located closer to the centre of the historic embankment); compare row E/F (Figure 8.36*a*), D15/F15 (Figure 8.36*b*) and C28/E28 (Figure 8.36*c*).

These difficulties led to a more cautious approach with longer column sockets the result and in turn, an increase in the overall cost and time taken for the ground improvement works. The variation in socket length of the 111 columns installed within the lower ground improvement level is shown in the histogram in Figure 8.37. The distribution of socket lengths resembles an approximate normal distribution with considerable skew to the right (i.e., longer socket lengths), the majority (62 %) of the column socket lengths are between 2.50 and 3.70 m. Ensuring that the correct socket length is reached is not only important to ensure cost effective ground improvement works but also to ensure a uniform axial load-deformation response of the columns. Significant scatter in their axial response translates to variable total settlement of the embankment due to the presence of "hard" columns (long socket length) and "soft" columns (short socket length) across the ground improvement area.

8.5.2 Assessment of applied load, capacity and dynamic test results

The installed columns were designed for a working load of 700 kN based on a minimum 2 m pile socket into the underlying Fishermens Bend Silt founding unit. In general, working loads acting on the columns are lower than the design working load. In Area #2 for example, the working load is approximately 380 kN assuming full load transfer by the load transfer platform (which is predicted to occur in the year 2028 based on the analysis presented in Chapter 5). The largest working loads occur at the eastern end of the embankment, beneath the gabion wall where it is highest. The additional load which acts under working conditions due to negative skin friction has been assessed

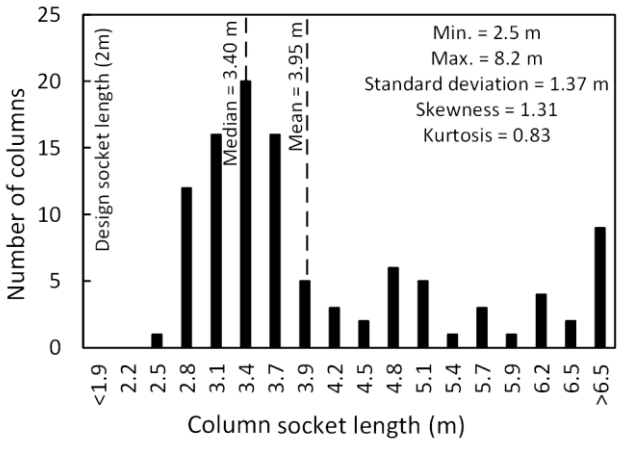

Figure 8.37. Variation in socket length of installed columns

using the method described by Poulos (2008) (see Appendix E1). Typical loads due to negative skin friction where assessed to be in the range of about 150 kN to 300 kN depending on Coode Island Silt thickness. The ultimate column capacity for the two tests columns, E11 and C27, has been assessed based on a total stress "*c*-α" approach and the method of Bustamante and Gianeselli (1993,1998) in Appendix E2. Test columns E11 and C27 were installed at an offset 10.5 m from CPT30 and offset 3.2 m from CPT29 respectively. Ultimate capacities for the two test columns where in the range of 1150 kN to 1250 kN using the *c*-α method and 1300 to 1700 kN using the method of Bustamante and Gianeselli (1993,1998). Serviceability capacities have a reduced length of shaft acting to resist load due to the action of negative skin friction. Serviceability capacities are approximately 200 kN lower than ultimate capacities (see Appendix E1, E2).

Columns C27 and E11 were also subjected to dynamic load testing of up to 100 % of working load. The results of the dynamic load tests are presented in Appendix E3 (Figure E7*a* and *b*) along with the adjacent CPT q_t profile and drilled rig torque profile. For column C27 approximately twice the working load is mobilised in base capacity alone and a serviceability capacity of approximately 1800 kN is assessed (the contribution of shaft capacity from the Fill and Coode Island Silt is ignored) which is measured at less than 10 mm of column head settlement. For column E11 the serviceability capacity is measured to be 1100 kN. Without further detailed assessment of the piling capacities and the dynamic pile test it is shown herein that measured serviceability capacities are typically in the order of 2 to 3 times working loads; the factor safety for ultimate limit state conditions is even greater.

It follows then, that where the 2 m embedment into the founding unit is achieved the column will have sufficient axial serviceability and ultimate capacity. The difficulties with the ground improvement works lies not in demonstrating that a column with a 2 m embedded shaft (into the founding unit) has adequate axial capacity but demonstrating that a 2 m column embedment (into the founding unit) has been achieved in the first instance, and furthermore, that this embedment can be reliable and repeatedly achieved. This is discussed further in the following section.

8.6 Discussion

8.6.1 Ground improvement works

From the analysis in the preceding section it has been shown that the installed columns have sufficient axial capacity as they exceeded their required design ultimate capacity of 700 kN considerable, although this is due in part to the columns having a socket length longer than the design 2 m length. For the design of the North Dynon embankment, a more significant risk identified during the design stage was the verification of the founding condition during the ground improvement works. This risk is primarily concerned with the suitability of the contractor's proposed installation methodology; i.e., whether the nominated 2 m socket could be reliably achieved and confirmed. A simple and conservative solution was to over-drill the socket (Figure 8.37), this inevitably results in additional construction costs, and depending on commercial and contractual arrangements, is often more advantageous to one party rather than the other depending on who carries these additional costs. For this case study, the risk was due to two main factors. These factors, mitigation measures and some comments are presented in Table 8.5. The installation effect is calculated by cumulatively summing at one-second intervals the product of normalised penetration index (Equation 8.24) and the normalised torque index (Equation 8.25).

$$\text{Normalised penetration index} = \frac{1}{\sqrt{\frac{PR}{PR_{base}}}} \quad \textbf{(8.24)}$$

$$\text{Normalised torque index} = 2.78\left(\frac{t_{fp}}{T_{base}}\right)^{1.36} \quad \textbf{(8.25)}$$

Where PR is the penetration rate and t is torque. These values are normalised relative to base values (denoted with a subscript). The Installation Effort method quantitatively assesses the installation process; however, the raw rig data was not available from the case study to allow this assessment to be undertaken. To be implemented effectively in this case study it would be necessary to ignore the shaft capacity derived in the fill and upper portion of the Coode Island Silt. This could be achieved by commencing calculation of the installation effort at approximately the neutral axis in the Coode Island Silt (Figure E1.). The error associated with selecting the commencement installation effort is minor as the contribution to shaft capacity from the Coode Island Silt is minor (see PDA test results in Appendix E3).

8.6.2 Sub-soil settlement and the ground improvement effect

The role of sub-soil settlement on the performance of the load transfer platform was assessed in Chapter 5 in terms of the development of arching and tensile load in the geosynthetic reinforcement. It was identified that there is a significant amount of uncertainty in the assessing time rate of sub-soil settlement arises primarily due to; 1) uncertainty in the applied load due to arching, the ground reaction curve method was shown to provide a significant improvement in reducing this source of uncertainty, and 2) the ground improvement effects resulting from the installation of an array of full displacement columns and the effect this has on (reducing) the compressibility of the

Table 8.5. Risk factors, mitigation measures and commentary on ground improvement works

Risk	Mitigation measures	Comments
Variability of the sub-surface conditions. (Specifically identifying the depth to the founding unit)	Additional site investigation to reduce the uncertainty in the assessing the depth to the interface. CPTs are generally the quickest and most cost-effective method to achieve this aim. Increase the amount of field testing/calibration undertaken in advance of the main ground improvement works.	For this case study, the difference in undrained shear strength between the Coode Island Silt and Fishermens Bend Silt was often minor at depth > 20 m. The field trial involved in the case study required the installation of columns within a 5 m radius of CPT test locations (or a borehole location) with the number of trial columns being dependent on the total number of production columns required for an area of ground improvement works. The minimum time required before columns can be tested (i.e., due to curing times) can lead to delays between the test columns and the start of production columns. In some cases, production columns were installed ahead of the completion of test columns.
Ability of the piling rig instrumentation to identify changes in the sub-surface strata.	The variation in torque is generally the most reliable indicator of penetration into the founding unit (see Figure 8.3 for example). The crowd pressure was found to be a useful additional indicator for identifying the founding unit. The rigs installing this type of ground	A measurable increase in the torque reading as the drilling tool penetrates the founding unit typically occurs between 0.4 m and 1.0 m after the interface has been penetrated. Installation resistance (assessed primarily through torque) can vary at locations with near-identical stratigraphy due to previous column installations causing increased *in situ* stress and pore water pressure. This variation was found to be in the order of 10 % to 20 %.

	improvement should be set up to measure crowd pressure. This was also recommended by Gniel et al. (2015). The "*Installation Effort*" method described by NeSmith (2003) can be implanted into the on-board piling rig computer to provide a real-time assessment of the column capacity. This is described in further detail below.	Identification of the founding unit based on constant value of torque can be a reasonable approach (provide calibration of the piling rig during the installation of test columns is undertaken), however, for the reasons outlined above this may become problematic as ground improvement works proceed owing to the increased influence of installation effects on the torque profile. On a number of occasions installation data was presented on an enlarged scale (due to a large spike in torque near the base of column) and the founding unit was difficult to identify. The torque scale should be set to highlight the penetration into the founding unit rather than base. Further improvements in piling rig capabilities can be expected to reduce this risk. For example, the latest Bauer piling rig (Bauer 2013) include an additional installation parameter termed the "α-value" for CFA/Drilled displacement pile installation monitoring. This value is based on penetration rate and torque. It is not clear what, if any, relationship this has to the "*Installation Effort*" described by NeSmith (2003).

soft soil. The ground improvement effect includes a reduction in the compressibility of the soft soil and also load transfer from the soft soil to the installed columns. Based on the analysis of the arching stress development presented in Chapter 5 and the assessment of installation effects presented in this chapter, it is apparent that the latter represents a greater source of uncertainty when predicting arching stress development using the ground reaction curve method.

8.7 Conclusion

Despite the significant amount of literature published in recent years on the topic of GRCSEs there is little practical advice in the literature that specifically addresses the installation effects and the interpretation of installation data. i.e., how does one assess whether a design minimum socket requirement has been achieved. It is thought that this is in part due to the number of proprietary drilling systems available, with much of the knowledge gained from the ground improvement works by the contractor staying "in-house". For this reason, and because the drilled displacement column technique is a relatively new technique compared with say CFA piling, there is little guidance in the published literature on assessing these installation effects and addressing these issues.

With little guidance in the published literature, the author has taken a relatively broad approach to assessing the installation effects associated with drilled displacement columns. The installation parameters are numerous and include; time of installation, depth, mast inclination, torque, auger rotation rate, penetration rate and crowd pressure and the concreting parameters include; concrete pressure and lifting speed. These two parameters are typically used to infer a "as-built" profile. Each of the parameters has its' own unique difficulties in assessing accurately, crowd pressure and concrete pressure being in the author's opinion the most problematic. A basic understanding of auger mechanics (Section 8.2.1) is therefore necessary to understand and interpret the installation data and from this it was found that a combination of penetration rate and torque are the most important parameters for interpreting installation data. These two parameters form the basis of the "Installation Effect" method by NeSmith (2003).

It is however important to recognise the practical limitations which apply in practice. Auger rotation rates, torque capacities, penetration rates and concrete pressures, amongst others, are constrained by the capabilities of the piling rig (and auxiliary equipment such as concrete pumps) and furthermore, the auger mechanics of a modern piling rig

is further constrained automatically by on-board software to avoid problems such as excessive flighting and excessive engine wear etc. The limitations do not necessarily apply in small scale physical modelling or in numerical simulations. For example, the physical and numerical modelling studies by Hird et al. (2011) and Pucker and Grabe (2012) respectively rotate and drive the simulated drilling tool at rotational and penetration rates significantly above, or below, the critical penetration rate (v_{cr}). In addition, the practical limitations of these parameters at full scale are not discussed, nor are the input parameters (rotation rate, penetration rate etc.) related to full scale behaviour. These studies provide insight into the relationship between the various installation parameters and column/pile performance, however, it is difficult to translate the variability in axial column capacity suggested by these physical and numerical studies to full scale. It is likely that these studies overstate the variability that can reasonably be expected under normal installation conditions at full-scale.

A number of findings are highlighted in this chapter that relate to mechanisms occurring at the column/soil interface during and immediately after column installation. On the basis of the data available from this case study, it is difficult to validate these further other than to highlight similar behaviour that has been observed in other studies. The key findings include:

- In addition to assessing the minimum penetration into a founding material that achieves ultimate column capacity and equally important questions is; What is the minimum penetration into a founding material that can be reliably identified during ground improvement works? In the majority of cases the latter will be greater in length and will often dictate the design embedment length of columns. For, this reason the author recommends a minimum 2 m socket due to the difficulties in reliably achieving adequate embedment as discussed in Section 8.6.1.
- Assessment of the pore water pressure data has shown that hydraulic fracturing of the soft soil likely has a considerable influence on the excess pore water pressure field which develops during ground improvement works. The cumulative installation effects are significant and this affects the rate of radial consolidation highlighted in the previous point.
- Effective stresses are out-of-balance at the interface immediately after installation. Radial stress "relaxation" or unloading of the soil mass must occur at the interface and this will be accompanied with a reduction in the cross sectional area of the column.
- Fluid pressures are initially out-of-balance at the interface immediately after installation and due to the difference in fluid pressure there must be a net inward pore pressure immediately after installation. The flow, or seepage, of groundwater into the column is not however calculated to have a detrimental effect on the quality of the concrete, for the columns considered here, due largely to the low permeability of the remoulded Coode Island Silt near the column shaft interface, the rapidly reducing excess pore water pressure and finally the likelihood that hydraulic cracking in the Coode Island Silt (described above) will limit the excess pore water pressures that develop in the soil mass.
- The development of shaft capacity for drilled displacement column/pile is expected to develop primarily due to radial consolidation in fine grain soils as the effective radial installation stresses are near zero. The development of shaft capacity is strongly time-dependent.

9 Global embankment behaviour

9.1 Background

There are typically six limit states which are considered when undertaking the design of a GRCSE (Rogbeck et al. 2004, Lawson 2013), these were presented in Fig 2.16. The pile group capacity limit state has been discussed in the preceding section and found to be adequate, likewise, the vertical loading shedding and surface deformation limit states were described in Chapter 5. In the following section the analysis is limited to the three limit states described in Figure 9.1. For this case study, the pile group extent limit state is satisfied by ensuring the limit states relating to the soil reinforced gabion wall construction; reinforcement failure/pull-out, analysis of connections and allowable eccentricity are met (see EBGEO; German Geotechnical Society, 2010) for a full list of limit states relating to soil-reinforced walls).

The assessment of the global embankment stability for this case study is concerned with assessment of the slope failure and lateral sliding mechanisms. Based on the survey, tiltmeter and inclinometer data the effect that ground improvement works have on these limit states are investigated. Lateral sliding, overall stability and column group extent limit states (Figure 9.1) are the limit states which may cause lateral deformation of a GRCSE. For this case study, the column group extent is satisfied by ensuring the limit states relating to the soil reinforced gabion wall construction; reinforcement failure/pull-out, analysis of connections and allowable eccentricity are met (see EBGEO; German Geotechnical Society, 2010, for a full list of limit states relating to soil-reinforced walls). The present study focuses on the assessment of overall stability and lateral sliding mechanisms.

9.2 Field case study

9.2.1 Vertical settlement

The ultimate axial capacity of the individual columns, and the column group capacity, has been investigated in the previous chapter (see Section 8.5.2) based on dynamic load test results; these results indicate sufficient single, and group, column capacity. Despite this, the observed vertical settlement of the gabion wall was between 10 mm and 40 mm post-construction (average 24 mm) over a period of about 1 year post-construction. The larger values of settlement correspond with sections of gabion wall that are highest (eastern end in Figure 3.4).

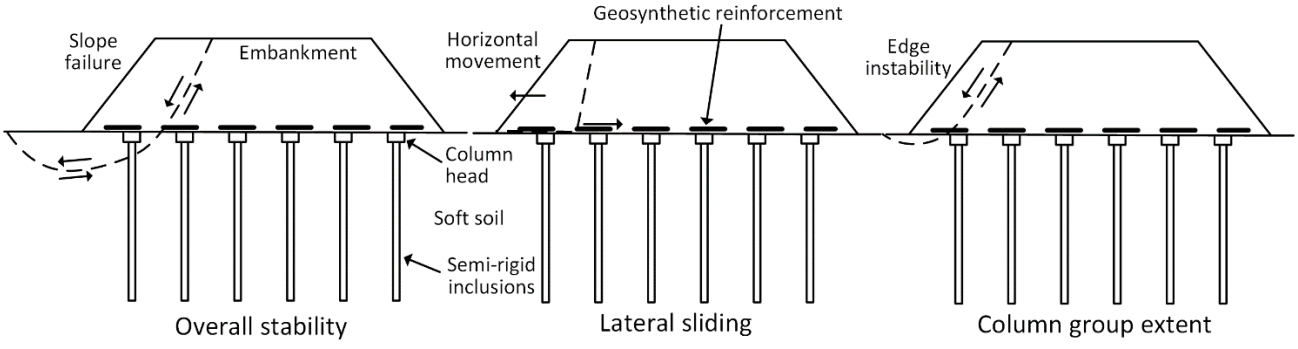

Figure 9.1. Various limit states of interest to case study

This post-construction settlement is explained by the post-construction development of arching which has been described in Chapter 5. Normalised settlement is plotted relative to arching development in Figure 9.2, quantified by the stress reduction ratio and the agreement is good. At the completion of embankment construction the stress reduction ratio was about 0.7, this decreased to a value of 0.1 as maximum arching conditions developed at about day 600 onwards. This is consistent with the column load increasing from 164 kN to 340 kN for the unit cell in Area #2; a 110% increase. This highlights the effect that the post-construction development of arching can have on the total embankment settlement. This results is however not entirely unexpected. The lateral deformation of the embankment also shows similar time-dependent post-construction behaviour, this is however, more difficult to explain and is examined over the remainder of the chapter.

9.2.2 Long term embankment behaviour

The long term lateral movement of the embankment is assessed through tiltmeter and inclinometer data as well as post-construction survey data. The magnitude of lateral displacement (day 182 to 894) is indicated with survey vectors in Figure 9.3 and shows between 10 mm and 25 mm of movement. The survey markers are located at the mid-height of the gabion wall which varies from between 5 m and 6.5m high (survey markers 1 to 4) and between 3 m and 4 m (survey markers 5 to 10). All of the 10 survey markers show consistent behaviour and indicate that the entire length of the gabion wall, and by inference a portion of the embankment itself, has moved in a southerly direction with larger movement generally occurring near the southeast end where the wall height is greatest. A large component of lateral deformation is in the longitudinal direction and this cannot be explained by (transverse) rotation of the soil-reinforced gabion wall, as is often the case. Furthermore, the lateral movement along the length of the gabion wall is not consistent with embankment behaviour caused by the overall stability or column group extent limit states as no significant wall rotation has been observed and the lateral movement is occurring out-of-plane (i.e., it is not occurring in the direction normal to the gabion wall).

The long term lateral movement (day 161 to 741) at the base of gabion wall, and through sub-surface profile, is shown in Figure 9.4 based on the data from Inclinometer #2 (offset 1.6 m from the gabion wall). The inclinometer data indicates about 10 mm of outward transverse movement and 5 mm of longitudinal movement (at R.L. + 2 m), a result of 11 mm in an approximate southerly direction that is consistent with survey data (survey marker 7) at this location. The uniform lateral movement at the base and mid-height of the gabion wall suggest a lateral sliding mechanism, not wall rotation, is primarily responsible for the post-construction movement.

In addition to the lateral movement at the base of the load transfer platform (R.L. + 2 m) there is also considerable lateral movement within the Coode Island Silt in an inward direction; the opposite to the outward

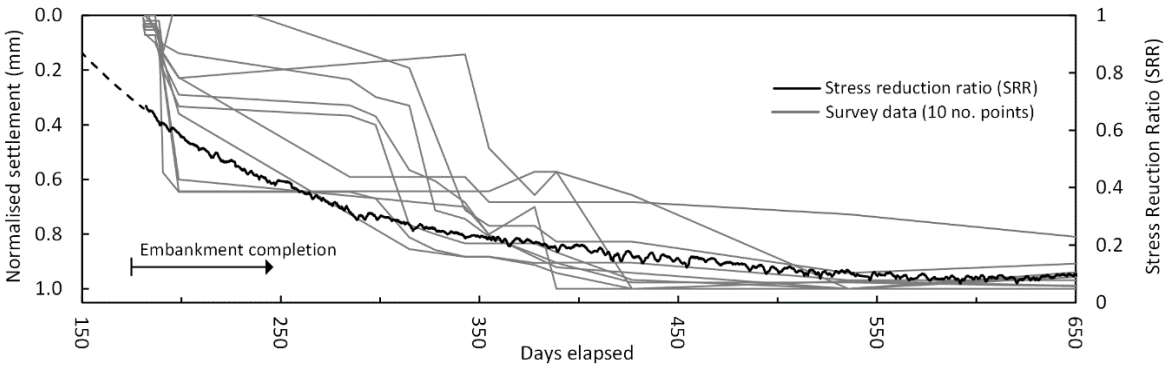

Figure 9.2. Normalised vertical settlement of gabion wall and arching development

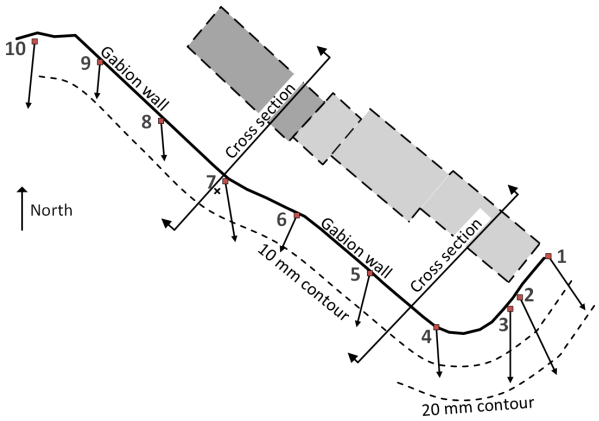

Figure 9.3. Post-construction survey monitoring – long term lateral displacement vectors

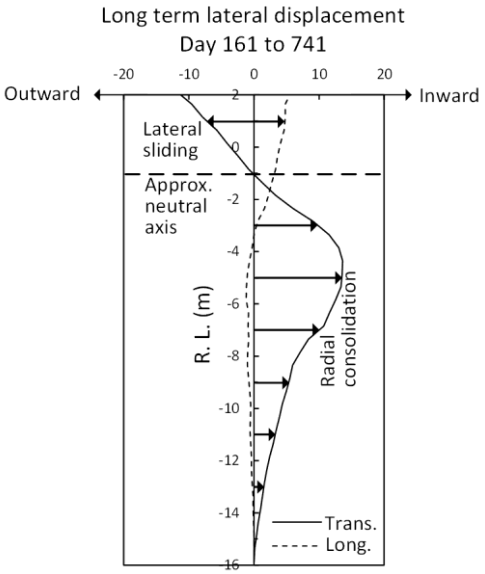

Figure 9.4. Long term lateral displacement - Inclinometer #2

transverse movement observed during drilled displacement column installation (see Figure 8.28 and Figure 8.29) that is due to radial equilibration of the installed columns. The lateral sliding and column equilibration mechanisms occur in approximately equal direction with a neutral axis in the transverse direction at about R.L. – 1 m.

The long term tiltmeter measurements (Figure 9.5) of C15 show the tilt in the outer row of columns supporting the gabion wall in Area #2 (see Figure 3.6). The transverse axis of the two tiltmeters show long term outward rotation consistent with the inclinometer profile (Figure 9.4). Between day 161 and 741 the rotation of tiltmeter 2 and 3 in the Y-axis direction was −0.36° and −0.32° respectively. Assuming the column and head rotate uniformly about a neutral axis at R.L. −1 m, then the lateral displacement at R.L. + 2 m (base of load transfer platform) is 17 mm based on the average of the two tiltmeter readings. In the longitudinal direction, the angle of tilt measured by the inclinometer above R.L. 0 m is just + 0.02° (72 arcseconds). The rotation of tiltmeter #2 and 3 in the X-axis is + 6 arcseconds and +79 arcseconds at a resolution of ±9 arcseconds. On this basis, it is inferred that the column head, load transfer platform and gabion wall are translating laterally with minimal rotation in the longitudinal direction. Due to the complex nature of the long term displacement profile of the column it is difficult to back-calculate a deflected profile based on discrete rotational measurements (tiltmeter data). Despite this, the agreement between the inclinometer, tiltmeters and survey data is considered good.

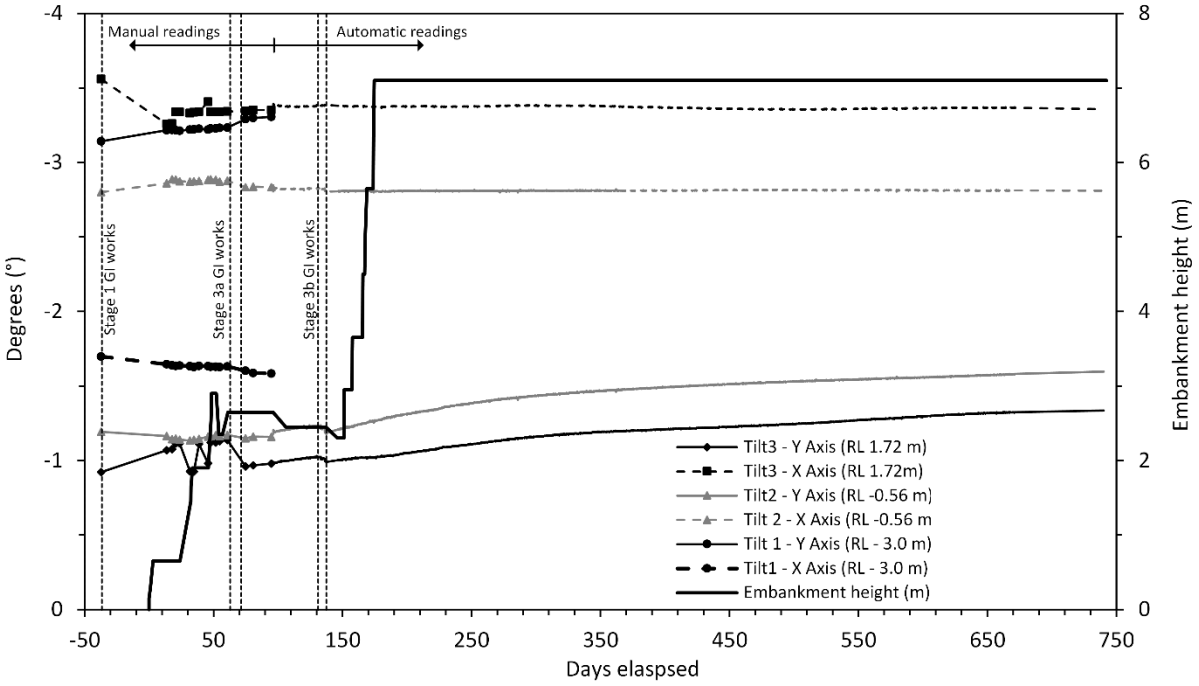

Figure 9.5. Long term tiltmeter data

In Figure 9.6 the long term lateral movement of the gabion wall is shown along with the excess pore water pressure. Both displacement and pore water pressure were normalised with respect to the maximum lateral displacement and maximum excess pore water pressure respectively. Lateral movement of the embankment stabilised by around day 400, which was consistent with the general dissipation of the excess pore water pressure. While the radial equilibration of the columns was governed by the dissipation of excess pore water pressure, it is shown here that the lateral sliding mechanism was also influenced by the dissipation of excess pore water pressure.

Based on the inclinometer, tiltmeter and survey data, the long term lateral movement of the GRCSE can be described by:

1) Outward lateral (block) sliding of the embankment due to the out of balance active earth pressure force acting on the gabion wall; the plane of sliding is however not sharply defined but represents a broad shear zone in the fill and upper portion of the Coode Island Silt, and
2) Inward lateral movement in the Coode Island Silt associated with radial equilibration of the numerous installed columns.

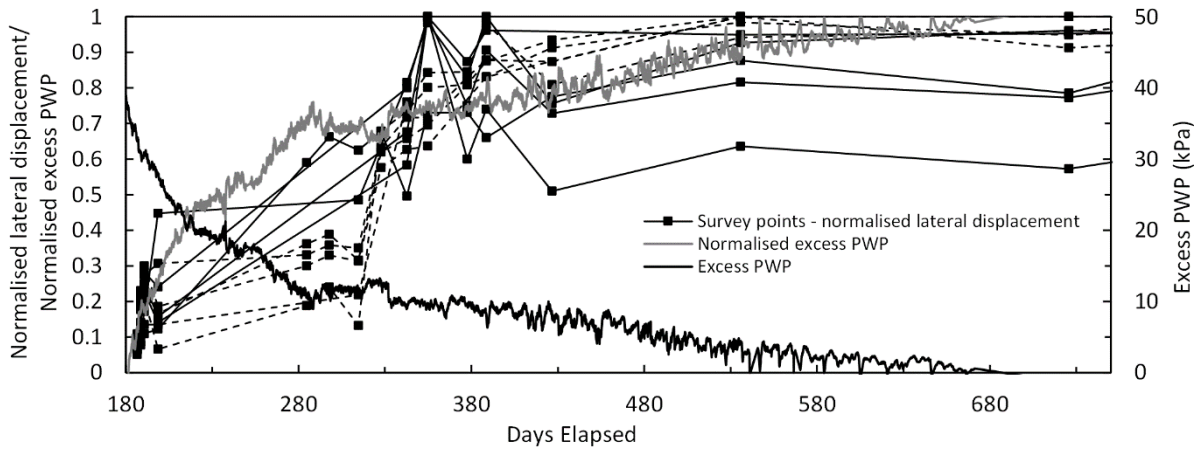

Figure 9.6. Lateral displacement of embankment and pore water pressure dissipation during the post-construction period

Both of these mechanisms act in approximately opposite directions, and are related to the dissipation of excess pore water pressure beneath the embankment due to column installation effects. This was measured directly through piezometer data, observed indirectly as heave/uplift (see section 8.4.1) and predicted based on cylindrical cavity expansion theory. The large build-up of excess pore water pressure beneath the GRCSE present at the completion of embankment construction is expected to have greatly reduced the effective stresses in the upper portion of the Coode Island Silt, and as a result, reduced the lateral resistance provided by the Coode Island Silt. This is inferred to have aided the lateral sliding mechanism and is consistent with the lateral sliding largely ceasing as excess pore water pressure in the upper portion of the Coode Island Silt dissipated by about day 400. The dissipation of excess pore water pressure in the middle of the Coode Island Silt is expected to have taken much longer and this is consistent with the tiltmeter data that indicates that the rotation of the columns did not stabilise until about day 700 as the equilibration of the columns continued; about two years after the completion of the ground improvement works.

It follows that the critical period with respect to embankment stability was the end of construction when the embankment was at full height and excess pore water pressure due to ground improvement works had not dissipated greatly. This is particularly the case where a GRCSE has been constructed quickly, which is a benefit frequently cited to justify their use in the first instance. Due to the reduction in effective stress in the upper portion of the Coode Island Silt, the lateral sliding mechanisms must therefore be resisted by the flexural capacity of the columns and the passive resistance provided by the fill unit around the periphery of the embankment. The combined effect of outward lateral sliding and inward equilibration subjects the columns to considerably greater internal stresses than would otherwise be expected if installation effects were ignored.

9.2.3 Response of drilled displacement columns

As instruments to measure bending moments directly are not currently available, it is common to calculate the bending moment indirectly from curvature and material properties as follows:

$$\mathrm{M} = \psi \mathrm{EI} \qquad \textbf{(9.1)}$$

Where M, ψ, E and I are the bending moment, curvature, modulus of elasticity and second moment of inertia of the column respectively. Where the bending moment exceeds M_{cr}, cracking of the column will occur and as result the cross sectional area is reduced. The effective moment of inertia I_e for a cracked section is calculated as follows (Branson 1977):

$$I_e = \left[\frac{M_{cr}}{M}\right]^3 I_g + \left[1 - \left(\frac{M_{cr}}{M}\right)^3\right] I_{cr} \leq I_g \qquad \textbf{(9.2)}$$

It is noted that flexural failure of an unreinforced concrete column is a brittle failure mechanism and that the use of Equation 9.1 and 9.2 is not strictly valid; the calculated crack depth should be considered as approximate only and is likely a lower bound. For inclinometer derived lateral displacement profiles, curvature can be calculated using Equation 9.3, however, typically dz/dw is assumed to be very close to zero and the approximate expression (Equation 9.4) is adopted. Curvature can be calculated directly from a lateral displacement profile using Equation 9.4, however, whilst the inclinometer profile with depth may appear "smooth" it is comprised of discrete inclination readings with depth, and as a result, the direct use of Equation 9.4 generally leads to erratic and unrealistic results.

To calculate the bending moment profile more accurately it is necessary to fit a continuous curve to the displacement profile (i.e., curve-fitting techniques are required).

$$\psi = \frac{\frac{\mathrm{d}^2 w}{dz^2}}{\left[1 + \left(\frac{dw}{dz}\right)^2\right]^{3/2}} \quad \textbf{(9.3)}$$

$$\psi \sim \frac{\mathrm{d}^2 w}{\mathrm{d}z^2} \quad \textbf{(9.4)}$$

Ooi et al. (2003) compared 12 curve fitting methods applied to 60 sets of inclinometer data and concluded that a piecewise cubic curve fitting over a 5-point window generally resulted in the best estimate of back-calculated bending moment profiles. The piecewise cubic curve fitting approach fits a cubic polynomial $w = Az^3 + Bz^2 + Cz + D$ over a moving window of adjacent data points. In Appendix E the 5-point data window recommended by Ooi et al. (2003) is shown along with larger data windows (9 no., 11 no., and 13 no.) and higher-order polynomial approximations (Figure E11*b* in Appendix E) based on the lateral displacement profile in Figure 9.4. Using the average of multiple piecewise cubic functions at a data point, the curvature can be calculated explicitly as follows:

$$\psi \sim \frac{d^2 w}{dz^2} = 6Az + 2B \quad \textbf{(9.5)}$$

The use of larger data windows results in increased "smoothing" of the data sets. Engineering judgement is required to obtain an appropriate balance between a profile that is "smoothed" and one which includes localised behaviour. The higher order polynomials generally provide a good fit of the displacement profile, however, the bending moment profiles show erratic and unpredictable behaviour at the top and bottom and are not utilised here; Ooi et al. (2003) made a similar recommendation. The 11-point data window is adopted herein as the preferred method based on analysis of the post-construction lateral displacement profile in Figure 9.4 (see Appendix E, Section E4 for details of this analysis).

It is interesting to note that post-construction survey of the embankment indicates that the outward deformation of the embankment is approximately within the allowable limits (i.e., about 20 mm) which satisfy a zero tensile strain (see Figure E9 in Appendix E), if it is assumed that the columns supporting the GRCSE rotate uniformly outwards due to lateral sliding alone. A zero tensile strain condition occurs where the tensile stress induced in the column due to flexure is less than, or equal to, the axial (compressive) stress (N) (see Appendix E). However, the bending moments induced in the columns are subjected to the combined effects of lateral sliding and equilibration acting in (approximately) the opposite direction (Figure 9.4) and when these actions are considered, not only are tensile stresses induced in the column, but cracking of the column occurs. Due to the rotational restraint provided by the drilled displacement column head, and to a lesser extent the fill unit, as well as the rotational restraint at the bottom of the column due to the socket into the Fishermens Bend Silt founding unit, flexural cracking is predicted beneath the column head (~R.L. – 1 m), above the location of maximum lateral deflection (~R.L. – 4 m) and above the column socket (~R.L. – 9 m). Post-construction survey does little to reveal the additional loadings due to radial equilibration occurring below the ground surface.

The behaviour of drilled displacement column C15 has however been subject to additional phases of ground improvement works, which occurred after the column was installed, in addition to the post-construction lateral sliding and equilibration. In Figure 9.7*a* the behaviour of the drilled displacement column C15 during the

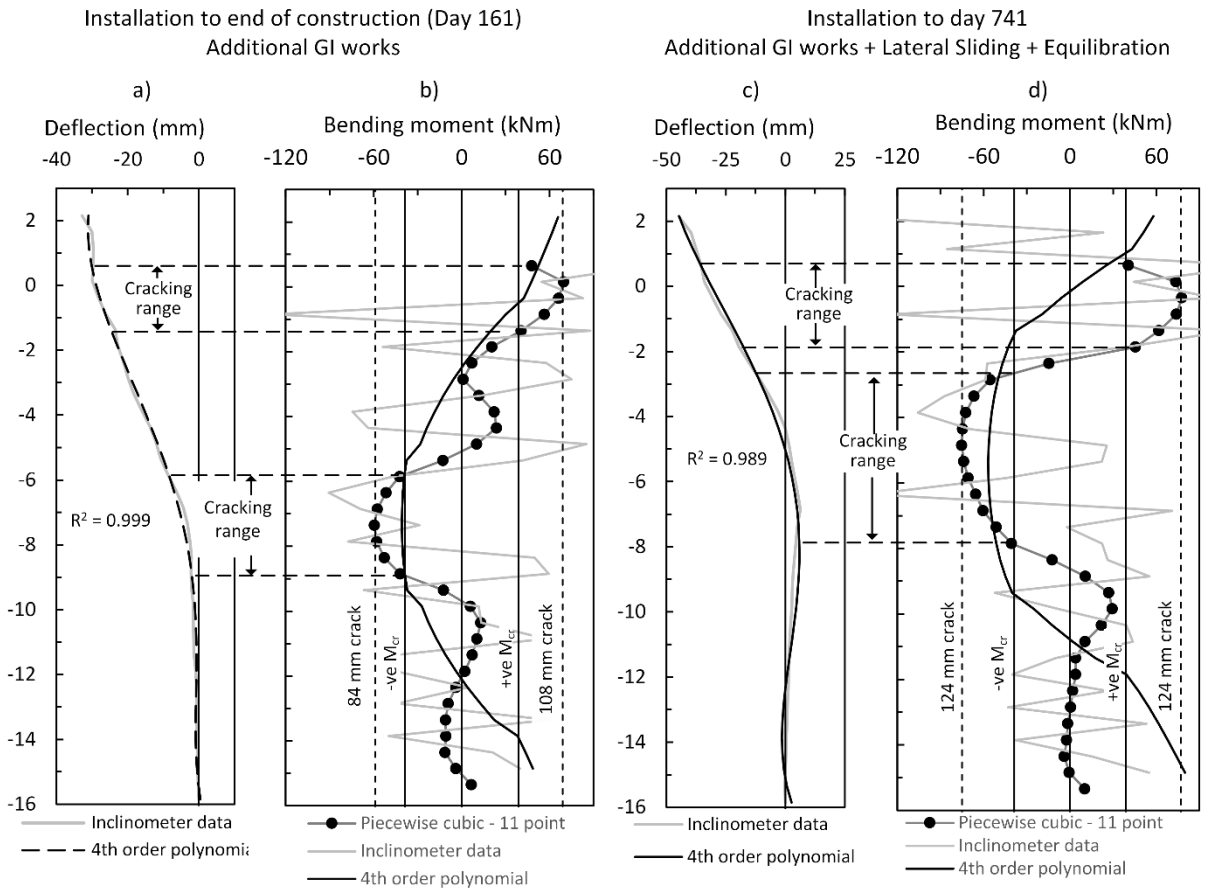

Figure 9.7. Inferred loading on drilled displacement column C15 during construction phase **(a)** displacement **(b)** bending moment profile and long term **(c)** displacement **(d)** bending moment profile

construction phase is shown (installation to day 161), this includes about 50 mm of lateral movement due to the Stage 3a/3b works. Between R.L. -6 m and -9 m, M_{cr} is exceeded. The long term condition (installation to day 741) is shown in Figure 9.7*b* and includes the additional displacement due to lateral sliding and equilibration. The long term behaviour of the drilled displacement column shows flexural cracking at two locations: 1) In the upper portion of the shaft due to the rotational rigidity of the drilled displacement column head and 2) at the mid depth due to the combined action of lateral sliding and equilibration.

9.2.4 Effects on drilled displacement column during installation

Installation effects arising as columns are installed in a dense grid is a problem that affects ground improvement works where semi-rigid inclusions are installed, these effects are not well understood. The installation layout plan adopted for the North Dynon embankment was a square array of columns on a grid size varying from 2 m to 2.5 m. A hit-1 miss-1 approach was adopted for column installation (Figure 9.8) similar to that described by Plomteux et al. (2004). There are two problems which arise: 1) where adjacent columns are installed in immediate succession and the concrete in the previously installed column has not set, the resulting lateral displacement acts to “squeeze” the previously installed “wet” concrete column, resulting in a loss of cross sectional area (column “necking”) and 2) where a column is installed adjacent to a partially or fully cured concrete column the previously installed column is subjected to lateral displacement which impose bending moments and shear forces.

9.2.5 Drilled displacement column necking

To assess column necking, the lateral displacement profiles due to the installation of column C15 (Inclinometer #2 - Phase 3 in Figure 8.28 and Table 8.3) and column D10 (Inclinometer #1 - Phase 3 in Figure 8.25 and Table 3.1) installed at radially offsets of 2.04 m and 2.41 m respectively are considered. The measured maximum lateral displacement resulting from the installation of these columns was about 20 mm and 10 mm for C15 and D10 respectively (Figure 9.9*a*). Lateral displacements of between 40 mm and 60 mm were measured following the installation of columns at offsets of 1.71 m and 1.12 m respectively. If displacement profiles of this magnitude are imposed on a column, prior to the column setting, lateral translation of the liquid column and simultaneous compression of the cross sectional area, due to the imposed lateral stresses, can be expected. Soil arching will have a beneficial effect, re-distributing lateral stresses around a liquid column, and reducing the lateral displacement in a manner analogous to compression of a tunnel subjected to vertical loading. However, relative displacement between the column interface and the surround soil is required to mobilise soil arching (Iglesia et al. 2013). For a 2 m square array of columns (2.8 m diagonal spacing), the worst-case scenario is the installation of the four diagonally adjacent columns (each at 2.8 m) and an increase in all-round radial stresses on the slurry column. The sum of free-field displacements in each direction (about 5 mm) results in a reduction in diameter of 10 mm that is less than 5 % of the column diameter; this ignores the development of hoop stresses in the soil and around the periphery of the column. A hit-1 miss-1 basis is reasonable and this is supported by field observations. However, at closer spacing's, say 1.5 m centre-to-centre spacing's (2.1 m diagonal spacing), where free field displacements were measured to be about 20 mm for an isolated column, it may be necessary to adopt a hit-1 miss-2 approach to increase the spacing between successive column installations to reduce the potential for loss of cross sectional area in the column that has not fully cured.

9.2.6 Column installation stresses

The bending moment profiles calculated from the lateral displacement profiles due to the installation of columns C15 and D10 are shown in Figure 9.9*b* and *c* respectively where these are calculated based on a zero axial stress condition during ground improvement works (column self-weight is ignored). The column is assumed to move laterally with the soil mass; the lateral displacement measured by the inclinometer is therefore considered representative of the column lateral movement. The columns are assessed to crack to a varying extent between about R.L. – 1 m and – 5 m however whether this cracking developed in the field is dependent on the extent to which the

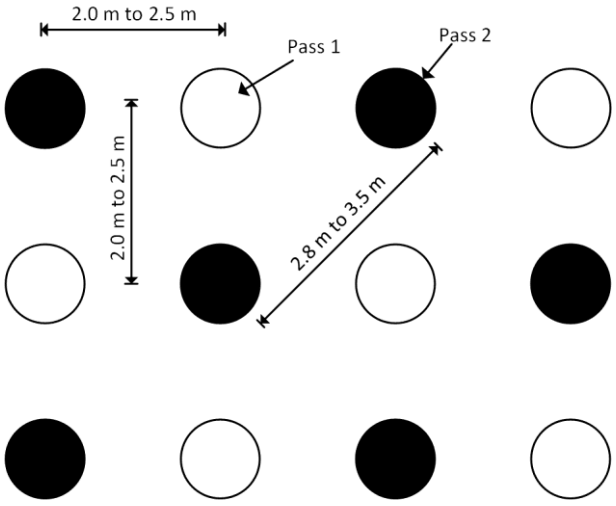

Figure 9.8. Hit-1 miss-1 installation process for square array

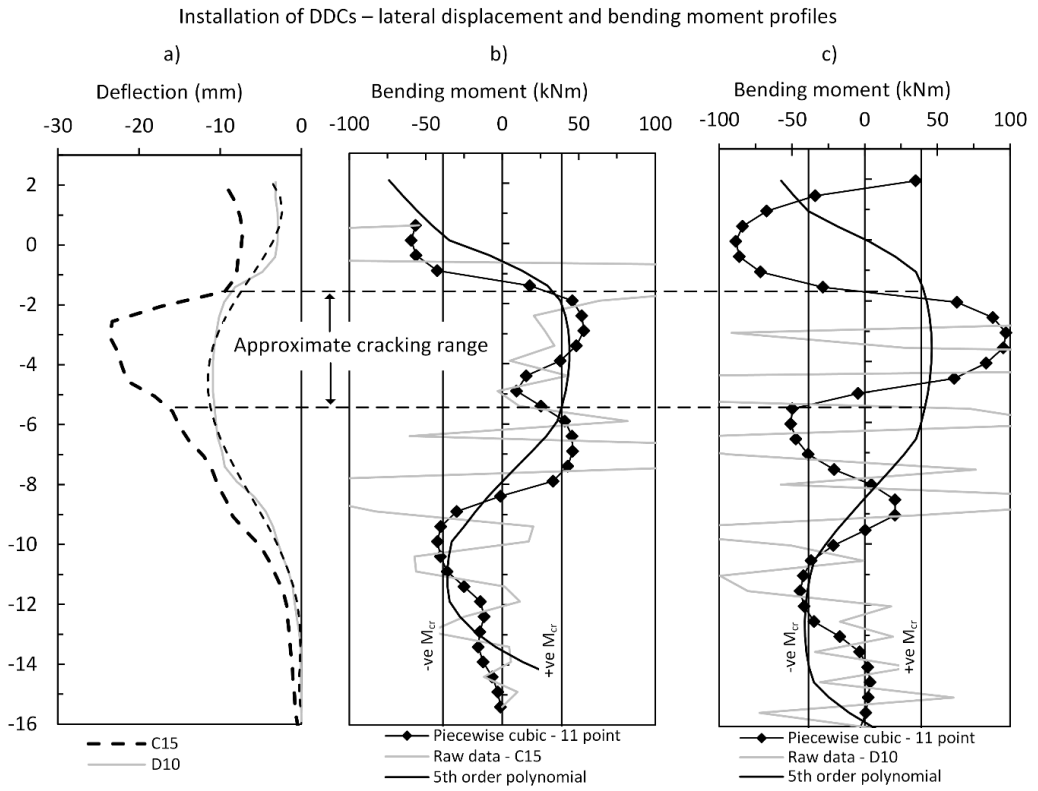

Figure 9.9. (a) Lateral displacement due to installation of columns C15 and D10 and equivalent bending moment profiles for **(b)** C15 and **(c)** D10

concrete has hardened and the ductility of the early set concrete. For a column situated within a 2 m by 2 m array, bending moments will develop cumulatively due to the installation of adjacent columns. Vector diagrams showing the displacement of an element of soil due to the installation of columns was presented in Figure 8.26 and Figure 8.29 for Inclinometer #1 and #2 respectively, provide an indication of the amount of lateral displacement that the soil mass (and by inference a column) undergoes due to the installation of the surround columns. In addition, lateral displacement of over 20 mm and nearly 10 mm where measured due to Stage 3a and 3b work (Figure 8.30) with a measurable change in column tilt (Figure 9.5).

A typical plot of time-dependent concrete strength (Figure 9.10) indicates that concrete develops around a third of its strength after 3 days, and 75 % after 7 days. Given the rate of concrete strength development, the time generally taken to complete multiple passes of installation as part of a ground improvement works program and the considerable amount of lateral displacement imposed on a column due to the installation of columns it would seem inevitable, that cracking of unreinforced columns will occur to some extent. The author is not aware of any

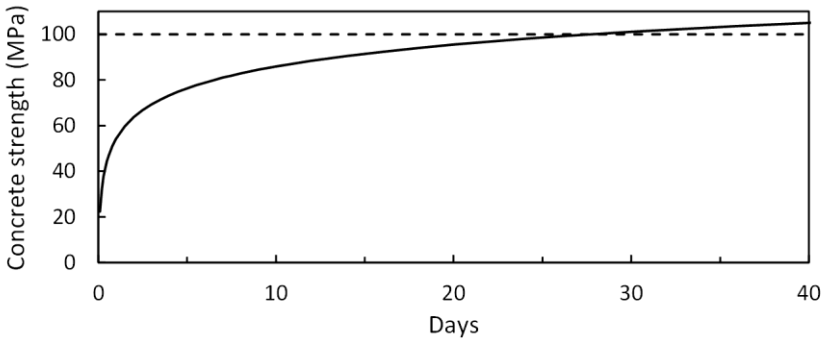

Figure 9.10. Typical rate of curing for Portland cement (Gilbert et al. 1990)

practically viable, and theoretically sound, ground improvement approaches that would mitigate these detrimental effects associated with column integrity during installation. Whilst the development of flexural cracking is not likely to impact the ability of these columns to carry vertical load in their intended manner, the analysis presented does however raise questions about the ability of the installed columns to provide lateral resistance to embankment lateral loading and to resist lateral sliding and global instability.

9.3 Discussion

9.3.1 Implications on the numerical modelling of GRCSEs under serviceability behaviour

For the North Dynon embankment case study considered here, as with many other GRCSEs, numerical methods are needed to assess the vertical and horizontal deformation of the embankment under serviceability conditions. This is particularly important for high embankments where lateral deformation under serviceability conditions may govern the acceptability of the proposed design. However, the traditional FEM techniques that are often utilised by design engineers are limited in their ability to explicitly model column installation effects and radial equilibration, yet alone group effects and in-turn the affect that these have on the performance of the other columns and embankment itself. These group effects are seldom modelled explicitly as part of routine design, if at all. These mechanisms include:

1) lateral displacement due to the installation of multiple columns in a dense array leading to induced internal forces and bending moments; the potential for column cracking is extremely high, if not inevitable, in unreinforced columnar elements
2) the build-up of excess pore water pressure beneath a GRCSE due to ground improvement, a reduction in effective stresses (in particular the vertical effective stress σ'_v), and by inference, enhanced lateral sliding due to the reduction in lateral resistance. This will further induce internal forces and bending moments in the columns supporting the embankment; the potential for column cracking is high.
3) radial equilibration of the columns, occurring as a group effect after ground improvement works. This acts in a direction opposite to lateral sliding and greatly increases the internal column forces and bending moments; the potential for column cracking is extremely high

These three mechanisms are all related to, and caused by, installation effects. The inability to assess this behaviour in GRCSE is not due to the lack of rigor in the structural assessment but the failure to explicitly model the geotechnical mechanisms involved due largely to the current limitations in the numerical techniques readily adopted in practice. The cavity expansion theories offer an analytical tool, or framework, to describe the governing mechanisms involved, to interpret and evaluate these effects, and by extension, a tool to evaluate group effects. However, the use of cylindrical cavity expansion theory to examine both excess pore water pressure and lateral deformation, as presented here, has limitations. At best, it provides a first-order assessment of the behaviour of installed columns. A solution to the problem of pile/column installation effects, and the group effects affecting a GRCSE is extremely complex. Advances in mesh-less methods (material point method, smooth particle hydrodynamics, discrete element method etc.) as well as other advanced numerical techniques, such as the Coupled Eulerian-Lagrangian (CEL), have enabled researchers to simulate the installation of an isolated drilled displacement column (Qiu et al. 2011, Pucker et al. 2012, Busch et al. 2013) with mixed success. However, the extension of these methods to model three-dimensional group effects on the scale of a typical GRCSE requires considerable computational power and further research to accurately model the coupled hydro-mechanical response of soft soils which is the unit of most interest when assessing the installation effects.

Despite these numerous limitations of traditional FEM techniques to model numerically, serviceability behaviour of a GRCSE, solution to these problems are required in practice. Recognition of the role that installation effects play in the performance of a GRCSE is an important starting point, and from that, an understanding of the need for "work-around" methods, at this time, to assess serviceability behaviour within a traditional FEM framework. Given the difficulties in explicitly modelling these mechanisms, and the many unknowns that cannot be directly accounted for numerically, a risk-based approach, which reflects this uncertainty it therefore, warranted.

This rationale largely underpins the design approach of modelling columns as "geotechnical" elements as described by Gniel et al. (2015) and Wong et al. (2012). This approach models the columns using plate elements with reduced bending stiffness to simulate the vertical stiffness and the loss of lateral resistance due to column cracking. The lateral spreading of the embankment is assessed by progressively reducing the plate element bending stiffness and assessing the dependency of the embankment deformation to the bending stiffness provided by the columns. The combined effects of lost bending and lateral shear capacity of a cracked column can be simulated, if required, by embedding the plate element in a thin finite element strip with a width of about 2/3 of the column diameter and material properties similar to that of cracked concrete. Typically, values of about 2 % uncracked moment capacity are adopted; a reasonable level of engineering judgement is required to assess the reliance on bending stiffness relative to the potential for column cracking. This is one such approach, that is time consuming, but does provide a more rational approach to dealing with installation effects associated with column integrity and behaviour. However, even with this approach, the build-up in excess pore water pressure and the corresponding reduction in lateral resistance is not explicitly accounted for.

By comparison, numerous studies (Liu et al. 2007, Jenck et al. 2009, Ariyarathne et al. 2012, Zhang et al. 2013, Bhasi et al. 2015) have modelled the construction and post-construction GRCSE performance with columns as "wished into place" structural elements (either a plate or linear-elastic material), with gross cross sectional properties (i.e., uncracked material properties) and have numerically simulated embankment construction starting with the load transfer platform construction. This approach ignores installation effects, equilibration, the potential for columnar cracking, and as a result, overestimates the lateral resistance provided by the installed columns. It is difficult to conceive a scenario where the ground improvement for a typical GRCSE could be undertaken and a dense array of unreinforced columns installed, without inducing considerable shear stresses and bending moments, and to a varying extent, cracking of the columns due to the ground improvement works alone. This does not include the effects of radial equilibration or any form of loading applied by the embankment itself. The basis for using gross cross sectional column properties, without strength or stiffness reduction, is poorly supported by experimental observation and has a weak theoretical basis.

An alternative approach suggested by a number of authors (Masse et al. 2004, Chatte et al. 2011) is to design the unreinforced columns as "structural" elements satisfying a zero tensile strain condition in order to limit the internal stresses and bending moments. A zero tensile strain condition is invalidated, in nearly all cases, during ground improvement works prior to the embankment construction even beginning, and due to the geotechnical mechanisms that are not explicitly modelled. Despite the findings of the numerical analysis, there can be little confidence that the as-built columns satisfy this zero tensile strain condition.

9.3.2 A column supported embankment or piled embankment

It is the author's experience that referring to these ground improvement elements as "piles" or as a "piled embankment" frequently leads to unnecessary confusion in design scenarios. Furthermore, this belies the design

intent of a GRCSE, and that is as a ground improvement option where unreinforced semi-rigid columns are installed and modelled numerically as "geotechnical elements" which reflects the risk of columns cracking. From a design perspective there is (presumably) a higher level of redundancy than a piled structure, and as a result, less onerous pile testing requirements are appropriate. This is this situation for most GRCSEs, as such, the term column, or alternatively, the more general term "semi-rigid inclusion", should be used.

There are of course certain design scenarios, where the geosynthetic reinforced embankment is required to be supported on piles. The piles may comprise driven pre-cast concrete piles, or columns with a reinforcement cage installed for example, that have large shear and flexural capacity and should be modelled as "structural elements" that satisfy traditional pile design requirements. Regardless of the piling technique adopted, the nomenclature should reflect the design intent of either a column supported, or pile supported geosynthetic reinforced embankment.

9.3.3 The "ground improvement effect" and the load transfer platform

The role that sub-soil settlement plays in the development of soil arching and on the performance of the load transfer platform was assessed by King et al. (2017a) for the case study considered here. At this time, there still remains considerable uncertainty in assessing the time rate of sub-soil settlement due to 1) uncertainty in the applied load (due to soil arching) acting on the sub-soil and 2) ground improvement affecting sub-soil behaviour. The ground improvement effect includes the radial consolidation of soft soil surrounding individual columns, the build-up of excess pore water pressure and the settlement interaction between columns and the soft soil. However, a large number of researchers have sought to address this first item – soil arching – and considerable progress has been made. At this time, it would seem apparent that the difficulties in describing accurately the ground improvement effects represents a greater barrier to fully understanding load transfer platform behaviour.

9.4 Summary of findings

A number of findings have been outlined based on the assessment of the case study considered herein:

- Total settlement of a GRCSE is affected by the development of maximum arching (see King et al. (2017a) due to the increase in load acting on the column. In the vast majority of embankments, this occurs post-construction.
- For the typical centre-to-centre spacing adopted for a GRCSE, the stress, displacement and pore water pressure fields arising due to installation effects will overlap; installation effects influence the behaviour of a GRCSE as a group effect.
- Excess pore water pressure will develop due to the embankment load distribution in the load transfer platform. However, in most cases, the build-up of excess pore water pressure due to ground improvement works will be considerably greater.
- The cumulative lateral displacement due to the ground improvement works can be expected to impose considerable lateral, shear and bending stresses on previously installed columns. Due to the slender unreinforced nature of the columns typically adopted for GRCSEs these bending moments will cause cracking of the columns during the installation phase. It is unlikely that a feasible ground improvement program could be implemented to avoid these detrimental effects.
- The dissipation of this excess pore water pressure (equilibration phase) leads to an inward movement of the soil mass beneath the embankment and imposes additional lateral/shear stresses and bending moments on the supporting columns. The assumption that the columns supporting a GRCSE will form an outward

cantilever shape during the post-construction phase is an oversimplification of the true behaviour and ignores this equilibration behaviour.

- Numerical analysis used to predict the imposed bending moments in columns supporting a GRCSE cannot be validated by post-construction survey data alone.
- The rapid construction of most GRCSEs limits the time available for the dissipation of excess pore water pressure (due to ground improvement) beneath the embankment. As a result, effective stresses in the soft soil underlying a GRCSE are reduced and, by inference, the lateral resistance available to resist overall stability and lateral sliding mechanisms are reduced. This behaviour is likely to be greater for high embankments.
- The dissipation of excess pore water pressure will lead to strength gain in the soft soil, an increase in effective stress, and will increase lateral resistance available with time, however, this may take a significant period of time post-construction (dependent on drainage conditions) for the embankment to reach lateral equilibrium. The complete dissipation of the excess pore water pressure through the full thickness of a soft soil will take longer and equilibration may continue for several years' post-construction.
- These installation effects may also have a detrimental effect on sensitive infrastructure (shallow foundations, footpaths, underground services etc.) surrounding a GRCSE, however these have not been investigated, the emphasis here has been on the effects to the embankment itself.

9.5 Conclusion

This chapter has investigated installation effects and the role that these have on the performance of a GRCSE. The emphasis is on high embankments, where lateral forces are greater, although many of these findings are not limited to these types of embankments. As a GRCSE increases in height, the performance of the load transfer platform becomes less critical and lateral embankment forces become increasingly critical for overall stability. The data and analysis presented herein have shown that the lateral behaviour of the columns for these high GRCSEs, and not their axial capacity, dictates their suitability in the design of a GRCSE for high embankments.

For these embankments numerical modelling is generally required to ensure that acceptable embankment performance can be achieved. Designers using numerical modelling to assess serviceability behaviour of a GRCSE, particularly horizontal deformation, should appreciate the limitations of traditional FEM software to describe the column installation effects, and the associated geotechnical mechanisms, outlined in this chapter. A significant quantity of data has been presented highlighting the behaviour of the columns supporting the embankment and questions are raised regarding the integrity of these columns, the likelihood of column cracking and their ability to provide lateral resistance. The numerical modelling of unreinforced concrete columns supporting a GRCSE using gross cross sectional properties, without strength or stiffness reduction, and with no account for the potential for column cracking is highly questionable. The design approach described by Gniel et al. (2015) and Wong et al. (2012), which considers the columns as geotechnical elements, provides an approach that is more robust and theoretically sound than many of the other design approaches currently in use.

10 Research findings and conclusion

The research presented in this thesis has been undertaken to assess the behaviour of GRCSEs, with an emphasis on localised load transfer platform behaviour and global scale behaviour. In this chapter, the key findings of the research are summarised and some areas for future research described.

10.1 Overview of research

GRCSEs have become an increasingly popular ground improvement option for soft soil sites owing to advances in the capabilities of piling rig equipment in recent years and improvements in the understanding of the behaviour of geosynthetic materials. The ability to rapidly construct the embankment, and the stringent settlement tolerances that can be achieved post-construction, are frequently cited as being two of the major factors justifying the use of this design approach. However, this study has highlighted that the advantages that these two factors present over other forms of ground improvement are not without limitations.

To investigate further the behaviour of GRCSEs, a field case study has been undertaken where a recently constructed GRCSE in Melbourne, Australia was extensively instrumented. The site chosen for this study is underlain by Coode Island Silt, a soft soil well known to the local geotechnical profession. The existing published literature on the Coode Island Silt and the availability of large amount of geotechnical site investigation information make this a good choice of site for the present study. Instrumentation has been installed in two areas within the embankment with an aim to assess both localised load transfer platform behaviour and global behaviour. In meeting these objectives, the data gathered has been separated to form two major components of research presented in this thesis.

10.2 Research findings

The main findings of the research presented in this thesis are discussed below.

10.2.1 Coode Island Silt

Through a review of historic and recent geotechnical site investigation data and a comprehensive laboratory testing program a high quality geotechnical site characterisation has been achieved and has largely met the aim of establishing a benchmark case study for GRCSE behaviour. The characterisation of this site for research purposes also presented an opportunity to further add to the current state of knowledge of the Coode Island Silt (as outlined in King et al. 2016a and presented in Appendix B).

Through the use of automated testing and modified testing parameters (load increment ratio and load duration) the yield point of the Coode Island Silt has been better characterised and the test completed in a shorter period of time compared with the traditional (24 hour load increment) oedometer test. The data gathered has provided a more comprehensive description of the structured nature of the Coode Island Silt, as evidenced through the S-shaped *e*-

log(p) plot and the variation in C_c as the soil yields. It has been noted that the use of the suggested test range described in AS1289.6.6.1 – 1998 is not likely to offer more than a first-order characterisation due to difficulties characterising σ'_p and $C_{c\,max}$. In addition, it was found that Becker's strain energy method provides a more reliable characterisation of σ'_p.

One shortcoming of the use of automated oedometer testing is not being able to assess $C_{\alpha\varepsilon}$. This is however offset by a better characterisation of the compression index in the yield range; C_α can then be assessed using a C_α/C_c ratio, which for Coode Island Silt was found here to be 0.039 based on a number of oedometer tests with extended creep stages. To the author's knowledge, the C_α/C_c ratio for Coode Island Silt has not been defined previously in the published literature. This ratio is in good agreement with the ratio for inorganic clays and silts which is typically quoted as 0.04 ± 0.01 (Terzaghi et al. 1996).

The C_α/C_c ratio, primary and secondary compression index data and the plot of the e *vs* k_v suggest that the Coode Island Silt has similar characteristics to many inorganic clays and silts found throughout the world. Long term historic measurements of surface settlement (presented in Ervin, 1992 and Srithar, 2010) in the Coode Island Silt delta show an apparent linear trend, rather than a diminishing rate, on a linear time scale. As noted by Srithar (2010), it is likely that this observation is due, in part, to construction activities over the past century. The data here further supports this contention and it would seem that whilst this long term trend is most likely real, it is not a direct manifestation of the secondary creep characteristics of the Coode Island Silt. Rather this observed behaviour occurs due to a combination of factors that included surcharge loading due to historic filling/reclamation works, de-watering/groundwater drawdown etc. as well as creep compression.

Comparison between the CPT data and σ'_p, calculated from laboratory test data, indicates that the expression described by Lunne et al. (1997) (See Appendix B, Equation B6) with a k value ranging from 0.27 to 0.33 (average value $k = 0.3$) can be used to provide a first-order estimate of the preconsolidation stress. The agreement between the laboratory data and the CPT correlations is reasonably good; a k value of 0.27 matches exactly. However, it is likely that the more disturbed samples with corresponding lower σ'_p values cause the laboratory derived trendline to underpredict the *in situ* σ'_p profile.

$$\sigma'_p = k(q_t - \sigma_{v0}) \qquad \textbf{(10.1)}$$

The Coode Island Silt data presented suggests that further insight into the compressibility and permeability of Coode Island Silt can be gained through consideration of its mineralogical composition although at this point in time there is only limited data available describing the mineralogical composition of Coode Island Silt.

10.2.2 Arching behaviour

A comparative analysis, of the type suggested by Terzaghi (1943), has been undertaken by the author to assess the various GRCSE arching models as part of the literature review in Chapter 2. This present study follows on from the earlier work of Tien (1996), which comprehensively outlined an extensive amount of experimental studies that have investigated soil arching. From the studies described by Tien (1996), along with more recent studies, a relatively consistent description of the theoretical aspects of arching stress development in active mode trapdoor tests has been developed through numerous investigations (Ladanyi et al. 1969, Vardoulakis et al. 1981, Evans 1983, Stone 1988, Iglesia 1991, Ono et al. 1993, Dewoolkar et al. 2007, Costa et al. 2009, Chevalier et al. 2011). The pertinent aspects of arching behaviour, as they relate to GRCSE include (Figure 2.5):

- Deformation dependency
- Initial, maximum, load recovery and terminal phases of arching
- Progressive shear band development characterising maximum, load recovery and terminal phases of arching
- Shear bands developing at an inclined angle equal to the dilatancy angle at that particular point and time in the soil mass (Evans 1983, Stone and Wood 1992, Santichaianant 2002). The inclination of these shear bands, and their height relative to the thickness of the load transfer platform, has important implications for the arching stress development in GRCSE.

Based on this understanding of soil arching behaviour, the various categories of arching models (rigid/fixed, limit equilibrium, frictional, models with mechanical elements, empirical model and hammock models) have been assessed in the literature review. The category of limit equilibrium models has found the most widespread use in recent years in the various design standards and particularly emphasis was placed on assessing these models in this study. These models include the Hewlett and Randolph model (1988), the method of Zaeske (2001) and the Concentric Arches model (Van Eekelen et al. 2013) and describe the vertical stress acting in the area between the columns based an assumed failure surface. The failure surface which forms the basis of these limit equilibrium methods, may, or may not, have a sound theoretical basis. That is to say, the failure surface (which is governed by the dilatancy angle) may, or may not, accurately describe the initial shear band development (line OA in Figure 2.5) which largely influences the maximum arching development. These theoretical aspects of arching, which are based on the works of others, is provided in the background of King et al. (2016, 2017a, b, c)

10.2.3 Load transfer platform behaviour – arching stress development

Based on the arching stress-deformation relationship described in the preceding section, and interpretation of the field case study data in Chapter 5 which showed time-dependent development of arching stresses, it is evident that the observed post-construction behaviour in the field case study is occurring as a function of sub-soil settlement/geogrid deflection. To assess the arching stress-deformation relationship the author has made us of the Ground Reaction Curve method (Iglesia et al. 1999, 2013), this requires converting the field case study geometry into an equivalent axisymmetric unit cell.

This method was found to be in good agreement with the strain gauge readings, the sub-settlement analysis and the back-calculated base settlement from the GRC which all indicated sub-soil settlement in the range of 30 mm to 60 mm. The observed behaviour at the North Dynon embankment is consistent with the development of maximum arching stress conditions and these conditions were shown to agree well with the method of Zaeske (2001) and the Concentric Arches model. While these limit equilibrium models do not explicitly state the arching stress conditions which they aim to describe, based on the concepts of “Concentric Arches” and “Multi shell arches” and their limit equilibrium formulation it is inferred that they knowingly, or unknowingly, formulated to describe maximum arching stress conditions. Regardless of the intention, knowingly or otherwise, the quantitative output of these limit equilibrium methods appears to agree well with observed maximum arching stress conditions in this study as well as others field case studies (see for example the “validation” of the Concentric Arches model by Van Eekelen et al. 2015).

However, it is predicted that with on-going base settlement, due to creep compression of the Coode Island Silt, that the arching stresses will transition into the load recovery phase over about the next 12 years as the loss of sub-soil support condition is reached. When comparing arching stress models in a GRCSE, the problem is one of

deformation compatibility. A number of arching stress-deformation relationship were compared in Chapter 2 and 7, these included: the bi-linear relationship adopted in the Load-Displacement compatibility method, the GRC and methods which describe this relationship as constant i.e., limit equilibrium models. The appropriateness of an arching model in load transfer platform behaviour is highlighted in Figure 2.18 through the use of an analogy with a material exhibiting pronounced strain softening behaviour.

When using limit analysis techniques, such as the slip-line method, limit analysis methods, and the limit equilibrium method as adopted here for GRCSE design, it is necessary to ignore the strain softening behaviour of the stress-strain curve when predicting collapse loads with the assumption of perfect plasticity (this is an implicit assumption of a limit equilibrium model). The validity of an assessed collapsed load, where perfectly plasticity is assumed, is dependent on the deformation range, the problem geometry and boundary stress; its' relative position will be somewhere between the bounds of peak and residual shear strength (Chen et al. 1975) (Figure 2.18*a*). This analogy resembles the description of arching stress development where the inverse of the load-deformation behaviour in Figure 2.18*a* is taken. The result is the SRR plotted in Figure 2.18*b*. However, a key difference between the two is that limit analysis is traditionally employed to assess a collapse load for structures where the problem is load dependent. However, limit analysis of arching stress development in a GRCSE is displacement controlled (by the geosynthetic reinforcement and sub-soil support), and as a result, the limiting load (or stress) which is predicted by the limit equilibrium method is not a collapse load.

This analogy highlights an important difference between traditional limit analysis techniques which aim to predict a collapse load for load controlled problem and the displacement controlled limit equilibrium analysis employed for LTP design. This analogy also highlights a key similarity between the two problems; the displacement range of the limit equilibrium method must be compatible with the problem it seeks to describe. For limit equilibrium models such as the method of Zaeske and Concentric Arches models, which describe maximum arching, this relative displacement range is 2 % to 4 %.

The appropriateness of an ultimate limit state arching model which is formulated to describe maximum arching is questionable on the following basis:

1) this is the least conservative position with respect to the stress acting in the area between the columns and is analogous to a collapse load formulated based on peak strength (Figure 2.18*a*),
2) deformation must be limited to about 4 % relative displacement in order for this arching stress formulation to remain valid; this is difficult to achieve even where very high strength geogrids are adopted. Alternatively, this may be achieved with considerable reliance on sub-soil support, which in itself is questionable at ultimate limit state.

10.2.4 Serviceability behaviour in shallow embankments

The serviceability behaviour of GRCSE embankments can be approximately delineated based on the McGuire line (Equation 10.2). For embankment which normalised geometry plotting above this line, the surface of the embankment is located above the H_{crit}, and the differential surface settlement associated with the serviceability reinforcement strain limit state is not likely to be critical. The limit state conditions associated with global embankment stability become increasingly important as the height of the embankment increases above this line. In the Load Displacement Compatibility method (Filz et al. 2012), it is recommended that this line defines the minimum embankment height. However, a number of design standards suggest minimum embankment heights well

below this line. For these geometries, differential surface settlement should be expected, and an assessment of the potential for differential settlement relative to the performance tolerances undertaken.

$$\frac{H_{\text{crit}}}{d} = 1.15\left(\frac{s'}{d}\right) + 1.44 \qquad (10.2)$$

An estimate of serviceability behaviour can be calculated using the differential settlement ratio from (McGuire 2011) and assessing the time-dependent base settlement. From this analysis, the construction- and post-construction phase settlement can be calculated. It has been shown in Chapter 7 that assessment of the base settlement is dependent on the arching stress-deformation relationship adopted. Accurate assessment of base settlement requires the use of a relationship which describes initial arching, maximum arching and load recovery. At this time, the GRC method is the only method available which enables this calculation to be performed.

Assessment of the base settlement using a constant value of stress, or the bi-linear relationship adopted in the Load Displacement Compatibility method will lead to an erroneous assessment of the time-rate of base settlement. The assessment of base settlement using an idealised example in Chapter 7 has shown that achieving the long term working condition requires considerable time under the action of arching stresses alone, even for very soft soil sites. In most cases this condition takes several years but can be accelerated by the presence of an unsupported fill layer and/or a working platform beneath the load transfer platform.

Understanding serviceability behaviour is critical to the successful long term performance of shallow height GRCSEs. The author considers that further research is required to develop serviceability limit state design methods for embankments below the McGuire line, if the design of these embankments is to be recommended in design standards, as is currently the case. Until such time, the author considers that it is unwise to construct shallow height embankments at, or near, the minimum height of 0.7 (s − a) for structure with sensitive surface settlement tolerances (road, rail infrastructure etc.) without detailed assessment of both the differential surface settlement and time required for the working condition to be achieved.

The assessment of serviceability behaviour in shallow height embankments has also highlighted the importance of the sub-soil support and the development of the working condition post-construction. In many cases, long term creep compression controls the development of the working condition. In contrast to the traditional view of GRCSE behaviour, detailed site investigation is not normally undertaken; this is often justified on the basis that the underlying soft soil does not greatly influence the GRCSE behaviour as the embankment load is transferred via the load transfer platform to the columns that then by-passes the soft soil. However, it has been shown in Chapter 7 that the compressibility and time-rate of settlement of the sub-soil plays an important role in the serviceability behaviour of GRCSE. In particular, the parameters σ_{p} and C_{α}. Often, these are not assessed accurately as part of site investigation works for GRCSEs. An assessment of the arching stress development and base settlement should reflect the uncertainty in these parameters if this is the case.

10.2.5 Dynamic loading and progressive collapse

The response of the arching mechanism to earthquake loading, cyclic dynamic loading (vehicular traffic) and other sources of dynamic loading (i.e., nearby construction works) is not well understood. The response of earthquake loading may cause the partial, or complete, collapse of the arching mechanism and re-establishment of overburden stress conditions. The partial collapse of soil arching was shown in model scale tests under cyclic dynamic load by Heitz et al. (2008) and was observed in the field case study (see Section 8.4.4) when columns were installed (at > 8

m) adjacent to a partially constructed GRCSE. Variations in the arching stresses due to vehicular loading was also observed and described at the N210 embankment (Haring et al. 2008) and Kyoto Rd (Van Eekelen et al. 2010). These studies highlight the sensitivity of the arching mechanism to external disturbance. Terzaghi's (1943) comments are noteworthy. Whilst emphasising that the state of stress defining the arching condition is no less permanent than any other state of stress that relies on shear stress, such as the stress conditions beneath a footing. Terzaghi also noted that external disturbance can influence this state of stress under static load conditions and that "*vibrations are the most important influence of this sort"*.

The re-establishment of overburden conditions will lead to further deformation and the re-establishment of some arching condition. However, the shear banding/failure surface, previously developed in the LTP, means that maximum arching will not re-establish, rather a weaker state of arching will develop (load recovery phase). This behaviour generates a positive feedback loop (i.e., increasing base settlement will lead to increasing stress leading to further base settlement, etc.) and will lead to progressive failure if enough sources of external disturbance are provided over the design life of a GRCSE. For the typical 100 year design life, at least one or more sources of external disturbance can, or should, be expected and engineering mechanisms employed to mitigate this risk. Some authors have suggested the removal of geosynthetic reinforcement under certain circumstances (i.e., for a thick fill layer beneath the LTP as suggested by Wong and Muttuvel, 2012), the reinforcement provides an engineering mechanism to guard against unrestrained base settlement under the progressive collapse mechanism outlined. Given the limited understanding at this time of the response of soil arching in GRCSE to dynamic loading, the removal of geosynthetic reinforcement is not recommended by the author.

The progressive collapse mechanism described above arises when the phases of arching stress development are considered, by contrast, the constant arching stress condition predicted by limit equilibrium models (and the bi-linear model), trend towards, a long term state of "equilibrium" under arching stresses; regardless of sub-soil deformation (Figure 7.8*c*) or soft-soil parameters (compare Figure 7.7 and Figure 7.8*c*). This is a short-coming of these arching models and can lead to erroneous conclusions regarding the long term performance of LTP (and GRCSE) behaviour.

10.2.6 Numerical modelling of soil arching

The deformation range of interest for GRCSE is up to 10 % relative displacement. This was described in the literature review and has been discussed based on the data from the field case study in Chapter 5. The FEM was used to model the GRC over this displacement range and number of computational difficulties were encountered. It was shown that it is difficult to achieve reliable results beyond the development of maximum arching due to the effects described below (these have been investigated numerically and through physical modelling in numerous studies):

- shear bands development (Roscoe 1970, Arthur et al. 1977, Vardoulakis 1980, Vardoulakis et al. 1981, Vermeer 1982, Bolton 1986, De Borst et al. 1993, Chu et al. 1996, Saada et al. 1999, Alshibli et al. 2000, Gajo et al. 2007)
- large relative displacement of the soft soil relative to the rigid pile heads (De Borst et al. 1984, Vermeer et al. 1984, Van Langen et al. 1991)
- severe mesh distortion at the corner of the pile heads, i.e., at the singularity point (De Borst et al. 1984, Vermeer et al. 1984, Van Langen et al. 1991)

Despite varying the material parameters (within reasonable limits) the maximum arching observed in the tests performed by Iglesia et al. (2013) was not accurately simulated. The development of shear banding, which is highlighted in Figure 6.10 shows quite clearly that the formulation of discontinuities within the soil mass is likely the primary reason for the difficulties in simulating maximum arching stress conditions as the shear band formation precedes the maximum arching stress development. The presence of these shear bands then poses significant on-going convergence issues where the tests is continued to greater values of relative displacement. Whilst this may seem like an obvious finding, it is evident from numerous publications that the limitations of FEM applied to arching stress development in a trapdoor tests, or a GRCSE which suffers from the same limitations, are not fully appreciated, and if these limitations are understood, there is no discussion as to the effects this introduces into the numerical analysis.

Numerous authors have undertaken FEM studies of full scale GRCEs and drawn a variety of conclusions based on the arching stresses calculated in the numerical simulations. In many cases, the load transfer mechanisms assessed in the numerical simulation are compared with the analytical methods describing ultimate limit state conditions despite the clear limitations in simulating ultimate behaviour using the FEM. These are often presented without reference to the limitations outlined above. Some examples of this have been discussed at Section 6.4 and include the studies of Bhasi et al. (2015), Bhasi et al. (2015), Jenck et al. (2009), Ariyarathne et al. (2012), Nunez et al. (2013), Briançon et al. 2011 and Zhuang et al. (2012) amongst others.

To address these difficulties, meshfree methods are required. In the present study, the SPH method has been introduced, although there are a number of other meshfree methods which could equally be used. The SPH method has been employed primarily to resolve the major difficulties associate with modelling the trapdoor problem; mesh distortion. Modelling of the large displacement trapdoor problem over the required relative displacement range (0 to 10 %) requires the issues associated with mesh distortion and shear band formation to be addressed. The SPH framework does not suffer from convergence issues due to mesh distortion and/or the formation of discontinuities, such as shear bands, within the problem geometry. However, while the issues associated with mesh distortion and shear band development were overcome a number of significant limitations were found with the constitutive model adopted within the SPH framework; the elastic-perfectly plastic model with a Drucker-Prager yield criterion. While this constitutive model may provide reasonable results for small strain problems, for large displacement problems, such as the trapdoor problem and the LTP behaviour in a GRCSE, where the failure mechanisms are strongly influenced by localised dilative behaviour this model is inadequate as it cannot describe the strain softening behaviour or the stress-dilatancy behaviour of the type described by Rowe (1962). The limitations of the constitutive model are not insurmountable and can be addressed, however, it is beyond the scope of the author's study to undertake such work. At the time of writing, work is on-going to address the limitations of the constitutive model.

10.2.7 Ground improvement for GRCSEs

Based on the assessment of the column capacity using the c-α method and the method of Bustamante and Gianeselli (1993, 1998) (see Appendix E1 and E2) along with the dynamic test results from two test columns (Appendix E3), it has been shown in Section 8.5.2 that the vertical axial capacity of the installed columns significantly exceeds the applied loads (serviceability capacities were shown to be typically 2 to 3 times greater than working loads). This result can reasonably be expected given the founding unit, the diameter of the columns and the relatively small applied loads. However, the difficulties with the ground improvement works lies not in demonstrating that a column with a 2 m embedded shaft (into the founding unit) has adequate axial capacity but demonstrating that a 2 m column

embedment (into the founding unit) has been achieved in the first instance, and furthermore, that this embedment can be reliable and repeatedly achieved. This is necessary to achieve uniform total column settlement (measured at the column head) across the ground improvement area. There are two factors which have been identified as important when considering the ability to confirm the founding socket length:

1. variability in the sub-surface conditions and
2. piling rig instrumentations

The use of CPTs is suggested as the quickest and most cost-effective method to reduce uncertainty in the sub-surface conditions. A strong correlation between CPT q_c profiles and the torque profiles of the piling rig was shown in Section 8.5.1. However, torque profiles tended to lag the CPT profile by between 0.4 m to 1.0 m due to differences in the geometries of the CPT cone and drilling tool; these effects tend to result in a conservative estimate of length of founding socket (i.e., the actual embedment length is greater than the length assessed based on the torque profile). The torque profile was found to be the most reliable indicator of founding conditions. This interpretation can be further aided if crowd pressure if measured, which in many cases it is not. The '*Installation Effort*' method of NeSmith (2003) is recommended as a field tool that can assist that the piling rig operator with the interpretation of founding conditions. Due to these difficulties, a recommended minimum socket embedded of at least 2 m is suggested to minimise the risk associated with inadequate penetration into the founding unit.

At this time, there is relatively poor understanding of the governing mechanism, relating to installation behaviour of drilled displacement columns, in an effective stress framework. The design methods that do exist for columns are largely semi-empirical and are concerned with the determination of bearing behaviour. These have largely been developed from *in situ* test results and relate unit base and shaft resistance to CPT tip resistance q_c or SPT blow count N. While these methods may provide a means to calculate bearing capacity, they provide limited insight into installation effects. Assessment of the installation behaviour and comparison with data from other case studies leads to a number of findings that relate to mechanisms occurring at the column/soil interface during and immediately after column installation:

- Effective stresses are out-of-balance at the interface immediately after installation. The unloading of radial stress (or relaxation) in the soil mass surrounding the column must occur, this is greatest at the soil/concrete slurry interface, and is accompanied by a reduction in column cross sectional area. This contention is well supported by the field data of Suleiman et al. (2015) (Section 8.3.3), (NeSmith 2002) and observations of lateral displacement behaviour from the present field case study which consistently under predicts displacement fields observed due to the installation of rigid driven piles.
- The construction records from drilled displacement columns are frequently used to validate the construction methodology and "confirm" that the design cross sectional area of the column has been achieved; this approach is questionable as it bears no relationship to the effective stress conditions at the soil/concrete shaft interface. This pressure-deformation relationship at the interface governs the final cross sectional area of the column.
- The development of shaft capacity is strongly time-dependent for displacement piles/columns. However, for drilled displacement columns, the radial stresses must develop from an initial near zero radial stress condition. The resulting shaft capacity of a drilled displacement pile will be less than that of an equivalent driven pile but greater than a non-displacement pile type such as a bored pile.

- For the typical centre-to-centre spacing adopted for a GRCSE (i.e., about 2m to 3 m), the stress, displacement and pore water pressure fields arising due to installation effects will overlap. This affects the rate of radial consolidation highlighted above.
- Fluid pressures are initially out-of-balance at the interface immediately after installation and due to the difference in fluid pressure there must be a net inward pressure condition immediately after installation. The flow, or seepage, of groundwater into the column is not however calculated to have a detrimental effect on the quality of the concrete, for the columns considered here, due largely to the low permeability of the remoulded Coode Island Silt near the column shaft interface, the rapidly reducing excess pore water pressure and finally the likelihood that hydraulic cracking in the Coode Island Silt (described above) will limit the excess pore water pressures that develop in the soil mass.

The cumulative lateral displacement due to the ground improvement works can be expected to impose considerable lateral, shear and bending stresses on previously installed columns. Due to the slender unreinforced nature of the columns typically adopted for GRCSEs these bending moments will cause cracking of the columns during the installation phase.

10.2.8 Global scale embankment behaviour

It has been shown in Chapter 8 and 9 that serviceability behaviour related to load transfer platform is likely to be the critical limit state condition for shallow height embankments. For high embankments above the McGuire line (McGuire, 2011), the global scale embankment limit state conditions, such as lateral sliding and overall stability become increasingly important as embankment height increases. It has been shown in this study that these mechanisms are affected considerably by installation effects, these include:

1) Lateral displacement due to the installation of multiple columns in a dense array leading to induced internal forces and bending moments in previously installed columns; the potential for column cracking is extremely high, if not inevitable, in unreinforced columnar elements.
2) The build-up of excess pore water pressure beneath a GRCSE due to ground improvement, a reduction in effective stresses, and by inference, enhanced lateral sliding due to the reduction in lateral resistance. This will further induce internal forces and bending moments in the columns supporting the embankment; the potential for column cracking is high as a result. The lateral sliding is predominately resisted by the columns which have a considerable higher stiffness relative to the transverse layers of geosynthetic reinforcement.
3) Radial equilibration of the columns, occurring as a group effect after ground improvement works. This acts in a direction opposite to lateral sliding and greatly increases the internal column forces and bending moments.

10.2.9 Numerical modelling global scale embankment behaviour

The inability to assess installation effects in a GRCSE is due to the inability to explicitly model the geotechnical mechanisms involved. Current FEM numerical techniques are limited in their ability to model large strain problems such as pile installation (Więckowski 2004) and generally advanced methods such as Coupled Eulerian-Lagrangian (CEL) (Qiu et al. 2011, Pucker et al. 2012) or point based (meshfree) methods such as smooth particle hydrodynamics (SPH) (Bui et al. 2008) or the material point method (MPM) are required. In some cases, “work-around” methods are adopted within a FEM analysis to account for installation effects.

The cavity expansion theories offer an analytical tool, or framework, to describe the governing mechanisms involved, to interpret and evaluate these effects, and by extension, a tool to evaluate group effects. However, the use of cylindrical cavity expansion theory to examine both excess pore water pressure and lateral deformation, as presented here, has limitations. It provides at best a first-order assessment of the behaviour of installed columns. A solution to the problem of pile installation effects, and the group effects affecting a GRCSE is extremely complex.

Recognition of the role that installation effects play in the performance of a GRCSE is an important starting point, and from that, an understanding of the need for "work-around" methods, at this time, to assess serviceability behaviour within a traditional FEM framework. Given the difficulties in explicitly modelling these mechanisms, and the many unknowns that cannot be directly accounted for numerically, a risk-based approach, which reflects this uncertainty it therefore, warranted. This rational largely underpins the design approach of modelling columns as "geotechnical" elements as described by Gniel et al. (2015) and Wong et al. (2012). This approach models the columns using plate elements with reduced bending stiffness to simulate the vertical stiffness and the loss of lateral resistance due to column cracking. Alternatively, numerical modelling techniques which assume gross cross sectional column properties, without strength or stiffness reduction, is poorly supported by experimental observation and has a weak theoretical basis.

The author considers that the nomenclature adopted for GRCSE should reflect the design intent of a GRCSE, and that is as a ground improvement option where unreinforced semi-rigid columns are installed and modelled numerically as "geotechnical elements" which reflects the risk of columns cracking and the potential for reduced bending and shear capacity. From a design perspective, there is (presumably) a higher level of redundancy than a piled structure, and as a result, less onerous pile testing requirements are appropriate. This is this situation for most GRCSEs, as such, the term column, or alternatively, the more general term "semi-rigid inclusion", should be used. The term "piled embankment" should be avoided unless it is the intention of the designer to design the piles as such, and in accordance with the relevant design standards.

10.3 Further research

The author recommends that further development of arching models for the purpose of load transfer platform design should incorporate sub-soil settlement as a governing parameter. While the GRC method describes these phases, further validation of the GRC method with various geometric and material properties is required. In particular, the properties characterising the GRC and developed based on the two-dimensional trapdoor tests, require validation (or otherwise) based on three-dimensional GRCSE tests. In the author's opinion, the GRC parameters of interest include: the empirically derived initial and secant arching modulus values of 63 and 125 respectively, the relative displacement range of maximum arching (2 % to 4 %), the relative displacement range at which maximum arching transitions to the load recovery phase (3 % to 5 %), and finally, how the equivalent relative displacement is assessed. i.e., is it assessed based on the settlement at the edge of the pile head, or the displacement where maximum sag occurs (as assumed here, or is there some other value representative of the sub-soil settlement that should be used?)

The results of the analysis presented in Chapter 5 suggest that the characteristic parameters of the GRC are, at the least, reasonable for describing the three-dimensional arching associated with a GRCSE, however further validation is required. Further work of this type is currently underway at Monash University where progressive development of soil arching in three-dimensional is being investigated using advanced Computed Tomography (CT) techniques, including neutron and synchrotron x-ray sources. This work builds on the limited studies that have examined the three-dimensional soil arching behaviour (Eskişar, et al. 2012, Chevalier and Otani 2011), by

implementing techniques that are able to achieve higher energies, greater radiation flux and less imaging artefacts compared to conventional x-ray CT. Model tests of small scale column supported embankments (without geosynthetic reinforcement) were undertaken at the neutron imaging station called DINGO (Garbe et al. 2015) located at the OPAL reactor (Australian Nuclear Science and Technology Organisation (ANSTO), New South Wales, Australia) and the Imaging and Medical Beamline at the Australian Synchrotron (ANSTO, Victoria, Australia). Some of the findings from this study along with an overview and preliminary results of this on-going research are presented in King et al. (2017c).

Further work to validate the differential settlement ratios contours in Figure 7.4 would be highly beneficial as this would increase the accuracy of the serviceability assessment carried out in Chapter 7 and would provide a more rigorous basis for this approach. In addition, in the author's opinion the current understanding of the effects of dynamic loading on the arching stresses in GRCSEs is poorly understood. Field data from the N210 embankment case study presented in Figure 7.11 showed quite clearly the determinantal effects which dynamic vehicular loading can have on a shallow embankment. There are other examples in the published literature. In addition, a portion of the live load is carried by the geosynthetic reinforcement each time a vehicle passes over the embankment. The potential for this repetitive behaviour to cause long term irrecoverable plastic deformation in the geosynthetic reinforcement represents a significant risk to the long term performance of this, and other, shallow height GRCSEs and further work to understand these long term mechanisms is warranted.

The other major area of GRCSE design which the author considers would benefit greatly from further research is the role of column installation effects on global scale embankment behaviour. The mechanism which require further consideration relate to the rate of sub-soil consolidation and therefore the time for which the phase arching develop in the field. These include:

1. The interaction between soft soil and piles and its' role in reducing the relative displacement between pile and sub-soil and
2. Role of the piling hardstand and the level of load transfer platform relative to the historic ground surface.

Small to medium scale laboratory testing to examine installation effects would be beneficial to better understand their effects on the soft soil and global scale embankment behaviour. Further research is also required to understand the pressure-deformation behaviour at the column interface, without a more comprehensive understanding of this behaviour it is difficult to; 1) confirm the conditions at the column/soil interface, and perhaps more importantly 2) assess the development of radial stresses acting on the column shaft with time.

10.4 Conclusion

Post-construction data of a recently constructed GRCSE supported on drilled displacement columns in Melbourne, Australia shows the time-dependent development of arching over the two-year monitoring period and a strong relationship between the development of arching stresses and sub-soil settlement. A ground reaction curve (based on the work of Iglesia et al. 1999, 2013) was adopted to describe the development of arching stresses and good agreement was found for the period observed thus far. Four phases of arching stress development (initial, maximum, load recovery and creep strain phase) have been proposed and were shown to describe the time-dependent, and sub-soil dependent, development of arching stresses that can be expected to occur in many field embankments. These findings highlight the need for coupled arching stress-deformation models to describe accurately ultimate limit state

conditions, and more importantly serviceability behaviour (i.e., deformation of the embankment) which typically governs the acceptability of a GRCSE design.

This approach contrasts the widely adopted "*two-step"* design approach, which uses limit-equilibrium models that de-couple the arching stress-deformation relationship to describe ultimate limit state behaviour. Of the four phases proposed by the author, the load recovery phase is the most important with respect to load transfer platform design as it predicts the breakdown of arching stresses in the long term due to increasing sub-soil settlement. These concepts were developed further and an approach was presented which provides a means to predict serviceability behaviour, and at the same time, raises questions about the long term performance and the manner in which acceptable performance has been achieved in the short term in several field case studies. In particular, those constructed at, or near, a minimum embankment height of $0.7(s - a)$.

In addition to the investigation of localised arching stress development in GRCSEs this study also examines the global scale behaviour of embankments. Traditional FEM techniques used in practice to model serviceability behaviour are limited in their ability to model the geotechnical mechanisms associated with column installation, equilibration and group installation effects. The role that column installation effects have on the performance of the GRCSE has been highlighted and the behaviour of the columns supporting the embankment was emphasised. It was shown that cracking of the unreinforced columns supporting the embankment is inevitable and that the reduction of lateral resistance provided by the columns should be accounted for in design. The suitability of various numerical approaches currently used in design that adopt gross cross sectional properties of the columns, without strength or stiffness reduction, and with no account for the potential for column cracking is highly questionable. The design approach described by Gniel et al. (2015) and Wong et al. (2012), which considers the columns as geotechnical elements with reduced column stiffness, provides an approach that is more robust and theoretically sound than other design approaches currently in use.

References

Acheson, D. J. (1990). *Elementary fluid dynamics*. Oxford University Press, Oxford, United Kingdom. pp. 408.

Ahmadi, M. and Robertson, P. (2005). Thin-layer effects on the CPT q_c measurement. *Canadian Geotechnical Journal,* **42**(5): 1302-1317. doi: 10.1139/t05-036

Almeida, M. S. S., Marques, M. E. S., Almeida, M. C. F. and Mendonca, M. B. (2008). Performance of two "low" piled embankments with geogrids at Rio de Janeiro. *Proceedings of the 1st Pan American Geosynthetics Conference and Exhibition*. Cancun, Mexico. 2-5 March 2008. pp. 1285-1295.

Alshibli, K. A. and Sture, S. (2000). Shear band formation in plane strain experiments of sand. *Journal of Geotechnical and Geoenvironmental Engineering,* **126**(6): 495-503. doi: 10.1061/(ASCE)1090-0241(2000)126:6(495)

Anantasech, C. (1984). *Stress-deformation and strength of soft alluvial clay.* Ph.D. thesis. Department of Civil Engineering, Monash University, Melbourne, Australia.

ARHS. (2014). *Victorian railways history, 1839 - 1899*. Australian Railway Historic Society - Victoria Division Inc., viewed May 5 2014. Available at; http://www.arhsvic.org.au/index.php/rail-history/victorian-railways-history-1839-1899

Ariyarathne, P., Liyanapathirana, D. and Leo, C. (2012). Comparison of different two-dimensional idealizations for a geosynthetic-reinforced pile-supported embankment. *International Journal of Geomechanics,* **13**(6): 754-768.

Arthur, J., Dunstan, T., Al-Ani, Q. and Assadi, A. (1977). Plastic deformation and failure in granular media. *Geotechnique,* **27**(1): 53-74.

AS1726 (1993). *Geotechnical Site Investigation.* Australian Standards, Sydney, NSW, Australia, SAI Global

AS1289 (1998). *Method 6.6.1: Soil strenth and consolidation tests - determination of the one-dimensional consolidation properties of a soil - Standard method (AS 1289.6.6.1 - 1998)*. Australian Standard - Method of testing soils for engineering purposes. Australian Standards, Sydney, NSW, Australia, SAI Global.

AS1289 (2007). *Method 5.8.1: Soil compaction and density tests - determination of field density and field moisture content of a soil using a nuclear surface moisture - density gauge - direct transmission mode (AS 1289.5.8.1-2007)*. Australian Standard - Method of testing soils for engineering purposes. Australian Standards, Sydney, NSW, Australia, SAI Global**:** pp. 21.

Asaoka, A., Kodaka, T. and Nozu, M. (1994). Undrained shear strength of clay improved with sand compaction piles. *Soils and foundations,* **34**(4): 23-32.

Aslam, R. and Ellis, E. A. (2008). Centrifuge modelling of piled embankments. *Proceedings of the 1st International Conference on Transportation Geotechnics - Advances in Transportation Geotechnics*. Nottingham, U.K. 25-27 August 2008. CRC Press. pp. 363-368.

Azzouz, A. S. and Morrison, M. J. (1988). Field measurements on model pile in two clay deposits. *Journal of geotechnical engineering,* **114**(1): 104-121.

Baligh, M. M. (1985). Strain path method. *Journal of Geotechnical Engineering,* **111**(9): 1108-1136.

Basu, P. and Prezzi, M. (2009). *Design and applications of drilled displacement (screw) piles*. Publication FHWA/IN/JTRP-2009/28. Joint Transportation Research Program, Indiana Department of Transportation and Purdue University, West Lafayette, Indiana. doi: 10.5703/1288284314278.

Basu, P., Prezzi, M. and Basu, D. (2010). Drilled displacement piles - current practice and design. *Deep Foundations Institute Journal* **4**(1): 3-20.

Basu, P., Prezzi, M. and Salgado, R. (2013). Modeling of installation and quantification of shaft resistance of drilled-displacement piles in sand. *International Journal of Geomechanics,* **14**(2): 214-229.

Bathurst, R. J., Blatz, J. A. and Burger, M. H. (2003). Performance of instrumented large-scale unreinforced and reinforced embankments loaded by a strip footing to failure. *Canadian geotechnical journal,* **40**(6): 1067-1083. doi: 10.1139/T03-052

Bauer. (2013). *Full displacement pile system - process and equipment*. Bauer Maschinen Gmbh, viewed 20 June 2016. Available at; https://www.bauer.de/export/shared/pdf/bma/products/methods/905-657-2.pdf

Becker, D. E., Crooks, J. H. A., Been, K. and Jefferies, M. G. (1987). Work as a criterion for determining in situ and yield stresses in clays. *Canadian Geotechnical Journal,* **24**(4): 549-564. doi: 10.1139/t87-070

Bell, G., Bowen, K., Douglas, J., Hancock, J., Jenkin, J., Kenley, P., Knight, J., Neilson, J., Spencer-Jones, D. and Talent, J. (1967). Geology of the Melbourne district, Victoria. *Geological Survey of Victoria Bulletin,* **59**: 19-30.

Belytschko, T., Krongauz, Y., Organ, D., Fleming, M. and Krysl, P. (1996). Meshless methods: an overview and recent developments. *Computer methods in applied mechanics and engineering,* **139**(1-4): 3-47.

Bhasi, A. and Rajagopal, K. (2013). Numerical investigation of time dependent behavior of geosynthetic reinforced piled embankments. *International Journal of Geotechnical Engineering,* **7**(3): 232-240.

Bhasi, A. and Rajagopal, K. (2015). Geosynthetic-Reinforced Piled Embankments: Comparison of Numerical and Analytical Methods. *International Journal of Geomechanics,* **15**(5). doi: 10.1061/(ASCE)GM.1943-5622.0000414

Bhasi, A. and Rajagopal, K. (2015a). Numerical study of basal reinforced embankments supported on floating/end bearing piles considering pile–soil interaction. *Geotextiles and Geomembranes,* **43**(6): 524-536.

Bishop, D. (2010). New approaches to understanding the structure and geotechnical characteristics of estuarine sediments. *Australian Geomechanics,* **45**(3): 111-122.

Bjerrum, L. (1954). Geotechnical properties of Norwegian marine clays. *Geotechnique,* **4**(2): 49-69.

Bjerrum, L. (1972). Embankments on soft ground. *Proceedings of the ASCE specialty Conference on Performance of Earth and Earth-Supported Structures*. Purdue University, Indiana. ASCE. pp. 1-54.

Blyth, F. and De Freitas, M. (1984). *A geology for engineers - 7th edition*. Elsevier, Butterworth-Heinemann, Burlington, Massachusetts, U.S.A. pp. 325.

Bolton, M. (1986). The strength and dilatancy of sands. *Geotechnique,* **36**(1): 65-78.

BOM (2015). Australian Government Bureau of Meteorology - Mean monthly maximum and minimum temperature - Melbourne regional office weather station [Data set]. Retrieved from http://www.bom.gov.au/climate/data/stations/

Bond, A. and Jardine, R. (1991). Effects of installing displacement piles in a high OCR clay. *Geotechnique,* **41**(3): 341-363.

Bouazza, A., Kwan, P. S. and Chapman, G. (2006). Strength improvement of Coode Island Silt by the soil mixing method. *Australian Geomechanics,* **41**(3): 101-106.

Bouazza, A., Singh, R. M., Wang, B., Barry-Macaulay, D., Haberfield, C., Chapman, G., Baycan, S. and Carden, Y. (2011). Harnessing on site renewable energy through pile foundations. *Australian Geomechanics,* **46**(4): 79-90.

Branson, D. E. (1977). *Deformation of concrete structures*. McGraw-Hill Companies, New York. pp. 576.

Brettmann, T. and NeSmith, W. (2005). Advances in auger pressure grouted piles: design, construction and testing. *Proceedings of the Advances in Designing and Testing Deep Foundations*. Austin, Texas, USA. 24-26 January 2005. ASCE. pp. 262-274.

Briançon, L. and Delmas, P. (2010). Study of the load transfer mechanisms in reinforced pile-supported embankments. *Proceedings of the 9th International Conference on Geosynthetics*. Gaurujà, Brazil. 23-27 May 2010. pp. 1917-1920.

Briançon, L., Faucheux, G. and Andromeda, J. (2008). Full-scale experimental study of an embankment reinforced by geosynthetics and rigid piles over soft soil. *Proceedings of the 4th European Geosynthetics Conference*. Edinburgh, Scotland, UK. 7-10 September 2008. CD-ROM.

Briançon, L. and Simon, B. (2011). Performance of pile-supported embankment over soft soil: full-scale experiment. *Journal of Geotechnical and Geoenvironmental Engineering,* **138**(4): 551-561. doi: 10.1061/(ASCE)GT.1943-5606.0000561.

Brinkgreve, R., Swolfs, W. and Engin, E. (2011). PLAXIS 2D - Reference manual - 2011. Plaxis bv, Delft, the Netherlands.

Brinkgreve, R. and Vermeer, P. (2013). Plaxis Scientific Manual. Plaxix bv. Delft, the Netherlands.

Britton, E. J. and Naughton, P. J. (2010). An experimental study to determine the location of the critical height in piled embankments. *Proceedings of the 9th International Conference on Geosynthetics*. Guarujá, Brazil. 23-27 May 2010.

Brown, D. and Drew, C. (2000). Axial capacity of augered displacement piles at Auburn University. *Proceedings of the New technological and design developments in deep foundations*. Denver, Colorado, U.S.A. 5-8 August 2000. American Society of Civil Engineers, Virginia, U.S.A. pp. 397-403.

Brown, D. A. (2005). Practical considerations in the selection and use of continuous flight auger and drilled displacement piles. *Proceedings of the Advances in deep foundations*. Austin, Texas, U.S.A. 24-26 January 2005. pp. 251-261.

Brown, D. A., Dapp, S. D., Thompson, W. R. and Lazarte, C. A. (2007). Geotechnical Engineering Circular No. 8 - Design and Construction of Continous Flight Auger (CFA) Piles. Washington, D.C., U.S. Department of Transportation - Federal Highway Administration.

Brown, E. T., Bray, J. W., Ladanyi, B. and Hoek, E. (1983). Ground response curves for rock tunnels. *Journal of Geotechnical Engineering,* **109**(1): 15-39.

BSI. (1995). Code of practice for strengthened/reinforced soils and other fills. *British Standard BS8006* (1995). British Standards Institution, London, U.K.

BSI. (2010). Code of practice for strengthened/reinforced soils and other fills. *British standard BS8006-1*. British Standards Institution, London, UK.

Bui, H., Nguyen, G., Kodikara, J. and Sanchez, M. (2015). Soil cracking modelling using the mesh-free SPH method. *Proceedings of the 12th Australian New Zealand Conference on Geomechanics* Wellington, New Zealand. 22-25 February 2015.

Bui, H. H. and Fukagawa, R. (2009). A first attempt to solve soil-water coupled problem by SPH. *Terramechanics,* **29**: 33-38.

Bui, H. H. and Fukagawa, R. (2013). An improved SPH method for saturated soils and its application to investigate the mechanisms of embankment failure: Case of hydrostatic pore‐water pressure. *International Journal for Numerical and Analytical Methods in Geomechanics,* **37**(1): 31-50.

Bui, H. H., Fukagawa, R., Sako, K. and Ohno, S. (2008). Lagrangian meshfree particles method (SPH) for large deformation and failure flows of geomaterial using elastic–plastic soil constitutive model. *International Journal for Numerical and Analytical Methods in Geomechanics,* **32**(12): 1537-1570.

Bui, H. H., Fukagawa, R., Sako, K. and Wells, J. (2011). Slope stability analysis and discontinuous slope failure simulation by elasto-plastic smoothed particle hydrodynamics (SPH). *Geotechnique,* **61**(7): 565-574.

Bui, H. H., Fukagawa, R., Sako, K., Wells, J. C., Nakagawa, M. and Luding, S. (2009). Numerical simulation of granular materials based on smoothed particle hydrodynamics (SPH). *American Institute of Physics,* **1145**(1): pp. 575-578.

Bui, H. H., Kodikara, J. K., Bouazza, A., Haque, A. and Ranjith, P. G. (2014). A novel computational approach for large deformation and post‐failure analyses of segmental retaining wall systems. *International Journal for Numerical and Analytical Methods in Geomechanics,* **38**(13): 1321-1340.

Bui, H. H., Sako, K. and Fukagawa, R. (2009). Slope stability analysis and slope failure simulation by SPH. *Proceedings of the 17th International Conference for Soil Mechanics and Geotechnical Engineering*. Bibliotheca Alexandrina, Egypt. 5-9 October 2009. pp. 1578-1581.

Bui, H. H., Sako, K., Fukagawa, R. and Wells, J. (2008). SPH-based numerical simulations for large deformation of geomaterial considering soil-structure interaction. *Proceedings of the 12th International Conference of International Association for Computer Methods and Advances in Geomechanics*. Goa, India. 1-6 October 2008. pp. 570-578.

Bullock, P. J., Schmertmann, J. H., McVay, M. C. and Townsend, F. C. (2005a). Side shear setup. I: Test piles driven in Florida. *Journal of Geotechnical and Geoenvironmental Engineering,* **131**(3): 292-300. doi: 10.1061/(ASCE)1090-0241(2005)131:3(292)

Bullock, P. J., Schmertmann, J. H., McVay, M. C. and Townsend, F. C. (2005b). Side shear setup. II: Results from Florida test piles. *Journal of Geotechnical and Geoenvironmental Engineering,* **131**(3): 301-310.

Busch, P., Grabe, J. and Gerressen, F. W. (2013). Influence of the installation process of full displacement bored piles on the subsoil. *Proceedings of the Conference on Baltic Piling*. Tallin, Estonia. 3-5 September 2012. Taylor and Francis Group, London, U.K. pp. 157-163.

Bustamante, M. and Gianeselli, L. (1993). Design of auger displacement piles from in situ tests. *Proceedings of the 2th international geotechnical seminar on deep foundation on bored and auger piles*. Ghent, Belgium. 1-4 June 1993. A.A. Balkema, Rotterdam, the Netherlands. pp. 21-34.

Bustamante, M. and Gianeselli, L. (1998). Installation parameters and capacity of screwed piles. *Proceedings of the 3rd International geotechnical seminar on deep foundations on bored and auger piles* Ghent, Belgium. 19-21 October 1998. A. A. Balkema, Rotterdam, the Netherlands. pp. 95-108.

Camp III, W. M. and Siegel, T. C. (2006). Failure of a column-supported embankment over soft ground. *Proceedings of the 4th International Conference on Soft Soil Engineering*. Vancouver, Canada. 4-6 October 2006. Taylor & Francis/Balkema. pp. 117-121.

Carlsson, B. (1987). Armerad jord beräkningsprinciper för vertikala väggar, branta slänter, bankar på lös undergrund, bankar på pålar (in Swedish) "Reinforced earth calculation principles for the vertical walls, steep slopes, embankments on soft ground, embankment of piles". Terratema AB, Linköping, Sweden.

Carter, J., Booker, J. and Yeung, S. (1986). Cavity expansion in cohesive frictional soils. *Geotechnique,* **36**(3): 349-358.

Carter, J. P., Randolph, M. and Wroth, C. (1979). Stress and pore pressure changes in clay during and after the expansion of a cylindrical cavity. *International Journal for Numerical and Analytical Methods in Geomechanics,* **3**(4): 305-322.

Carter, J. P., Randolph, M. F. and Wroth, P. (1980). Some Aspects of the Performance of Open and Closed-ended Piles. *Proceedings of the International Conference on Numerical Methods in Offshore Piling*. Institute of Civil Engineers, London. pp. 165-170.

Chapra, S. C. and Canale, R. P. (2010). *Numerical methods for engineers, 6th edition*. McGraw-Hill. pp. 960.

Charles, J. A. and Watts, K. (1980). The influence of confining pressure on the shear strength of compacted rockfill. *Geotechnique,* **30**(4): 353-367.

Chatte, R. and Lauzon, M. (2011). Embankment Construction Using Controlled Modulus Columns for Nouvelle Autoroute 30 Project in Beauharnois (Qc). *Proceedings of the Pan-American Canadian Geotechnical Society - Geotechnical Conference*. Toronto, Ontario, Canada. 2-6 October 2011.

Chen, R., Wang, Y., Ye, X., Bian, X. and Dong, X. (2016). Tensile force of geogrids embedded in pile-supported reinforced embankment: A full-scale experimental study. *Geotextiles and Geomembranes,* **44**(2): 157-169.

Chen, W.-F. and Baladi, G. Y. (1985). *Soil plasticity: theory and implementation*. Elsevier Science Publisers B.V., Amsterdam, the Netherlands. pp. 244.

Chen, W.-F. and Liu, X. L. (1975). *Limit Analysis and Soil Plasticity*. Elsevier Scientific Publishing B.V., Amsterdam, the Netherlands. pp. 656.

Chen, Y.-M., Cao, W.-P. and Chen, R.-P. (2008). An experimental investigation of soil arching within basal reinforced and unreinforced piled embankments. *Geotextiles and Geomembranes,* **26**(2): 164-174. doi: 10.1016/j.geotexmem.2007.05.004

Cherubini, C. and Vessia, G. (2007). Reliability approach for the side resistance of piles by means of the total stress analysis (α Method). *Canadian Geotechnical Journal,* **44**(11): 1378-1390.

Chevalier, B. and Otani, J. (2011). Arching observation in three-dimensional trapdoor problem with X-ray CT and discrete element method. *Soils and foundations,* **51**(3): 459-469.

Chew, S., Phoon, H., Le Hello, B. and Villard, P. (2006). Geosynthetic Reinforced Piled Embankment-Large-Scale Model Tests and Numerical Modeling. *Proceedings of the 8th International Conference on Geosynthetics*. Yokohama, Japan. 18-22 September 2006. pp. 901-904.

Chow, F., Jardine, R., Brucy, F. and Nauroy, J. (1998). Effects of time on capacity of pipe piles in dense marine sand. *Journal of Geotechnical and Geoenvironmental Engineering,* **124**(3): 254-264.

Chu, J., Lo, S.-C. and Lee, I. (1996). Strain softening and shear band formation of sand in multi-axial testing. *Geotechnique,* **46**(1): 63-82.

Coduto, D. P. (1994). *Foundation Design, Principle and Practice*. Prentice Hall, Engewood Cliffs, New Jersey, U.S.A. pp. 796.

Coghlin, J. (2005). Neurtal Citation No. (2005) NIQB 68. *Brian Blair and Joan Blair (and other individuals identified in the schedule attached to the writ of summons dated 17 April 2003) v AWG Residential Limited and Brendan Loughran, Enda Loughran, Dermot Loughran and Eunin Loughran Trading as Brendan Loughran and Sons and Rossorry Development and TPA Taylor, GI Black, RG Kerr and N Magill Practising as Taylor and Boyd (a firm) and Tensar International Limited,* Northern Ireland Court Service.

Collin, J. (2004). Column supported embankment design considerations. *Proceedings of the 52nd Annual Geotechnical Engineering Conference*. St. Paul, Minnesota, U.S.A. 26 February 2004. pp. 51-78.

Collin, J., Watson, C. and Han, J. (2005). Column-supported embankment solves time constraint for new road construction. *Proceedings of the Geo-Frontiers Congress* Austin, Texas, United States. 24-26 January 2005. American Society of Civil Engineers. pp. 1-10.

Collin, J. G., Han, J. and Huang, J. (2005). Geosynthetic reinforced column support embankment design guidelines. *Proceedings of the The North America Geosynthetics Society Conference (NAGS)/GRI 19 Cooperative Conference*. Las Vegas, Nevada, USA. 14-16 December 2005.

Combarieu, O., Gestin, F. and Pioline, M. (1993). Remblais sur sols amérliorès par inclusions rigides: premiers chanters. *Bulletin de Liaison des Laboratoires des Ponts et Chaussées*, No. 191, Paris, France.

Coop, M. R. and Wroth, C. P. (1989). Field studies of an instrumented model pile in clay. *Géotechnique,* **39**(4): 679-696. doi: 10.1680/geot.1989.39.4.679

Corbet, S. P., Jenner, C. and Horgan, G. (2011). Revisions to BS8006 for reinforced soil - what do these mean for industry? Ground Engineering, April, 2011.

Costa, Y. D., Zornberg, J. G., Bueno, B. S. and Costa, C. L. (2009). Failure mechanisms in sand over a deep active trapdoor. *Journal of Geotechnical and Geoenvironmental Engineering,* **135**(11): 1741-1753. doi: 10.1061/(ASCE)GT.1943-5606.0000134.

Cotecchia, F. and Chandler, R. J. (2000). A general framework for the mechanical behaviour of clays. *Géotechnique,* **50**(4): 431-447. doi: 10.1680/geot.2000.50.4.431

Coulomb, C. A. (1776). Essai sur une application des règles de maximis & minimis à quelques problèmes de statique, relatifs à l'architecture (An attempt to apply the rules of maxima and minima to several problems of stability related to architecture). Mem. Div. Sav., Academie des Sciences, Paris.

Courant, R., Friedrichs, K. and Lewy, H. (1928). Über die partiellen Differenzengleichungen der mathematischen Physik. *Mathematische annalen,* **100**(1): 32-74.

Cupper, M. L., White, S. and Neilson, J. L. (2003). *Quaternary: Ice Ages - environments of change. In: Geology of Victoria. Birch, W. D. (Eds.). Geological Society of Australia, pp. 337-359.*

CUR. 2010. Ontwerprichtlijin paalmatrassyststemen. [Design Guideline Piled Embankments.] Dutch standard CUR226. Stichting CUR, Gouda. ISBN 978-90-376-0518-1. [In Dutch.]

CUR. 2015. Ontwerprichtlijin paalmatrassyststemen. [Design Guideline Piled Embankments.] Dutch standard CUR226. Updated version. Stichting CUR, Gouda. [In Dutch.]

Dave, T. N. and Dasaka, S. M. (2011). A review on pressure measurement using earth pressure cell. *International Journal of Earth Science and Engineering,* **4**(6): 1031-1034.

Day, R. A. and Woods, P. (2007). Verification of consolidation parameters of a near-normally consolidated clay by back-analysis of an instrumented wick drain reclamation. *Proceedings of the 10th Australian New Zealand Conference on Geomechanics*. Brisbane, Australia. 21-24 October 2007. pp. 54-59.

De Borst, R., Sluys, L., Muhlhaus, H.-B. and Pamin, J. (1993). Fundamental issues in finite element analyses of localization of deformation. *Engineering computations,* **10**(2): 99-121.

De Borst, R. and Vermeer, P. (1984). Finite element analysis of static penetration tests. *Géotechnique,* **34**(2): 199-210.

Deb, K. (2010). A mathematical model to study the soil arching effect in stone column-supported embankment resting on soft foundation soil. *Applied Mathematical Modelling,* **34**(12): 3871-3883. doi: 10.1016/j.apm.2010.03.026

Deb, K., Chandra, S. and Basudhar, P. (2007). Nonlinear analysis of multilayer extensible geosynthetic-reinforced granular bed on soft soil. *Geotechnical and Geological Engineering,* **25**(1): 11-23.

Deb, K., Chandra, S. and Basudhar, P. (2008). Response of multilayer geosynthetic-reinforced bed resting on soft soil with stone columns. *Computers and Geotechnics,* **35**(3): 323-330.

Deere, D., Peck, R., Monsees, J. and Schmidt, B. (1969). Design of tunnel liners and support systems. Department of Civil and Environmental Engineering, University of Illinois, Urbana-Champaign. Report prepared for the National Technical Information Service, Alexandria, Virginia, U.S.A. pp. 419

Demerdash, M. A. (1996). *An experimental study of piled embankments incorporating geosynthetic basal reinforcement.* Ph.D. thesis. Department of Civil Engineering, University of Newcastle-Upon-Tyne, UK.

Dewoolkar, M. M., Santichaianant, K. and Ko, H.-Y. (2007). Centrifuge modeling of granular soil response over active circular trapdoors. *Soils and Foundations,* **47**(5): 931-945. doi:10.3208/sandf.47.931.

DGSI (2009). Durham Geo Slope Indicator (DGSI) - Product Manual - MEMS Tiltmeter. Available at http://www.slopeindicator.com/pdf/manuals/mems-tiltmeter-manual.pdf (accessed 4 April 2017).

Donald, I. B. and Ellwood, R. B. (1962). Geotechnical investigation for the proposed crossing of the lower Yarra River, Melbourne. *Australian Road Research Board,* **1**(2): 1173 - 1212.

DOT. (2014). *Department of Transport, Planning and Local Infrastructure, State Government of Victoria, Australia - Regional Rail Link - Fact sheet*. viewed 5 May 2014. Available at; http://www.regionalraillink.vic.gov.au/

Douglas, K. J. (2003). *The shear strength of rock masses.* Ph.D. thesis. Department of Civil and Environmental Engineering, The University of New South Wales, Australia.

Drucker, D. C. and Prager, W. (1952). Soil mechanics and plastic analysis or limit design. *Quarterly of applied mathematics,* **10**(2): 157-165.

Duncan, J. M. and Chang, C.-Y. (1970). Nonlinear analysis of stress and strain in soils. *Journal of Soil Mechanics & Foundations Div,* **96**(5): 1629-1653.

Dunnicliff, J. (1988). *Geotechnical Instrumentation for monitoring field performance*. Wiley, New York. pp. 608.

Eigenbrod, K. D. and Issigonis, T. (1996). Pore-water pressures in soft to firm clay during driving of piles into underlying dense sand. *Canadian Geotechnical Journal,* **33**(2): 209-218.

Ellis, E. and Aslam, R. (2009a). Arching in piled embankments: comparison of centrifuge tests and predictive methods - Part 1 of 2. *Ground Engineering,* **42**(6): 34-38.

Ellis, E. and Aslam, R. (2009b). Arching in piled embankments: comparison of centrifuge tests and predictive methods - Part 2 of 2. *Ground Engineering,* **42**(7): 28-31.

Ervin, M. C. (1992). *Engineering properties of Quaternary age sediments of the Yarra Delta: In Engineering Geology of Melbourne. Edited by W.A. Peck, J.L. Neilson, R.J. Olds and K.D. Seddon.* A. A. Balkema, Rotterdam, Netherlands. pp. 245-259.

Ervin, M. C., Benson, N. D., Morgan, J. R. and Pavlovic, N. (2004). Melbourne's Southbank Interchange: a permanent excavation in compressible clay. *Canadian Geotechnical Journal,* **41**(5): 861-876. doi: 10.1139/t04-043

Ervin, M. C. and Morgan, J. R. (2001). Groundwater control around a large basement. *Canadian Geotechnical Journal,* **38**(4): 732-740. doi: 10.1139/t01-011

Eskişar, T., Otani, J. and Hironaka, J. (2012). Visualization of soil arching on reinforced embankment with rigid pile foundation using X-ray CT. *Geotextiles and Geomembranes,* **32**(June 2012): 44-54. doi: 10.1016/j.geotexmem.2011.12.002

Evans, C. H. (1983). *An examination of arching in granular soils.* M.Sc. thesis. Department of Civil Engineering, Massachusetts Institute of Technology, Massachusetts, U.S.A.

Fagundes, D. F., Almeida, M. S. S., Thorel, L. and Blanc, M. (2017). Load transfer mechanism and deformation of reinforced piled embankments. *Geotextiles and Geomembranes,* **45**(2): 1-10. doi: 10.1016/j.geotexmem.2016.11.002

Fannin, R., Eliadorani, A. and Wilkinson, J. (2005). Shear strength of cohesionless soils at low stress. *Geotechnique,* **55**(6): 467-478.

Fell, R., MacGregor, P., Stapledon, D. and Bell, G. (2005). *Geotechnical engineering of dams*. Taylor and Francis Group, London, U.K. pp. 912.

Filz, G. and Plaut, R. (2009). Practical Implications of Numerical Analyses of Geosynthetic Reinforcement in Column‐Supported Embankments. *Proceedings of the Advances in ground improvement: Research to practice in the United States and China*. Orlando, Florida, U.S.A. 14 March 2009. American Society of Civil Engineers. pp. 55-62.

Filz, G., Sloan, J., McGuire, M. P., Collin, J. and Smith, M. (2012). Column-supported embankments: settlement and load transfer. *Proceedings of the Geotechnical Engineering State of the Art and Practice: Keynote lectures from GeoCongress 2012*. Oakland, California, United States. 25-29 March 2012. ASCE. pp. 54-77.

Filz, G. M. and Smith, M. E. (2006). Design of bridging layers in geosynthetic-reinforced, column-supported embankments. Report prepared for Virginia Department of Transport, Richmond, Virginia, U.S.A. pp. 48.

Fleming, W. (1995). The understanding of Continous Flight Auger piling, its monitoring and control. *Proceedings of the Insititue of Civil Engineers - Geotechnical Engineering,* **113**(3): 157-165.

Fok, N., Qui, T., Vincent, P. and Kreminsky, M. (2012). A case study of ground improvement using semi-rigid inclusions for breakwater road bridge. *Proceedings of the International Conference on Ground Improvement and Ground Control*. Wollongong. 30 October - 2 November 2012. pp. 629 - 643.

Frossard, E., Hu, W., Dano, C. and Hicher, P.-Y. (2012). Rockfill shear strength evaluation: a rational method based on size effects. *Geotechnique,* **62**(5): 415-427.

Gajo, A., Wood, D. M. and Bigoni, D. (2007). On certain critical material and testing characteristics affecting shear band development in sand. *Géotechnique,* **57**(5): 449-462.

Galavi, V. (2010). Groundwater flow, fully coupled flow deformation and undrained analyses in PLAXIS 2D and 3D, Technical report, Plaxis BV 2010, Research department.

Gnanendran, C. and Selvadurai, A. (2001). Strain measurement and interpretation of stabilising force in geogrid reinforcement. *Geotextiles and Geomembranes,* **19**(3): 177-194.

Garbe, U., Randall, T., Hughes, C., Davidson, G., Pangelis, S. and Kennedy, S. (2015). A new neutron radiography/tomography/imaging station DINGO at OPAL. *Physics Procedia,* **69**: 27-32. doi: 10.1016/j.phpro.2015.07.003

Geofabrics. (2015). *Geofabrics - Maccaferri gabion wire baskets*. viewed 29 April 2015. Available at; http://www.geofabrics.com.au/products/products/35-maccaferri-gabion-wire-baskets/literature

Geokon (2011). Instruction Manual - Models 4800, 4810, 4815, 4820 and 4830 - Vibrating Wire Earth Pressure Cells. Lebanon, New Hampshire, USA.

German Geotechnical Society. 2010. Empfehlungen für den Entwurf und die Berechnung von Erdkörpern mit Bewehrungen aus Geokunststoffen EBGEO, vol. 2. German Geotechnical Society, Auflage, ISBN 978-3-433-02950-3 (in German). Also available in English: Recommendations for Design and Analysis of Earth Structures using Geosynthetic Reinforcements EBGEO, 2011. ISBN: 978-3-433-02983-1 and digital in English ISBN: 978-3-433-60093-1. German Geotechnical Society. Ernst & Sohn, Germany.

Gibbs, H. J. and Holtz, W. G. (1957). Research on determing the density of sand by spoon penetration test. *Proceedings of the 4th International Conference on Soil Mechanics and Foundation Engineering*. London, U.K. 12-24 August 1957. Butterworths Scientific Publications, London, U.K. pp. 35-39.

Gibson, R. and Anderson, W. (1961). In situ measurement of soil properties with the pressuremeter. *Civil Engineering and Public Works Review,* **56**(658): 615-618.

Gilbert, R. I. and Mickleborough, N. C. (1990). *Design of prestressed concrete*. CRC Press, London, U.K. pp. 528.

Gingold, R. A. and Monaghan, J. J. (1977). Smoothed particle hydrodynamics: theory and application to non-spherical stars. *Monthly notices of the Royal Astronomical Society,* **181**(3): 375-389.

Giroud, J. P. (1995). Determination of geosynthetic strain due to deflection. *Geosynthetics International,* **2**(3): 635-641. doi: 10.1680/gein.2.0028

Girout, R., Blanc, M., Thorel, L., Fagundes, D. F. and Almeida, M. S. (2016). Arching and Deformation in a Piled Embankment: Centrifuge Tests Compared to Analytical Calculations. *Journal of Geotechnical and Geoenvironmental Engineering,* **142**(12). doi: 10.1061/(ASCE)GT.1943-5606.0001557

Gniel, J. and Haberfield, C. (2015). Design, construction and performance of a tied-wall embankment supported on concrete column ground improvement. *Proceedings of the International Conference on Geotechnical Engineering: Soil-Structure Interaction, Underground Structures and Retaining Walls* St. Petersburg, Russia. 17 June 2014. IOS Press. pp. 18-27.

Goel, S. and Patra, N. (2008). Effect of arching on active earth pressure for rigid retaining walls considering translation mode. *International Journal of Geomechanics,* **8**(2): 123-133.

Golder (1984b). Golder Associates - Geotechnical Investigation - Moonee Ponds Ck. bridge. Internal report (Reference: 84612060) - June 1984.

Golder (2013). Golder Associates - Geotechnical investigation and design report. Regional Rail Link project. Internal report (Ref: 127612029-009-R-Rev2, dated 21 Feb 2013).

Gottardi, G., Cavallari, L. and Marchi, M. (2008). Soil fracturing of soft silty clays for the reinforcement of a bell tower foundation. *Proceedings of the 2nd International Workshop on Geotechnics of Soft Soils*. Glasgow, Scotland. 3-5 September 2008. CRC Press. pp. 31-41.

Gray, J., Monaghan, J. and Swift, R. (2001). SPH elastic dynamics. *Computer methods in applied mechanics and engineering,* **190**(49): 6641-6662.

GSA (2005). HMA - Geotechnical Systems Australia (GSA) - 7040: Inclinometer Casing Installation Manual.

Guido, V., Knueppel, J. and Sweeny, M. (1987). Plate loading tests on geogrid-reinforced earth slabs. *Proceedings of the Geosynthetic '87 Conference*. New Orleans, U.S.A. pp. 216-225.

Gwede, D. and Horgan, G. J. (2008). Design, construction and in-service performance of a low height geosynthetic refinforced piled embankment: A650 Bingley relief Road. *Proceedings of the 4th European Geosynthetics Conference*. Edinburgh, Scotland. 7-10 September 2008.

Haberfield, C. M. and Szymakowski, J. (2003). Applications of large scale direct shear testing. *Australian Geomechanics,* **38**(1): 29-39.

Halliday, D., Walker, J. and Resnick, R. (2001). *Fundamentals of Physics, Sixth Edition*. John Wiley & Sons. pp. 1056.

Hamidi, B., Nikraz, H. and Varaksin, S. (2009). Arching in Ground Improvement. *Australian Geomechanics,* **44**(4): 99-108.

Han, J. and Gabr, M. A. (2002). Numerical analysis of geosynthetic-reinforced and pile-supported earth platforms over soft soil. *Journal of Geotechnical and Geoenvironmental Engineering,* **128**(1): 44-53. doi: 10.1061/(ASCE)1090-0241(2002)128:1(44)

Handy, R. L. (1985). The arch in soil arching. *Journal of Geotechnical Engineering,* **111**(3): 302-318.

Haring, W., Profittlich, M. and Hangen, H. (2008). Reconstruction of the national road N210 Bergambacht to Krimpen a.d. IJssel, NL: design approach, construction experiences and measurement results. *Proceedings of the 4th European Geosynthetics Conference*. Edinburgh, Scotland. 7-10 September 2008.

Head, K. H. (1982). *Manual of soil laboratory testing - Volume 2: Permeability, shear strength and compressibility tests*. Pentech Press, Plymouth, Devon, UK. pp. 749.

Heitz, C. (2006). *Bodengewölbe unter ruhender und nichtruhender Belastung bei Berücksichtigung von Bewehrungseinlagen aus Geogittern.* Ph.D. thesis. kassel university press GmbH.

Heitz, C., Lüking, J. and Kempfert, H.-G. (2008). Geosynthetic reinforced and pile supported embankments under static and cyclic loading. *Proceedings of the 4th European Geosynthetics Conference*. Edinburgh, Scotland. 7-10 September 2008.

Henke, S. (2010). Influence of pile installation on adjacent structures. *International journal for numerical and analytical methods in geomechanics,* **34**(11): 1191-1210.

Hewlett, W. J. and Randolph, M. (1988). Analysis of piled embankments. *Ground Engineering,* **21**(3): 12-18.

Hill, R. (1950). *The mathematical theory of plasticity*. Clarendon Press, Oxford, UK. pp.

Hilsdorf, H. and Kropp, J. (2004). *Performance criteria for concrete durability*. CRC Press. pp. 226.

Hird, C., Ni, Q. and Guymer, I. (2011). Physical modelling of deformations around piling augers in clay. *Geotechnique,* **61**(11): 993-999.

Holtz, R. D., Kovacs, W. D. and Sheahan, T. C. (2010). *An introduction to geotechnical engineering - 2nd edition*. Prentice Hall, Upper Saddle River, NJ. pp. 863.

Hsu, H. H. a. H., Y.H. (2008). Behavior of geogrids under different strain level. *Proceedings of the 1st Pan American Geosynthetics Conference and Exhibition*. Cancun, Mexico. 2-5 March 2008.

Huang, J., Han, J. and Oztoprak, S. (2009). Coupled mechanical and hydraulic modeling of geosynthetic-reinforced column-supported embankments. *Journal of Geotechnical and Geoenvironmental Engineering,* **135**(8): 1011-1021.

Hughes, J., Ervin, M., Holden, J. and Harvey, R. (1980). Determination of the engineering properties of the Coode Island Silts using a self boring pressuremeter. *Proceedings of the 3rd Australian-New Zealand Conference on Geomechanics*. Wellington, New Zealand. 12-16 May 1980. pp. 249-254.

Hughes, J., Wroth, C. and Windle, D. (1977). Pressuremeter tests in sands. *Geotechnique,* **27**(4): 455-477.

Hussein, M. H., Likins, G. E. and Hannigan, P. J. (1993). Pile evaluation by dynamic testing during restrike. *Proceedings of the 11th South-East Asian Geotechnical Conference* Singapore, Malayasia. 4-8 May 1993. pp. 535-539.

Idelsohn, S. R. and Onate, E. (2006). To mesh or not to mesh. That is the question…. *Computer methods in applied mechanics and engineering,* **195**(37): 4681-4696.

Iglesia, G. R. (1991). *Trapdoor experiments on the centrifuge- a study of arching in geomaterials and similitude in geotechnical models.* Ph.D. thesis. Department of Civil Engineering, Massachusetts Institute of Technology, Massachusetts, U.S.A.

Iglesia, G. R. and Einstein, H. H. (2015). Closure to "Investigation of Soil Arching with Centrifuge Tests" by Geraldo R. Iglesia, Herbert H. Einstein, and Robert V. Whitman. *Journal of Geotechnical and Geoenvironmental Engineering,* **141**(7). doi: 10.1061/(ASCE)GT.1943-5606.0001276

Iglesia, G. R., Einstein, H. H. and Whitman, R. V. (1999). Determination of vertical loading on underground structures based on an arching evolution concept. *Proceedings of the 3rd National Conference - Geo-Engineering for Underground Facilities*. University of Illinois, Urbana-Champaign, Illinois, U.S.A. 13-17 June 1999. pp. 495-506.

Iglesia, G. R., Einstein, H. H. and Whitman, R. V. (2011). Validation of centrifuge model scaling for soil systems via trapdoor tests. *Journal of Geotechnical and Geoenvironmental Engineering,* **137**(11): 1075-1089. doi: 10.1061/(ASCE)GT.1943-5606.0000517

Iglesia, G. R., Einstein, H. H. and Whitman, R. V. (2013). Investigation of soil arching with centrifuge tests. *Journal of Geotechnical and Geoenvironmental Engineering,* **140**(2). doi: 10.1061/(ASCE)GT.1943-5606.0000998

Indraratna, B., Wijewardena, L. and Balasubramaniam, A. (1993). Large-scale triaxial testing of grey wacke rockfill. *Geotechnique,* **43**(1): 37-51.

Islam, S., Haque, A., Wilson, S. A. and Ranjith, P. G. (2013). Improvement of acid sulfate soils using lime-activated slag. *Proceedings of the ICE-Ground Improvement,* **167**(4): 235-248.

Jackson, A. (1969). *Undrained shear strength of a marine sediment.* M. Eng. Sci. thesis. Civil Engineering, Monash University, Melbourne, Australia.

Jacobsz, S. W. (2016). Trapdoor experiments studying cavity propagation. *Proceedings of the 1st Southern African Geotechnical Conference*. Durban, South Africa 18-19 October 2016. CRC Press. pp. 159-165.

Jefferies, M. and Been, K. (2006). *Soil liquefaction: a critical state approach, 2nd edition*. CRC Press. pp. 690.

Jefferies, M. G. and Davies, M. P. (1991). Soil classification by the cone penetration test: Discussion. *Canadian Geotechnical Journal,* **28**(1): 173-176.

Jenck, O., Dias, D. and Kastner, R. (2009). Three-Dimensional Numerical Modeling of a Piled Embankment. *International Journal of Geomechanics,* **9**(3): 102-112. doi: 10.1061/(ASCE)1532-3641(2009)9:3(102)

Jones, B. M. (2008). *Three-Dimensional Finite Difference Analysis of Geosynthetic Reinforcement Used in Column-Supported Embankments.* M.Sc. thesis. Department of Civil and Environmental Engineering, Virginia Polytechnic Institute and State University, Blacksburg, Virginia, USA.

Jones, B. M., Plaut, R. H. and Filz, G. M. (2010). Analysis of geosynthetic reinforcement in pile-supported embankments. Part I: 3D plate model. *Geosynthetics International,* **17**(2): 59-67. doi: 10.1680/gein.2010.17.2.59

Jones, C., Lawson, C. and Ayres, D. (1990). Geotextile reinforced piled embankments. *Proceedings of the 4th International Conference on Geotextiles, Geomembranes and Related Products*. The Hague, Netherlands. 28 May - 1 June 1990. AA Balkema, Rotterdam. pp. 155-160.

Karlsrud, K. and Haugen, T. (1986). Axial static capacity of steel model piles in overconsolidated clay. *Publikasjon-Norges Geotekniske Institutt,*(163).

Kempfert, H., Göbel, C., Alexiew, D. and Heitz, C. (2004). German recommendations for reinforced embankments on pile-similar elements. *Proceedings of the 3rd European Geosynthetics Conference*. Munich, Germany. 1-3 March 2004. pp. 279-284.

Kempfert, H., Stadel, M. and Zaeske, D. (1997). Design of geosynthetic-reinforced bearing layers over piles. *Bautechnik,* **74**(12): 818-825.

King, D. J., Gniel, J., Bouazza, A., Bui, H. H. and Rowe, R. K. (2014). Preliminary observations from a geosynthetic reinforced piled embankment. *Proceedings of the 10th International Conference on Geosynthetics*. Berlin, Germany. 21 - 24 September 2014. German Geotechnical Society.

King, D. J. and Bouazza, A. (2016b). Arching in geosynthetic reinforced column supported embankments - recent findings from a field case study. *Proceedings of the 11th Australian and New Zealand Young Geotechnical Professionals Conference*. Queenstown, New Zealand.

King, D. J., Bouazza, A., Gniel, J. and Bui, H. H. (2016a). The compressibility, permeability and structured nature of the Coode Island Silt. *Australian Geomechanics,* **50**(2): pp. 45-62.

King, D. J., Bouazza, A., Gniel, J., Rowe, K. R. and Bui, H. H. (2017a). Load transfer platform behaviour in embankments supported on semi-rigid columns: implications of the ground reaction curve. *Canadian Geotechnical Journal*, **54**(8):1158-1175. doi: 10.1139/cgj-2016-0406

King, D. J., Bouazza, A., Gniel, J., Rowe, K. R. and Bui, H. H. (2017b). Serviceability behaviour in geosynthetic reinforced column supported embankments. Geotextiles and Geomembranes, **45**(4): 261-279. doi: 10.1016/j.geotexmem.2017.02.006

King, D. J., Bouazza, A., Gniel, J., Rowe, K. R. and Bui, H. H. (2018a). Geosynthetic reinforced column supported embankments and the role of ground improvement effects (accepted). *Canadian Geotechnical Journal*.

King, D. J., Bui, H. H., Bouazza, A., Rowe, K. R. and Gniel, J. (2018b). Mesh-based and meshless numerical methods for assessing arching in geosynthetic reinforced column supported embankments. *Geotechnique (in preparation)*.

King, D. J. and Haberfield, C. (2017). Global scale numerical modelling of a geosynthetic reinforced, column supported embankment (*in preparation*). *Proceedings of the 19th International Conference on Soil Mechanics and Geotechnical Engineering - TC207 Workshop*. Seoul, Korea. 17 - 22 September 2017.

King, D. J., King, L., Bouazza, A., Gniel, J. and Bui, H. H. (2017c). The development of arching in geosynthetic reinforced embankments on semi-rigid inclusions (*accepted*). *Proceedings of the 19th International Conference on Soil Mechanics and Geotechnical Engineering*. Seoul, Korea. 17 - 22 September 2017.

Kitazume, M. and Maruyama, K. (2007). Internal stability of group column type deep mixing improved ground under embankment loading. *Soils and Foundations,* **47**(3): 437-455.

Kitazume, M. and Terashi, M. (2013). *The deep mixing method*. CRC Press, London, UK. pp. 410.

Kreyszig, E. (2010). *Advanced engineering mathematics, 9th edition*. John Wiley & Sons. pp. 1094.

Krynine, D. (1945). Discussion of "*Stability and stiffness of cellular cofferdams*" by Karl Terzaghi. *ASCE,* **110**: 1175-1178.

Ladanyi, B. and Hoyaux, B. (1969). A study of the trap-door problem in a granular mass. *Canadian Geotechnical Journal,* **6**(1): 1-14.

Ladd, C. C. and DeGroot, D. J. (2003). Recommended practice for soft ground site characterization: Arthur Casagrande Lecture. *Proceedings of the 12th Panamerican Conference on Soil Mechanics and Geotechnical Engineering*. Massachusetts Institute of Technology, Cambridge, Massachusetts. 22-26 June 2003. Verlag Gluckauf, Essen, Germany. pp. 3-57.

Larisch, M. (2014). *Behaviour of stiff, fine-grained soil during the installation of screw auger displacement piles.* Ph.D. thesis. School of Civil Engineering, University of Queensland, Brisbane, Australia.

Larisch, M., Arnold, M., Uhlig, M., Schwiteilo, E., Williams, D. and Scheuermann, A. (2013). Stress and displacement monitoring of auger displacement piles. *Proceedings of Pile 2013 – State of the Art of Pile foundations and Case Histories*. Bandung, Indonesia. 2-4 June 2013. pp. 1-13.

Larisch, M., Nacke, E., Arnold, M., Williams, D. and Scheuermann, A. (2012). Simulation of auger displacement pile installation. *Proceedings of the 11th Australia-New Zealand Conference on Geomechanics*. Melbourne, Australia. pp. 37-42.

Larisch, M. D., Nacke, E., Arnold, M., Williams, D. and Scheuermann, A. (2014). Simulation of auger displacement pile installation. *International Journal of Geotechnical Engineering,* **8**(4): 458-462.

Lawson, C. R. (2012). Role of modelling in the development of design methods for basal reinforced piled embankments. *Proceedings of the EuroFuge 2012*. Delft, Netherlands. 23-24 April 2012.

Lawson, C. R. (2013). Design, Analysis and Performance of Basal Reinforced Embankments - Reinforced Soil Course. Melbourne, Australia 2013, TenCate Geosynthetics Group.

Lee, K. L. and Seed, H. B. (1967). Drained strength characteristics of sands. *Journal of Soil Mechanics & Foundations Division,* **93**(6): 117-141.

Lehane, B. and Jardine, R. (1994). Displacement-pile behaviour in a soft marine clay. *Canadian Geotechnical Journal,* **31**(2): 181-191.

Leps, T. M. (1970). Review of shearing strength of rockfill. *Journal of Soil Mechanics & Foundations Division,* **96**(4): 1159-1170.

Leroueil, S. and Vaughan, P. (1990). The general and congruent effects of structure in natural soils and weak rocks. *Geotechnique,* **40**(3): 467-488.

Libersky, L. D. and Petschek, A. (1991). Smooth particle hydrodynamics with strength of materials. *Proceedings of the Advances in the free lagrange method*. Moran, Wyoming, USA. 3-7 June 1990. Springer. pp. 248-257.

Liu, G.-R. (2009). *Meshfree methods: moving beyond the finite element method*. CRC Press, Taylor & Francis. pp. 712.

Liu, K.-W., and Rowe, R.K. 2015. Numerical study of the effects of geosynthetic reinforcement viscosity on behaviour of embankments supported by deepmixing-method columns. Geotextiles and Geomembranes, 43(6): 567–578. doi: 10.1016/j.geotexmem.2015.04.020

Liu, H.-L., Chu, J. and Deng, A. (2009). Use of large-diameter, cast in-situ concrete pipe piles for embankment over soft clay. *Canadian Geotechnical Journal,* **46**(8): 915-927.

Liu, H., Ng, C. W. and Fei, K. (2007). Performance of a geogrid-reinforced and pile-supported highway embankment over soft clay: case study. *Journal of Geotechnical and Geoenvironmental Engineering,* **133**(12): 1483-1493.

Liu, M. and Liu, G. (2010). Smoothed particle hydrodynamics (SPH): an overview and recent developments. *Archives of computational methods in engineering,* **17**(1): 25-76.

Livesey, J., Webber, I., Whaley, A. and Horgan, G. J. (2008). Design, construction and in-service performance of a low height geosynthetic reinforced piled embankment: A614 Welham tridge to Spaldington. *Proceedings of the 4th European Geosynthetic Conference*. Edinburgh, Scotland. 7-10 September 2008.

Low, B., Tang, S. and Choa, V. (1994). Arching in piled embankments. *Journal of Geotechnical Engineering,* **120**(11): 1917-1938.

Lowe, J. (1964). Shear strength of coarse embankment dam materials. *Proceedings of the 8th International Congress on Large Dams*. Edinburgh, Scotland. International Commission on Large Dams. pp. 745-761.

Lucy, L. B. (1977). A numerical approach to the testing of the fission hypothesis. *The astronomical journal,* **82**: 1013-1024.

Lunne, T., Robertson, P. K. and Powell, J. J. M. (1997). *Cone Penetration Testing in Geotechnical Practice*. Taylor & Francis, London, UK. pp. 352.

Maccaferri (2003). Maccaferri Pty. Ltd. - Quality Assurance (QA) Specification - TS14 - Galmac Coated Maccaferri Gabion and TerraMesh Panels - Reinforced Soil Structures. pp. 27.

Maccaferri. (2015). *Maccaferri (UK & Ireland) - Geogrid Para products* viewed 19 May 2015. Available at; http://www.maccaferri.com/uk/products/geogrid-para-products-2/

Magnan, J.-P. (1994). Methods to reduce the settlement of embankments on soft clay: a review. *Proceedings of the Vertical and Horizontal Deformations of Foundations and Embankments (Settlement '94, Geotechnical Special Publication 40)*. College Station, Texas, USA. 16-18 June 1994. American Society of Civil Engineers. pp. 77-91.

Maheshwari, P. and Viladkar, M. (2009). A mathematical model for beams on geosynthetic reinforced earth beds under strip loading. *Applied Mathematical Modelling,* **33**(4): 1803-1814.

Marachi, N. (1969). *Strength and deformation characteristics of rockfill materials.* PhD. thesis. Department of Civil Engineering, University of California, Berkeley, USA.

Marachi, N. D., Chan, C. K. and Seed, H. B. (1972). Evaluation of properties of rockfill material. *Journal of Soil Mechanics & Foundations Div,* **97**: 95-114.

Marchi, M., Gottardi, G. and Soga, K. (2013). Fracturing Pressure in Clay. *Journal of Geotechnical and Geoenvironmental Engineering,* **140**(2). doi: 10.1061/(ASCE)GT.1943-5606.0001019

Marsal, R. J. (1973). *Mechanical properties of rockfill. In: Embankment-dam Engineering, Hirschfeld R.C., Poulos S.J. (Eds.)*. John Wiley and Sons, New York, USA. pp. 109-200.

Marston, A. and Anderson, A. O. (1913). The Theory of Loads on Pipes in Ditches and Tests of Cement and Clay Drain Tile and Sewer Pipe, Iowa State University Engineering Experiment Station Bulletin 31. Ames, Iowa, USA.

Mašín, D. (2005). A hypoplastic constitutive model for clays. *International Journal for Numerical and Analytical Methods in Geomechanics,* **29**(4): 311-336.

Massarsch, K. R. and Broms, B. B. (1977). Fracturing of soil caused by pile driving in clay. *Proceedings of the 9th International Conference on Soil Mechanics and Foundation Engineering*. Tokyo, Japan. 10-15 July 1977. Kluwer Academic. pp. 197-200.

Masse, F., Brockbank, B. and Pearlman, S. (2004). CMC: potential application to Canadian soils with a new trend in ground improvement. *Proceedings of the Geo-Quebec 2004*. Quebec, Canada. 22 - 27 October 2004. Session 4F - pp. 32 - 39.

Mayne, P. W. (1991). Determination of OCR in clays by piezocone tests using cavity expansion and critical state concepts. *Soils and Foundations,* **31**(2): 65-76. doi: 10.3208/sandf1972.31.2_65

Mayne, P. W. (2005). Integrated ground behavior: In-situ and lab tests. *Proceedings of the International Symposium on Deformation Characteristics of Geomaterials*. Lyon, France. 22–24 September 2005. Taylor & Francis Group, London. pp. 155–177.

McDonald, P. (1988). The real world of embankment settlement. *Proceedings of the 5th Australian-New Zealand Conference on Geomechanics*. Sydney, Australia. 22-23 August 1988. Institution of Engineers Australia. pp. 110-117.

McDonald, P. and Cimino, D. J. (1984). Settlement of low embankments on thick compressible soils. *Proceedings of the 4th Australia and New Zealand Geomechanics Conference*. Perth, Western Australia. 14-18 May 1984. Institute of Engineers Australia. pp. 310-315.

McGown, A., Yogarajah, I., Andrawes, K. and Saad, M. A. (1995). Strain behavior of polymeric geogrids subjected to sustained and repeated loading in air and in soil. *Geosynthetics International,* **2**(1): 341-355.

McGuire, M. P. (2011). *Critical height and surface deformation of column-supported embankments.* Ph.D. thesis. Department of Civil Engineering, Virginia Polytechnic Institute and State University, Virginia, U.S.A.

McGuire, M. P. and Filz, G. M. (2008). Quantitative comparison of theories for geosynthetic reinforcement of column-supported embankments. *Proceedings of the 1st Pan American Geosynthetics Conference and Exhibition*. Cancun, Mexico. 1-5 March 2008. pp. 1303–1312.

McKelvey III, J. A. (1994). The anatomy of soil arching. *Geotextiles and geomembranes,* **13**(5): 317-329.

Mesri, G. (2003). Primary compression and secondary compression. *Proceedings of the Symposium on Soil Behavior and Soft Ground Construction, Geotechnical Special Publication (GSP) No. 119*. Cambridge, Massachusetts, USA. Germaine, J. T., Sheahan, T.C., Whitman, R.V. (Eds.). October 5-6, 2001. pp. 122-166.

Mesri, G. and Castro, A. (1987). C_α/C_c concept and K_0 during secondary compression. *Journal of Geotechnical Engineering,* **113**(3): 230-247.

Mesri, G. and Godlewski, P. M. (1977). Time and stress-compressibility interrelationship. *Journal of the Geotechnical Engineering Division,* **103**(5): 417-430.

Mesri, G. and Olson, R. E. (1971). Mechanisms controlling the permeability of clays. *Clays and Clay minerals,* **19**: 151-158.

Mesri, G., Stark, T., Ajlouni, M. and Chen, C. (1997). Secondary compression of peat with or without surcharging. *Journal of Geotechnical and Geoenvironmental Engineering,* **123**(5): 411-421.

Mikkelsen, P. E. (2002). Cement-bentonite grout backfill for borehole instruments. *Geotechnical News,* **20**(4): 38-42.

Mikkelsen, P. E. (2003). Advances in inclinometer data analysis. *Proceedings of the 6th International Symposium on Field Measurements in Geomechanics*. Oslo, Norway. 15 - 18 September 2003.

Monaghan, J. J. (2000). SPH without a tensile instability. *Journal of Computational Physics,* **159**(2): 290-311.

Monaghan, J. J. (2005). Smoothed particle hydrodynamics. *Reports on progress in physics,* **68**(8): 1703.

Monaghan, J. J. and Lattanzio, J. C. (1985). A refined particle method for astrophysical problems. *Astronomy and astrophysics,* **149**: 135-143.

Nagalingam, S. P. (1986). *Strength and Deformation Properties of Coode Island Silt.* M.Eng.Sc. thesis. Department of Civil Engineering, University of Melbourne, Australia.

Naughton, P. (2007). The significance of critical height in the design of piled embankments. *Proceedings of the Geo-Denver 2007 (GSP 172)*. Denver, Colorado, USA. 18-21 February 2007. pp. 13-23.

Naughton, P. J. and Kempton, G. T. (2005). Comparison of analytical and numerical analysis design methods for piled embankments. *Proceedings of the Geo-Frontiers 2005 Congress*. Austin, Texas, USA. 24-26 January 2005.

Navy (1982). Foundations and earth structures design manual 7.2. Deptartment of the Navy, Navy Facilities Engineering Command, Alexandria, Virginia, USA.

Neilson, J. L. (1988). *Yarra Delta*. *In*: Geology of Victoria. Douglas, J. G. Ferguson, J.A. (Eds.). Geological Society of Australia, Victoria Division, Melbourne**:** pp. 387-392.

Neilson, J. L. (1992). *Geology of the Yarra Delta. In: Engineering Geology of Melbourne. Peck, W.A., Neilson, J.L., Olds, R.J. and Seddon, K.D. (Eds.)*. A. A. Balkema, Rotterdam, Netherlands. pp. 223-245.

NeSmith, W. M. (2002). Static Capacity Analysis of Augered, Pressure - Injected Displacement Piles. *Proceedings of the International Deep Foundations Congress* Orlando, Florida, United States. 14-16 February 2002. American Society of Civil Engineers, Reston, Virginia, USA. pp. 1174-1186.

NeSmith, W. M. (2003). Installation effort as an indicator of displacement screw pile capacity. *Proceedings of the 4th International Geotechnical Seminar on Deep Foundations on Bored and Auger Piles*. Ghent, Belgium. 8-10 September 2008. CRC Press, Taylor & Francis Group.

NeSmith, W. M. and Fox, J. (2009). Practical considerations for design and installation of drilled displacement piles. *Proceedings of the Contemporary Topics in Deep Foundations*. Orlando, Florida, USA. 15-19 March 2009. ASCE. pp. 438-446.

NeSmith, W. M. and NeSmith, W. M. (2006a). Anatomy of a data acquisition system for drilled displacement piles. *Proceedings of the GeoConGress 2006*. Atlanta, Georgia, USA. 26 February - 1 March 2006. American Society of Civil Engineers, Reston, Virginia, USA. pp. 1-6.

Ng, K. W., Roling, M., AbdelSalam, S. S., Suleiman, M. T. and Sritharan, S. (2012a). Pile setup in cohesive soil. I: experimental investigation. *Journal of Geotechnical and Geoenvironmental Engineering,* **139**(2): 199-209.

Ng, K. W., Suleiman, M. T. and Sritharan, S. (2012b). Pile setup in cohesive soil. II: Analytical quantifications and design recommendations. *Journal of Geotechnical and Geoenvironmental Engineering,* **139**(2). doi: 10.1061/(ASCE)GT.1943-5606.0000753

Nguyen, V. P., Rabczuk, T., Bordas, S. and Duflot, M. (2008). Meshless methods: a review and computer implementation aspects. *Mathematics and computers in simulation,* **79**(3): 763-813.

Nunez, M., Briançon, L. and Dias, D. (2013). Analyses of a pile-supported embankment over soft clay: Full-scale experiment, analytical and numerical approaches. *Engineering Geology,* **153**: 53-67.

Nyame, B. and Illston, J. (1981). Relationships between permeability and pore structure of hardened cement paste. *Magazine of Concrete Research,* **33**(116): 139-146.

O'Neill, M. W., Hawkins, R. A. and Audibert, J. M. (1982). Installation of pile group in overconsolidated clay. *Journal of the Geotechnical Engineering Division,* **108**(11): 1369-1386.

Oglesby, J. W., Mahmoodzadegan, B. and Griffin, P. M. (1992). Evaluation of methods and materials used to attach strain gages to polymer grids for high strain conditions. Louisiana Transportation Research Center. Baton Rouge, Louisiana, USA. pp. 66.

Olsen, R. and Mesri, G. (1970). Mechanisms controlling compressibility of clays. *Journal of Soil Mechanics & Foundations Division,* **96**(6): 1863-1978.

Ono, K. and Yamada, M. (1993). Analysis of the arching action in granular mass. *Géotechnique,* **43**(1): 105-120. doi: 10.1680/geot.1993.43.1.105

Ooi, P. and Ramsey, T. (2003). Curvature and bending moments from inclinometer data. *International Journal of Geomechanics,* **3**(1): 64-74.

Paik, K. and Salgado, R. (2003). Estimation of active earth pressure against rigid retaining walls considering arching effects. *Geotechnique,* **53**(7): 643-654.

Palmer, A. C. (1971). Undrained plane-strain expansion of a cylindrical cavity in clay: a simple interpretation of the pressuremeter test. *Geotechnique,* **22**(3): 451-457.

Park, S., Roberts, L. A. and Misra, A. (2012). Design methodology for axially loaded auger cast-in-place and drilled displacement piles. *Journal of Geotechnical and Geoenvironmental Engineering,* **138**(12): 1431-1441.

Paul, D., Barrett, S., Stewart, P. and Webster, M. (2014). The engineering geological evolution of the jolimont valley, Melbourne, Australia. *Australian Geomechanics,* **49**(2): 15-30.

Peattie, K. R. and Sparrow, R. (1954). The fundamental action of earth pressure cells. *Journal of the Mechanics and Physics of Solids,* **2**(3): 141-155.

Pestana, J. M., Hunt, C. E. and Bray, J. D. (2002). Soil deformation and excess pore pressure field around a closed-ended pile. *Journal of Geotechnical and Geoenvironmental Engineering,* **128**(1): 1-12.

Piscsalko, G. and Likins, G. (2004). Automatic Inspection Control of Augercast Piles. *Proceedings of the 83rd Transportation Research Board Annual Meeting*. Washington, D.C. USA. 11-15 January 2004. pp. 11-16.

Plomteux, C. and Porbaha, A. (2004). CMC foundation system for embankment support. *Proceedings of the Geosupport Conference*. Orlando, Florida, United States. December 29 - 31, 2004. American Society of Civil Engineers.

Poulos, H. (1994). Effect of pile driving on adjacent piles in clay. *Canadian geotechnical journal,* **31**(6): 856-867.

Poulos, H. and Davis, E. (1974). *Elastic solutions for soil and rock mechanics*. John Wiley and Sons, New York, U.S.A. pp. 411.

Poulos, H. G. (2008). A practical design approach for piles with negative friction. *Proceedings of the ICE-Geotechnical Engineering,* **161**(1): 19-27.

Preim, M. J., March, R. and Hussein, M. (1989). Bearing capacity of piles in soils with time dependent characteristics. *Proceedings of the 3rd International Conference on Piling and Deep Doundations*. London, UK. 15 - 18 May 1989. pp. 363-370.

Prezzi, M. and Basu, P. (2005). Overview of construction and design of auger cast-in-place and drilled displacement piles. *Proceedings of the 30th Annual Conference on Deep Foundations*. Chicago, Illinois, USA. pp. 497-512.

Pritchard, G. B. (1910). The geology of Melbourne. 8 vo, Tait, Melbourne.

Pucker, T. and Grabe, J. (2012). Numerical simulation of the installation process of full displacement piles. *Computers and Geotechnics,* **45**: 93-106. doi: 10.1016/j.compgeo.2012.05.006

Qiu, G., Henke, S. and Grabe, J. (2011). Applications of coupled Eulerian–Lagrangian method to geotechnical problems with large deformations. *Computers and Geotechnics,* **38**: 30-39. doi: 10.1016/j.compgeo.2010.09.002

Raithel, M., Kirchner, A. and Kempfert, H. (2008). Pile-supported embankments on soft ground for a high speed railway-Load Transfer, Distribution and Concentration by different construction methods. *Proceedings of the Advances in Transportation Geotechnics*. Nottingham, UK. 25-27 August 2008. CRC Press. pp. 401-407.

Raithel, M., Kirchner, A. and Kempfert, H. (2009). German Recommendations for reinforced Embankments on Pile-similar elements. *Proceedings of the 4th Asian regional conference on geosynthetics*. 17-20 June 2008. Springer. pp. 697-702.

Randolph, M. (2003). Science and empiricism in pile foundation design. *Geotechnique,* **53**(10): 847-875.

Randolph, M. F., Carter, J. and Wroth, C. (1979). Driven piles in clay—the effects of installation and subsequent consolidation. *Geotechnique,* **29**(4): 361-393.

Randolph, M. F. and Wroth, C. (1979). An analytical solution for the consolidation around a driven pile. *International Journal for Numerical and Analytical Methods in Geomechanics,* **3**(3): 217-229.

Rex, S., Chapman, M., Haque, A., Kamruzzaman, A. H. M. and Wilkinson, A. (2008). Strength and compressibility behaviour of lime-slag treated Coode Island Silt. *Australian Geomechanics,* **43**(4): 31-40.

Robertson, P. (2009). Interpretation of cone penetration tests-a unified approach. *Canadian Geotechnical Journal,* **46**(11): 1337-1355.

Robertson, P. (2010). Soil behaviour type from the CPT: an update. *Proceedings of the 2nd International symposium on cone penetration testing*. Huntington Beach, California, USA. 9-11 May 2010. pp. 2-56.

Robertson, P., Sully, J., Woeller, D. J., Lunne, T., Powell, J. and Gillespie, D. (1992). Estimating coefficient of consolidation from piezocone tests. *Canadian Geotechnical Journal,* **29**(4): 539-550.

Robertson, P. K. (1990). Soil classification using the cone penetration test. *Canadian Geotechnical Journal,* **27**(1): 151-158. doi: 10.1139/t90-014

Robinson, R. G. and Allam, M. M. (1998). Effect of clay mineralogy on coefficient of consolidation. *Clays and Clay minerals,* **46**(5): 596-600.

Rogbeck, Y., Alen, C., Gunilla, F., Kjeld, A., Oden, K., Rathmayer, H., Watn, A. and Oiseth, E. (2004). *Nordic guidelines for reinforced soils and fills*, Nordic Geotechnical Societies.

Roscoe, K. H. (1970). The influence of strains in soil mechanics. *Geotechnique,* **20**(2): 129-170.

Rowe, P. W. (1962). The stress-dilatancy relation for static equilibrium of an assembly of particles in contact. *Proceedings of the Royal Society of London. Series A. Mathematical and Physical Sciences,* **269**(1339): 500-527.

Rowe, R. K. and Liu, K.-W. (2015). Three-dimensional finite element modelling of a full-scale geosynthetic-reinforced, pile-supported embankment. *Canadian Geotechnical Journal,* **52**(12): 2041-2054.

RST-Instruments (2010). RST - MEMS Digital Inclinometer System Instruction Manual.

Russell, D., Naughton, P. and Kempton, G. (2003). A new design procedure for piled embankments. *Proceedings of the 56th Canadian Geotechnical Conference and 2003 NAGS Conference*. Winnipeg, Canada. 29 September - 1 October 2003. pp. 858-865.

Russell, D. and Pierpoint, N. (1997). An assessment of design methods for piled embankments. *Ground Engineering,* **30**(10): 39-44.

Saada, A., Liang, L., Figueroa, J. and Cope, C. (1999). Bifurcation and shear band propagation in sands. *Geotechnique,* **49**(3): 367-385.

Saboya Jr, F. and Byrne, P. M. (1993). Parameters for stress and deformation analysis of rockfill dams. *Canadian Geotechnical Journal,* **30**(4): 690-701.

Sagaseta, C. and Whittle, A. J. (2001). Prediction of ground movements due to pile driving in clay. *Journal of Geotechnical and Geoenvironmental Engineering,* **127**(1): 55-66.

Samson, L. and Authier, J. (1986). Change in pile capacity with time: case histories. *Canadian Geotechnical Journal,* **23**(2): 174-180. doi: 10.1139/t86-027

Santichaianant, K. (2002). *Centrifuge modeling and analysis of active trapdoor in sand.* Ph.D. thesis. Department of Civil, Environmental and Architectural Engineering, University of Colorado, Boulder, Colorado, USA.

Satibi, S. (2009). *Numerical analysis and design criteria of embankments on floating piles.* Ph.D. thesis. Civil and Environmental Engineering, University of Stuttgart, Germany.

Schanz, T. and Vermeer, P. (1996). Angles of friction and dilatancy of sand. *Géotechnique,* **46**(1): 145-152.

Schanz, T., Vermeer, P. and Bonnier, P. (1999). The hardening soil model: formulation and verification. *Proceedings of the Plaxis symposium - Beyond 2000 in computational geotechnics*. Amsterdam, the Netherlands. 18-20 March 1999. Balkema, Rotterdam, Netherlands. pp. 281-296.

Shen, S.-L. and Miura, N. (1999). Soil fracturing of the surrounding clay during deep mixing column installation. *Soils and Foundations,* **39**(5): 13-22.

Shen, S.-L., Miura, N. and Koga, H. (2003). Interaction mechanism between deep mixing column and surrounding clay during installation. *Canadian Geotechnical Journal,* **40**(2): 293-307.

Shen, S.-L. M., Han, J. and Koga, H. (2004). Evaluation of property changes in surrounding clays due to installation of deep mixing columns. *Proceedings of the 3rd International Conference on Grouting and Ground Treatment* New Orleans, Louisiana, United States 10-12 February 2003. American Society of Civil Engineers, Reston, Virginia, USA.

Shinoda, M. and Bathurst, R. J. (2004). Strain measurement of geogrids using a video-extensometer technique. *Geotechnical Testing Journal,* **27**(5): 456-463. doi: 10.1520/GTJ11940

Shukla, S. K. and Yin, J.-H. (2006). *Fundamentals of geosynthetic engineering*. Taylor & Francis. pp. 410.

Singh, R. M., Bouazza, A. and Wang, B. (2015). Near-field ground thermal response to heating of a geothermal energy pile: Observations from a field test. *Soils and Foundations,* **55**(**6**): 1412-1426. doi: 10.1016/j.sandf.2015.10.007

Skinner, H., Powell, J., Morris, J. and England, M. (2003). Results from a piling trial on bored, CFA and rotary displacement piles in stiff clay. *Proceedings of the British Geotechnical Association - International conference on foundations: innovations, observations, design and practice*. Dundee, Scotland. 2-5 September 2003. pp. 825-834.

Skov, R. and Denver, H. (1988). Time-dependence of bearing capacity of piles. *Proceedings of the 3rd International Conference on the Application of Stress-Wave Theory to Piles*. Ottawa, Canada. 25-27 May 1988. pp. 879-888.

Sladen, J. (1992). The adhesion factor: applications and limitations. *Canadian Geotechnical Journal,* **29**(2): 322-326.

Slatter, J. (2000). *The fundamental behaviour of displacement screw piling augers.* Ph.D. thesis. Department of Civil Engineering, Monash University, Melbourne, Australia.

Slatter, J. (2006). Recent developments in Continuous Flight Auger (CFA) and Cast-in-situ Displacement Screw Piles in Melbourne. *Australian Geomechanics,* **41**(3): 17 - 24.

Sloan, J. A. (2011). *Column-supported embankments: full-scale tests and design recommendations.* Ph.D. thesis. thesis. Department of Civil Engineering, Virginia Polytechnic Institute and State University, Virginia, U.S.A.

Sloan, J. A., Filz, G. M. and Collin, J. G. (2013). Field-scale column-supported embankment: test facility. *Geotechnical Testing Journal,* **36**(6): 12.

Sluis, J. (2012). *Validation of embedded pile row in PLAXIS 2D.* M.Sc. thesis. Delft University of Technology, Delft, Netherlands.

Smith, M. E. (2005). *Design of bridging layers in geosynthetic-reinforced column-supported embankments.* Ph.D. thesis. Department of Civil and Environmental Engineering, Virginia Polytechnic Institute and State University, Blacksburg, Virginia, USA.

Soga, K., Ng, M. and Gafar, K. (2005). Soil fractures in grouting. *Proceedings of the 11th International Conference on Computer Methods and Advances in Geomechanics*. Torino, Italy 19-24 June 2005. Patron Editore. pp. 397-406.

Soroush, A. and Araei, A. A. (2006). Analysis of behaviour of a high rockfill dam. *Proceedings of the ICE-Geotechnical Engineering,* **159**(1): 49-59.

Srithar, S. T. (2010). Settlement characteristics of Coode Island Silt. *Australian Geomechanics,* **45**(1): 55-64.

Stanley, B., Chowdhury, B. and Haque, A. (2012). A preliminary study of strength behaviour of lime-slag treated pyrite bearing soft Coode Island Silt. *Australian Geomechanics,* **47**(2): 17-23.

Stanley, B., Singh, G., Haque, A., Ranjith, P. and Bouazza, A. (2010). Lime optimisation in lime-slag treated soft Coode island Silt in Melbourne. *Australian Geomechanics,* **45**(1): 65-76.

Stone, K. J. and Wood, D. M. (1992). Effects of dilatancy and particle size observed in model tests on sand. *Soils and Foundations,* **32**(4): 43-57. doi: 10.3208/sandf1972.32.4_43.

Stone, K. J. L. (1988). *Modelling of rupture development in soils.* Ph.D. thesis. thesis. Department of Civil Engineering, University of Cambridge, Cambridge, U.K.

Suleiman, M. T., Ni, L., Davis, C., Lin, H. and Xiao, S. (2015). Installation Effects of Controlled Modulus Column Ground Improvement Piles on Surrounding Soil. *Journal of Geotechnical and Geoenvironmental Engineering,* **142**(1). doi: 10.1061/(ASCE)GT.1943-5606.0001384

Surenee. (2017). *Surenee Piling*. viewed 9 February 2015. Available at; http://www.pilefoundation.in/rotary.html

Svanø, G., Ilstad, T., Eiksund, G. and Want, A. (2000). Alternative calculation principle for design of piled embankments with base reinforcement. *Proceedings of the 4th International conference on ground improvement geosystems. Finnish Geotechnical Society.* Helsinki, Finland. 7-9 June 2000. pp. 541-548.

Svinkin, M. R., Morgano, C. M. and Morvant, M. (1994). Pile capacity as a function of time in clayey and sandy soils. *Proceedings of the 5th International Conference and Exhibition on Piling and Deep Foundations*. Bruges, Belgium. 13-15 June 1994. Deep Foundations Institute, Hawthorne, New Jersey, USA. pp. 1.11.11-11.11.18.

Swegle, J., Hicks, D. and Attaway, S. (1995). Smoothed particle hydrodynamics stability analysis. *Journal of computational physics,* **116**(1): 123-134.

Talesnick, M. (2013). Measuring soil pressure within a soil mass. *Canadian Geotechnical Journal,* **50**(7): 716-722. doi: 10.1139/cgj-2012-0347

Terzaghi, K. (1936). Stress distribution in dry and in saturated sand above a yielding trap-door. *Proceedings of the 1st International Conference of Soil Mechanics and Foundation Engineering*. Harvard University, Cambridge, U.S.A. pp. 307-311.

Terzaghi, K. (1943). *Theoretical Soil Mechanics*. John Wiley and Sons, New York, USA. pp. 510. doi: 10.1002/9780470172766

Terzaghi, K. and Peck, R. B. (1967). *Soil Mechanics in Engineering Practice - 2nd edition*. John Wiley & Sons, New York, USA. pp. 729.

Terzaghi, K., Peck, R. B. and Gholamreza, G. (1996). *Soil mechanics in engineering practice - 3rd edition*. John Wiley and Sons, New York, USA. pp. 549.

Theroux, B., Labuz, J. F. and Dai, S. (2001). Field installation of an earth pressure cell. *Transportation Research Record: Journal of the Transportation Research Board,* **1772**(1): 12-19.

Theroux, B., Labuz, J.F. and Drescher, A. (2000). Calibration of an earth pressure cell. (Report no. MN/RC - 2000-34). Minnesota Department of Transportation. St. Paul, Minnesota, USA. pp. 114.

Thomas, H. and Ward, W. (1969). The design, construction and performance of a vibrating-wire earth pressure cell. *Geotechnique,* **19**(1): 39-51.

Tien, H.-J. (1996). *A literature study of the arching effects.* M.Sc. thesis. Department of Civil and Environmental Engineering, Massachusetts Institute of Technology, Cambridge, Massachusetts, USA.

USBR (1975). *Concrete manual, 8th edition*. United States Bureau of Reclamation. Denver, Colorado, USA, US Department of the Interior and Bureau of Reclamation.

Van der Peet, T. C. (2014). *Arching in basal reinforced piled embankments - Validation of the concentric arches model.* M.Sc. thesis. Department of Geoscience and Engineering, Delft University of Technology, Delft, Netherlands.

Van der Stoel, A., Brok, C., De Lange, A. and Van Duijnen, P. (2010). Construction of the first railroad widening in the Netherlands on a Load Transfer Platform (LTP). *Proceedings of the 9th International Geosynthetic Conference*. Guarujá, Brazil. 23-27 May 2010. Brazilian Geosynthetics Society. pp. 1969-1972.

Van Duijnen, P. G., Van Eekelen, S. J. M. and Van der Stoel, A. E. C. (2010). Monitoring of a railway piled embankment. *Proceedings of the 9th International Geosynthetics Conference*. Guarujá, Brazil. 23-27 May 2010. Brazilian Geosynthetics Society pp. 1461-1464.

Van Eekelen, S., Bezuijen, A. and Van Tol, A. (2015). Validation of analytical models for the design of basal reinforced piled embankments. *Geotextiles and Geomembranes,* **43**(1): 56-81.

Van Eekelen, S. J. M. and Bezuijen, A. and van Duijnen, P. G. (2012). Does a piled embankment 'feel'the passage of a heavy truck? High frequency field measurements. *Proceedings of the 5th European Geosynthetics Congress*. Valencia, Spain. 16-19 September 2012. pp. 162-166.

Van Eekelen, S. J. M., Bezuijen, A. and Alexiew, D. (2010). The Kyoto road piled embankment: 3.5 years of measurements. *Proceedings of the 9th International Conference on Geosynthetics*. Guaruja, Brazil. 23-27 May 2010. pp. 1941-1944.

Van Eekelen, S. J. M., Bezuijen, A., Lodder, H. J. and Van Tol, A. F. (2012a). Model experiments on piled embankments. Part I. *Geotextiles and Geomembranes,* **32**: 69-81. doi: 10.1016/j.geotexmem.2013.07.005

Van Eekelen, S. J. M., Bezuijen, A., Lodder, H. J. and Van Tol, A. F. (2012b). Model experiments on piled embankments. Part II. *Geotextiles and Geomembranes,* **32**: 82-94. doi: https://doi.org/10.1016/j.geotexmem.2013.07.005

Van Eekelen, S. J. M., Bezuijen, A. and Van Tol, A. F. (2011a). Analysis and modification of the British Standard BS8006 for the design of piled embankments. *Geotextiles and Geomembranes,* **29**(3): 345-359.

Van Eekelen, S. J. M., Bezuijen, A. and Van Tol, A. F. (2013). An analytical model for arching in piled embankments. *Geotextiles and Geomembranes,* **39**: 78-102. doi: 10.1016/j.geotexmem.2013.07.005

Van Eekelen, S. J. M., Van, M. A. and Bezuijen, A. (2007). The Kyoto Road, a full-scale test, measurements and calculations. *Proceedings of the 14th European Conference on Soil Mechanics and Geotechnical Engineering*. Madrid, Spain. 24-27 September 2007. Millpress, Rotterdam, the Netherlands. pp. 1533-1538.

Van Langen, H. and Vermeer, P. (1991). Interface elements for singular plasticity points. *International journal for numerical and analytical methods in geomechanics,* **15**(5): 301-315.

VandenBerg, A. (1973). Geology of the Melbourne district. *In:* Regional Guide to Victorian Geology. McAndrew, J. and Marsden M.A.H. (Eds.). pp. 14-30.

Varadarajan, A., Sharma, K., Venkatachalam, K. and Gupta, A. (2003). Testing and modeling two rockfill materials. *Journal of Geotechnical and Geoenvironmental Engineering,* **129**(3): 206-218.

Vardoulakis, I. (1980). Shear band inclination and shear modulus of sand in biaxial tests. *International Journal for Numerical and Analytical Methods in Geomechanics,* **4**(2): 103-119.

Vardoulakis, I., Graf, B. and Gudehus, G. (1981). Trap - door problem with dry sand: a statical approach based upon model test kinematics. *International Journal for Numerical and Analytical Methods in Geomechanics,* **5**(1): 57-78.

Vardoulakis, I. G. and Sulem, J. (2004). *Bifurcation analysis in geomechanics*. CRC Press. pp. 462.

Vermeer, P. (1982). A simple shear-band analysis using compilances. *Proceedings of the International Union of Theoretical and Applied Mechanics - International Conference on Deformation and Failure of Granular Materials*. Deflt, Netherlands. 31 August - 3 September 1982. Balkema, Rotterdam, Netherlands. pp. 493-499.

Vermeer, P. A. and De Borst, R. (1984). Non-associated plasticity for soils, concrete and rock. *Heron,* **29**(3): pp. 1 - 64.

Vermeer, P. A., Punlor, A. and Ruse, N. (2001). Arching effects behind a soldier pile wall. *Computers and geotechnics,* **28**(6): 379-396.

VicRoads (1990). Geotechnical Investigation Report, Moonee Ponds Ck. bridge. Internal report dated August 1990.

VicRoads (1993). VicRoads - Invitation to submit firm offers to build, own and operate the Wester & Southern Bypass, Volume 6A – Initial Geotechnical Investigations, Western Bypass – Additional boreholes and CPTs.

Viggiani, C. (1989). Influenza dei fattori tecnologici sul comportamento dei pali. *Atti del XVII Convegno di Geotecnica*. Taormina, vol. 2, pp. 83-91.

VMM. (2010a). *Vishay Micro Measurements. Tech Note 505-4 Strain Gage Selection: Criteria, Procedures, Recommendations*. viewed 4 December 2015. Available at; http://www.vishaypg.com/micro-measurements/stress-analysis-strain-gages/technotes-list/

VMM. (2010b). *Vishay Micro Measurements. Instructional Bulletin B-137. Strain gage applications with M-Bond AE-10, AE-15 and GA-2 adhesive systems*. viewed 4 December 2015. Available at; http://www.vishaypg.com/micro-measurements/stress-analysis-strain-gages/instruction-list/

VMM. (2010c). *Vishay Micro Measurements. Application Note TN-609 Strain gage soldering techniques*. viewed 4 December 2015. Available at; http://www.vishaypg.com/micro-measurements/stress-analysis-strain-gages/appnotes-list/

VMM. (2010d). *Vishay Micro Measurements. Application Note VMM-21 Three leadwire attachment*. viewed 4 December 2015. Available at; http://www.vishaypg.com/micro-measurements/stress-analysis-strain-gages/appnotes-list/

VMM. (2011). *Vishay Micro Measurements. Instruction Bulletin B-129-8. Surface Preparation for strain gage bonding*. viewed 4 December 2015. Available at; http://www.vishaypg.com/micro-measurements/stress-analysis-strain-gages/instruction-list/

Wachman, G., Biolzi, L. and Labuz, J. (2009). Structural behavior of a pile-supported embankment. *Journal of geotechnical and geoenvironmental engineering,* **136**(1): 26-34.

Wachman, G. and Labuz, J. (2008). TH 241 column-supported embankment. Department of Civil Engineering, University of Minnesota. Report prepared for the Minnesota Department of Transport, St Paul, Minnesota, U.S.A. pp. 111.

Walker, L. K. and Morgan, J. R. (1977). Field performance of a firm silty clay. *Proceedings of the 9th International Conference on Soil Mechanics and Foundation Engineering*. Toyko, Japan. 10-15 July 1977. pp. 341–346.

Waltham, T., Bell, F. G. and Culshaw, M. (2007). *Sinkholes and subsidence: karst and cavernous rocks in engineering and construction*. Springer Berlin-Heidelberg, Berlin, Germany. pp. pp. 384.

Wang, B., Bouazza, A., Singh, R. M., Haberfield, C., Barry-Macaulay, D. and Baycan, S. (2014). Posttemperature Effects on Shaft Capacity of a Full-Scale Geothermal Energy Pile. *Journal of Geotechnical and Geoenvironmental Engineering,* **141**(4). doi: https://doi.org/10.1061/(ASCE)GT.1943-5606.0001266

Ward, W. (1978). Ground supports for tunnels in weak rocks (18th Rankine Lecture). *Geotechnique,* **28**(2): 133-171.

Waugh, A. (2000). *Victorian Railway Maps 1860 - 2000*. viewed 9 November 2014. Available at; http://www.vrhistory.com/VRMaps/index.html

Weiler, W. A. and Kulhawy, F. H. (1982). Factors affecting stress cell measurements in soil. *Journal of the Geotechnical Engineering Division,* **108**(12): 1529-1548.

Więckowski, Z. (2004). The material point method in large strain engineering problems. *Computer methods in applied mechanics and engineering,* **193**(39): 4417-4438.

Wong, M. (2015). *Rail Geelong - Essendon Flyover* viewed 9 November 2015. Available at; http://www.railgeelong.com/location/essendon-flyover

Wong, P. and Muttuvel, T. (2012). Design of embankments supported on controlled modulus columns. *International Journal of Geotechnical Engineering* **6**(2): 207-213. doi: 10.3328/IJGE.2012.06.02.207-213

Wood, D. M. (2003). *Geotechnical modelling*. Spon Press, Abingdon, Oxfordshire, UK. pp. 488.

Youd, T., Idriss, I., Andrus, R., Arango, I., Castro, G., Christian, J., Dobry, R., Finn, W., Harder, L. J., M., H., Ishihara, K., Koester, J., Liao, S., Marcuson, W. I., Martin, G., Mitchell, J., Moriwaki, Y., Power, M., Robertson, P., Seed, R. and Stokoe, K., II (2001). Liquefaction Resistance of Soils: Summary Report from the 1996 NCEER and 1998 NCEER/NSF Workshops on Evaluation of Liquefaction Resistance of Soils. *Journal of Geotechnical and Geoenvironmental Engineering,* **127**(10): 817-833. doi: 10.1061/(ASCE)1090-0241(2001)127:10(817)

Yu, H.-S. (2007). *Plasticity and geotechnics*. Springer Science & Business Media, New York, USA. pp. 522.

Yu, H.-S. (2013). *Cavity expansion methods in geomechanics*. Springer Science & Business Media, New York, USA. pp. 401.

Yu, H. and Carter, J. (2002). Rigorous similarity solutions for cavity expansion in cohesive-frictional soils. *International Journal of Geomechanics,* **2**(2): 233-258.

Yu, H. and Houlsby, G. (1991). Finite cavity expansion in dilatant soils: loading analysis. *Geotechnique,* **41**(2): 173-183.

Yun-Min, C., Wei-Ping, C. and Ren-Peng, C. (2008). An experimental investigation of soil arching within basal reinforced and unreinforced piled embankments. *Geotextiles and Geomembranes,* **26**(2): 164-174.

Zaeske, D. (2001). *Zur Wirkungsweise von unbewehrten und bewehrten mineralischen Tragschichten über pfahlartigen Gründungselementen (in German).* Ph.D. thesis. thesis. Department of Civil Engineering, Univeristy Kassel, Hesse, Germany.

Zarnani, S., Scott, J. D. and Sego, D. C. (2004). Long term performance of geogrid strain gauges. *Proceedings of the 57th Canadian Geotechnical Conference*. Québec City, Québec, Canada. 24-27 October 2004. pp. 24-27.

Zhang, J., Zheng, J.-J., Chen, B.-G. and Yin, J.-H. (2013). Coupled mechanical and hydraulic modeling of a geosynthetic-reinforced and pile-supported embankment. *Computers and Geotechnics,* **52**: 28-37.

Zhang, L., Zhao, M., Hu, Y., Zhao, H. and Chen, B. (2012). Semi-analytical solutions for geosynthetic-reinforced and pile-supported embankment. *Computers and Geotechnics,* **44**: 167-175.

Zhuang, Y. (2009). *Numerical modelling of arching in piled embankments including the effects of reinforcement and subsoil.* Ph.D. thesis. Department of Civil Engineering, University of Nottingham, Nottingham, U.K.

Zhuang, Y., Cui, X. Y. and Liu, H. L. (2012). Analytical analyses of a failure department project in northern ireland. *Advanced Materials Research,* **594**: 2968-2975.

Zhuang, Y., Ellis, E. and Yu, H. S. (2012). Three-dimensional finite-element analysis of arching in a piled embankment. *Geotechnique,* **62**(12): 1127-1131. doi: 10.1680/geot.9.P.113

Zhuang, Y. and Wang, K. Y. (2015). Three-dimensional behavior of biaxial geogrid in a piled embankment: numerical investigation. *Canadian Geotechnical Journal,* **52**: 1629-1635. doi: 10.1139/cgj-2014-0538

Zhuang, Y., Wang, K. Y. and Liu, H. L. (2014). A simplified model to analyze the reinforced piled embankments. *Geotextiles and Geomembranes,* **42**(2): 154-165. doi: 10.1016/j.geotexmem.2013.07.005

APPENDIX A. Field case study

A1. Site Geology information

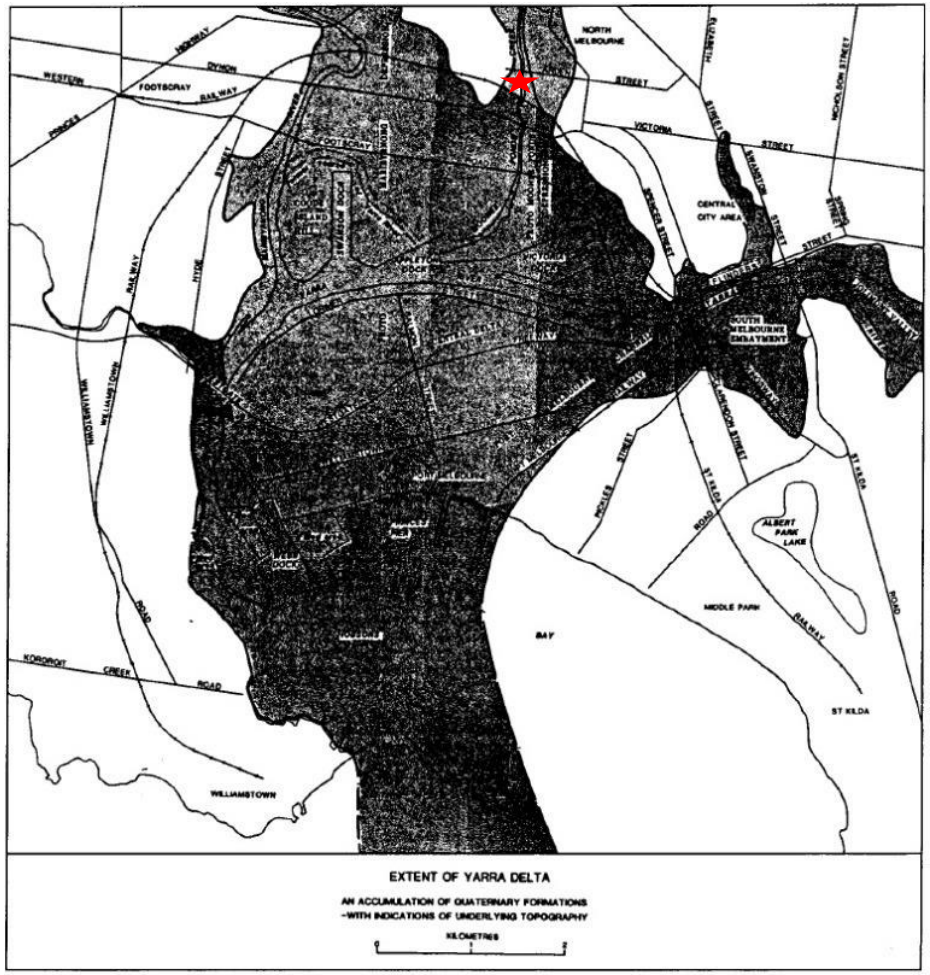

Figure A1. Extent of Yarra Delta with site location (reproduced from Neilson, 1992)

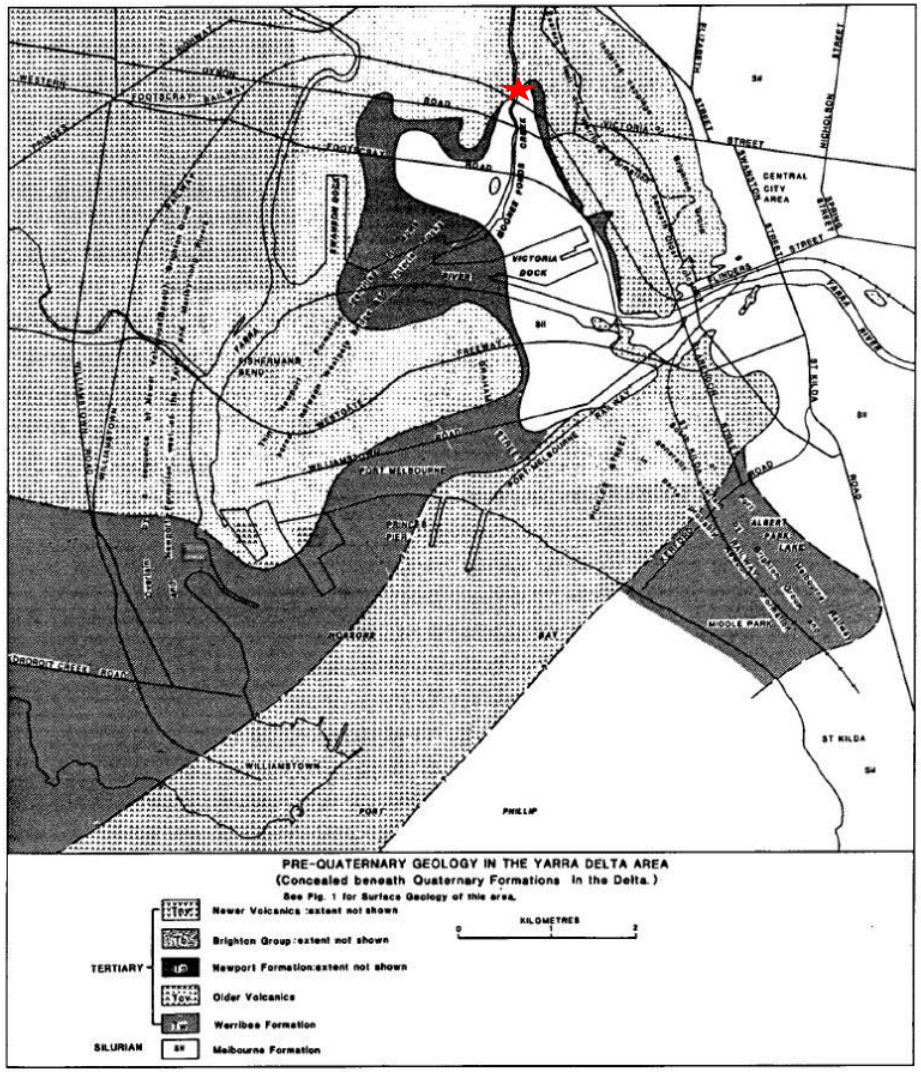

Figure A2. Pre-Quaternary geology in the Yarra Delta region with site location (reproduced from Neilson, 1992)

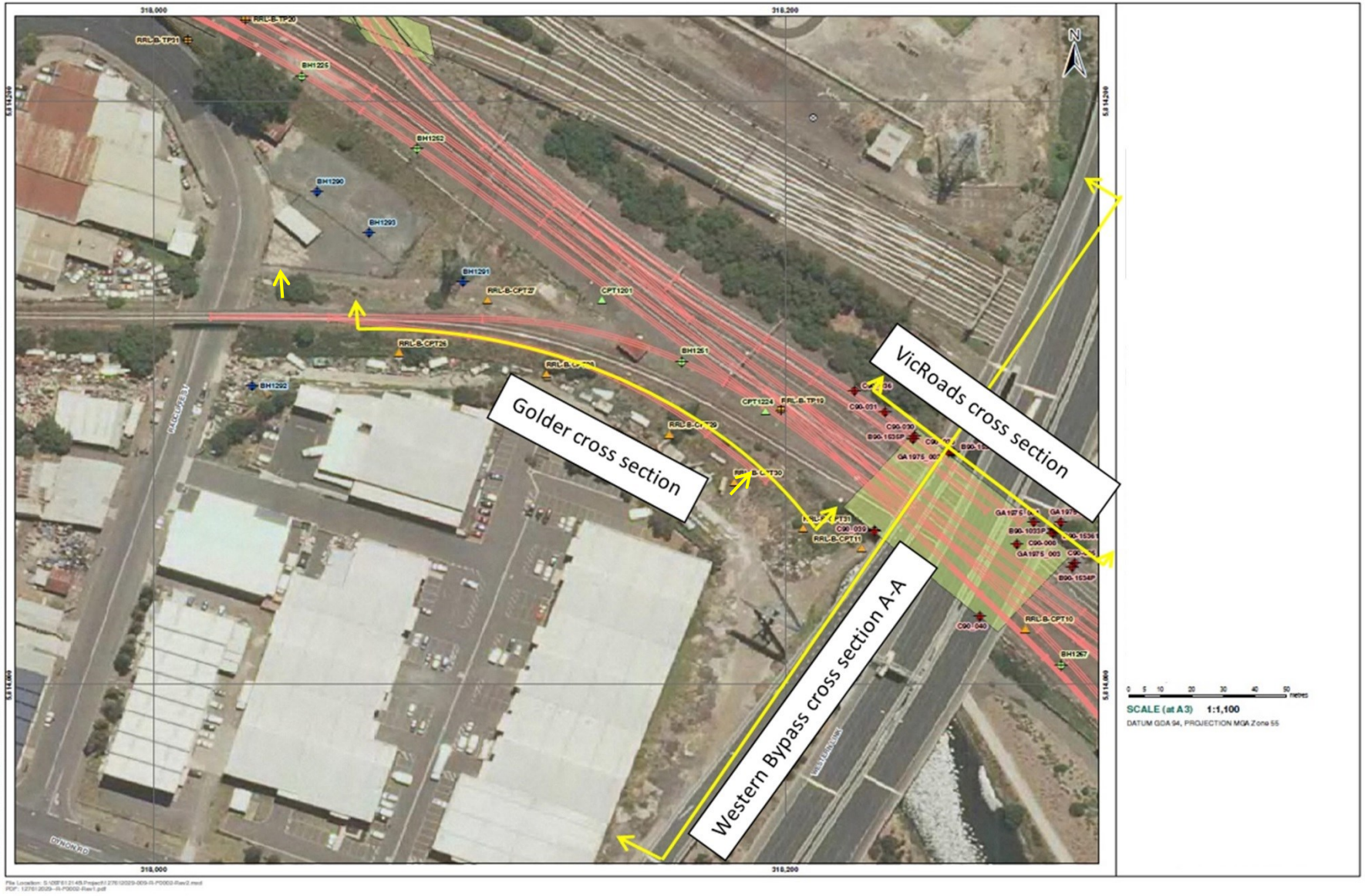

Figure A3. Geotechnical Investigation Location Plan modified from Golder (2013)

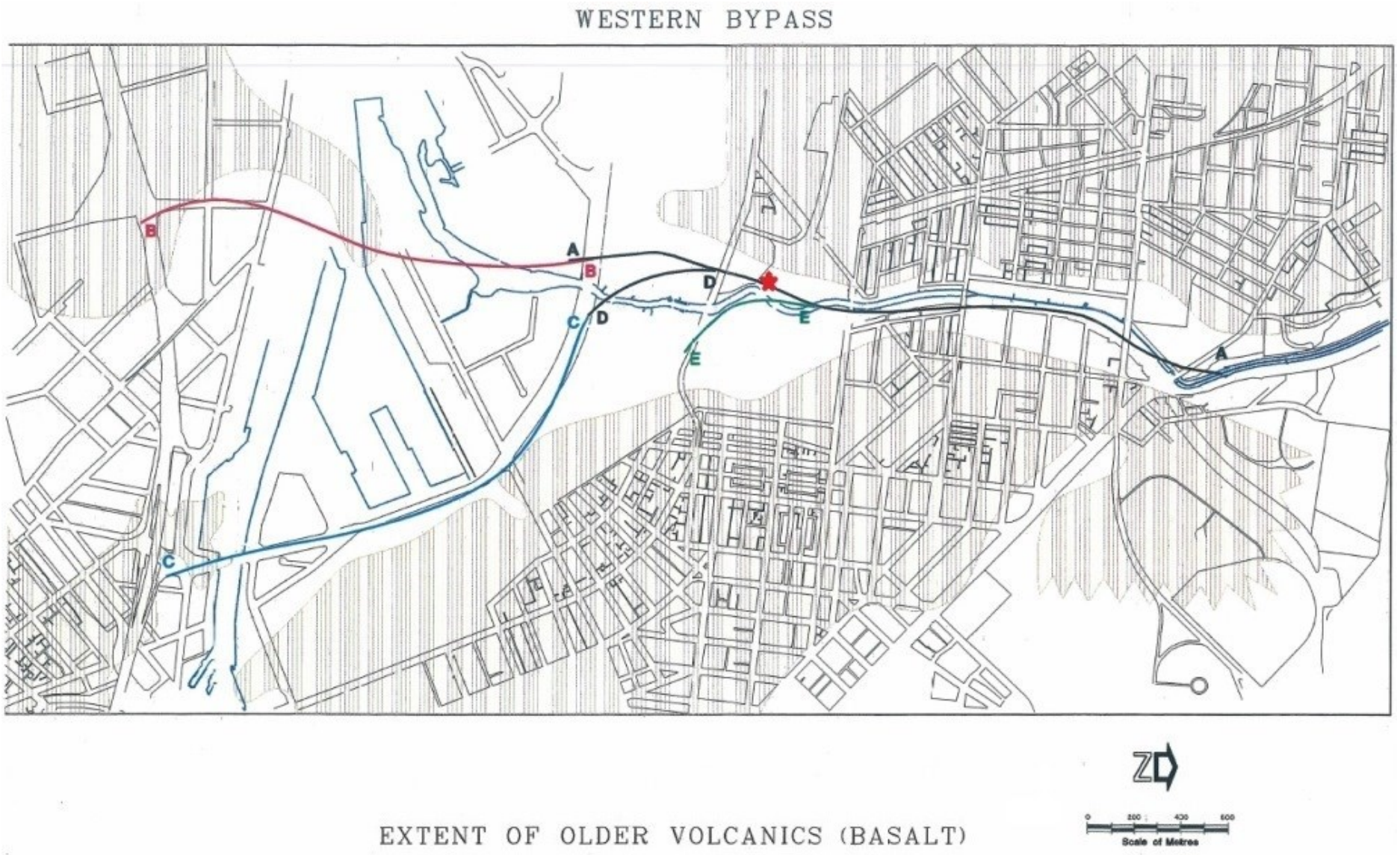

Figure A4. Extent of Older Volcanics – from Western bypass project (VicRoads 1993)

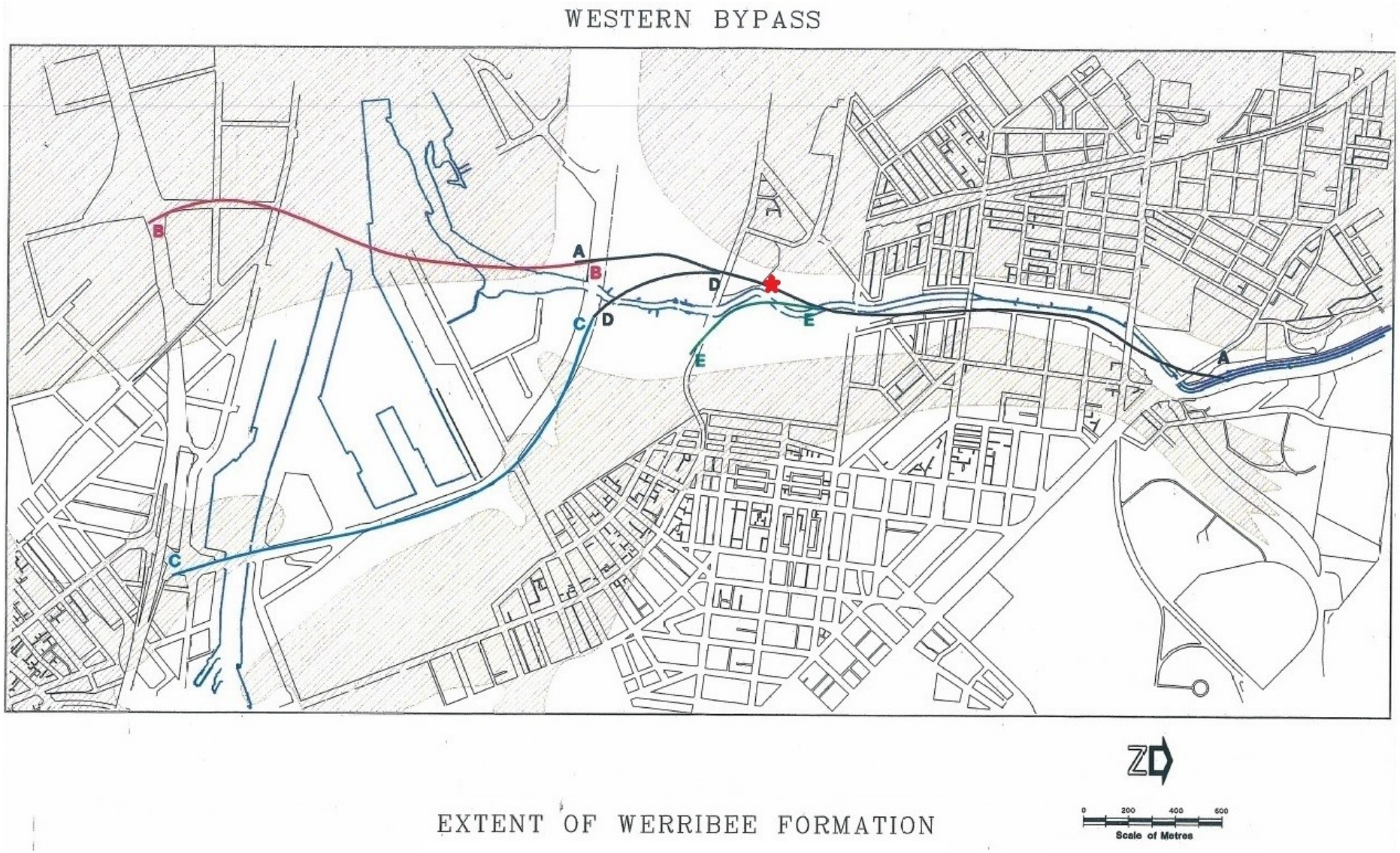

Figure A5. Extent of Werribee formation – from Western bypass project (VicRoads 1993)

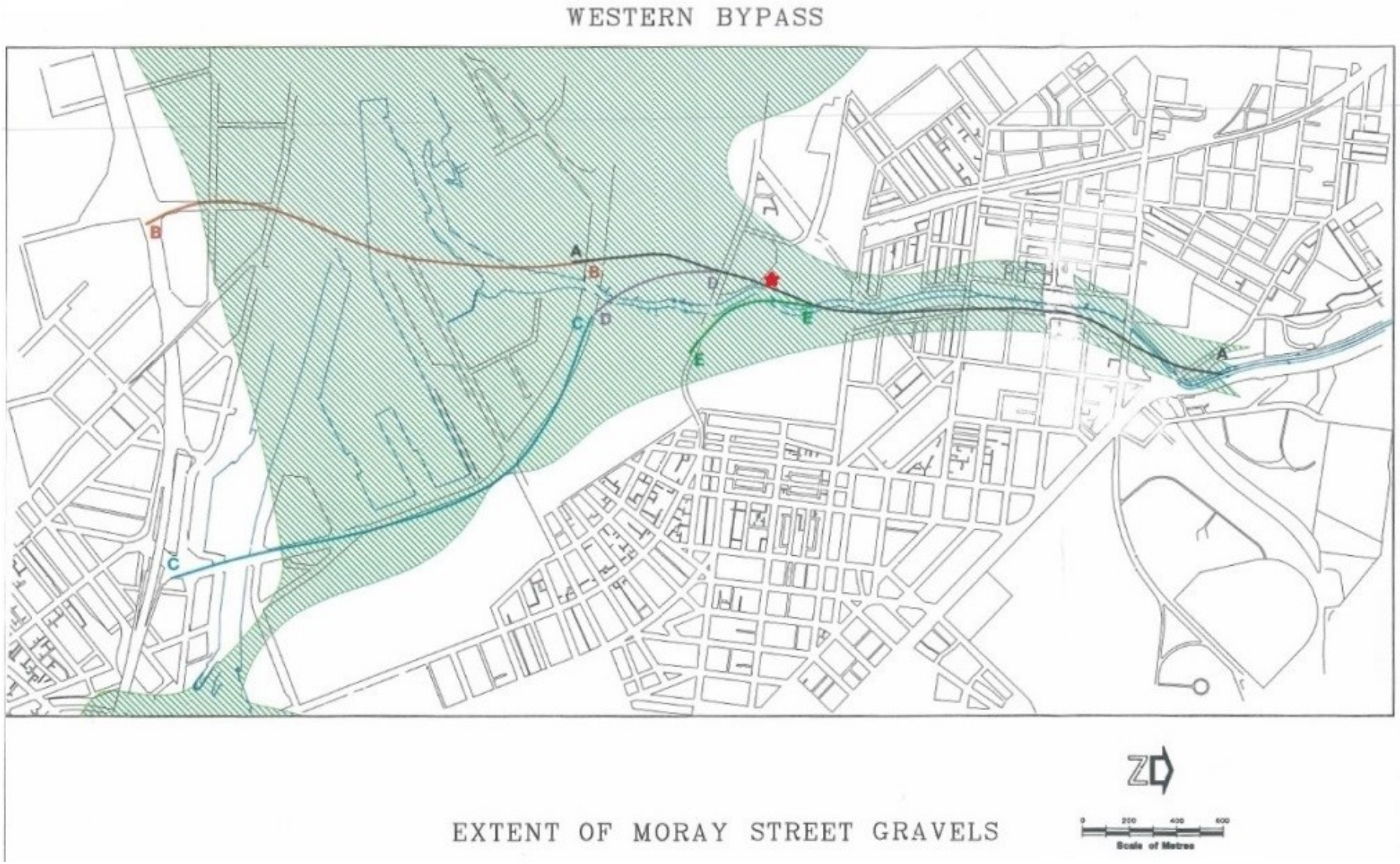

Figure A6. Extent of Moray Street Gravel – from Western bypass project (VicRoads 1993)

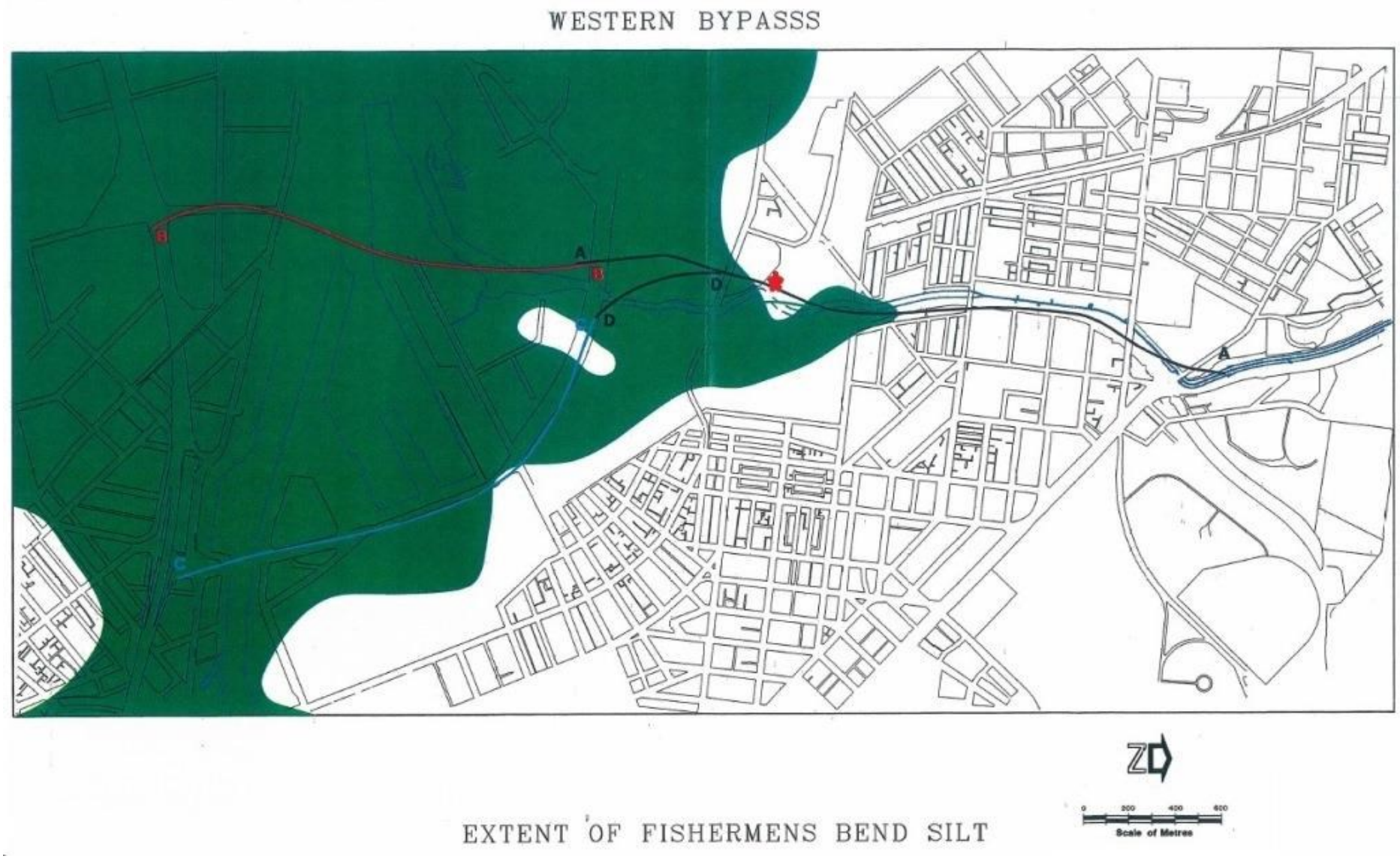

Figure A7. Extent of Fishermens Bend Silt – from Western bypass project (VicRoads 1993)

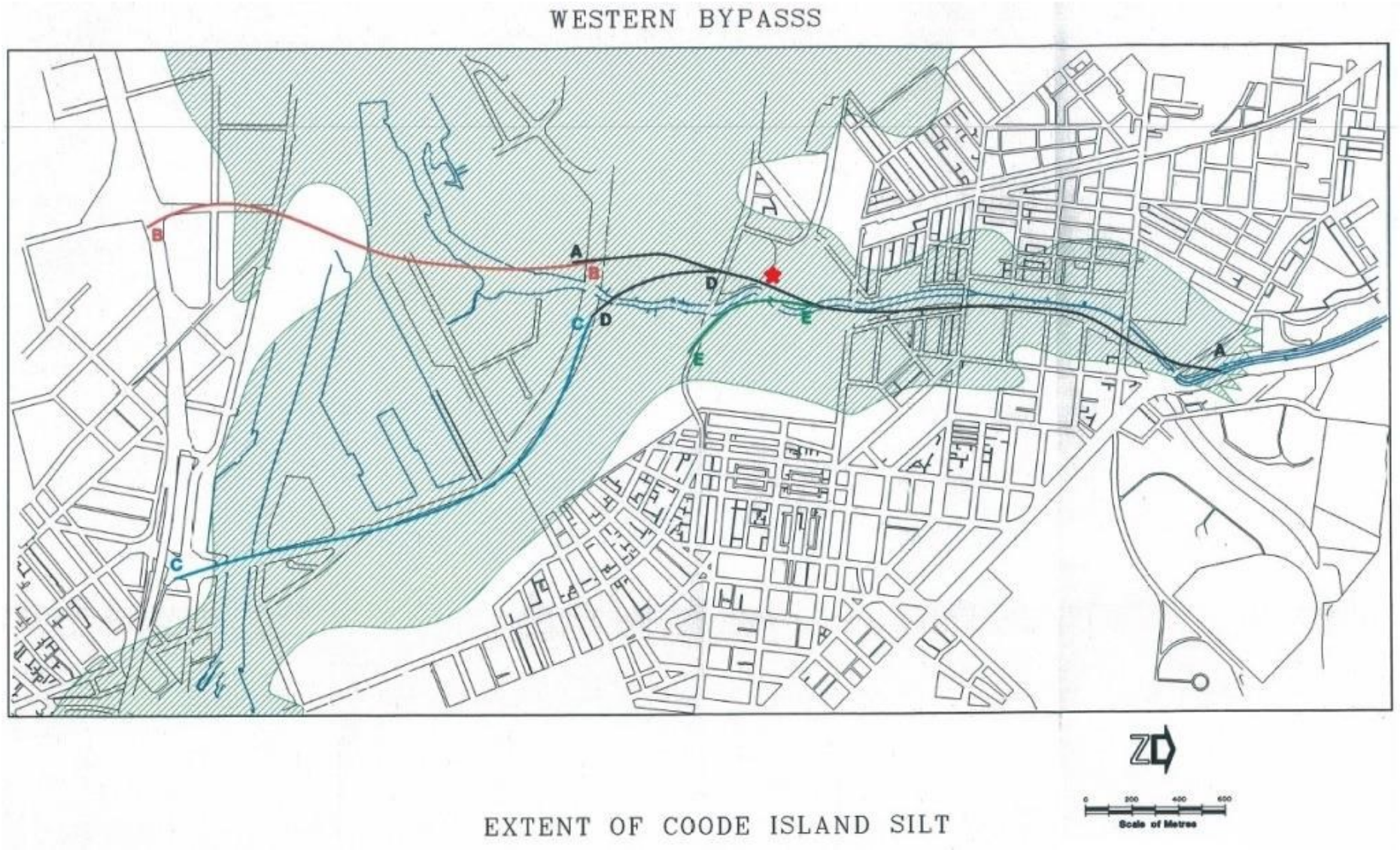

Figure A8. Extent of Werribee formation – from Western bypass project (VicRoads 1993)

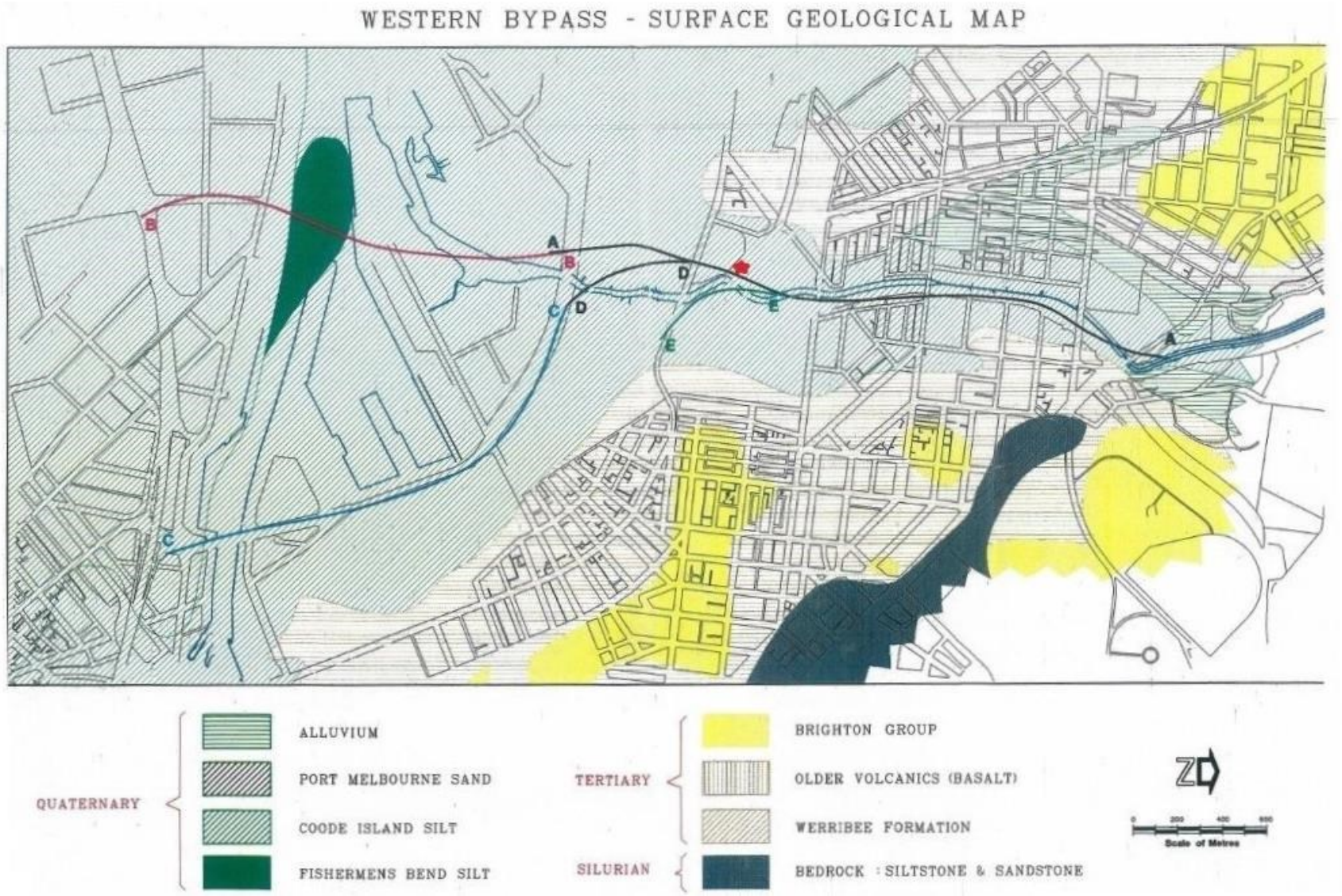

Figure A9. Surface geology map - from Western bypass project (VicRoads 1993)

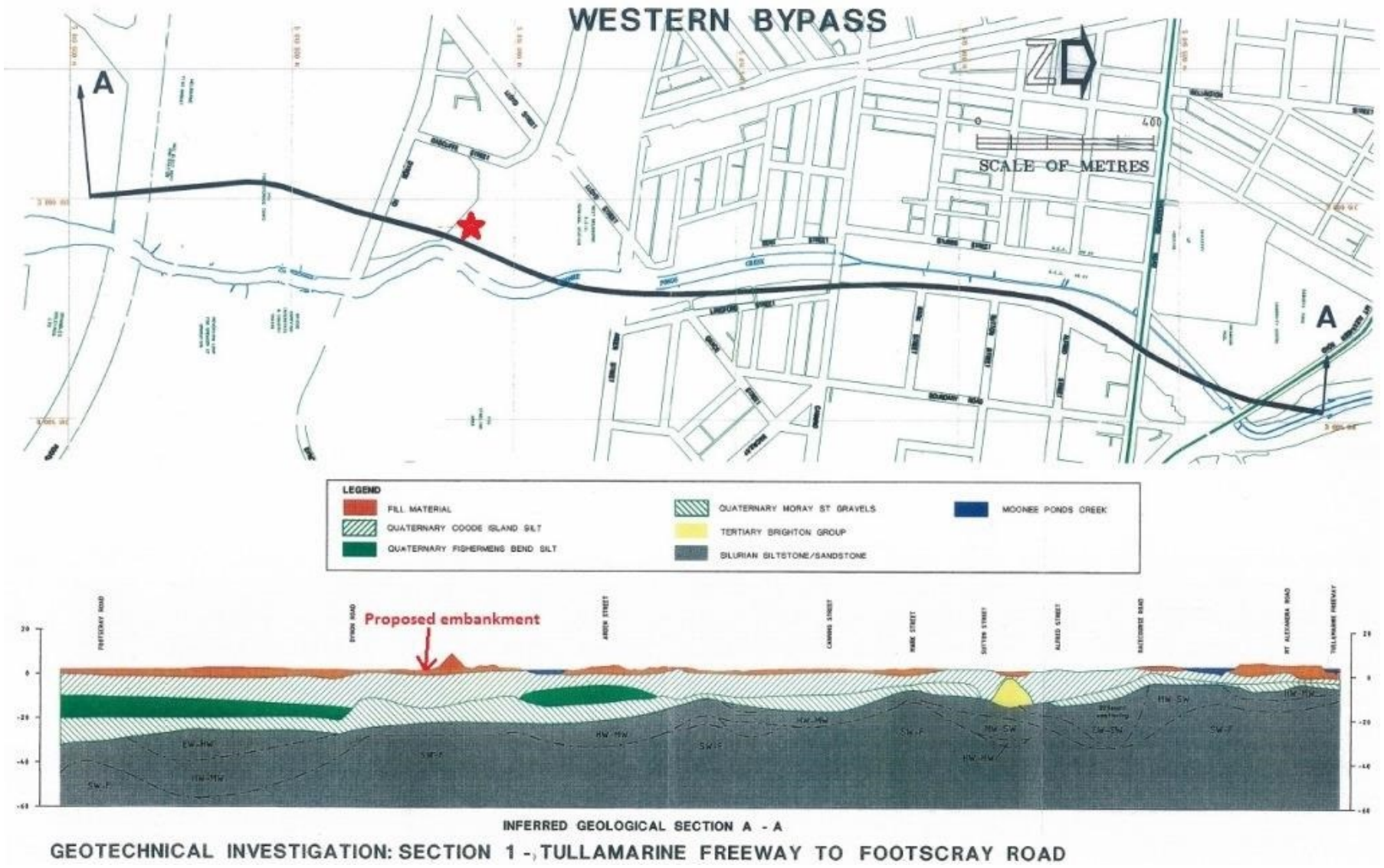

Figure A10. Inferred geological section A- A from Western bypass project (VicRoads 1993)

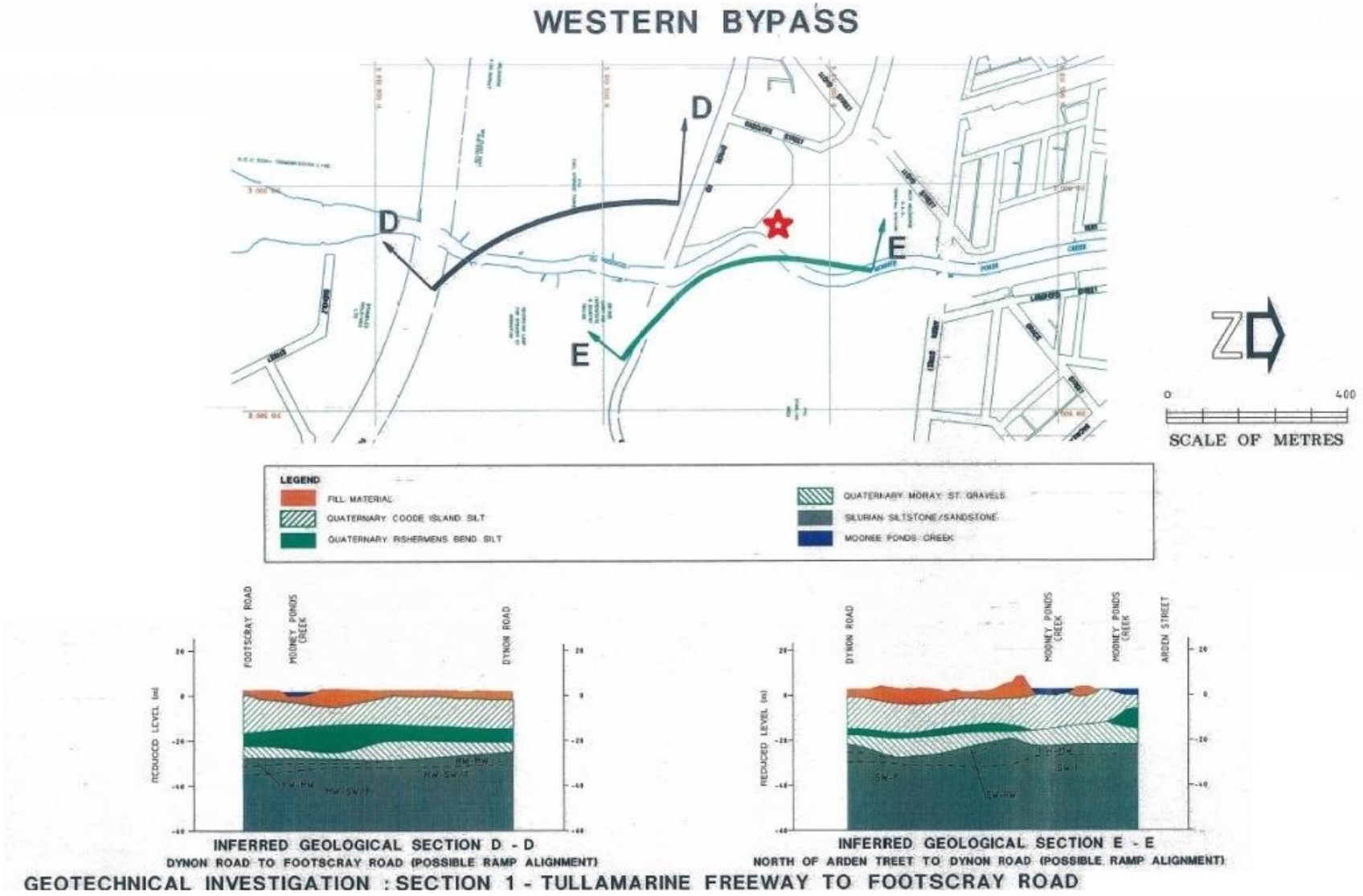

Figure A11. Inferred geological section D - D/E - E from Western bypass project (VicRoads 1993)

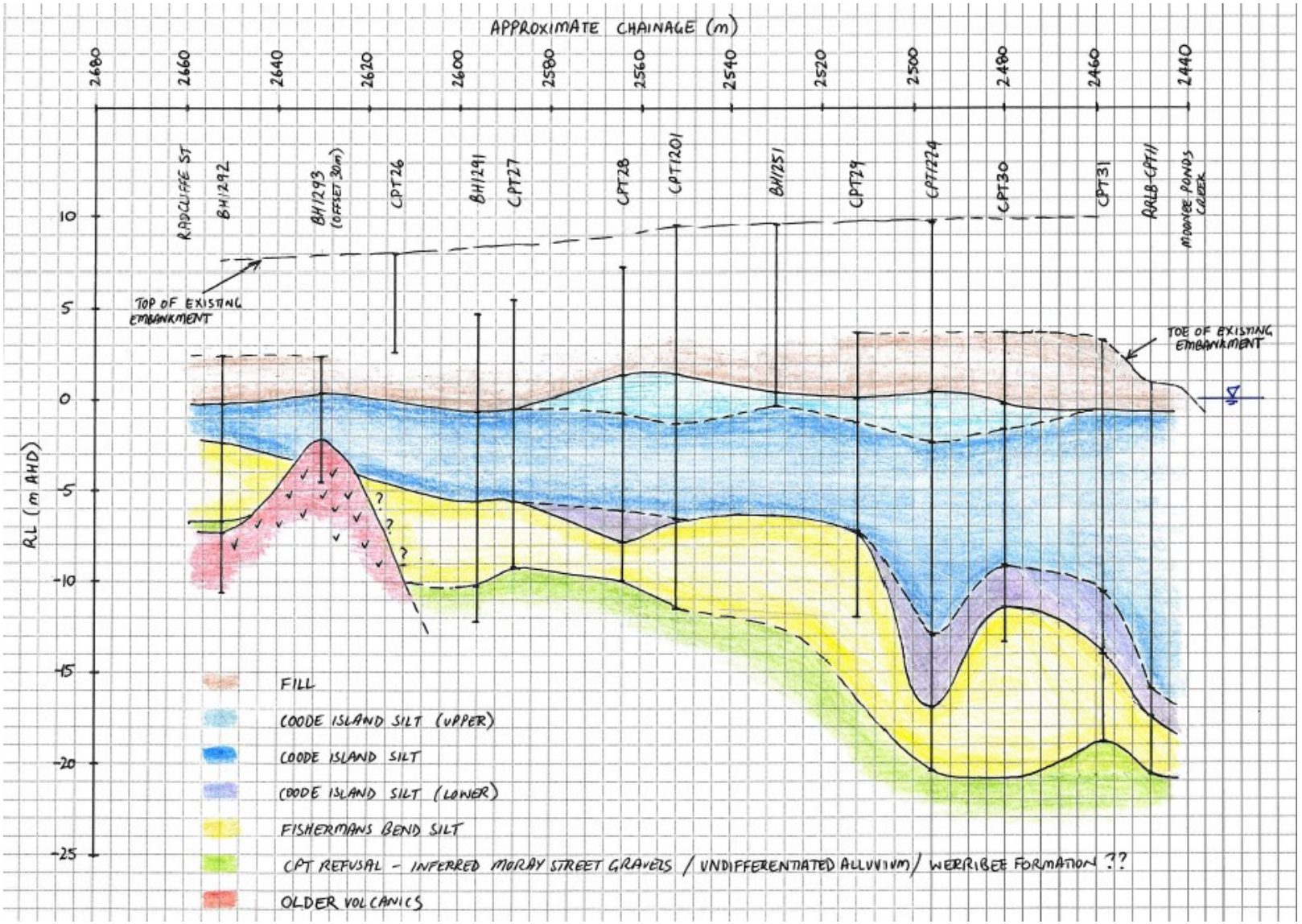

Figure A12. North Dynon embankment - geological long section from Golder (2013)

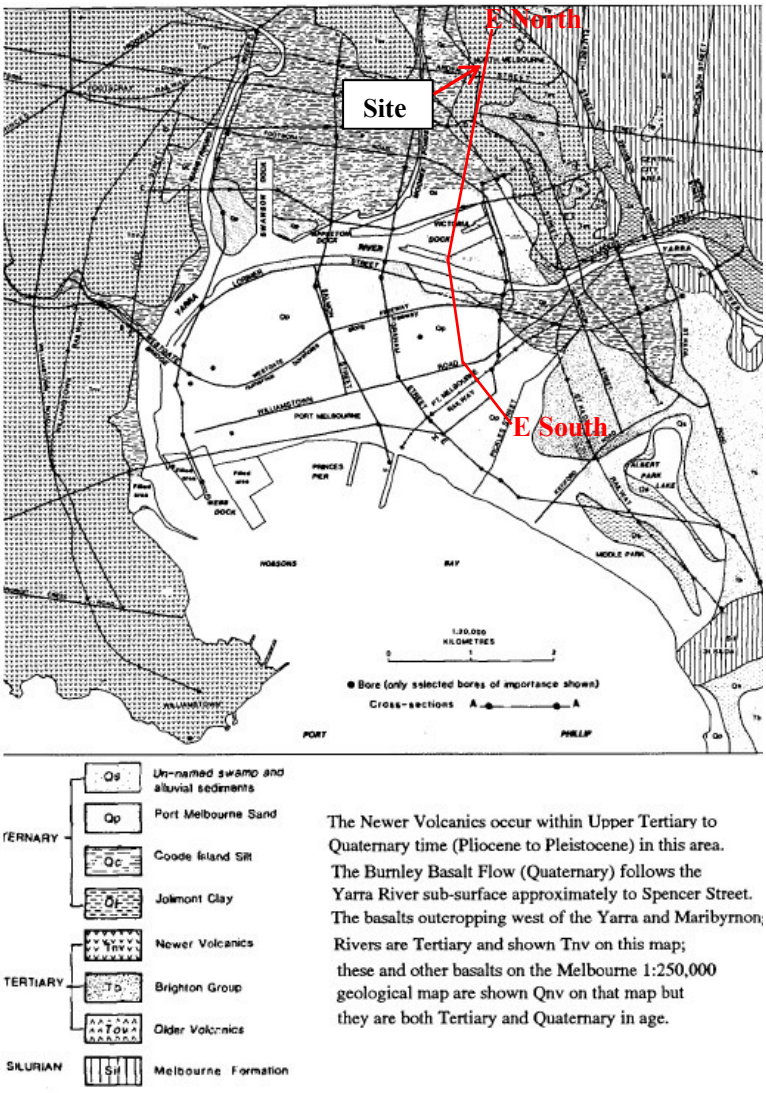

Figure A13. Surficial Geology of the Yarra Delta from Neilson (1992)

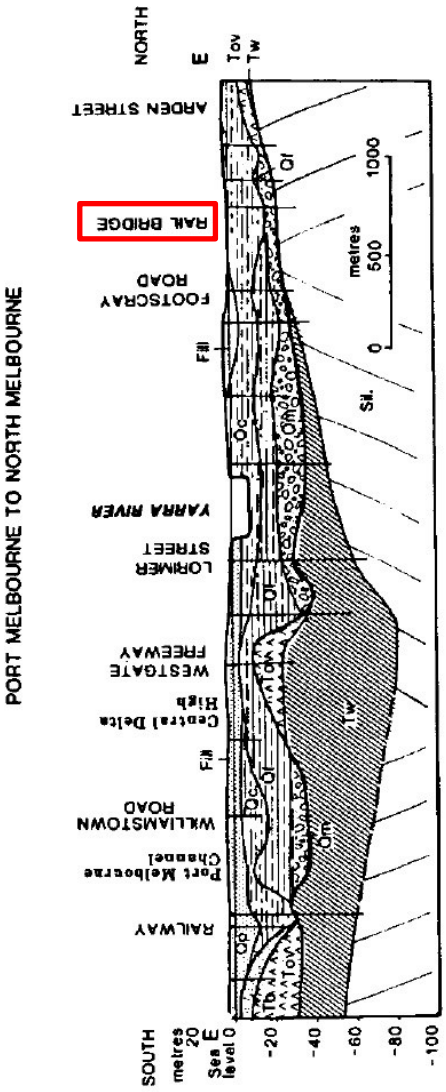

Figure A14. Geological long section E - E from Neilson (1992)

A2. Geotechnical Site Characterisation – Additional data

CPT Figures (CPT28 – CPT31, CPT11 and BH41)

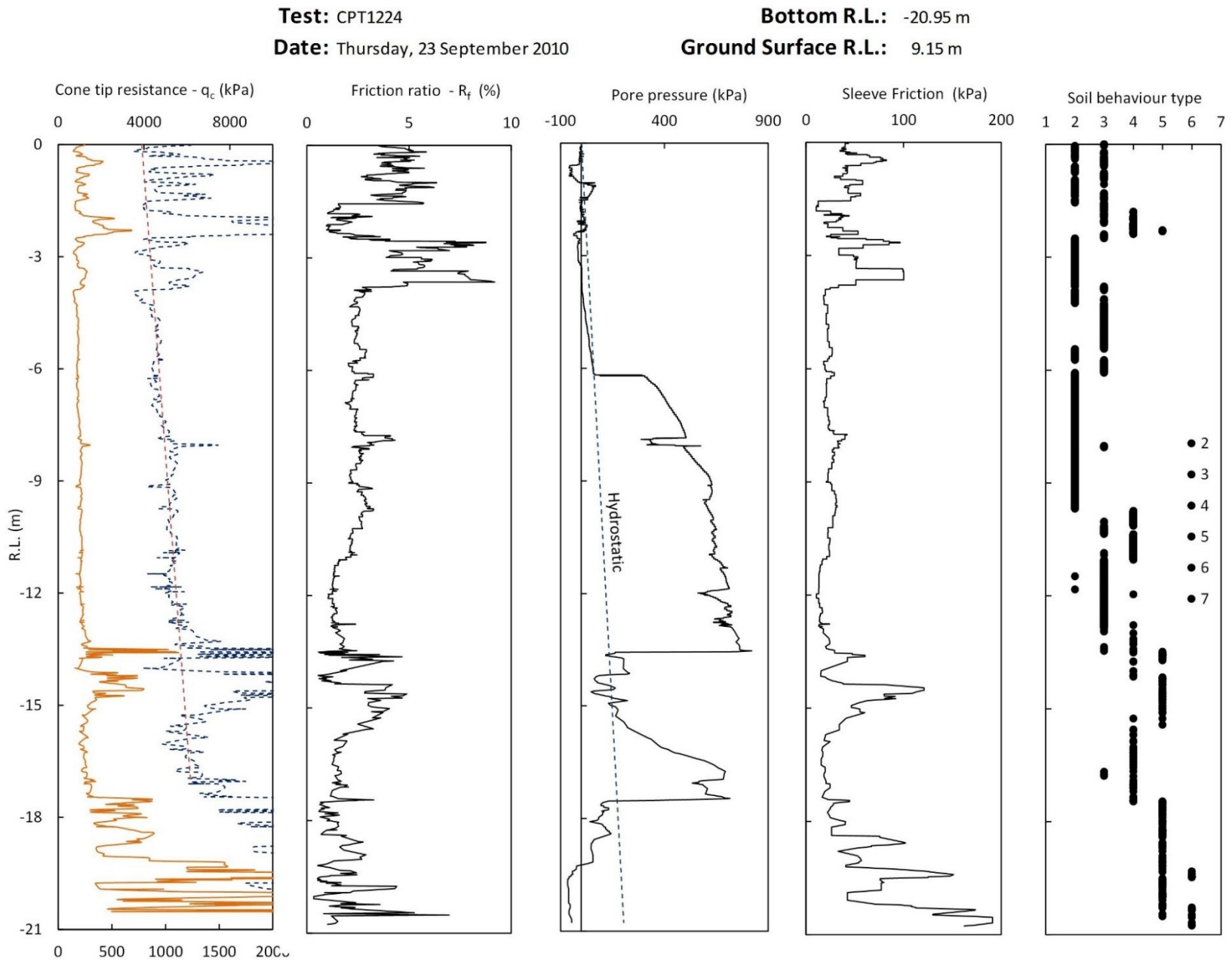
Test: CPT1224
Date: Thursday, 23 September 2010
Bottom R.L.: -20.95 m
Ground Surface R.L.: 9.15 m
Cone tip resistance - q_c (kPa)
Friction ratio - R_f (%)
Pore pressure (kPa)
Sleeve Friction (kPa)
Soil behaviour type
R.L. (m)
Hydrostatic
0
4000
8000
5
10
-100
400
900
100
200
1
2
3
4
5
6
7
-3
-6
-9
-12
-15
-18
-21
500
1000
1500

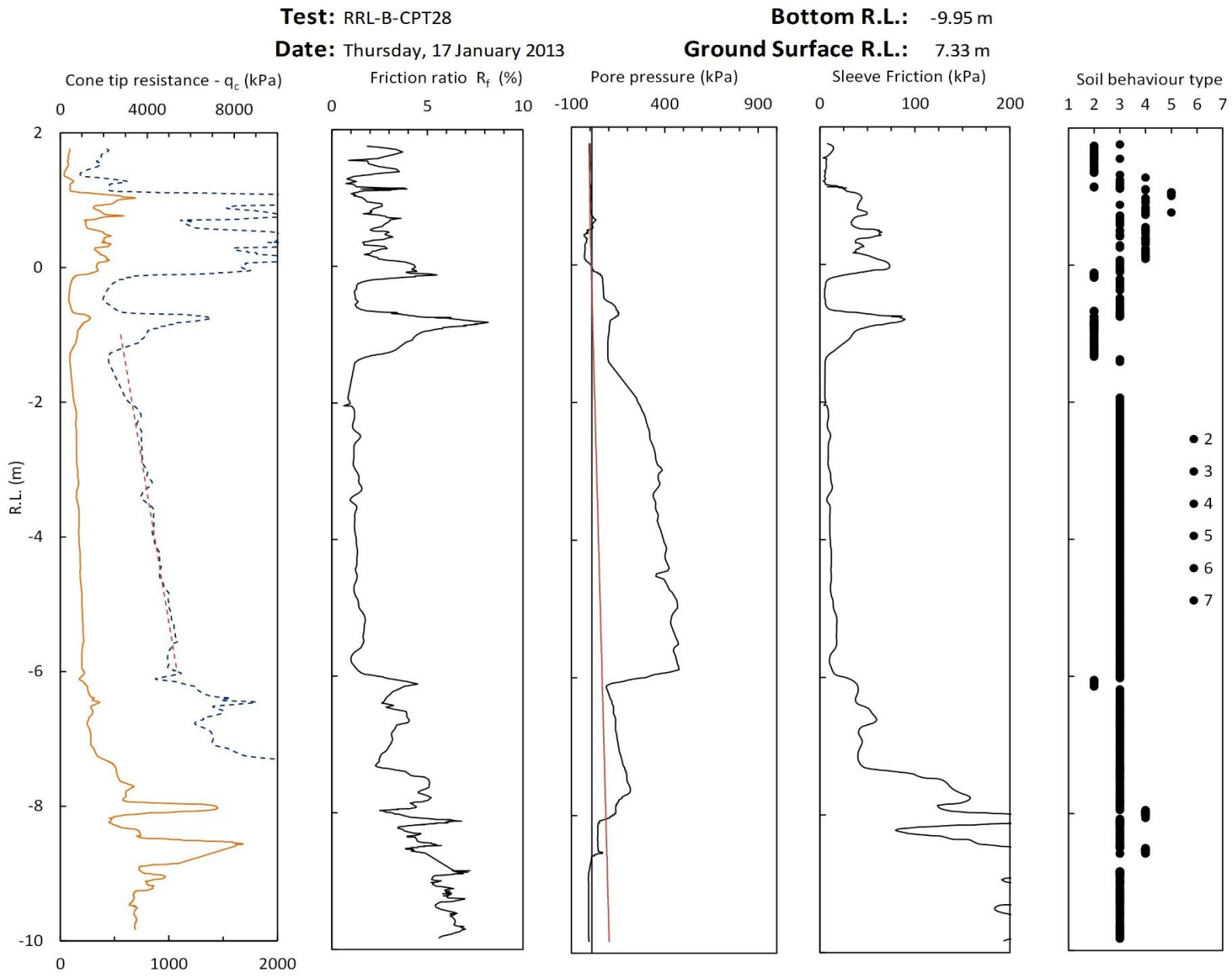
Test: RRL-B-CPT28
Date: Thursday, 17 January 2013
Bottom R.L.: -9.95 m
Ground Surface R.L.: 7.33 m
Cone tip resistance - q_c (kPa)
Friction ratio R_f (%)
Pore pressure (kPa)
Sleeve Friction (kPa)
Soil behaviour type
R.L. (m)
0
4000
8000
0
5
10
-100
400
900
0
100
200
1
2
3
4
5
6
7
2
0
-2
-4
-6
-8
-10
0
1000
2000

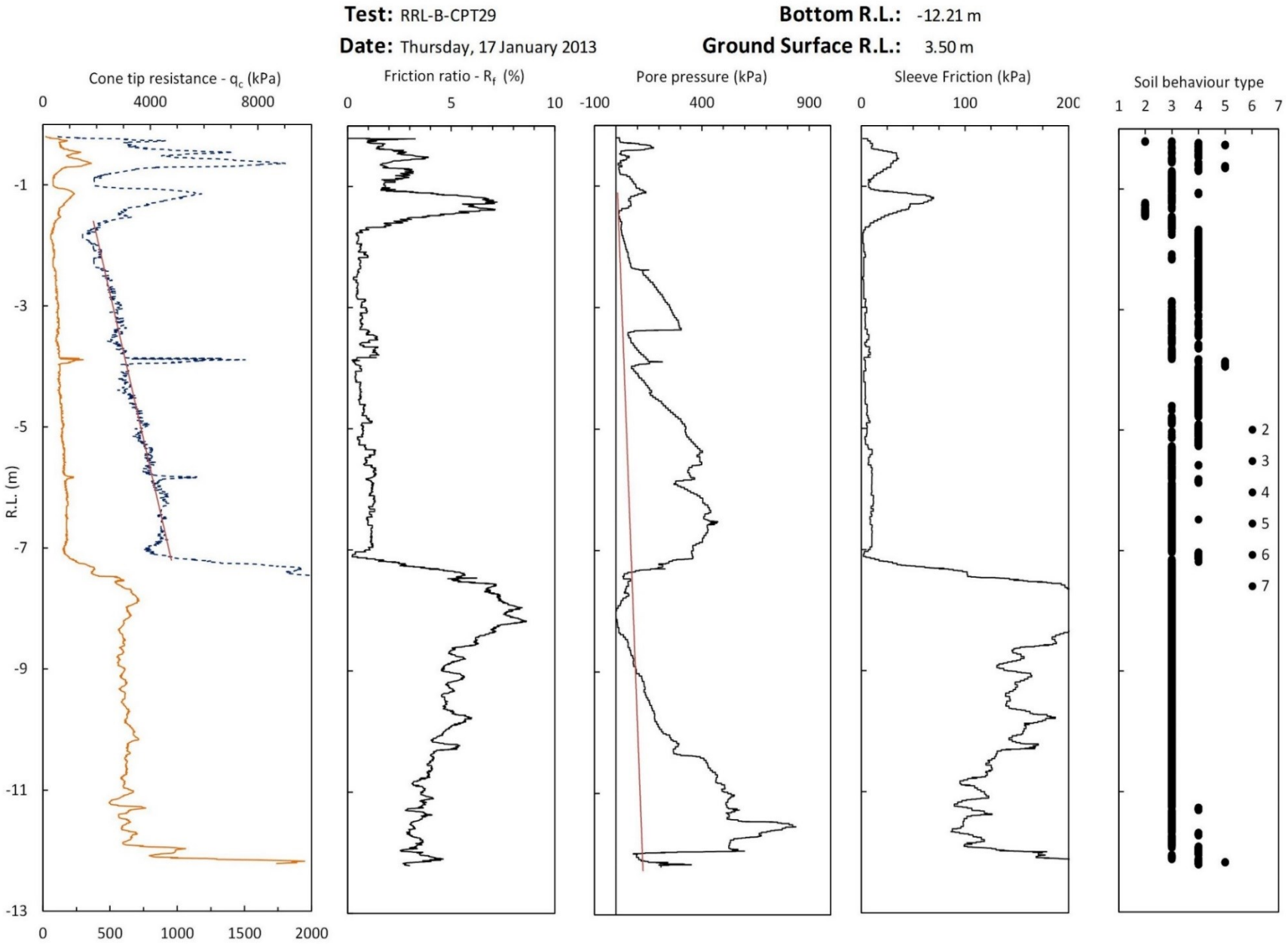
Test: RRL-B-CPT29
Bottom R.L.: -12.21 m
Date: Thursday, 17 January 2013
Ground Surface R.L.: 3.50 m
Cone tip resistance - q_c (kPa)
Friction ratio - R_f (%)
Pore pressure (kPa)
Sleeve Friction (kPa)
Soil behaviour type
R.L. (m)
0
4000
8000
0
5
10
-100
400
900
0
100
200
1
2
3
4
5
6
7
-1
-3
-5
-7
-9
-11
-13
0
500
1000
1500
2000

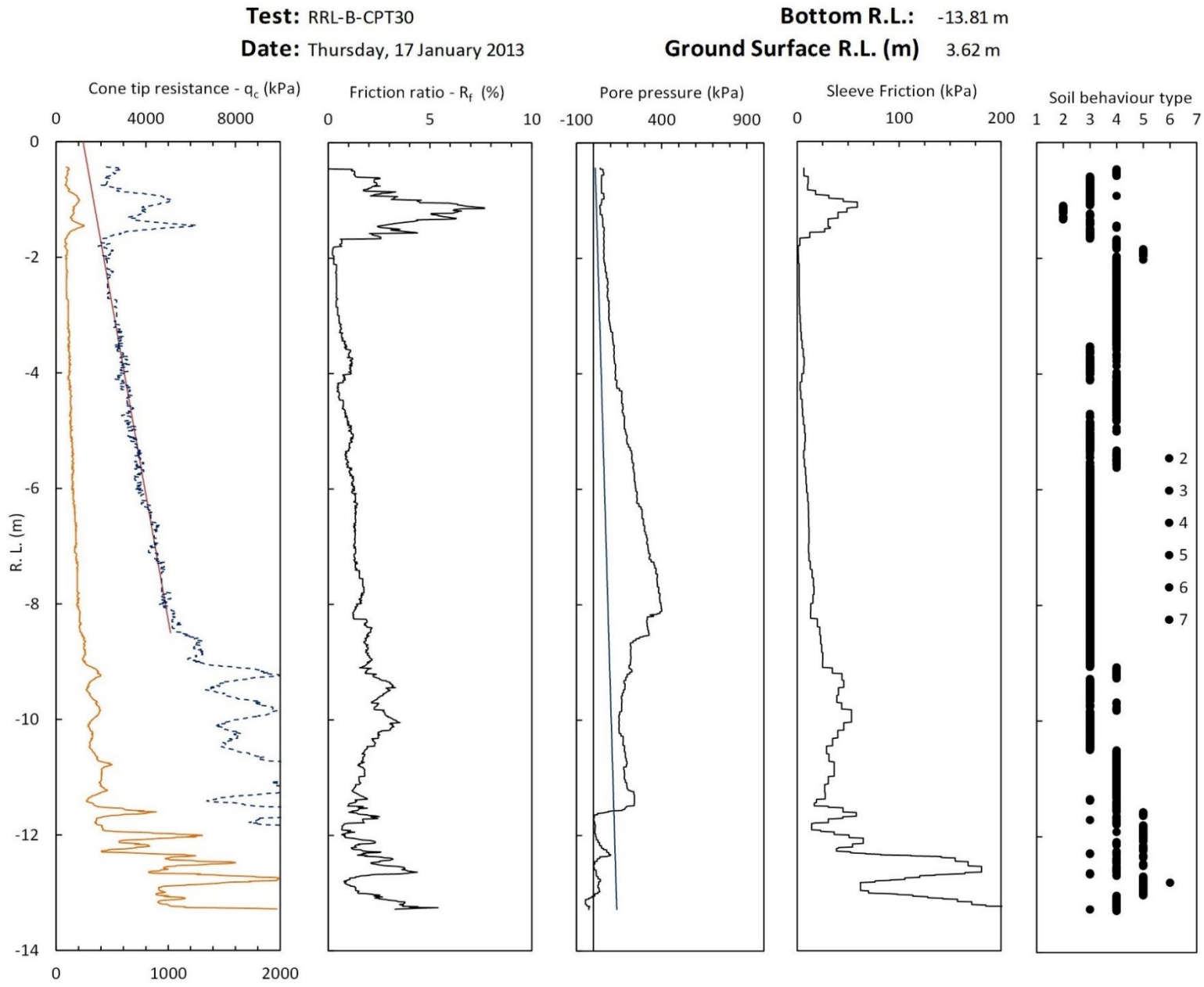
Test: RRL-B-CPT30
Date: Thursday, 17 January 2013
Bottom R.L.: -13.81 m
Ground Surface R.L. (m) 3.62 m
Cone tip resistance - q_c (kPa)
Friction ratio - R_f (%)
Pore pressure (kPa)
Sleeve Friction (kPa)
Soil behaviour type
R. L. (m)
0
4000
8000
5
10
-100
400
900
100
200
1 2 3 4 5 6 7
0
-2
-4
-6
-8
-10
-12
-14
1000
2000
2
3
4
5
6
7

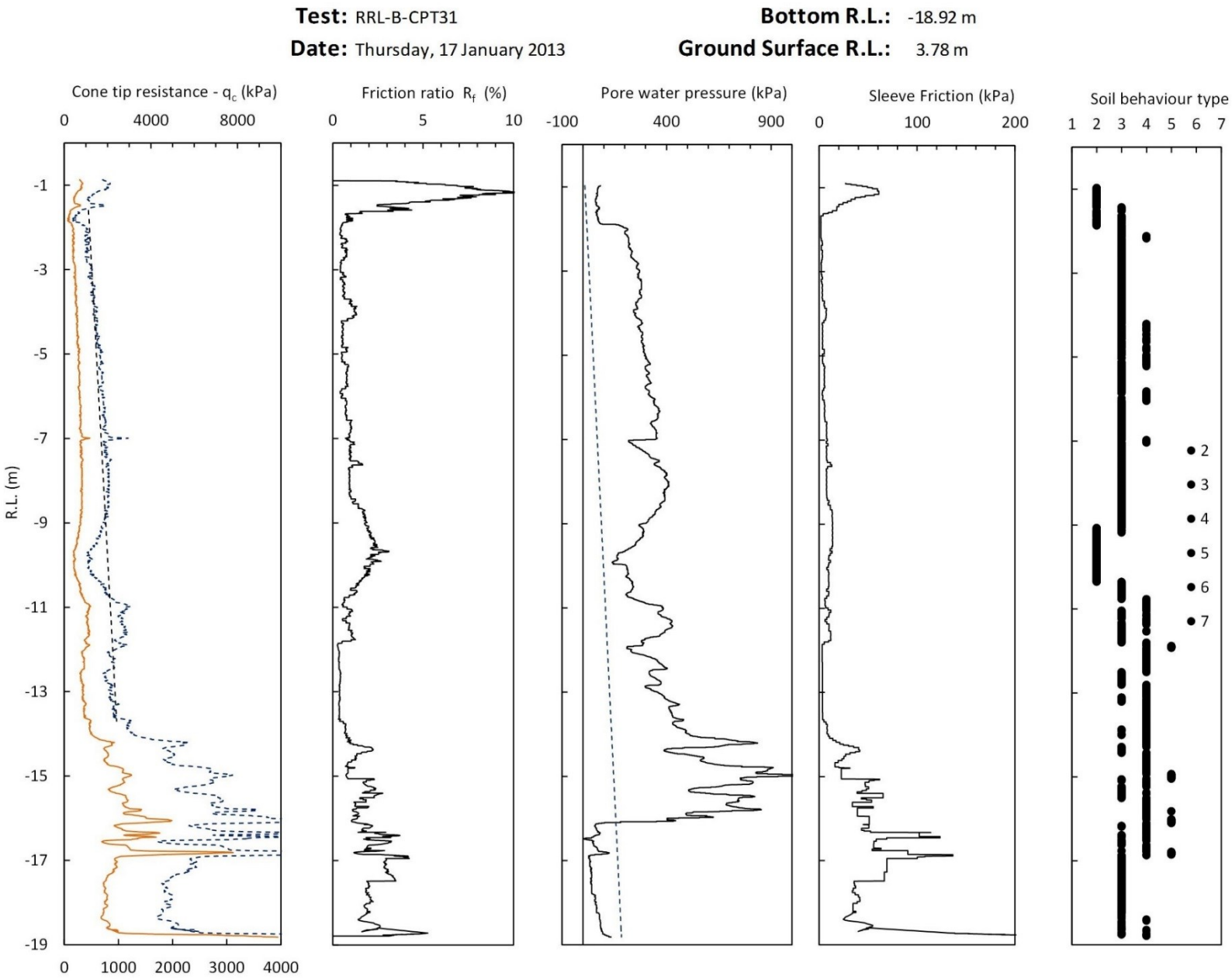
Test: RRL-B-CPT31
Date: Thursday, 17 January 2013
Bottom R.L.: -18.92 m
Ground Surface R.L.: 3.78 m
Cone tip resistance - q_c (kPa)
Friction ratio R_f (%)
Pore water pressure (kPa)
Sleeve Friction (kPa)
Soil behaviour type
R.L. (m)
0 4000 8000
0 5 10
-100 400 900
0 100 200
1 2 3 4 5 6 7
-1 -3 -5 -7 -9 -11 -13 -15 -17 -19
0 1000 2000 3000 4000
2 3 4 5 6 7

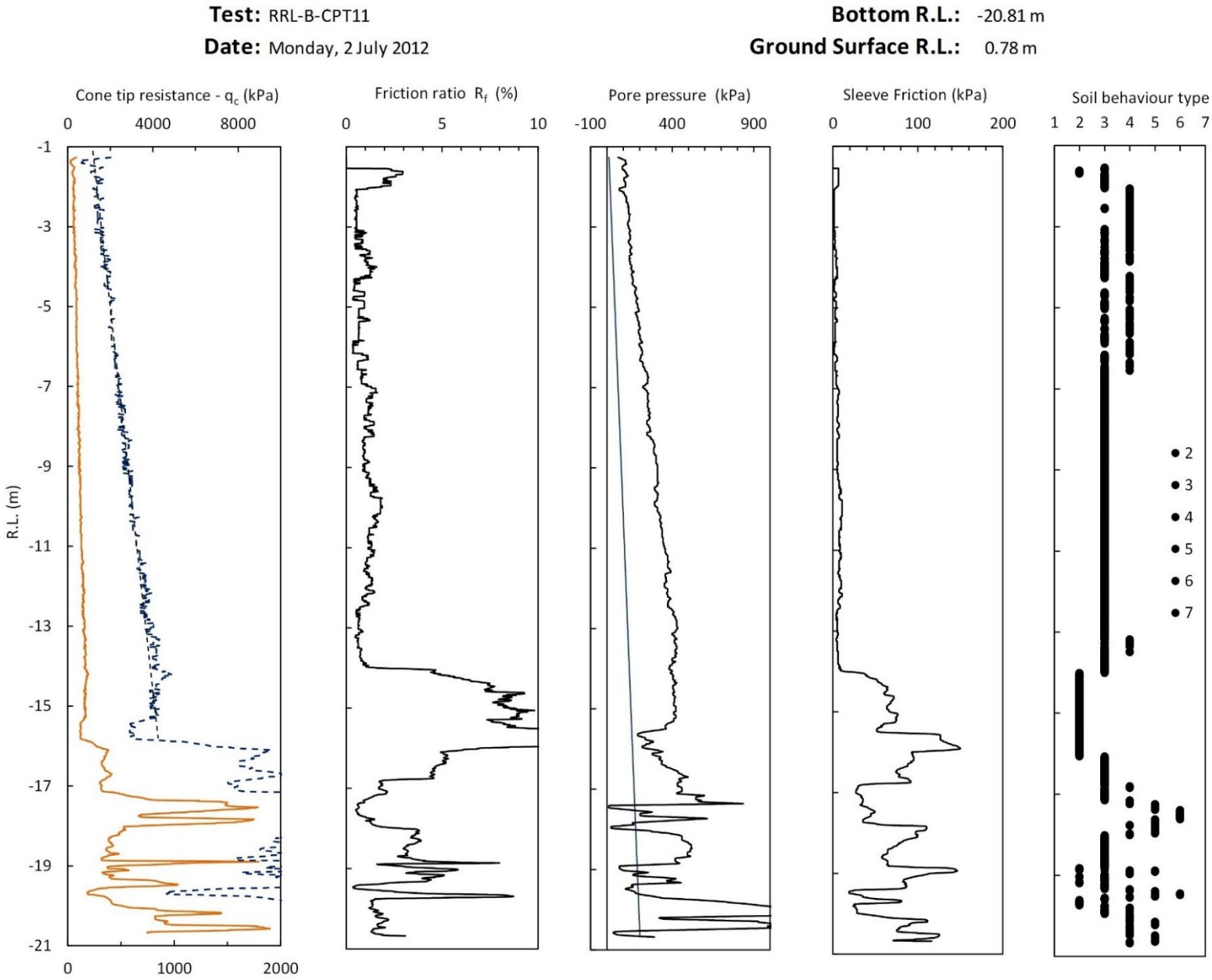
Test: RRL-B-CPT11
Date: Monday, 2 July 2012
Bottom R.L.: -20.81 m
Ground Surface R.L.: 0.78 m
Cone tip resistance - q_c (kPa)
Friction ratio R_f (%)
Pore pressure (kPa)
Sleeve Friction (kPa)
Soil behaviour type
R.L. (m)
0
4000
8000
0
5
10
-100
400
900
0
100
200
1 2 3 4 5 6 7
-1
-3
-5
-7
-9
-11
-13
-15
-17
-19
-21
0
1000
2000
2
3
4
5
6
7

APPENDIX B. Geotechnical characterisation – Coode Island Silt

This Appendix presents the results of the laboratory study and assessment of field data undertaken to characterise the Coode Island Silt for the case study. This was presented in (King et al. 2016a). Some additional findings relating to the sensitivity of the Coode Island Silt (Section B.1.2), laboratory horizontal permeability (Section B.1.4), undrained shear strength (Section B.2.7) and *in situ* dissipation tests and field coefficient of horizontal consolidation (Section B.2.8) are also presented.

B1. Coode Island Silt – laboratory testing

A borehole (BH41) was drilled adjacent to CPT31 in order to recover samples for laboratory testing and to calibrate the material properties assessed through the CPTs. Laboratory tests on the Coode Island Silt and Fishermens Bend Silt comprised Atterberg limits, particle size distribution (PSD), oedometer and triaxial tests. This section describes the Coode Island Silt laboratory testing and analysis of data undertaken.

The results of 14 no. Atterberg limits tests on Coode Island Silt samples are overlain on Casagrande's mineralogical identification chart in Figure B1. The test data matches well with the trendline described by Nagalingam (1986) in Equation B1. The three results with w_L less than 40 % are samples containing a fine sand portion near the upper (R.L. 0 m to – 3 m) and lower surfaces of the Coode Island Silt (R.L. – 13 m to – 14.2 m). The mineralogical composition assessed using X-ray diffraction analysis from Coode Island Silt sampled at a site in South Melbourne (Stanley et al. 2012) is shown in Figure B1*b*. The percentage composition of the dominant clay minerals; illite, kaolinite and smectite (primarily montmorillonite), is generally consistent with Nagalingam's trendline which passes between and parallel to these clay mineral groups on Casagrande's chart.

It is postulated that the location of Coode Island Silt samples on this trendline is primarily due to a varying portion of quartz and that the relative difference in the composition of the dominant clay minerals (illite, kaolinite and smectite) does not vary significantly; considerable variation in the vertical direction about the trendline would be expected if this was not case. As noted above, the fine sand portion (quartz) explains the lower w_L of 3 no. tests.

a)

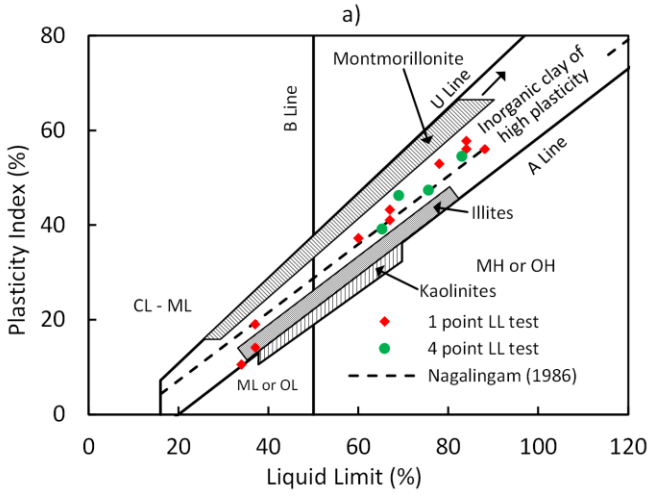

b)

Mineralogical type	% composition
Quartz	30
Feldspar	5
Illite	15
Kaolinite	20
Smectite	27
Pyrite	3

Figure B1. (a) Casagrande's mineralogy identification chart after Holtz et al. (2010) with Coode Island Silt test results and **(b)** mineralogical composition of a Coode Island Silt sample from a site in South Melbourne after Stanley et al. (2012)

However, there is insufficient quantitative data of Coode Island Silt mineralogy to verify the relationship between Nagalingam's trendline and clay mineralogy. Additional data on the moisture content-void ratio relationship and unit weight of Coode Island Silt samples is presented in Figure B2*a* and *b*, respectively; the agreement with data from Ervin (1992) is good. A typical cross section of a Coode Island Silt sample is shown in Figure B3*a* along with a thin bedding of shells in the same sample (Figure B3*b*), the occurrence of which is common in the Coode Island Silt.

$$PL = 0.72\ (LL - 10) \qquad \textbf{(B1)}$$

B.1.1 Oedometer testing and pre-consolidation stress

Oedometer tests were performed in order to assess settlement of the Coode Island Silt beneath the load transfer platform. Initial instrumentation data indicated low applied stresses acting on the Coode Island Silt, as a result, secondary (creep) compression of the Coode Island Silt is expected to play an important part in the long term behaviour of the load transfer platform. Therefore, in addition to accurately characterising the σ'_p profile with depth, oedometer tests with extended secondary creep incremental load stages were performed to assess the secondary compression index C_α. Eight conventional (manual) 24-hour incremental load oedometer tests were performed with a load increment ratio of 1.0 and a one week creep stage (1 log cycle) based on the detailed procedure outlined by

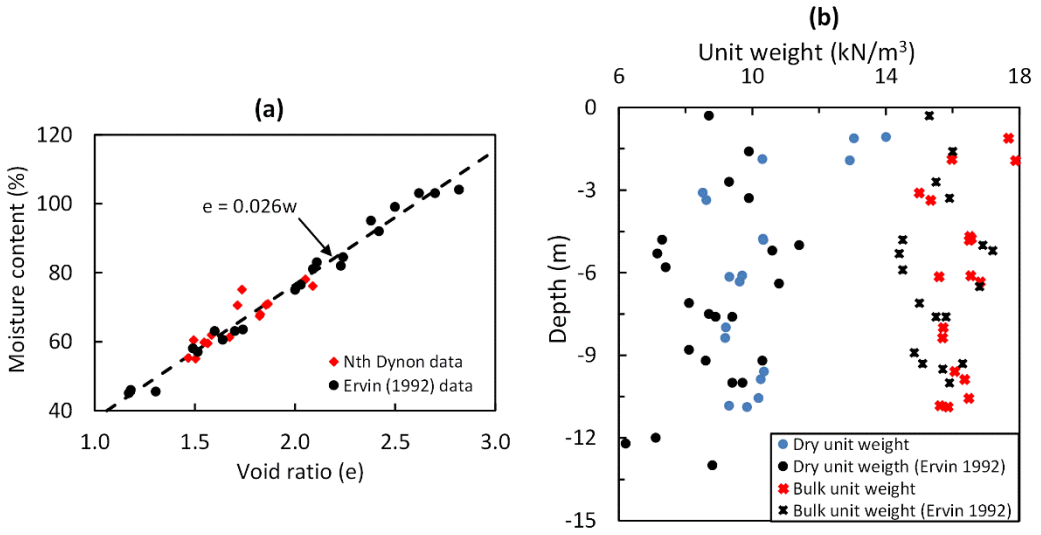

Figure B2. Comparison with Ervin's (1992) data **(a)** *e* vs *w* and **(b)** dry and bulk unit weights

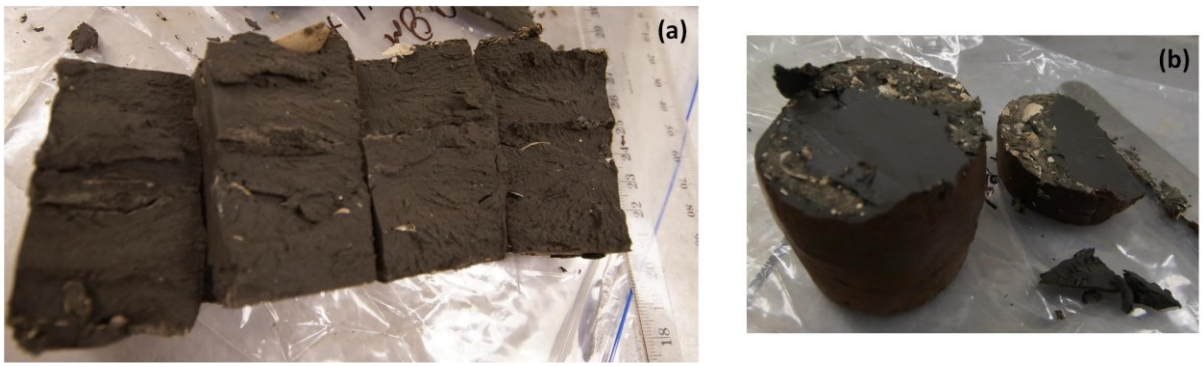

Figure B3. (a) Cross section of triaxial samples of Coode Island Silt at R.L. – 9.95 to – 10.07 m and **(b)** thin (10 mm thick) bedding of shells in upper portion of triaxial sample

Head (1982) and in accordance with AS1289 (1998). The extended creep stage was performed at ratios of applied stress over *in situ* vertical effective stress (σ'_{vc} /σ'_{v}) ranging from 0.9 to 2.2. Ervin (1992) previously showed that for Coode Island Silt C_{α} tends to increase with increasing σ'_{vc} /σ'_{v}. Two no. (automated) 24-hour incremental load oedometer tests were performed with load stages; 6.25, 12.5, 25, 50, 100, 200, 400 and 800 kPa, as suggested by AS1289 (1998). Not surprisingly, σ'_{p} values from these 10 tests show considerable scatter due to the load increment ratio adopted (i.e., lack of data points in the vicinity of σ'_{p}), and in the case of the extended creep tests, the effect of the creep stage on the *e*-log(*p*) plot.

The effect of the load increment ratio is consistent with observations described by Ladd et al. (2003), who noted that the S-shaped portion of the *e*-log(*p*), when compared with traditional 24-hour incremental tests, is better captured with an incremental end-of-primary test with reduced load increment ratio or constant-rate of strain (CRS) tests, with Ladd et al. (2003) recommending the latter test. These tests methods result in better characterisation of the yield point and the initial post-yield behaviour (de-structuring of the clay) as assessed through σ'_{p} and the maximum virgin compression index ($C_{c\,max}$) respectively. The effect that sample disturbance, load increment ratio and duration has on these parameters is illustrated in Figure B4*a*, *b* and *c*, respectively.

The recommendations by Ladd et al. (2003) were adopted for the next 10 tests although automated incremental end-of-primary tests were performed as the equipment for CRS testing was not available. These automated tests were loaded to 50 kPa with an increment ratio equal to 1.0, then typically loaded between 50 kPa to 896 kPa with a load increment ratio of 0.3 (Load stages: 6.25, 12.5, 25, 50, 65, 84.5, 109.9, 142.8, 185.6, 241.3, 313.7, 407.9, 530.2, 689.3 and 896.0 kPa), the load increment duration was equal to the time to end of primary consolidation. A benefit of performing end-of-primary tests was that the time to complete a test was typically 3 to 4 days, compared with around 2 weeks for a 24-hour load increment test. Using this test method it was possible to complete several tests in the same period of time as a traditional 24-hour incremental load test; the large amount of oedometer test data enabled the use of statistical techniques to interpret the σ'_{p} profile as described below.

Three oedometer tests on the sample recovered from between R.L. – 10.52 and – 10.92 m are shown in Figure B5*a*. The σ'_{p} stress has been assessed using both the Casagrande graphical technique and the strain energy method proposed by Becker et al. (1987), this is shown for an end-of-primary test in Figure B5*b* and *c*, respectively. The strain energy method (SEM) plots work per unit volume versus applied stress σ'_{vc}, note that work is calculated using incremented natural strain which differs from engineering strain ε_{v} referred to below to assess sample disturbance. The SEM method calculates the σ'_{p} stress as the intercept of the initial linear portion of the work curve prior to σ'_{vc}

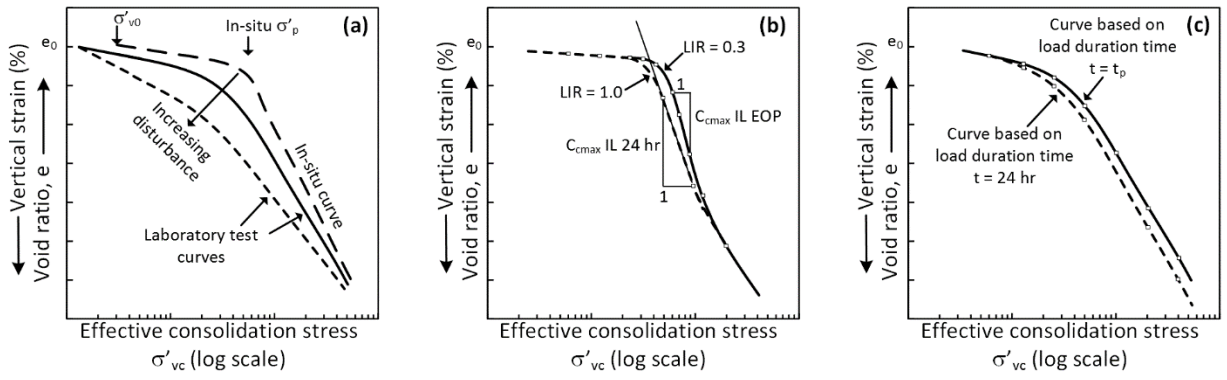

Figure B4. Factors affecting laboratory determination of σ'_{p} **(a)** sample disturbance **(b)** load increment ratio and **(c)** load increment duration after Holtz et al. (2010) and Ladd et al. (2003)

and the linear post-yield portion of the work curve; this is well defined over several data points in work-stress space in Figure B5*c*.

By comparison, calculation of σ'_p in *e*-log(*p*) space is quite subjective. The linear portions of the *e*-log(*p*) plot at σ'_v and post-yield, which defines the "most probable" value of σ'_p, are poorly defined in Figure B5*b*. This is often the case for tests on Coode Island Silt samples which exhibit a curved portion in the vicinity of σ'_p and the recompression range ($\sigma'_v < \sigma' < \sigma'_p$). The graphical Casagrande method requires assessment of the point of maximum curvature (κ), this too is subjective, particularly in the case of the traditional 24-hour tests where the curve in the vicinity of σ'_p for Coode Island Silt is typically defined by just 3 data points; 50 kPa, 100 kPa and 200 kPa. However, the main difference between the two approaches is the stress axis, compared with the linear axis used with the SEM, the *e*- log(*p*) methods amplify the potential error range due to the log scale. A more rigorous approach might be to calculate κ explicitly using Equation B2, however, this requires a continuous function and therefore interpolation between the *e*-log(*p*) data points. This in turn introduces a numerical bias as the yield point established is biased towards the curve fitting method adopted.

$$\kappa(x) = \frac{|y''|}{(1 + (y')^2)^{\frac{3}{2}}} \qquad \textbf{(B2)}$$

Regardless of the method adopted, assessing σ'_p based on the traditional 24 hr (with load increment ratio = 1.0) tests generally results in a poorly defined yield point; this cannot be resolved through graphical or numerical interpolation methods.

The borehole stratigraphy, Atterberg limits, particle size distribution, liquidity index and SBT zones from BH41 as well as the q_c profile from CPT31 are shown in Figure B6*a*, *b*, *c*, *d*, *e* and *f* respectively. Ladd et al. (2003) suggest using the vertical strain ε_{v0} of the oedometer samples measured at overburden stress (σ'_{v0}) to provide an indication of relative disturbance between samples at equivalent depths, this is shown in Figure B6*g* along with the specimen quality designation (SQD). Figure B6*g* indicates that the majority of the samples undergo considerable deformation (strain) when recompressed back to their *in situ* vertical stress, particularly samples at depth. This was also the case for over 80 research quality oedometer samples on Boston Blue clay described by Ladd et al. (2003). In

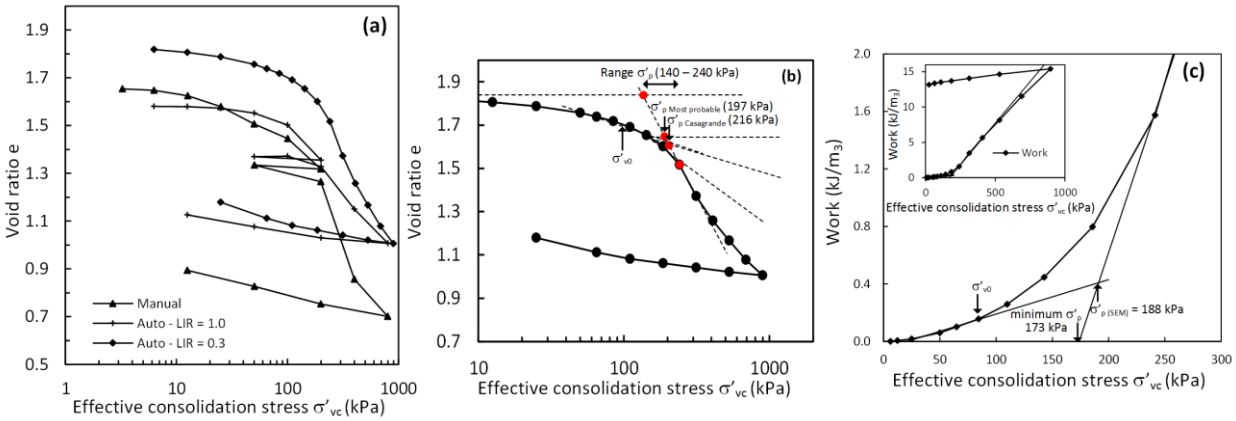

Figure B5. *e*-log(*p*) plots for sample from R.L. – 10.52 to – 10.92 m: **(a)** comparison of 3 test methods and calculation of σ'_p for end-of-primary test sample using the **(b)** Casagrande graphical technique and **(c)** Strain energy method

addition to assessing relative sample disturbance, ε_{v0} for the manual tests (load increment ratio = 1.0) and automated tests (load increment ratio= 0.3) are compared in Figure B6*g*.

This comparison provides an indication of the relative quality of the resulting S-shaped oedometer curve in *e*-log(*p*) space for the two test methods. For the various reasons described above, the end-of-primary tests alone are used to develop the σ_p' profile in Figure B6*h*. Comparison of the ε_{v0} values for load increment ratio = 0.3 tests tends to indicate that tests with a higher ε_{v0} have a corresponding lower σ_p'; this suggests that sample disturbance affects the fabric and structure of the clay resulting in a poorly defined yield point. The effect is well illustrated by Ladd et al. (2003) based on a number of oedometer tests on Boston Blue clay. The inclusion of these data points at higher relative ε_{v0} values likely leads to the underestimation of the σ_p' profile. As suggested previously by Srithar (2010), the expression by Mayne (1991) can be used to relate q_c and σ_p'. Mayne (1991) developed an analytical model in terms of cavity expansion theory and critical state soil mechanics to link σ_p' and net cone tip resistance ($q_t - \sigma_p'$). A simplified version of this expression is given below based on Mayne (2005):

$$\sigma_p' = \frac{(q_t - \sigma_{vo})}{(M/3) \cdot [\ln(I_R) + 2.928]} \qquad \textbf{(B3)}$$

Where M is the slope of the critical state line Equation B3, I_R the rigidity index defined as G/s_u where G is the shear modulus and s_u the undrained shear strength, q_t and σ_{v0} have been defined previously.

$$M = \frac{6 \sin \phi'}{3 - \sin \phi'} \qquad \textbf{(B4)}$$

Adopting an I_R value of 100 and $\phi' = 30^o$ (average value based on the results of 28 CU triaxial tests with measurements on Coode Island Silt presented by Ervin (1992), σ_p' can be expressed as:

$$\sigma_p' = 0.33(q_t - \sigma_{v0}) \qquad \textbf{(B5)}$$

This is similar to Equation B6 which is the expression described by Lunne et al. (1997) with an average value of k = 0.3. The k value has a range of 0.2 to 0.5, with higher values recommended for clays with a high OCR.

$$\sigma_p' = 0.30(q_t - \sigma_{v0}) \qquad \textbf{(B6)}$$

The expressions described by Mayne (2005) and Lunne et al. (1997) are shown in Figure B6*h* along with the linear regression trendline based on the laboratory test data. The agreement between the laboratory data and the CPT correlations is reasonably good; a k value of 0.27 matches exactly. However, it is likely that the more disturbed samples with corresponding lower σ_p' values cause the laboratory derived trendline to under predict the *in situ* σ_p' profile. On the basis of the data presented a k value in the range of 0.27 to 0.33 will likely provide a reasonable first order estimate of *in situ* pre-consolidation stresses for the Coode Island Silt. A lower bound k value is suggested where this correlation is to be used in practice without site specific laboratory testing to assess σ_p'.

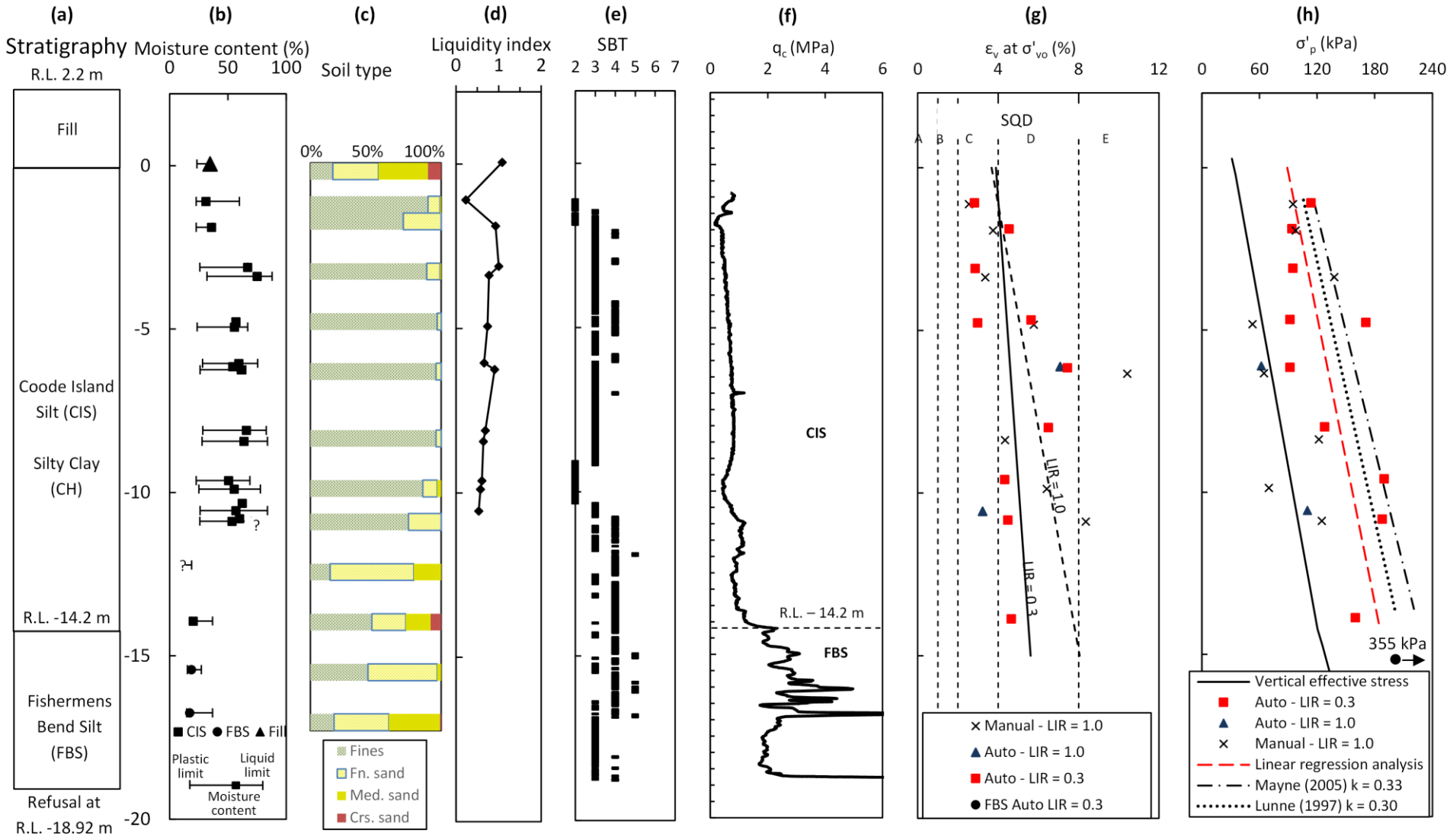

Figure B6. CPT31 and BH41 **(a)** Soil stratigraphy **(b)** Atterberg limits **(c)** Soil type **(d)** Liquidity index **(e)** SBT zones **(f)** q_c profile **(g)** BH41 - vertical strain measured in oedometer tests at *in situ* overburden pressure **(h)** σ'_p profiles from laboratory tests and CPT correlations

B.1.2 Compression index

The S-shaped portion of an *e*-log(*p*) plot is a characteristic of soft soils which exhibit structured behaviour under load. There are a number of parameters used to define the s-shaped portion of an *e*-log(*p*) plot, here the terminology used by Terzaghi et al. (1996) and Holtz et al. (2010) is adopted and defined in Figure B7*a*. Figure B7 illustrates the difficulties in establishing a simple correlation between the compression index (C_c) with material parameters (such I_P, e_0, etc.) where the soft soil exhibits the characteristic S-shape curve of a structured clay. For settlement analysis, it is typically the initial post-yield behaviour in the normally consolidated (NC) range, defined by $C_{c\,max}$, which is of most importance.

In Figure B7*b* a correlation with the strain based maximum modified compression index $C_{c\varepsilon\,max}$ ($\Delta\varepsilon/\log \sigma'_{vc}$) is presented as functions of w_L (%) and it can be seen that the correlation is poor. The widely used correlation proposed by Terzaghi et al. (1967) $C_c = 0.009\,(w_L - 10)$ is also shown, considerable scatter about this trendline is also observed. Although for this correlation it is noted that it should not be used when the soil exhibits a sensitivity greater than 4, w_L greater than 100 or when the clay contains a high organic content. The Coode Island Silt does not meet at least one of these criteria and perhaps provides some indication as to why compression index shows a poor correlation with w_L. This finding is consistent with Ervin (1992) who also attempted to correlate C_c and $C_{c\varepsilon}$ and did not found a strong correlation; Ervin (1992) suggested *in situ* moisture content (w_0) as a better alternative.

In Figure B8*a* and *b*, $C_{c\varepsilon\,max}$ and $C_{c\,max}$, respectively, are plotted against w_0. A strong correlation is found, a similarly good fit is also achieved with e_0. The maximum compression ratio has been assessed by adopting a cubic spline interpolation of the *e*-log(*p*) data points, this interpolated function provides a more realistic assessment of $C_{c\,max}$ than the use of a linear slope between data points. The $C_{c\varepsilon\,max}$ parameter is approximately linear with respect to moisture content, and indeed many correlations of this type are linear, however, a power function expression ($C_{c\varepsilon\,max} = 5.065 \times 10^{-4} \times w^{1.66}$) provides the best fit with a coefficient of determination (R^2) equal to 0.95. This expression converted to $C_{c\,max}$ ($C_{c\,max} = C_{c\varepsilon\,max}/(1+e_0)$) has an $R^2 = 0.91$. The outlier at RL – 6.15 m ($w = 67$ %, $C_{c\,max} = 0.59$) is not considered, this is the most disturbed test sample both in terms of absolute ε_{v0} and ε_{v0} relative to the mean (Figure B6*c*) used in the automated test.

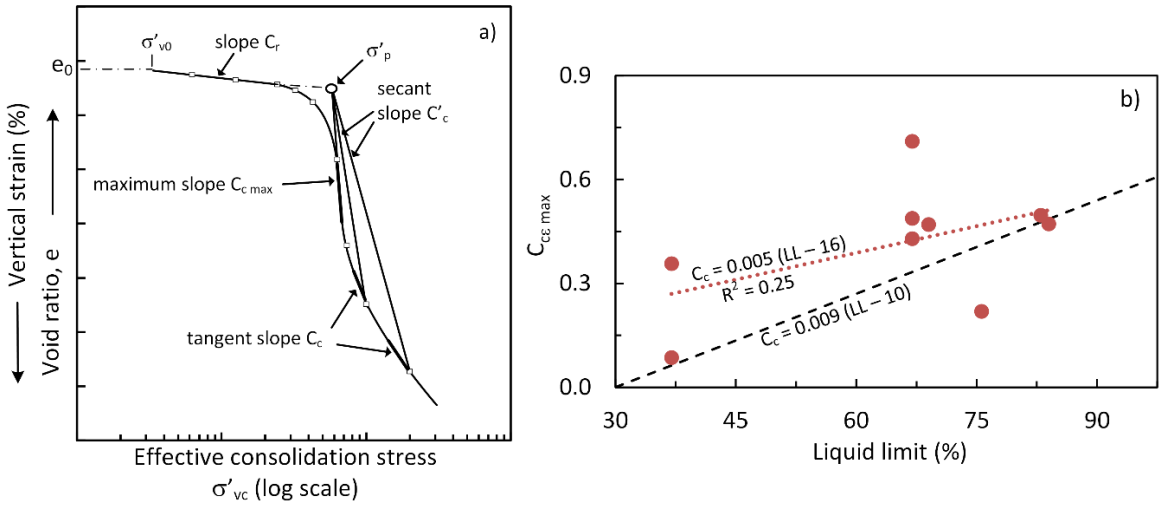

Figure B7. (a) Definition of recompression index C_r, max. compression index $C_{c\,max}$, compression index C_c and secant compression index C'_c and laboratory data correlations and **(b)** $C_{c\varepsilon\,max}$ vs w_L data

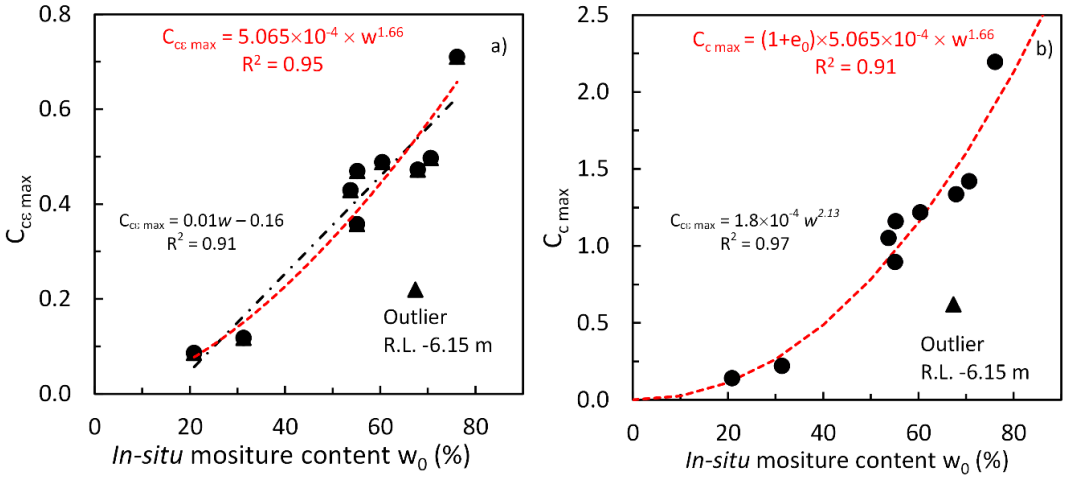

Figure B8. (a) $C_{c\varepsilon\ max}$ vs. w (%) and **(b)** $C_{c\ max}$ vs. w (%)

At higher σ'_{vc} stresses the e-log(p) curve tends to be approximately linear. In Figure B9*a* the slope of the linear portion of the e-log(p) curve is plotted against void ratio e_0. For the traditional 24-hour tests this is the linear portion between the 400 to 800 kPa load stages. The automated and manual test data are both shown in Figure B9*a*, a power function relationship provides a best fit for this data $C_{c400\rightarrow800\ kPa} = 0.26e_0^{1.39}$. The trendlines for $C_{c\ max}$ and $C_{c400\rightarrow800\ kPa}$ as a function of moisture content provide an approximate upper and lower bound of the compression index respectively and also bound the compression index data previously reported by Srithar (2010) and Ervin (1992) quite well (Figure B9*b*). This is similar to what is likely the earliest developed relationship describing the variation in C_c for Coode Island Silt by Donald et al. (1962), in this case C_c was plotted against liquid limit.

However, using the secant compression index (C'_c), the post-yield portion of the S-shaped e-log(p) curve (Figure 11) can be completely defined with isochronous e_0 curves as a function of normalised vertical effective stress σ'_{vc}/σ'_p. The S-shaped portion of the e-log(p) plot is reasonably well defined for the majority of the automated tests with reduced load increment ratio, however, for the traditional 24-hour tests, reliable assessment of $C_{c\ max}$ and the C'_c curve is not possible. The C'_c isochronous curves for the automated oedometer tests are shown in Figure B10*b*, while the individual curves are not true isochronous curves the general features are evident from the trendlines of

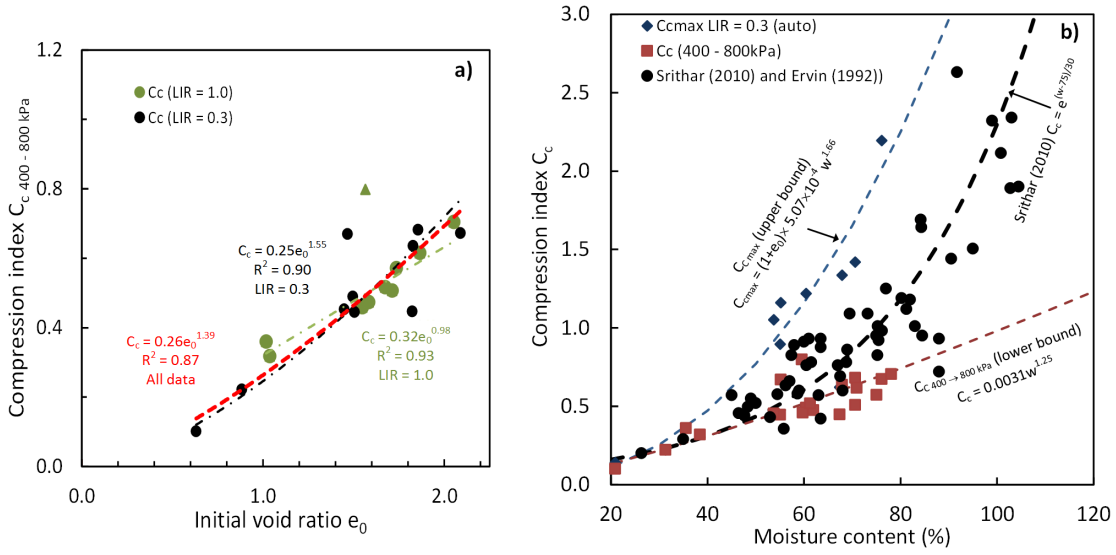

Figure B9. Compression index correlations - **(a)** $C_{c\ 400\rightarrow800kPa}$ vs. w (%) and **(b)** Laboratory data, upper and lower bounds and C_c data by Srithar (2010) and Ervin (1992).

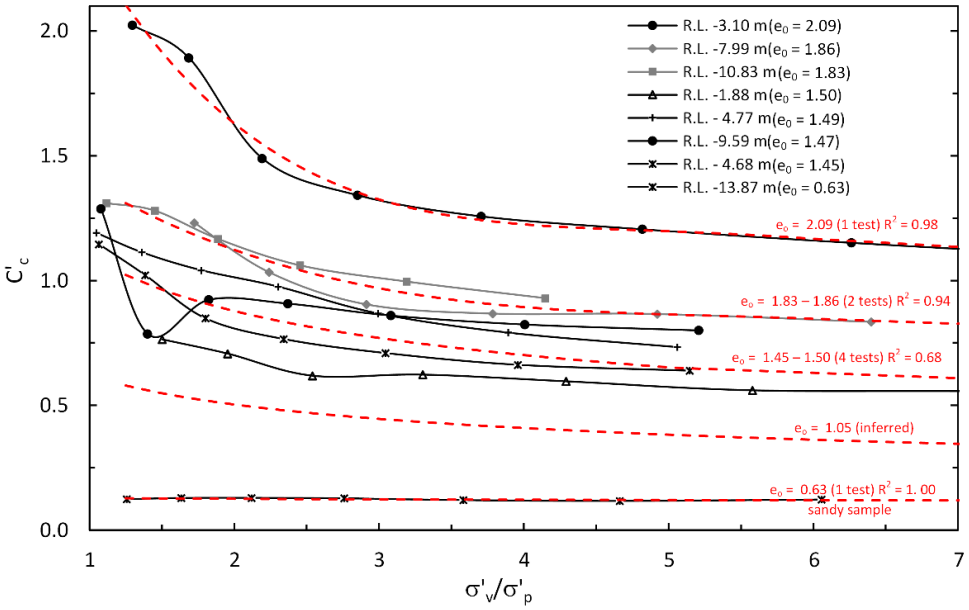

Figure B10. Secant compression index C'_c data for Coode Island Silt from eight no. tests.

curves with similar void ratios, these general features include: 1) a maximum C'_c value just past the pre-consolidation stress corresponding to initial post-yield behaviour, 2) samples with a higher void ratio showing higher C'_c values (or C_c values) representing increased compressibility and more structured behaviour and 3) a general reduction in C'_c values with increasing stress and a gradual reduction in C'_c values at stresses greater than about $\sigma'_{vc}/\sigma'_p = 4$. This last feature is due to the near constant C_c values at higher stresses (on an e-log(p) plot) where the sample has undergone significant yield and approaches remoulded behaviour.

B.1.3 Sensitivity

Ervin (1992) previously assessed the sensitivity (S_t) of the Coode Island Silt based on field shear vane data from a range of sites, this data is reproduced in Table B1 along with data from Donald et al. (1962). The sensitivity of Coode Island Silt samples recovered from the North Dynon embankment is assessed in Figure B11*a* based on e-log(p) profiles which have been converted to liquidity index (I_L) – log (σ'_{vc}) profiles and compared with data from Cotecchia et al. (2000). The liquidity index is expressed as $I_L = (w - w_P)/I_P$. This data suggests sensitivity in the range of about 3 to 5 which, compared with the field vane data, indicates lower values of sensitivity. This is likely due to the effects of sample disturbance on the oedometer samples. The effect sample disturbance has on the yield point was discussed previously and the effect on the I_L – log (σ'_v) plot is similar. i.e., yield point is shifted towards the lower left hand corner of Figure B11*a*.

The relationship between sensitivity and liquidity index after Bjerrum (1954) is shown in Figure B11*b*. The liquidity index was shown Figure B6*d* and varied from between 0.7 to 1.0, this is also consistent with data

Table B1. Sensitivity of Coode Island Silt samples from field vane data (from Ervin 1992)

Source of data	Site (no. of readings)	S_t - range (average) kPa
Donald et al. (1962)	Port Melbourne (12)	2.4 – 6.7 (4.2)
McDonald et al. (1984)	South Melbourne	? (5)
Ervin (1992)	Webb Dock (15)	2.6 – 10.3 (5.9)
	Appleton Dock (25)	4.5 – 12 (7.3)

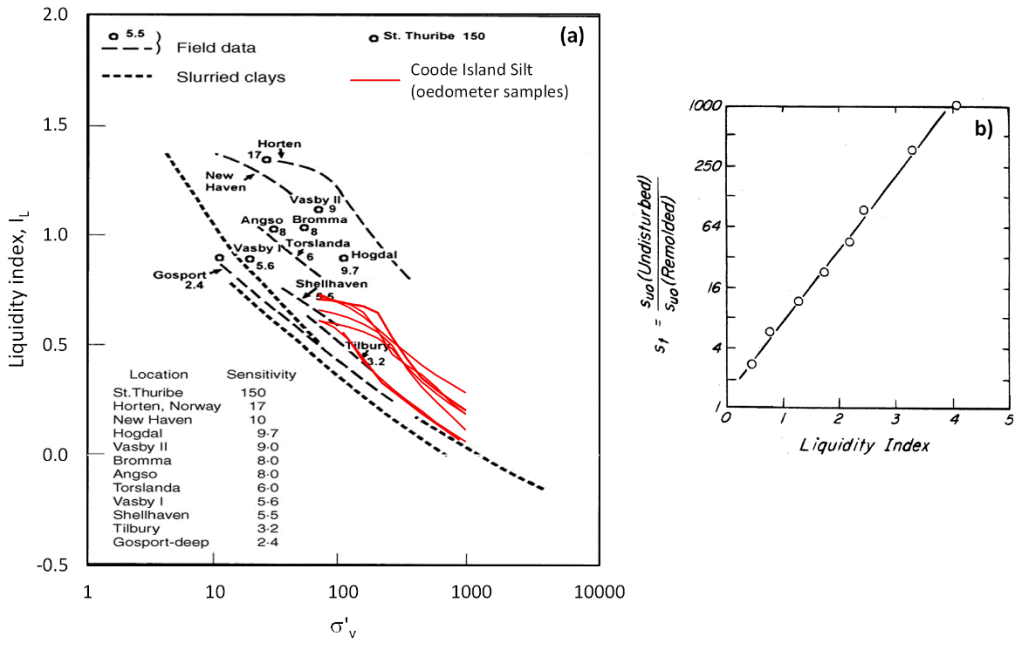

Figure B11. (a) Sensitivity of Coode Island Silt samples based on liquidity index after Cotecchia et al. (2000) and **(b)** Relation between sensitivity and liquidity index (after Bjerrum 1954)

presented by Donald et al. (1962) which showed a similar range. The sensitivity assessed based on liquidity index and the correlation presented by Bjerrum (1954) indicates a range of sensitivity of 4 to 8 which is consistent with the sensitivity assessed based on *in situ* shear vane testing.

B.1.4 Time rate of consolidation

The coefficient of consolidation can be assessed incrementally from oedometer test data with a double drainage condition using Equation B7 where $\bar{H}$ is the mean sample height (mm) over a load increment, t_{50} (minutes) is the time to 50 % primary consolidation and c_v is in units of m^2/year. The time to end of primary consolidation t_{100} and t_{50} for an incremental load can both be assessed using either the log-time or square root-time fitting methods, details can be found in Head (1982).

$$c_v = \frac{0.026 \times (\bar{H})^2}{t_{50}} \text{m}^2/\text{year} \qquad \textbf{(B7)}$$

As a clay sample is loaded in an oedometer cell the coefficient of consolidation is not constant. The value calculated depends a great deal on whether the soil is in the recompression (RC) or normally consolidated (NC) range with a marked reduction in the coefficient of consolidation as the soil yields and transitions to the normally consolidated range. The ratio of c_v in the recompression to virgin compression ranges (i.e., c_v(RC)/c_v(NC)) is typically 5 to 10 for soft soils but can be up to 100 for highly structured sensitive clays found for example in parts of Canada (Terzaghi et al. 1996). After an initial minimum c_v(NC) value just past of the pre-consolidation stress the value of c_v can either increase slightly or remain constant (Terzaghi et al. 1996).

Robinson et al. (1998) showed that the variation of c_v in a de-structured state can be related to clay mineralogy based on the assessment of c_v for various reconstituted clay mineral samples and can therefore explain the variation in c_v as a soft soil sample transitions from initial post-yield behaviour to a fully structured state at higher stresses in an oedometer test. For the samples tested by Robinson et al. (1998) comprising the clay mineral groups whose

behaviour is dominated by "mechanical" interaction (powdered quartz, illite and kaolinite), c_v increased with increasing stress while a montmorillonite sample, whose behaviour is dominated by "physio-chemical" interaction, c_v decreased with increasing stress. Where the terms mechanical and physio-chemical, after Olsen et al. (1970), refer to short range particle interaction (particle shape, geometric arrangement of particles and surface friction) and long-range particle interaction (particle shape, geometric arrangement of particles and chemical variables) respectively. The mineralogical composition of the Coode Island Silt described previously suggests that Coode Island Silt predominately comprises the "mechanical" clay mineral types and therefore an increase in c_v in the NC range is more likely.

The variation of c_v as a function of normalised stress is shown in Figure B12*a*. The considerable reduction in c_v as the Coode Island Silt samples yield just past the preconsolidation stress is evident, as are the effects of sample disturbance on c_v in the recompression range for the two disturbed samples shown. In the destructured state (NC range) the sample show a relatively small range of variation in c_v values (about $0.3 < c_v < 0.8$ m^2/year) compared with the RC range, with the later likely due to sample disturbance. The ratio of c_v (RC)/c_v (NC) is about 3 to 7 with the least disturbed samples showing a higher ratio. It is likely that the variation of c_v, as Coode Island Silt undergoes yielding *in situ*, is more accurately represented by ratio values near the upper end of this range and may be higher

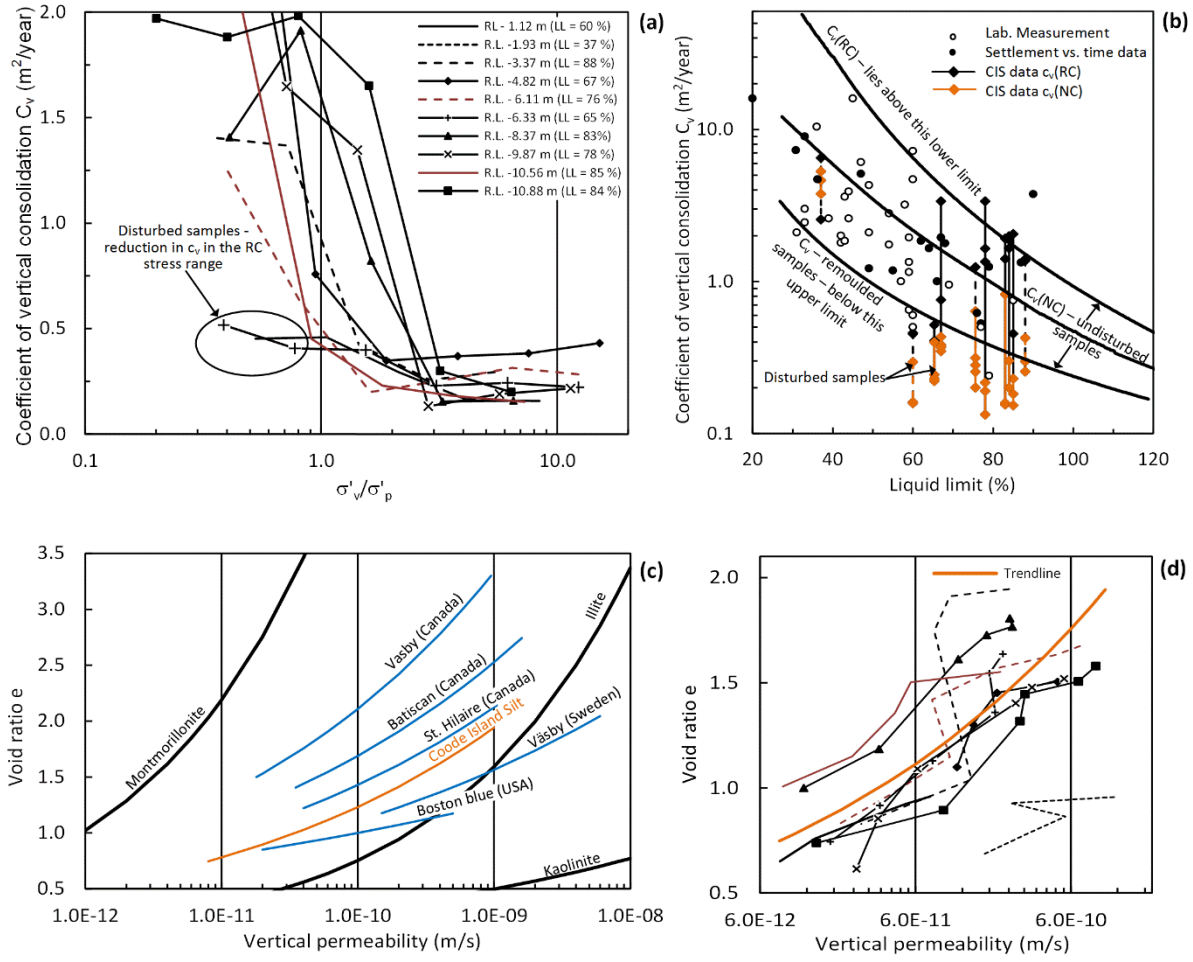

Figure B12. (a) Vertical coefficient of consolidation c_v vs. normalised applied loading σ'_{vc}/σ'_p for manual oedometer tests and **(b)** c_v vs. w_L for Coode Island Silt samples and c_v values for various clays from direct measurement of k_v and computed from settlement-time data after Terzaghi et al. (1996). Approximate correlations of c_v for recompression, virgin compression and remoulded states after U.S. Navy (1982). **(c)** Void ratio e vs. vertical permeability k_v for Coode Island Silt, various soft clays (after Terzaghi et al. 1996) and clay minerals (after Mesri and Olson, 1971). **(d)** e vs k_v for Coode Island Silt samples

still due to sample disturbance effects on c_v(RC). All of the samples show some variation in c_v(NC) although it is difficult to establish any clear trend. It is worth noting that the magnitude of variation in the NC stress range is minor compared to the substantial reduction in c_v as the soil yields in the vicinity of the pre-consolidation stress. The behaviour of c_v in the latter case, is in most cases more important for engineering design.

The data in Figure B12*a* is also presented as a function of liquid limit in Figure B12*b*. In Figure B12*b* the Coode Island Silt data is compared with data reported by Terzaghi et al. (1996) based on direct k_v measurements and settlement vs time data along with delineated RC, NC and remoulded c_v zones suggested in a design chart by the US Navy (1982). The values of c_v (RC) for Coode Island Silt site is in the NC range or near the boundary of the NC/RC zone, this further supports the notion that sample disturbance has likely resulted in a reduction in c_v(RC). During the process of consolidation the variation in void ratio results in a decrease in the permeability of a soft soil. It is possible to indirectly measure the vertical permeability k_v of an oedometer sample using Equation B8 where c_v (m^2/year) is as defined previously and the coefficient of volume compressibility m_v has units of m^2/MN.

The values of void ratio are plotted against k_v in Figure B12*d* on a semi-logarithmic plot. The samples at R.L. – 1.93 m with a fine sand portion have a higher permeability, however, for the remaining samples there is a general near linear reduction in k_v with decreasing void ratio. The parameter $C_k = \Delta e/\Delta\log(k_v)$ is approximately 0.53 for the Coode Island Silt samples shown (excluding the sandy sample), there is approximately 1 order of magnitude of total scatter in k_v across e values. The values of k_v compare reasonably well with the value of $k_v = 3 \times 10^{-10}$ m/s at the initial void ratio adopted by Ervin et al. (2001) for the design of a large basement excavation into Coode Island Silt in Southbank. Their design value was based on six no. constant-head triaxial permeability tests on Coode Island Silt.

In Figure B12*c* the Coode Island Silt e-k_v trendline is compared with various soft soils from Canada, Sweden and the U.S.A. In general, the curvature and relative position of the trendline compares well with these other soils. In addition, a comparison of the Coode Island Silt e-k_v trendline and trendlines for clay mineral samples of montmorillonite, illite and kaolinite (in Figure B12*c*) suggests that the trendline is influenced by the main clay mineral types which make up the Coode Island Silt samples. The apparent influence of clay mineralogy on the e-k_v trendline shares similarities with Nagalingam's trendline of material behaviour shown in Figure B12*a*. The data presented herein suggests that further insight into the compressibility and permeability of Coode Island Silt can be gained through consideration of its mineralogical composition.

$$k_v = c_v m_v \times 0.31 \times 10^{-9} \text{m/s} \qquad \textbf{(B8)}$$

B.1.5 Horizontal coefficient of consolidation

Two no. radial oedometer tests were performed to assess the horizontal coefficient of consolidation and anisotropic nature of the Coode Island Silt. Tests were performed on samples at R.L. – 8.4 m and – 10.80 m. The variation in horizontal coefficient of consolidation (c_h) against normalised applied loading σ'_{vc}/σ'_p for the two tests is shown in Figure B13. The variation in c_h due to applied stress is similar in many respects to the variation observed in c_v plotted against σ'_{vc}/σ'_p in Figure B12*a*. A ratio of c_h/c_v at equivalent values of σ'_{vc} varies from 0.8 to 2.0 over the stress range of 85 kPa to 240 kPa. These values are discussed further along with CPT dissipation test results in Section B.2.3.

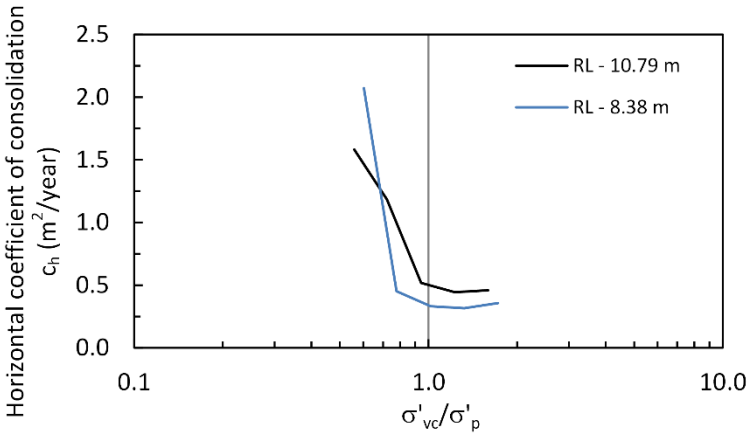

Figure B13. Horizontal coefficient of consolidation assessed from oedometer tests on radially oriented samples

B.1.6 Secondary compression

Consistent with the approach taken above, the secondary compression index C_α and modified secondary compression index $C_{\alpha\varepsilon}$, are defined as void ratio ($\Delta e/\Delta\log(\text{time})$) and strain expressions ($\Delta\varepsilon/\Delta\log(\text{time})$) respectively, similar to the definitions of $C_{c\varepsilon}$ and $C_{c\varepsilon}$ presented above. It is $C_{c\varepsilon}$ which is calculated directly from the extended incremental load stage of an oedometer tests, typically the duration of this load stage is 1 week (1000 mins to 10,000 minutes) which allows the assessment of deformation over 1 log cycle (see Head (1982) for further details). The so-called C_α/C_c concept developed by Mesri et al. (1977) describes the relationship between the C_α and C_c and has been shown to be approximately constant for a large range of soft soils (Mesri et al. 1987, Mesri et al. 1997, Mesri 2003) during the loading stages of an oedometer test (and by inference in the field). As the σ'_{vc} stress increases and approaches the pre-consolidation stress, the magnitude of C_α increases and reaches a peak just after σ'_p, C_α then reduces as a soil yields in the NC range. The general behaviour is the same for $C_{\alpha\varepsilon}$ and is shown conceptually in Figure B14*a* with a normalised stress axis σ'_{vc}/σ'_p.

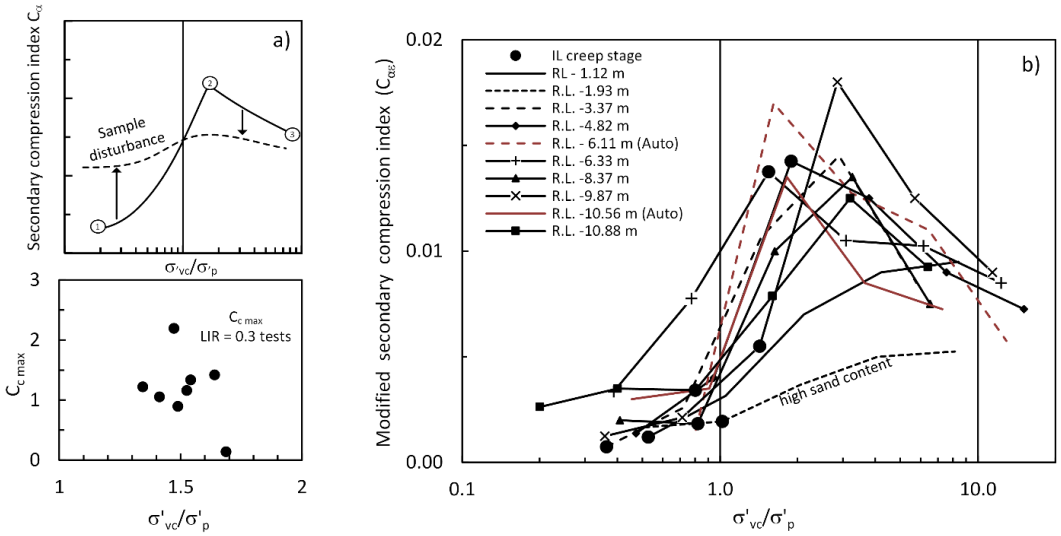

Figure B14. Fundamental one dimensional consolidation behaviour after Ladd et al. (2003) **(a)** Secondary compression index vs. σ'_{vc}/σ'_p **(b)** $C_{\alpha\varepsilon}$ vs. $C_{c\varepsilon}$ and **(c)** Range of $C_{c\,max}$ values vs normalised (point 2) from automated tests

The measured data from the traditional 24-hour (manual) tests is shown in Figure B14*b*, note that secondary compression parameters cannot be calculated from the automated tests as the duration of the load stages is equal to t_p. This is one short-coming with automated tests where a reduced load increment ratio and load duration equal to t_p is adopted. The data presented in Figure B14*b* compares well with similar data presented by Ervin (1992). However, the previous data was presented with the stress axis normalised as $\sigma'_{vc}/\sigma'_{v0}$, this results in the data presented by Ervin (1992) being shifted to the right. This can be observed by comparing the range of maximum $C_{c\varepsilon}$ values for the data shown in Figure B14*b*, the maximum is in the range of about $1.5 < \sigma'_{vc}/\sigma'_{p} < 3.0$ whereas Ervin's data is in the range of about $2 < \sigma'_{vc}/\sigma'_{v0} < 5$. Based on the automated test data shown in Figure B14*c* it can be seen that the maximum values of $C_{c\,max}$ (point 2 in Figure B14*a*) occurs in a narrow range of $1.3 < \sigma'_{vc}/\sigma'_{p} < 1.7$.

Based on the C_α/C_c concept, the range of maximum $C_{\alpha\varepsilon}$ (or C_α) values should be in the same range. The reason for the scatter in these maxima in Figure B14*b* is due to the uncertainty associated with the calculation of σ'_p from the manual tests and the limited number of data points defining the maxima, it is likely that higher $C_{\alpha\varepsilon}$ values would be obtained if load increments fell within the initial post-yield range ($1.3 < \sigma'_{vc}/\sigma'_{p} < 1.7$). The data presented by Ervin (1992) supports his data indicating a number of maximum $C_{\alpha\varepsilon}$ data points in the range of $0.02 < C_{c\varepsilon} < 0.03$ somewhat higher than the maximum $C_{\alpha\varepsilon}$ reported here. The variation of C_c with respect to normalised stress is similar to the variation in C_α shown in Figure B14*a*; the result is a constant C_α/C_c ratio as shown in Figure B15*a*. The graphical method for calculating the C_α/C_c is shown in Figure B15*b* and *c* after Mesri et al. (1987), note that C_c is the tangential slope on the *e*-log(*p*) plot at the stress increment applied for the corresponding C_α load stage. The approach described above of fitting a cubic spline interpolation of the *e*-log(*p*) data points is again adopted to calculate the tangential slope (i.e., C_c) for the 24-hour oedometer tests.

The corresponding pairs of C_α , C_c values and $C_{\alpha\varepsilon}$, $C_{c\varepsilon}$ values are shown in Figure B16*a* and *b*, respectively. The majority of the scatter in the data is due to the data points in the vicinity of the pre consolidation stress i.e., point 2 in Figure B14*a* and Figure B15*a*. This uncertainty in assessing $C_c/C_{c\varepsilon}$ is again due to the lack of data points defining the *e*-log(σ'_{vc}) curve in this stress range as discussed previously. The ratio assessed from both the compression and modified compression indices is 0.039 with a reasonably good coefficient of determination. The typical range of

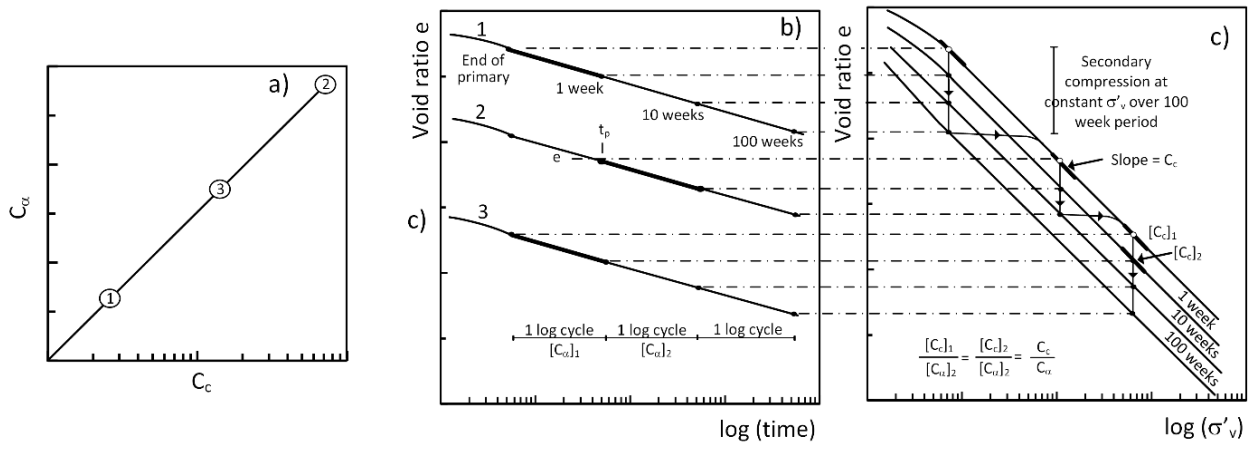

Figure B15. (a) $C_{\alpha\varepsilon}$ vs. $C_{c\varepsilon}$ linear relationship, **(b)** and **(c)** C_α/C_c concept – calculating C_α and C_c values at any (*e*, σ'_{vc}, time) during secondary consolidation after Mesri et al. (1987)

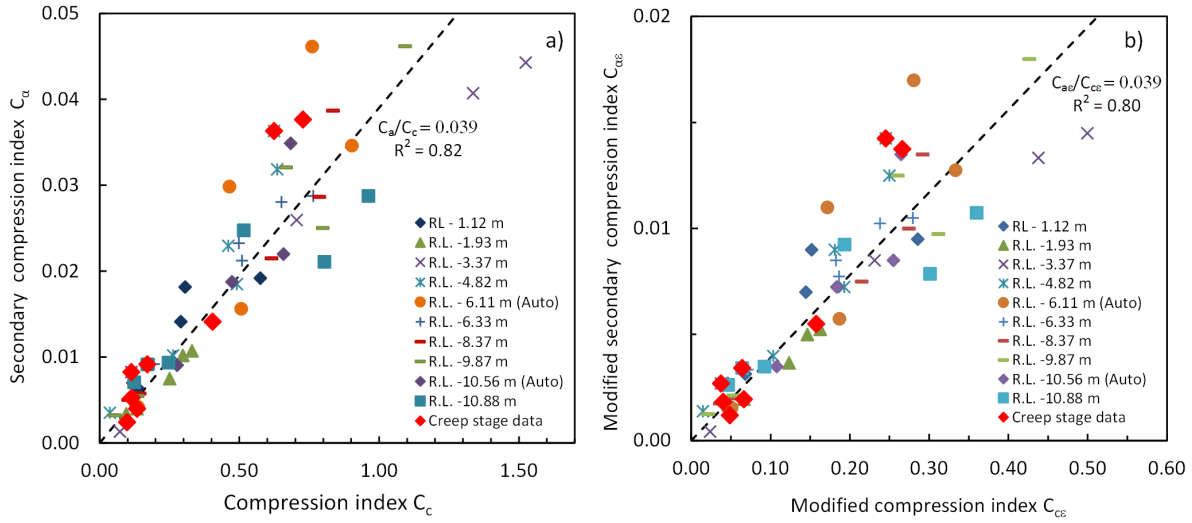

Figure B16. Oedometer test data (24-hour load increments) **(a)** C_α vs. C_c and **(b)** $C_{\alpha\varepsilon}$ vs. $C_{c\varepsilon}$

C_α/C_c values varies from 0.01 to 0.07 for all geotechnical materials (Terzaghi et al. 1996) and for inorganic soft soils is 0.04±0.01. This compares well with the value of 0.039 reported here for the Coode Island Silt samples investigated in this study which predominately comprise high plasticity inorganic clay based on Casagrande's mineralogical chart shown in Figure B1. The presence of organic content in the Coode Island Silt is well documented and it is therefore possible that locally higher values of C_α/C_c may be encountered.

B2. Coode Island Silt – field testing

B.2.1 CPT Analysis

Profiles of the corrected cone tip resistance (q_t) with depth for CPT29, CPT30 and CPT11 are shown in Figure B17*a*, *b* and *c* respectively. The value of q_t corrects for the unequal end area effect as follows:

$$q_t = q_c + u_2(1 - a) \quad \textbf{(B9)}$$

Where q_c is the cone tip resistance and a the cone area ratio which typically varies between 0.75 and 0.85 depending on cone manufacturer (equal to 0.8 for the cones used herein). This correction is typically insignificant in sands but can be significant in fine grain soils (Robertson 2009) and for this reason has been applied to these CPT profiles. The q_t profiles commence at about R.L. – 1 m as the overlying fill material was pre-drilled and are typical for tests performed in the Yarra Delta area. Addition plots of cone tip resistance q_c, friction ratio R_f, pore water pressure u, sleeve friction f_s and soil behaviour type I_c against depth for CPTs CPT28, CPT29, CPT30, CPT31, RRL-B-CPT11 and CPT1224 are presented in Appendix A2. Where the Fill units are penetrated, this interface with the upper surface of the Coode Island Silt is indicated by a considerable drop in q_c, in the authors experience this upper surface is often poorly defined. The q_t profile in CPT11 is observed to increase at a linear rate of 37 kPa/m, Ervin (1992) noted that the rate of increase of q_c (approximately the same for q_t) with depth is in the range of 30 kPa/m to 50 kPa/m based on CPT data across the Yarra Delta. CPT28 to CPT31 and CPT1224 show a rate of increase in q_c which is also in this range.

As also noted by Ervin (1992), assessment of the Coode Island Silt/Fishermens Bend Silt interface based on undrained shear strength (s_u) alone can be difficult as the increasing s_u of the Coode Island Silt with depth can approach that of the underlying Fishermens Bend Silt. For the ground improvement works, accurate assessment of Coode Island Silt/Fishermens Bend Silt interface depth was important as the columns were designed based on a minimum 2 m socket into the Fishermens Bend Silt unit. To assist with this assessment, and improve the general site characterisation, the CPTu material index (I_c) has been calculated using Equation B10 reported by Jefferies et al. (2006). The three dimensionless and normalised CPT$_u$ parameters are calculated as follow: $Q_t = (q_t - \sigma_{vo})/ \sigma'_{v0}$, $F_r = 100\% \times f_s/(q_t - \sigma_{vo})$ and $B_q = (u_2 - u_0)/(q_t - \sigma_{vo})$. Where q_t, f_s (sleeve friction) and u_2 (pore water pressure) are normalised by the total and effective vertical stress, σ_{vo} and σ'_{v0}, respectively, and the hydrostatic pore water pressure u_0. The I_c values can then be used to evaluate various soil types, referred to as soil behaviour type (SBT) zones. The relationship between I_c and SBT zones are shown in Figure B17 along with plots of the SBT zones for CPT29, CPT30 and CPT11 with depth.

$$I_c = \sqrt{\{3 - \log(Q_t[1 - B_q] + 1)\}^2 + \{1.5 + 1.3\log(F_r)\}^2} \qquad \textbf{(B10)}$$

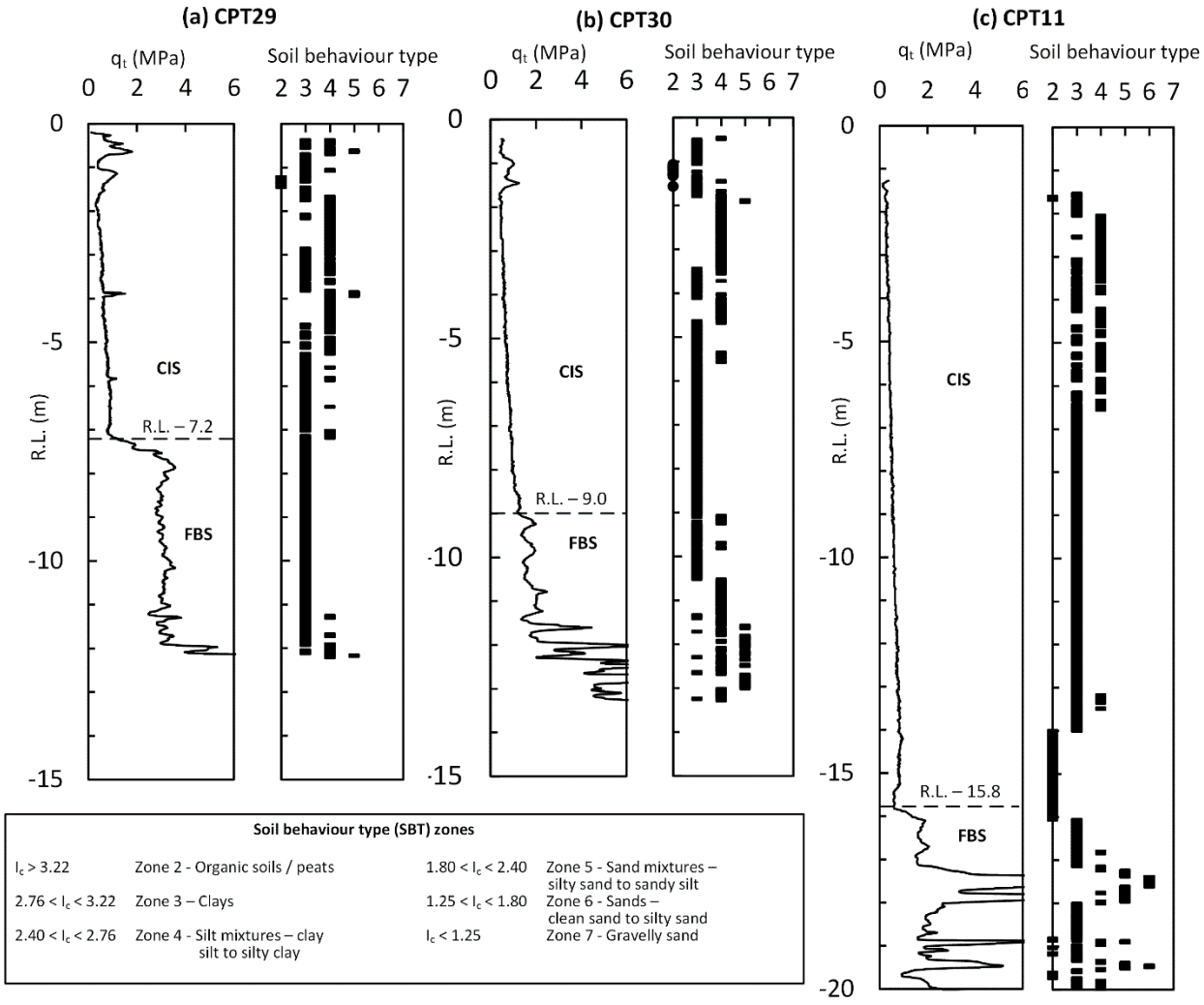

Figure B17. q_t profiles and soil behaviour type **(a)** CPT29, **(b)** CPT30, **(c)** CPT11

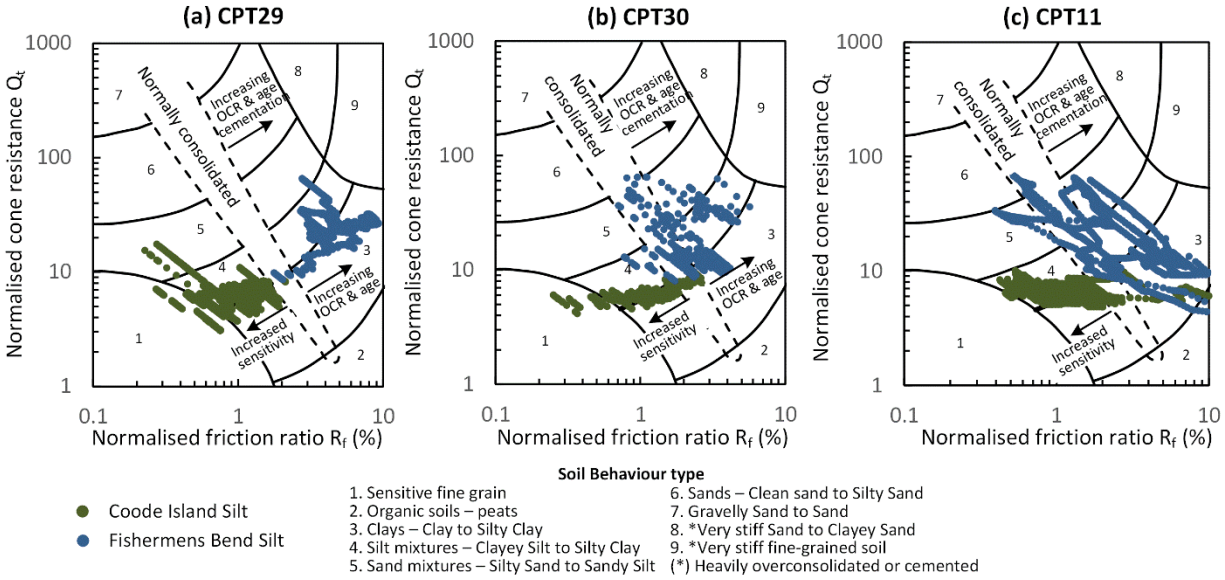

Figure B18. Soil behaviour type on Robertson (1990) and Jefferies et al. (1991) **(a)** CPT29 **(b)** CPT30 **(c)** CPT11

The Coode Island Silt is observed to vary between zone 3 (clay mixtures) and zone 4 (silt mixtures) which is inferred to represent interbedded layers and lenses of coarser material (silt and fine sand) within a predominately clayey unit. The Fishermens Bend Silt plots as a mixture of zone 4, 5 and 6 soil types. These soil behaviour types compare reasonably well with the sub-surface conditions assessed through laboratory testing and presented earlier in the chapter. An alternative means to assess the soil type is to plot Q_t vs F_r directly using the interpretation chart of Robertson (1990) as shown in Figure B18. This method provides additional information on the sensitivity and OCR/cementation of a soil type, however, the variability of soil type with depth is difficult to assess when plotted in this manner. From Figure B18 it can be seen that the Coode Island Silt plots relatively consistently between the zone 3 and 4 soil types and between the sensitive fine grain and normally consolidated regions. Banding within the Coode Island Silt markers is also evident and is consistent with fining-up or coarsening-up sedimentation sequences as described by Bishop (2010).

Whilst the Coode Island Silt may appear to be relatively uniform, subtle variation is common. This variability can take the form of sand lenses, these were assessed by Srithar (2010) for a site in the Yarra Delta based on a continuously sampled borehole, and changes in Atterberg limits over small distances as described by Ervin (1992). In general, anisotropy, soil fabric and the presence of partings, lenses and thicker layers of coarse silt, fine sand and sand can have a considerable effect on the permeability and compressibility of soft soils. Srithar (2010) describes these effects on the time rate of consolidation of Coode Island Silt based on observations from a number of sites located across the Yarra Delta. It is worth then considering the extent to which a CPTu can assess this variability, in particular the presence of interbedded layers/lenses of sand.

It is reasonably well understood that the measured cone tip resistance represents the behaviour of the soil within the CPT cone's zone of influence, which extends several cone diameters ahead of the cone tip. Based on experimental observations, Lunne et al. (1997) showed that for soft soils this zone of influence can be as small as 2 or 3 cone diameters and up to 20 diameters in stiff material. As a result, when a CPT cone passes through an interlayer boundary, rather than observing an abrupt change in q_c, a gradual increase is often registered ahead of the boundary and once the cone passes the interlayer boundary. The ability to detect a strata change is dependent on the relative stiffness between the two strata and the thickness of the layer which is being penetrated; in general, a CPT may not always measure the correct (full) cone resistance in thin interbedded layers, rather it will measure an

average of material behaviour in its' zone of influence. This can be overcome to some extent by using a correction factor to increase q_c for thin sand layers to more accurately reflect the full cone resistance.

Ahmadi et al. (2005) investigated the effects of thin interbedded layers in CPT profiles based on numerical analysis. For thin sand layers interbedded within soft clay it was found that no correction factor was required for very loose sand layers where the thickness exceeded 8 cone diameters i.e., a thickness > 0.3 m for a typical 10 cm^2 cone with diameter of 35.7 mm. For interbedded dense sand layers this minimum thickness increased to 28 cone diameters (> 1 m thickness). Ahmadi et al. (2005) recommended the lower bound correction factors suggested by Youd et al. (2001).

Based on the Coode Island Silt profile near the Swan Street bridge described by Srithar (2010), it is clear that nearly all of the interbedded sand layers encountered at that particular site would require a correction factor if they are to be properly characterised with a CPT. However, given that the majority of the sand lenses (or partings) had a thickness in the range of 5 mm to 30 mm, characterisation of these features is difficult. It is likely that they may be "detected" as subtle variations in the SBT (Figure B17) and perhaps evident as banding in the Q_t vs R_f plots (Figure B18). Therefore, if relying solely on CPT methods, characterisation of the Coode Island Silt profile to a level of detail similar to the continuous profile described by Srithar (2010) is unlikely.

B.2.2 Undrained shear strength (CPT and *in situ* shear vane)

Ervin (1992) notes that the Coode Island Silt is typically encountered in an over-consolidated state owing to either the overlying Port Melbourne Sand or a thin covering of fill where areas of marginal ground underlain by Coode Island Silt have been historically reclaimed. An undrained shear strength profile can be calculated using Equation B11, where N_k (test) is the cone factor corresponding to s_u (test). Depending on the test type which the CPT is calibrated against, the value of s_u (test) can be s_u (FV), s_u (UU), s_u (mob) etc.

$$s_u(\text{test}) = \frac{q_c - \sigma_{vo}}{N_k\,(\text{test})} \qquad \textbf{(B11)}$$

For two Coode Island Silt sites in South Melbourne (Site A, Site B) with UU and CU triaxial tests and self-boring pressuremeter tests, Ervin (1992) showed that laboratory test data (CU and UU triaxial) was well bounded by CPT s_u profiles with a cone factor of 10 and 15, with N_k of 15 generally showing a better fit (Figure B19*a*) . Note that Ervin (1992) used q_c/N_k and that an distinction between N_k (test) types was not made, this data was also originally presented against depth. The data has been converted to a R.L. based on an estimated site R.L. of + 1.5 m; direct comparison between the data is difficult owing to differences in R.L and the omission of the overburden term. The q_c/15 profile for CPT11 is also shown along with uncorrected shear vane data and agrees well with the South Melbourne sites, however, where the s_u profile is based on Equation B11, an N_k value of 11 better matches the data. In Figure B19*b* data for Webb dock is shown and again compared with CPT q_c/15 profile.

At the present case study site, the CPT s_u profile of CPT11 is correlated with field vane shear tests from a number of boreholes (Golder 1984b) in the immediate vicinity. Bjerrum (1972) empirical correction factor (μ) has been applied, where a μ value of 0.8 (I_p = 50 % for Coode Island Silt based on laboratory testing below) is adopted. The corrected undrained shear strength s_u (FV) data is shown in Figure B19*c*. A trendline through the field vane data shows excellent agreement with the CPT11 s_u profile where N_k = 15 is adopted based on Equation B11. The various CPT s_u profiles (N_k = 15) are shown in Figure B19*d* along with the historic site RL. The CPT s_u profiles show an

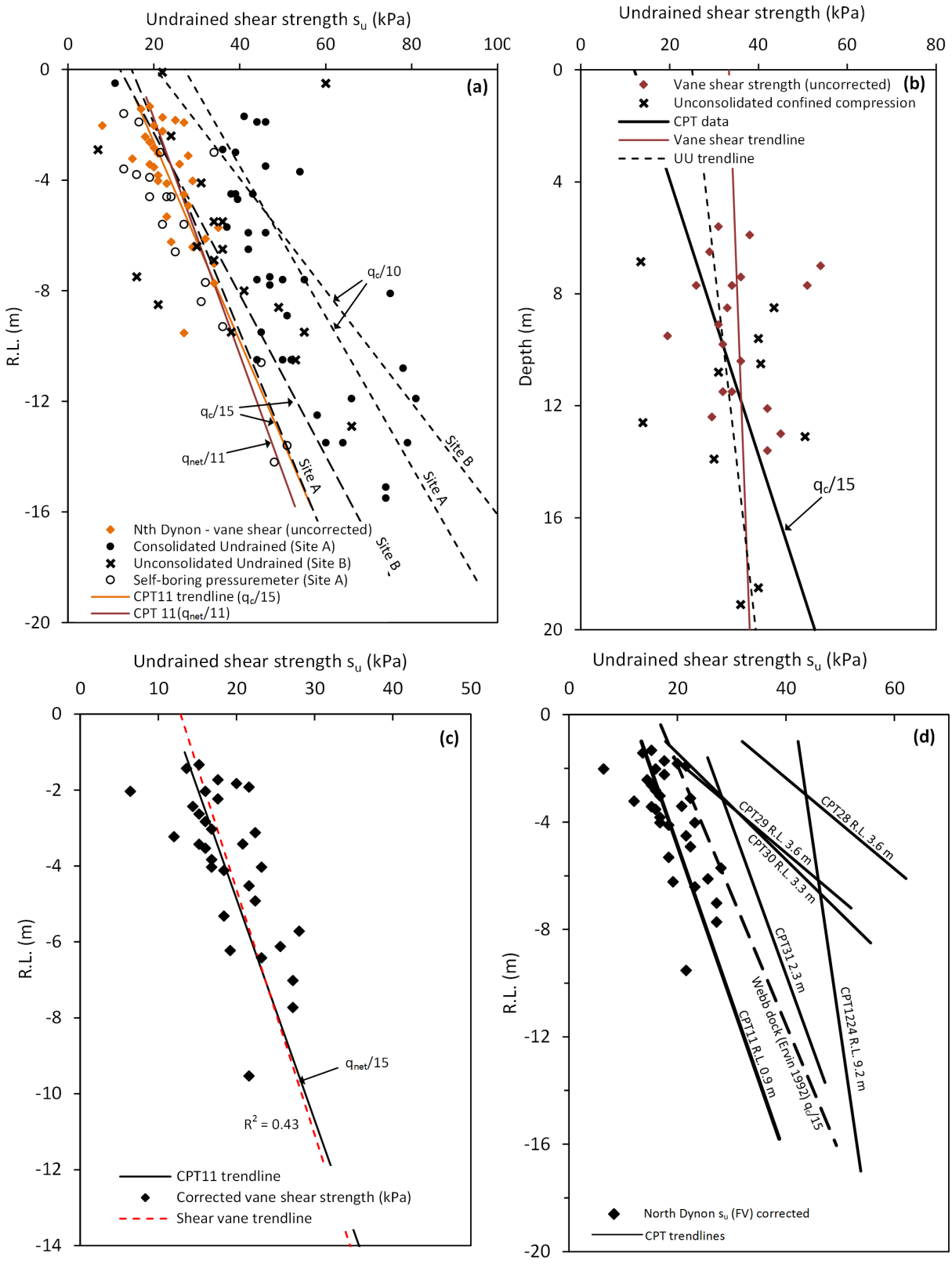

Figure B19. (a) CPT s_u profiles compared with laboratory and field s_u data from South Melbourne and North Dynon, **(b)** Laboratory and field data compared with CPT s_u profile from Webb dock, **(c)** Field vane data and CPT s_u profile from North Dynon and **(d)** North Dynon CPT s_u profiles and similar Coode Island Silt sites in South Melbourne after Ervin (1992)

increased strength profile which is generally consistent with the thickness of the overlying Fill (inferred from R.L.). This is most apparent in the undrained shear strength profile of CPT1224 (Figure B19*d*). The Coode Island Silt at

this location underlies the Historic Rail Embankment (R.L. 9.15 m) which dates back to approximately the 1920s. The effect of close to 100 years of surcharging is evident in the s_u profile.

B.2.3 In-situ dissipation tests and horizontal coefficient of consolidation

The horizontal coefficient of consolidation (c_h) has been calculated based on the results of two CPT dissipation tests performed in CPT1224 at depths of 17.01 m (R.L. – 7.9 m) and 22.94 m (R.L. – 13.79 m). This CPT was performed on the Historic Rail Embankment from an R.L. of 9.15 m. The horizontal coefficient of consolidation was calculated based on the procedure described by Lunne et al. (1997) and is summarised below:

1. The early part (less than 10 % dissipation) of the dissipation tests is plotted on an enlarged scale and the initial pore pressure (u_i) is calculated
2. Based on the ground water level the hydrostatic pore pressure (u_0) is calculated
3. Normalised excess pore pressure is plotted against log(time):

$$U = \frac{u_t - u_0}{u_i - u_0} \quad \textbf{(B12)}$$

4. The time to 50 % dissipation (t_{50}) is defined
5. The horizontal coefficient of consolidation (c_h) can be estimated from the chart from Robertson et al. (1992) based on t_{50} and rigidity index ($I_r = G/s_u$) for the Coode Island Silt taken as 200. The pore pressure reading is u_2 type.

The results are summarised in Table B2 with the normalised excess pore pressure plots presented in Figure B20. The soil behaviour type (I_c) calculated for CPT1224 indicates that dissipation test no. 2 is located within a sand layer; this explains the higher rate of excess pore pressure dissipation compared with test no. 1. The dissipation test data is presented along with laboratory vertical and horizontal coefficient of consolidation parameters and data from Day et al. (2007) and Srithar (2010) in Table B3 for comparison. As noted by Srithar (2010), comparison of field dissipation data with laboratory c_v values can be problematic owing to differences in the void ratio at which the coefficient of consolidation is assessed.

The c_v data presented shows reasonable agreement between sites, however, there is considerable variability in values of c_h. Srithar (2010) noted that the use of laboratory assessed values of c_v frequently resulted in the under-estimation of the time rate of consolidation of Coode Island Silt based on field monitoring of embankments on Coode Island Silt and it was postulated that this was caused largely by the presence of sand lenses; these often difficult to detect using common site investigation methods as described previously. Based on data from a number of sites, Srithar (2010) proposed the time rate of consolidation presented in Figure B21.

From this graph it is possible to assess combinations of c_v and maximum drainage length (H) values which provide a time rate of consolidation as shown in Figure B21, combination of values are presented in Figure B22.

Table B2. Summary of CPT dissipation tests analysis

Test no.	Depth of test (m)	R.L. (m)	u_0 (kPa)	u_i (kPa)	t_{50} (seconds)	c_h (m^2/year)
1	17.01	-7.90	71	512	12182*	2.1
2	22.94	-13.79	129	543	1381	10.5

*t_{50} calculated from extrapolation based on linear plot of u vs √t plot

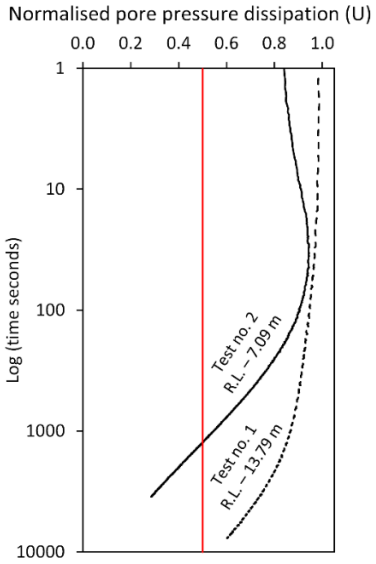

Figure B20. CPT1224 dissipation tests

Values of c_v and H in the NC range have a maximum drainage length between 0.5 m to 1.0 m. This shows good agreement with the continuously sampled borehole described by Srithar (2010) at the Swan Street bridge site where the Coode Island Silt was encountered between depths of 4.2 m and 20.8m; a total of 16 no. sand lenses were recorded with thicknesses ranging from 3 mm to 400 mm. The total thickness of the sand lenses was 935 mm (5.6 % of total thickness); the soft soil therefore has a thickness of 15.67 m (total thickness less sand lens thickness). The average thickness of the clay between sand lenses was 0.92 m.

Table B3. Typical vertical and horizontal coefficient of consolidation values

Source	Site	Parameters	Coode Island Silt (m/year)
North Dynon case study		c_v (RC)	1.3 to 3.4
		c_v (NC)	0.1 to 0.4 (see Figure B12)
		$c_{h\ field}$	2.1 to 10.5
		$c_{h\ lab}$ / $c_{v\ lab}$	0.9 to 1.7 (see Figure B13)
		$c_{h\ field}$ / c_v (RC)	0.6 to 8
Day and Wood (2007)	Moonee Ponds Creek (downstream of site)	c_v (range)	0.4 (0.2 to 1.0)
		c_h / c_v	3 to 5
		c_h (range)	1.2 to 2.0 (.6 to 5.0)
Srithar (2010)	Swan Street bridge	c_v	0.4 to 1.2
	Docklands	c_v	0.3 to 1.4
		c_h	10 to 17
		c_h / c_v (approximate)	12 to 33
	Laboratory testing (typical)	$c_{v\ lab}$	0.1 to 2
		$c_{h\ field}$ / $c_{v\ lab}$	5 to 10

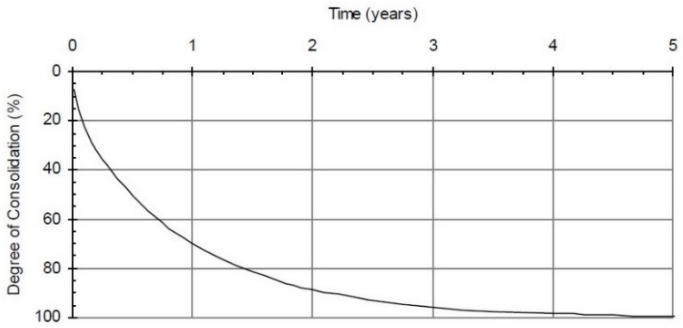

Figure B21. Time rate of consolidation for Coode Island Silt after Srithar (2010)

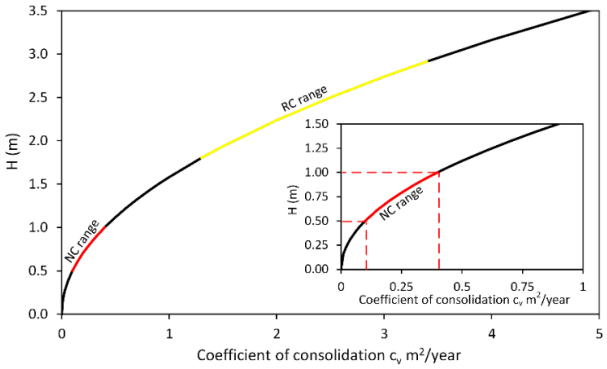

Figure B22. Value of c_v and H satisfying Srithar's time rate of consolidation expression

B.2.4 Coode Island Silt findings

The data presented here provides an overview of the compressibility and permeability characteristics of Coode Island Silt in the Moonee Ponds creek depositional zone based on laboratory and field tests. Compared with previous published literature available on Coode Island Silt, a more comprehensive description of the structured nature of the Coode Island Silt is presented, as evidenced through the S-shaped e-log(p) plot and the variation in C_c as the soil yields. This has been made possible primarily through the use of more sophisticated (automated) oedometer testing. The suggested test range described in AS1289.6.6.1 – 1998 for oedometer testing has a load increment ratio = 1.0. However, this suggested loading sequence is of limited use when characterising a soft soil due to the lack of data points in the vicinity of the pre-consolidation stress. A first order characterisation of soft soil behaviour is the best result likely, for Coode Island Silt a similar result can be achieved simply through empirical correlations with moisture content for C_c and correlations with q_c for σ'_p. Through the use of automated testing and modified testing parameters (load increment ratio and load duration) the yield point of a soft soil can be better characterised and the test completed in a shorter period of time compared with the traditional oedometer test. The automated test also avoids the need for numerous and repetitive manual readings by a laboratory technician over a period of weeks.

One shortcoming of the automated testing is not being able to assess $C_{\alpha\varepsilon}$. However, this is offset by a properly characterised compression index in the yield range; C_α can then be assessed using a C_α/C_c ratio, found here to be 0.039 for the Coode Island Silt. For settlement analysis of sites underlain by Coode Island Silt, the stress range which the Coode Island Silt is subjected to in most design scenarios is generally in the recompression to initial post yield stress range i.e., about $\sigma'_{v0} < \sigma < 2\sigma'_p$. Accurately defining the yield point of the Coode Island Silt is therefore critical to achieve an accurate estimate of settlement. With that being said, Becker's strain energy method was found to provide a more reliable characterisation of σ'_p and was also recommended by Ladd et al. (2003) as the preferred method to assess σ'_p.

The description of the structured nature of the Coode Island Silt presented here is by no means comprehensive. It is generally necessary to use large diameter samples and/or block samples of soft soils in order to preserve the soil structure (Leroueil et al. 1990). The U63 tube samples used in the current study whilst "undisturbed" would have inevitably resulted in some sample disturbance and as a result, some loss of soil structure. The recovery of undisturbed samples using the likes of a Laval sampler (200 mm diameter sample), Sherbrooke sampler (350 mm diameter sample) or large hand-carved block samples are required to preserve and fully characterise the structure of

the Coode Island Silt. The structured nature of the Coode Island Silt can also be better characterised in the laboratory through the use of constant-rate-of-strain (CRS) tests, as previously suggested by Srithar (2010), although this more advanced testing method will not eliminate sample disturbance effects.

The data presented suggests that further insight into the compressibility and permeability of Coode Island Silt can be gained through consideration of its mineralogical composition although at this point in time there is only limited data available describing the mineralogical composition of Coode Island Silt. It is the experience of the various authors that there is a reasonable amount of spatial variability in the Coode Island Silt parameters across the Yarra Delta, although this is also not well understood. Therefore, the compressibility and permeability characteristics of the Coode Island Silt assessed from this site in the Moonee Ponds Creek depositional zone may not be applicable across other areas of the Yarra Delta. It is likely that spatial variability exists and care should be taken if empirical correlations described here are to be used elsewhere.

APPENDIX C. Numerical modelling

This appendix comprises two components of numerical analysis. In Section C1 the global scale numerical analysis is presented. Some background information is first provided and then the analysis which was undertaken to assess the overburden stress at Area #2 is presented. This analysis supports the analysis and interpretation of the instrumentation data in Chapter 5.

In Section C2 the Smooth Particle Hydrodynamics numerical method is derived. The SPH code that has been implemented as part of this study was primarily developed by Dr. Ha Bui (co-supervisor). The derivation presented follows a similar course to derivations presented previously by Bui et al. (2008). Numerous modifications (improvements) have been made by Dr. Ha Bui and colleagues over the past decade to the original SPH code developed by Dr. Ha Bui in the mid-2000s. The relevant updated are described as part of the derivation.

C1. FE modelling of global embankment behaviour

The global embankment behaviour was described in Chapter 8 and 9 where a number of a complex issues relating to the use FEM numerical techniques to simulate embankment behaviour were highlighted. In addition, limitations in modelling the arching development at small scale (i.e., a single "soil arch") have been investigated and discussed in Chapter 6. These limitations are further exacerbated when modelling in three-dimensions where arching is developing at a numerous of locations within the embankment. As a result, the singularity point in plain strain is now present as a line extending around the periphery of each column head.

The key difficulties with successful numerical implementation are numerous and include; column installation, equilibration, excess porewater pressure, column cracking and arching development. Modelling each of these geotechnical mechanisms using current FEM techniques is considerably difficult, accurately modelling the combined effects in three-dimensions is not possible. In addition, modelling accurately the long term base settlement requires the use of a visco-plastic constitutive models (i.e., Soft soil creep model in PLAXIS) to simulate the initial stress conditions due to the historic embankment construction in order to describe the development of creep settlement. The use of this type of constitutive model further complicates the analysis. Work around methods are therefore required to assess these geotechnical mechanisms, as discussed at the conclusion of Chapter 9. Several approaches were used to extend this initial FEM model (presented in the following section) to describe various aspects of global embankment behaviour, with varying degrees of success. The results of this work is presented in King et al. (2017d) which was under preparation at the time of thesis submission.

C.1.1 Embankment model – overburden stress

In this section the overburden pressure is assessed in order to support the interpretation of the field data in Chapter 5, is presented. The design of the North Dynon embankment has been outlined in Section 3.2, a timeline of construction was presented in Table 3.1 and shown graphically in Figure 3.7*b* for Area #2. The overburden stress is

assessed using a two-dimensional plane strain model based on the embankment cross section for Area #2 in Figure 3.5. The construction phases modelled (12 in total) are presented in Table C1, Phase number 13 is the application of live train load and is not investigated in detail. The embankment height is shown in meters and is defined as the height of embankment above R.L. 2.0 m (base of LTP). Material parameters adopted are outlined Table C2. These are based on the site characterisation presented in Chapter 4 and summarised in Table 4.8 for the Coode Island Silt and Table 4.9 for the Fishermens Bend Silt. The LTP zone is modelled as "rigid" with high stiffness and strength values in order to avoid the development of arching and allow the calculation of overburden stresses. The embankment geometry is shown in Figure C1.

Modelling geogrid

The geogrid used for the Gabion wall in the vicinity of Area #2 was Paralink® 100 and extends 6 m behind the wall. The ultimate tensile strength (T_c) is 100 kN/m which is the machine average roll value (mean less 2 standard deviations). The mean ultimate tensile strength is taken as 110 kN/m. The partial factors for creep (RF_{creep} = 1.38), durability ($RF_{durability}$) and installation ($RF_{installation}$) have been used in Equation C1 to calculate the long term design tensile strength (T_d):

$$T_d = \frac{T_c}{RF_{installation} \cdot RF_{durability} \cdot RF_{creep}} \qquad \textbf{(C1)}$$

The multiplication of partial factors $RF_{durability} \times RF_{installation}$ is equal to 1.09. $RF_{durability}$ is taken as 1.01 (value for Paralink200 – Paralink1000 products) and $RF_{installation}$ is therefore 1.08. Similar to the modelling of the ACEGRID® in Chapter 6, the Paralink® 100 is modelled with the installation partial factor applied to the ultimate tensile strength to calculate the stiffness for the numerical analysis. The geogrid stiffness at 5 % strain ($J_{5\%}$) is 1280 kN/m.

Gabion Baskets

The gabion baskets are modelled as linear-elastic units with high stiffness to simulate a block-like response. The bulk density is calculated as $\gamma = (1 - v)\ \gamma_s$; where v (void ratio of rock fill is taken as 0.35) and γ_s is taken as 27 kN/m^3 for basalt rock. A bulk density of 17.5 kN/m^3 is calculated.

Table C1. PLAXIS construction phases

Construction phase number	Description	Embankment height (m)	R. L. (m)
0	Initial phase – gravity loading	0	2.0
1	Plastic nil step	0	2.0
2	LTP construction	0.65	2.65
3	Embankment lift no. 1	1.9	3.9
4	Embankment lift no. 2	2.65	4.65
5	Embankment lift no. 2.5	2.65	4.65
6	Upper level - batter slope cut	2.65	4.65
7	Upper level ground improvement	2.65	4.65
8	Upper level – LTP construction	2.65	4.65
9	Embankment lift no. 4	3.6	5.6
10	Embankment lift no. 5	5.6	7.6
11	Embankment lift no. 6	6.7	8.7
12	Track formation	7.0	9.0
13	Live loading	7.0	9.0

Overburden stress

In Figure C2 the vertical stress, calculated at the location of EPC #2 in Area #2, is shown as a function of phase number. Selected phases of embankment construction are shown in Figure C3*a* to *d* to illustrate the embankment construction process; the location where vertical stress is assessed is shown with a red arrow in Figure C3*d*. At the completion of embankment construction (Phase 12) the vertical stress is 74 kPa. After the upper level ground improvement (Phase 6), the subsequent increases in embankment height results in smaller increases in vertical stress.

Table C2. Material parameters for two-dimensional plain strain finite element analysis

Material Type	Model type	γ (kN/m^3)	E (MPa)	ν	c' (kPa)	ϕ' (°)	ψ (°)
Embankment fill	M-C* (Drained)	19.0	40	.25	5	28	1
Existing embankment fill	M-C (Drained)	18.5	30	.25	5	28	1
General fill	M-C (Drained)	18	10	.25	3	28	1
Rockfill (LTP)	H-S† (Drained)	20	50	.30	1	50	0
Gabion baskets	LE‡ (Non-porous)	17.5	100	.30	-	-	-
Ground improvement	LE‡ (Non-porous)	18	115	0	-	-	-

*M-C Mohr-Coulomb, ‡LE Linear elastic, †H-S Hardening soil

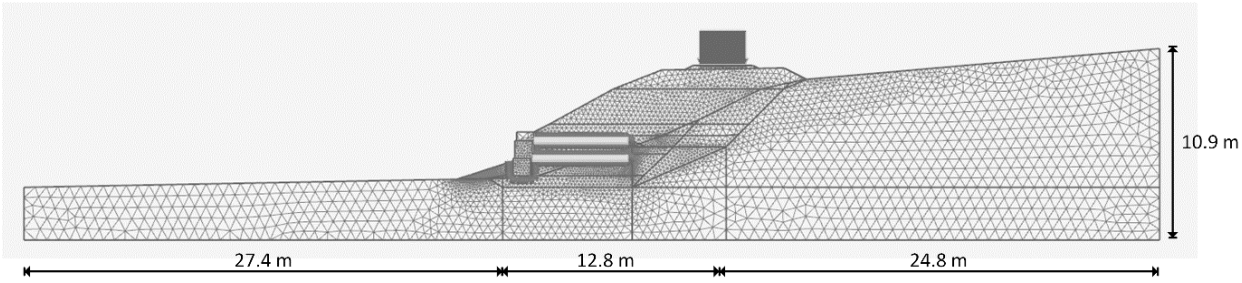

Figure C1. Embankment geometry for finite element analysis

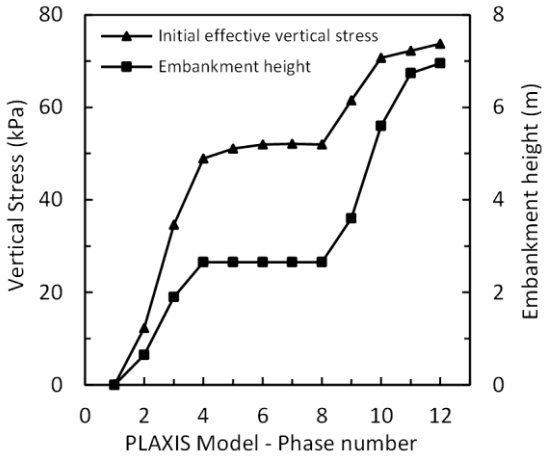

Figure C2. Vertical stress at CMC D15 versus time

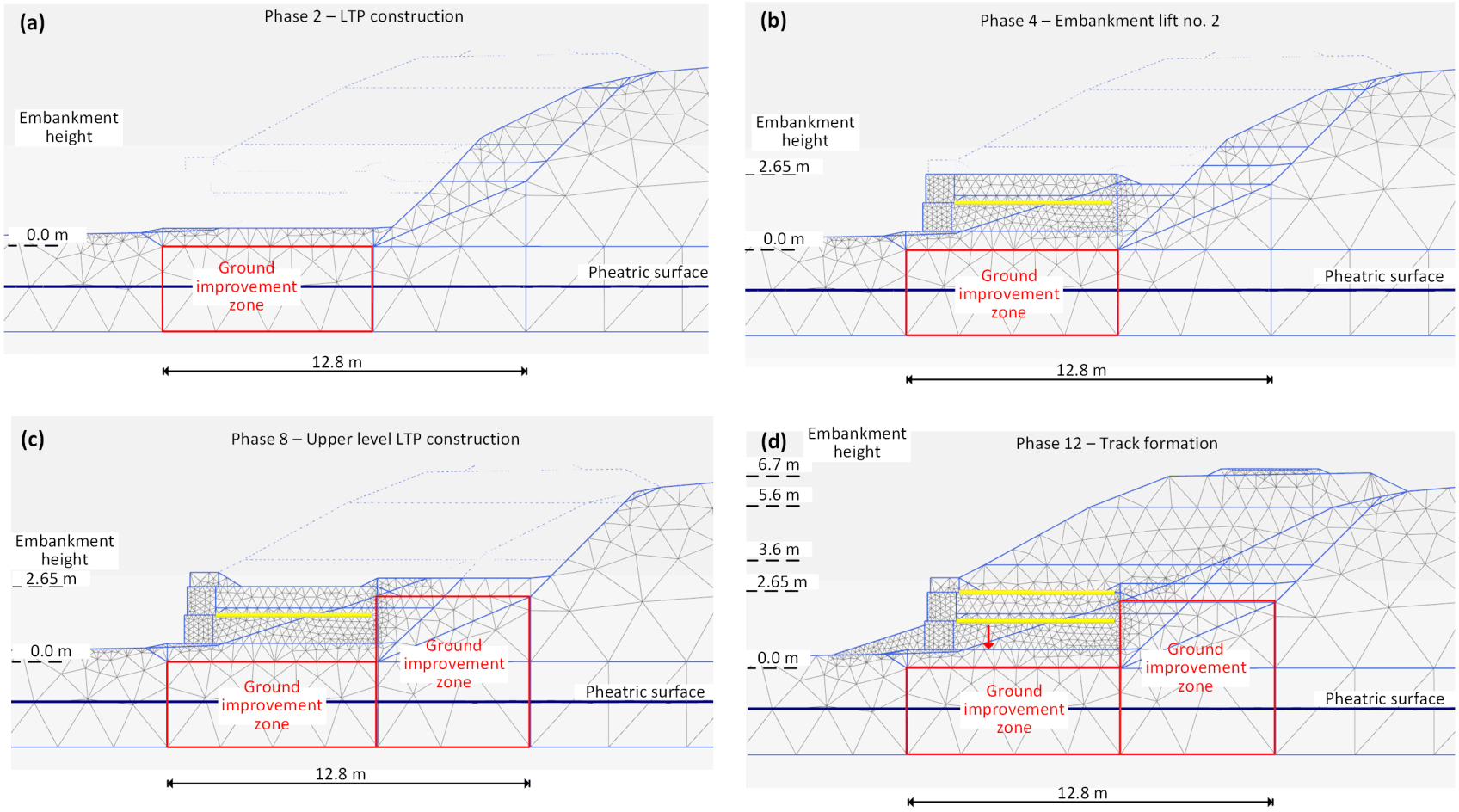

Figure C3. Selected phases of PLAXIS analysis showing embankment construction; **a)** LTP construction, **b)** Embankment lift no. 2, **c)** Upper level LTP construction and **d)** Track formation

C2. Smooth particle hydrodynamics

The derivation of the SPH framework, SPH governing equations and the soil constitutive model adopted within the SPH framework is presented below and follows a similar course to that presented in Bui et al. (2008) with relevant modifications made to the SPH code since that publication included (see for example (Bui et al. 2011, Bui and Fukagawa, 2013).

C.2.2 SPH Framework

The derivation of the kernel and particle approximation is well described in the literature which covers the SPH method (see for example (Libersky et al. 1991, Monaghan 2005, Liu 2009, Liu et al. 2010). The basic steps in the derivation are outlined below.

Kernel approximation

The field variables assigned to each particle are calculated using an interpolation process over their neighboring particles. This interpolation process is based on an integral representation of a field function f (**x**) as:

$$\langle f(\mathbf{x})\rangle = \int_{\Omega} f(\mathbf{x}')W(\mathbf{x}-\mathbf{x}',h)\,d\mathbf{x}' \qquad \textbf{(C2)}$$

Where W is the smoothing function (or kernel), Ω is the integration (problem) domain that contains ***x***, and *h* is the smoothing length which defines the influence domain of W. The adopted smoothing function must satisfy three conditions:

1) Normalisation condition (or unity condition)

$$\int_{\Omega} f(\mathbf{x}')W(\mathbf{x}-\mathbf{x}',h)\,d\mathbf{x}' = 1 \qquad \textbf{(C3)}$$

2) Delta function property

$$\lim_{h\to 0}(\mathbf{x}-\mathbf{x}',h) = \delta(\mathbf{x}-\mathbf{x}') \qquad \textbf{(C4)}$$

3) Compact support condition

$$W(\mathbf{x}-\mathbf{x}',h) = 0 \qquad when\ |\mathbf{x}-\mathbf{x}'| > \kappa h \quad \text{when} \qquad \textbf{(C5)}$$

Where κ is a constant that defines the non-zero area of the smoothing function for a point at position vector **x** (referred to as the support domain). From Equation C5, the integration domain (Ω) becomes the same as the support domain.

The choice of kernel or smoothing function is very important in an SPH formulation and has been studied extensively as it directly affects the accuracy, efficiency and stability of the numerical approach (Bui et al. 2008, Liu et al. 2010). For the SPH adopted herein, the cubic B-spline function, proposed by Monaghan et al. (1985), is adopted (see Bui et al. 2008). This is formulated as follows:

$$W_{ij} = \alpha_d \begin{cases} \frac{2}{3} - q^2 + \frac{1}{2}q^3, & 0 \le q < 1 \\ \frac{1}{6}(2-q)^3, & 1 \le q < 2 \\ 0 & q \ge 2 \end{cases} \quad \textbf{(C6)}$$

Where α_d is the normalisation parameter, which is $15/(7\pi h^2)$ for two-dimensional space and q is the normalised distance between particles i and j which is defined as $q = r/h$. The parameter k is equal to 2 for the numerical analyses presented herein and defines the support domain as shown in Figure C4.

Particle approximation

The integral representation of a field function f (**x**) (Equation C2) is discretised for N number of particles as follows:

$$\langle f(\mathbf{x}) \rangle \approx \sum_{j=1}^{N} \frac{m_j}{\rho_j} f(\mathbf{x}_j) W(\mathbf{x} - \mathbf{x_j}, h) \quad \textbf{(C7)}$$

Where j = 1, 2, …, N are particles within the support domain, as shown in Figure C4, m_j and ρ_j are mass and density respectively.

To obtain the discretised approximation of the partial derivative of a field function f (**x**), f (**x**) in Equation C2 is substituted with $\partial f(\mathbf{x})/\partial \mathbf{x}$, integrated by parts and the divergence theorem is used to obtain:

$$\langle \frac{\partial f(\mathbf{x})}{\partial \mathbf{x}} \rangle \approx \int_S f(\mathbf{x}') W(\mathbf{x} - \mathbf{x}', h) \cdot \mathbf{n}\, dS - \int_\Omega f(\mathbf{x}') \frac{W(\mathbf{x} - \mathbf{x}', h)}{\partial \mathbf{x}'} d\mathbf{x}' \quad \textbf{(C8)}$$

Where **n** is the unit normal vector to the surface S. Since the smoothing function must satisfy the compact support condition (Equation C5) the surface integral on the right hand side of Equation C8 must be equal to zero (Bui et al. 2008). The integral of the field function in Equation C8 can then be discretised using an approach similar to that adopted for the field function f (x) (Equation C7). The following discretised form of the partial derivative of a field function $\partial f(\mathbf{x})/\partial \mathbf{x}$ is obtained:

$$\langle \frac{\partial f(\mathbf{x})}{\partial \mathbf{x}} \rangle \approx -\sum_{j=1}^{N} \frac{m_j}{\rho_j} f(\mathbf{x}_j) \cdot \frac{\partial W(\mathbf{x} - \mathbf{x_j}, h)}{\partial \mathbf{x_j}} \quad \textbf{(C9)}$$

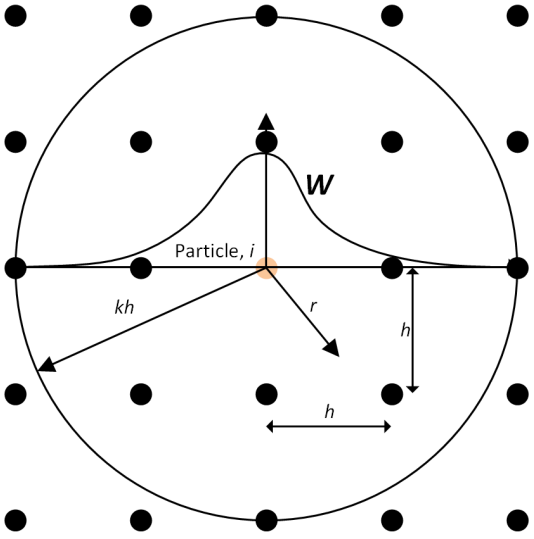

Figure C4. Example showing numerical "particles" in SPH simulation with smoothing function (W) of particle i and support domain (kh) shown.

The particle approximation of the field function f (**x**) (Equation C7) and the partial derivative of the field function ∂f (**x**)/ ∂**x** (Equation C9) can be expressed in condensed form for a particle *i*, as follows:

$$f(\mathbf{x}_i) \approx \sum_{j=1}^{N} \frac{m_j}{\rho_j} f(\mathbf{x}_j)\, W_{ij} \qquad \textbf{(C10)}$$

$$\langle \frac{\partial f(\mathbf{x})}{\partial \mathbf{x}} \rangle \approx -\sum_{j=1}^{N} \frac{m_j}{\rho_j} f(\mathbf{x}_j) \cdot \frac{W_{ij}}{\partial \mathbf{x_j}} \qquad \textbf{(C11)}$$

$$W_{ij} = W(\mathbf{x_i} - \mathbf{x_j}, h) \quad \text{and} \quad \frac{\partial W_{ij}}{\partial \mathbf{x_j}} = \left(\frac{\mathbf{x_i} - \mathbf{x_j}}{r}\right) \frac{\partial W_{ij}}{\partial r} \qquad \textbf{(C12)}$$

Where *r* is the relative distance between particles *i* and *j* and is defined as r = $|\mathbf{x}_i - \mathbf{x}_j|$. The minus sign in Equation C9 does not appear in Equation C11 as the gradient $\partial W_{ij}/\partial \mathbf{x}_i$ is taken with respect to $\mathbf{x}_i$ rather than $\mathbf{x}_j$ (Bui et al. 2008). In the following sections these discretised condensed versions of field function f (x) (Equation C10) and the partial derivative of the field function ∂f (x)/ ∂x (Equation C11) are used to discretised the soil constitutive equations as well as the equations of mass and momentum conservation.

C.2.3 Governing equations

The soil mass within a SPH framework must satisfy the governing equations of mass and momentum conservation. In continuum mechanics, the conservation mass can be expressed in a general differential form as an exact conservation law as follows (Halliday et al. 2001):

$$\frac{\partial \rho}{\partial \mathrm{t}} = -\nabla \cdot \mathbf{j} \qquad \textbf{(C13)}$$

Where ∇ is the divergence and **j** is flux, in this case the flux is mass where the flow of mass into and out of a unit volume is conserved. For mass continuity, **j** = $\rho \boldsymbol{v}$, where **v** is the velocity at each point (i.e., at the point where mass moves into and out of a unit volume). Equation C13 can be expanded as follows:

$$\frac{\partial \rho}{\partial \mathrm{t}} = -\rho \left(\frac{\partial}{\partial x}, \frac{\partial}{\partial y}, \frac{\partial}{\partial z}\right) \cdot (v_\mathrm{x}, v_\mathrm{y}, v_\mathrm{z}) = -\rho \left(\frac{\partial v_\mathrm{x}}{\partial x}, \frac{\partial v_\mathrm{y}}{\partial y}, \frac{\partial v_\mathrm{z}}{\partial z}\right) \qquad \textbf{(C14)}$$

Using Einstein summation convention (where α denotes Cartesian components *x*, *y* and *z*), the mass conservation equation can be written as follows:

$$\frac{\partial \rho}{\partial \mathrm{t}} = -\rho \frac{\partial v^\alpha}{\partial x^\alpha} \qquad \textbf{(C15)}$$

The conservation of moment equation is the Cauchy momentum equation (Acheson 1990), which describes non-relativistic momentum as follows:

$$\frac{Dv^\alpha}{Dt} = \frac{1}{\rho} \nabla \cdot \boldsymbol{\sigma} + f^\alpha \qquad \textbf{(C16)}$$

Where D/D*t* is the material derivative, $\boldsymbol{\sigma}$ is a second order tensor known as the Cauchy stress tensor and f_α is the component of acceleration due to an external force (i.e., gravity) and is denoted g_α herein. The material derivative is defined in a fixed Eulerian frame as follows:

$$\frac{D}{Dt} = \frac{\partial}{\partial t} + v^{\alpha}\frac{\partial}{\partial x^{\alpha}} \quad \textbf{(C17)}$$

Similar to the mass conservation equation (C13), the divergence of the Cauchy stress tensor can be expanded and written using Einstein summation convention (where β denotes Cartesian components x, y and z) and the resulting momentum conservation equation is as follows:

$$\frac{Dv^{\alpha}}{Dt} = \frac{1}{\rho}\frac{\partial \sigma^{\alpha\beta}}{\partial x^{\alpha}} + g^{\alpha} \quad \textbf{(C18)}$$

Where the Cauchy stress tensor ($\boldsymbol{\sigma}$), or $\sigma^{\alpha\beta}$ where written using Einstein summation convention, is a total stress tensor as follows (Chen et al. 1985):

$$\sigma^{\alpha\beta} = \begin{bmatrix} \sigma_{xx} & \sigma_{xy} & \sigma_{xz} \\ \sigma_{yx} & \sigma_{yy} & \sigma_{yz} \\ \sigma_{zx} & \sigma_{zy} & \sigma_{zz} \end{bmatrix} \equiv \begin{bmatrix} \sigma_{x} & \tau_{xy} & \tau_{xz} \\ \tau_{yx} & \sigma_{y} & \tau_{yz} \\ \tau_{zx} & \tau_{zy} & \sigma_{z} \end{bmatrix} \quad \textbf{(C19)}$$

The total stress tensor ($\sigma^{\alpha\beta}$) requires a constitutive equation. Where SPH is applied to computational fluid dynamics it is common to express $\sigma^{\alpha\beta}$ in two parts; isotropic hydrostatic pressure p and deviatoric shear stress s (Bui et al. 2008):

$$\sigma^{\alpha\beta} = -p\delta^{\alpha\beta} + s^{\alpha\beta} \quad \textbf{(C20)}$$

Where $\delta^{\alpha\beta}$ is Kronecker's delta, $\delta^{\alpha\beta} = 1$ if $\alpha = \beta$ and $\delta^{\alpha\beta} = 0$ if $\alpha \neq \beta$ (Kreyszig 2010). In contrast to SPH models for fluids, and other SPH applications applied to solids, where ρ is calculated from an equation of state, Bui et al. (2008) proposed calculating the hydrostatic pressure directly form the soil constitutive equations using the standard definition of mean stress:

$$p = -\frac{1}{3}(\sigma_{\mathrm{x}} + \sigma_{\mathrm{y}} + \sigma_{\mathrm{z}}) \quad \textbf{(C21)}$$

This approach is also adopted in the present study. In this study compressive stress is defined as negative.

Discretisation of mass continuity equation

Combining Equation C15 and C17, the mass conservation equation can be written as follows:

$$\frac{\mathrm{D}\rho}{\mathrm{D}t} = -\left(\frac{\partial}{\partial x^{\alpha}}(\rho v^{\alpha}) - v^{\alpha}\cdot\frac{\partial \rho}{\partial x^{\alpha}}\right) \quad \textbf{(C22)}$$

This form of the mass conservation equation can be approximated by replacing the two gradient terms on the right hand side of Equation C22 with the SPH particle approximation equations derived above for the partial derivative of the field function $\partial f(\mathbf{x})/\partial \mathbf{x}$ (Equation C9). If the velocity term in the last term of Equation C22 is evaluated, the following is obtained:

$$\frac{\mathrm{D}\rho_i}{\mathrm{D}t} = -\sum_{j=1}^{N} m_j\,(v_i^{\alpha} - v_j^{\alpha})\cdot\frac{W_{ij}}{\partial x_i^{\alpha}} \quad \textbf{(C23)}$$

Discretisation of momentum equation

The term on the right hand side of the momentum conservation equation can be written as follows:

$$\frac{1}{\rho}\frac{\partial \sigma^{\alpha\beta}}{\partial x^{\alpha}} = \frac{\partial}{\partial x^{\beta}}\left(\frac{\sigma^{\alpha\beta}}{\rho}\right) + \frac{\sigma^{\alpha\beta}}{\rho^2}\frac{\partial \rho}{\partial x^{\beta}} \quad \textbf{(C24)}$$

Using the same approach as used above for the mass conservation equation the following expression is obtained:

$$\frac{\mathrm{D}v_i^{\alpha}}{\mathrm{D}t} = -\sum_{j=1}^{N} m_j \left(\frac{\sigma_i^{\alpha\beta}}{\rho_i^2} + \frac{\sigma_j^{\alpha\beta}}{\rho_j^2}\right)\frac{W_{ij}}{\partial x^{\beta}} + g^{\alpha} \quad \textbf{(C25)}$$

C.2.4 Soil constitutive model

The SPH method developed herein adopts an elastic-perfectly plastic model with a Drucker-Prager yield criterion to describe the yield surface. The total strain rate tensor is defined as follows:

$$\dot{\epsilon}^{\alpha\beta} = \frac{1}{2}\left(\frac{\partial v^{\alpha}}{\partial x^{\beta}} + \frac{\partial v^{\beta}}{\partial x^{\alpha}}\right) \quad \textbf{(C26)}$$

For an elastic-perfectly plastic material the total strain rate is written in terms of elastic strain rate ($\dot{\varepsilon}_e^{\alpha\beta}$) and plastic strain rate ($\dot{\varepsilon}_p^{\alpha\beta}$) components:

$$\dot{\epsilon}^{\alpha\beta} = \dot{\varepsilon}_e^{\alpha\beta} + \dot{\varepsilon}_p^{\alpha\beta} \quad \textbf{(C27)}$$

Generalised Hooke's law is used to describe the elastic strain rate tensor ($\dot{\varepsilon}_e^{\alpha\beta}$):

$$\dot{\varepsilon}_e^{\alpha\beta} = \frac{\dot{s}^{\alpha\beta}}{2G} + \frac{1-2\nu}{3E}\dot{\sigma}^{\gamma\gamma}\delta^{\alpha\beta} \quad \textbf{(C28)}$$

Where $\dot{s}^{\alpha\beta}$ is the deviatoric shear stress rate tensor, ν is Poisson's ratio, E is Young's modulus, G is the shear modulus and $\dot{\sigma}^{\gamma\gamma}$ is the sum of the three normal stress components (i.e., $\dot{\sigma}^{\gamma\gamma} = \dot{\sigma}^{xx} + \dot{\sigma}^{yy} + \dot{\sigma}^{zz}$). The plastic strain rate tensor ($\dot{\varepsilon}_p^{\alpha\beta}$) is computed using the plastic flow rule:

$$\dot{\varepsilon}_p^{\alpha\beta} = \dot{\lambda}\frac{\partial g}{\partial \sigma^{\alpha\beta}} \quad \textbf{(C29)}$$

Where $\dot{\lambda}$ is the rate of change of the plastic multiplier (λ), g is the plastic potential function which describes the direction which plastic strain develops. Both an associated and non-associated flow rule can be incorporated with the later used in the models presented herein. The plastic multiplier λ has to satisfy the following yield conditions for a yield function f:

- $\lambda = 0$ when $f < 0$ or $f = 0$ and $\mathrm{d}f < 0$ for elastic and plastic unloading
- $\lambda > 0$ when $f = 0$ and $\mathrm{d}f = 0$ for plastic loading

To ensure that the stress states that develop on the yield surface remain on the yield surface, a consistency conditions is employed ($\mathrm{d}f = \frac{\partial f}{\partial \sigma^{\alpha\beta}} d\sigma^{\alpha\beta} = 0$). This assures that a new stress state will satisfy the following yield criterion:

$$f\left(\sigma^{\alpha\beta} + \mathrm{d}\sigma^{\alpha\beta}\right) = f\left(\sigma^{\alpha\beta}\right) + \mathrm{d}f = f(\sigma^{\alpha\beta}) \quad \textbf{(C30)}$$

Substituting Equations C28 and C29 into the equation for total strain rate (Equation C27), the following is obtained:

$$\dot{\epsilon}^{\alpha\beta} = \frac{\dot{s}^{\alpha\beta}}{2G} + \frac{1-2\nu}{3E}\dot{\sigma}^{\gamma\gamma}\delta^{\alpha\beta} + \dot{\lambda}\frac{\partial g}{\partial \sigma^{\alpha\beta}} \quad \textbf{(C31)}$$

By combining the equation for the total stress tensor (Equation C20) with Equation C21) ($\sigma^{\alpha\beta} = s^{\alpha\beta} - \frac{1}{3}\dot{\varepsilon}^{\gamma\gamma}\delta^{\alpha\beta}$) and substituting in Equation C31, then rearranging, the following expression for the stress-strain relationship for an elastic-perfectly plastic material is obtained:

$$\dot{\sigma}^{\alpha\beta} = 2G\dot{e}^{\alpha\beta} + K\dot{\varepsilon}^{\gamma\gamma}\delta^{\alpha\beta} - \dot{\lambda}\left[\left(K - \frac{2G}{3}\right)\frac{\partial g}{\partial \sigma^{mn}}\delta^{mn}\delta^{\alpha\beta} + 2G\frac{\partial g}{\partial \sigma^{\alpha\beta}}\right] \quad \textbf{(C32)}$$

Where α and β are free indices and m and n are dummy indices, K is the bulk modulus, which is related to G and ν as follows:

$$K = \frac{E}{3(1-2\nu)} \quad \text{and} \quad G = \frac{E}{2(1+\nu)} \quad \textbf{(C33)}$$

The deviatoric shear strain rate tensor ($\dot{e}^{\alpha\beta}$) is defined as follows:

$$\dot{e}^{\alpha\beta} = \dot{\varepsilon}^{\alpha\beta} - \frac{1}{3}\dot{e}^{\gamma\gamma}\delta^{\alpha\beta} \quad \textbf{(C34)}$$

By substituting the general stress-strain relationship (Equation C32) into the consistency criterion (Equation C30) the equation for rate of change of the plastic multiplier ($\dot{\lambda}$) for an elastic-perfectly plastic material can be obtained:

$$\dot{\lambda} = \frac{2G\dot{\varepsilon}^{\alpha\beta}\frac{\partial f}{\partial \sigma^{\alpha\beta}} + \left(K - \frac{2G}{3}\right)\dot{\varepsilon}^{\gamma\gamma}\frac{\partial f}{\partial \sigma^{\alpha\beta}}\delta^{\alpha\beta}}{2G\frac{\partial f}{\partial \sigma^{mn}}\frac{\partial g}{\partial \sigma^{mn}} + \left(K - \frac{2G}{3}\right)\frac{\partial f}{\partial \sigma^{mn}}\delta^{mn}\frac{\partial g}{\partial \sigma^{mn}}\delta^{mn}} \quad \textbf{(C35)}$$

Drucker-Prager model

The Drucker-Prager yield criterion is defined by Drucker et al. (1952) as follows:

$$\sqrt{J_2} = \mathrm{A} + \mathrm{B}\, I_1 \quad \textbf{(C36)}$$

Where A, B are material constants, I_1 is the first stress invariant of the Cauchy stress tensor and J_2 is the second deviatoric stress invariant. These are defined as follows (Yu 2007):

$$I_1 = \sigma_{xx} + \sigma_{yy} + \sigma_{zz} \quad \text{and} \quad J_2 = \frac{1}{2}s^{\alpha\beta}s^{\alpha\beta} \quad \textbf{(C37)}$$

Where using a Drucker-Prager yield criterion the yield function *f* is written as follows:

$$f(I_1, J_2) = 0 = \sqrt{J_2} + \alpha_\phi I_1 - k_c \quad \textbf{(C38)}$$

Where material constants A, B are replaced with the Drucker-Prager constants k_c and α_ϕ as shown in Figure C5*a*. The constants k_c and α_ϕ can be related to the Mohr-Coulomb material constants *c* (cohesion) and ϕ (internal friction)

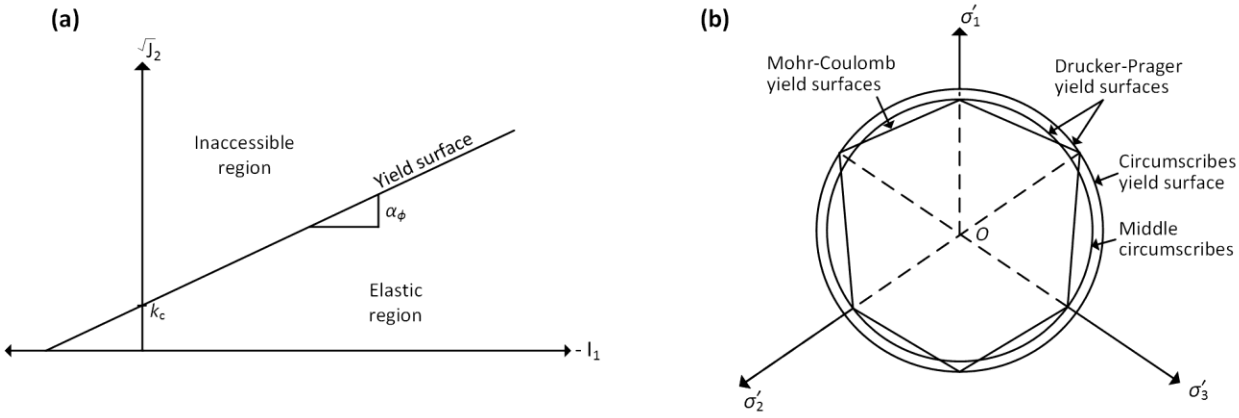

Figure C5. Drucker-Prager yield criterion; **(a)** – I_1, $\sqrt{J_2}$ space and **(b)** π-plane ($\sigma_1 + \sigma_2 + \sigma_3 = 0$) (after Bui et al. 2008)

in various ways. Two examples are shown in Figure C5, in one example the Drucker-Prager yield criterion circumscribes the Mohr-Coulomb yield surface in the second it middle circumscribes the Mohr-Coulomb yield surface. An alternative approach is to match the yield surface so that they give identical collapse loads in plane-strain conditions (Drucker et al. 1952). This approach is adopted herein and the constants k_c and α_ϕ are defined as follows:

$$\alpha_\phi = \frac{\tan\phi}{\sqrt{9 + 12\tan^2\phi}} \quad \text{and} \quad k_c = \frac{3c}{\sqrt{9 + 12\tan^2\phi}} \tag{C39}$$

To describe the plastic potential function, both an associated and non-associated flow rule are developed by Bui et al. (2008). Only the non-associated plastic flow rule case is presented herein. This has the form:

$$g = \sqrt{J_2} + 3I_1 \sin\psi \tag{C40}$$

Where ψ is the dilatancy angle. By substituting the equation for the non-associated plastic flow rule into the stress-strain relationship for an elastic-perfectly plastic soil (Equation C32) and the equation for the rate of change of plastic multiplier ($\dot{\lambda}$) then the following equation is obtained (a detailed derivation is presented in Bui et al. 2008):

$$\dot{\sigma}^{\alpha\beta} = 2G\dot{e}^{\alpha\beta} + K\dot{\varepsilon}^{\gamma\gamma}\delta^{\alpha\beta} - \dot{\lambda}\left[9K\sin\psi\,\delta^{\alpha\beta} + \frac{G}{\sqrt{J_2}}s^{\alpha\beta}\right] \tag{C41}$$

With the plastic multiplier ($\dot{\lambda}$) expressed as follows:

$$\dot{\lambda} = \frac{3\alpha_\phi K\dot{\varepsilon}^{\gamma\gamma} + \left(\frac{G}{\sqrt{J_2}}\right)s^{\alpha\beta}\dot{\varepsilon}^{\alpha\beta}}{27\alpha_\phi K\sin\psi + G} \tag{C42}$$

Within the SPH framework adopted for the models in Chapter 6 Equations C41 and C42 are solved directly using an updated Lagrangian formulation rather than building a stiffness matrix as is done in a FEM simulation. For large displacement problems it is necessary to employ a stress rate that is invariant with respect to rigid body motion for the constitutive equations. Bui et al. (2008) adopts the Jaumann stress rate ($\mathring{\dot{\sigma}}^{\alpha\beta}$):

$$\dot{\sigma}^{\alpha\beta} = \dot{\sigma}^{\alpha\beta} - \sigma^{\alpha\gamma}\dot{\omega}^{\beta\gamma} - \sigma^{\gamma\beta}\dot{\omega}^{\alpha\gamma} \tag{C43}$$

Where $\dot{\omega}$ is the spin rate tensor defined as:

$$\dot{\omega}^{\alpha\beta} = \frac{1}{2}\left(\frac{\partial v^{\alpha}}{\partial x^{\beta}} - \frac{\partial v^{\beta}}{\partial x^{\alpha}}\right) \tag{C44}$$

The final form of the stress-strain relationship with a non-associated plastic flow rule is as follows:

$$\dot{\sigma}^{\alpha\beta} - \sigma^{\alpha\gamma}\dot{\omega}^{\beta\gamma} - \sigma^{\gamma\beta}\dot{\omega}^{\alpha\gamma} = 2G\dot{e}^{\alpha\beta} + K\dot{\varepsilon}^{\gamma\gamma}\delta^{\alpha\beta} - \dot{\lambda}\left[9K\sin\psi\,\delta^{\alpha\beta} + \frac{G}{\sqrt{J_2}}s^{\alpha\beta}\right] \tag{C45}$$

Discretisation of the soil constitutive equations

In order to solve Equation C45 the equations must be discretised into the SPH framework for every particle and then interpolated using the updated Lagrangian formulation. Use the discretised equations for the field function f (x) (Equation C10) and the partial derivative of the field function ∂f (x)/ ∂x (Equation C11) the stress-strain relationship with a non-associated plastic flow rule (Equation C41) can be discretised as follows:

$$\frac{\mathrm{D}\sigma_i^{\alpha\beta}}{\mathrm{D}t} = \sigma_i^{\alpha\gamma}\dot{\omega}_i^{\beta\gamma} - \sigma_i^{\gamma\beta}\dot{\omega}_i^{\alpha\gamma} + 2G\dot{e}_i^{\alpha\beta} + K\dot{\varepsilon}_i^{\gamma\gamma}\delta_i^{\alpha\beta} - \dot{\lambda}_\iota\left[9K\sin\psi\,\delta^{\alpha\beta} + \frac{G}{\sqrt{J_2}}s_i^{\alpha\beta}\right] \tag{C46}$$

With the rate of change of the plastic multiplier ($\dot{\lambda}$) for a non-associated plastic flow rule expressed as follows:

$$\dot{\lambda} = \frac{3\alpha_\phi K\dot{\varepsilon}^{\gamma\gamma} + \left(\frac{G}{\sqrt{J_2}}\right)s_i^{\alpha\beta}\dot{\varepsilon}_i^{\alpha\beta}}{27\alpha_\phi K\sin\psi + G} \tag{C47}$$

It is also necessary to discretise the strain rate tensor (Equation C26) and the spin rate tensor (Equation C44), these are written as follows:

$$\dot{\epsilon}^{\alpha\beta} = \frac{1}{2}\left(\frac{\partial v^{\alpha}}{\partial x^{\beta}} + \frac{\partial v^{\beta}}{\partial x^{\alpha}}\right) = \frac{1}{2}\left[\sum_{j=1}^{N}\frac{m_j}{\rho_j}\left(v_j^{\alpha} - v_i^{\alpha}\right)\cdot\frac{\partial W_{ij}}{\partial x_i^{\beta}} + \sum_{j=1}^{N}\frac{m_j}{\rho_j}\left(v_j^{\beta} - v_i^{\beta}\right)\cdot\frac{\partial W_{ij}}{\partial x_i^{\alpha}}\right] \tag{C48}$$

$$\dot{\omega}^{\alpha\beta} = \frac{1}{2}\left(\frac{\partial v^{\alpha}}{\partial x^{\beta}} - \frac{\partial v^{\beta}}{\partial x^{\alpha}}\right) = \frac{1}{2}\left[\sum_{j=1}^{N}\frac{m_j}{\rho_j}\left(v_j^{\alpha} - v_i^{\alpha}\right)\cdot\frac{\partial W_{ij}}{\partial x_i^{\beta}} + \sum_{j=1}^{N}\frac{m_j}{\rho_j}\left(v_j^{\beta} - v_i^{\beta}\right)\cdot\frac{\partial W_{ij}}{\partial x_i^{\alpha}}\right] \tag{C49}$$

C.2.5 Other aspects of numerical implementations

In the following section, a few numerical topics specific to the SPH method are briefly discussed. These numerical issues have been studies extensively by Dr. Bui (see Bui et al. 2008).

Artificial viscosity

During the implementation of the SPH method large unphysical oscillations in the numerical solutions have been observed. These occur where there is a “shock” to the system, these are most often are problem during the initial stages where initial stress conditions are generated. A dissipative term Π_{ij} is included in the momentum equation (Equation C25) to dampen out these oscillations as follows:

$$\frac{\mathrm{D}v_i^\alpha}{\mathrm{D}t} = -\sum_{j=1}^{N} m_j \left(\frac{\sigma_i^{\alpha\beta}}{\rho_i^2} + \frac{\sigma_j^{\alpha\beta}}{\rho_j^2} + \Pi_{ij}\delta^{\alpha\beta} \right) \frac{W_{ij}}{\partial x^\beta} + g^\alpha \qquad \textbf{(C50)}$$

$$\text{where} \quad \Pi_{ij} = \begin{cases} \dfrac{-\alpha_\Pi c_{ij}\phi_{ij} + \beta_\Pi \phi^2}{\rho_{ij}}, & v_{ij}\cdot x_{ij} < 0 \\ 0, & v_{ij}\cdot x_{ij} \geq 0 \end{cases} \qquad \textbf{(C51)}$$

$$\phi_{ij} = \frac{h_{ij} v_{ij}\cdot x_{ij}}{|x_{ij}|^2 + 0.01h_{ij}^2}, \quad c_{ij} = \frac{c_i + c_j}{2}, \quad \rho_{ij} = \frac{\rho_i + \rho_j}{2}$$
$$h_{ij} = \frac{1}{2}(h_i + h_j), \quad x_{ij} = x_i + x_j, \quad v_{ij} = v_i + v_j \qquad \textbf{(C52)}$$

In Equation C51 α_Π and β_Π are constants both equal to 0.1 and c is the speed of sound (i.e., a primary wave) in the soil mass. For the present study, *c* is taken as 600 m/s. While the use of large values of α_Π can introduce shear viscosity into the flow of granular material (i.e., dissipation of energy) the small values used herein mean that this effect is minor. Similarly, Bui et al. (2008) has shown that the second term β_Π has a very small effect on the simulation due to the speed of *c* adopted.

Tensile instability

One particular problem which is encountered in SPH simulations is the unphysical "clumping" of numerical particles. This instability is termed "*tensile instability*" and was first studied by Swegle et al. (1995). Numerous techniques which have been employed to address this issue, the approach described by Monaghan (2000) and Gray et al. (2001) is adopted by Bui et al. (2008) and this essentially involves introducing a small repulsive force to prevent particles becoming too close together. To do this, Equation C50 is modified as follows:

$$\frac{\mathrm{D}v_i^\alpha}{\mathrm{D}t} = -\sum_{j=1}^{N} m_j \left(\frac{\sigma_i^{\alpha\beta}}{\rho_i^2} + \frac{\sigma_j^{\alpha\beta}}{\rho_j^2} + \Pi_{ij}\delta^{\alpha\beta} + f_{ij}^n (R_i^{\alpha\beta} + R_j^{\alpha\beta}) \right) \frac{W_{ij}}{\partial x^\beta} + g^\alpha \qquad \textbf{(C53)}$$

Where *n* is exponent of the repulsive force term f_{ij}, defined in terms of the smoothing function as follows:

$$f_{ij}^n = \frac{W_{ij}}{W(\Delta d, h)} \qquad \textbf{(C54)}$$

Where Δd is the initial particle spacing and as the smoothing length is also constant the term W(Δd, h) is also constant. For this study *n* is equal to 2.55.

For the two-dimensional problems considered herein the artificial stress tensor $R_i^{\alpha\beta}$ is calculated from prinicipal stress components $R_i'^{xx}$ and $R_i'^{yy}$ as follows:

$$R_i^{xx} = R_i'^{xx}\cos^2\theta_i + R_i'^{yy}\sin^2\theta_i \qquad \textbf{(C55)}$$

$$R_i^{yy} = R_i'^{xx}\sin^2\theta_i + R_i'^{xx}\cos^2\theta_i \qquad \textbf{(C56)}$$

$$R_i^{xy} = (R_i'^{xx} - R_i'^{yy})\sin\theta_i\cos\theta_i \qquad \textbf{(C57)}$$

Where the angle θ_i is defined as follows:

$$\tan 2\theta_i = \frac{2\sigma_i^{xy}}{\sigma_i^{xx} - \sigma_i^{yy}} \quad \textbf{(C58)}$$

The principal stress component $R_i'^{xx}$ forms one of two diagonal components of the artificial stress tensor defined in principle stress space x' and y'. $R_i'^{xx}$ is calculated as follows:

$$R_i'^{xx} = \begin{cases} -\varepsilon \dfrac{\sigma_i'^{xx}}{\rho_i^2} & \text{if } \sigma_i'^{xx} > 0 \\ 0 & \text{otherwise} \end{cases} \quad \textbf{(C59)}$$

Gray et al. (2001) noted that the constant ε = 0.3 is the best value for an elastic solid. The other diagonal principal stress component $R_i'^{yy}$ is calculated using the same approach as Equation C59, however, the superscripts *xx* are replaced with subscripts *yy*.

Time integration

There are a variety of numerical methods which can be used to numerically integrate ordinary differential equations. Here the Leap-Frog algorithm is used to integrate the discrete SPH equations. The velocity, density, stress tensor and position are updated as follows:

$$\rho_{n+1/2} = \rho_{n-1/2} + \Delta t \left(\frac{\mathrm{D}\rho}{\mathrm{D}t}\right)_n \quad \textbf{(C60)}$$

$$\upsilon_{n+1/2} = \upsilon_{n-1/2} + \Delta t \left(\frac{\mathrm{D}\upsilon}{\mathrm{D}t}\right)_n \quad \textbf{(C61)}$$

$$\sigma_{n+1/2}^{\alpha\beta} = \sigma_{n-1/2}^{\alpha\beta} + \Delta t \left(\frac{\mathrm{D}\sigma^{\alpha\beta}}{\mathrm{D}t}\right)_n \quad \textbf{(C62)}$$

$$x_{n+1/2} = x_n + \Delta t \upsilon_{n+1/2} \quad \textbf{(C63)}$$

To solve the discrete SPH equations in ordinary differential form the Courant-Freidrich-Lewy condition (Courant et al. 1928) is imposed in order to ensure convergence. This condition requires the time step to be less than a critical time step Δ*t*, the Courant-Freidrich-Lewy condition is as follows:

$$\Delta t \leq C_{\mathrm{cour}} \left(\frac{h}{c}\right) \quad \textbf{(C64)}$$

Where C_{cour} is the Courant coefficient takes as equal to 0.2, and as noted above, c = 600 m/s for the simulations presented herein.

APPENDIX D. Rockfill behaviour

D1. Material behaviour of granular material

Before investigating the material behaviour of rockfill it is necessary to first describe some of the fundamental mechanism relating to the behaviour of granular soil (sand, gravel and rockfill). When a granular material undergoes shear, particle movement does not occur entirely in the primary direction of shearing. For granular material, shearing is also accompanied by particles pushing and particle rearrangement as well as particles moving/climbing up and over other particles within the vicinity of the shearing surface (Terzaghi et al. 1996). As noted by Lee et al. (1967) the measured shear strength of a granular material comprises four components: sliding friction (ϕ_μ) ± dilation (ψ) + particle rearranging + particle crushing. The angle of interparticle sliding friction (ϕ_μ) is a function of the roughness, texture and hardness and ranges from 20° to 40°, more commonly it is between 25° to 35° (Terzaghi et al. 1996).

To understand the behaviour of granular material the concept of the critical state is important. When a granular material is sheared to a sufficiently large displacement, on-going shearing continues with zero volume change. This critical state condition is characterised by a unique ratio $\tau/\sigma' = \tan(\sigma'_{\text{crit}})$ and comprises the components of sliding friction and particle rearrangement which is generally in the range of 5° to 6° (Terzaghi et al. 1996). Whether this state critical state is achieved, in laboratory and field applications, following volumetric expansion or compression depends largely on the initial density of the granular material and the confining pressure.

The mobilised friction angle can therefore be described as follows:

$$\phi' = \phi'_{\text{crit}} + \psi \qquad \textbf{(D1)}$$

The author has previously recommended using granular material of large aggregate size (for example 20 mm base course material, or larger) to enhance the development of arching in GRCSE. It is shown in subsequent sections that the low confining pressure typically found at the base of the embankment coupled with a relatively densely packed granular material is conducive for maximising the contribution of the dilative component in the friction angle,

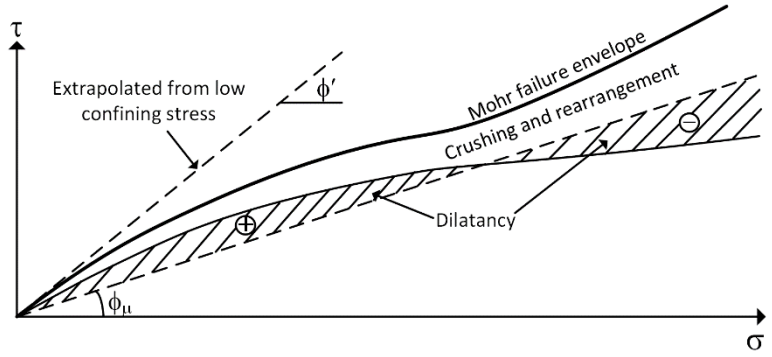

Figure D1. Components of Mohr failure envelope for a granular soil (after Lee et al. (1967)

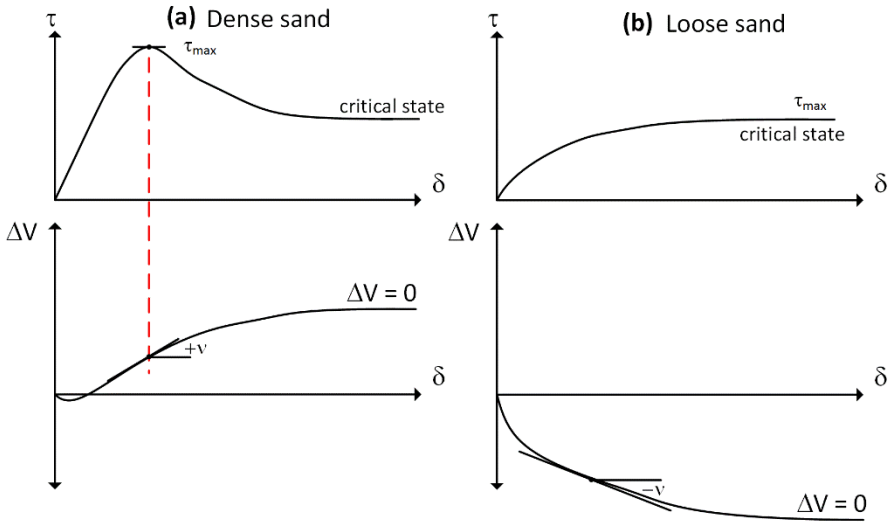

Figure D2. Shear and volume change in direct shear test **(a)** dense **(b)** loose sand after Holtz et al. (2010)

resulting in a large mobilised friction angle (ϕ_{mob}). It follows then, that in many cases, accurate assessment of ψ will be important in order to fully describe the development of arching in the LTP.

D2. Shear strength of rockfill

Much of the information on the rockfill material behaviour arose out of a need to understand better the behaviour of rockfill dams. As with the testing of soils, the triaxial cell has been the most common method to assess the mechanical properties of rockfill material. However, the large particle sizes associated with rockfill material generally leads to significant difficulties in testing the rockfill. Marachi (1969), for example, suggested a minimum triaxial cell diameter equal to 6 × D_{max} (450 mm diameter triaxial cell for the 75 mm minus rockfill in consideration here). No surprisingly then, due to a lack of large scale triaxial cells, the availability of data on the mechanical behaviour of rockfill lagged behind that of soil data.

In 1970, Leps (1970) described (to the authors knowledge) just 10 large scale triaxial cells which had been developed and were in use in the western hemisphere at the time. The results of large scale triaxial tests by Leps (1970), and a significant number of additional tests, were summarised by Douglas (2003) who investigated the various factors affecting the shear strength of rockfill (Figure D3). A clear trend of increasing shear strength with reducing normal (confining) pressure is shown. Although the significant influence that confining pressure has on

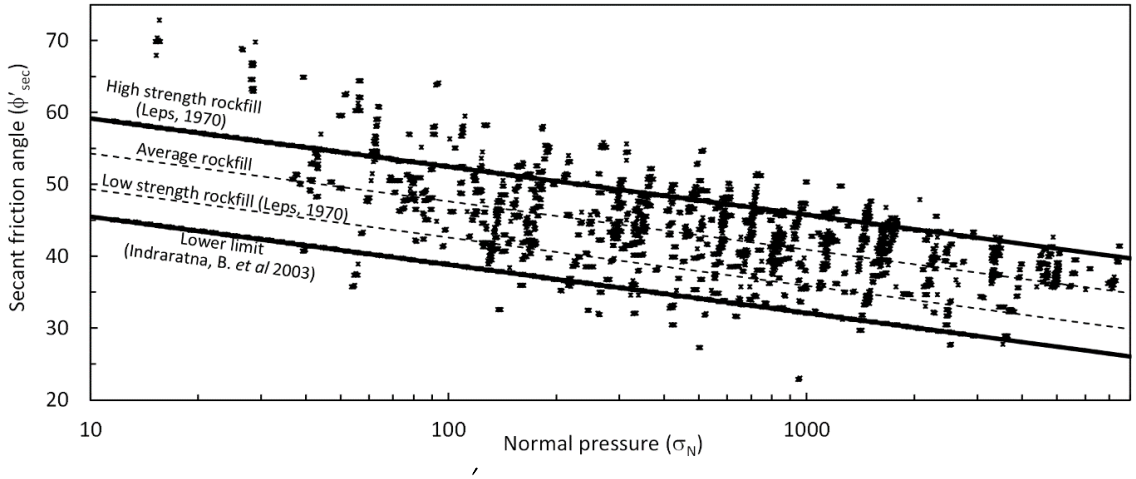

Figure D3. Secant friction angle ($\boldsymbol{\phi'_{sec}}$) with normal stress ($\boldsymbol{\sigma_N}$) – modified from Douglas (2003)

shear strength is highlighted in this data, a number of other factors are not, namely: effects of relative density, gradation, crushing strength, particle shape and degree of saturation (Leps 1970). The influencing effect of these factors and other is described by Fell et al. (2005) and reproduced in Table D1. This is based largely on the work of Marsal (1973) and Douglas (2003).

It was shown previously in Figure D2 that the initial density of a granular material has a considerable effect on the stress-strain response, with dense sand showing a pronounced peak in shear strength followed by softening behaviour. Confining pressure can also affect the response of a granular material when subjected to shear. Triaxial compression test data from Marachi et al. (1972), and reproduced by Terzaghi et al. (1996), is shown in Figure D4. below. Where the dense rockfill shears under high confining pressure (σ'_3 = 4485 kPa) it shows only a minor peak in shear strength, compresses as it undergoes shear, and shows an overall stress-strain response similar to loose granular material (Figure D2*b*). This response illustrates that dilatant behaviour is stress-dependent and demonstrate how the volumetric response can be suppressed under high confining pressure. The difference in response is due largely to the increased prevalence of particle breakage at high confining pressures. For the dense rockfill in Figure D4, the major principal (axial) stress acting on the triaxial sample is in the order of 18 MPa at peak shear strength, compared with about 1.6 MPa for the sample sheared at the lower confining pressure. The increased prevalence of particle breakage for rockfill tested under high confining pressures leads to a general reduction in the peak shear strength of rockfill with increasing confining pressure.

Table D1. Factors affecting the shear strength of rockfill (Fell et al. 2005)

Rockfill variable	**Effect on shear strength**	**Importance in present case study**	**References**
Confining pressure	The secant friction angle (ϕ_{sec}) reduces with increasing confining pressures. As a result, the Mohr-Coulomb shear strength envelope is curved. This is discussed further below.	Significant – see Figure D2. (Douglas 2003)	Leps (1970), Fannin et al. (2005), Douglas (2003), Charles et al. (1980) and Marsal (1973)
Density or void ratio	Shear strength increases with increased density (lower value of void ratio, e). This effect is more significant at low confining pressure, little effect at high confining pressure	Medium to minor – see Figure D2	Douglas (2003), and Marsal (1973)
Unconfined compressive strength of the rock	Shear strength increases with increasing rock strength for UCS below 100 MPa, little effect for rocks stronger than 100 MPa. Marsal (1973) showed that mineralogy is responsible for grain strength, the crushing strength and breakage index is high dependent on mineralogy.	Minor (at low confining pressure) to medium (at high confining pressure)	Douglas (2003)
Uniformity coefficient	Uniformly graded rockfill exhibits more curvature in the M-C strength envelope than well graded rockfill. Douglas (2003) however noted that there was no clear effect on shear strength.	Minor	Douglas (2003)
Maximum particle size	Generally accepted that shear strength decreases with particle size (Chui, Douglas (2003), some claim no effect (Charles et al. 1980), some claim the opposite.	Minor	Douglas (2003) and Marsal (1973)
Finer particles content	Shear strength reduced significantly with more than 30 – 50 % silty or clayey sand passing 2 mm size sieve (USBR)	Medium	Douglas (2003)
Particle angularity	Angular particles have higher shear strength than sub-angular and rounded particles at low confining pressures, little difference at high confining pressures due to particle breakage.	Some influence at low confining pressure, Minor at high confining pressure	Douglas (2003)

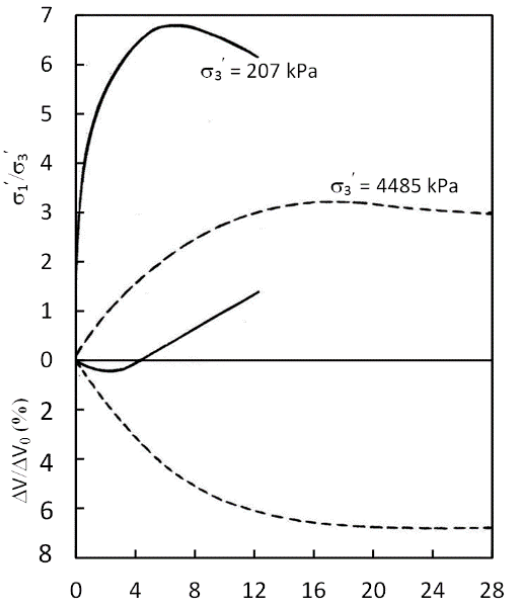

Figure D4. Stress-strain and volumetric response for triaxial test on dense rockfill (from Terzaghi et al. 1996)

The breakage index B_g can be used to quantify the amount of particles breakage under load. The breakage factor is assessed by comparing the particle size distribution curve of a rockfill before and after testing. Where breakage occurs, a decrease in the number of particles retained in the larger sieves is expected, a corresponding increase in particles retained in the smaller sized sieves likewise occurs. The sum of the percentage increase (or decrease) is the breakage factor, B_g, expressed as a percentage (Lowe 1964).

In addition to the effects of confining pressure on shear strength. It has also been shown that an increasing particle size has the effect of also reducing the shear strength when all other factors remain the same. The so-called "*size effect*". Frossard et al. (2012) developed a method for the evaluation of the shear strength of granular material, with incorporated size effects, by applying concepts of fracture mechanics to the behaviour of quasi-brittle material. Frossard et al. (2012) demonstrated that, statistically, the "*size effect*" can be expressed as a reduction in intrinsic strength with increasing sample size and noted that this behaviour must be due to the increased presence (statistically) of micro cracks in larger sized particles, which under loading conditions, grow and interconnect to form a macrocrack failure. This has important implications when using the parallel gradation techniques described below and where test results on medium sized rockfill are extrapolated to predict the shear strength behaviour of larger sized rockfill of the type used in dams.

The "parallel gradation technique" described by Lowe (1964) uses samples of rockfill with laboratory gradings which plot parallel to the field grading on a semi-logarithmic particle size distribution graph. Based on principles of similitude it is postulated that similar behaviour can be achieved providing the following four conditions are satisfied:

1) Similar particle size distribution,
2) Comparable field and laboratory compaction
3) Similar particle angularity
4) Simple sample size ratios

With the exception of particle angularity, these conditions can generally be achieved when using the parallel gradation technique. Ensuring consistent particle angularity between field and laboratory gradings can be difficult as the angularity can vary between different size grains in a rockfill sample (Indraratna et al. 1993). The particle

breakage factor is shown to increase with increasing confining pressure in Figure D5 (Varadarajan et al. 2003). In addition, the size effect is demonstrated with a higher breakage factor for samples with a larger d_{max} value. The particle breakage at confining pressures of less than about 200 kPa is negligible. The slightly higher breakage factor of the Ranjit Sagar rockfill compared with the Purulia rockfill, at low confining stresses, can be attributed to the poorer quality material which comprises the Ranjit Sagar rockfill (lower values of aggregate impact value, aggregate crushing value and Los Angeles abrasion value).

Indraratna et al. (1993) performed large-scale triaxial tests on greywacke rockfill as part of construction for several dams in Thailand, including the Chiew Larn dam. Triaxial tests were performed on samples at confining pressures between 100 kPa and 600 kPa. A considerable reduction in d_{50} was noted at high confining pressures, however, when confining pressures were below 200 kPa the degree of grain crushing was insignificant (Indraratna et al. 1993). These findings suggest that the Rockfill unit, which comprises Granodiorite with a UCS > 100 MPa, will have negligible particle breakage when tested at low confining pressures.

Based on the work of Marsal (1973), Saboya Jr et al. (1993) noted that more angular rockfill material was, statistically, likely to have fewer interparticle contact points. A corresponding increase in interparticle contact forces is expected to lead to an increased breakage factor, at higher confining pressures and a reduction in shear strength. The Ranjit Sagar and Purulia rockfill in Figure D5 are described as a rounded/subrounded sedimentary alluvium and angular/subangular blasted metamorphic rock respectively. Despite the Purulia rockfill having a higher intrinsic strength the rockfill exhibits a greater increase in breakage factor with increasing confining pressure. It is likely that angularity of the Purulia rockfill is a contributing factor which is causing the increased breakage factor at higher confining pressures.

Based on the discussion above, and assuming the rockfill is comprised of reasonable intrinsic strength, it can be concluded that rockfill behaviour in the context of LTP design at low confining pressures will exhibit the following characteristics:

- A negligible (or very low) breakage factor.
- Due to the negligible breakage factor, the size effect at these low confining pressure is not expected to affect the scaling of rockfill when the using the “parallel gradation technique”.
- Increased particle angularity, at low confining pressure, is further expected to increase shear strength (Douglas 2003).

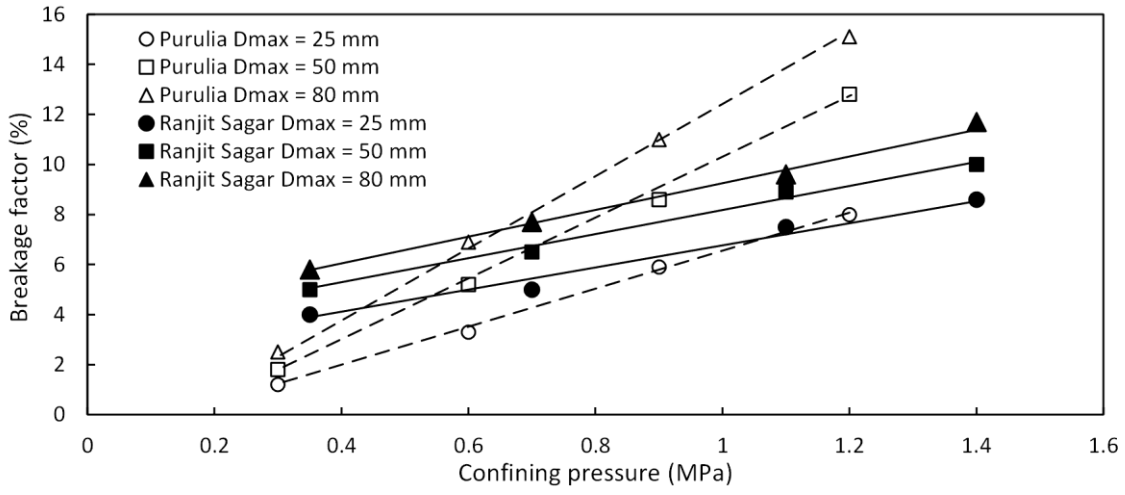

Figure D5. Variation of breakage factor with confining pressure from Varadarajan et al. (2003)

While it has been noted that increasing maximum particle size results in a reduced shear strength, this observation is largely derived from, and relates to, test data from large size rockfill (>100 mm D_{max}). In general, rockfill will exhibit a higher friction angle than gravel, and gravel in turn, will exhibit a higher friction angle than sand. This arises because the principles of similitude do not generally hold for naturally occurring granular materials, the angularity, mineralogy, surface roughness and void ratio/relative density vary. For this reason, it is generally desirable to adopt a rockfill material, which will typically exhibit a high friction angle, in the LTP design to enhance the development of arching. The potential benefits offered through the use of rockfill need to be considered relative to the potential detrimental effects arising due to increased damage to the GR layer during installation.

D.2.1 Curvature of the failure envelope

The following empirical relationship was developed by Charles et al. (1980) to describe the curved shear stress failure envelope which describes rockfill shear strength:

$$\tau = A(\sigma')^b \quad \textbf{(D2)}$$

The relationship (Figure D6) is shown for a range of rockfill types based on triaxial test data described by Charles et al. (1980), the failure envelope for the North Dynon Rockfill is also indicated. This result is described in further detail below. Douglas (2003) described the following relationship to relate φ'_{sec} with σ_n based on a non-linear least squares regression analysis of the data in Figure D3:

$$\phi'_{\text{sec}} = a + b\sigma_n'^c \quad \textbf{(D3)}$$

Where

a = 36.43 – 0.267ANG – 0.172FINES + .756(C_c - 2) + 0.0459(UCS – 150)

b = 69.51 + 10.27ANG + 0.549FINES – 5.105(C_c -2) – 0.408(UCS – 150) – 0.408

c = -0.3974

$$C_C \text{ coefficient of curvature} = \frac{d_{30}^2}{d_{10}d_{60}}$$

ANG = (angularity rating – 5) for angularity rating > 5.5; otherwise = 0

FINES = percentage of fines passing 0.075 mm (%)

UCS = unconfined compressive strength of intact rock (MPa)

Angularity rating is a subjective value ranging from 0 to 8

1 – 2 Rounded

2 – 3 Sub-rounded

5 – 6 Sub-angular

7 – 8 Angular

For the North Dynon Rockfill unit the following values are assessed:

Example based on North Dynon rockfill (see Section 3.2.1 for material properties)

D_{10} = 0.1 mm, D_{30} = 2.0 mm, D_{60} = 14 mm and C_c = 2.86

Angularity rating = 6, ANG = 1

FINES = 5

UCS = 150 MPa (assumed for Fresh Granodiorite)

$$\phi'_{\text{sec}} = 35.95 + \frac{77.73}{\sigma'^{.3974}_{\text{n}}} \qquad \textbf{(D4)}$$

This is compared with laboratory test data below (Figure D6).

D.2.2 Strain softening behaviour

Some data showing rockfill behaviour that is denser than that used in the field case study is shown in Figure D7. (after Charles and Watts, 1980) . The deviatoric and volumetric response against axial strain is presented for the four rockfill materials shown in Figure D7. at a confining pressure (σ'_3) of 100 kN/m^2. Note that these four rockfill samples were heavily compacted which is not the case for the field case study rockfill which was only subjected to light compaction. With the exception of the B2 rockfill, which could be reasonable rejected on the grounds that its' intrinsic strength is not representative of a good quality engineering rockfill (Charles et al. 1980), all the of the rockfill samples show a peak in shear strength followed by significant post-peak strain softening. Whilst this strain softening behaviour is not expected to be as pronounced (the rockfill is not heavily compacted) for the North Dynon rockfill it is expected to be considerable. This has important implications when undertaking numerical analysis of the trapdoor test and arching development in a GRCSE. This is discussed further in the Chapter 6.

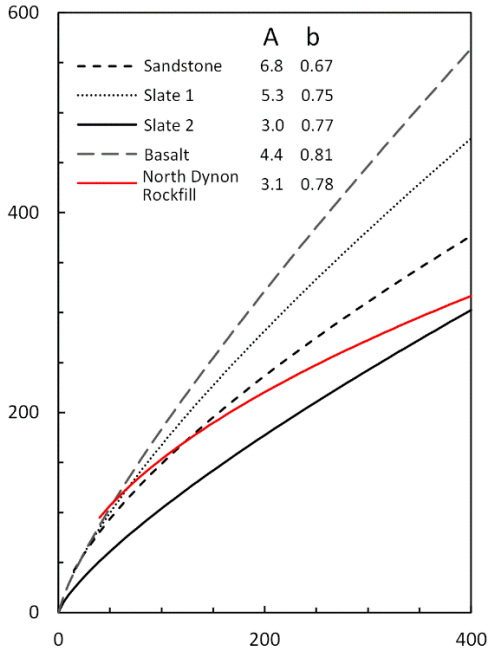

Figure D6. Curved failure enveloped for rockfill described by Charles et al. (1980)

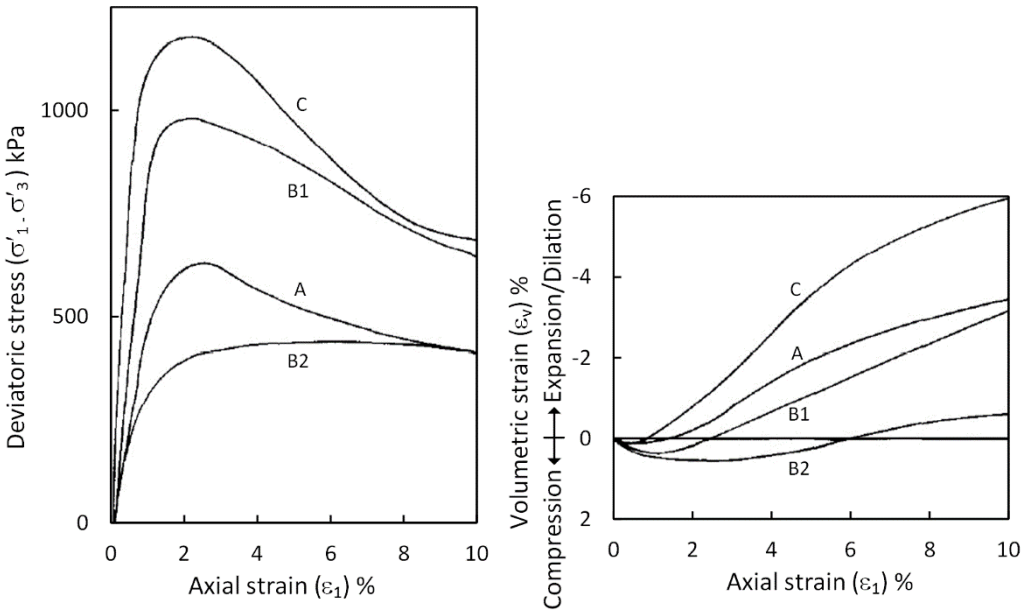

Figure D7. Drained triaxial tests on heavily compacted rockfill (σ'_3 = 100kPa) (Charles et al. 1980)

D3. Laboratory testing of Rockfill

Due to difficulties finding a suitable sized direct shear box test apparatus owing to the large particle size of the rockfill, the parallel gradation technique originally developed by Lowe (1964) has been used to assess the shear strength properties of the Rockfill unit. The Particle-size distribution for the 75 mm minus rockfill (typical curve) and for the scaled 26 mm minus rockfill tested is shown in Figure D8.

The direct shear tests were performed on the scaled rockfill using the Monash University's Constant Normal Stiffness direct shear apparatus (Haberfield et al. 2003)(Figure D9.). This test equipment was developed primarily for testing of the interface strength of rock-socketed piles. The tests performed on the Rockfill were all performed under constant normal load. The shear box used has a plan area of 600 mm by 200 mm and a height of 135 mm which was reduced with spacers to 100 mm for this test.

The Rockfill was compacted in the shear box in about 40 mm layers and the dry density was calculated to be 18.7 kN/m^3. Compaction was done in non-planar layers, above and below the shear plane, to avoid having a planar compaction boundary between layers at the shear plane. The *in situ* Rockfill did not have a target density, this was to

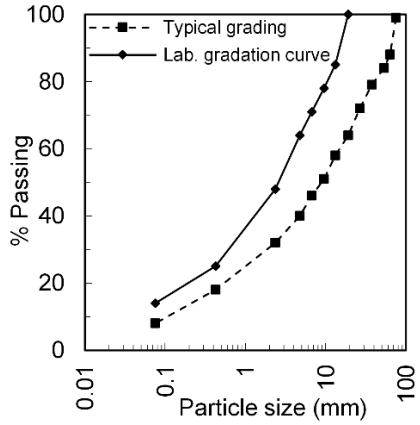

Figure D8. Parallel graduation technique applied to 75 minus rockfill

Figure D9. Large scale direct shear apparatus (from Haberfield et al. 2003)

avoid damaging the geogrid layers. However, the *in situ* Rockfill was subjected to compaction. The bottom 100 mm of rockfill was lightly compacted before placing the geogrid layers. Light compaction was applied after placing about 300 mm of rockfill over the upper longitudinal geogrid layer and further compaction was provided to achieve the 650 mm thickness of rockfill specified for the load transfer platform. The laboratory dry density of 89 % of modified proctor compaction is considered to approximate the field conditions.

Samples were tested at confining pressures of 50 kPa, 100 kPa and 200 kPa, results are shown in Figure D10*a*, *b* and *c* respectively. Values of ϕ'_{sec} of 51°, 49° and 44°, and dilation angles 14°, 14° and 11° were measured at confining pressures of 50 kPa, 100 kPa and 200 kPa respectively. From Equation D2, values of A and b equal to 3.10 and 0.78 were found to provide the best fit through the data using linear regression analysis and was also shown in Figure D10. The relationship suggested by Douglas (2003) in Equation D4 is also plotted and shows a good fit through the two tests at confining pressures of 50 kPa and 100 kPa. The Rockfill failure envelope developed from the laboratory data under predicts the relationship described by Douglas (2003) at stresses greater than 200 kPa and also under predicts the rockfill failure envelope of other rockfill materials in Figure D3 at higher stresses. This behaviour at higher confining pressures may be due to the well graded nature and angular nature of the Rockfill unit, or due to the results of the direct shear tests at 200 kPa, the reason for this is not clear. Regardless, the friction angle and dilation angle derived over the stress range of interest (50 kPa to 100 kPa) appears reasonable.

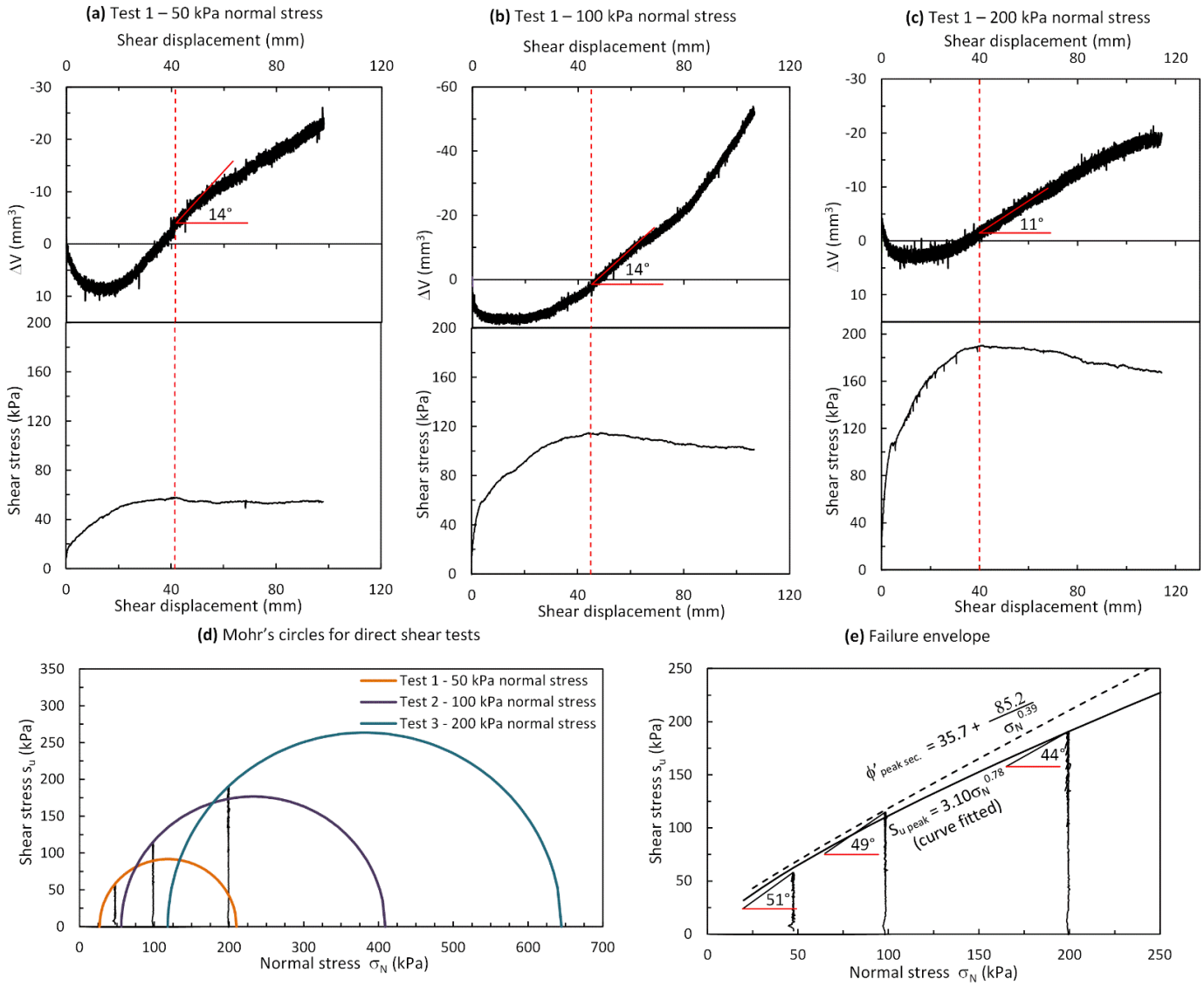

Figure D10. Direct shear tests results; **(a)** 50 kPa normal stress, **(b)** 100 kPa normal stress, **(c)** 200 kPa normal stress, **(d)** Mohr circles and **(e)** failure envelope

APPENDIX E. Assessment of column capacity and bending moments

E1. Assessment of applied load on columns supporting the GRCSE

The installed columns were designed for a working load of 700 kN based on a minimum 2 m pile socket into the underlying Fishermens Bend Silt founding unit. In general loads acting on the columns are significantly lower than the design working load. In Area #2 for example, the working load is approximately 380 kN assuming full load transfer by the load transfer platform (which is predicted to occur in the year 2028 based on the analysis presented in Chapter 5). The largest working loads occur at the eastern end of the embankment, beneath the gabion wall where it is highest. The additional load due to negative skin friction is also considered below.

Negative skin friction

There was considerable debate during design phases as to whether or not assessment of skin friction is required when assessing the working loads of the ground improvement elements. Based on the analysis presented in Chapter 5 it is assumed here that the end bearing columns will have additional load caused by ongoing creep settlement of the Coode Island Silt relative to the rigid columns. The negative downdrag force is calculated (Equation E1 and Figure E1*a*) using the method described by Poulos (2008) and is plotted against the base R.L. of the Coode Island Silt (Figure E1*b*).

$$F_{nf} = \mathrm{C} f_n L \qquad \textbf{(E1)}$$

Where $f_n = K_0(1 - \sin\phi)\tan(\gamma)\,\sigma_{v(average)}$

$f_n \approx 0.3\sigma_{v(average)}$ for Coode Island Silt

C = Circumference of column

L = Length of downdrag zone. Taken as 75 % of the Coode Island Silt thickness (shown in red in Figure E1.)

Based on this assessment, additional pile load due to negative skin friction is 92 kN for columns in Area #2 (base of Coode Island Silt at R.L. − 8.5 m) and 196 kN for columns in Area #1 (base of Coode Island Silt at R.L. − 13.5 m). For the columns at Area #2 this increases the working loads by about 25 % to a total load of 472 kN.

E2. Assessment of capacity of columns supporting the GRCSE

Three different methods are used to assess the column capacity of the two tests columns, E11 and C27, which were installed offset 10.5 m from CPT30 and offset 3.2 m from CPT29 respectively. The test columns are described in more detail in the next section where the dynamic testing is assessed. The inferred load distribution acting on the columns for serviceability limit state based on method of Poulos (2008) is shown for column E11 and C27 in Figure E2*b* and *d*. The ultimate capacity is derived from the full shaft capacity. The working load and negative skin friction

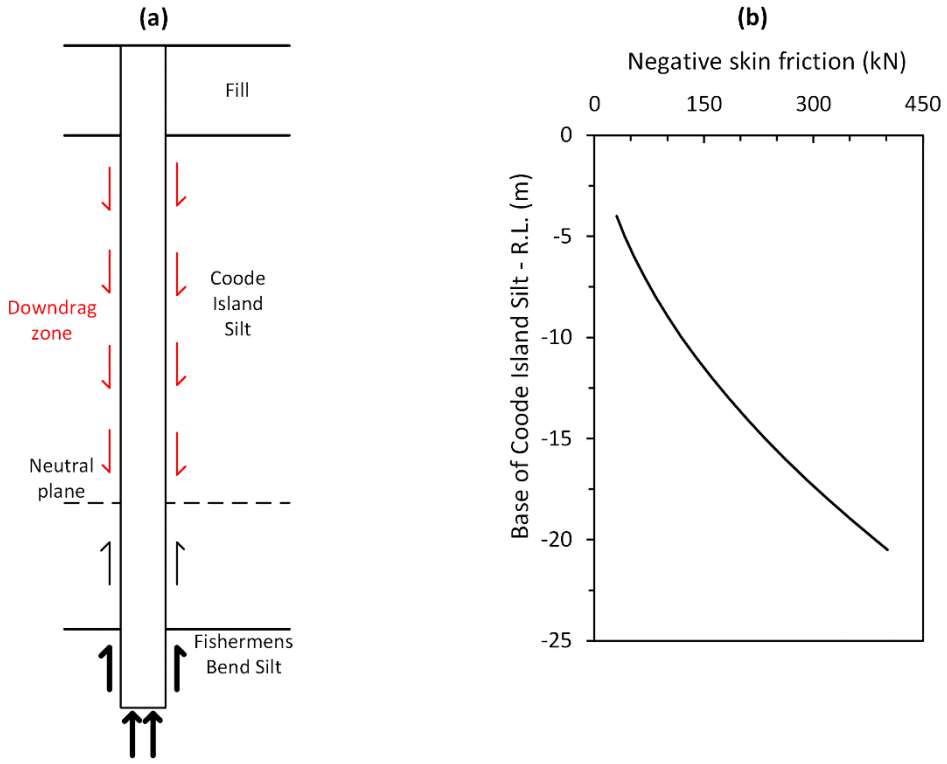

Figure E1. (a) Forces acting on typical a column (serviceability limit state) and **(b)** negative skin friction based on method of Poulos (2008)

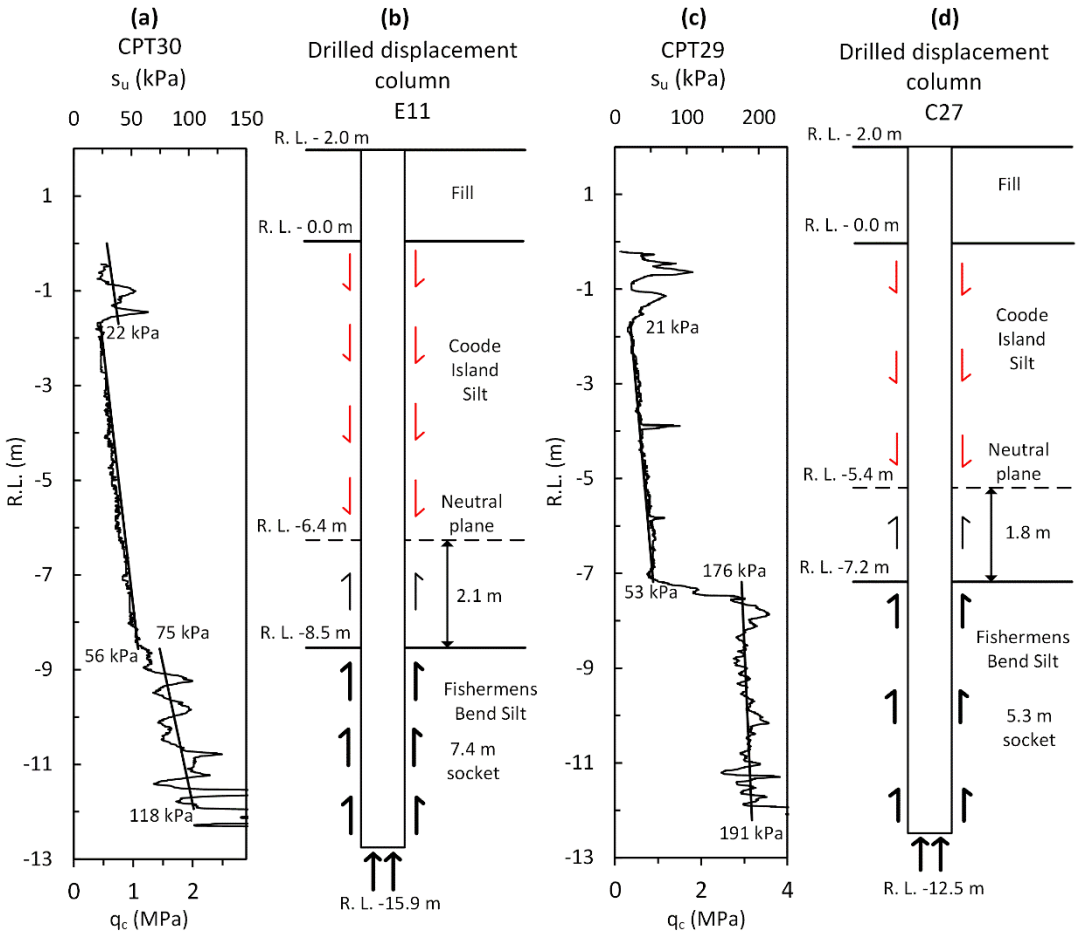

Figure E2. (a) CPT30 **(b)** Column E11 and interpreted (serviceability) pile loading **(c)** CPT29 **(d)** Column C27 and interpreted (serviceability) pile loading

is resisted by the columns shaft below the neutral plane. This comprises the socket into the Fishermens Bend Silt as well as a length of socket in the lower portion of the Coode Island Silt.

C-α method

The ultimate capacity of a column can be calculated using the total stress "c-α" approach. The ultimate capacity of the pile (Q_{ult}) is the sum of ultimate base capacity (Q_{ub}) and ultimate shaft capacity (Q_{us}). This does not explicitly account for installation effects but this behaviour can be indirectly included using a modified adhesion factor (α).

$$Q_{ult} = Q_{us} + Q_{ub} \quad \textbf{(E2)}$$

For a pile founded in clay, Q_{ult} can be expressed as follows:

$$Q_{ult} = A_s \alpha c_s + A_b c_b N_c \quad \textbf{(E3)}$$

where: A_s = area of pile shaft (m^2) = 1.41 m^2/m length for 450 mm diameter column
s_{us} = Undrained shear strength - shaft
A_b = area of pile base (m^2) = 0.16 m^2
s_{ub} = Undrained shear strength - base
N_c = bearing capacity factor = 9
c_b, c_s = cohesion at base, (average) cohesion on shaft

Cherubini et al. (2007) described a number of different methods to assess pile capacity using the total stress approach (c-α approach). Various adhesion factors summarised by Sladen (1992) (Figure E3) were presented as was a similar correlation for driven piles from Coduto (1994) (Figure E4). The trendline described by Coduto (1994) is adopted here and the calculated serviceability and ultimate state column capacities are presented in Table E1.

Table E1. Calculated column capacities (c-α method)

		Shaft capacity (kN)		Base (kN)	Total (kN)
		Coode Island Silt	Fishermens Bend Silt		
E11	Serviceability	85	551	273	909
	Ultimate	337		262	1162
C27	Serviceability	85		273	909
	Ultimate	405			1230

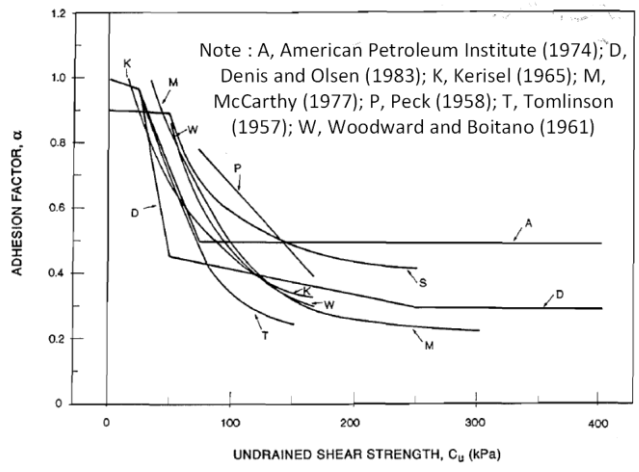

Figure E3. Adhesion factors recommended by various authors (from Sladen 1992)

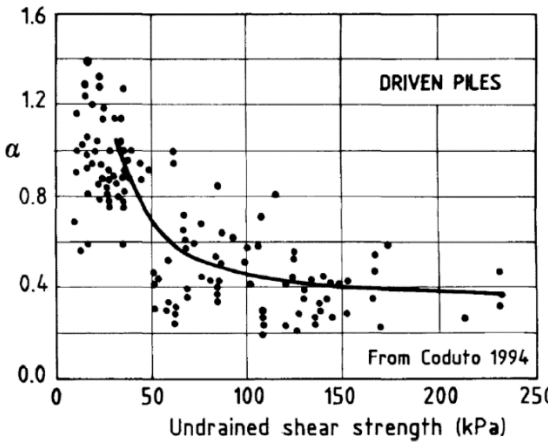

Figure E4. Adhesion factors for driven piles from Coduto (1994)

Method of Bustamante and Gianeselli (1993,1998

The method of Bustamante and Gianeselli (1993,1998) was developed based on the analysis of 24 Atlas piles which were performed in France and Belgium between 1984 and 1988. The method describes the pile capacity for cast-in-place screw piles (Atlas pile) and cased screw piles (Fundex pile). Larisch (2014) reported the successful use of this method for full displacement auger piles by treating these as cast-in-place screw piles for the purpose of this design method. This approach is also adopted here. This method calculates Q_{ub} as follows:

$$Q_b = K\alpha \quad \textbf{(E4)}$$

Where K is taken from Table E2 and the parameter α is an average of *in situ* test results (SPT, CPT or pressuremeter) in the influence zone.

Based on the soil behaviour type for CPT30 and CPT29 (Appendix B), a K value of 0.65 is adopted for both profiles. For the CPT data used here, the influence zone extends a distance a above and below the column base where a is defined as $1.5D$. A four-step procedure is used to calculate a modified q_c profile (q_{ce}) in the influence zone:

(1) the q_c profile is first smoothed to remove irregularities
(2) an arithmetic mean q_{ca} is calculated in the influence zone
(3) a q_{ce} profile is obtained by clipping the q_c profile at minimum ($0.7q_{ca}$) and maximum ($1.3q_{ca}$) values
(4) the α value is the arithmetic mean q_{ce} value calculated from the q_{ce} profile developed in the preceding step

The q_c values used by Bustamante and Gianeselli (1993,1998) to develop the method were based on a mechanical CPT cone (M1 type). Where an electric CPT cone is used, as is the case here, the following correction is applied:

$$q_{c,\text{mechanical}} = \beta q_{c,\text{electrical}} \quad \textbf{(E5)}$$

where β is 1.4 – 1.7 for clayey soils and 1.3 for saturated sands (Bustamante and Gianeselli, 1993). A value of 1.55 is adopted for the Coode Island Silt and 1.4 for the Fishermens Bend Silt here based on the interpreted soil behaviour types described in Appendix B.

An example of the CPT procedure applied to the bottom 1.5 m of the CPT30 q_c profile is shown in Figure E5. Calculated values of $q_{c\ \text{average}}$ and $q_{ce\ \text{average}}$ are 6.94 MPa and 6.83 MPa respectively. For CPT29 these values were 4.36 MPa and 4.30 MPa. This CPT procedure appears to be most beneficial in interbedded deposits that show large variability in q_c, however for homogeneous deposits, particularly clay deposits this procedure has minimal influence on the average q_c value as seen from the results for CPT29 q_c profile. The unit shaft q_{us} is calculated from the design curves (Q1, Q2, Q3, Q4, Q5) in Figure E6. Table E3 is used to identify the design curve based on the soil type, this has been assessed in 0.5 m increments along the column shaft. The calculated column capacities are shown in Table E4.

Others

The U.S. Department of Transport – Federal Highway Administration developed a state-of-the-art design manual for the design and construction of CFA piles – Geotechnical Engineering Circular No. 8 (Brown et al. 2007). This manual also includes recommendations on the design of auger-cast-in-place piles, drilled displacement piles and screw piles. Based on the study of 22 full-scale compression load tests and six full-scale pull out tests of drilled displacement piles (NeSmith 2002), methods for assessing the axial capacity of drilled displacement piles based on

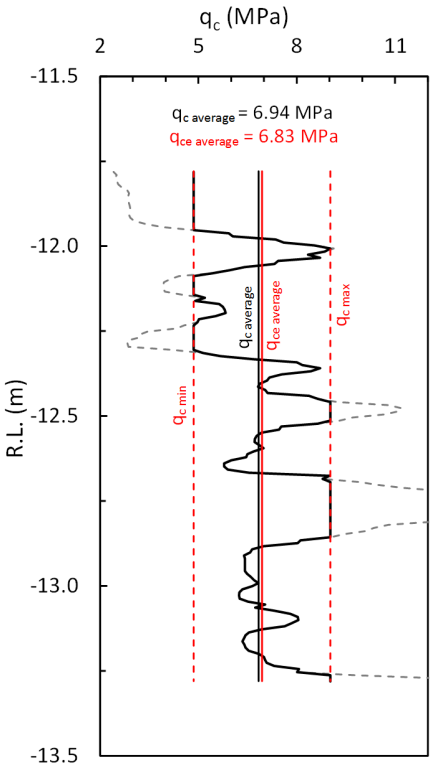

Figure E5. Calculation of modified q_c profile for CPT30 (E11)

Tble E2. *K* values for various soil types (Bustamante and Gianeselli, 1998)

Soil type	*In situ* tests		
	Pressuremeter	CPT	SPT
Clay	1.6 – 1.8	0.55 – 0.65	0.9 – 1.2
Sand	3.6 – 4.2	0.50 – 0.75	1.8 – 2.1
Gravel	≥ 3.6	≥ 0.5	-
Marl	2.0 – 2.6	≥ 0.7	≥ 1.2
Chalk	≥ 2.6	≥ 0.6	≥ 2.6

Table E3. Selection of design curve for Figure E6 (Bustamante and Gianeselli, 1998)

Soil type	Limit pressure from pressuremeter (MPa)	CPT q_c (MPa)	Curves	
			C	M
Clay / Clayey Silt / Sandy Clay	<0.3	< 1.0	Q1	Q1
	>0.5	>1.5	Q3	Q2
	≥1.0	≥3.0	Q4	Q2
Sand / Gravel	<0.3	< 1.0	Q1	Q1
	>0.5	>3.5	Q4	Q2
	≥1.2	>8.0	Q5	Q2
Marl	<1.2	< 4.0	Q4	Q2
	≥1.5	≥5.0	Q5	Q2
Chalk	>0.5	< 1.5	Q4	Q2
	≥1.2	>4.5	Q5	Q2

Table E4. Pile capacities – Method of Bustamante and Gianeselli (1993,1998)

		Shaft capacity (kN)		Base (kN)	Total (kN)
		Coode Island Silt	Fishermens Bend Silt		
E11	Serviceability	50	965	502	1517
	Ultimate	219			1686
C27	Serviceability	21	723	445	1189
	Ultimate	171			1339

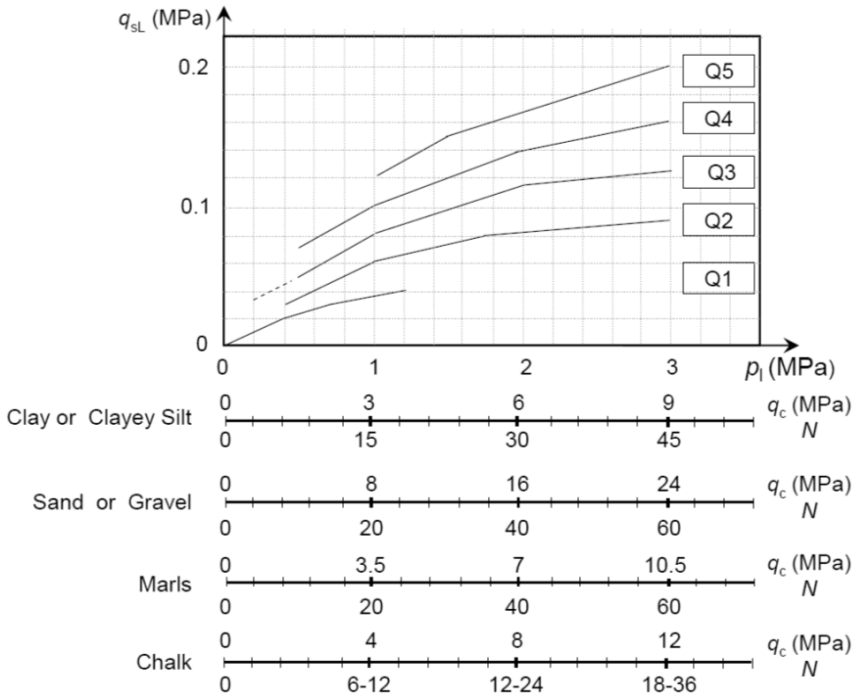

Figure E6. Unit shaft resistance q_{us} (Bustamante and Gianeselli, 1998)

SPT N-values and CPT data are presented. However, these recommendations "*should only be applied to cohesionless soils in which displacement of the spoils into the borehole wall during construction will result in densification of the surrounding soil.*" For this reason the methods suggested by NeSmith (2002) are not pursued here. Despite this, the general design and construction advice relating to drilled displacement piles (columns) by Brown et al. (2007), is in the author's opinion, the most comprehensive source of information on this topic (see also Brown and Drew 2000 and Brown 2005).

A considerable amount of research into drilled displacement piles has been undertaken at Purdue University (see, (Prezzi et al. 2005, Basu et al. 2009, Basu et al. 2013). The "Design and Application of Drilled Displacement (Screw) Piles" (Basu et al. 2009) describes three methods to assess the axial capacity: (1) The method of Bustamante and Gianeselli (1993,1998) , outlined above, (2) the method of NeSmith (2002) and Brettmann et al. (2005) also described above and (3) the "Belgium pile design practice" which is not discussed here. The design method of Basu et al. (2009) also provides a good overview of the numerous proprietary drilling tools used to construct drilled displacement pile (Atlas, De Waal, Fundex pile types etc.).

E3. Dynamic test results

As part of the ground improvement works, testing of trial columns was recommended in order to calibrate the piling rig instrumentation and to ensure rig instrumentation was sensitive enough to detect the Fishermens Bend Silt (founding unit). The pre-production testing involved the installation of columns as close as practical to CPT and borehole test locations. Columns C27 (near CPT29) and E11 (near CPT30) were nominated and subjected to Pile Integrity Testing (PIT) and dynamic load testing, comprising a Case Pile Wave Analysis Program (CAPWAP) and Pile Driving Analyser (PDA) analysis.

Dynamic loading to 100 % of the working load was proposed with this capacity to be fully mobilised in the column socket at not more than 50 mm settlement (i.e., ignoring shaft contributions from fill and Coode Island Silt).

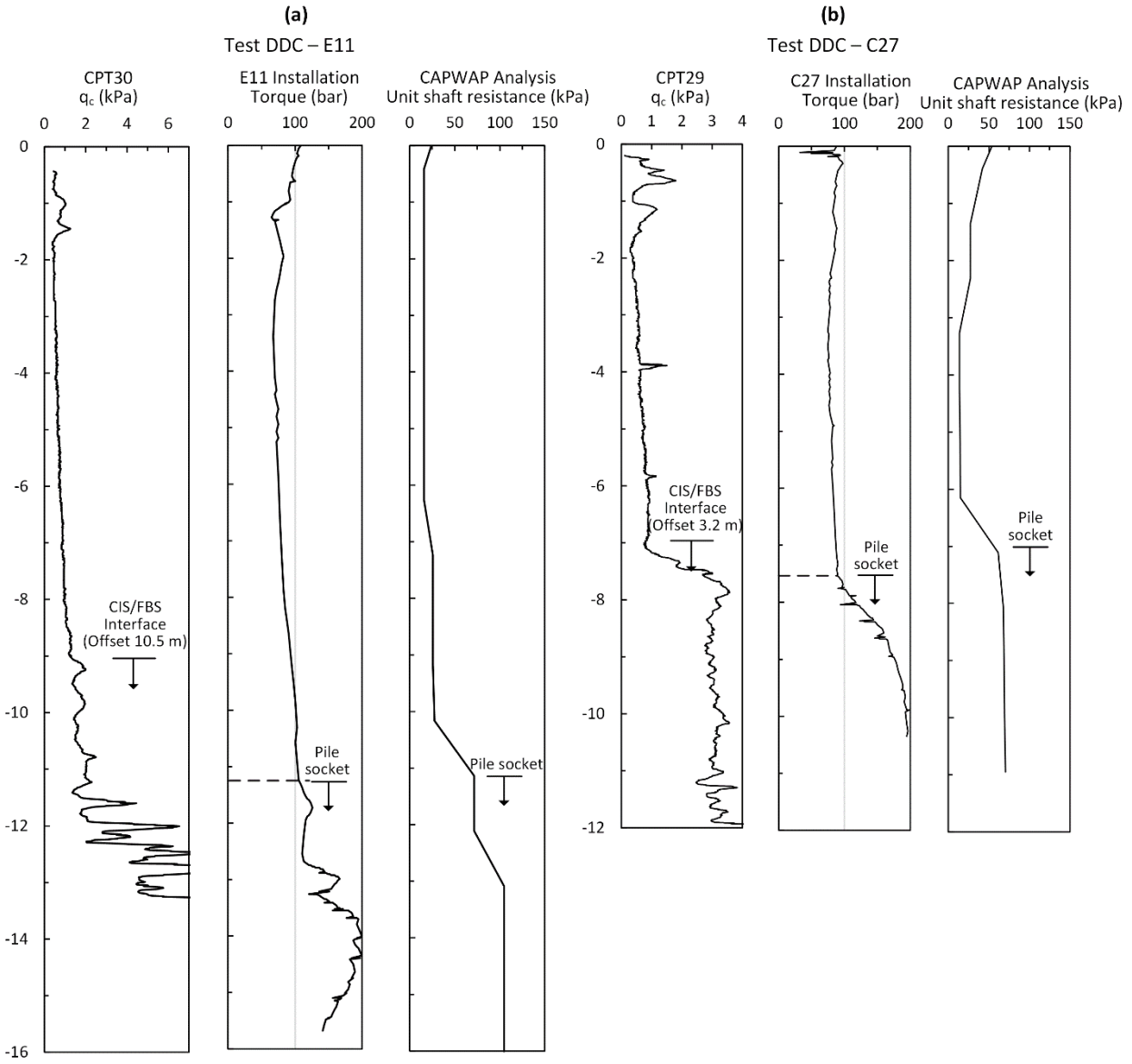

Figure E7. CPT q_t, torque and CAPWAP unit shaft resistance profiles for; **(a)** Test column E11 and **(b)** Test column C27

The results of the two test columns, E11 and C27, are shown in Figure E7*a* and *b*, respectively along with the adjacent CPT q_t profile and drilled rig torque profile. The interpreted Coode Island Silt/Fishermens Bend Silt interface (top of socket) is shown based on assessment of the three types of available data; CPT, installation records and CAPWAP data. In Figure E8 the CAPWAP *p-s* curves are shown along with Davisson's criteria (Equation E6) for assessing ultimate load. Where *P* is applied load and *D* diameter, *L* length, A cross sectional area and *E* Young's modulus are column parameters. In the case of C27 approximately twice the working load is mobilised in base capacity alone at 12 mm deflection with approximately 1600 kN mobilised at 10 mm deflection in a 2.9 m length socket into the Fishermens Bend Silt.

$$S\,(\text{mm}) = 3.81 + \frac{D}{120} + \left(\frac{PL}{AE}\right) \qquad \textbf{(E6)}$$

E4. Inclinometer derived bending moment profiles

As instruments to measure bending moments directly are not currently available it is common to calculate the bending moment indirectly from curvature and material properties as follows:

$$M = \psi EI \qquad \textbf{(E7)}$$

Where M, ψ, E and I are the bending moment, curvature, modulus of elasticity and second moment of inertia of the column respectively. A zero tensile strain condition occurs where the tensile stress induced in the column due to flexure is less than, or equal to, the axial (compressive) stress as shown in Figure E9. To provide an indication of the range of allowable lateral displacement under the zero tensile strain condition, profiles of (idealised) lateral displacement are shown in Figure E10 for cases where applied stresses of 75 kPa (σ_N = 472 kPa) and 150 kPa (σ_N = 943 kPa) are acting on the 1 m by 1 m square column head and where σ_N is the stress acting in the 450 mm diameter column shaft. These two cases approximate the stress acting on the column head under conditions on no arching (i.e., overburden pressure) and maximum arching respectively. The idealised lateral displacement profiles assume a fixed base, pinned rotational condition at the head and uniform curvature along the shaft. As a result, the bending moment is uniform along the length of the column. For the case of maximum arching, the maximum lateral displacement satisfying a zero tensile strain condition is 18 mm at the column head. If tensile strain is permitted, the

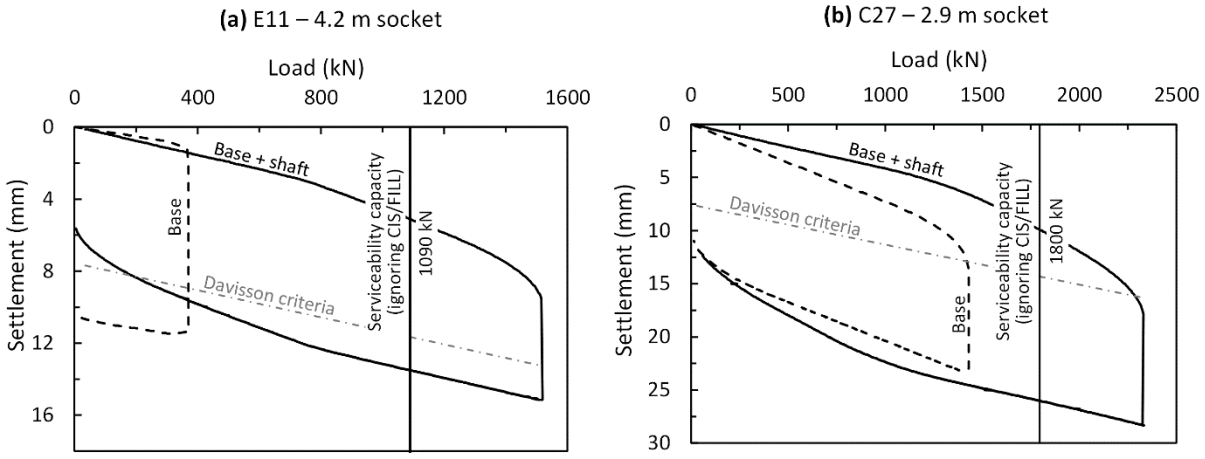

Figure E8. CAPWAP P-S curves for columns; **(a)** E11 (4.2 m shaft based on torque profile) and **(b)** C27 (2.9 m shaft based on torque profile)

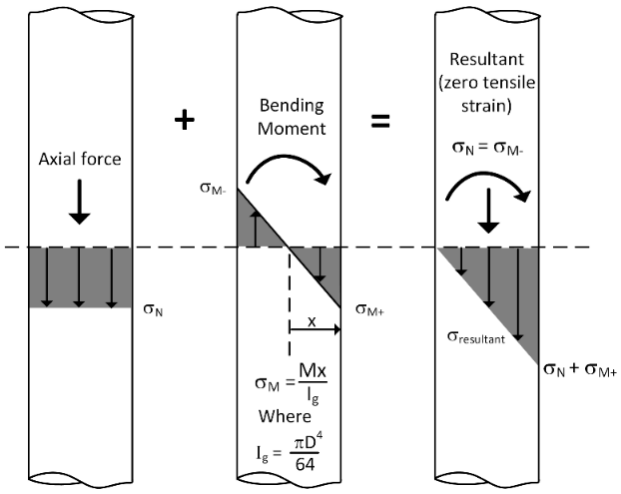

Figure E9. Calculation of applied loading on columns

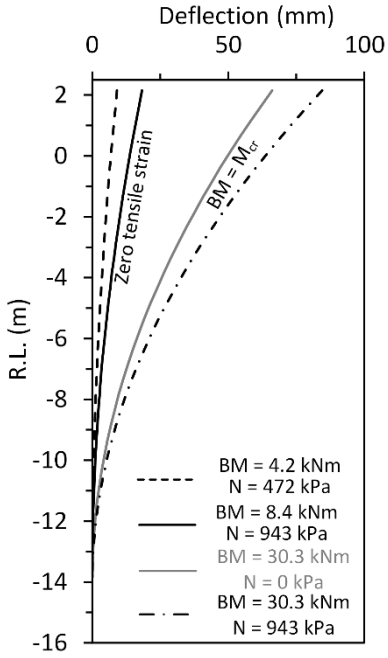

Figure E10. Idealised lateral displacement profiles for zero tensile strain condition and bending moment = M_{cr} condition

columns can be displaced 85 mm laterally at the column head under maximum arching before cracking occurs. Under this condition the bending moment is equal to the cracking moment (M_{cr}) calculated from Equation E8. Where f_r is the flexural tensile strength of concrete (modulus of rupture), I_g the gross second moment of inertia and y_t the distance from the centroid to the extreme fibre.

$$M_{cr} = \frac{f_r I_g}{y_t} \qquad \textbf{(E8)}$$

In addition, a zero applied load condition is considered. This is similar to the conditions that exist during ground improvement works where a column is displaced by an adjacent column (contribution of column self weight is minimal and ignored).

In Figure 9.4 the long term transverse movement (day 161 to 741) of the inclinometer was considered. It is assumed that the lateral displacement profile of the column C15 is approximated by Inclinometer #2; the general agreement between the embedded tiltmeters and Inclinometer #2 has been described previously and the correlation was very good. Furthermore, lateral soil arching can be expected to lead to increased lateral load attraction, due to columns being stiffer than the surround soft soil. This makes the columns more likely to more with the soft soil. In Figure E10 idealised lateral displacement profiles were shown; the behaviour is similar to that which may be expected if lateral sliding is considered in isolation. However, the long term behaviour is more complex due to the combined effect of lateral sliding and equilibration (radial consolidation). As a result, the lateral displacement profile (Figure E11*a*) and the internal bending moments in the column are also more complex.

For inclinometer derived lateral displacement profiles, curvature can be calculated using Equation E9 however, typically d*z*/d*w* is assumed to be very close to zero and the approximate expression (Equation E10) is adopted. Using this approach the curvature can be calculated quite simply and directly from a lateral displacement profile, however, this typically leads to quite erratic results (Figure E11*b*). To more accurately calculate the bending moment profile curve fitting techniques applied to the displacement profile are required.

$$\psi = \frac{\frac{\mathrm{d}^2 w}{\mathrm{d}z^2}}{\left[1 + \left(\frac{\mathrm{d}w}{\mathrm{d}z}\right)^2\right]^{3/2}} \quad \textbf{(E9)}$$

$$\psi \sim \frac{\mathrm{d}^2 w}{\mathrm{d}z^2} \quad \textbf{(E10)}$$

In Figure E11*a* the lateral displacement is globally fitted with a higher (6th) order polynomial and an excellent fit is obtained (R^2 = 0.986). In Figure E11*b* the bending moment profile is shown based on the higher order polynomial as well as the bending moment profile calculated directly from the inclinometer data with the latter case showing a highly erratic result. The various sources of error in the inclinometer measurement which leads these erratic results are summarised by Ooi et al. (2003); it is the variability in the back-calculated bending moment profile which necessitates the use of curve fitting methods. Ooi et al. (2003) presented a comprehensive comparison of 12 curve fitting methods applied to 60 sets of inclinometer data and concluded that a piecewise cubic curve fitting over a 5-point window generally resulted in the best estimate of back-calculated bending moment profiles. The piecewise cubic curve fitting approach fits a cubic polynomial $w = Az^3 + Bz^2 + Cz + D$ over a moving window of data points, in Figure E11 the 5-point data window recommended by Ooi et al. (2003) is shown along with larger data windows (9 no., 11 no., and 13 no.). These piecewise cubic functions are fitted over a moving window of adjacent data points. in the bending moment profile at the top and bottom of the column, this is observed as a "kick" at the top and

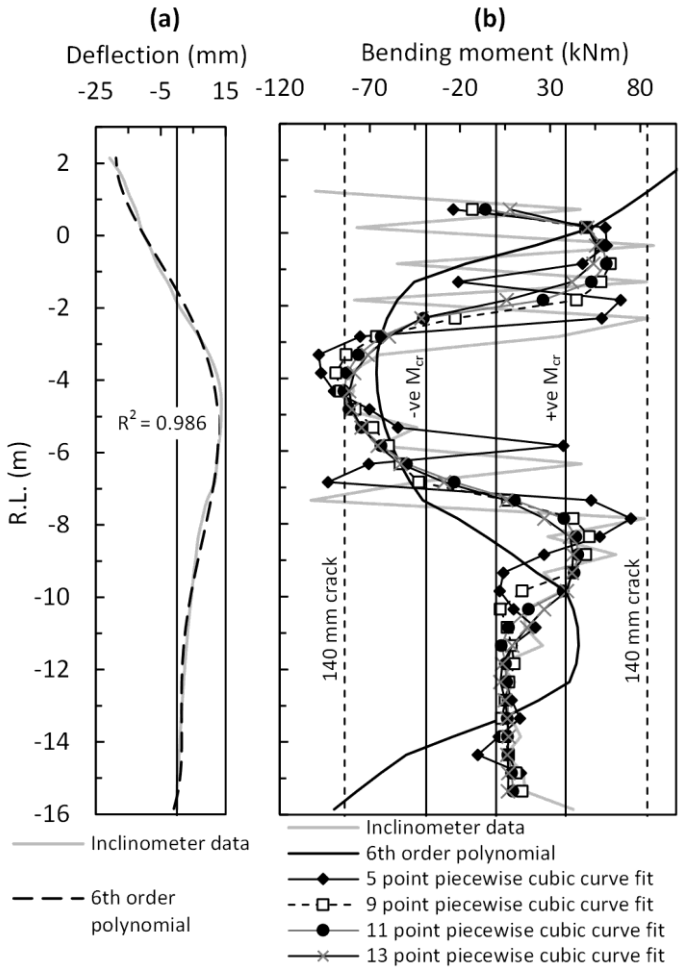

Figure E11. (a) Post-construction inclinometer profile and **(b)** Inferred bending moment acting on column C15

bottom of the fitted displacement profile and is a common source of error when using higher order polynomials (Ooi et al. 2003). Furthermore, the higher order polynomial does not appear to capture the localisation of larger BMs well. Similar behaviour was observed with 4th and 5th order polynomials and as recommended by Ooi et al. (2003) these are not used here. Where the bending moment exceeds M_{cr}, cracking of the column will occur and as result the cross sectional area is reduced. The effective moment of inertia I_e for a cracked section is calculated as follows (Branson 1977):

$$I_e = \left[\frac{M_{cr}}{M}\right]^3 I_g + \left[1 - \left(\frac{M_{cr}}{M}\right)^3\right] I_{cr} \leq I_g \qquad \textbf{(E12)}$$

Where I_{cr} is the second moment of inertia of a transformed cracked section. The bending moment profiles shown in Figure E11*b* is calculated based on the axial stress at on the column head of 150 kPa and approximates the stress acting on column C15 post-construction. The values of positive and negative M_{cr} are indicated in Figure E11*b* with a bending moment of 88 kNm occurring at R.L. −4 m. The depth of cracking is assessed to be 140 mm at this depth. It is important to note that flexural failure of unreinforced concrete is a brittle failure mechanism and that the use of Equation E7 and E12 is not strictly valid; the calculated crack depth should be considered as first order approximation only. The brittle failure mechanism of unreinforced concrete means that crack depths may be greater. The bending moment profile also exceeds M_{cr} in the lower and upper portion of the shaft.

However, despite the long term lateral sliding been approximately within the allowable limits which satisfy the zero tensile strain (Figure E10) i.e., about 20 mm, bending moments induced in the column are significantly larger than those predicted based on a lateral sliding mechanism alone. Furthermore, the embankment post-construction survey which is commonly employed in design scenarios validates only the lateral sliding behaviour and does little to reveal the additional loadings due to radial equilibration occurring below the ground surface. The additional lateral displacement induced in the columns due to the radial equilibration, which has acted long term in the opposite direction, has significantly increased the BMs and as a result increased the amount of cracking of the column shaft than would have otherwise been expected based on lateral sliding alone.